

Transition Metal Clusters Supported by
Multinucleating Ligand Frameworks as Models
of Biological Active Sites

Thesis by
Emily Yuan Tsui

In Partial Fulfillment of the Requirements for the
degree of
Doctor of Philosophy

CALIFORNIA INSTITUTE OF TECHNOLOGY
Pasadena, California
2014
(Defended February 18, 2014)

To hell with dignity! I'll leave when the job's done.

- M, *Skyfall* (2012)

ACKNOWLEDGMENTS

My time at Caltech over the past several years has been an experience that will stay with me for the rest of my life, primarily due to my interactions with a number of very special individuals. Although it is entirely inadequate to express my feelings for them in words, I will try, briefly, below:

Theodor Agapie, my advisor, is the root of it all. His excitement about all kinds of chemistry is what first drew me to Caltech and has been representative of most of my interactions with him and the other members of the chemistry department throughout my time here. Thank you, Theo, for always pushing me out of my intellectual comfort zone and for asking hard questions about the research in order to extend the limits of what we think we can accomplish. I really appreciate that, despite your constant eagerness for new chemistry and new results, you have always been patient with me when the going's been tough. I aspire to achieve your standards of excellence someday, at long last!

The members of my committee, Nate Lewis, Jim Heath, and Jonas Peters, have all been helpful in discussing research, propositions, and career plans. Many thanks to John Bercaw for allowing us all to run amok through your labs and for showing me how to use the Toepler pump. I would also like to thank Harry Gray and Jay Winkler for being willing to discuss my research and to provide new ideas. Bruce Brunschwig was a great help with the SQUID measurements.

Before I came to Caltech, I was fortunate to work with a number of scientists who have inspired me to continue my studies in chemistry. At college, I worked in the labs of Joseph Sadighi and Tim Swager, two fantastic mentors who have been great inspirations for me. David Laitar, my graduate student mentor, was very patient in teaching me lab techniques

and for showing me that it is possible (for some) to get through graduate school with an intact sense of humor.

In the Agapie group, I have been privileged to work with many creative and intelligent colleagues with unique personalities. I am grateful to have had the opportunity to learn from all of them. Jacob Kanady has been a close collaborator on the manganese projects for the past four years. I have learned a lot from him and from his intellectual curiosity and excitement, and I enjoyed our trip to Northern California together. Discussions with the other members of the metal oxide subgroup have been invaluable; Po-Heng Lin, Dave Herbert, Sandy Suseno, and Davide Lionetti were unflagging in their weekly presentations. I have learned a lot about molecular magnetism and relationships from Po-Heng; you owe me dinner in Taiwan! Dave was a hairy, but unharried baymate and boxmate; I enjoyed talking chemistry and getting advice from him over coffee. Sandy, thanks for being a great boxmate and for always providing solutions to everybody's problems. Davide, thank you for sharing a bay with me for several years and for being a fun drinking and hiking buddy. Josh Buss has been a patient hoodmate and boxmate over the past year and half and certainly has a bright future ahead of him; thank you for babysitting me during hiking trips and for teaching me many things that I never wanted to know. Guy Edouard was a fellow Box 2 worker for a period of time; thank you for putting up with me during that time and for your great stories. Justin Henthorn, thanks for killing zombies with me! Kyle Horak, never stop Horak styling. Josh Wiensch, thank you for being a great fitness coach over the summer. Best of luck to the new group members, Heui Beom Lee, Marcus Low, Jessica Sampson, and Graham de Ruiter.

In particular, I would like to thank Paul Kelley, Sibbo Lin, and Madalyn Radlauer, who were fellow members of the first class of students in the Agapie group and have been there for the past five and half years. It was exciting to set up the lab with you all and we made it through all the growing pains with each other's support. Paul, you are a synthetic inspiration; I wish I had half of your ligand synthesis abilities. Thanks also for going to Taco Bell with me – other people have no taste! Maddy, thank you for always being positive and upbeat. I have been very impressed with your dedication and organization. You are one of the most effective people I know. Sibbo, thank you for always being around during the late night shift and for being perhaps the strangest person I have ever met. You've always been there to provide a unique perspective (when you're awake).

The undergraduates have been an important part of the lab environment. Alexandra Velian was the very first Agapie group member and provided a cheerful presence when we were first setting up the labs. Best of luck to Eva Nichols and Jade Shi in their graduate school careers; I learned a lot from them. Special thanks to Christine Cheng, who worked with me for two summers and has a truly incredible tolerance both for my nonsense and for ethanol (and mercury poisoning?).

I have been lucky to be able to discuss science with many other students and postdoctoral associates at Caltech. When we first started, the Bercaw group members, particularly Alex Miller, Steve Baldwin, and Nilay Hazari were always willing to help and teach me what I needed to know. Charles McCrory has been an invaluable source of information about electrochemical techniques. Kyle Lancaster had many ideas about paramagnetic NMR studies and copper EPR studies, and performed XAS measurements on

the tricopper complexes before we could get single crystals that diffracted. Wes Sattler was a great help with stopped-flow measurements.

Many thanks to the staff at Caltech who make the department what it is. In particular, Larry Henling, thank you for spending many hours in the X-ray facility helping me mount my terrible crystals. I have learned a lot from you. Dave VanderVelde, thank you for helping me with NMR experiments.

Finally, I would like to thank my family. My parents and my brother, Daniel, provided unfailing love and support and listened to my many complaints over the years. Any successes that I may have experienced I owe to them (though I will take credit for the far more numerous failures!).

PREFACE

Parts of this thesis have been adapted from articles co-written by the author.

The following articles were reproduced in part with permission from the American Chemical Society:

“Oxygen Atom Transfer and Oxidative Water Incorporation in Cuboidal Mn_3MO_n Complexes Based on Synthetic, Isotopic Labeling, and Computational Studies” Jacob S. Kanady, Jose L. Mendoza-Cortes, Emily Y. Tsui, Robert J. Nielsen, William A. Goddard III, and Theodor Agapie. *J. Am. Chem. Soc.* **2013**, *135*, 1073-1082.

“Synthetic Cluster Models of Biological and Heterogeneous Manganese Catalysts for O_2 Evolution” Emily Y. Tsui, Jacob S. Kanady, and Theodor Agapie. *Inorg. Chem.* **2013**, *52*, 13833-13848.

The following article was reproduced in part with permission from Wiley-VCH:

“Trinucleating Copper: Synthesis and Magnetostructural Characterization of Complexes Supported by a Hexapyridyl 1,3,5-Triarylbenzene Ligand” Emily Y. Tsui, Michael W. Day, and Theodor Agapie. *Angew. Chem. Int. Ed.* **2011**, *50*, 1668-1672.

The following article was reproduced in part with permission from The Royal Society of Chemistry:

“Trinuclear First Row Transition Metal Complexes of a Hexapyridyl, Trialkoxy 1,3,5-Triarylbenzene Ligand” Emily Y. Tsui, Jacob S. Kanady, Michael W. Day, and Theodor Agapie. *Chem. Commun.* **2011**, *47*, 4189-4191.

The following article was reproduced in part with permission from the American Association for the Advancement of Science:

“A Synthetic Model of the Mn_3Ca Subsite of the Oxygen-Evolving Complex in Photosystem II” Jacob S. Kanady, Emily Y. Tsui, Michael W. Day, and Theodor Agapie. *Science* **2011**, 333, 733-736.

The following article was reproduced in part with permission from Nature Publishing Group:

“Redox-Inactive Metals Modulate the Reduction Potential in Heterometallic Manganese-Oxido Clusters” Emily Y. Tsui, Rosalie Tran, Junko Yano, and Theodor Agapie. *Nat. Chem.* **2013**, 5, 293-299.

The following article was reproduced in part with permission from the National Academy of Sciences of the United States of America:

“Reduction Potentials of Heterometallic Manganese-Oxido Cubane Complexes Modulated by Redox-Inactive Metals” Emily Y. Tsui and Theodor Agapie. *Proc. Natl. Acad. Sci. USA* **2013**, 110, 10084-10088.

RESPECTIVE CONTRIBUTIONS

Much of the work described in this thesis is the result of collaborative efforts. Specific notes are included for compounds not synthesized by the author; some general comments are given here.

Many of the studies of multimetallic clusters were carried out in close collaboration with Mr. Jacob S. Kanady. He synthesized and characterized the trimanganese(II) triacetate complex that served as a precursor to most of the heterometallic manganese oxido clusters, as well as the structurally related tricobalt(II) triacetate and trinickel(II) triacetate complexes for which magnetic susceptibility data are presented in Chapter 2. Mr. Kanady was the first to isolate and characterize structurally and with NMR spectroscopy the $[\text{CaMn}_3\text{O}_4]$ cubane cluster **6**-Ca discussed in Chapter 4 as well as the $\{[\text{Mn}_3\text{O}]_2\text{Ca}\}^{2+}$ cluster **3** discussed in Chapter 3. Additionally, the PMe_3 studies of the oxidized heterometallic cubane clusters (Chapter 5) were run in collaboration with Mr. Kanady.

In Chapter 3, the X-ray absorption spectroscopy studies were carried out by Drs. Rosalie Tran and Junko Yano. In Chapter 4, the magnetic susceptibility studies of the tetraoxido cubane clusters were carried out in collaboration with Dr. Po-Heng Lin, who performed the SQUID measurements. The late Dr. Michael Day solved many of the single crystal X-ray diffraction structures presented in Chapters 2 and 4, and in Appendix C.

ABSTRACT

This dissertation describes efforts to model biological active sites with small molecule clusters. The approach used took advantage of a multinucleating ligand to control the structure and nuclearity of the product complexes, allowing the study of many different homo- and heterometallic clusters. Chapter 2 describes the synthesis of the multinucleating hexapyridyl trialkoxy ligand used throughout this thesis and the synthesis of trinuclear first row transition metal complexes supported by this framework, with an emphasis on tricopper systems as models of biological multicopper oxidases. The magnetic susceptibility of these complexes were studied, and a linear relation was found between the Cu–O(alkoxide)–Cu angles and the antiferromagnetic coupling between copper centers. The triiron(II) and trizinc(II) complexes of the ligand were also isolated and structurally characterized.

Chapter 3 describes the synthesis of a series of heterometallic tetranuclear manganese dioxido complexes with various incorporated apical redox-inactive metal cations ($M = Na^+$, Ca^{2+} , Sr^{2+} , Zn^{2+} , Y^{3+}). Chapter 4 presents the synthesis of heterometallic trimanganese(IV) tetraoxido complexes structurally related to the $CaMn_3$ subsite of the oxygen-evolving complex (OEC) of Photosystem II. The reduction potentials of these complexes were studied, and it was found that each isostructural series displays a linear correlation between the reduction potentials and the Lewis acidities of the incorporated redox-inactive metals. The slopes of the plotted lines for both the dioxido and tetraoxido clusters are the same, suggesting a more general relationship between the electrochemical potentials of heterometallic manganese oxido clusters and their “spectator” cations. Additionally, these

studies suggest that Ca^{2+} plays a role in modulating the redox potential of the OEC for water oxidation.

Chapter 5 presents studies of the effects of the redox-inactive metals on the reactivities of the heterometallic manganese complexes discussed in Chapters 3 and 4. Oxygen atom transfer from the clusters to phosphines is studied; although the reactivity is kinetically controlled in the tetraoxido clusters, the dioxido clusters with more Lewis acidic metal ions (Y^{3+} vs. Ca^{2+}) appear to be more reactive. Investigations of hydrogen atom transfer and electron transfer rates are also discussed.

Appendix A describes the synthesis, and metallation reactions of a new dinucleating bis(*N*-heterocyclic carbene)ligand framework. Dicopper(I) and dicobalt(II) complexes of this ligand were prepared and structurally characterized. A dinickel(I) dichloride complex was synthesized, reduced, and found to activate carbon dioxide. Appendix B describes preliminary efforts to desymmetrize the manganese oxido clusters via functionalization of the basal multinucleating ligand used in the preceding sections of this dissertation. Finally, Appendix C presents some partially characterized side products and unexpected structures that were isolated throughout the course of these studies.

TABLE OF CONTENTS

| | |
|--|------|
| Acknowledgements | iv |
| Preface | viii |
| Respective Contributions | x |
| Abstract..... | xi |
| Table of Contents | xiii |
| Chapter 1: General Introduction..... | 1 |
| Structural and mechanistic studies of the OEC | 3 |
| Heterogeneous metal oxides as water oxidation catalysts..... | 6 |
| Synthetic manganese clusters..... | 6 |
| This work..... | 12 |
| Chapter 2: Synthesis, Structure, and Magnetic Susceptibilities of Trinuclear Transition Metal Clusters of a Hexapyridyl 1,3,5- Triarylbenzene Ligand Framework | 21 |
| Abstract..... | 22 |
| Introduction | 23 |
| Results and Discussion..... | 24 |
| Ligand synthesis and NMR studies | 24 |
| Synthesis and structure of tricopper complexes | 28 |
| Magnetic susceptibility and EPR studies of tricopper(II) complexes | 35 |
| Trinuclear complexes of other first row transition metals..... | 42 |
| Conclusions | 48 |
| Experimental Details | 49 |
| References | 73 |
| Chapter 3: Heterometallic Manganese Dioxido Complexes: Reduction Potential Modulation by Lewis Acidic Redox-Inactive Metals..... | 77 |
| Abstract..... | 78 |
| Introduction | 79 |
| Results and Discussion..... | 81 |
| Synthesis of $[\text{CaMn}_3\text{O}_2]$ clusters | 81 |
| Synthesis of $[\text{MMn}_3\text{O}_2]$ complexes | 86 |
| Magnetic susceptibility and X-ray absorption studies..... | 90 |
| Electrochemical studies of $[\text{MMn}_3\text{O}_2]$ complexes | 94 |
| Conclusions | 100 |
| Experimental Section | 100 |
| References | 123 |
| Chapter 4: Synthesis, Structure, and Electrochemical Studies of Heterometallic Manganese Tetraoxido Cubane Clusters | 127 |
| Abstract..... | 128 |
| Introduction | 129 |
| Results and Discussion..... | 131 |
| Synthesis of a $[\text{CaMn}_3\text{O}_4]$ cluster | 131 |
| Synthesis of $[\text{MMn}_3\text{O}_4]$ complexes | 135 |
| Chemical reductions of cubane complexes..... | 141 |

| | |
|---|-----|
| Magnetic susceptibility measurements | 143 |
| Electrochemical studies..... | 148 |
| Conclusions | 152 |
| Experimental Section | 152 |
| References | 162 |
| Chapter 5: Reactivity Studies of Heterometallic Manganese Oxido Clusters | 165 |
| Abstract..... | 166 |
| Introduction | 167 |
| Results and Discussion..... | 170 |
| Oxygen atom transfer reactions of [MMn ₃ O ₄] complexes..... | 170 |
| Phosphine reactivity of dioxido complexes..... | 176 |
| Hydrogen atom transfer to dioxido clusters..... | 180 |
| Electron transfer rates..... | 182 |
| Conclusions | 183 |
| Experimental Section | 184 |
| References | 190 |
| Appendix A: Bimetallic Complexes of a Dinucleating | |
| Bis(N-heterocyclic Carbene) Framework | 193 |
| Abstract..... | 194 |
| Introduction | 195 |
| Results and Discussion..... | 196 |
| Conclusions | 208 |
| Experimental Section | 209 |
| References | 220 |
| Appendix B: Synthesis and Preliminary Metallation Reactions of an | |
| Asymmetric Multinucleating Ligand Framework..... | 223 |
| Abstract..... | 224 |
| Introduction | 225 |
| Results and Discussion..... | 226 |
| Ligand design and synthesis | 226 |
| Metallation of monooxime ligand..... | 228 |
| Conclusions | 231 |
| Experimental Section | 232 |
| References | 237 |
| Appendix C: Side Products and Other Structures..... | 239 |
| Introduction | 240 |
| Results and Discussion..... | 240 |
| Trinuclear complexes | 240 |
| Tetrametallic monooxo complexes..... | 246 |
| Complexes derived from dioxido clusters | 249 |
| Products derived from tetraoxido cubane clusters..... | 254 |
| Conclusions | 259 |
| Experimental Section | 260 |
| References | 265 |
| Appendix D: NMR Spectra..... | 267 |

Chapter 1

GENERAL INTRODUCTION

The text for this chapter was reproduced in part from:

Tsui, E. Y.; Kanady, J. S.; Agapie, T. *Inorg. Chem.* **2013**, 52, 13833-13848.

Introduction

Photosynthesis, the sunlight-powered process by which plants, algae, and cyanobacteria convert carbon dioxide and water into carbohydrates and O_2 , is responsible for the dioxygen in Earth's atmosphere.¹ Light-driven water oxidation occurs at photosystem II (PSII), a membrane protein assembly that absorbs four photons to sequentially oxidize a $CaMn_4O_5$ cluster, known as the water oxidizing complex (WOC) or the oxygen-evolving complex (OEC), through a sequence of S_n states called the Kok cycle.² At the most oxidized state, S_4 , dioxygen is released. Water acts as the source of the electrons that are transferred through a series of cofactors and stored as NADPH.¹ The reducing equivalents and proton gradient generated by photochemical water oxidation power carbon dioxide fixation and other processes of life. Overall, solar energy is converted and stored as chemical bonds. Many efforts have been devoted to structural, spectroscopic, and biochemical studies of the OEC because understanding how plants form oxygen from water will have implications for designing artificial catalysts for solar fuels. Heterogeneous metal oxide water oxidation catalysts have been proposed to perform their function at discrete multimetallic sites reminiscent of the OEC.³ Artificial water oxidation catalysts have been prepared from Ca-doped manganese oxide materials to mimic the composition of the OEC, despite the limited structural understanding.^{3c, 4} Other mixed metal oxides have intriguing catalytic properties, both for water oxidation and oxygen reduction.⁵ Metal oxides are also important as battery materials.⁶ Access to and study of well-defined metal oxide clusters structurally analogous to the active sites of these catalysts are expected to provide insight into the interactions between different types of metals and their effect on the properties of the cluster and the catalytic material.

1.1 Structural and mechanistic studies of the OEC

X-ray absorption spectroscopy (XAS)⁷ and electron paramagnetic resonance (EPR)⁸ methods have been employed to identify oxidation state, electronic structure, and coordination environment changes during the S-state progression. Recent single crystal X-ray diffraction (XRD) studies have shown that the OEC consists of a CaMn_3O_4 cubane cluster with the fourth “dangler manganese” center bridged via oxide moieties (Figure 1).⁹ Subsequent computational studies, however, have suggested that this structure corresponds to a more reduced manganese cluster due to X-ray damage,¹⁰ consistent with previous studies on X-ray-induced reduction,¹¹ or to an equilibrium of multiple structural forms at similar energies.¹² More open cubane structures of the S_2 state have been proposed by calculations that are consistent with OEC geometries advanced from EPR and XAS studies (Figure 2).^{7e, 8c, 12b, 13}

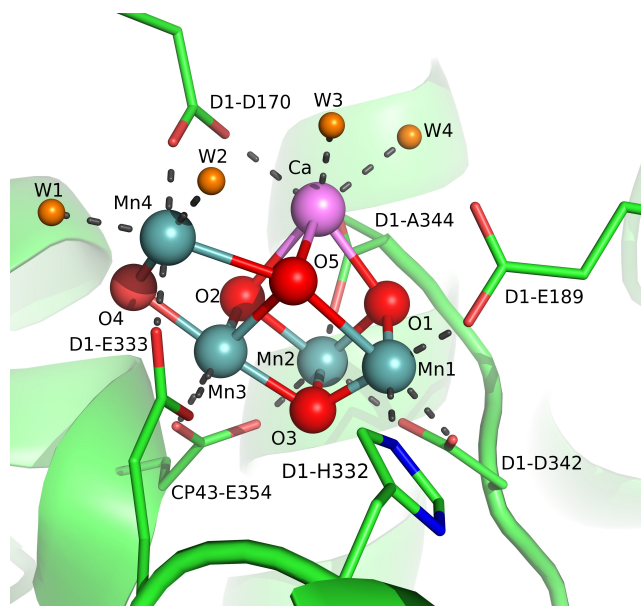


Figure 1. Structure of OEC from single crystal X-ray diffraction studies.^{9b}

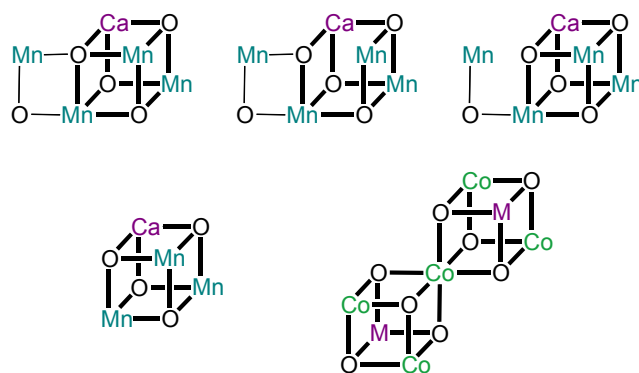


Figure 2. Proposed structure of the OEC from single crystal XRD studies (top left)⁹ and more open structures proposed from XAS and computational studies (top middle, right).¹² Proposed structure of catalytic sites in calcium manganese oxide water oxidation catalysts (bottom left)^{3c, 3d} and of cobalt oxide water oxidation catalysts (bottom right).^{3a}

Due to these uncertainties in the structural details of the S states of the OEC, the mechanism of O–O bond formation during water oxidation remains controversial. Isotopic labeling studies using mass spectrometry and magnetic resonance techniques have been used to analyze substrate water exchange rates with bulk water within the OEC.¹⁴ Based on these studies and spectroscopic data, several mechanisms for O–O bond formation have been proposed. These proposals differ in the nature and location of the substrate oxo moieties that undergo O–O bond formation to generate O₂. Early proposals, such as the manganese-only adamantane and the double-pivot mechanisms, proved incorrect based on structural grounds.¹⁵ Heterolytic pathways involve a water or hydroxide ligand bound to Ca²⁺ attacking a Mn(V) oxo or Mn(IV) oxyl.¹⁶ Other mechanisms have suggested that a terminal oxyl reacts with a bridging oxido moiety via a radical mechanism (Figure 3).^{13a, 17} Distinguishing the different mechanisms through computational and experimental studies remains a challenge.

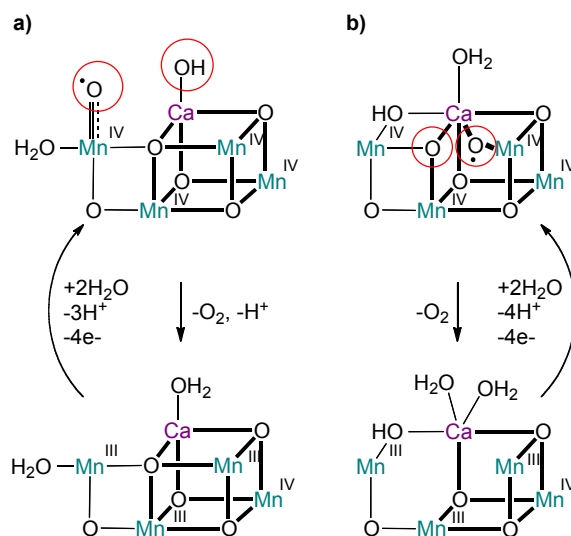


Figure 3. Recent proposed mechanisms of O–O bond formation in the OEC,^{16a, 18} with sites of substrate incorporation highlighted in red.

The role of calcium, which is known to be necessary for activity, is an unclear aspect of water oxidation at the OEC.¹⁹ In particular, the association of Ca²⁺, a redox-inactive metal, with an active site that performs a multielectron redox transformation is puzzling and departs from other roles of Ca²⁺ in biological systems. XAS and XRD studies have revealed that Ca²⁺ is bridged by oxido moieties to the manganese centers in the OEC, but does not function solely as a structural component. Substitution of other metal ions for Ca²⁺ leads to inhibition of catalysis, except for Sr²⁺, which recovers activity, albeit to a lower extent (ca. 40%).^{1c, 19a, 20} The Sr²⁺-substituted OEC shows subtle changes in geometry (XAS)²¹ and electronic structure (EPR)²² compared to the native CaMn₄O_x cluster. The ability of Sr²⁺ and Ca²⁺ to maintain catalysis has been explained in terms of their similar Lewis acidities in the context of binding and activating a water substrate.^{16a, 16c, 23} Size or charge effects were deemed secondary, as Cd²⁺, an ion with the same ionic radius as Ca²⁺, does not support water oxidation.^{1c, 23a} Others have proposed that Ca²⁺ affects proton

coupled electron transfer and the redox properties of the cluster, possibly via interactions through a H-bond network with the neighboring tyrosine residue or by affecting the protonation state of a coordinated water molecule.^{7c, 24} Despite detailed biochemical and spectroscopic studies, the role of calcium in the OEC remains under debate. Synthetic models to complement these investigations were extremely scarce and not structurally accurate, until recently.

1.2 Heterogeneous metal oxides as water oxidation catalysts

Heterogeneous manganese-containing materials have been studied for their water oxidation activities, and parallels have been drawn to the biological system. Although undoped manganese oxides have been demonstrated to catalyze water oxidation at low efficiencies, addition of calcium greatly increases the reaction efficiency, raising the possibility that the mechanism of dioxygen formation is related to that of the biological OEC.^{4a, 4d} XAS studies of these materials determined that the Mn centers are of the +3 and +4 oxidation state, and that the redox-inactive ions may be bridged to the Mn centers by oxido moieties in similar MMn_3O_4 cuboidal subsites as in the OEC.^{3c, 3d} These results suggest that further understanding of PSII may allow for the rational design of more efficient heterogeneous water oxidation catalysts. Beyond manganese water oxidation catalysts, the proposed catalytic site of cobalt oxide has been illustrated with redox-inactive cations at positions reminiscent of the Ca^{2+} position in the OEC (Figure 2),^{3a, 3b} (although alkaline metals were not detected by EXAFS).²⁵

1.3 Synthetic manganese clusters

Synthetic biomimetic complexes have been targeted to supplement the structural, spectroscopic, and mechanistic studies of biological systems while at the same time

exploring the possibilities of catalysis. Structural and functional modeling of the OEC has been challenging, in particular due to the propensity of the oxido moieties to bridge and generate oligomeric structures in uncontrolled fashion. Many mononuclear, dinuclear, trinuclear, and tetranuclear manganese complexes have been prepared as models and have been extensively reviewed in the literature.^{1b, 26} These high oxidation state manganese oxido complexes are often synthesized by spontaneous self-assembly by oxidation of manganese(II) salts; for these compounds, the choice of oxidant is crucial. Bridging oxides are known to stabilize higher oxidation state Mn centers, but also to significantly affect the geometry, Mn–Mn distance, and magnetic exchange of these compounds.^{26a} A second important aspect is the choice of ancillary ligands. These ligands, often polydentate O- or N-donors, are chosen to limit aggregation and to stabilize certain oxidation states. Manganese carboxylate chemistry especially has been heavily studied, due to the carboxylate-containing residues in the OEC binding site.^{26d} In the following section, selected examples of manganese oxide clusters will be discussed, with emphasis on tetramanganese complexes and heterometallic complexes as they are particularly relevant to the composition of the OEC.

Mixed-valent $\text{Mn}^{\text{III,IV}}_2$ bis(μ -oxo) dimers stabilized by polydentate N-donor ligands have been of particular interest in OEC biomimetic chemistry since they were first prepared and studied for their magnetic exchange coupling properties (Fig. 4, **A**).²⁷ Although these lower nuclearity complexes were clearly not structural mimics of the tetramanganese OEC cluster, they were heavily studied because of the Mn–Mn distance of 2.7 Å, which is similar to distances in the OEC measured by XAS studies,²⁸ as well as a multiline EPR signal that is similar to the multiline signal observed for the S_2 state of the OEC.^{27c, 29} From

a structural perspective, a dimer-of-dimers model was proposed for the S_2 state OEC based on these observations,^{7c, 30} and synthetic models were prepared (Fig. 4, **B**).³¹ The dimer-of-dimers model was later shown to be inconsistent with EPR spectroscopic measurements that support a 3+1 arrangement of the manganese centers.^{8c} From a functional aspect, Brudvig and co-workers have used a terpyridine-supported $Mn^{III,IV}_2$ bis(μ -oxo) complex for water oxidation using oxone or hypochlorite as the oxidant.³² Based on kinetic and isotope-labeling studies, a terminal $Mn^V O$ moiety was proposed as an intermediate for dioxygen formation.³³

One of the earliest high oxidation state tetramanganese oxido clusters, prepared by Christou and co-workers, was a $[Mn_4O_2]$ complex in which the Mn centers are in a “butterfly” arrangement (Fig. 4, **C**).³⁴ This structure was proposed to participate in the Kok cycle through a “double-pivot” mechanism to rearrange to more cubane-like structures.^{15b} Tetramanganese cubane structures had previously been proposed as intermediates in the water oxidation pathway of the OEC,^{15b, 15c} but were not synthetically accessed until Christou and coworkers isolated an acetate-bridged tetramanganese trioxido chloride cubane complex (Fig. 4, **D**).³⁵ A diarylphosphinate-supported tetraoxido $[Mn_4O_4]^{n+}$ cubane variant was later isolated by Dismukes and coworkers via the spontaneous assembly of mononuclear or dinuclear manganese precursors (Fig. 4, **E**).³⁶ These clusters are proposed to be stabilized by π -interactions between the aryl groups of the phosphinate ligands.^{36b} The diarylphosphinate stabilized system was also proposed to photoelectrochemically oxidize water to dioxygen when embedded in a Nafion film;³⁷ however, an amorphous manganese oxide material was later found to be the active catalyst.³⁸ Adamantane-type tetramanganese clusters have also been described (Fig. 4, **F**).³⁹

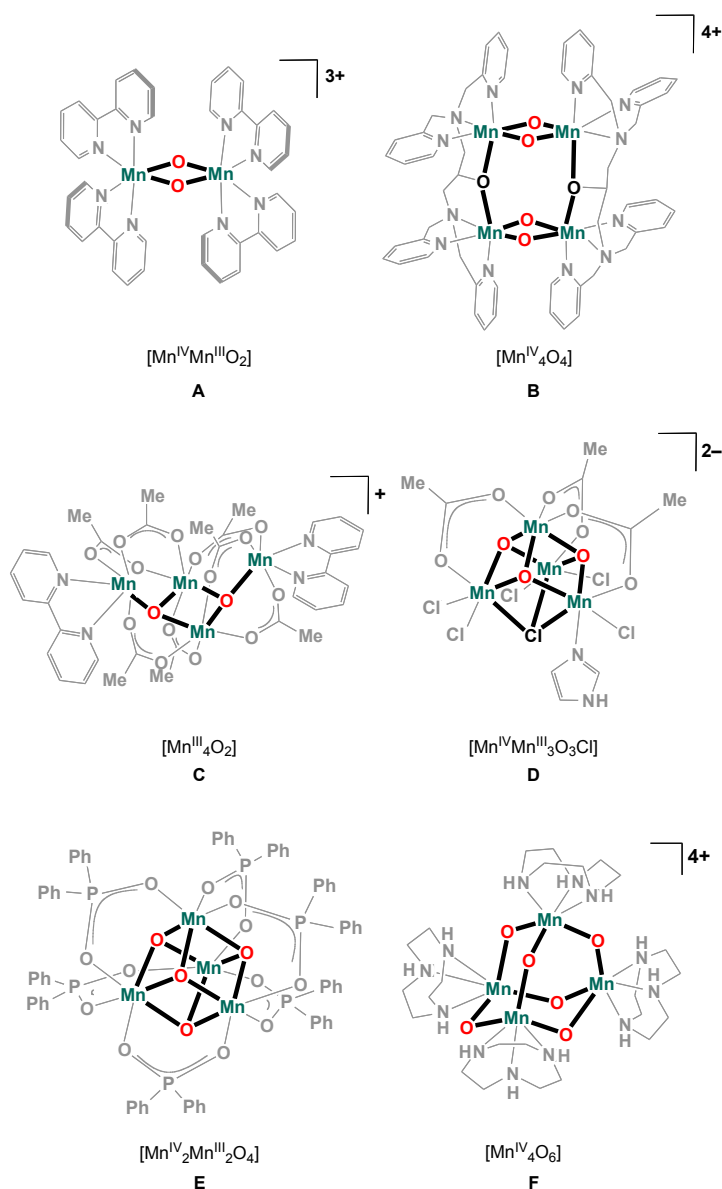


Figure 4. Selected examples of di- and tetramanganese oxido clusters.^{27a, 31a, 34b, 35-36, 39a}

One of the most important, but least explored, problems in preparing accurate structural models of the OEC has been the incorporation of calcium in the clusters. Heterometallic manganese clusters are relatively rare, and have been isolated as molecular species only in recent years.⁴⁰ The first high oxidation state manganese cluster with incorporated calcium, $[Mn_{13}Ca_2O_{10}(OH)_2(OMe)_2(O_2CPh)_{18}(H_2O)_4] \cdot 10MeCN$ (Fig. 5, **G**) was prepared by

Christou and coworkers from calcium salts such as $\text{Ca}(\text{NO}_3)_2 \cdot 4\text{H}_2\text{O}$, $\text{Ca}(\text{ClO}_4)_2$, or $\text{Ca}(\text{O}_2\text{CPh})_2$ and $(\text{NBu}_4)[\text{Mn}_4\text{O}_2(\text{O}_2\text{CPh})_9(\text{H}_2\text{O})]$.^{40a} Although this is a high nuclearity $[\text{Mn}_{13}\text{Ca}_2]$ cluster much larger than the $[\text{Mn}_4\text{Ca}]$ motif found in PSII, one portion resembled the OEC in that it had a CaMn_3O_4 cubane subunit with a fourth manganese center bridged to the cluster via an oxide moiety. A similar compound with Sr^{2+} rather than Ca^{2+} was also later isolated and studied.^{40b, 41} Powell and coworkers used a chelating Schiff base ligand to generate CaMn_4 clusters, though with only one incorporated oxide moiety (Fig. 5, **H**).^{40c, 40d} A heterometallic polymeric material with a Mn_3O unit in proximity to a Ca^{2+} center was isolated (Fig. 5, **I**).⁴² To the authors' knowledge, only three other Mn/Ca clusters had been reported and characterized by crystallography prior to 2011, all with no bridging oxido ligands: a Mn_4 metallacrown moiety with a Ca^{2+} center coordinated to one side of the crown and chelated by carboxylates;⁴³ a $\text{Mn}^{\text{II}}_4\text{Ca}_2$ cluster with bridging alkoxides;⁴⁴ and a Mn_3NaCa coordination polymer.⁴⁵ The oxidation state of Mn in these compounds varies from mixed-valent $\text{Mn}^{\text{II}}/\text{Mn}^{\text{III}}/\text{Mn}^{\text{IV}}$ or $\text{Mn}^{\text{II}}/\text{Mn}^{\text{III}}$ to all- Mn^{II} or all- Mn^{III} . These synthetically novel heterometallic compounds demonstrate that although the self-assembly strategy is structurally very versatile, control of oxidation state, oxide incorporation, and level of aggregation to form the desired molecular model clusters remains challenging.

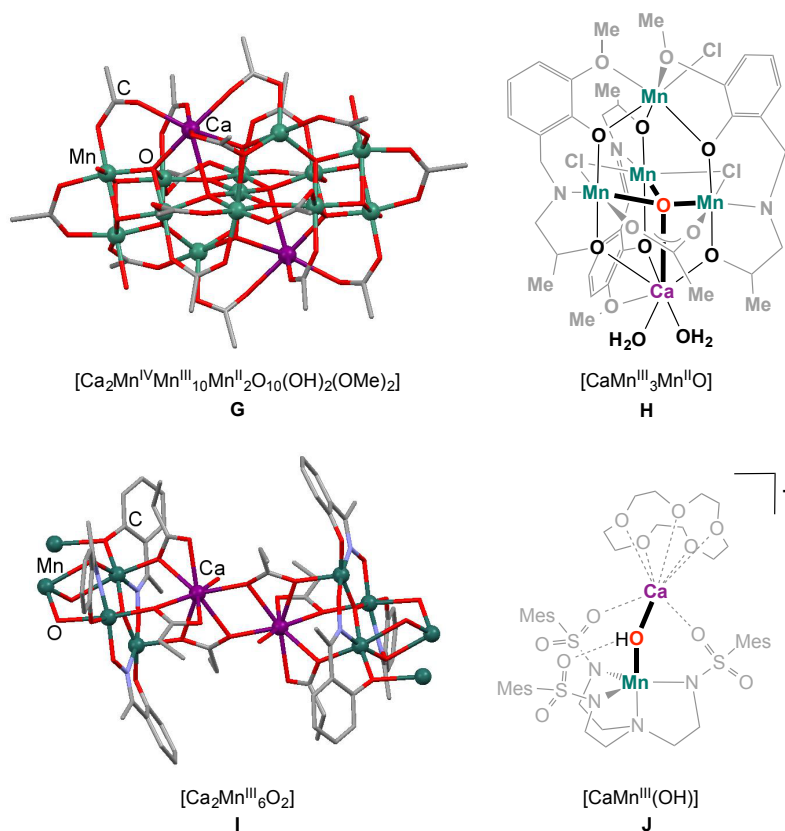


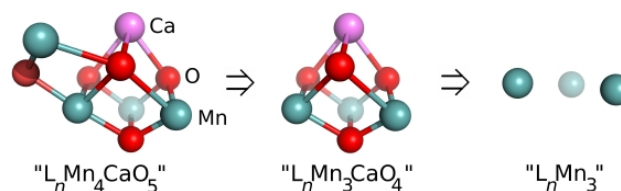
Figure 5. Structurally characterized heterometallic calcium-manganese clusters with bridging oxide or hydroxide moieties.^{40a, 40c, 40e, 42}

A complementary approach reported concurrently with our work on clusters investigated the effects of Ca^{2+} and other redox-inactive metals in heterometallic binuclear complexes. Borovik and co-workers exploited a tripodal tris(sulfonamide) ligand framework to access complexes of transition metals such as Mn, Fe, and Co associated via a bridging hydroxide with Ca^{2+} , Sr^{2+} , and Ba^{2+} centers that are also coordinated by two sulfonamide oxygen donors (Fig. 5, J).^{40e, 40g, 46} The redox-inactive metal was reported to affect the reduction potentials of the complexes as well as the rate of reaction with O_2 . Although not structurally characterized, Sc^{3+} association to $\text{Mn}^{\text{IV}}\text{O}$ moieties have been reported by Fukuzumi, Nam et al. to affect the reduction potential as well as reactivity,

including the rates of electron transfer, O-atom transfer, and H-atom abstraction.⁴⁷ Related effects have been observed for Fe^{IV}O moieties coordinated with redox-inactive metals, the Sc³⁺ version being structurally characterized.⁴⁸ Valence tautomerism was reported by Goldberg, de Visser, et al. for Mn^VO-porphyrinoid complexes upon addition of Zn²⁺, which affected redox and H-atom transfer chemistry.⁴⁹ These elegant studies show clearly that redox-inactive metals significantly affect the chemistry of transition metal-oxo species. Implications to the chemistry of the OEC have been proposed; however, more structurally accurate cluster models of the OEC remain very desirable to interrogate the effects on the physical properties and chemical reactivity of the complexes by changing various aspects such as structure, oxidation state, nature of redox-inactive metal, and number of oxido moieties.

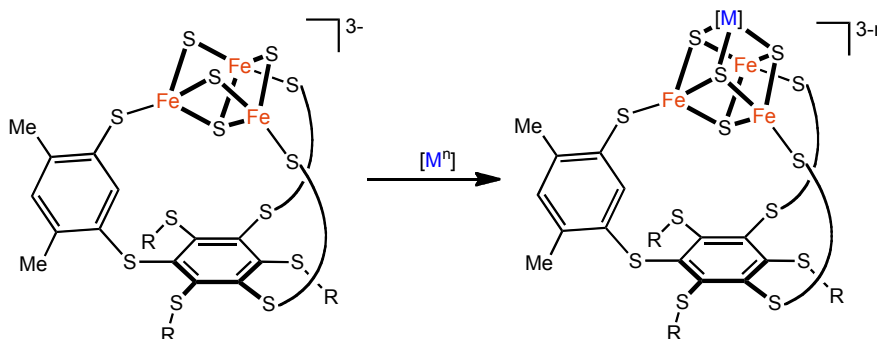
1.4 This work

Access to models of the active sites in biological and heterogeneous catalysts for water oxidation represents a significant synthetic challenge for several reasons, including the relatively large number of atoms, the presence of two types of metals, metal lability, and cluster asymmetry. In one possible strategy for modeling the OEC, outlined in a retrosynthetic fashion (Scheme 1), the “dangler” is attached late in the synthesis to a CaMn₃O₄ cubane structure. Accessing the simpler and higher-symmetry CaMn₃O₄ cubane presents the challenge (vide supra) of incorporating two types of metals bridged by oxides in the same cluster in a 3:1 ratio. A precursor to such species was envisioned in a trimetallic manganese complex.



Scheme 1. Retrosynthetic analysis for the synthesis of an OEC model.

This synthetic approach is reminiscent of Holm's methodology for the preparation of site-differentiated cuboidal iron-sulfur clusters.⁵⁰ Site-differentiated Fe_4S_4 cubanes are found in several metalloenzymes, with one of the supporting cysteinyls bridged to another metal fragment. In order to model such moieties, a semirigid tris-thiolate ligand was employed to support three of the four metals of the cubane moiety. Incomplete iron sulfur clusters, Fe_3S_4 , supported by this trinucleating ligand could be isolated and utilized as precursors to homo- and hetero-metallic Fe_3MS_4 moieties (Scheme 2).



Scheme 2. Metal incorporation into subsite-differentiated Fe_3MS_4 clusters.^{50e}

Toward heterometallic manganese oxido complexes, pre-formed trimanganese clusters were targeted that could be oxidized with concomitant addition of a fourth metal center. A multinucleating ligand based upon a semi-rigid 1,3,5-triarylbenzene framework was synthesized, with the three peripheral aryl groups functionalized by a dipyridylmethanol moiety. The lability of the dipyridylalkoxymethyl moiety is well documented in the coordination chemistry of dipyridylketone and the *gem*-diol or hemiacetal form thereof,

which chelate and bridge metal ions in a wide variety of binding modes.⁵¹ Such coordinative flexibility was expected to support the formation of different types of clusters on the ligand architecture. Additionally, these donor moieties were expected to support high oxidation state metal centers and be relatively stable to oxidative reaction conditions.

Chapter 2 describes the design and synthesis of this trinucleating ligand framework, as well as NMR studies of its temperature-dependent solution behavior. Tricopper(I) and tricopper(II) complexes of this ligand were synthesized and can be interconverted using proton- and electron-transfer reagents, demonstrating the structural versatility of the different donor moieties of the ligand. Additionally, variation of the counterions of the tricopper(II) complexes results in small structural changes in the $[\text{Cu}_3(\text{OR})_3]$ cores of these complexes and allows tuning of the antiferromagnetic exchange interactions between neighboring copper(II) centers. The syntheses and structural characterization of trinuclear complexes of this ligand using other divalent first row transition metals, including manganese(II), iron(II), cobalt(II), nickel(II), and zinc(II), further demonstrates that this ligand is a useful framework upon which to build larger inorganic clusters that may serve as bioinorganic models.

The trimanganese(II) triacetate complex of the trinucleating ligand framework is a useful precursor for the synthesis of site-differentiated *tetrametallic* complexes. Chapter 3 describes the synthesis of a series of isostructural heterometallic trimanganese dioxido complexes in which a redox-inactive metal is bridged to the basal trimanganese core via a μ_4 -oxido and a μ_2 -oxido bridge. Chapter 4 describes the synthesis of heterometallic trimanganese tetraoxido cubane clusters that are structurally related to the CaMn_3 subsite of

the OEC. These complexes demonstrate the utility of this synthetic strategy in modeling complicated structures that are difficult to achieve using self-assembly methods.

The ability to use this synthetic method to incorporate different redox-inactive metals in isostructural manganese oxido clusters allows systematic study of the roles of redox-inactive metal ions in the chemical properties of larger clusters. Electrochemical studies of the complexes described in Chapters 3 and 4 show that the reduction potentials of these manganese clusters are dependent upon the Lewis acidity of the incorporated redox-inactive metals. Despite the structure and oxidation state differences between the dioxido and tetraoxido clusters, the linear correlations between Lewis acidities and reduction potentials are the same, suggesting that Ca^{2+} may play a role in modulating the redox potentials of the OEC for water oxidation. Chapter 5 describes some preliminary studies investigating the roles of redox-inactive metal ions in the reactivity behavior of these complexes, including oxygen atom transfer, hydrogen atom transfer, and electron transfer rates.

The studies described in this work are primarily of fundamental interest because the biomimetic complexes presented herein allow spectroscopic and reactivity studies that help to improve our understanding of more complicated biological architectures. Ultimately, however, these studies may lead to practical applications in the design of new homogeneous and heterogeneous catalysts for water oxidation or oxygen reduction.

References

1. (a) Wydrzynski, T. J.; Satoh, K., *Photosystem II: The Light-Driven Water: Plastoquinone Oxidoreductase*. Springer: Dordrecht, The Netherlands, 2005; Vol. 22, p 11-22; (b) McEvoy, J. P.; Brudvig, G. W. *Chem. Rev.* **2006**, *106*, 4455-4483; (c) Brudvig, G. W. *Philos. Trans. R. Soc. London, Ser. B* **2008**, *363*, 1211-1218.

2. (a) Joliot, P.; Barbieri, G.; Chabaud, R. *Photochem. Photobiol.* **1969**, *10*, 309-329; (b) Kok, B.; Forbush, B.; McGloin, M. *Photochem. Photobiol.* **1970**, *11*, 457-475.
3. (a) Symes, M. D.; Surendranath, Y.; Lutterman, D. A.; Nocera, D. G. *J. Am. Chem. Soc.* **2011**, *133*, 5174-5177; (b) Risch, M.; Klingan, K.; Ringleb, F.; Chernev, P.; Zaharieva, I.; Fischer, A.; Dau, H. *Chemsuschem* **2012**, *5*, 542-549; (c) Zaharieva, I.; Najafpour, M. M.; Wiechen, M.; Haumann, M.; Kurz, P.; Dau, H. *Energy Environ. Sci.* **2011**, *4*, 2400-2408; (d) Wiechen, M.; Zaharieva, I.; Dau, H.; Kurz, P. *Chem. Sci.* **2012**; (e) Zaharieva, I.; Chernev, P.; Risch, M.; Klingan, K.; Kohlhoff, M.; Fischer, A.; Dau, H. *Energy Environ. Sci.* **2012**, *5*, 7081-7089.
4. (a) Najafpour, M. M.; Ehrenberg, T.; Wiechen, M.; Kurz, P. *Angew. Chem. Int. Ed.* **2010**, *49*, 2233-2237; (b) Najafpour, M. M.; Nayeri, S.; Pashaei, B. *Dalton Trans.* **2011**, *40*, 9374-9378; (c) Shevela, D.; Koroidov, S.; Najafpour, M. M.; Messinger, J.; Kurz, P. *Chem. Eur. J.* **2011**, *17*, 5415-5423; (d) Najafpour, M. M.; Pashaei, B.; Nayeri, S. *Dalton Trans.* **2012**, *41*, 4799-4805.
5. (a) Suntivich, J.; May, K. J.; Gasteiger, H. A.; Goodenough, J. B.; Shao-Horn, Y. *Science* **2011**, *334*, 1383-1385; (b) Smith, R. D. L.; Prévot, M. S.; Fagan, R. D.; Zhang, Z.; Sedach, P. A.; Siu, M. K. J.; Trudel, S.; Berlinguette, C. P. *Science* **2013**, *340*, 60-63; (c) Liang, Y.; Wang, H.; Zhou, J.; Li, Y.; Wang, J.; Regier, T.; Dai, H. *J. Am. Chem. Soc.* **2012**, *134*, 3517-3523; (d) Suntivich, J.; Gasteiger, H. A.; Yabuuchi, N.; Nakanishi, H.; Goodenough, J. B.; Shao-Horn, Y. *Nat Chem* **2011**, *3*, 546-550; (e) Hamdani, M.; Singh, R. N.; Chartier, P. *Int. J. Electrochem. Sci.* **2010**, *5*, 556-577.
6. (a) Goodenough, J. B.; Kim, Y. *Chem. Mater.* **2009**, *22*, 587-603; (b) Whittingham, M. S. *Chem. Rev.* **2004**, *104*, 4271-4302; (c) Reddy, M. V.; Subba Rao, G. V.; Chowdari, B. V. R. *Chem. Rev.* **2013**, *113*, 5364-5457; (d) Melot, B. C.; Tarascon, J. M. *Acc. Chem. Res.* **2013**, *46*, 1226-1238.
7. (a) Kirby, J. A.; Robertson, A. S.; Smith, J. P.; Thompson, A. C.; Cooper, S. R.; Klein, M. P. *J. Am. Chem. Soc.* **1981**, *103*, 5529-5537; (b) Kirby, J. A.; Goodin, D. B.; Wydrzynski, T.; Robertson, A. S.; Klein, M. P. *J. Am. Chem. Soc.* **1981**, *103*, 5537-5542; (c) Yachandra, V. K.; Sauer, K.; Klein, M. P. *Chem. Rev.* **1996**, *96*, 2927-2950; (d) Sauer, K.; Yano, J.; Yachandra, V. *Photosynth Res* **2005**, *85*, 73-86; (e) Yano, J.; Kern, J.; Sauer, K.; Latimer, M. J.; Pushkar, Y.; Biesiadka, J.; Loll, B.; Saenger, W.; Messinger, J.; Zouni, A.; Yachandra, V. K. *Science* **2006**, *314*, 821-825.
8. (a) Messinger, J.; Nugent, J. H. A.; Evans, M. C. W. *Biochemistry* **1997**, *36*, 11055-11060; (b) Messinger, J.; Robblee, J. H.; Yu, W. O.; Sauer, K.; Yachandra, V. K.; Klein, M. P. *J. Am. Chem. Soc.* **1997**, *119*, 11349-11350; (c) Peloquin, J. M.; Campbell, K. A.; Randall, D. W.; Evanchik, M. A.; Pecoraro, V. L.; Armstrong, W. H.; Britt, R. D. *J. Am. Chem. Soc.* **2000**, *122*, 10926-10942; (d) Dismukes, G. C.; Siderer, Y. *Febs Lett* **1980**, *121*, 78-80; (e) Dismukes, G. C.; Siderer, Y. *P Natl Acad Sci-Biol* **1981**, *78*, 274-278; (f) Dismukes, G. C.; Ferris, K.; Watnick, P. *Photobioch Photobiop* **1982**, *3*, 243-256.
9. (a) Ferreira, K. N.; Iverson, T. M.; Maghlaoui, K.; Barber, J.; Iwata, S. *Science* **2004**, *303*, 1831-1838; (b) Umena, Y.; Kawakami, K.; Shen, J. R.; Kamiya, N. *Nature* **2011**, *473*, 55-U65.
10. (a) Luber, S.; Rivalta, I.; Umena, Y.; Kawakami, K.; Shen, J.-R.; Kamiya, N.; Brudvig, G. W.; Batista, V. S. *Biochemistry* **2011**, *50*, 6308-6311; (b) Ames, W.; Pantazis, D. A.;

- Krewald, V.; Cox, N.; Messinger, J.; Lubitz, W.; Neese, F. *J. Am. Chem. Soc.* **2011**, *133*, 19743-19757.
11. Yano, J.; Kern, J.; Irrgang, K.-D.; Latimer, M. J.; Bergmann, U.; Glatzel, P.; Pushkar, Y.; Biesiadka, J.; Loll, B.; Sauer, K.; Messinger, J.; Zouni, A.; Yachandra, V. K. *Proc. Natl. Acad. Sci. USA* **2005**, *102*, 12047-12052.
 12. (a) Kusunoki, M. *J. Photochem. Photobiol., B* **2011**, *104*, 100-110; (b) Pantazis, D. A.; Ames, W.; Cox, N.; Lubitz, W.; Neese, F. *Angew. Chem. Int. Ed.* **2012**, *51*, 9935-9940.
 13. (a) Siegbahn, P. E. M. *Chem. Eur. J.* **2008**, *14*, 8290-8302; (b) Grundmeier, A.; Dau, H. *Biochim. Biophys. Acta Bioenergetics* **2012**, *1817*, 88-105.
 14. (a) Messinger, J.; Badger, M.; Wydrzynski, T. *Proc. Natl. Acad. Sci. USA* **1995**, *92*, 3209-3213; (b) Hillier, W.; Messinger, J.; Wydrzynski, T. *Biochemistry* **1998**, *37*, 16908-16914; (c) Rapatskiy, L.; Cox, N.; Savitsky, A.; Ames, W. M.; Sander, J.; Nowaczyk, M. M.; Rögner, M.; Boussac, A.; Neese, F.; Messinger, J.; Lubitz, W. *J. Am. Chem. Soc.* **2012**, *134*, 16619-16634.
 15. (a) Dasgupta, J.; van Willigen, R. T.; Dismukes, G. C. *Phys. Chem. Chem. Phys.* **2004**, *6*, 4793-4802; (b) Vincent, J. B.; Christou, G. *Inorg. Chim. Acta* **1987**, *136*, L41-L43; (c) Brudvig, G. W.; Crabtree, R. H. *Proc. Natl. Acad. Sci. USA* **1986**, *83*, 4586-4588.
 16. (a) Pecoraro, V. L.; Baldwin, M. J.; Caudle, M. T.; Hsieh, W. Y.; Law, N. A. *Pure Appl. Chem.* **1998**, *70*, 925-929; (b) Vrettos, J. S.; Limburg, J.; Brudvig, G. W. *Biochim. Biophys. Acta Bioenergetics* **2001**, *1503*, 229-245; (c) Vrettos, J. S.; Stone, D. A.; Brudvig, G. W. *Biochemistry* **2001**, *40*, 7937-7945.
 17. (a) Siegbahn, P. E. M.; Crabtree, R. H. *J. Am. Chem. Soc.* **1999**, *121*, 117-127; (b) Siegbahn, P. E. M. *Philos. Trans. R. Soc. London, Ser. B* **2008**, *363*, 1221-1228.
 18. (a) Sproviero, E. M.; Gascón, J. A.; McEvoy, J. P.; Brudvig, G. W.; Batista, V. S. *J. Am. Chem. Soc.* **2008**, *130*, 3428-3442; (b) Siegbahn, P. E. M. *Acc. Chem. Res.* **2009**, *42*, 1871-1880.
 19. (a) Ghanotakis, D. F.; Babcock, G. T.; Yocum, C. F. *Febs Lett* **1984**, *167*, 127-130; (b) Boussac, A.; Zimmermann, J. L.; Rutherford, A. W. *Biochemistry* **1989**, *28*, 8984-8989; (c) Yocum, C. F. *Biochim. Biophys. Acta Bioenergetics* **1991**, *1059*, 1-15; (d) Yocum, C. F. *Coord. Chem. Rev.* **2008**, *252*, 296-305.
 20. Boussac, A.; Rutherford, A. W. *Biochemistry* **1988**, *27*, 3476-3483.
 21. Pushkar, Y.; Yano, J.; Sauer, K.; Boussac, A.; Yachandra, V. K. *Proc. Natl. Acad. Sci. USA* **2008**, *105*, 1879-1884.
 22. Cox, N.; Rapatskiy, L.; Su, J.-H.; Pantazis, D. A.; Sugiura, M.; Kulik, L.; Dorlet, P.; Rutherford, A. W.; Neese, F.; Boussac, A.; Lubitz, W.; Messinger, J. *J. Am. Chem. Soc.* **2011**, *133*, 3635-3648.
 23. (a) Lee, C.-I.; Lakshmi, K. V.; Brudvig, G. W. *Biochemistry* **2007**, *46*, 3211-3223; (b) Yachandra, V. K.; Yano, J. *J. Photochem. Photobiol., B* **2011**, *104*, 51-59.
 24. (a) Riggs-Gelasco, P. J.; Mei, R.; Ghanotakis, D. F.; Yocum, C. F.; Penner-Hahn, J. E. *J. Am. Chem. Soc.* **1996**, *118*, 2400-2410; (b) Lohmiller, T.; Cox, N.; Su, J.-H.; Messinger, J.; Lubitz, W. *J. Biol. Chem.* **2012**, *287*, 24721-24733.
 25. Kanan, M. W.; Yano, J.; Surendranath, Y.; Dincă, M.; Yachandra, V. K.; Nocera, D. G. *J. Am. Chem. Soc.* **2010**, *132*, 13692-13701.
 26. (a) Wieghardt, K. *Angew. Chem. Int. Ed.* **1989**, *28*, 1153-1172; (b) Cady, C. W.; Crabtree, R. H.; Brudvig, G. W. *Coord. Chem. Rev.* **2008**, *252*, 444-455; (c) Sproviero, E. M.; Gascón, J. A.; McEvoy, J. P.; Brudvig, G. W.; Batista, V. S. *Coord. Chem. Rev.*

- 2008**, 252, 395-415; (d) Christou, G. *Acc. Chem. Res.* **1989**, 22, 328-335; (e) Pecoraro, V. L.; Baldwin, M. J.; Gelasco, A. *Chem. Rev.* **1994**, 94, 807-826; (f) Manchanda, R.; Brudvig, G. W.; Crabtree, R. H. *Coord. Chem. Rev.* **1995**, 144, 1-38; (g) Yagi, M.; Kaneko, M. *Chem. Rev.* **2000**, 101, 21-36; (h) Mukhopadhyay, S.; Mandal, S. K.; Bhaduri, S.; Armstrong, W. H. *Chem. Rev.* **2004**, 104, 3981-4026; (i) Wu, A. J.; Penner-Hahn, J. E.; Pecoraro, V. L. *Chem. Rev.* **2004**, 104, 903-938; (j) Mullins, C. S.; Pecoraro, V. L. *Coord. Chem. Rev.* **2008**, 252, 416-443.
27. (a) Plaksin, P. M.; Stouffer, R. C.; Mathew, M.; Palenik, G. J. *J. Am. Chem. Soc.* **1972**, 94, 2121-2122; (b) Cooper, S. R.; Calvin, M. *J. Am. Chem. Soc.* **1977**, 99, 6623-6630; (c) Cooper, S. R.; Dismukes, G. C.; Klein, M. P.; Calvin, M. *J. Am. Chem. Soc.* **1978**, 100, 7248-7252.
28. Kirby, J. A.; Robertson, A. S.; Smith, J. P.; Thompson, A. C.; Cooper, S. R.; Klein, M. P. *J. Am. Chem. Soc.* **1981**, 103, 5529-5537.
29. Dismukes, G. C.; Siderer, Y. *Proc. Natl. Acad. Sci. USA* **1981**, 78, 274-278.
30. Guiles, R. D.; Zimmermann, J. L.; McDermott, A. E.; Yachandra, V. K.; Cole, J. L.; Dexheimer, S. L.; Britt, R. D.; Wieghardt, K.; Bossek, U. *Biochemistry* **1990**, 29, 471-485.
31. (a) Chan, M. K.; Armstrong, W. H. *J. Am. Chem. Soc.* **1991**, 113, 5055-5057; (b) Chen, H.; Faller, J. W.; Crabtree, R. H.; Brudvig, G. W. *J. Am. Chem. Soc.* **2004**, 126, 7345-7349; (c) Philouze, C.; Blondin, G.; Girerd, J.-J.; Guilhem, J.; Pascard, C.; Lexa, D. *J. Am. Chem. Soc.* **1994**, 116, 8557-8565.
32. (a) Limburg, J.; Brudvig, G. W.; Crabtree, R. H. *J. Am. Chem. Soc.* **1997**, 119, 2761-2762; (b) Limburg, J.; Vrettos, J. S.; Liabe-Sands, L. M.; Rheingold, A. L.; Crabtree, R. H.; Brudvig, G. W. *Science* **1999**, 283, 1524-1527.
33. Limburg, J.; Vrettos, J. S.; Chen, H.; de Paula, J. C.; Crabtree, R. H.; Brudvig, G. W. *J. Am. Chem. Soc.* **2000**, 123, 423-430.
34. (a) Vincent, J. B.; Christmas, C.; Chang, H. R.; Li, Q.; Boyd, P. D. W.; Huffman, J. C.; Hendrickson, D. N.; Christou, G. *J. Am. Chem. Soc.* **1989**, 111, 2086-2097; (b) Vincent, J. B.; Christmas, C.; Huffman, J. C.; Christou, G.; Chang, H.-R.; Hendrickson, D. N. *J. Chem. Soc., Chem. Commun.* **1987**, 0, 236-238.
35. Li, Q.; Vincent, J. B.; Libby, E.; Chang, H.-R.; Huffman, J. C.; Boyd, P. D. W.; Christou, G.; Hendrickson, D. N. *Angew. Chem. Int. Ed.* **1988**, 27, 1731-1733.
36. (a) Ruettinger, W. F.; Campana, C.; Dismukes, G. C. *J. Am. Chem. Soc.* **1997**, 119, 6670-6671; (b) Dismukes, G. C.; Brimblecombe, R.; Felton, G. A. N.; Pryadun, R. S.; Sheats, J. E.; Spiccia, L.; Swiegers, G. F. *Acc. Chem. Res.* **2009**, 42, 1935-1943.
37. Brimblecombe, R.; Swiegers, G. F.; Dismukes, G. C.; Spiccia, L. *Angew. Chem. Int. Ed.* **2008**, 47, 7335-7338.
38. Hocking, R. K.; Brimblecombe, R.; Chang, L.-Y.; Singh, A.; Cheah, M. H.; Glover, C.; Casey, W. H.; Spiccia, L. *Nat. Chem.* **2011**, 3, 461-466.
39. (a) Wieghardt, K.; Bossek, U.; Gebert, W. *Angew. Chem. Int. Ed.* **1983**, 22, 328-329; (b) Dubé, C. E.; Wright, D. W.; Pal, S.; Bonitatebus Jr., P. J.; Armstrong, W. H. *J. Am. Chem. Soc.* **1998**, 120, 3704-3716.
40. (a) Mishra, A.; Wernsdorfer, W.; Abboud, K. A.; Christou, G. *Chem. Commun.* **2005**, 54-56; (b) Mishra, A.; Yano, J.; Pushkar, Y.; Yachandra, V. K.; Abboud, K. A.; Christou, G. *Chem. Commun.* **2007**, 1538-1540; (c) Hewitt, I. J.; Tang, J.-K.; Madhu, N. T.; Clerac, R.; Buth, G.; Anson, C. E.; Powell, A. K. *Chem. Commun.* **2006**, 2650-

- 2652; (d) Nayak, S.; Nayek, H. P.; Dehnen, S.; Powell, A. K.; Reedijk, J. *Dalton Trans.* **2011**, 40, 2699-2702; (e) Park, Y. J.; Ziller, J. W.; Borovik, A. S. *J. Am. Chem. Soc.* **2011**, 133, 9258-9261; (f) Mukherjee, S.; Stull, J. A.; Yano, J.; Stamatatos, T. C.; Pringouri, K.; Stich, T. A.; Abboud, K. A.; Britt, R. D.; Yachandra, V. K.; Christou, G. *Proc. Natl. Acad. Sci. USA* **2012**, 109, 2257-2262; (g) Park, Y. J.; Cook, S. A.; Sickerman, N. S.; Sano, Y.; Ziller, J. W.; Borovik, A. S. *Chem. Sci.* **2013**, 4, 717-726.
41. Mishra, A.; Pushkar, Y.; Yano, J.; Yachandra, V. K.; Wernsdorfer, W.; Abboud, K. A.; Christou, G. *Inorg. Chem.* **2008**, 47, 1940-1948.
 42. Kotzabasaki, V.; Siczek, M.; Lis, T.; Milios, C. J. *Inorg. Chem. Commun.* **2011**, 14, 213-216.
 43. Koumoussi, E. S.; Mukherjee, S.; Beavers, C. M.; Teat, S. J.; Christou, G.; Stamatatos, T. C. *Chem. Commun.* **2011**, 47, 11128-11130.
 44. Jerzykiewicz, L. B.; Utko, J.; Duczmal, M.; Sobota, P. *Dalton Trans.* **2007**, 825-826.
 45. Li, N.; Wang, M.; Ma, C.-B.; Hu, M.-Q.; Zhou, R.-W.; Chen, H.; Chen, C.-N. *Inorg. Chem. Commun.* **2010**, 13, 730-732.
 46. Lacy, D. C.; Park, Y. J.; Ziller, J. W.; Yano, J.; Borovik, A. S. *J. Am. Chem. Soc.* **2012**, 134, 17526-17535.
 47. (a) Chen, J.; Lee, Y.-M.; Davis, K. M.; Wu, X.; Seo, M. S.; Cho, K.-B.; Yoon, H.; Park, Y. J.; Fukuzumi, S.; Pushkar, Y. N.; Nam, W. *J. Am. Chem. Soc.* **2013**, 135, 6388-6391; (b) Yoon, H.; Lee, Y.-M.; Wu, X.; Cho, K.-B.; Sarangi, R.; Nam, W.; Fukuzumi, S. *J. Am. Chem. Soc.* **2013**, 135, 9186-9194.
 48. (a) Fukuzumi, S.; Morimoto, Y.; Kotani, H.; Naumov, P.; Lee, Y. M.; Nam, W. *Nat. Chem.* **2010**, 2, 756-759; (b) Morimoto, Y.; Kotani, H.; Park, J.; Lee, Y. M.; Nam, W.; Fukuzumi, S. *J. Am. Chem. Soc.* **2011**, 133, 403-405.
 49. Leeladee, P.; Baglia, R. A.; Prokop, K. A.; Latifi, R.; de Visser, S. P.; Goldberg, D. P. *J. Am. Chem. Soc.* **2012**, 134, 10397-10400.
 50. (a) Stack, T. D. P.; Holm, R. H. *J. Am. Chem. Soc.* **1987**, 109, 2546-2547; (b) Venkateswara Rao, P.; Holm, R. H. *Chem. Rev.* **2003**, 104, 527-560; (c) Stack, T. D. P.; Holm, R. H. *J. Am. Chem. Soc.* **1988**, 110, 2484-2494; (d) Ciurli, S.; Carrie, M.; Weigel, J. A.; Carney, M. J.; Stack, T. D. P.; Papaefthymiou, G. C.; Holm, R. H. *J. Am. Chem. Soc.* **1990**, 112, 2654-2664; (e) Zhou, J.; Raebiger, J. W.; Crawford, C. A.; Holm, R. H. *J. Am. Chem. Soc.* **1997**, 119, 6242-6250.
 51. Stamatatos, T. C.; Efthymiou, C. G.; Stoumpos, C. C.; Perlepes, S. P. *Eur. J. Inorg. Chem.* **2009**, 2009, 3361-3391.

Chapter 2

SYNTHESIS, STRUCTURE, AND MAGNETIC SUSCEPTIBILITIES OF TRINUCLEAR TRANSITION METAL CLUSTERS OF A HEXAPYRIDYL 1,3,5- TRIARYLBENZENE LIGAND FRAMEWORK

The text for this chapter was reproduced in part from:

Tsui, E. Y.; Day, M. W.; Agapie, T. *Angew. Chem. Int. Ed.* **2011**, *50*, 1668-1672.

Tsui, E. Y.; Kanady, J. S.; Day, M. W.; Agapie, T. *Chem. Commun.* **2011**, *47*, 4189-4191.

Abstract

Targeting synthetic model complexes of multimetallic enzyme active sites such as the multicopper oxidases, a trinucleating ligand based upon a 1,3,5-triarylbenzene framework with six pyridyl and three alkoxide donors was synthesized, and its fluxional solution behavior was characterized using variable temperature NMR studies. Tricopper(I) and tricopper(II) complexes supported by this ligand were prepared, and their chemical interconversion was studied. A magnetostructural study of tricopper(II) complexes with various counteranions revealed a relationship between the Cu–O–Cu angles of the alkoxide-bridged tricopper core and the magnitude of the antiferromagnetic coupling of the neighboring spins. Trinuclear complexes of other first row transition metals were prepared and structurally characterized, and their magnetic susceptibilities were studied.

Introduction

Multimetallic active sites are common in enzymes responsible for the catalysis of challenging multielectron chemical reactions such as O_2 activation, H_2O oxidation, CO_2 reduction, and N_2 reduction.¹ In the context of reproducing the activity of such enzymes and understanding the electronic structure and reactivity of the active sites, the design of ligand architectures capable of nucleating several metal centers is of interest. The active sites of oxidases (laccase, ascorbate oxidase) and oxygenases (particulate methane monooxygenase), which are known or proposed to contain multicopper centers, have been appealing synthetic targets due to the potential applications in fuel cell technology, functionalization of organic substrates, and liquefaction of methane.² Treatment of mononuclear copper diamines with O_2 was found to generate a self-assembled Cu_3O_2 moiety; reduction, however, causes the loss of the trinuclear core.³ Multinucleating ligands represent an appealing alternate approach for accessing multinuclear copper complexes.⁴ Of the variety of trinucleating ligands designed and investigated,⁵ most are rather flexible and do not enforce cooperative trinuclear reactivity or a well-defined arrangement of the metal centers. Macrocyclic frameworks have shown promise for forming tricopper(II) complexes, but reactivity with O_2 has yet to be reported for most of these systems.⁶

We report here the design of a trinucleating ligand based upon a 1,3,5-triphenylbenzene core that can closely constrain three copper centers. The synthesis, oxygen reactivity, and spectroscopic characterization of trinuclear copper(I) and copper(II) complexes based upon this framework are reported. Trinuclear complexes of Fe^{II} , Cu^{II} , and Zn^{II} supported by this ligand architecture were also synthesized and characterized structurally and magnetically.

Results and Discussion

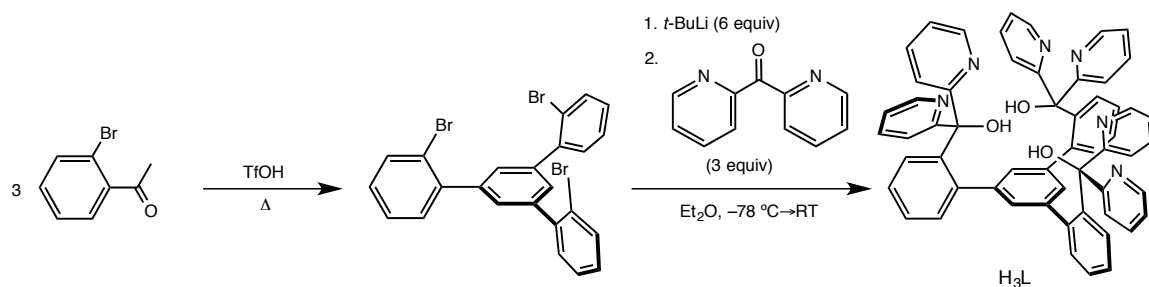
2.1 Ligand synthesis and NMR studies

We envisioned that building a ligand upon a 1,3,5-triarylbenzene core would impart rigidity to the framework that would help maintain the proximity of the three copper centers, as only rotation about the aryl-aryl bonds would be allowed. Pyridyl donors were incorporated due to their relative oxidative stability in comparison to donor groups connected to sp^3 C–H bonds that might be oxidized or oxygenated by reduced dioxygen intermediates. In addition to three bidentate dipyriddy copper binding sites, the ligand variant discussed here (H_3L , Scheme 1) contains three hydroxyl moieties that may serve as shuttles for the protons necessary for dioxygen reduction to water.

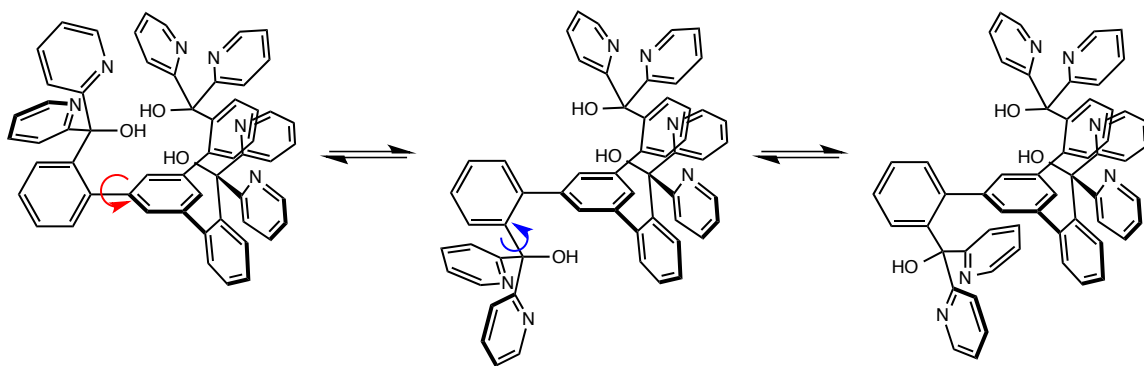
The compound H_3L was prepared in two steps from commercially available materials (Scheme 1). 1,3,5-tri(2'-bromophenyl)benzene⁷ was prepared by acid-promoted condensation of 2'-bromoacetophenone. Lithium-halogen exchange followed by addition of three equivalents of di(2-pyridyl)ketone yielded H_3L in moderate yield (ca. 60%). This synthetic route can be reproducibly run on a multi-gram scale.

The solution behavior of H_3L was studied using 1H NMR spectroscopy. Variable temperature 1H NMR studies were conducted on solutions of H_3L in C_6D_6 (Fig. 1) and CD_2Cl_2 (Fig. 2). At room temperature, the 1H NMR signals are broad, indicating site exchange due to fluxional behavior. These broad signals sharpen at higher temperature, indicating faster exchange of the different conformational isomers of H_3L (Fig. 1). The spectrum at $-50\text{ }^\circ C$ has 24 signals corresponding to an isomer of H_3L with one dipyriddy moiety located on the opposite face of the central aryl ring from the other two (Fig. 2). At lower temperatures other exchange processes are observed, possibly corresponding to

freezing of rotational isomers about the aryl–alkyl bonds (Scheme 2). The ^1H NMR spectrum of H_3L was assigned using gCOSY NMR studies at room temperature and at -50°C (Figs. 3 and 4).



Scheme 1. Synthesis of H_3L .



Scheme 2. Fluxional processes and conformational isomers of H_3L .

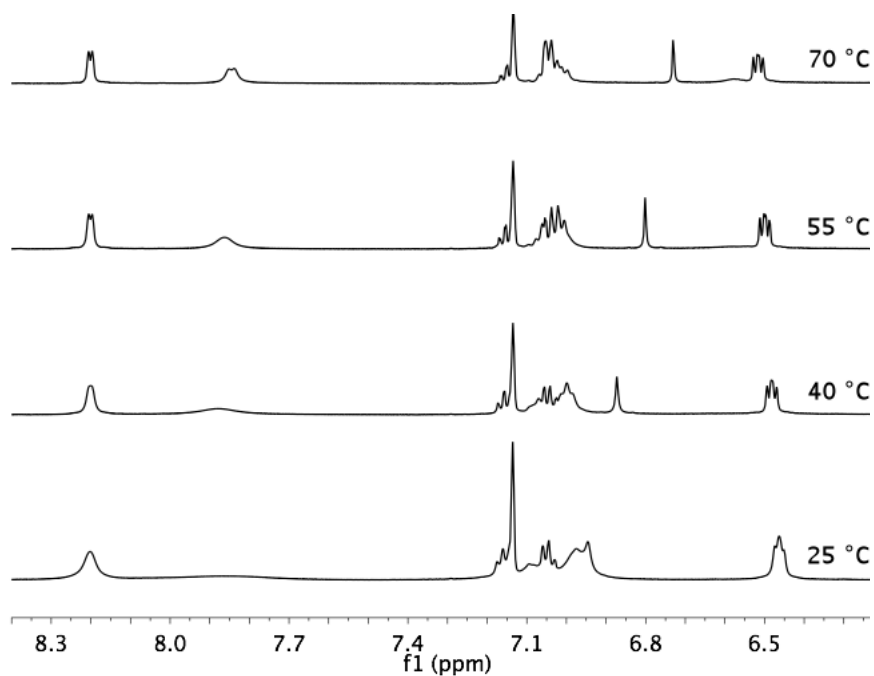


Figure 1. High temperature variable temperature ^1H NMR spectra of H_3L in C_6D_6 .

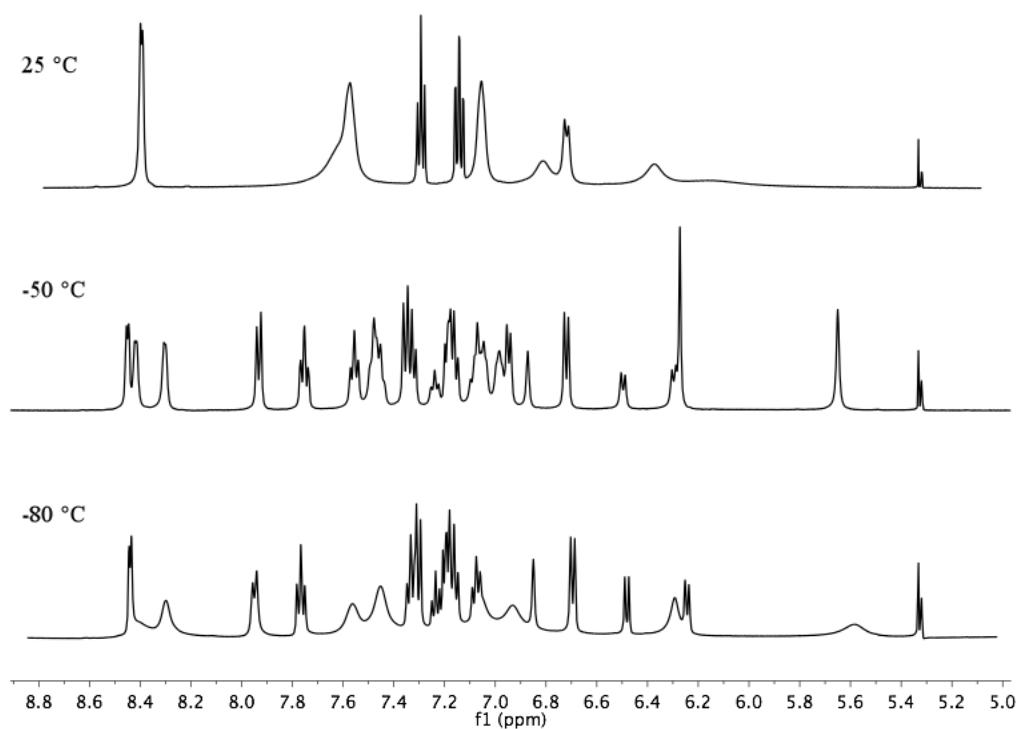


Figure 2. Low temperature variable temperature ^1H NMR spectra of H_3L in CD_2Cl_2 .

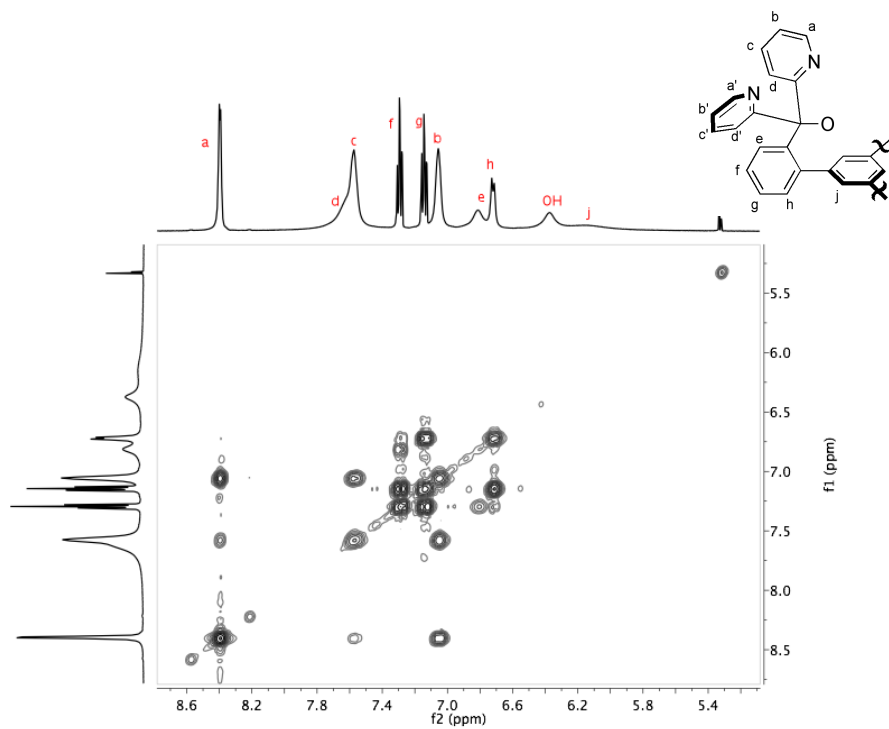


Figure 3. gCOSY NMR spectrum of H₃L in CD₂Cl₂ at 25 °C.

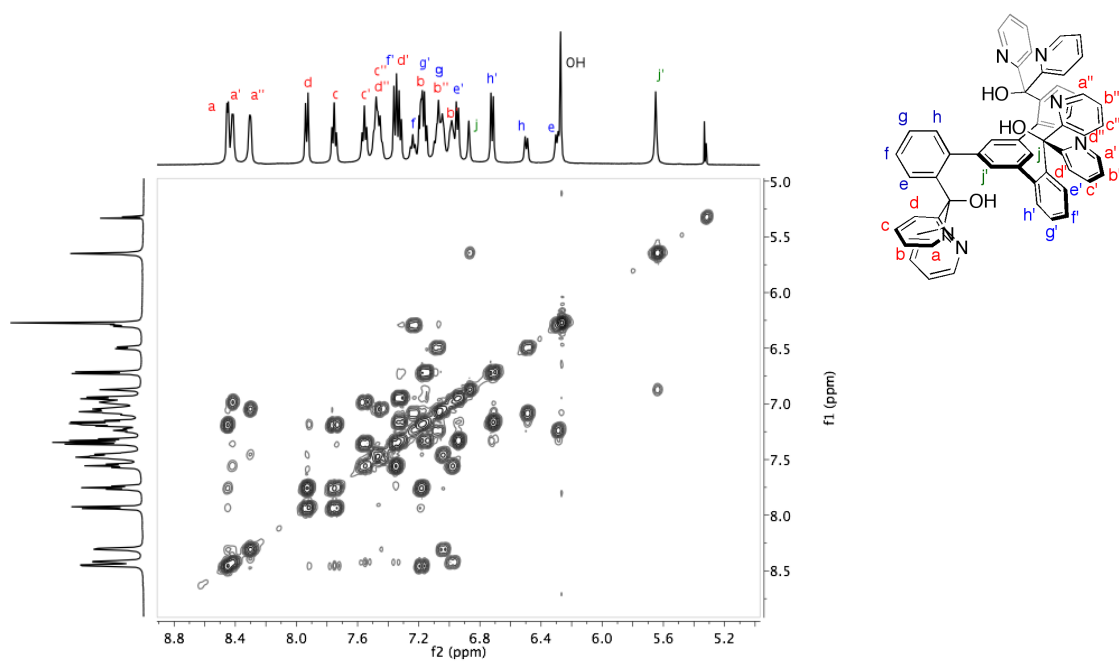


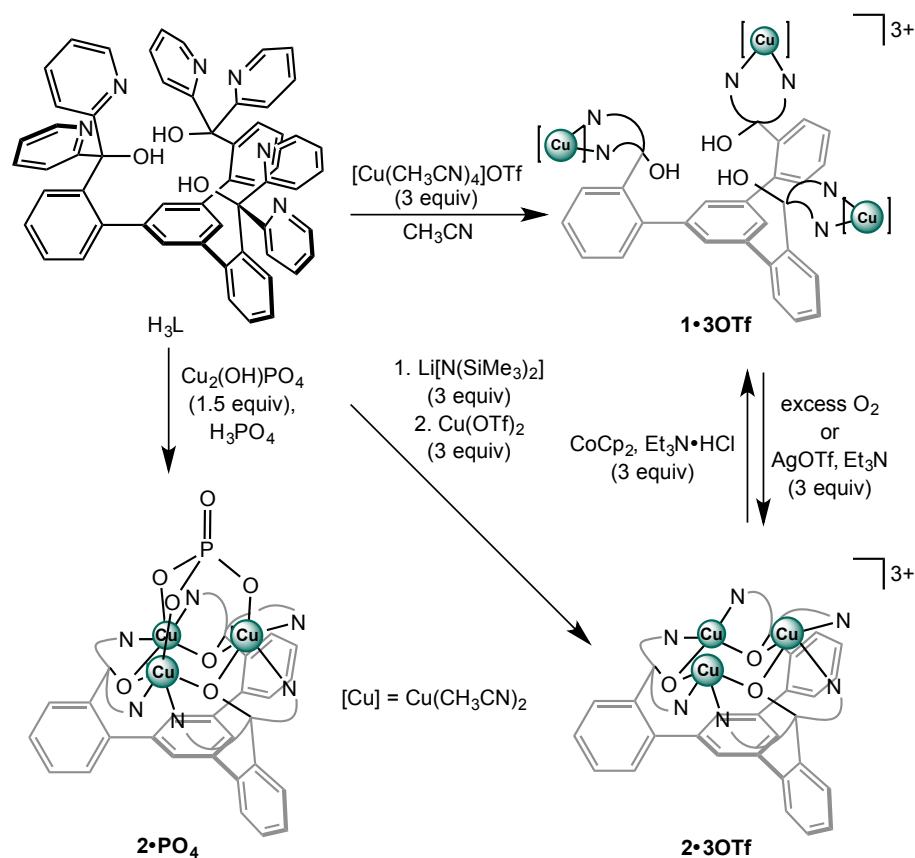
Figure 4. gCOSY NMR spectrum of H₃L in CD₂Cl₂ at -50 °C.

2.2 Synthesis and structure of tricopper complexes

Addition of three equivalents of a copper(I) salt such as $[\text{Cu}(\text{CH}_3\text{CN})_4]\text{OTf}$ or $[\text{Cu}(\text{CH}_3\text{CN})_4]\text{BF}_4$ to H_3L (Scheme 3) forms the yellow compounds $[\text{Cu}_3(\text{H}_3\text{L})]\cdot 3\text{X}$ ($\text{X} = \text{OTf}, \text{BF}_4$), **1•3X**. The copper centers are each expected to bind two pyridyl nitrogens and solvent molecules or anion. Variable temperature ^1H NMR spectra of **1•3BF₄** are indicative of fluxional processes in solution similar to those of H_3L ; the three copper centers are not constrained to remain together and likely have rotational freedom about both aryl-aryl and aryl-alkyl bonds. At low temperatures, **1•3OTf** likely adopts the same conformation as free H_3L , with one copper center located on the opposite face of the central aryl ring from the other two copper ions. Addition of excess dioxygen to a propionitrile solution of **1•3OTf** at $-78\text{ }^\circ\text{C}$ does not result in a reaction within 24 h. However, the reaction of **1•3OTf** with dioxygen in acetonitrile over 15 h at room temperature forms a green compound $[\text{Cu}_3\text{L}]\cdot 3\text{OTf}$ (**2•3OTf**) quantitatively, as determined by ^1H NMR spectroscopy using an internal standard.

In the reaction with O_2 , complex **1•3OTf** formally acts as a source of both protons and electrons for the reduction of between 0.75 and 1 equivalent of O_2 (Toepler pump measurement). The product derived from O_2 in the oxidation of **1•3OTf** has not been identified to date, but a peroxotitanyl test indicates that H_2O_2 is not present in solution when the conversion to **2•3OTf** is complete.⁸ In the absence of dioxygen, oxidation of **1•3OTf** in acetonitrile with three equivalents of silver(I) triflate in the presence of triethylamine cleanly forms **2•3OTf**. Addition of fewer equivalents of silver(I) does not form a mixed valence compound but rather a mixture of **1•3OTf** and **2•3OTf** in the expected ratio as judged by ^1H NMR spectroscopy (Fig. 5). For the reverse reaction,

2•3OTf can be converted to **1•3OTf** upon addition of three equivalents of cobaltocene in the presence of an acid such as triethylamine hydrochloride or upon treatment with benzoin.



Scheme 3. Synthesis and reactions of tricopper complexes.

Compound **2•3OTf** was independently prepared by deprotonation of **H₃L** with three equivalents of base followed by addition of three equivalents of $\text{Cu}(\text{OTf})_2$. The solid-state structures of **2•3OTf** and of a phosphate analogue, **2•PO₄**, show that the trinuclear complexes are pseudo- C_3 symmetric alkoxo-bridged trinuclear copper clusters capped by a triflate or phosphate anion (Fig. 6).⁹ The copper(II) centers and the alkoxo oxygens are linked in a chair-like $[\text{Cu}_3(\text{OR})_3]$ core and each copper(II) center is further coordinated by two pyridyl nitrogens from neighboring dipyridyl moieties. The Cu–O (alkoxide) and

Cu–N distances are typical of other Cu^{II} compounds (1.91–2.01 Å), although the Cu–O (anion) distances are longer (ca. 2.4 and 2.2 Å respectively), indicating weaker coordination of the triflate or phosphate.

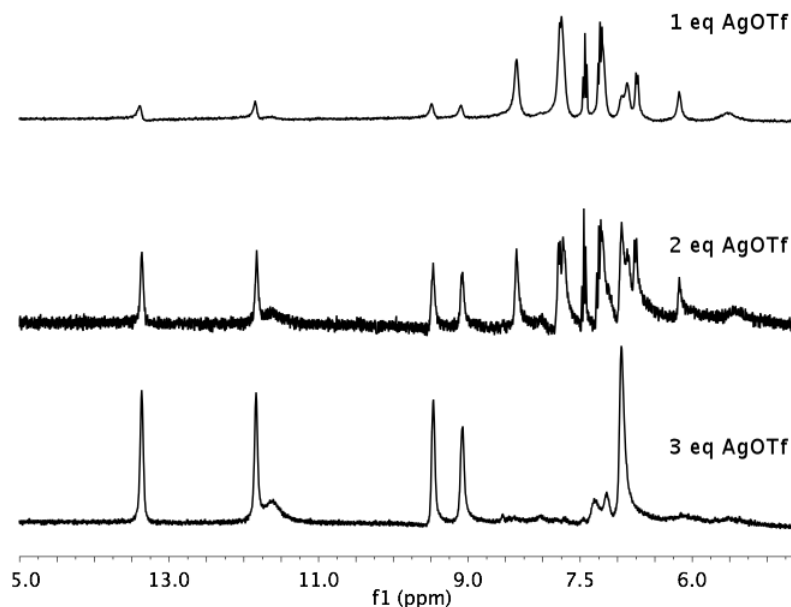


Figure 5. ¹H NMR spectra of the reactions mixtures of the addition of AgOTf and Et₃N to **1·3OTf**.

NMR spectroscopy data suggest that the [Cu₃O₃N₆] geometry observed in the solid-state structures remains intact in solution allowing for three potentially accessible coordination sites on the same face of the tricopper unit. The ¹H NMR spectra of both **2·3OTf** and **2·PO₄** contain thirteen signals (Fig. 7), indicating that the molecules are C₃-symmetric in solution; a higher symmetry structure would give rise to nine peaks. The peaks are very well resolved, indicating the presence of low-lying excited states of the copper(II) complex that allow for fast electronic relaxation.^{6b, 10} The signals were assigned by comparing longitudinal relaxation times to distances in the X-ray diffraction structure

(Table 1), as well as using gCOSY experiments (Fig. 8) and NMR spectra of complexes with a deuterium labeled ligand.

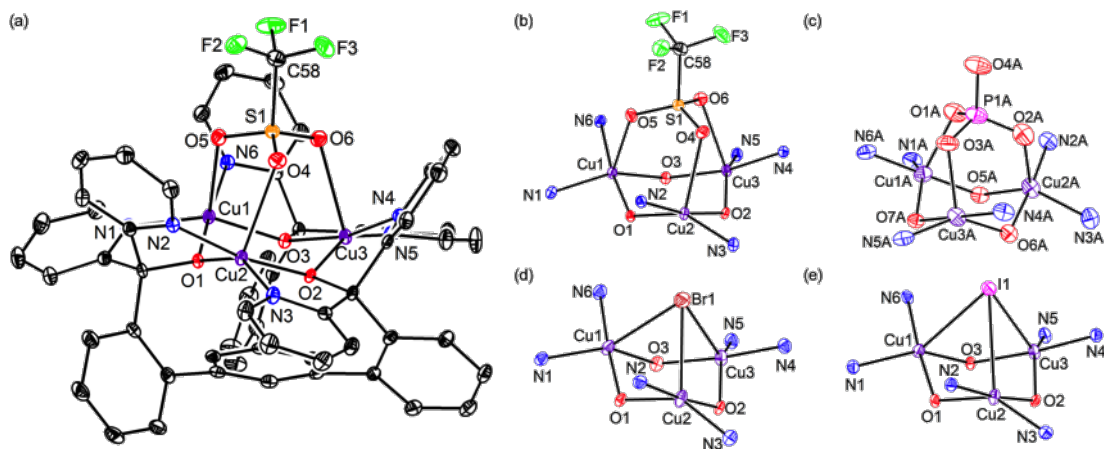


Figure 6. Solid-state structure of **2•3OTf** as 50% thermal ellipsoids. Outer-sphere triflate anions and solvent molecules omitted for clarity. Truncated view of solid-state structures of b) **2•3OTf**, c) **2•PO₄**, d) **2•Br•2OTf**, and e) **2•I•2OTf**. Selected bond lengths (Å): b) Cu–Cu 3.4426(3)–3.4624(3), Cu–O(alkoxide) 1.9087(9)–1.954(1), Cu–N 1.9350(9)–1.986(1), Cu–O(OTf) 2.425(1)–2.508(1). c) Cu–Cu 3.2948(5)–3.3309(5), Cu–O(alkoxide) 1.931(2)–1.994(2), Cu–N 1.972(2)–2.014(2), Cu–O(PO₄) 2.194(2)–2.215(2). d) Cu–Cu 3.2959(5)–3.3217(5), Cu–O(alkoxide) 1.907(2)–1.975(2), Cu–N 1.965(2)–2.000(2), Cu–Br 2.8243(5)–2.8851(5). e) Cu–Cu 3.3192(5)–3.3612(5), Cu–O(alkoxide) 1.909(2)–1.969(2), Cu–N 1.959(2)–1.993(2), Cu–I 3.0442(5)–3.1308(4).

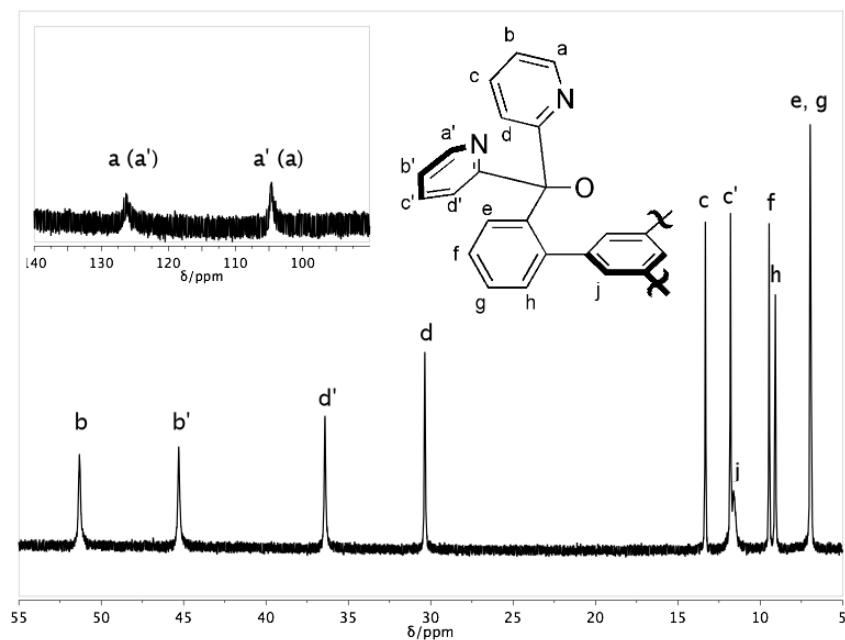


Figure 7. ^1H NMR spectrum of **2•3OTf** in CD_3CN at 25 $^\circ\text{C}$.

Table 1. Signal assignments, shifts, and relaxation times of the ^1H NMR spectrum of **2•3OTf**.

| H | δ (ppm) | T1 (ms) | T2 (ms) |
|---------|----------------|---------|---------|
| a or a' | 126.72 | 3 | 1 |
| a or a' | 104.99 | 4 | 1 |
| b | 51.44 | 27 | 7 |
| b' | 45.43 | 20 | 8 |
| d' | 36.53 | 40 | 11 |
| d | 30.42 | 56 | 14 |
| c | 13.34 | 91 | 20 |
| c' | 11.81 | 67 | 20 |
| j | 11.61 | 8 | 5 |
| f | 9.47 | 98 | 20 |
| h | 9.08 | 46 | 18 |
| g | 6.96 | 105 | 19 |
| e | 6.91 | 32 | 19 |

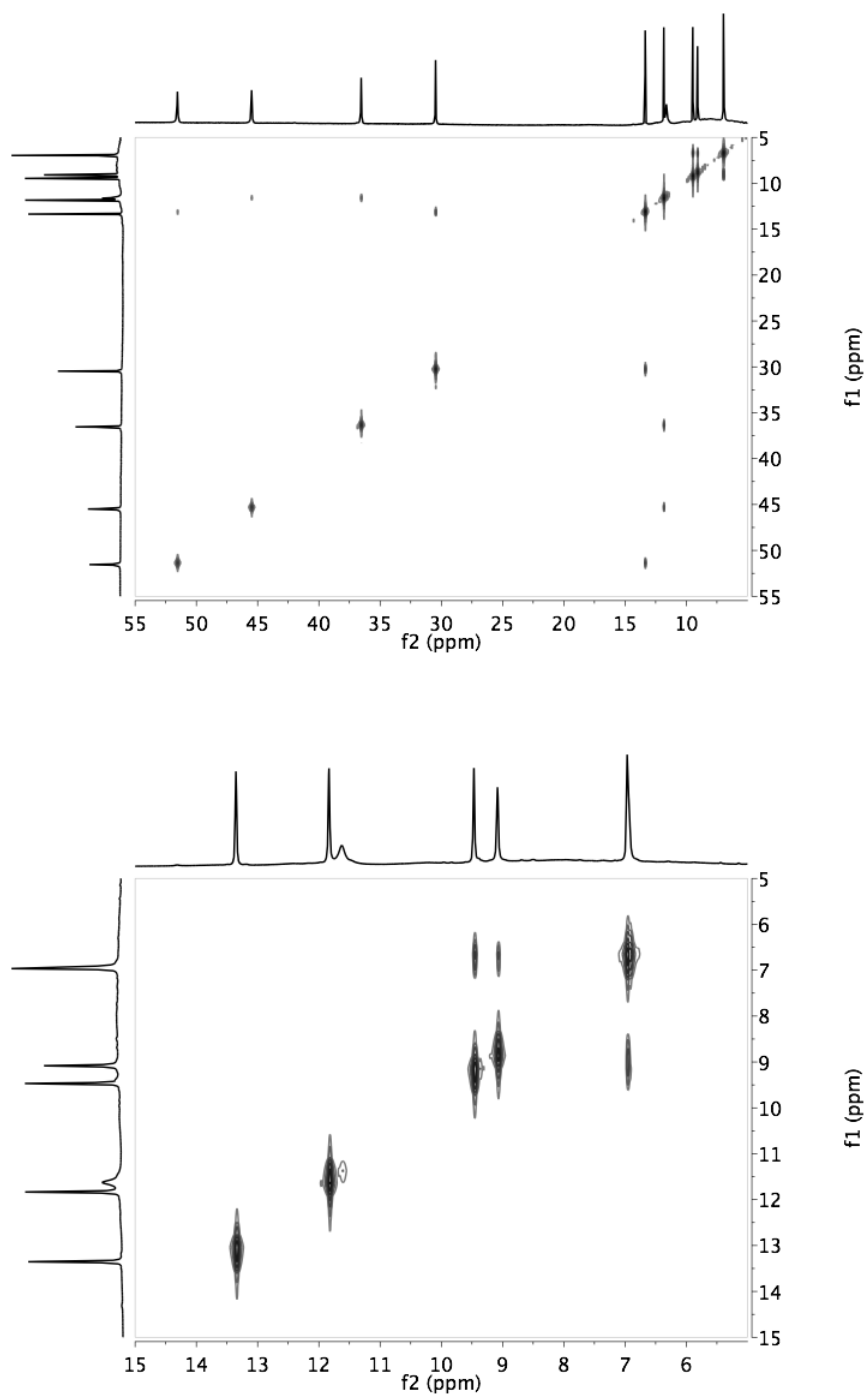


Figure 8. gCOSY NMR spectra of **2•3OTf** in CD_3CN at 25°C .

To test the lability of the coordinated anions, a solution **2•3OTf** in CD_3CN was titrated with $n\text{Bu}_4\text{NX}$ ($\text{X} = \text{Br}, \text{I}$) (Scheme 4). Addition of less than one equivalent of halide led to

gradual changes in the ^1H NMR spectra of the mixture. After the addition of one equivalent of $n\text{Bu}_4\text{NX}$, the spectra of the mixture remain unchanged even upon adding three equivalents of halide. This behavior suggests that only one halide ion can bind to the $[\text{Cu}_3(\text{OR})_3]$ cluster. X-ray diffraction studies of single crystals of **2**•**Br**•**2OTf** and **2**•**I**•**2OTf** confirm that a single halide atom bridges the three copper centers of each cluster, with the triflate anions remaining outer sphere (Figs. 9 and 10). Based on the ^1H NMR spectra, it is likely that these halide-capped structures are preserved in acetonitrile solution. Similar halide-bridged clusters have previously been observed in tricopper(II) complexes of other ligand systems.¹¹

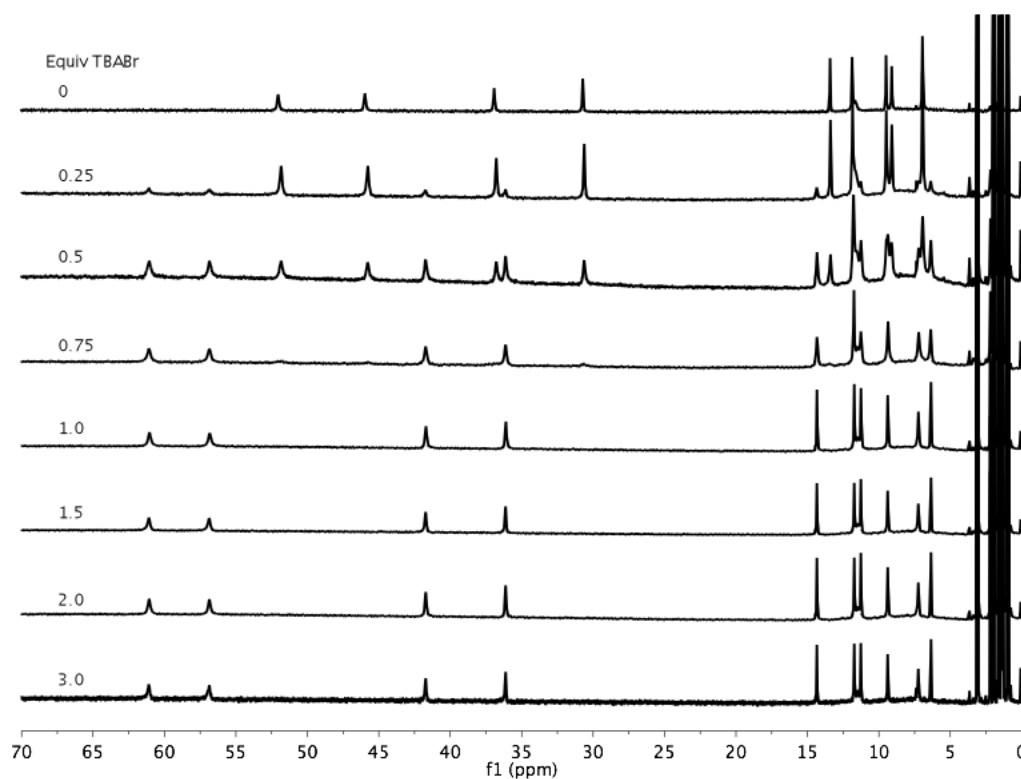


Figure 9. Room temperature ^1H NMR spectra of reactions mixtures upon addition of $n\text{Bu}_4\text{NBr}$ to a CD_3CN solution of **2**•**3OTf**. Four broad signals downfield of 70 ppm not shown for clarity.

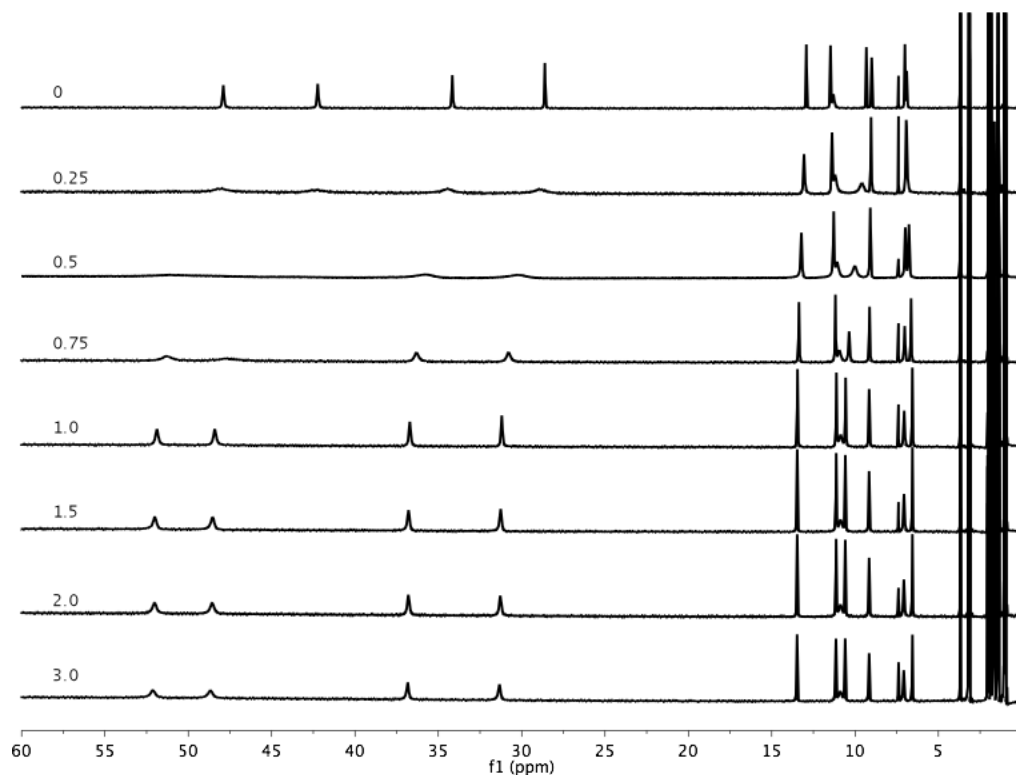
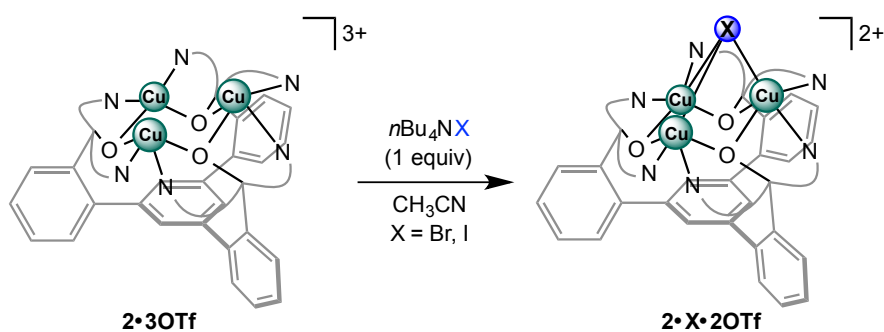


Figure 10. ^1H NMR spectra taken at 65 °C of reaction mixtures upon addition of $n\text{Bu}_4\text{NI}$ to a CD_3CN solution of **2•3OTf**. Two broad signals downfield of 60 ppm not shown for clarity.



Scheme 4. Synthesis of **2•X•2OTf** (X = Br, I).

2.3 Magnetic susceptibility and EPR studies of tricopper(II) complexes

Alkoxo-bridged tricopper(II) clusters with similar $[\text{Cu}_3(\text{OR})_3]$ motifs are known, but generally form via self-assembly of mononuclear copper(II) moieties.^{11a, 12} The magnetic

behavior of these complexes has been studied because spin frustrated triangular complexes may exhibit interesting ground states. It has been shown that varying the anion bridges of linear¹³ and triangular¹⁴ trinuclear copper(II) complexes changes the magnetic coupling, but no systematic study has been made of these effects on μ -alkoxo-bridged trimers lacking a strongly μ_3 -coordinated ligand.^{11a, 15} Since the synthesis of anion variants of the tricopper(II) complexes supported by the trinucleating ligand L described above is facile, a magnetostructural investigation of the effect of the capping anion the $[\text{Cu}_3\text{O}_3\text{N}_6]$ core was performed.

The variable temperature magnetic susceptibilities of compounds **2** were studied, and plots of $\chi_{\text{M}}T$ vs. T are shown in Figure 11. For **2•PO₄**, the $\chi_{\text{M}}T$ value at 300 K is close to $1.2 \text{ cm}^3 \text{ mol}^{-1} \text{ K}$ as expected for three nearly independent $S = 1/2$ centers. The room temperature $\chi_{\text{M}}T$ values for the other complexes are below $1.2 \text{ cm}^3 \text{ mol}^{-1} \text{ K}$ due to antiferromagnetic exchange between the copper centers. The slope of these curves decreases at low temperatures, with most approaching a plateau around $\chi_{\text{M}}T = 0.4 \text{ cm}^3 \text{ mol}^{-1} \text{ K}$, which agrees with the spin-only value for an $S = 1/2$ system. When cooled below 20 K, **2•3OTf** and **2•3BF₄** have $\chi_{\text{M}}T$ values below $0.4 \text{ cm}^3 \text{ mol}^{-1} \text{ K}$, indicating intermolecular antiferromagnetic interactions.^{6d, 11c, 12b}

The intramolecular exchange coupling was modeled for a triangle of $S = 1/2$ centers, and the energies of the spin states of the systems were calculated using the isotropic spin Hamiltonian (Eq. 1). The fits were not significantly improved by varying two coupling constants. As a result, it was assumed that $J = J_{13}$ in an approximately equilateral arrangement of the copper(II) centers. Application of the Van Vleck equation yielded the magnetic susceptibility equation (Eq. 2).¹⁶ The fitted magnetic susceptibility parameters for

each complex are shown in Table 2. Except for **2**·**3BF₄**,¹⁷ the fits ($R \sim 10^{-4}$)¹⁸ were obtained by varying only J , g , and the Curie-Weiss parameter θ .¹⁹

$$H = -2J[(S_1S_2) + (S_2S_3)] - 2J_{13}(S_3S_1) \quad (1)$$

$$\chi_M = \frac{Ng^2\beta^2}{4k(T-\theta)} \left[\frac{5 + \exp(-3J/kT)}{1 + \exp(-3J/kT)} \right] \quad (2)$$

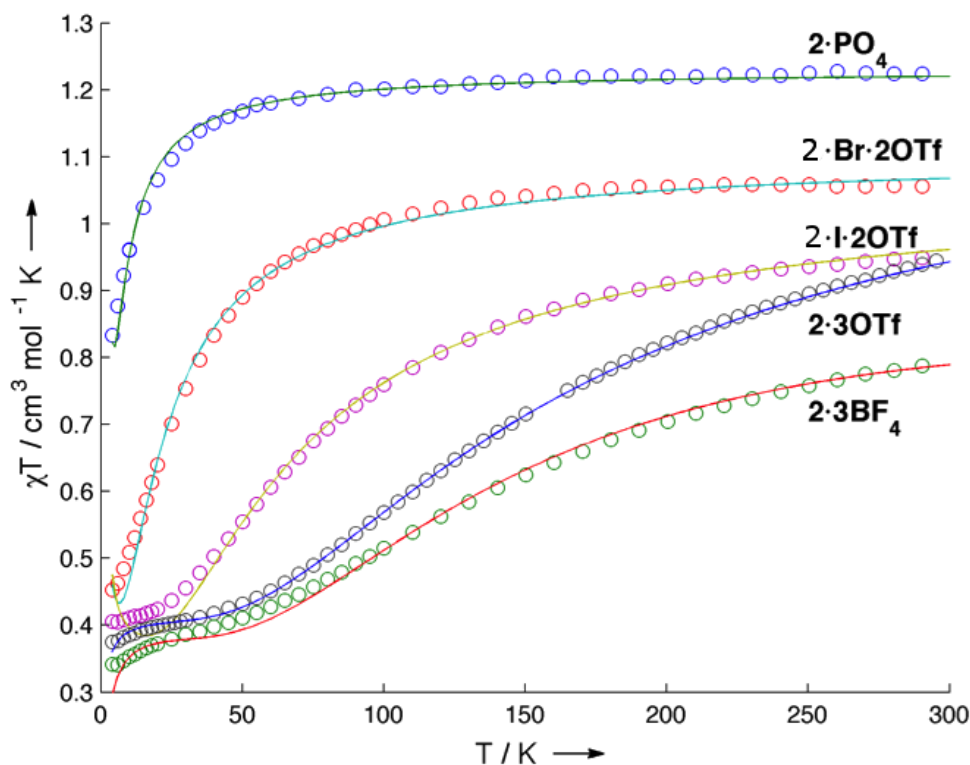


Figure 11. Plots of $\chi_M T$ vs. T for compounds **2** at an applied field of 0.5 T. Solid lines represent the best fits obtained.

The above data show that the antiferromagnetic exchange between spins varies considerably with the character of the coordinated anion. Triangular copper(II) complexes that couple through μ_3 -hydroxy or μ_3 -oxo groups display the strongest antiferromagnetic interactions in structures with large Cu–O–Cu angles, where the bridged clusters are more

planar.^{14a, 14b, 15, 20} Since compounds **2** contain more weakly coordinated capping anions, exchange between copper(II) centers is expected to occur primarily via the μ -alkoxo moieties. This is consistent with the fact that complexes **2•Br•2OTf** and **2•I•2OTf** display antiferromagnetic exchange and have longer Cu–halide bond lengths (by ~ 0.4 Å) compared to trinuclear copper complexes with μ_3 -halide ligands in which ferromagnetic exchange is proposed to occur via the μ_3 -halide.^{14b} Furthermore, the complexes containing the least coordinating anions in the series, **2•3OTf** and **2•3BF₄**, show the largest exchange. The facially coordinated capping ligand distorts the geometry of the [Cu₃(OR)₃] core and changes the Cu–O–Cu angles (Table 2). As the capping ligand binds more strongly, the [Cu₃(OR)₃] core distorts from a planar geometry by decreasing the Cu–O–Cu angles; this correlates with a weakening of antiferromagnetic exchange.

Table 2. Magnetic susceptibility and structural parameters.

| Compound | Cu–O–Cu | J | g | θ [K] |
|--------------------------|-------------|---------------------|------|--------------|
| | Angle [°] | [cm ^{−1}] | | |
| 2•PO₄ | 114.6–118.5 | −2.7 | 2.09 | 1.7 |
| 2•3OTf | 125.9–126.5 | −52.0 | 2.10 | −0.6 |
| 2•3BF₄ | -- | −52.2 | 2.10 | −1.6 |
| 2•I•2OTf | 116.7–120.8 | −22.0 | 1.95 | 1.0 |
| 2•Br•2OTf | 116.1–118.5 | −7.3 | 1.98 | 0.8 |

This behavior is consistent with the solid- and solution-state EPR spectra of compounds **2**. The EPR spectrum of **2•3OTf** in ethanol solution at 10 K (Fig. 12) shows a feature at around $g = 2$ arising from the doublet ground state. The EPR spectra of **2•3BF₄**, **2•I•2OTf**, and **2•Br•2OTf** are similar, with varying amounts of broadness (see experimental section). However, the EPR spectrum of **2•PO₄** shows an additional broad feature at around 1700 G (Fig. 12). The low-field signal is characteristic of a $S = 3/2$ excited state.²¹ As the temperature increases, the intensity of the low-field signal increases relative to that of the higher-field feature (Fig. 13), suggesting a spin equilibrium between the quartet and doublet spin states, with the doublet state as the ground state in agreement with the small antiferromagnetic exchange interaction determined from the magnetic susceptibility data (Table 2). The variation in EPR spectra between **2•3OTf** and **2•PO₄** is explained by the antiferromagnetic exchange between copper centers. Since $J = -2.7 \text{ cm}^{-1}$ in **2•PO₄**, the $S = 3/2$ state is thermally populated even at 10 K and EPR transitions within this quartet state can be observed. In contrast, at the same temperatures no low field EPR signals are observed in the other copper(II) complexes due to the larger antiferromagnetic exchange and doublet-quartet state energy splittings.

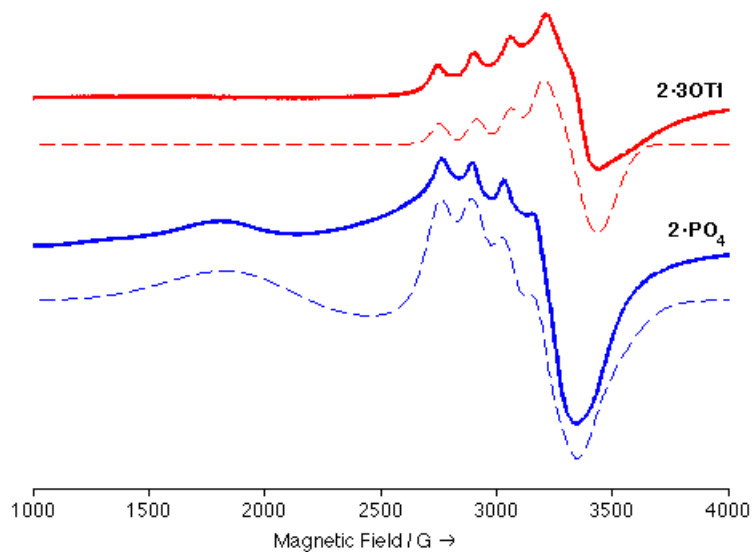


Figure 12. Experimental (—) and simulated (---) X-band EPR spectra of **2•3OTf** and **2•PO₄** in ethanol solution at 10 K. Simulated parameters: **2•3OTf**: $g_{\perp} = 1.98$, $g_{\parallel} = 2.24$, and $A_{\parallel} = 0.015 \text{ cm}^{-1}$. **2•PO₄** was simulated as two systems: a) $g_{\perp} = 2.08$, $g_{\parallel} = 2.24$, $A_{\perp} = 0.011 \text{ cm}^{-1}$, $A_{\parallel} = 0.014 \text{ cm}^{-1}$ and b) $g_{\perp} = 3.40$, $g_{\parallel} = 2.00$, $A_{\perp} = 0.007 \text{ cm}^{-1}$, and $A_{\parallel} = 0.001 \text{ cm}^{-1}$.

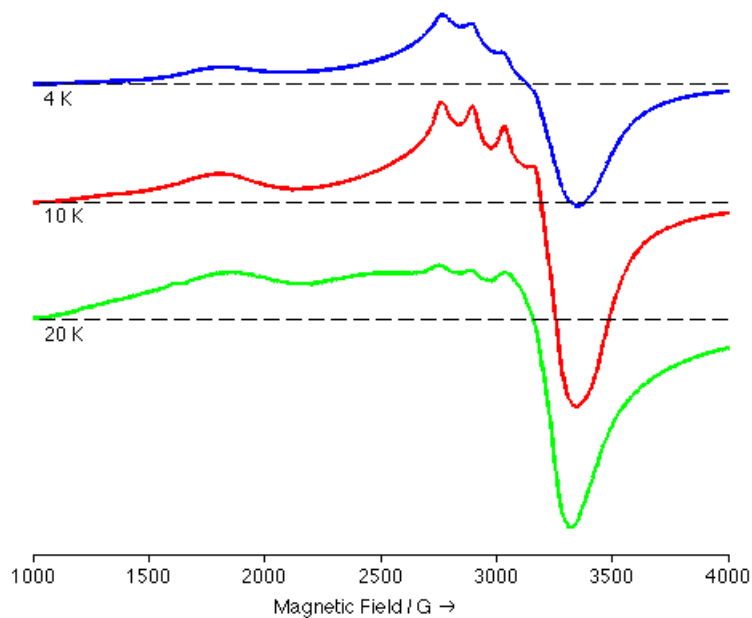


Figure 13. EPR spectra of **2•PO₄** in ethanol solution at 4, 10, and 20 K.

A linear dependence of the exchange interactions of di-hydroxo-bridged copper(II) dimers with the Cu–O–Cu angles has been reported.²² Similar trends extended to more complex systems have been complicated by the presence of multiple exchange pathways. Nevertheless, a non-linear trend has been reported for the Cu–(μ_3 -X)–Cu angle for μ_3 -bridged trimers.^{14b, 14c} The present compounds allow systematic magnetostructural study. When the exchange parameters of compounds **2** are plotted against the average Cu–O–Cu angle in the respective structure, the data indeed follow an approximately linear trend (Fig. 14). This dependence also holds when the available structural and magnetic data from other μ -alkoxo and μ -hydroxo copper(II) trimers of pseudo- C_3 symmetry are included.^{6d, 11a, 12b, 23} This behavior reflects the exchange through the μ_2 -O donors rather than the weakly coordinated capping ligands; the exchange parameters for tricopper systems with μ_3 -hydroxy or μ_3 -oxo ligands do not lie along this trend. It is noteworthy that the linear trend holds despite significant variations in the nature of the non-bridging ligands (pyridines, alkyl amines, pyrrolides, and alkoxides). This magnetostructural behavior suggests that, as in hydroxo-bridged dimers, there is a Cu–O–Cu angle at which the copper centers switch from antiferromagnetic to ferromagnetic coupling. Such distorted structures may be difficult to access, however.

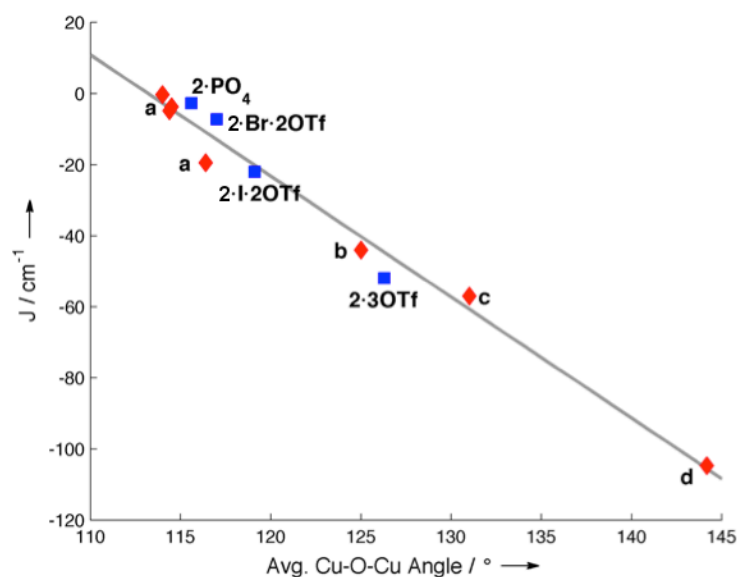
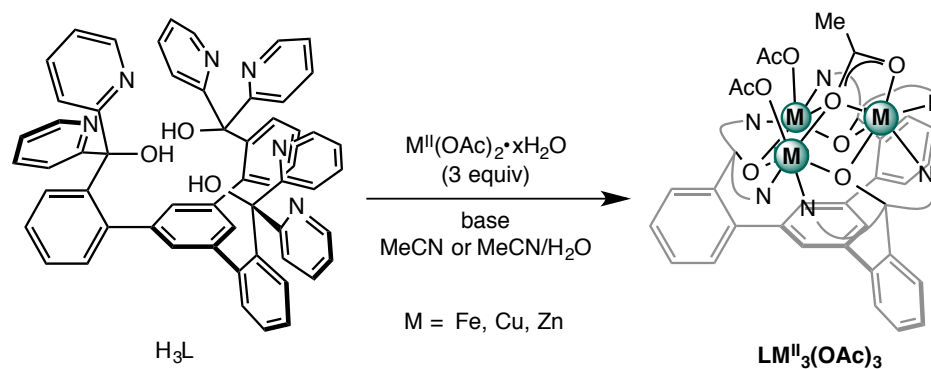


Figure 14. J vs. bridge angle (ϕ) for a series of alkoxo- or hydroxo-bridged copper(II) trimers. (■) This work. (♦) (a) Ref. 11a (b) Ref. 6d (c) Ref. 12b (d) Ref. 23. Straight line was calculated from $J = -3.41\phi + 386 \text{ cm}^{-1}$.

2.4 Trinuclear complexes of other first row transition metals

To further investigate the metal coordination potential of H_3L and its control over cluster nuclearity, trinuclear complexes of L containing other first row transition metals were targeted. Metallation studies were initiated with the acetate salts of the first-row metals Fe^{II} , Cu^{II} , and Zn^{II} in the presence of base (Scheme 5). Addition of three equivalents of solid $\text{M}^{\text{II}}(\text{OAc})_2 \cdot x\text{H}_2\text{O}$ to a suspension of H_3L in acetonitrile or a mixture of acetonitrile/water followed by three equivalents of a base such as sodium hydroxide or triethylamine resulted in complete dissolution of insoluble materials within 12 hours. Analytically pure crystals were obtained by vapor diffusion of diethyl ether into dichloromethane or chloroform solutions of the reaction products.



Scheme 5. Synthesis of trinuclear complexes of Fe^{II} , Cu^{II} , and Zn^{II} . Related complexes of Mn^{II} , Co^{II} , and Ni^{II} also synthesized by Mr. Jacob Kanady.

Single crystal X-ray diffraction (XRD) studies demonstrate the trinucleating nature of the deprotonated H_3L framework to give complexes generally formulated as $\text{LM}_3(\text{OAc})_3$ (Figs. 15–17). The three metal centers are bridged by three alkoxides forming a six membered ring, and the pendant pyridines coordinate with the two pyridines of each dipyriddy moiety bound to adjacent metal centers. The coordination environment is completed by acetate counterions. Systematically changing the nature of the metal centers does not disrupt the trinuclear core, but changes the binding mode of the acetates. Three capping acetates are present for $\text{LFe}_3(\text{OAc})_3$; two acetates bind in monodentate and one in bidentate fashion (Fig. 15). The bidentate acetate bridges two or three metal centers via a μ_2 -oxygen atom. For $\text{M} = \text{Cu}$ and Zn , single crystal XRD studies show two acetates bound to the trimetallic core (Figs. 16, 17). However, a third outer sphere acetate required for charge balance could not be located due to disorder. This change in coordination mode may be due to the smaller size of $\text{Cu}(\text{II})$ and $\text{Zn}(\text{II})$ hindering the binding of a third acetate.

^1H NMR spectroscopy and mass spectrometry studies confirm that the trinuclear cores of the complexes are maintained in solution. The ^1H NMR spectra of $\text{LM}^{\text{III}}_3(\text{OAc})_3$ ($\text{M} = \text{Fe–Zn}$) display fourteen resonances, with chemical shifts between -20 and 160 ppm for the

paramagnetic species.²⁴ Thirteen peaks correspond to protons on framework L, consistent with the C_3 -geometry observed in the solid-state. The single peak assigned to the acetate counterions is indicative of fluxional processes that exchange the capping ligands on the NMR time scale.

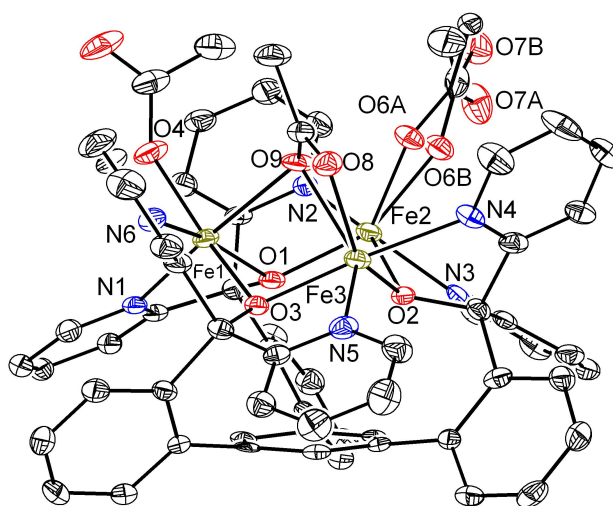


Figure 15. Structural drawing of $LFe_3(OAc)_3$ with 50% thermal probability ellipsoids. One acetate is disordered over two populations, denoted A and B.

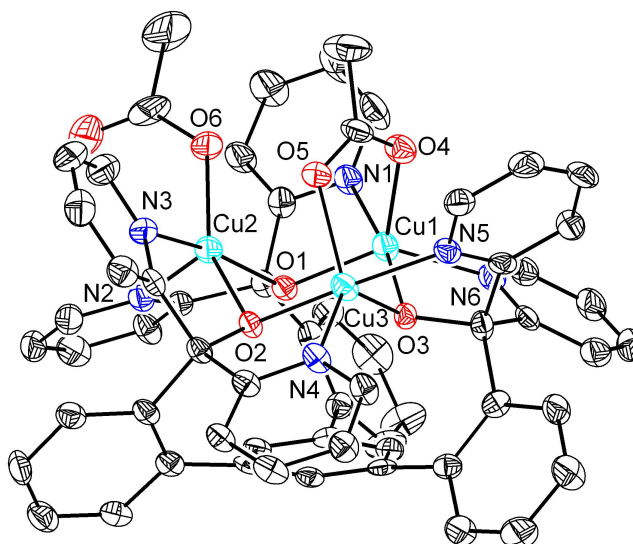


Figure 16. Structural drawing of $LCu_3(OAc)_3$ with 50% thermal probability ellipsoids.

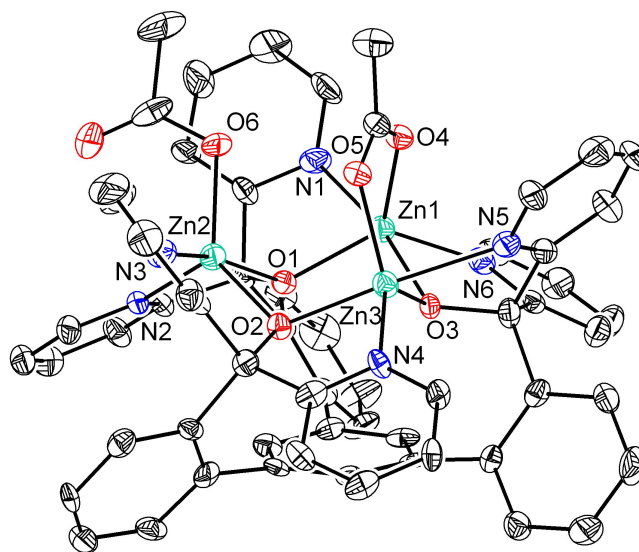


Figure 17. Structural drawing of $\text{LZn}_3(\text{OAc})_3$ with 50% thermal probability ellipsoids.

The magnetism of triangular clusters has been studied in the context of spin frustration and molecular magnets.^{14c, 25} Although several alkoxo-bridged Ni^{II}_3 and Cu^{II}_3 complexes have been studied,^{11a, 26} there have been fewer investigations of Mn^{II}_3 , Fe^{II}_3 , and Co^{II}_3 cores. Triangular clusters of manganese and iron more commonly contain higher oxidation state metal centers.²⁷ The present $\text{LM}_3(\text{OAc})_3$ family provides an opportunity to systematically study the magnetic interactions of several divalent transition metals in a single trinuclear system, allowing for better understanding of the magnetostructural characteristics of trinuclear complexes.

Magnetic susceptibility measurements were performed on powdered crystalline samples of $\text{LM}_3(\text{OAc})_3$ ($\text{M} = \text{Mn}, \text{Fe}, \text{Co}, \text{Ni}, \text{Cu}$) in the temperature range 4–300 K. At room temperature, the $\chi_{\text{M}}T$ values approach 12.0, 9.0, 6.7, 3.3, and 1.0 $\text{cm}^3 \text{K mol}^{-1}$, respectively (Fig. 18). The difference between these and the spin-only values may be due to spin-orbit coupling and population of excited states.²⁸ Upon cooling, the $\chi_{\text{M}}T$ values decrease gradually and then drop sharply below 40 K, indicating the presence of

antiferromagnetic exchange interactions. With the exception of the $\chi_M T$ values of $\text{LCu}_3(\text{OAc})_3$, which approach a plateau near the expected value for the spin-only $S = 1/2$ state (ca. $0.4 \text{ cm}^3 \text{ K mol}^{-1}$), the $\chi_M T$ plots do not approach obvious limiting values at 4 K.

To determine the magnitude of exchange between neighboring metal centers, the magnetic behavior of the compounds was analyzed using the isotropic spin Hamiltonian (Eq. 3) considering the two exchange pathways of an isosceles triangular arrangement. Application of the Van Vleck equation according to the Kambe vector method¹⁶ yields the magnetic susceptibility equation (Eq. 4).

$$H = -2J[(S_1 S_2) + (S_2 S_3)] - 2J_{13}(S_3 S_1) \quad (3)$$

$$\chi_M = \frac{N_A \beta^2 g^2}{3kT} \frac{\sum S'(S'+1)(2S'+1)\Omega(S')\exp(-W(S')/kT)}{\sum (2S'+1)\Omega(S')\exp(-W(S')/kT)} \quad (4)$$

The Curie-Weiss parameter θ was included to account for possible intermolecular interactions.^{22a} The fits were not appreciably improved when modeling two J values instead of one; as a result, the magnetism data were simulated for an equilateral triangle arrangement of spins, despite small anisotropies in the solid-state geometries.²⁹ In accordance with the $\chi_M T$ plots, the simulated parameters show that compounds $\text{LM}_3(\text{OAc})_3$ display weak antiferromagnetic exchange coupling (Table 3). Except for $\text{LCu}_3(\text{OAc})_3$ ($J = -13.7 \text{ cm}^{-1}$), the best fits were obtained with $|J| < 2 \text{ cm}^{-1}$. Although the ground states are predicted to be $S = 0$ or $S = 1/2$ for an equilateral triangle of antiferromagnetically coupled ions, such small J values indicate that higher spin states are thermally populated even at low temperatures.³⁰ For these complexes, the presence of spin equilibria between these states is consistent with the observation that no limiting values of $\chi_M T$ are reached at 4 K.

Due to the presence of multiple types of bridging ligands, it is difficult to definitively assign the exchange pathways in these $\text{LM}_3(\text{OAc})_3$ complexes.³¹ Since there are few alkoxo-bridged trinuclear complexes containing metals other than Cu^{II} —and none with Fe^{II} to our knowledge—there is yet no clear correlation between the J constants and common structural parameters such as M–M distances or M–O–M angles.^{11c} Previously studied acetate-bridged trinuclear clusters of divalent metals have been shown to have similar intramolecular exchange interactions.³² Alkoxo- and phenoxo-bridged tricobalt(II), trinickel(II), and triiron(III) clusters all show small antiferromagnetic coupling.³³ While there are no examples of Mn^{II} bridged by alkoxides, amido-bridged³⁴ or carboxylate-bridged³⁵ Mn^{II} clusters also demonstrated antiferromagnetic coupling of magnitudes similar to $\text{LMn}_3(\text{OAc})_3$.

Table 3. Magnetic susceptibility parameters.³⁶

| Compound | $J(\text{cm}^{-1})$ | g | $\theta(\text{K})$ | $R(\times 10^{-4})$ |
|------------------------------|---------------------|------|--------------------|---------------------|
| $\text{LMn}_3(\text{OAc})_3$ | −1.1 | 1.97 | 0.53 | 10 |
| $\text{LFe}_3(\text{OAc})_3$ | −1.4 | 1.99 | 2.35 | 1.6 |
| $\text{LCo}_3(\text{OAc})_3$ | −1.2 | 2.30 | 0.23 | 1.9 |
| $\text{LNi}_3(\text{OAc})_3$ | −1.2 | 2.11 | 0.74 | 0.4 |
| $\text{LCu}_3(\text{OAc})_3$ | −13.7 | 2.01 | 0.75 | 12 |

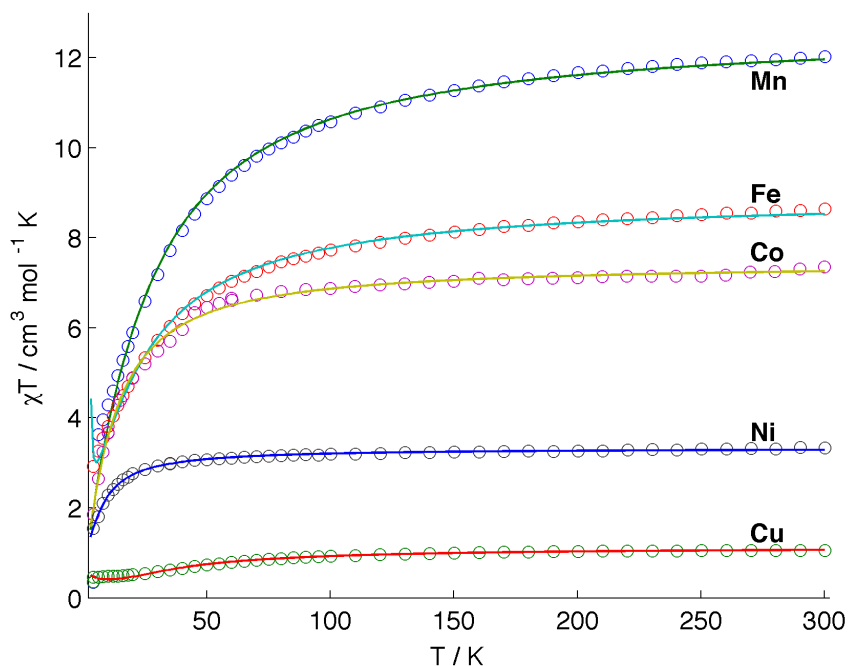


Figure 18. Plots of $\chi_M T$ vs. T for reported trinuclear complexes $LM^{\text{II}}_3(\text{OAc})_3$. Solid lines show the best fits obtained. Compounds $M = \text{Mn}$, Co , and Ni synthesized by Jacob Kanady.

Conclusions

In summary, a trinucleating ligand containing six pyridine and three alcohol donors on a 1,3,5-triarylbenzene platform has been used to assemble a tricopper(I) complex which, upon reaction with O_2 , leads to alcohol deprotonation and oxidation of copper. The C_3 -symmetric trinuclear core is robust by spectroscopy and chemical reactivity. Changing the capping anion facially coordinated to the tricopper(II) cluster alters the Cu-O-Cu angle to lead to changes of the antiferromagnetic exchange coupling between neighboring copper ions, providing a strategy for tuning the magnetism of the trinuclear core. The observed linear trend between the antiferromagnetic exchange coupling and the Cu-O-Cu angle holds for a variety of previously reported trinuclear species providing an extension to more

complex systems of the classical dependence observed for di-hydroxo-bridged copper(II) dimers. Complexes of the present ligand provide a versatile framework for mechanistic studies related to O₂ and other small molecule reactivity at trinuclear centers and current studies are targeted toward further exploring Cu₃-O₂ chemistry as well as a variety of first row transition metal trinuclear clusters. These trinuclear clusters may also serve as versatile precursors to more complex multimetallic structures, as will be discussed in the next few chapters.

Experimental Details

General Considerations.

Unless stated otherwise, all synthetic manipulations were carried out using standard Schlenk techniques under a nitrogen atmosphere, or in a M. Braun glovebox under an atmosphere of nitrogen. Reactions were carried out in oven-dried glassware cooled under vacuum. Anhydrous THF was purchased from Aldrich in 18 L Pure-PacTM containers. Anhydrous dichloromethane, acetonitrile, diethyl ether, and THF were purified by sparging with nitrogen for 15 minutes and then passing under nitrogen pressure through a column of activated A2 alumina (Zapp's). All non-dried solvents used were reagent grade or better. All NMR solvents were purchased from Cambridge Isotope Laboratories, Inc. NMR solvents were dried as follows: CD₂Cl₂ and CD₃CN over calcium hydride, and *d*₆-acetone over calcium sulfate. All NMR solvents were degassed by three freeze-pump-thaw cycles and vacuum-transferred prior to use. ¹H NMR and ¹³C NMR spectra were recorded on a Varian 300 MHz instrument or a Varian 500 MHz instrument or a Varian 600 MHz instrument, with shifts reported relative to the residual solvent peak. ¹⁹F NMR spectra were referenced to an external standard of CFCI₃ (0 ppm). Elemental analyses were performed

by Midwest Microlab, LLC, Indianapolis, IN. High resolution mass spectra (HRMS) were obtained at the California Institute of Technology Mass Spectral Facility. UV–Vis spectra were taken on a Varian Cary 50 spectrophotometer using a quartz crystal cell. IR spectra were recorded on a Nicolet 6700 FT-IR spectrometer using a solution cell with CaF₂ plates.

Unless indicated otherwise, all commercial chemicals were used as received. Copper(II) hydroxide phosphate, benzoin, and lithium bis(trimethylsilyl)amide was purchased from Aldrich. Di(2-pyridyl)ketone was purchased from Aldrich or from Frontier Chemicals. Copper(II) triflate and copper(II) tetrafluoroborate hydrate were purchased from Strem. Copper(I) triflate toluene dimer,³⁷ tetrakis(acetonitrile)copper(I) perchlorate,³⁸ and 1,3,5-tris(2-bromophenyl)benzene⁷ were prepared according to literature procedures.

For ¹H NMR spectra discussed below, refer to Fig. 19 for signal assignments. In some of the compounds, the protons of the two pyridine moieties are related by symmetry and protons assigned as (a, b, c, d) will refer to protons (a', b', c', d') as well.

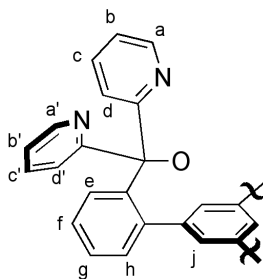


Figure 19. Proton assignments for complexes of H₃L.

Synthesis of 1, 3, 5-Tris(2-di(2'-pyridyl)hydroxymethylphenyl)benzene (H₃L). In the glovebox, a Schlenk flask equipped with a stir bar was charged with 1,3,5-tris(2-bromophenyl)benzene (4.0 g, 7.37 mmol) and diethyl ether (80 mL). On the Schlenk line, the suspension was cooled to –78 °C, and *t*-BuLi (1.61 M, 27.9 mL, 44.9 mmol) was added slowly via syringe. The mixture was stirred for 15 min. at –78 °C, and a solution of di(2-

pyridyl)ketone (4.21 g, 22.8 mmol) in diethyl ether (30 mL) was added slowly via cannula transfer. The reaction mixture was allowed to warm to room temperature and stirred for 8 h under nitrogen. The mixture was quenched with methanol (30 mL), and the orange solution was diluted with water and extracted with dichloromethane. The organic layer was washed with brine and dried over magnesium sulfate, then filtered. The solvent was removed under reduced pressure, and the yellow residue was recrystallized from acetone/dichloromethane to yield the product as a white solid (2.65 g, 42%). ^1H NMR (300 MHz, CDCl_3 , 25 °C): δ 8.41 (d, J = 6 Hz, 6 H, *a*), 7.66 (bs, 6 H, *c*), 7.55 (bs, 6 H, *d*), 7.25 (t, J = 7.5 Hz, 3 H, *f*), 7.13 (t, J = 7.5 Hz, 3 H, *g*), 7.02 (bs, 6 H, *b*), 6.81 (bs, 3 H, *e*), 6.74 (J = 6 Hz, 3 H, *h*), 6.37 (bs, 3 H, OH), 6.14 (bs, 3 H, *j*). ^{13}C NMR (CDCl_3): δ 164.0, 147.2, 144.0, 143.5, 139.5, 136.2, 133.2, 129.2, 126.6, 126.1, 123.7, 121.9, 81.9. IR (CH_2Cl_2): 3330, 1751 cm^{-1} . HRMS (FAB+): calcd. for $\text{C}_{57}\text{H}_{43}\text{N}_6\text{O}_3$: 859.3397; found: 859.3436 [M+H].

Synthesis of $[(\text{H}_3\text{L})\text{Cu}_3](3\text{OTf})$ (1•3OTf**).** In the glovebox, a 20-mL scintillation vial equipped with a stir bar was charged with a suspension of **H₃L** (0.100 g, 0.116 mmol) in acetonitrile (10 mL). A solution of $[\text{CuOTf}]_2 \cdot \text{toluene}$ (0.090 g, 0.175 mmol) in acetonitrile (5 mL) was added slowly. The resulting yellow solution was stirred for 15 min. at room temperature, and the solvent was removed under reduced pressure to yield a yellow-orange solid (172 mg, 85%). ^1H NMR (300 MHz, CD_3CN): δ 8.32 (bs, 6 H, *a*), 7.81 (bs, 12 H, *c* & *d*), 7.45 (t, J = 7.5 Hz, 3 H, *f*), 7.23 (m, 6 H, *g*), 7.23 (bs, 3 H, *b*), 6.87 (bs, 3 H, *e*), 6.74 (bs, 3 H, *h*), 6.22 (bs, 3 H, OH), 5.23 (bs, 3 H, *j*). ^{13}C NMR (125.7 MHz, CD_3CN): δ 163.7, 149.5, 144.1, 142.8, 138.9, 135.1, 131.7, 129.8, 129.1, 127.9, 124.4, 123.8, 121.3, 82.9. ^{19}F NMR (282.3 MHz, CD_2Cl_2): δ 78.97. IR (CH_2Cl_2): 3337, 1600 cm^{-1} . UV-vis

(CH₃CN, λ_{max} (ϵ)): 260 (35,500 M⁻¹ cm⁻¹); 381 (610 M⁻¹ cm⁻¹) nm. Anal. Calcd. for C₇₂H₆₀Cu₃F₉N₁₂O₁₂S₃ (6 CH₃CN): C, 49.61; H, 3.47; N, 9.64. Anal. Calcd. for C₆₆H₅₁Cu₃F₉N₉O₁₂S₃ (3 CH₃CN): C, 48.93; H, 3.17; N, 7.78. Found: C, 47.25; H, 3.16; N, 7.52.

Synthesis of [(H₃L)Cu₃](3ClO₄) (1•3ClO₄**).** In the glovebox, a 20-mL scintillation vial equipped with a stir bar was charged with a suspension of **H₃L** (0.050 g, 0.058 mmol) in acetonitrile (5 mL). While stirring, a solution of tetrakis(acetonitrile) copper(I) perchlorate (0.057 g, 0.175 mmol) in acetonitrile (5 mL) was added, and the yellow solution was stirred at room temperature for 5 h. The reaction mixture was concentrated under vacuum to a volume of 5 mL, and a yellow solid was then precipitated out upon addition of diethyl ether (10 mL). The yellow solid was collected and washed with diethyl ether, then extracted with dichloromethane (10 mL). The solvent was removed under reduced pressure from the yellow dichloromethane extract to yield the product as a yellow solid (57 mg, 61%). ¹H NMR spectra in CD₃CN and CD₂Cl₂ match that of **1•3OTf**. IR (CH₂Cl₂): 3393, 1599, 1103 cm⁻¹. UV-vis (CH₃CN, λ_{max} (ϵ)): 262 (42,000 M⁻¹ cm⁻¹); 378 (670 M⁻¹ cm⁻¹) nm. Anal. Calcd. for C₆₉H₆₀Cl₃Cu₃N₁₂O₁₅: C, 51.98; H, 3.79; N, 10.54. Found: C, 51.37; H, 3.69; N, 10.30.

Synthesis of [(L)Cu₃](3OTf) (2•3OTf**).**

Method A: In the glovebox, a 20-mL scintillation vial equipped with a stir bar was charged with a solution of **H₃L** (0.500 g, 0.582 mmol) in THF (8 mL). The solution was frozen in a cold well. While stirring, a solution of LiHMDS (0.292 g, 1.75 mmol) in THF was added slowly to the thawing solution. The yellow solution was stirred at room temperature for 15 min., then frozen again. A suspension of copper(II) trifluoromethanesulfonate (0.632 g,

1.75 mmol) in 1:1 THF/CH₃CN (4 mL) was added to the thawing solution, and the green suspension was stirred at room temperature for 1 h. The green precipitate was collected on a fritted glass funnel over Celite, and washed with THF, then extracted with acetonitrile. The solution was concentrated under reduced pressure to yield the product as a blue-green solid (0.604 g, 70%). The product can be recrystallized from CH₃CN/THF to yield hexagonal blue green crystals (0.110 g, 13%). ¹H NMR (600 MHz, CD₃CN): δ 126.72 (bs, 3 H, *a/a'*), 104.99 (bs, 3 H, *a/a'*), 51.44 (s, 3 H, *b*), 45.43 (s, 3 H, *b'*), 36.53 (s, 3 H, *d'*), 30.42 (s, 3, *d*), 13.34 (s, 3 H, *c*), 11.81 (s, 3 H, *c'*), 11.61 (bs, 3 H, *j*), 9.46 (s, 3 H, *f*), 9.08 (s, 3 H, *h*), 6.96 (s, 3 H, *e*), 6.91 (s, 3 H, *g*). ¹⁹F NMR (282 MHz, CD₃CN): δ -78.77. UV-Vis (CH₃CN, λ_{max} (ε)): 253 (63,600 M⁻¹ cm⁻¹); 681 (330 M⁻¹ cm⁻¹) nm. HRMS (FAB+): calcd. for C₅₇H₃₉Cu₃N₆O₃ (no ⁻OTf): 1046.0965; found: 1046.0985 [M⁺]; 1195.0427 [M•1OTf]; 1343.9903 [M•2OTf]. Anal. Calcd. for C₆₀H₃₉Cu₃F₉N₆O₁₂S₃: C, 48.24; H, 2.63; N, 5.63. Found: C, 47.91; H, 2.90; N, 5.76.

Method B: In the glovebox, a J Young NMR tube was charged with **1•3OTf** (16.9 mg, 0.01 mmol) in 0.7 mL CD₃CN. On a Schlenk line, the solution was degassed with one freeze-pump-thaw cycle. The solution was frozen again, and the tube was evacuated and put under an atmosphere of O₂. The solution was then allowed to warm up to room temperature. The yellow solution turned green and then darker blue-green over the course of 12 h. The ¹H NMR spectrum matches that of **2•3OTf** prepared in the way described above.

The ¹H NMR spectra of the other derivatives of compound **2** have not been assigned, but are similar to that of **2•3OTf**.

Synthesis of [(L)Cu₃](BF₄)₃ (2•3BF₄**).** Under ambient conditions, a scintillation vial equipped with a stir bar was charged with **H₃L** (0.200 g, 0.233 mmol) and Cu(BF₄)₂•XH₂O (0.193 g, ca. 0.815 mmol). The mixture was suspended in acetonitrile (5 mL), and triethylamine (0.16 mL, 1.16 mmol) was added via syringe. The blue-green mixture was stirred at room temperature for 10 h, and the solvent was removed *in vacuo*. The blue-green residue was washed with THF, then extracted with acetonitrile. The solution was concentrated *in vacuo*, then recrystallized from CH₃CN/Et₂O to yield the product as blue-green crystals of **2•3BF₄•Et₂O** (0.043 g, 13%). ¹H NMR (300 MHz, CD₃CN): δ 125.66 (bs, 3 H), 100.08 (bs, 3 H), 49.31 (s, 3 H), 46.62 (s, 3 H), 37.46 (s, 3 H), 28.93 (s, 3 H), 13.18 (s, 3 H), 11.72 (s, 3 H), 11.30 (s, 3 H), 9.69 (s, 3 H), 9.12 (s, 3 H), 6.85 (s, 3 H), 6.64 (s, 3 H). ¹⁹F NMR (282.3 MHz, CD₃CN): δ -149.25. UV-Vis (CH₃CN, λ_{max} (ε)): 246 (53,300 M⁻¹ cm⁻¹), 730 (336 M⁻¹ cm⁻¹) nm. Anal. Calcd. for C₅₇H₃₉B₃Cu₃F₁₂N₆O₃: C, 52.39; H, 3.01; N, 6.43. Calcd. for C₆₁H₄₉B₃Cu₃F₁₂N₆O₄ (**2•3BF₄•Et₂O**): C, 53.05; H, 3.58; N, 6.08. Found: C, 53.29; H, 3.68; N, 6.13.

Synthesis of [(L)Cu₃](PO₄) (2•PO₄**).** Under ambient conditions, a scintillation vial equipped with a stir bar was charged with **H₃L** (0.200 g, 0.233 mmol) and Cu₂(OH)PO₄ (0.084 g, 0.349 mmol). The mixture was suspended in 2:1 H₂O/acetone (15 mL), and phosphoric acid (85%, 0.016 mL) was added via syringe. The green mixture was stirred for 1 day, then filtered through Celite. The solvent was removed from the green filtrate *in vacuo* to yield the product as a green solid (0.210 g, 79%). ¹H NMR (300 MHz, D₂O): δ 148.94 (bs, 3 H), 101.47 (bs, 3 H), 56.33 (s, 3 H), 50.50 (s, 3 H), 39.66 (s, 3 H), 29.70 (s, 3 H), 13.44 (s, 3 H), 11.19 (bs, 3 H), 10.81 (s, 3 H), 10.21 (s, 3 H), 9.58 (s, 3 H), 6.64 (s, 3 H), 5.76 (s, 3 H). UV-Vis (H₂O, λ_{max} (ε)): 245 (28,500 M⁻¹ cm⁻¹), ~800 (260 M⁻¹ cm⁻¹)

nm. Anal. Calcd. for $C_{57}H_{56}Cu_3N_6O_{18}P_2$ (**2•PO₄•H₃PO₄•6H₂O**): C, 50.80; H, 4.04, N, 6.24. Found: C, 49.91; H, 3.88; N, 6.00. A X-ray diffraction study of a single crystal of **2•PO₄** showed that the compound crystallizes with a disordered amount of H₂O and additional phosphate anions within the unit cell.

Synthesis of [(L)Cu₃]Br(OTf)₂ (2•Br•2OTf**).** Under ambient conditions, a scintillation vial equipped with a stir bar was charged with **2•3OTf** (0.056 g, 0.0372 mmol) in acetonitrile (6 mL). A solution of tetrabutylammonium bromide (0.012 g, 0.0372 mmol) in acetonitrile (2 mL) was added, and the green solution was stirred at room temperature for 3 h. The solvent was removed *in vacuo*, and the green residue was washed with THF, then extracted with acetonitrile. The solution was concentrated to yield the product as a green solid (0.047 g, 89 %). The compound crystallizes from vapor diffusion of THF into a CH₃CN solution of **2•Br•2OTf** with an additional equivalent of THF. ¹H NMR (300 MHz, CD₃CN): δ 154.39 (s, 3 H), 124.72 (s, 3 H), 61.15 (s, 3 H), 56.92 (s, 3 H), 41.73 (s, 3 H), 36.15 (s, 3 H), 14.33 (s, 3 H), 11.73 (s, 3 H), 11.47 (s, 3 H), 11.25 (s, 3 H), 9.38 (s, 3 H), 7.24 (s, 3 H), 6.36 (s, 3 H). ¹⁹F NMR (282.3 MHz, CD₃CN): δ -78.54. UV-Vis (CH₃CN, λ_{max} (ε)): 245 (75,000 M⁻¹ cm⁻¹), 725 (707 M⁻¹ cm⁻¹) nm. Anal. Calcd. for $C_{63}H_{46}BrCu_3F_6N_6O_{10}S_2$ (**2•Br•2OTf•THF**): C, 50.59; H, 3.10; N, 5.62. Found: C, 50.32; H, 3.32; N, 5.41.

Synthesis of [(L)Cu₃]I(OTf)₂ (2•I•2OTf**).** Under ambient conditions, a scintillation vial equipped with a stir bar was charged with **2•3OTf** (0.051 g, 0.034 mmol) in acetonitrile (6 mL). A solution of tetrabutylammonium iodide (0.012 g, 0.034 mmol) in acetonitrile (2 mL) was added, and the green solution was stirred at room temperature for 3 h. The solvent was removed *in vacuo*, and the green residue was washed with THF, then extracted with acetonitrile. The solution was concentrated to yield the product as a green solid that was

recrystallized from CH₃CN/THF to yield hexagonal green crystals (0.032 g, 64 %). ¹H NMR (300 MHz, CD₃CN): δ 141.31 (s, 3 H), 116.58 (s, 3 H), 57.45 (s, 3 H), 53.43 (s, 3 H), 40.13 (s, 3 H), 34.07 (s, 3 H), 14.11 (s, 3 H), 11.57 (s, 3 H), 11.32 (s, 3 H), 10.86 (s, 3 H), 8.30 (s, 3 H), 7.10 (s, 3 H), 6.47 (s, 3 H). ¹⁹F NMR (282.3 MHz, CD₃CN): δ -78.60. UV-Vis (CH₃CN, λ_{max} (ε)): 246 (41,500 M⁻¹ cm⁻¹), 406 (shoulder, 805 M⁻¹ cm⁻¹), 709 (545 M⁻¹ cm⁻¹) nm. Anal. Calcd. for C₅₉H₃₉Cu₃F₆IN₆O₉S₂: C, 48.15; H, 2.67; N, 5.71. Found: C, 48.24; H, 2.70; N, 5.49.

D₃-2'-bromoacetophenone. A Schlenk flask equipped with a stir bar was charged with NaOH (0.03 g) and flame-dried under vacuum. D₂O (8 mL, 400 mmol) and 2'-bromoacetophenone (1.6 mL, 12 mmol) were added via syringe, and the mixture was stirred at room temperature under nitrogen for 40 h. Anhydrous diethyl ether (10 mL) was added, and the organics were extracted, dried over magnesium sulfate, and filtered. The solvent was removed under reduced pressure to yield the product as a colorless oil. ¹H NMR spectroscopy indicated 16% of the doubly deuterated compound. The product was carried on without further purification.

D₃-1,3,5-tris(2-bromophenyl)benzene. A flame-dried Schlenk flask equipped with a stir bar was charged with D₃-2'-bromoacetophenone and then fit with a Teflon stopper. The flask was evacuated for 5 min., then fit with a septum. Trifluoromethanesulfonic acid (0.05 mL) was added via syringe. The yellow-orange mixture was stirred at 130 °C for 14 h, then cooled to room temperature. The mixture was quenched with D₂O (2 mL) and CH₂Cl₂. The organics were extracted, dried over magnesium sulfate, and filtered. The solvent was removed *in vacuo*, and the red residue was taken up in CH₂Cl₂ (5 mL). The product precipitated out of solution was a white solid upon addition of methanol. The solid was

collected on a fritted glass funnel and further washed with methanol, then dried under vacuum (0.896 g, 41%). ^1H NMR spectroscopy indicated 30% of the doubly-deuterated product.

D₃-H₃L. In a glove box, D₃-1,3,5-tris(2-bromophenyl)benzene (0.57 g, 1.05 mmol) was added to a scintillation vial equipped with a stir bar and then suspended in diethyl ether (10 mL). The mixture was frozen in a cold well. To the stirred, thawing mixture, *t*-BuLi (1.61 M in hexanes, 3.97 mL, 6.39 mmol) was added via syringe. The dark red mixture was stirred for 10 min. at room temperature, then frozen again. To the thawing red mixture was added a thawing solution of di(2-pyridyl)ketone in THF (4 mL). The mixture was allowed to warm to room temperature and stirred for 7 h, turning green and then brown. The vial was removed from the glovebox, and the reaction was quenched with water. The precipitated orange solid was collected on a fritted funnel and washed with H₂O and diethyl ether. The solid was dissolved in CH₂Cl₂, and the solution was washed with H₂O and brine. The organic layer was dried over magnesium sulfate and filtered, and the solvent was removed *in vacuo*. The residue was recrystallized from CH₂Cl₂/diethyl ether to yield the product as a white solid (0.108 g, 12%).

D₃-1•3OTf. In a glove box, **D₃-H₃L** (0.050 g, 0.058 mmol) and (CuOTf)₂•toluene (0.045 g, 0.087 mmol) were added to a scintillation vial equipped with a stir bar and dissolved in acetonitrile (5 mL). The orange solution was stirred at room temperature for 15 min. The solvent was removed under reduced pressure to yield the product as an orange-yellow solid (0.090 g, 88%).

Oxidation of **1•3OTf**

1 equiv: In the glovebox, a scintillation vial equipped with a stir bar was charged with a solution of **1•3OTf** (0.050 g, 0.0287 mmol) in acetonitrile (8 mL). A stock solution (0.020 mL Et₃N/5 mL CH₃CN) was prepared in a second vial, and 1 mL (1 equiv) was added to the yellow solution. A second stock solution (0.037 g AgOTf/5 mL CH₃CN) was prepared in a vial, and 1 mL (1 equiv) was added to the solution of **1•3OTf**. The yellow mixture was stirred at room temperature for 12 h, during which the solution turned pale green and a silver mirror was formed. The mixture was filtered, and the green filtrate was concentrated *in vacuo* to a green solid. The ¹H NMR spectrum of a portion of the residue in CD₃CN corresponds to a 1:2 mixture of **2•3OTf** and **1•3OTf** (Figure S20).

2 equiv: The same mixture from before was redissolved in CH₃CN (8 mL), and 1 mL each of the stock solutions of Et₃N and AgOTf were added. The green mixture was stirred for another 12 h at room temperature, filtered, and concentrated. The ¹H NMR spectrum of a portion of the residue in CD₃CN corresponds to a 2:1 mixture of **2•3OTf** and **1•3OTf**.

3 equiv: The procedure above was repeated with an additional equivalent of Et₃N and AgOTf. The mixture was stirred for 12 h at room temperature, filtered, and concentrated. The ¹H NMR spectrum of a portion of the residue in CD₃CN shows complete conversion of **1•3OTf** to **2•3OTf**.

Reduction of **2**

A Schlenk tube with a Teflon stopper and equipped with a stir bar was charged with **2•3OTf** (0.015 g, 0.01 mmol) and Et₃N•HCl (0.004 g, 0.03 mmol) in acetonitrile (5 mL). The green mixture was degassed with three freeze-pump-thaw cycles, then fitted with a septum under N₂. A solution of CoCp₂ (0.005 g, 0.03) in THF (1.2 mL) was added, and the

mixture turned yellow-brown. The solvent was removed from the mixture under reduced pressure. The ^1H NMR spectrum of the residue in CD_3CN matches that of **1•3OTf**.

Synthesis of $\text{LFe}_3(\text{OAc})_3$. In a glovebox, a scintillation vial equipped with a stir bar was charged with a suspension of $\text{Fe}(\text{OAc})_2$ (0.061 g, 0.349 mmol) in CH_2Cl_2 (2 mL). Triethylamine (0.052 mL, 0.407 mmol) was added via syringe, and then a solution of **H₃L** (0.100 g, 0.116 mmol) in CH_2Cl_2 (3 mL) was added. The pale yellow mixture was stirred at room temperature and slowly darkened over 20 h to form a homogeneous orange solution. The solvent was removed under reduced pressure and the residue was recrystallized twice from CH_2Cl_2 /diethyl ether to yield the product as orange-red crystals (0.087 g, 62%). ^1H NMR (300 MHz, CD_2Cl_2 , 25 °C): δ 109.04 (3 H), 69.06 (3 H), 65.32 (6 H), 43.77 (3 H), 38.34 (9 H), 37.96 (3 H), 28.40 (3 H), 13.43 (3 H), 12.93 (3 H), 9.47 (3 H), 8.08 (3 H), 3.49 (3 H), -4.13 (3 H). UV-Vis (CH_2Cl_2 , λ_{max} (ϵ)): 254 (50,500 $\text{M}^{-1} \text{cm}^{-1}$); 443 (2610 $\text{M}^{-1} \text{cm}^{-1}$); 793 (83 $\text{M}^{-1} \text{cm}^{-1}$) nm. Anal. Calcd. for $\text{C}_{63}\text{H}_{48}\text{Fe}_3\text{N}_6\text{O}_9$: C, 63.02; H, 4.03; N, 7.00. Found: C, 62.91; H, 3.97; N, 6.90.

Synthesis of $\text{LCu}_3(\text{OAc})_3$. A scintillation vial equipped with a stir bar was charged with **H₃L** (0.100 g, 0.116 mmol) and $\text{Cu}(\text{OAc})_2 \cdot \text{H}_2\text{O}$ (0.071 g, 0.355 mmol). Dichloromethane (5 mL) was added, and then triethylamine (0.052 mL, 0.407 mmol) was added via syringe. The mixture was stirred at room temperature for 12 h, becoming a homogeneous green mixture. The solvent was removed under reduced pressure and the green residue was washed with THF (5 mL), then recrystallized from CH_2Cl_2 /diethyl ether to yield $\text{LCu}_3(\text{OAc})_3$ as clusters of pale green needles (0.041 g, 29%). ^1H NMR (500 MHz, CDCl_3 , 25 °C): δ 126.26 (3 H), 49.44 (3 H), 36.45 (3 H), 33.15 (3 H), 22.02 (3 H), 12.93 (3 H), 10.96 (3 H), 9.80 (9 H), 8.78 (6 H), 8.12 (3 H), 6.55 (3 H), 6.08 (3 H). UV-Vis (CH_2Cl_2 ,

λ_{max} (ϵ): 253 (49,100 $\text{M}^{-1} \text{cm}^{-1}$); 860 (270 $\text{M}^{-1} \text{cm}^{-1}$) nm. Anal. Calcd. for $\text{C}_{63}\text{H}_{48}\text{Cu}_3\text{N}_6\text{O}_9$: C, 61.83; H, 3.95; N, 6.87. Anal. Calcd. for $\text{C}_{63}\text{H}_{50}\text{Cu}_3\text{N}_6\text{O}_{10}$ ($\text{LCu}_3(\text{OAc})_3 \cdot \text{H}_2\text{O}$): C, 60.94; H, 4.06; N, 6.77. Found: C, 60.79; H, 4.04; N, 6.92.

Synthesis of $\text{LZn}_3(\text{OAc})_3$. A scintillation vial equipped with a stir bar was charged with H_3L (0.100 g, 0.116 mmol) and $\text{Zn}(\text{OAc})_2$ (0.065 g, 0.355 mmol). Dichloromethane (5 mL) was added, then triethylamine (0.052 mL, 0.407 mmol) was added via syringe. The yellow solution was stirred at room temperature for 12 h, and the solvent was removed under reduced pressure. The pale pink residue was washed with THF, then recrystallized twice from CH_2Cl_2 /diethyl ether to yield $\text{LZn}_3(\text{OAc})_3$ as colorless crystals (0.024 g, 17%). ^1H NMR (500 MHz, CDCl_3 , 25 $^\circ\text{C}$): δ 8.70 (d, $J = 4.5$ Hz, 3 H, *a*), 8.02 (t, $J = 7.5$ Hz, 3 H, *f*), 7.86 (t, $J = 7.5$ Hz, 3 H, *g*), 7.80 (d, $J = 8$ Hz, 3 H, *d*), 7.74 (d, $J = 4.5$ Hz, 3 H, *a'*), 7.37 (dd, $J = 7.5, 4.5$ Hz, 3 H, *b* or *b'*), 7.25 (dd, $J = 7.5, 4.5$ Hz, 3 H, *b* or *b'*), 7.21 (t, $J = 8$ Hz, 3 H, *c* or *c'*), 7.17 (t, $J = 7.5$ Hz, 3 H, *c* or *c'*), 7.16 (d, $J = 8$ Hz, 3 H, *d'*), 6.98 (d, $J = 7.5$ Hz, 3 H, *e*), 6.51 (d, $J = 7.5$ Hz, 3 H, *h*), 5.66 (s, 3 H, *j*), 1.42 (s, 9 H, OAc). ^{13}C NMR (125.70 MHz, CDCl_3 , 25 $^\circ\text{C}$): δ 177.5, 165.7, 164.0, 150.6, 147.1, 144.7, 142.5, 141.5, 140.0, 138.7, 131.3, 130.5, 127.7, 127.0, 126.7, 126.2, 123.8, 123.6, 121.6, 84.4, 23.6. UV-Vis (CH_2Cl_2 , λ_{max} (ϵ)): 253 (48,700 $\text{M}^{-1} \text{cm}^{-1}$) nm. Anal. Calcd. for $\text{C}_{63}\text{H}_{48}\text{N}_6\text{O}_9\text{Zn}_3$: C, 61.56; H, 3.94; N, 6.84. Anal. Calcd. for $\text{C}_{63}\text{H}_{50}\text{N}_6\text{O}_{10}\text{Zn}_3$ ($\text{LZn}_3(\text{OAc})_3 \cdot \text{H}_2\text{O}$): C, 60.67; H, 4.04; N, 6.74. Found: C, 60.93; H, 4.09; N, 6.71.

Magnetic Susceptibility Measurements

General Considerations.

The magnetic susceptibility measurements were carried out in the Molecular Materials Research Center in the Beckman Institute of the California Institute of Technology on a Quantum Design MPMS instrument running MPMS Multivu software. Crystalline samples (0.030–0.100 g) were powdered and suspended in a clear plastic straw in gel caps. Data were recorded at 0.5 and 5 T from 4–300 K. Diamagnetic corrections were made using the average experimental magnetic susceptibility of **H₃L** at 0.5 T from 100–300 K ($-593 \times 10^{-6} \text{ cm}^3/\text{mol}$) in addition to the values of Pascal's constants for amounts of anion and solvent quantified for each sample using elemental analysis.

The $\chi_M T$ data taken at 0.5 T were initially fit to the magnetic susceptibility equation derived from the isotropic spin Hamiltonian for two coupling constants, J and J_{13} [Eq. (5)]. The best fit was found with $\alpha = J_{13}/J = 1$, so the data were instead modeled to an equilateral triangle of $S = 1/2$ spins [Eq. (6, 7)].

$$\hat{H} = -2J[(\hat{S}_1\hat{S}_2) + (\hat{S}_2\hat{S}_3)] - 2J_{13}(\hat{S}_3\hat{S}_1) \quad (5)$$

$$\hat{H} = -2J[(\hat{S}_1\hat{S}_2) + (\hat{S}_2\hat{S}_3) - (\hat{S}_3\hat{S}_1)] \quad (6)$$

$$\chi_M = \frac{Ng^2\beta^2}{4k(T-\theta)} \frac{5 + \exp(-3J/kT)}{1 + \exp(-3J/kT)} \quad (7)$$

The data were fit using Matlab³⁹ (contact author for code) by minimizing $R = \sum |(\chi_M T)_{obs} - (\chi_M T)_{calcd}|^2 / \sum (\chi_M T)_{obs}^2$. The data for **2•3BF₄•Et₂O** could not be satisfactorily fit without the inclusion of a temperature independent magnetism $-500 \times 10^{-6} \text{ cm}^3/\text{mol}$, which may be attributed to the presence of diamagnetic impurities such as unaccounted for solvent in the material.

The magnetic parameters when the data are fit with an additional Curie-Weiss parameter θ are shown in Table 4. The variables were modeled from multiple starting values, and the fitted parameters were stable within reasonable ranges for J (-60 to 0 cm^{-1}), g (1.90 to 2.10), and θ (-2 to 2 K), except for compound **2•PO₄**, whose fit showed a second local minimum with values of $J = 1.0 \text{ cm}^{-1}$, $g = 2.10$, and $\theta = -4.5 \text{ K}$. This set of parameters was not favored because of its large θ value and because the R value was slightly higher (0.9×10^{-4}).

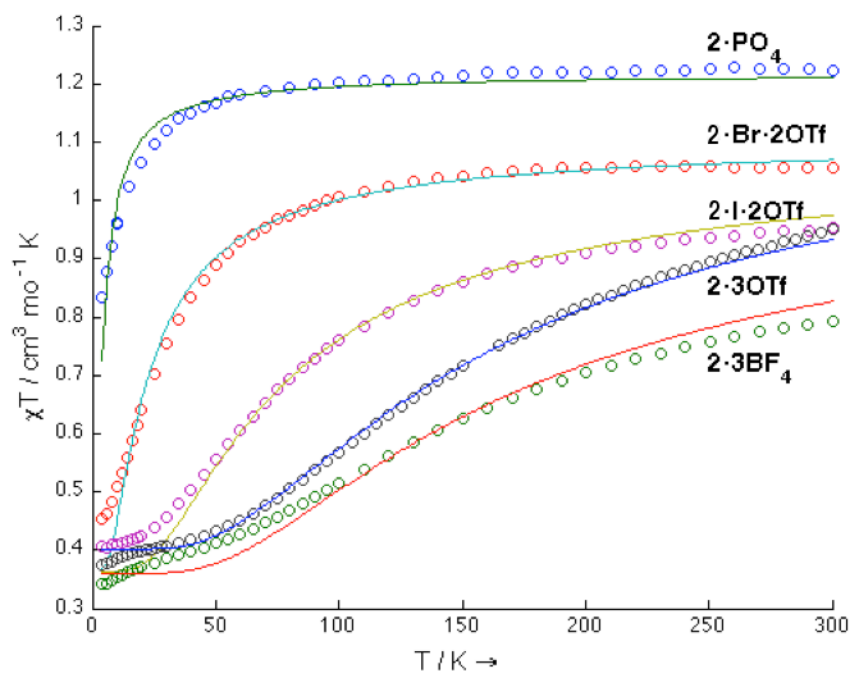
The parameters fit without θ are shown in Table 5 and Figure 20.

Table 4. Magnetic parameters with included θ .

| Compound | Diamagnetic Correction (\times $10^6 \text{ cm}^3/\text{mol}$) | $J (\text{cm}^{-1})$ | g | $\theta (\text{K})$ | $R (\times 10^{-4})$ |
|---|--|----------------------|------|---------------------|----------------------|
| 2•PO₄•H₃PO₄•6H₂O | -782 | -2.7 | 2.09 | 1.6 | 0.7 |
| 2•3OTf | -881 | -52 | 2.10 | -0.6 | 0.3 |
| 2•3BF₄•Et₂O | -737 | -52.2 | 2.10 | -1.6 | 4.2 |
| 2•Br•2OTf•THF | -837 | -7.3 | 1.98 | 0.8 | 2.3 |
| 2•I•2OTf | -803 | -22.0 | 1.95 | 1.0 | 5.7 |

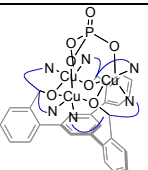
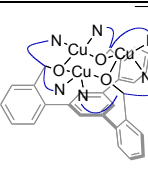
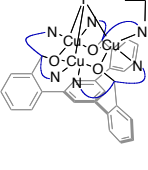
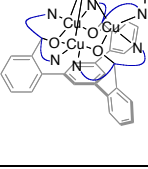
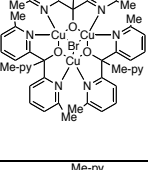
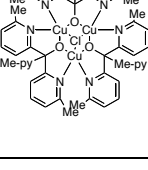
Table 5. Parameters when fit without θ .

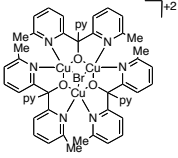
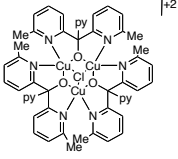
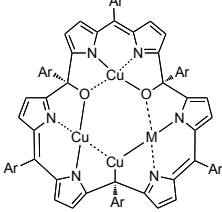
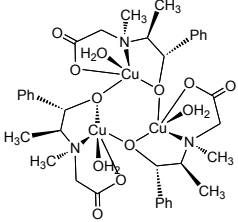
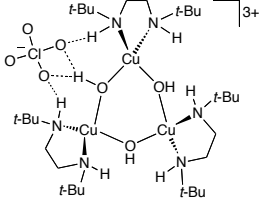
| Compound | $J(\text{cm}^{-1})$ | g | $R(\times 10^{-4})$ |
|---|---------------------|------|---------------------|
| 2•PO₄•H₃PO₄•6H₂O | −1.3 | 2.08 | 4.5 |
| 2•3OTf | −49.1 | 2.07 | 1.6 |
| 2•3BF₄•Et₂O | −51.3 | 1.96 | 13 |
| 2•Br•2OTf•THF | −6.5 | 1.98 | 7.6 |
| 2•I•2OTf | −22.7 | 1.97 | 12 |

**Figure 20.** $\chi_{\text{M}}T$ vs. T plots with fits for compounds **2** using parameters from Table 5.

Magnetostructural Study

Table 6. Structural and magnetic parameters for alkoxo- or hydroxo-bridged copper(II) trimers in this work and in the literature.

| Compound | Structure | Cu–O–Cu Angle (°) | J (cm ⁻¹) |
|-------------------------|---|----------------------|-------------------------|
| 2•PO₄ |  | 114.6–118.5 | –2.7 |
| 2•3OTf |  | 125.9–126.5 | –52.0 |
| 2•I•2OTf |  | 116.7–120.8 | –22.0 |
| 2•Br•2OTf |  | 116.1–118.5 | –7.3 |
| a1^{IIa} |  | 116.4 | –19.5 |
| a2^{IIa} |  | 114.5 | –3.7 |

| | | | |
|--------------------------|---|-------------|--------|
| a3 ^{11a} |  | 114.4 | −4.8 |
| a4 ^{11a} |  | 114.0 | −0.3 |
| b ^{6d} |  | 121.2–125.2 | −44 |
| c ^{12b} |  | 131.1 | −57 |
| d ²³ |  | 144.3 | −104.7 |

EPR Measurements

X-band EPR spectra were obtained on a Bruker EMX Biospin spectrometer. Variable temperature measurements were conducted with an Oxford continuous-flow helium cryostat. EPR parameters were simulated using W95EPR.⁴⁰

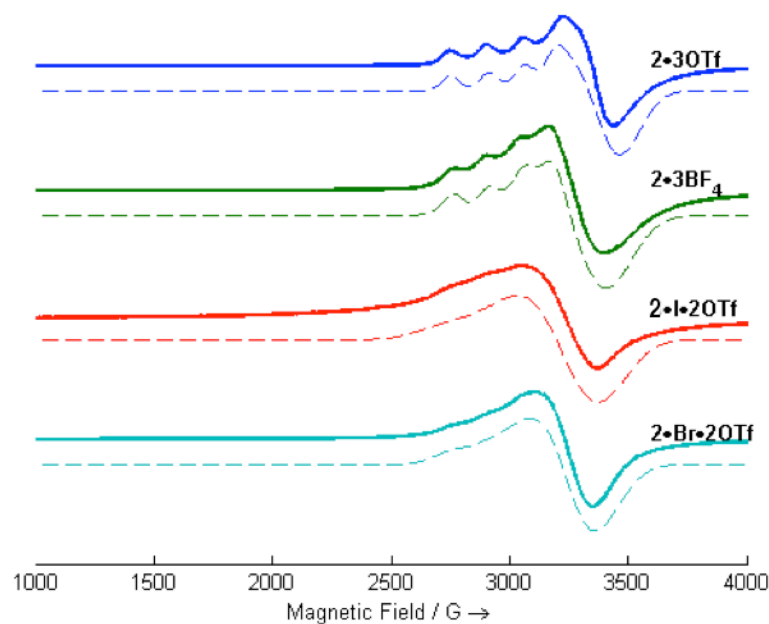


Figure 21. Experimental (–) and simulated (– –) EPR spectra of CH_3CN solutions of **2•3OTf**, **2•3BF₄**, **3•I•2OTf**, **3•Br•2OTf** at 10 K. Simulated parameters: **2•3OTf**: $g_{\perp} = 1.97$, $g_{\parallel} = 2.24$, $A_{\perp} = 0 \text{ cm}^{-1}$, $A_{\parallel} = 0.015 \text{ cm}^{-1}$. **2•3BF₄**: $g_{\perp} = 2.01$, $g_{\parallel} = 2.23$, $A_{\perp} = 0.001 \text{ cm}^{-1}$, $A_{\parallel} = 0.014 \text{ cm}^{-1}$. **2•I•2OTf**: $g_{\perp} = 2.04$, $g_{\parallel} = 2.29$, $A_{\perp} = 0.007 \text{ cm}^{-1}$, $A_{\parallel} = 0.015 \text{ cm}^{-1}$. **2•Br•2OTf**: $g_{\perp} = 2.05$, $g_{\parallel} = 2.25$, $A_{\perp} = 0 \text{ cm}^{-1}$, $A_{\parallel} = 0.015 \text{ cm}^{-1}$. Parameters for **2•I•2OTf** and **2•Br•2OTf** are approximate due to the broadness of the signals.

Crystallographic Information:

Crystallographic data have been deposited at the CCDC, 12 Union Road, Cambridge CB2 1EZ, UK and copies can be obtained on request, free of charge, by quoting the publication citation and the deposition numbers 803594 (LFe₃(OAc)₃), 803593 (LCu₃(OAc)₃), 803592 (LZn₃(OAc)₃), 797194 (**2•3OTf**), 755941 (**2•PO₄**), 797196 (**2•Br•2OTf**), and 797195 (**2•I•2OTf**).

Table 7. Crystal and refinement data for compounds **2**.

| | 2•3OTf | 2•PO₄ | 2•Br•2OTf | 2•I•2OTf |
|---|---|---|--|--|
| empirical formula | [C ₅₈ H ₃₉ N ₆ O ₃ Cu ₃] + ³ 3[CF ₃ O ₃ S] [−] • C ₄ H ₁₀ O • 2(C ₂ H ₃ N) | [C ₅₇ H ₃₉ N ₆ O ₇ PCu ₃] + ³ | [C ₅₇ H ₃₉ N ₆ O ₃ C u ₃ Br] ⁺² 2[CF ₃ O ₃ S] [−] • C ₄ H ₁₀ O • 2(C ₂ H ₃ N) | [C ₅₇ H ₃₉ N ₆ O ₃ Cu ₃ I] ⁺² 2[CF ₃ O ₃ S] [−] • C ₄ H ₁₀ O • 2(C ₂ H ₃ N) |
| formula wt | 1650 | 1141.53 | 1580.84 | 1627.83 |
| T (K) | 100 | 100 | 100 | 100 |
| a, Å | 16.5204(7) | 18.5968(7) | 16.2366(5) | 16.3795(9) |
| b, Å | 17.6508(8) | 18.9030(7) | 17.5618(5) | 17.228(1) |
| c, Å | 23.620(1) | 20.0033(7) | 23.2387(7) | 23.452(1) |
| α, deg | 90 | 80.451(2) | 90 | 90 |
| β, deg | 90 | 80.179(2) | 90 | 90 |
| γ, deg | 90 | 69.214(2) | 90 | 90 |
| V, Å ³ | 6887.7(5) | 6435.3(4) | 6626.4(3) | 6617.9(6) |
| Z | 4 | 4 | 4 | 4 |
| cryst syst | orthorhombic | triclinic | orthorhombic | orthorhombic |
| space group | P2 ₁ 2 ₁ 2 ₁ | P-1 | P2 ₁ 2 ₁ 2 ₁ | P2 ₁ 2 ₁ 2 ₁ |
| d _{calcd} , g/cm ³ | 1.591 | 1.178 | 1.585 | 1.634 |
| θ range, deg | 1.90-33.23 | 1.16-28.64 | 2.10-30.90 | 1.52-30.79 |
| μ, mm ^{−1} | 1.103 | 1.055 | 1.702 | 1.567 |
| abs cor | none | none | none | none |
| GOF | 1.603 | 2.525 | 2.155 | 1.964 |
| R1, ^a wR2 ^b (I > 2σ(I)) | 0.0266, 0.0457 | 0.0458, 0.0775 | 0.0395, 0.0646 | 0.0346, 0.0661 |

$$^a R1 = \cdot ||F_o| - |F_c|| \cdot |F_o|. \quad ^b wR2 = \{ \cdot [w(F_o^2 - F_c^2)^2] \cdot [w(F_o^2)] \}^{1/2}.$$

Special Refinement Details for 2•3OTf

Crystals were mounted on a glass fiber using Paratone oil then placed on the diffractometer under a nitrogen stream at 100K.

This crystal is twinned with the twin component of the diastereomer at 25.6%.

Refinement of F2 against ALL reflections. The weighted R-factor (wR) and goodness of fit (S) are based on F2, conventional R-factors (R) are based on F, with F set to zero for negative F2. The threshold expression of $F2 > 2\sigma(F2)$ is used only for calculating R-factors(gt) etc. and is not relevant to the choice of reflections for refinement. R-factors based on F2 are statistically about twice as large as those based on F, and R-factors based on ALL data will be even larger.

All esds (except the esd in the dihedral angle between two l.s. planes) are estimated using the full covariance matrix. The cell esds are taken into account individually in the estimation of esds in distances, angles and torsion angles; correlations between esds in cell parameters are only used when they are defined by crystal symmetry. An approximate (isotropic) treatment of cell esds is used for estimating esds involving l.s. planes.

Special Refinement Details for 2•PO₄

Crystals were mounted on a glass fiber using Paratone oil then placed on the diffractometer under a nitrogen stream at 100K.

The crystal contains disordered solvent, presumably water and acetone, as well as disordered counterion, PO₄⁻³. The total solvent accessible volume (including counterion) of this crystal is 2207 Å³ (34% of total volume). In light of the difficulty in obtaining a satisfactory model including the solvent and counterion, the program SQUEEZE⁴¹ was

employed to adjust observed intensities in order to remove the contribution for this area. In this way a total of 1016 electrons were compensated for. This is in reasonable agreement with what would be expected for phosphate and approximately 25 water molecules.

Refinement of F^2 against ALL reflections. The weighted R-factor (wR) and goodness of fit (S) are based on F^2 , conventional R-factors (R) are based on F , with F set to zero for negative F^2 . The threshold expression of $F^2 > 2s(F^2)$ is used only for calculating R-factors(gt) etc. and is not relevant to the choice of reflections for refinement. R-factors based on F^2 are statistically about twice as large as those based on F , and R-factors based on ALL data will be even larger.

All esds (except the esd in the dihedral angle between two l.s. planes) are estimated using the full covariance matrix. The cell esds are taken into account individually in the estimation of esds in distances, angles and torsion angles; correlations between esds in cell parameters are only used when they are defined by crystal symmetry. An approximate (isotropic) treatment of cell esds is used for estimating esds involving l.s. planes.

Special Refinement Details for 2•Br•2OTf

Crystals were mounted on a glass fiber using Paratone oil then placed on the diffractometer under a nitrogen stream at 100K.

Refinement of F^2 against ALL reflections. The weighted R-factor (wR) and goodness of fit

(S) are based on F^2 , conventional R-factors (R) are based on F , with F set to zero for negative F^2 . The threshold expression of $F^2 > 2s(F^2)$ is used only for calculating R-factors(gt) etc. and is not relevant to the choice of reflections for refinement. R-factors

based on F^2 are statistically about twice as large as those based on F , and R-factors based on ALL data will be even larger.

All esds (except the esd in the dihedral angle between two l.s. planes) are estimated using the full covariance matrix. The cell esds are taken into account individually in the estimation of esds in distances, angles and torsion angles; correlations between esds in cell parameters are only used when they are defined by crystal symmetry. An approximate (isotropic) treatment of cell esds is used for estimating esds involving l.s. planes.

Special Refinement Details for 2•I•2OTf

Crystals were mounted on a glass fiber using Paratone oil then placed on the diffractometer under a nitrogen stream at 100K.

The crystal is a racemic twin with a refined twin ratio of 66:44.

Refinement of F^2 against ALL reflections. The weighted R-factor (wR) and goodness of fit (S) are based on F^2 , conventional R-factors (R) are based on F , with F set to zero for negative F^2 . The threshold expression of $F^2 > 2s(F^2)$ is used only for calculating R-factors(gt) etc. and is not relevant to the choice of reflections for refinement. R-factors based on F^2 are statistically about twice as large as those based on F , and R-factors based on ALL data will be even larger.

All esds (except the esd in the dihedral angle between two l.s. planes) are estimated using the full covariance matrix. The cell esds are taken into account individually in the estimation of esds in distances, angles and torsion angles; correlations between esds in cell parameters are only used when they are defined by crystal symmetry. An approximate (isotropic) treatment of cell esds is used for estimating esds involving l.s. planes.

Table 8. Crystal and refinement data for LM₃(OAc)₃ (M = Fe, Cu, Zn).

| | LFe ₃ (OAc) ₃ | LCu ₃ (OAc) ₃ | LZn ₃ (OAc) ₃ |
|---|---|---|---|
| empirical formula | C ₆₃ H ₄₈ Fe ₃ N ₆ O ₉ | C ₆₃ H ₄₈ Cu ₃ N ₆ O ₉ | C ₆₃ H ₄₈ Zn ₃ N ₆ O ₉ |
| formula wt | 1200.62 | 1164.65 | 1170.14 |
| T (K) | 100 | 100 | 100 |
| a, Å | 10.6327(4) | 18.9118(5) | 19.106(1) |
| b, Å | 18.9722(8) | 19.0501(5) | 18.7848(9) |
| c, Å | 19.6009(8) | 36.0732(9) | 36.130(2) |
| α, deg | 72.453(2) | 90 | 90 |
| β, deg | 89.924(2) | 90 | 90 |
| γ, deg | 75.857(2) | 90 | 90 |
| V, Å ³ | 3644.5(3) | 12996.1(6) | 12967(1) |
| Z | 2 | 8 | 8 |
| cryst syst | triclinic | orthorhombic | orthorhombic |
| space group | P-1 | P <i>bcn</i> | P <i>bcn</i> |
| d _{calcd} , g/cm ³ | 1.094 | 1.190 | 1.199 |
| θ range, deg | 1.98–30.60 | 1.89–26.40 | 2.13–26.43 |
| μ, mm ⁻¹ | 0.638 | 1.023 | 1.151 |
| abs cor | none | none | none |
| GOF | 3.896 | 2.988 | 2.297 |
| R1, ^a wR2 ^b (I > 2σ(I)) | 0.0576, 0.1052 | 0.0481, 0.0898 | 0.0519, 0.0954 |

$$^a R1 = \cdot ||F_o| - |F_c|| / \cdot |F_o|. \quad ^b wR2 = \{ \cdot [w(F_o^2 - F_c^2)^2] / \cdot [w(F_o^2)^2] \}^{1/2}.$$

Special refinement details for LFe₃(OAc)₃. Crystals were mounted on a glass fiber using Paratone oil then placed on the diffractometer under a nitrogen stream at 100K. Approximately 35% of the unit cell volume is solvent and poorly ordered. To account for solvent the program SQUEEZE⁴¹ was employed to apply bulk solvent flattening. A total of 685 electrons were accounted for. One of the bound acetate is disordered and was modeled without restraints. Refinement of F² against ALL reflections. The weighted R-factor (wR) and goodness of fit (S) are based on F², conventional R-factors (R) are based on F, with F set to zero for negative F². The threshold expression of F² > 2s(F²) is used only for calculating R-factors(gt) etc. and is not relevant to the choice of reflections for refinement. R-factors based on F² are statistically about twice as large as those based on F, and R-factors based on ALL data will be even larger. All esds (except the esd in the dihedral angle between two l.s. planes) are estimated using the full covariance matrix. The cell esds are

taken into account individually in the estimation of esds in distances, angles and torsion angles; correlations between esds in cell parameters are only used when they are defined by crystal symmetry. An approximate (isotropic) treatment of cell esds is used for estimating esds involving l.s. planes.

Special refinement details for $\text{LCu}_3(\text{OAc})_3$. Crystals were mounted on a glass fiber using Paratone oil then placed on the diffractometer under a nitrogen stream at 100K. Presumably the solvent region of the crystal contains an acetate which would balance the charge on the Cu complex. Approximately 32% of the unit cell volume contains potential solvent. Electron density in this space is poorly defined suggesting disorder and a suitable solvent model was not obtained. SQUEEZE⁴¹ was employed to produce a bulk solvent correction which accounted for 964 electrons which is a good fit to two chloroform and one acetate per unit cell. Refinement of F^2 against ALL reflections. The weighted R-factor (wR) and goodness of fit (S) are based on F^2 , conventional R-factors (R) are based on F , with F set to zero for negative F^2 . The threshold expression of $F^2 > 2s(F^2)$ is used only for calculating R-factors(gt) etc. and is not relevant to the choice of reflections for refinement. R-factors based on F^2 are statistically about twice as large as those based on F , and R-factors based on ALL data will be even larger. All esds (except the esd in the dihedral angle between two l.s. planes) are estimated using the full covariance matrix. The cell esds are taken into account individually in the estimation of esds in distances, angles and torsion angles; correlations between esds in cell parameters are only used when they are defined by crystal symmetry. An approximate (isotropic) treatment of cell esds is used for estimating esds involving l.s. planes.

Special refinement details for $\text{LZn}_3(\text{OAc})_3$. Crystals were mounted in a loop using oil then placed on the diffractometer under a nitrogen stream at 100K. Presumably the solvent region of the crystal contains an acetate which would balance the charge on the Zn complex. Approximately 31% of the unit cell volume contains potential solvent. Electron density in this space is poorly defined suggesting disorder and a suitable solvent model was not obtained. SQUEEZE⁴¹ was employed to produce a bulk solvent correction which accounted for 1066 electrons which is a good fit to two chloroform and one acetate per unit cell. Refinement of F^2 against ALL reflections. The weighted R-factor (wR) and goodness of fit (S) are based on F^2 , conventional R-factors (R) are based on F , with F set to zero for negative F^2 . The threshold expression of $F^2 > 2s(F^2)$ is used only for calculating R-factors(gt) etc. and is not relevant to the choice of reflections for refinement. R-factors based on F^2 are statistically about twice as large as those based on F , and R-factors based on ALL data will be even larger. All esds (except the esd in the dihedral angle between two l.s. planes) are estimated using the full covariance matrix. The cell esds are taken into account individually in the estimation of esds in distances, angles and torsion angles; correlations between esds in cell parameters are only used when they are defined by crystal symmetry. An approximate (isotropic) treatment of cell esds is used for estimating esds involving l.s. planes.

References

1. (a) McEvoy, J. P.; Brudvig, G. W. *Chem. Rev.* **2006**, *106*, 4455-4483; (b) Holm, R. H.; Kennepohl, P.; Solomon, E. I. *Chem. Rev.* **1996**, *96*, 2239-2314.
2. (a) Solomon, E. I.; Augustine, A. J.; Yoon, J. *Dalton Trans.* **2008**, 3921-3932; (b) Solomon, E. I.; Chen, P.; Metz, M.; Lee, S. K.; Palmer, A. E. *Angew. Chem. Int. Ed.* **2001**, *40*, 4570-4590; (c) Balasubramanian, R.; Rosenzweig, A. C. *Acc. Chem. Res.* **2007**, *40*, 573-580; (d) Lieberman, R. L.; Rosenzweig, A. C. *Nature* **2005**, *434*, 177-182; (e) Chan, S. I.; Yu, S. S. F. *Acc. Chem. Res.* **2008**, *41*, 969-979; (f) Mirica, L. M.; Ottenwaelder, X.; Stack, T. D. P. *Chem. Rev.* **2004**, *104*, 1013-1045; (g)

- Balasubramanian, R.; Smith, S. M.; Rawat, S.; Yatsunyk, L. A.; Stemmler, T. L.; Rosenzweig, A. C. *Nature* **2010**, *465*, 115-119.
3. Cole, A. P.; Root, D. E.; Mukherjee, P.; Solomon, E. I.; Stack, T. D. P. *Science* **1996**, *273*, 1848-1850.
 4. Chen, P. P. Y.; Yang, R. B. G.; Lee, J. C. M.; Chan, S. I. *Proc. Natl. Acad. Sci. USA* **2007**, *104*, 14570-14575.
 5. (a) Ohi, H.; Tachi, Y.; Itoh, S. *Inorg. Chem.* **2006**, *45*, 10825-10835; (b) Brown, E. C.; Johnson, B.; Palavicini, S.; Kucera, B. E.; Casella, L.; Tolman, W. B. *Dalton Trans.* **2007**, 3035-3042; (c) Frey, S. T.; Sun, H. H. J.; Murthy, N. N.; Karlin, K. D. *Inorg. Chim. Acta* **1996**, *242*, 329-338; (d) Karlin, K. D.; Gan, Q. F.; Farooq, A.; Liu, S. C.; Zubieta, J. *Inorg. Chem.* **1990**, *29*, 2549-2551; (e) Karlin, K. D.; Gan, Q. F.; Tyeklar, Z. *Chem. Commun.* **1999**, 2295-2296; (f) Maiti, D.; Woertink, J. S.; Ghiladi, R. A.; Solomon, E. I.; Karlin, K. D. *Inorg. Chem.* **2009**, *48*, 8342-8356.
 6. (a) Adams, H.; Bailey, N. A.; Dwyer, M. J. S.; Fenton, D. E.; Hellier, P. C.; Hempstead, P. D.; Latour, J. M. *J. Chem. Soc., Dalton Trans.* **1993**, 1207-1216; (b) Gonzalez-Alvarez, A.; Alfonso, I.; Cano, J.; Diaz, P.; Gotor, V.; Gotor-Fernandez, V.; Garcia-Espana, E.; Garcia-Granda, S.; Jimenez, H. R.; Lloret, F. *Angew. Chem. Int. Ed.* **2009**, *48*, 6055-6058; (c) Suh, M. P.; Han, M. Y.; Lee, J. H.; Min, K. S.; Hyeon, C. *J. Am. Chem. Soc.* **1998**, *120*, 3819-3820; (d) Inoue, M.; Ikeda, C.; Kawata, Y.; Venkatraman, S.; Furukawa, K.; Osuka, A. *Angew. Chem. Int. Ed.* **2007**, *46*, 2306-2309.
 7. Feng, X. L.; Wu, J. S.; Enkelmann, V.; Mullen, K. *Org. Lett.* **2006**, *8*, 1145-1148.
 8. Eisenberg, G. M. *Ind. Chem. Anal. Ed.* **1943**, *15*, 327-328.
 9. Vincent, J. B.; Christou, G. *Inorg. Chim. Acta* **1987**, *136*, L41-L43.
 10. Murthy, N. N.; Karlin, K. D.; Bertini, I.; Luchinat, C. *J. Am. Chem. Soc.* **1997**, *119*, 2156-2162.
 11. (a) Kodera, M.; Tachi, Y.; Kita, T.; Kobushi, H.; Sumi, Y.; Kano, K.; Shiro, M.; Koikawa, M.; Tokii, T.; Ohba, M.; Okawa, H. *Inorg. Chem.* **2000**, *39*, 226-234; (b) Afrati, T.; Dendrinou-Samara, C.; Raptopoulou, C.; Terzis, A.; Tangoulis, V.; Kessissoglou, D. P. *Dalton Trans.* **2007**, 5156-5164; (c) Jiang, Y.-B.; Kou, H.-Z.; Wang, R.-J.; Cui, A.-L.; Ribas, J. *Inorg. Chem.* **2005**, *44*, 709-715.
 12. (a) Gautier-Luneau, I.; Phanon, D.; Duboc, C.; Luneau, D.; Pierre, J. L. *Dalton Trans.* **2005**, 3795-3799; (b) Lopez-Sandoval, H.; Contreras, R.; Escuer, A.; Vicente, R.; Bernes, S.; Noth, H.; Leigh, G. J.; Barba-Behrens, N. *J. Chem. Soc., Dalton Trans.* **2002**, 2648-2653.
 13. (a) Gehring, S.; Fleischhauer, P.; Paulus, H.; Haase, W. *Inorg. Chem.* **1993**, *32*, 54-60; (b) Das, O.; Zangrando, E.; Paine, T. K. *Inorg. Chim. Acta* **2009**, *362*, 3617-3623; (c) Gehring, S.; Astheimer, H.; Haase, W. *J. Chem. Soc., Faraday Trans. 2* **1987**, *83*, 347-354.
 14. (a) Sarkar, B.; Ray, M.; Li, Y. Z.; Song, Y.; Figuerola, A.; Ruiz, E.; Cirera, J.; Cano, J.; Ghosh, A. *Chem. Eur. J.* **2007**, *13*, 9297-9309; (b) Boca, R.; Dihan, L. u. r.; Mezei, G.; Ortiz-Perez, T.; Raptis, R. G.; Telser, J. *Inorg. Chem.* **2003**, *42*, 5801-5803; (c) Wang, L.-L.; Sun, Y.-M.; Yu, Z.-Y.; Qi, Z.-N.; Liu, C.-B. *J. Phys. Chem. A* **2009**, *113*, 10534-10539; (d) Angaridis, P. A.; Baran, P.; Boca, R.; Cervantes-Lee, F.; Haase, W.; Mezei, G.; Raptis, R. G.; Werner, R. *Inorg. Chem.* **2002**, *41*,

- 2219-2228; (e) Sinha Ray, M.; Chattopadhyay, S.; Drew, M. G. B.; Figuerola, A.; Ribas, J.; Diaz, C.; Ghosh, A. *Eur. J. Inorg. Chem.* **2005**, 2005, 4562-4571.
15. Mukherjee, P.; Drew, M. G. B.; Estrader, M.; Diaz, C.; Ghosh, A. *Inorg. Chim. Acta* **2008**, 361, 161-172.
 16. (a) Kambe, K. *J. Phys. Soc. Jpn.* **1950**, 5, 48-51; (b) Sinn, E. *Coord. Chem. Rev.* **1970**, 5, 313-&.
 17. An improved fit for the magnetism susceptibility of compound **2•3BF₄** was calculated by including a temperature independent magnetism of $-500 \times 10^{-6} \text{ cm}^{-1}$. This discrepancy may due to diamagnetic impurities such as an unknown number of solvent molecules or other salts.
 18. The data were fit by minimizing $R = \sum |(\chi_M T)_{obs} - (\chi_M T)_{calcd}|^2 / \sum (\chi_M T)_{obs}^2$.
 19. The parameter θ was included in the magnetic susceptibility equation to account for antiferromagnetic ($\theta < 0$) or ferromagnetic ($\theta > 0$) intermolecular interactions. See Ref. 14e and Ref. 22a for examples.
 20. Butcher, R. J.; Oconnor, C. J.; Sinn, E. *Inorg. Chem.* **1981**, 20, 537-545.
 21. (a) Fleischhauer, P.; Gehring, S.; Saal, C.; Haase, W.; Tomkowicz, Z.; Zanchini, C.; Gatteschi, D.; Davidov, D.; Barra, A. L. *J. Magn. Magn. Mater.* **1996**, 159, 166-174; (b) Koval, I. A.; Akhidenov, H.; Tanase, S.; Belle, C.; Duboc, C.; Saint-Aman, E.; Gamez, P.; Tooke, D. M.; Spek, A. L.; Pierre, J.-L.; Reedijk, J. *New J. Chem.* **2007**, 31, 512-518; (c) Gutierrez, L.; Alzuet, G.; Real, J. A.; Cano, J.; Borrás, J.; Castineiras, A. *Inorg. Chem.* **2000**, 39, 3608-3614; (d) Banci, L.; Bencini, A.; Gatteschi, D. *Inorg. Chem.* **1983**, 22, 2681-2683.
 22. (a) Crawford, V. H.; Richardson, H. W.; Wasson, J. R.; Hodgson, D. J.; Hatfield, W. E. *Inorg. Chem.* **1976**, 15, 2107-2110; (b) Ruiz, E.; Alemany, P.; Alvarez, S.; Cano, J. *J. Am. Chem. Soc.* **1997**, 119, 1297-1303.
 23. Mirica, L. M.; Stack, T. D. P. *Inorg. Chem.* **2005**, 44, 2131-2133.
 24. Grundmeier, A.; Dau, H. *Biochim. Biophys. Acta Bioenergetics* **2012**, 1817, 88-105.
 25. Ferrer, S.; Lloret, F.; Bertomeu, I.; Alzuet, G.; Borrás, J.; Garcia-Granda, S.; Liu-Gonzalez, M.; Haasnoot, J. G. *Inorg. Chem.* **2002**, 41, 5821-5830.
 26. Inoue, M.; Ikeda, C.; Kawata, Y.; Venkatraman, S.; Furukawa, K.; Osuka, A. *Angew. Chem. Int. Ed.* **2007**, 46, 2306-2309.
 27. Dasgupta, J.; van Willigen, R. T.; Dismukes, G. C. *Phys. Chem. Chem. Phys.* **2004**, 6, 4793-4802.
 28. Drago, R. S., *Physical methods for chemists*. Surfside Scientific Publishers: Gainesville, 1992.
 29. Rapatskiy, L.; Cox, N.; Savitsky, A.; Ames, W. M.; Sander, J.; Nowaczyk, M. M.; Rögnér, M.; Boussac, A.; Neese, F.; Messinger, J.; Lubitz, W. *J. Am. Chem. Soc.* **2012**, 134, 16619-16634.
 30. (a) Mabbs, F. E.; Machin, D. J., *Magnetism and Transition Metal Complexes*. Dover Publications, Inc.: Mineola, 2008; (b) Haddadpour, S.; Niedermeyer, H.; Clerac, R.; Dehnen, S. *Dalton Trans.* **2009**, 8162-8164.
 31. Kahn, O., *Molecular Magnetism*. VCH Publishers, Inc.: New York, 1993.
 32. Reynolds, R. A.; Yu, W. O.; Dunham, W. R.; Coucouvanis, D. *Inorg. Chem.* **1996**, 35, 2721-2722.

- 33. (a) Labisbal, E.; Rodriguez, L.; Souto, O.; Sousa-Pedrares, A.; Garcia-Vazquez, J. A.; Romero, J.; Sousa, A.; Yanez, M.; Orallo, F.; Real, J. A. *Dalton Trans.* **2009**, 8644-8656; (b) Adams, H.; Fenton, D. E.; Cummings, L. R.; McHugh, P. E.; Ohba, M.; Okawa, H.; Sakiyama, H.; Shiga, T. *Inorg. Chim. Acta* **2004**, 357, 3648-3656; (c) Boskovic, C.; Rusanov, E.; Stoeckli-Evans, H.; Gidel, H. U. *Inorg. Chem. Commun.* **2002**, 5, 881-886.
- 34. Hatnean, J. A.; Raturi, R.; Lefebvre, J.; Leznoff, D. B.; Lawes, G.; Johnson, S. A. *J. Am. Chem. Soc.* **2006**, 128, 14992-14999.
- 35. Christian, P.; Rajaraman, G.; Harrison, A.; Helliwell, M.; McDouall, J. J. W.; Raftery, J.; Winpenny, R. E. P. *Dalton Trans.* **2004**, 2550-2555.
- 36. Brudvig, G. W.; Crabtree, R. H. *Proc. Natl. Acad. Sci. USA* **1986**, 83, 4586-4588.
- 37. Gillespie, K. M.; Sanders, C. J.; O'Shaughnessy, P.; Westmoreland, I.; Thickitt, C. P.; Scott, P. *J. Org. Chem.* **2002**, 67, 3450-3458.
- 38. Liang, H.-C.; Karlin, K. D.; Dyson, R.; Kaderli, S.; Jung, B.; Zuberbühler, A. D. *Inorg. Chem.* **2000**, 39, 5884-5894.
- 39. *Matlab*, 7.10.0.499 (R2010a); The MathWorks, Inc.: Natick, MA, 2010.
- 40. Neese, F. *QCPE Bull.* **1995**, 15.
- 41. Spek, A. L. *PLATON - A Multipurpose Crystallographic Tool*, Utrecht, The Netherlands, 2006.

Chapter 3

HETEROMETALLIC MANGANESE DIOXIDO COMPLEXES: REDUCTION POTENTIAL MODULATION BY LEWIS ACIDIC REDOX-INACTIVE METALS

The text for this chapter was reproduced in part from:

Tsui, E. Y.; Tran, R.; Yano, J.; Agapie, T. *Nat. Chem.* **2013**, 5, 293-299.

Abstract

Redox-inactive metals are found in biological and heterogeneous water oxidation catalysts, but their roles in catalysis are currently not well understood. A series of high oxidation state tetranuclear-dioxido clusters comprised of three manganese centers and a redox-inactive metal (M) of various charge is reported. Crystallographic studies show an unprecedented $\text{Mn}_3\text{M}(\mu_4\text{-O})(\mu_2\text{-O})$ core that remains intact upon changing M or the manganese oxidation state. Electrochemical studies reveal that the reduction potentials of the $\text{Mn}^{\text{IV}}\text{Mn}^{\text{III}}_2/\text{Mn}^{\text{III}}_3$ couples of the complexes span a window of ca. 700 mV, dependent upon the Lewis acidity of the second metal. With the $\text{p}K_{\text{a}}$ of the redox-inactive metal-aqua complex as a measure of Lewis acidity, these compounds display a linear dependence between reduction potential and Lewis acidity, with a slope of ca. 100 mV per $\text{p}K_{\text{a}}$ unit. The Sr^{2+} and Ca^{2+} compounds show similar potentials, an observation that correlates with the behavior of the OEC, which is active only in the presence of one of these two metals.

Introduction

Redox-inactive metal ions are critical components in many biological electron transfer reactions.¹ For example, Ca^{2+} is essential for activity in the oxygen-evolving complex (OEC) of Photosystem II (PSII), although its exact role in catalysis is still unclear.² There have been numerous studies of electron transfer to synthetic organic substrates,^{1a, 3} but studies of electron transfer to metal oxo complexes relevant to the active sites of a number of metalloenzymes have been fewer, possibly due to the challenge of isolating complexes with bound metal ions. Recently, a non-heme $\text{Fe}^{\text{IV}}\text{O}$ complex with a bound Sc^{3+} ion was characterized crystallographically, and it was found that the presence of Sc^{3+} or Ca^{2+} in solution allowed the two-electron reduction of the complex using ferrocene.⁴ The addition of other Lewis acidic metal ions to a different $\text{Fe}^{\text{IV}}\text{O}$ compound greatly enhanced electron transfer rates, although the adducts were not structurally characterized.⁵ With a monomeric Mn^{II} complex, faster rates of oxygen reduction were observed in the presence of Ca^{2+} , and a $\text{Mn}^{\text{III}}-(\mu\text{-OH})\text{-Ca}^{\text{II}}$ complex was isolated as the product.⁶ Substitution of Sr^{2+} for Ca^{2+} in this complex showed a similar reduction potential, while substitution with Ba^{2+} resulted in a more negative reduction potential.⁷ O-atom transfer from some manganese oxo complexes has also been promoted by the binding of redox-inactive metals such as lithium.⁸

Redox-inactive metal ions also play a role in non-biological electron transfer reactions such as water oxidation catalyzed by heterogeneous cobalt⁹ and manganese oxides¹⁰ containing alkali or alkali earth metals. In these examples, there has been speculation that the redox-inactive metal is associated with the transition metal catalyst in cubane-like structures reminiscent of the crystallographically determined structure of the OEC, an

oxide-bridged CaMn_4 cluster in which the calcium center is associated with three of the manganese centers in a cubane motif (Fig. 1).¹¹ A recent study varying the redox-inactive metal (K^+ , Ca^{2+} , Sr^{2+} , Mg^{2+}) in layered heterogeneous manganese oxides showed that, as in the OEC, the presence of Ca^{2+} allows for the highest catalytic activity.^{10a} Additionally, heterogeneous mixed oxides of cobalt show different water oxidation behavior dependent on the nature of the redox-inactive metal present in the mixture.¹² The role of the redox-inactive metal on electron transfer and catalysis within the material remains unclear in these systems.

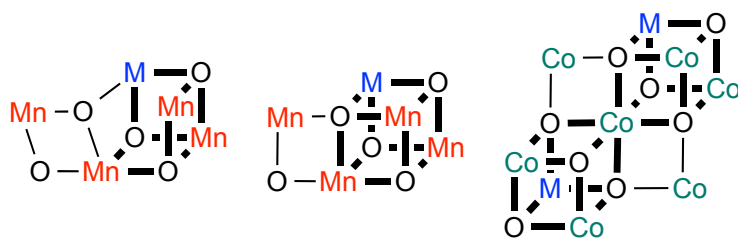


Figure 1. Proposed structures of water oxidation catalysts containing redox-inactive metals (M) in the OEC (left, middle) and in heterogeneous cobalt oxide water oxidation catalysts (right).^{9a, 13} The OEC is known to contain a Mn_3M core: one major model is based on extended X-ray absorption fine structure (EXAFS) and electron paramagnetic resonance (EPR) studies (left)¹⁴ and one on X-ray crystallography (middle).¹¹ Bold bonds emphasize the Mn_3M and Co_3M cluster cores.

Our recent report of a structural model of the CaMn_3 subsite of the OEC containing a high oxidation state heterometallic $\text{Mn}^{\text{IV}}_3\text{CaO}_4$ moiety and comparison to a tetramanganese analog suggested a significant influence of the calcium center on the redox properties of the cluster (see Chapter 4).¹⁵ To study the scope and chemical basis of this phenomenon in multimetallic oxide clusters such as those found in the OEC and in heterogeneous systems, access to well-defined and structurally related heterometallic oxido clusters of redox-active

and inactive metals is desirable. Based on a multinucleating ligand-based synthetic strategy developed by our group,¹⁶ we targeted heteronuclear clusters supported by the hexapyridyl trisalkoxido 1,3,5-triarylbenzene ligand (H_3L). In this chapter, we describe the synthesis of a series of tetranuclear heterometallic trimanganese dioxo clusters $[Mn_3M(\mu_4-O)(\mu_2-O)]$ containing a redox-inactive cation bridging via oxido moieties to manganese centers. Electrochemical characterization reveals that large changes in the Lewis acidity of the redox-inactive metal have a systematic effect on the redox properties of the cluster.

Results and discussion

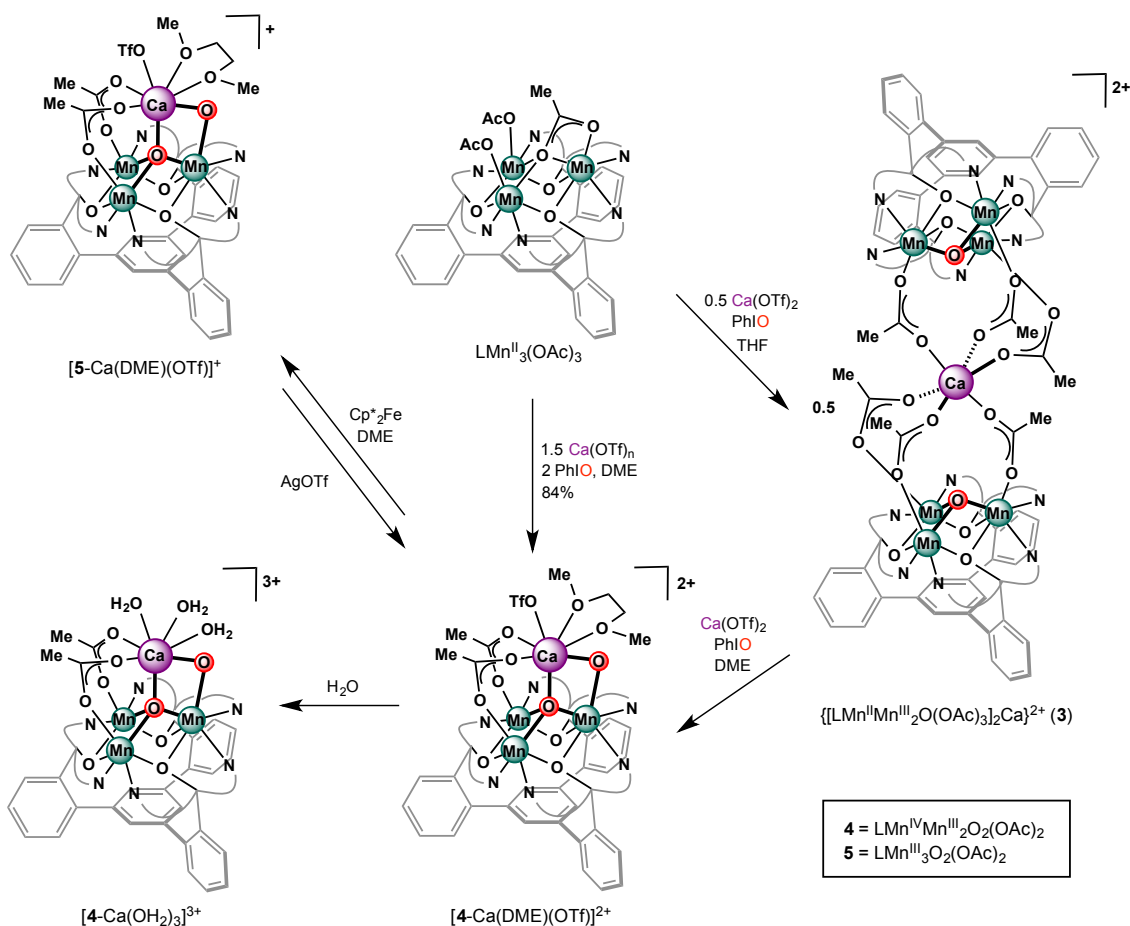
Heterometallic clusters have been targeted by several groups as proposed structural models of the OEC as evidence it contained a mixed Mn-Ca-oxido cluster emerged.¹⁷ Calcium-manganese clusters remain uncommon, though recently there have been a number of such complexes that have been isolated and structurally characterized.^{6, 15, 17b-g} Because heterometallic clusters are often synthesized by self-assembly, controlling the composition and relative arrangement of metals has been a challenge. Furthermore, these synthetic protocols are not necessarily easily extended to the incorporation of other redox-inactive metals instead of calcium. To develop general syntheses of heterometallic clusters, we employed a multinucleating ligand that affords versatile trimetallic (M^{II}_3) precursors (see Chapter 2).^{16b} These Mn^{II}_3 species could be elaborated to site-differentiated tetramanganese cubanes, Mn_4O_4 , as well as heteronuclear Mn_3CaO_4 clusters.¹⁵ Strategies for general synthetic protocols to related heteronuclear complexes were then explored.

3.1 Synthesis of $[CaMn_3O_2]$ clusters

A dicationic calcium-bridged hexamanganese complex $([LMn_2^{III}Mn^{II}O(OAc)_3]_2Ca(OTf)_2)$ (**3**) in which each trimanganese unit is coordinated by a

μ_3 -oxide was prepared by treatment of $\text{LMn}^{\text{II}}_3(\text{OAc})_3$ with $\text{Ca}(\text{OTf})_2$ (0.5 equiv) and iodosobenzene (Scheme 1).¹⁵ In an effort to isolate other manganese clusters of high oxidation state relevant for the preparation of structural mimics of the OEC, $[\text{LMn}_2^{\text{III}}\text{Mn}^{\text{II}}\text{O}(\text{OAc})_3]_2\text{Ca}(\text{OTf})_2$ was treated with $\text{Ca}(\text{OTf})_2$ and PhIO in 1,2-dimethoxyethane (DME) to form a red-purple compound (Scheme 1). The same compound was also independently synthesized in high yield (84%) in one step from the more reduced $\text{LMn}^{\text{II}}_3(\text{OAc})_3$ precursor. A single crystal X-ray diffraction (XRD) study of this species confirmed the material to be a calcium trimanganese dioxido complex ($[\mathbf{4}\text{-Ca}(\text{DME})(\text{OTf})]^{2+}$, $\mathbf{4} = \text{LMn}^{\text{IV}}\text{Mn}^{\text{III}}_2\text{O}_2(\text{OAc})_2$, Fig. 2). The metal oxidation states were assigned based on crystallographic, XAS, and magnetism data (vide infra). In this complex, as in $\text{LMn}^{\text{II}}_3(\text{OAc})_3$, the three manganese centers are bridged by three alkoxide donors from L, forming a six-membered ring, and the pyridine nitrogens of each dipyridyloxymethyl moiety coordinate to adjacent metal centers. Ca^{2+} is bridged to the trimanganese cluster by a μ_4 -oxido, to the Mn^{IV} center by a μ_2 -oxido, and to the remaining Mn^{III} centers by bridging acetate moieties. The Ca^{2+} is further coordinated by a bidentate DME ligand and a trifluoromethanesulfonate anion. Two trifluoromethanesulfonate ions remain outer-sphere. The isolated compounds reported here display diagnostic ^1H NMR spectra, although the paramagnetically broadened and shifted signals have not been assigned. The addition of excess water to a CD_2Cl_2 solution of $[\mathbf{4}\text{-Ca}(\text{DME})(\text{OTf})]^{2+}$ forms a new species by ^1H NMR spectroscopy (Fig. 4) that was identified by XRD as the tris(aqua) complex $[\mathbf{4}\text{-Ca}(\text{OH}_2)_3]^{3+}$ (Fig. 3). Addition of DME to the CD_2Cl_2 solution of $[\mathbf{4}\text{-Ca}(\text{OH}_2)_3]^{3+}$ converts the complex back to $[\mathbf{4}\text{-Ca}(\text{DME})(\text{OTf})]^{2+}$ (^1H NMR spectroscopy). In the solid state, $[\mathbf{4}\text{-Ca}(\text{DME})(\text{OTf})]^{2+}$ is stable for weeks under ambient conditions.

Treatment of a DME suspension of $[4\text{-Ca(DME)(OTf)}]^{2+}$ with the one-electron reductant decamethylferrocene yields the singly reduced product $[5\text{-Ca(DME)(OTf)}]^+$ (Scheme 1, **5** = $\text{LMn}^{\text{III}}_3\text{O}_2(\text{OAc})_2$). The chemical reversibility of this conversion is evidenced upon treatment of $[5\text{-Ca(DME)(OTf)}]^+$ with AgOTf to convert back to $[4\text{-Ca(DME)(OTf)}]^{2+}$. ^1H NMR analysis is consistent with clean interconversion of these two clusters. A XRD study of $[5\text{-Ca(DME)(OTf)}]^+$ reveals a cluster isostructural to $[4\text{-Ca(DME)(OTf)}]^{2+}$ with only slight bond distance changes (vide infra), indicating little rearrangement of the cluster upon reduction (Fig. 5).



Scheme 1. Synthesis of tetrametallic trimanganese dioxido complexes.

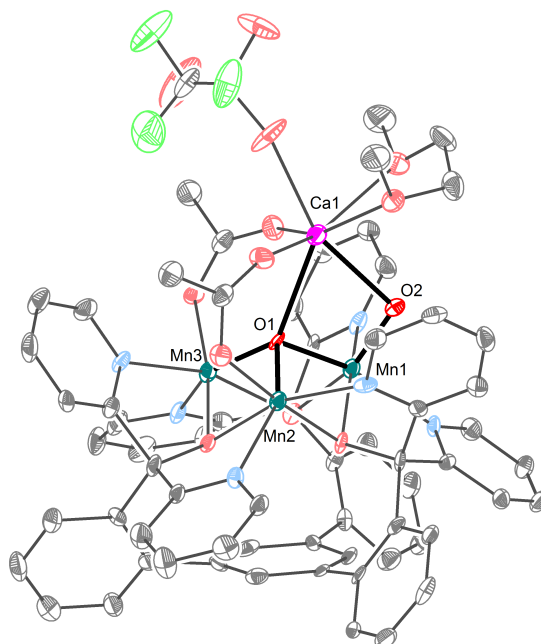


Figure 2. Solid-state structure of $[4\text{-Ca}(\text{DME})(\text{OTf})]^{2+}$ as 50% thermal ellipsoids. Outer-sphere anions and hydrogen atoms not shown for clarity.

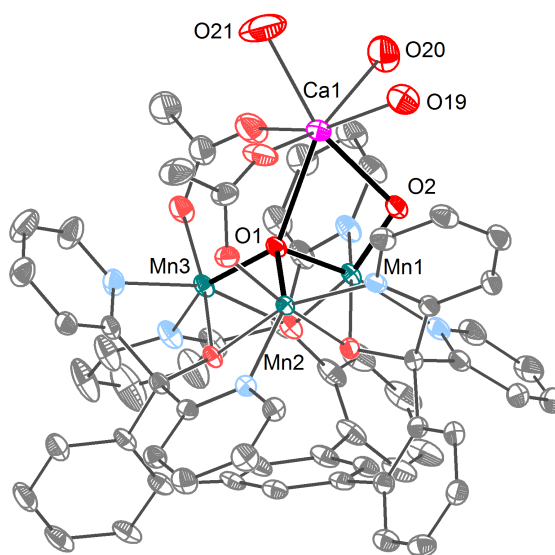


Figure 3. Structural drawing of $[4\text{-Ca}(\text{H}_2\text{O})_3](\text{OTf})_3$ with 50% probability ellipsoids. Outer-sphere trifluoromethanesulfonate anions and hydrogen atoms not pictured for clarity.

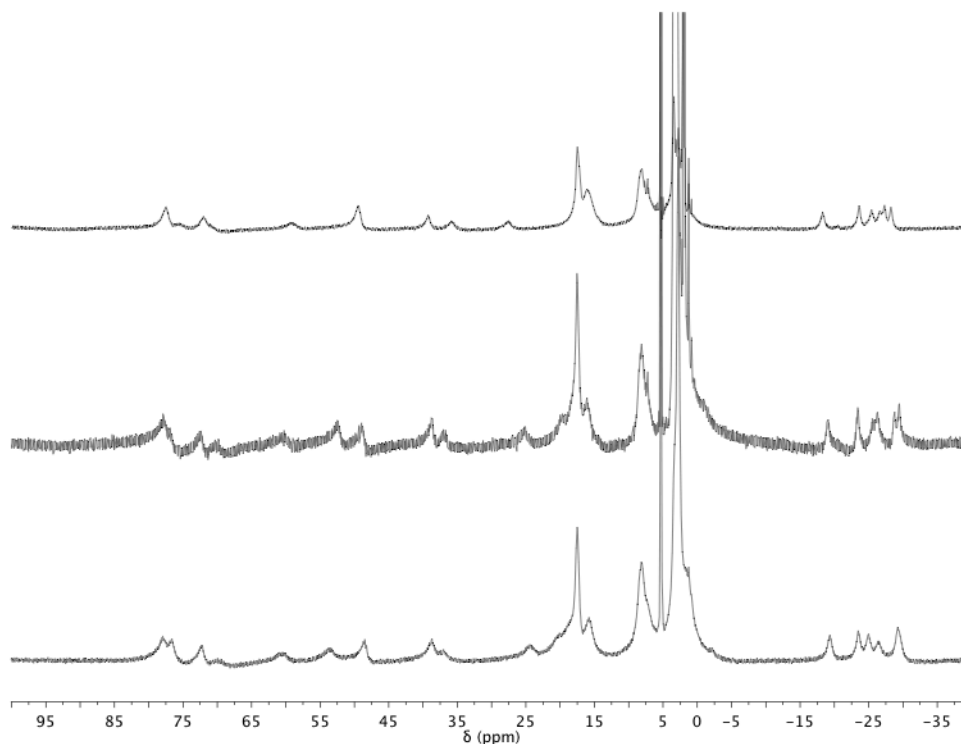


Figure 4. ^1H NMR spectra of CD_2Cl_2 solutions of $[\mathbf{4}\text{-Ca}(\text{H}_2\text{O})_3]^{3+}$ (top), $[\mathbf{4}\text{-Ca}(\text{H}_2\text{O})_3]^{3+}$ with added DME (middle), and $[\mathbf{4}\text{-Ca}(\text{DME})(\text{OTf})]^{2+}$ (bottom) at 25 °C.

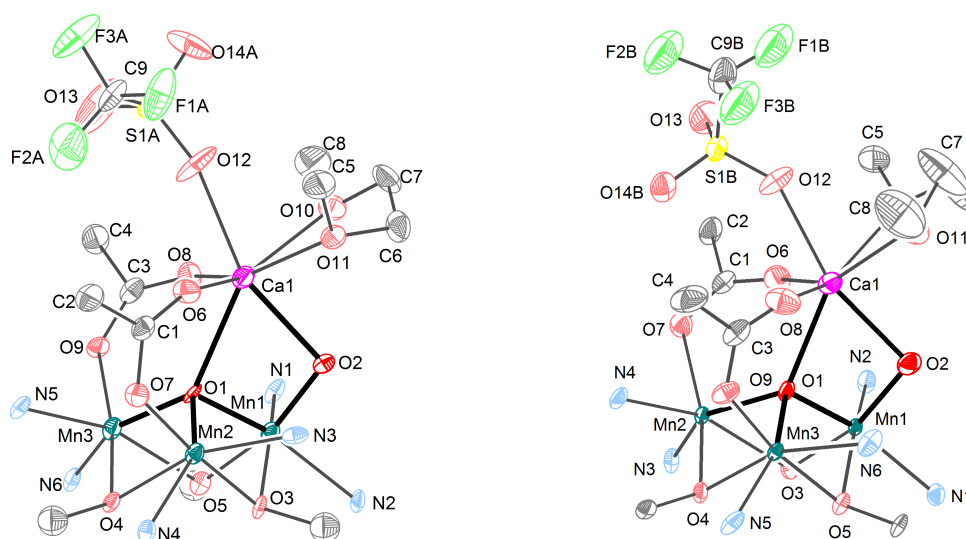
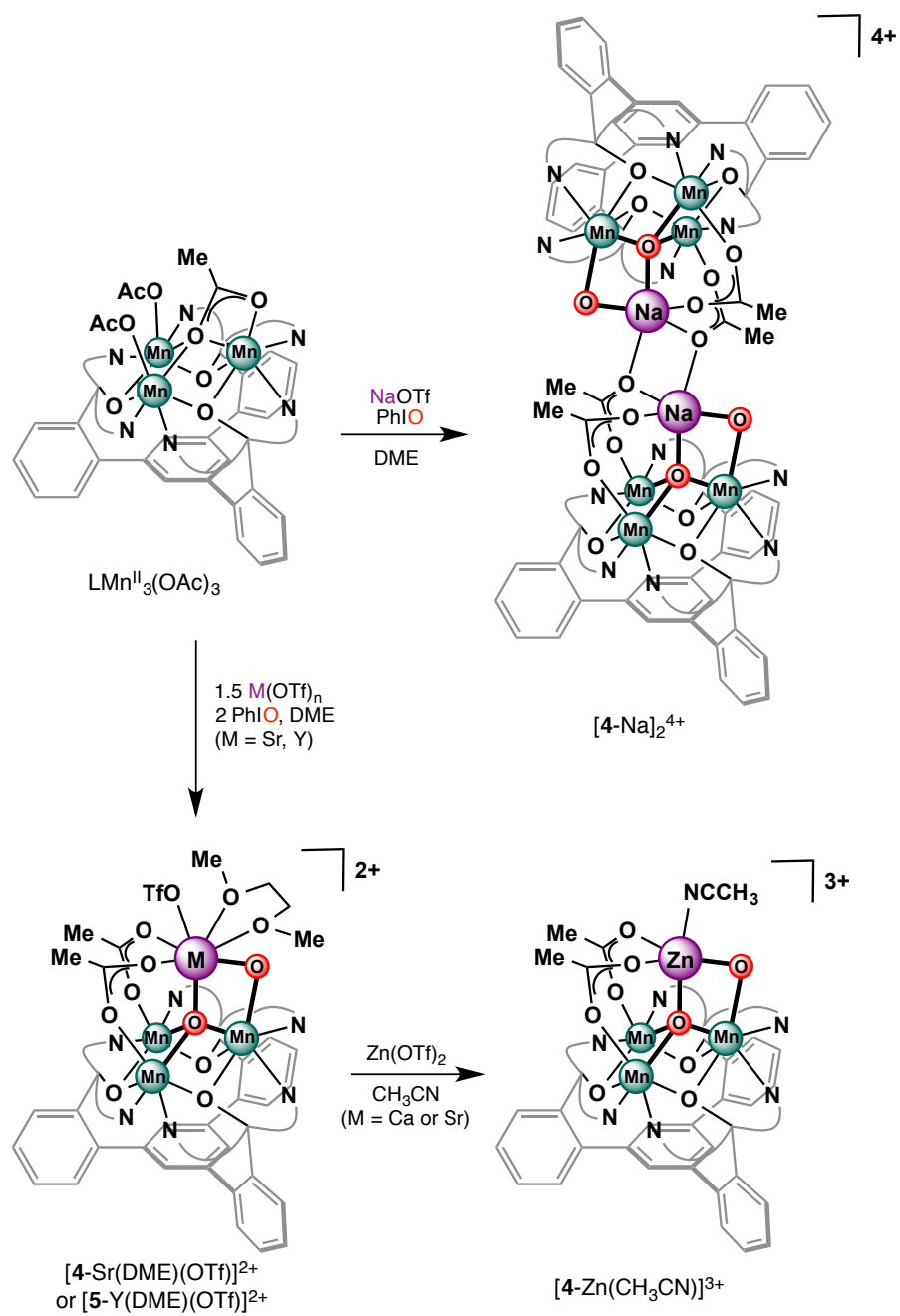


Figure 5. Solid-state structures of reported complexes (thermal ellipsoids shown at 50% level). Hydrogen atoms and outer-sphere anions not shown for clarity. Bolded bonds emphasize the dioxido core. Truncated view of $[\mathbf{4}\text{-Ca}(\text{DME})(\text{OTf})][\text{OTf}]_2$ (left). Truncated view of $[\mathbf{5}\text{-Ca}(\text{DME})(\text{OTf})][\text{OTf}]$ (right).

3.2 Synthesis of $[MMn_3O_2]$ complexes

To study the effects of the redox-inactive center on the properties of the $[Mn_3O_2]$ core, the analogous Sr^{2+} -, Y^{3+} -, Na^+ -, and Zn^{2+} -capped trimanganese dioxo complexes were targeted. Treatment of $LMn^{II}_3(OAc)_3$ with PhIO and $M(OTf)_n$ (Scheme 2, $M = Na, Sr, Y$), led to new species with 1H NMR spectroscopic characteristics similar to compounds **[4-Ca(DME)(OTf)] $^{2+}$** and **[5-Ca(DME)(OTf)] $^+$** . Complexes **[4-Sr(DME)(OTf)] $^{2+}$** and **[5-Y(DME)(OTf)] $^{2+}$** are structurally analogous to **[4-Ca(DME)(OTf)] $^{2+}$** with the redox-inactive metal bridged by two oxido moieties to the trimanganese cluster and further coordinated by a DME molecule and a triflate anion (Fig. 6). The yttrium-capped dioxo compound was isolated in the more reduced Mn^{III}_3 state rather than the $Mn^{IV}Mn^{III}_2$ state observed under the same reaction conditions for the calcium and strontium dioxo compounds. Similar to the reduction of **[4-Ca(DME)(OTf)] $^{2+}$** to **[5-Ca(DME)(OTf)] $^+$** , the reduced strontium compound **[5-Sr(DME)(OTf)] $^+$** was prepared by treating **[4-Sr(DME)(OTf)] $^{2+}$** with decamethylferrocene. The Na-capped dioxo complex **[4-Na] $_2^{4+}$** was isolated in the solid-state as a dimer of $[Mn_3NaO_2]$ subunits via bridged by acetate ligands. Each $[Mn_3NaO_2]$ core is structurally similar to the Ca^{2+} , Sr^{2+} and Y^{3+} analogs, with the Na^+ cation bridged by two oxidos to the trimanganese moiety (Fig. 6). Preparation of the Zn-capped compound **[4-Zn(CH₃CN)] $^{3+}$** was accomplished by addition of $Zn(OTf)_2$ to a CH_3CN solution of **[4-Ca(DME)(OTf)] $^{2+}$** , leading to substitution of Ca^{2+} with Zn^{2+} . A XRD study of **[4-Zn(CH₃CN)] $^{3+}$** grown from an acetonitrile/diethyl ether mixture shows one acetonitrile coordinated to the Zn^{2+} center. The Mn_3ZnO_2 core is structurally similar to the other Mn_3MO_2 moieties reported here.



Scheme 2. Synthesis of heterometallic manganese dioxido complexes.

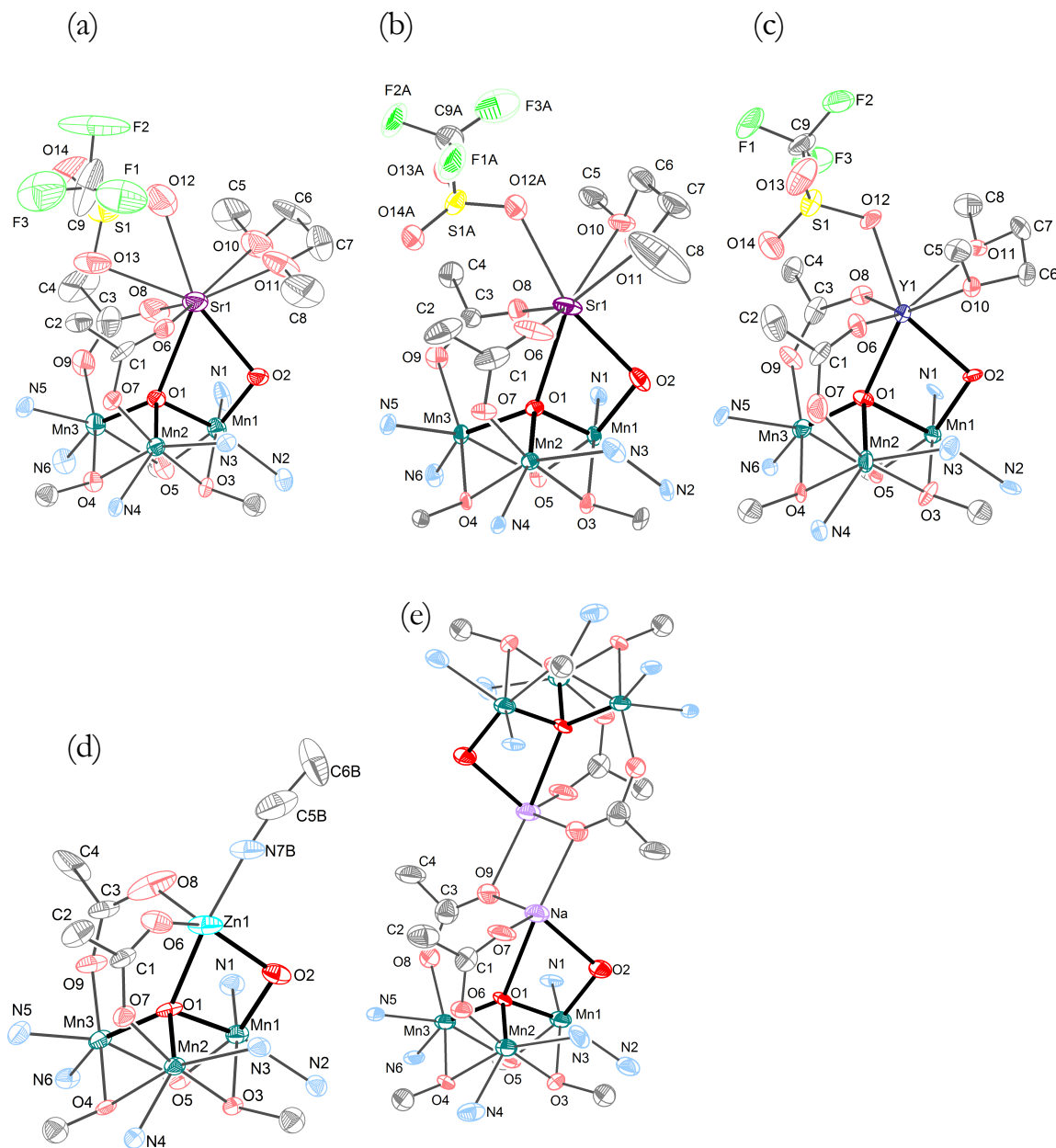


Figure 6. (a) Truncated view of $[4\text{-Sr}(\text{DME})(\text{OTf})][\text{OTf}]_2$. (b) Truncated view of $[5\text{-Sr}(\text{DME})(\text{OTf})][\text{OTf}]$. (c) Truncated view of $[5\text{-Y}(\text{DME})(\text{OTf})][\text{OTf}]_2$. (d) Truncated view of $[4\text{-Zn}(\text{CH}_3\text{CN})][\text{OTf}]_3$. (e) Truncated view of $[4\text{-Na}]_2[\text{OTf}]_4$.

Analysis of the solid-state structures show that the distances from the redox-inactive metals to the bridging oxido moieties vary as expected based on the ionic radius of the ion M , with the $M\text{-O}$ distances increasing from $[4\text{-Zn}(\text{CH}_3\text{CN})]^{3+}$ [2.008(3), 2.090(3) Å] to $[4\text{-$

$\text{Sr}(\text{DME})(\text{OTf})]^{2+}$ [2.510(5), 2.651(4) Å] (Table 1). Upon reduction of the $\text{Mn}^{\text{IV}}\text{Mn}^{\text{III}}_2$ clusters $[\mathbf{4}\text{-Ca}(\text{DME})(\text{OTf})]^{2+}$ and $[\mathbf{4}\text{-Sr}(\text{DME})(\text{OTf})]^{2+}$ to form the Mn^{III}_3 complexes $[\mathbf{5}\text{-Ca}(\text{DME})(\text{OTf})]^+$ and $[\mathbf{5}\text{-Sr}(\text{DME})(\text{OTf})]^+$, the $\text{M}-(\mu_4\text{-O})$ distances contract, indicating a stronger interaction with the redox-inactive metal as the interaction of the μ_4 -oxido with the trimanganese core weakens due to increased population of σ -antibonding orbitals in d^4 , Mn^{III} centers. As expected, the Mn-O distances increase upon reduction (compounds **5** vs **4**), but only small variations are observed based upon the redox-inactive metal. $[\mathbf{5}\text{-Y}(\text{DME})(\text{OTf})]^{2+}$ displays the longest Mn-oxido average distance, consistent with the yttrium center, the most Lewis acidic metal of the series, drawing more electron density from the oxido moieties and weakening the Mn-O interactions. Notably, the bond distances of the Mn_3O_2 core are essentially the same between $[\mathbf{4}\text{-Ca}(\text{DME})(\text{OTf})]^{2+}$ and $[\mathbf{4}\text{-Sr}(\text{DME})(\text{OTf})]^{2+}$. These observations are consistent with XAS studies of Sr-substituted PSII indicating no significant structural change in the OEC from Ca-substituted PSII.^{2a}

Table 1. Selected bond lengths (Å) for reported complexes. All e.s.d.s were calculated rigorously from the full covariance matrix.¹⁸

| | $[\mathbf{4}\text{-Ca}(\text{DME})(\text{OTf})]^{2+}$ | $[\mathbf{5}\text{-Ca}(\text{DME})(\text{OTf})]^+$ | $[\mathbf{4}\text{-Sr}(\text{DME})(\text{OTf})]^{2+}$ | $[\mathbf{5}\text{-Sr}(\text{DME})(\text{OTf})]^+$ | $[\mathbf{4}\text{-Na}]_2^{4+}$ | $[\mathbf{4}\text{-Zn}(\text{ACN})]_2^{3+}$ | $[\mathbf{5}\text{-Y}(\text{DME})(\text{OTf})]^{2+}$ |
|-----------|---|--|---|--|---------------------------------|---|--|
| M–Mn1 | 3.317(1) | 3.283(1) | 3.476(1) | 3.424(1) | 3.216(3) | 3.0005(8) | 3.3011(6) |
| M–Mn2 | 3.749(1) | 3.802(1) | 4.005(1) | 3.923(1) | 3.739(3) | 3.3495(9) | 3.7533(6) |
| M–Mn3 | 4.042(1) | 4.034(1) | 4.149(1) | 4.166(1) | 3.942(3) | 3.7595(9) | 3.8592(6) |
| Mn1–Mn2 | 3.0480(9) | 3.0111(9) | 3.062(1) | 3.020(2) | 3.076(2) | 3.065(1) | 3.2110(7) |
| Mn1–Mn3 | 3.0486(9) | 3.1537(9) | 3.051(1) | 3.142(2) | 3.000(2) | 3.038(1) | 3.0494(7) |
| Mn2–Mn3 | 3.0179(9) | 3.0541(9) | 3.025(1) | 3.064(2) | 3.004(2) | 3.0739(9) | 3.1223(7) |
| M–O2 | 2.349(3) | 2.368(3) | 2.510(5) | 2.508(5) | 2.300(6) | 2.008(3) | 2.269(2) |
| M–O1 | 2.452(3) | 2.397(3) | 2.651(4) | 2.536(5) | 2.422(6) | 2.090(3) | 2.232(2) |
| Mn1–O2 | 1.842(3) | 1.887(3) | 1.841(4) | 1.869(5) | 1.840(5) | 1.862(3) | 1.889(2) |
| Mn1–O1 | 2.017(3) | 1.939(3) | 2.022(4) | 1.943(5) | 1.995(5) | 1.981(3) | 2.150(2) |
| Mn2–O1 | 1.913(3) | 2.159(3) | 1.932(4) | 1.856(5) | 1.936(5) | 1.946(3) | 2.177(2) |
| Mn3–O1 | 1.958(3) | 1.860(3) | 1.936(4) | 2.172(5) | 1.889(5) | 1.960(3) | 1.895(2) |
| Av. Mn–O1 | 1.96 | 1.99 | 1.96 | 1.99 | 1.94 | 1.96 | 2.07 |

3.3 Magnetic susceptibility and X-ray absorption studies of dioxido complexes

The variable temperature magnetic susceptibilities of [4-Ca(DME)(OTf)][OTf]₂ and [5-Ca(DME)(OTf)][OTf] were studied (Fig. 7). For [4-Ca(DME)(OTf)][OTf]₂, dominant ferromagnetic coupling between Mn ions is observed (see Table 2 for fitting parameters). At 14 K, the $\chi_M T$ value increases to a maximum of 18.7 cm³ mol⁻¹ K, which is close to the expected spin-only value of a $S = 11/2$ system (17.9 cm³ mol⁻¹ K, $g = 2$). Different values would be expected for a more oxidized $S = 5$ system (15 cm³ mol⁻¹ K, $g = 2$) or a more reduced $S = 6$ system (21 cm³ mol⁻¹ K, $g = 2$). These results support the oxidation state assignment of [4-Ca(DME)(OTf)]²⁺ as Mn^{IV}Mn^{III}₂. The $\chi_M T$ value of [5-Ca(DME)(OTf)][OTf] approaches 10.2 cm³ mol⁻¹ K at 300 K, which is near the expected spin-only value of three uncoupled Mn^{III} ions ($S = 2$ spins, 3 cm³ mol⁻¹ K, $g = 2$). The $\chi_M T$ value decreases at low temperatures, reaching 2.6 cm³ mol⁻¹ K at 4 K, which shows a dominant antiferromagnetic interaction (Table 2). To further confirm the oxidation state assignment of the isolated species, Mn XANES spectra were collected for [4-Ca(DME)(OTf)][OTf]₂ and [5-Ca(DME)(OTf)][OTf] (Fig. 8a). The rising edge energy, taken as a zero-crossing point of the 2nd derivative spectrum (Fig. 8b), is shifted to a higher energy by ca. 1.0 eV step from [5-Ca(DME)(OTf)][OTf] (6548.66 eV) to [4-Ca(DME)(OTf)][OTf]₂ (6549.76 eV). Such step-wise edge shift is consistent with an one-electron oxidation state change in redox-active Mn complexes,¹⁹ when the geometry and type of ligands are highly conserved. This result, correlated with charge balance in the solid state structure, magnetism, and chemical reactivity, therefore, supports the formal oxidation state assignments for [4-Ca(DME)(OTf)][OTf]₂ and [5-Ca(DME)(OTf)][OTf] as Mn^{IV}Mn^{III}₂ and Mn^{III}₃ respectively. The magnetic susceptibilities of the Mn^{IV}Mn^{III}₂

complexes $[\mathbf{4}\text{-Sr(DME)(OTf)}][\text{OTf}]_2$, $[\mathbf{4}\text{-Na}]_2[\text{OTf}]_4$, and $[\mathbf{4}\text{-Zn(CH}_3\text{CN)}][\text{OTf}]_3$ were measured, and all demonstrate ferromagnetic coupling of spins close to that of $[\mathbf{4}\text{-Ca(DME)(OTf)}][\text{OTf}]_2$, supporting the same formal oxidation state assignment (Fig. 7).

Table 2. Magnetic susceptibility fitting parameters.

| Compound | Diamagnetic Correction ($\times 10^{-6} \text{ cm}^3/\text{mol}$) | $J (\text{cm}^{-1})$ | $\mathcal{J} (\text{cm}^{-1})$ | g | R ($\times 10^{-5}$) |
|---|---|----------------------|--------------------------------|------|------------------------|
| $[\mathbf{4}\text{-Ca(DME)(OTf)}][\text{OTf}]_2$ | −938 | 12.9 | −0.7 | 2.05 | 3.3 |
| $[\mathbf{4}\text{-Sr(DME)(OTf)}][\text{OTf}]_2$ | −947 | 12.4 | 0.6 | 2.02 | 2.5 |
| $[\mathbf{4}\text{-Na}]_2[\text{OTf}]_4$ | −715 | 17.3 | −5.1 | 2.07 | 7.9 |
| $[\mathbf{4}\text{-Zn(CH}_3\text{CN)}][\text{OTf}]_3$ | −715 | 17.3 | −3.2 | 2.06 | 3.5 |
| $[\mathbf{5}\text{-Ca(DME)(OTf)}][\text{OTf}]$ | −831 | −2.3 | 25.3 | 1.95 | 1.7 |

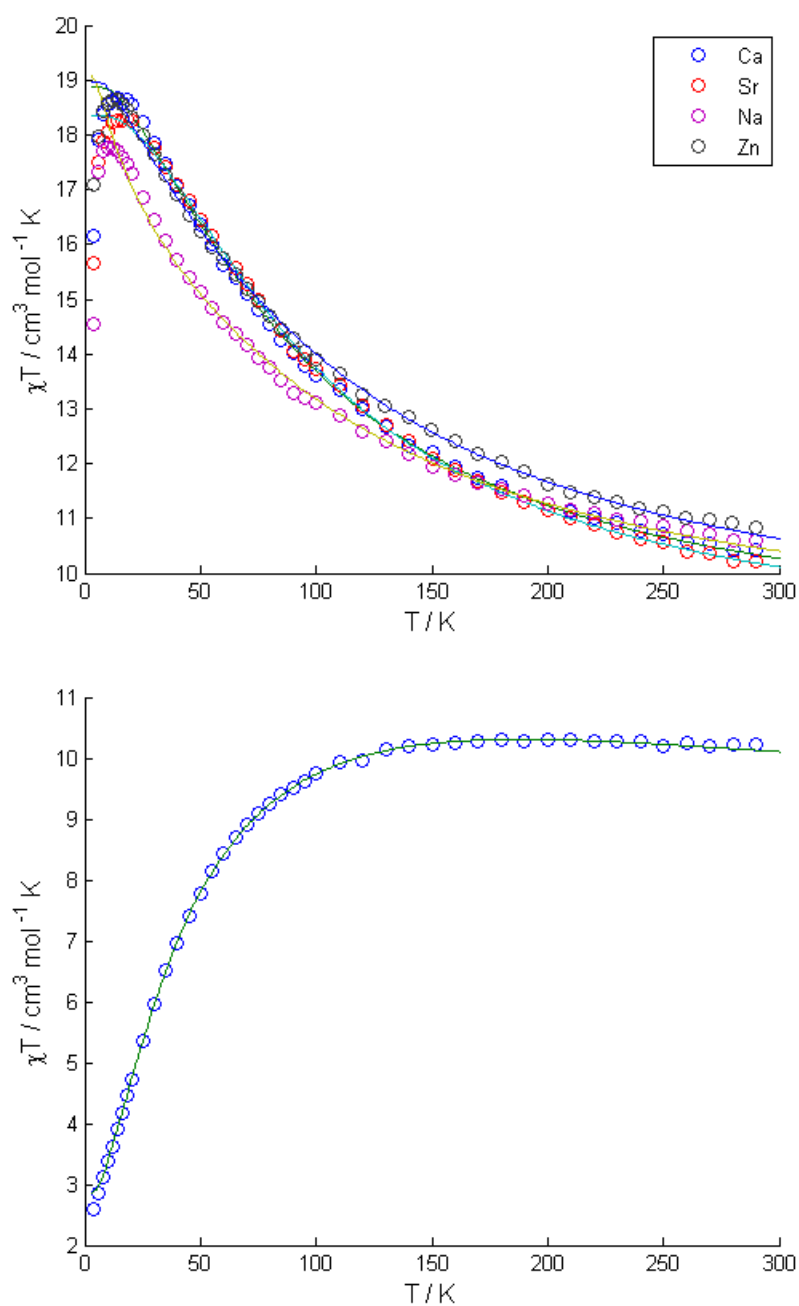


Figure 7. $\chi_M T$ vs. T data and fits for [4-Ca(DME)(OTf)][OTf]₂, [4-Sr(DME)(OTf)][OTf]₂, [4-Na]₂[OTf]₄, and [4-Zn(CH₃CN)][OTf]₃ (top), and $\chi_M T$ vs. T data and fit for [5-Ca(DME)(OTf)][OTf] (bottom). See Table 2 for fit parameters.

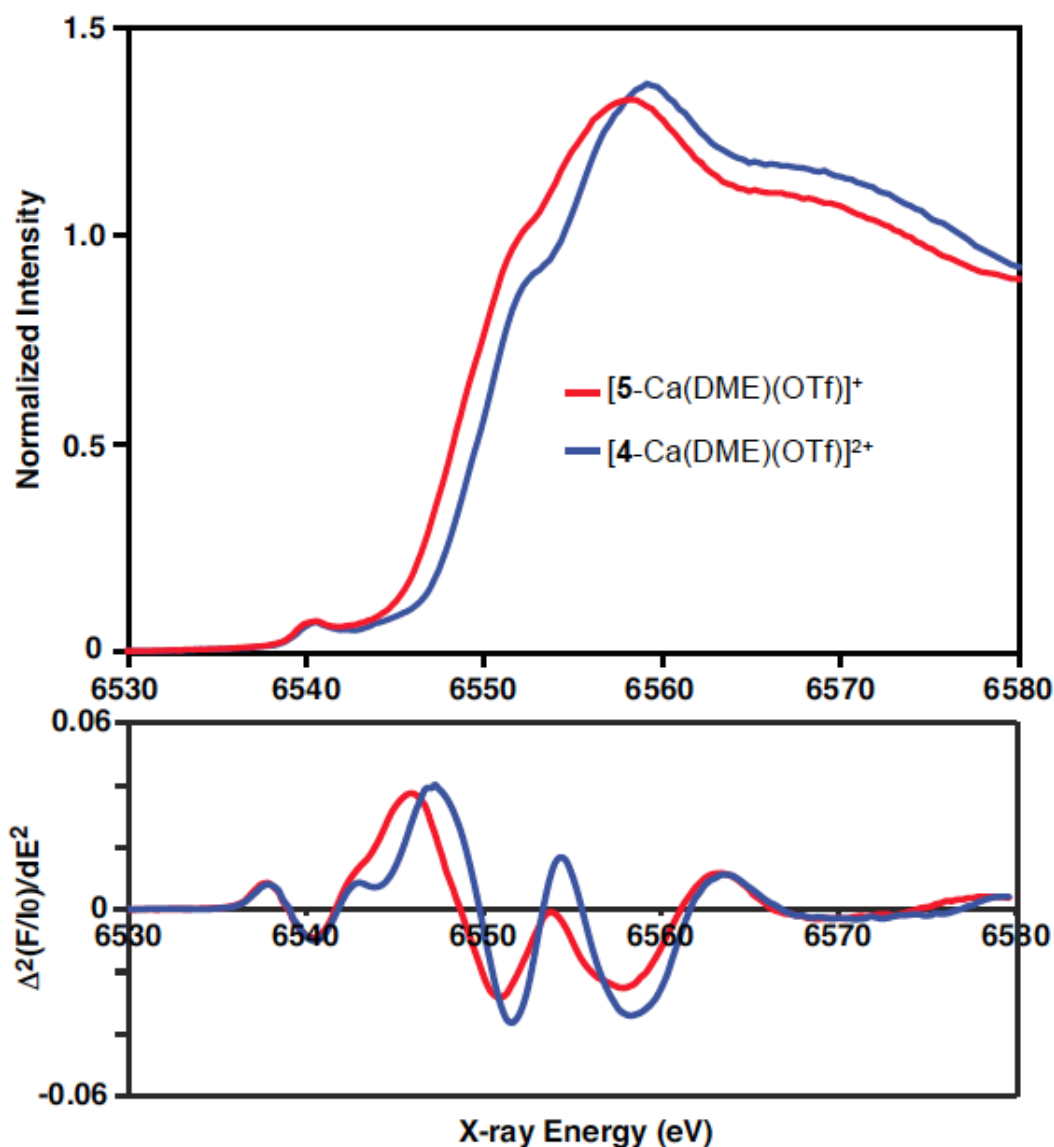


Figure 8. The shift in the rising edge energy in the Mn XANES spectra. The shift for $[4\text{-Ca(DME)(OTf)}][\text{OTf}]_2$ (blue line) and $[5\text{-Ca(DME)(OTf)}][\text{OTf}]$ (red line) (6,549.76 and 6,548.66 eV, respectively) suggests a one-electron oxidation state change. Mn XANES spectra (a) and second derivative spectra (b). XANES measurements collected by Rosalie Tran and Junko Yano.

3.4 Electrochemical studies of $[MMn_3O_2]$ complexes

We and others have reported studies that suggest a significant effect of redox-inactive metals on the electron transfer properties of metal-oxido species, phenomenon of particular relevance in biological systems and heterogeneous mixed metal oxides.^{4-5, 10a, 15, 17a, 20} With a series of well-defined and structurally analogous Mn_3MO_2 complexes in hand, the effect of metal M on the reduction potential of the clusters was investigated. The cyclic voltammogram (CV) of a 10:1 CH_2Cl_2 /DME solution of $[4-Ca(DME)(OTf)]^{2+}$ (0.1 M NBu_4PF_6) shows two quasireversible redox couples at -70 and -530 mV versus the ferrocene/ferrocenium couple (Fc/Fc^+) (Fig. 9 left). Since $[4-Ca(DME)(OTf)]^{2+}$ is chemically reduced to $[5-Ca(DME)(OTf)]^+$ by the addition of one equivalent of decamethylferrocene ($E^O \sim -0.48$ V vs. Fc/Fc^+ in CH_2Cl_2), the couple centered at -70 mV is assigned as the $[Mn^{IV}Mn^{III}_2/Mn^{III}_3]$ couple. A 10:1 CH_2Cl_2 /DME solution of $[4-Ca(DME)(OTf)]^{2+}$ (0.05 M LiOTf electrolyte) was electrolyzed at a potential of -0.25 V vs. Ag/Ag^+ to form a new species by 1H NMR spectroscopy. The amount of current passed at that potential supports the assignment of the wave at -80 mV as the one electron reduction of $[4-Ca(DME)(OTf)]^{2+}$. Independently prepared $[5-Ca(DME)(OTf)]^+$ reacts with excess LiOTf to cleanly form a product whose 1H NMR spectrum matches that of the controlled potential electrolysis product described above (Fig. 10). Under the same conditions, $[4-Ca(DME)(OTf)]^{2+}$ does not react with LiOTf. The more negative redox couple at -530 mV is presumed to correspond to the $[Mn^{III}_3/Mn^{III}_2Mn^{II}]$ couple, but the more reduced product has not yet been isolated.

Since the electrochemical studies are presumed to be of intact clusters, the solution stability of the $[MMn_3O_2]$ core was studied. Isotopically labelled

$\text{LCaMn}_3^{18}\text{O}_2(\text{OAc})_2(\text{DME})(\text{OTf})_3$ ($[\mathbf{4}^*-\text{Ca}(\text{DME})(\text{OTf})][\text{OTf}]_2$) was prepared and mixed with one equivalent of natural abundance $[\mathbf{4}-\text{Ca}(\text{DME})(\text{OTf})]^{2+}$ in dichloromethane at room temperature, and the mixture was analyzed over time using electrospray ionization mass spectrometry (ESI-MS). Less than 20% isotopic scrambling occurs on the timescale of the electrochemical experiments (ca. 18% after 1 h at RT). Additionally, methylene chloride solutions of $[\mathbf{4}-\text{Ca}(\text{DME})(\text{OTf})]^{2+}$ are stable at room temperature under anhydrous conditions for days (^1H NMR spectroscopy). The addition of 10 equivalents of $\text{Ca}(\text{OTf})_2$ to the solution of $[\mathbf{4}-\text{Ca}(\text{DME})(\text{OTf})]^{2+}$ does not change the reduction potential of the complex indicating that any equilibrium toward dissociation of the clusters lies toward Ca^{2+} association. To interrogate the effect of the Ca-coordinated ligands, under the same conditions, the reduction of $[\mathbf{4}-\text{Ca}(\text{OH}_2)_3]^{3+}$ occurs within 30 mV of that of $[\mathbf{4}-\text{Ca}(\text{DME})(\text{OTf})]^{2+}$ (see experimental section) suggesting that the capping ligands on the Ca^{2+} center do not significantly affect the reduction potentials of the clusters.

CVs of $[\mathbf{4}-\text{Sr}(\text{DME})(\text{OTf})]^{2+}$, $[\mathbf{5}-\text{Y}(\text{DME})(\text{OTf})]^{2+}$, $[\mathbf{4}-\text{Zn}(\text{CH}_3\text{CN})]^{3+}$, and $[\mathbf{4}-\text{Na}]_2^{4+}$ all display the $[\text{Mn}^{\text{IV}}\text{Mn}^{\text{III}}_2/\text{Mn}^{\text{III}}_3]$ couple observed for $[\mathbf{4}-\text{Ca}(\text{DME})(\text{OTf})]^{2+}$, although at different potentials (Fig. 9, Table 3). Although the peak-to-peak separations of the observed couples are large when measured at a glassy carbon electrode ($\Delta E_p \sim 400$ mV), indicating slow electron transfer to the complexes, the $E_{1/2}$ values calculated from the CVs of $[\mathbf{4}-\text{Ca}(\text{DME})(\text{OTf})]^{2+}$, $[\mathbf{4}-\text{Sr}(\text{DME})(\text{OTf})]^{2+}$, and $[\mathbf{4}-\text{Na}]_2^{4+}$ are in good agreement with CVs collected using a hanging drop mercury electrode, with $\Delta E_p \sim 200$ mV (see experimental section). The $E_{1/2}$ corresponding to the reduction of $[\mathbf{4}-\text{Ca}(\text{DME})(\text{OTf})]^{2+}$ to $[\mathbf{5}-\text{Ca}(\text{DME})(\text{OTf})]^+$ was also measured by monitoring the electronic absorption spectrum

upon titration with dimethylferrocene, and the calculated values (-0.1 V vs. Fc/Fc^+) are close to the value from the CV (-0.08 V vs. Fc/Fc^+).

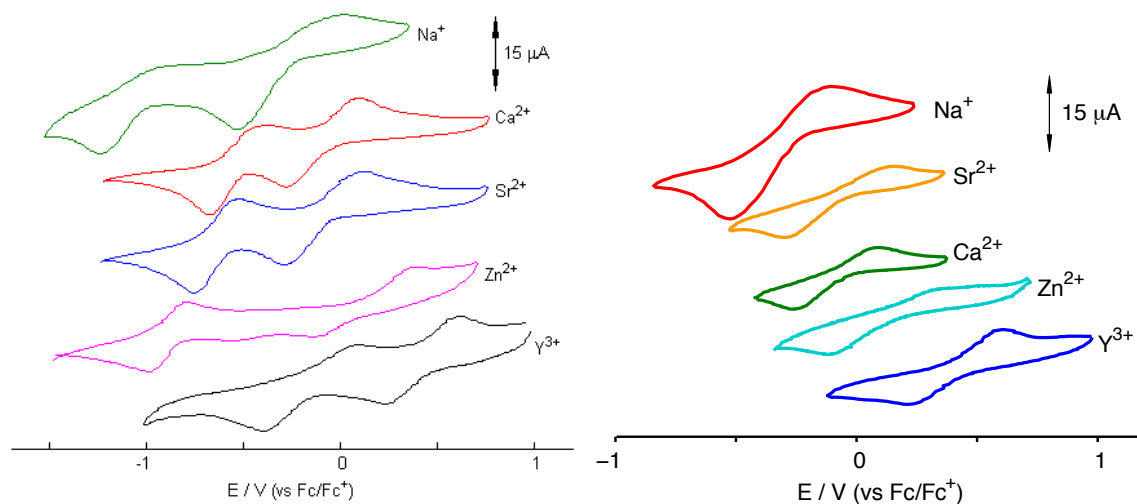


Figure 9. Cyclic voltammograms of complexes using a GCE at 20 °C showing both redox events (left) and the $\text{Mn}^{\text{IV}}\text{Mn}^{\text{III}}_2/\text{Mn}^{\text{III}}_3$ couple (right). CVs were taken at a scan rate of 100 mV/s and referenced to an internal Fc/Fc^+ standard.

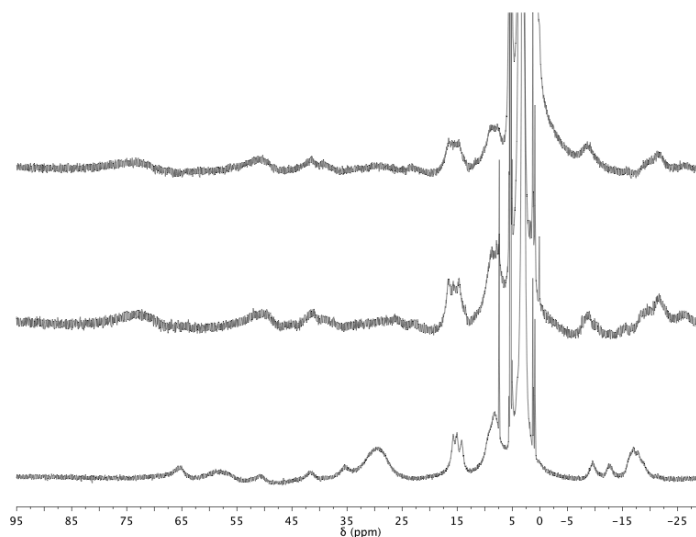


Figure 10. ^1H NMR spectra at 25 °C of CD_2Cl_2 solutions of the controlled-potential electrolysis product (top), $[\mathbf{5}\text{-Ca}(\text{DME})(\text{OTf})][\text{OTf}]$ after addition of LiOTf (middle), and $[\mathbf{5}\text{-Ca}(\text{DME})(\text{OTf})][\text{OTf}]$ (bottom).

As structural characterization was obtained only for clusters displaying the $\text{Mn}^{\text{IV}}\text{Mn}^{\text{III}}_2$ and Mn^{III}_3 oxidation states, these are the reduction potentials that are compared below. Moreover, the more highly oxidized species are pertinent to the moieties present in the OEC and proposed for water oxidation catalysts. The $E_{1/2}$ values of the $[\text{Mn}^{\text{IV}}\text{Mn}^{\text{III}}_2/\text{Mn}^{\text{III}}_3]$ couple become more positive as the charge of the redox-inactive metal increases. This trend suggests that the increased charge of the proximal redox-inactive cation facilitates reduction of the manganese centers. The $E_{1/2}$ value for the Zn^{2+} complex appears at potentials ca. 230 mV more positive compared to the Ca^{2+} and Sr^{2+} species. Although $[\text{4-Zn}(\text{CH}_3\text{CN})]^{3+}$ is tricationic while $[\text{4-Ca}(\text{DME})(\text{OTf})]^{2+}$ and $[\text{4-Sr}(\text{DME})(\text{OTf})]^+$ are dicationic, the $E_{1/2}$ of the $[\text{Mn}^{\text{IV}}\text{Mn}^{\text{III}}_2/\text{Mn}^{\text{III}}_3]$ couple of $[\text{4-Ca}(\text{OH}_2)]^{3+}$, also a tricationic complex, is more positive than that of $[\text{4-Ca}(\text{DME})(\text{OTf})]^{2+}$ by less than 30 mV. The more positive potential of the Zn^{2+} compound is inconsistent with a purely electrostatic explanation of the change in reduction potentials, as proposed for oxo-bridged manganese dimers with alkali and alkali earth metal ions associated via salen ligands modified with crown ether moieties.^{20b}

Table 3. $E_{1/2}$ values of the $[\text{MMn}_3\text{O}_2]^{n+6}/[\text{MMn}_3\text{O}_2]^{n+5}$ couple vs. Fc/Fc^+ using the glassy carbon electrode (GCE) and the hanging mercury drop electrode.

| M | GCE (V) | Hg (V) |
|----|---------|--------|
| Na | −0.30 | −0.31 |
| Sr | −0.07 | −0.06 |
| Ca | −0.07 | −0.07 |
| Zn | 0.16 | -- |
| Y | 0.42 | -- |

The effect of redox-inactive metals on the kinetics of electron transfer to a non-heme $\text{Fe}^{\text{IV}}\text{O}$ species has been previously linked to the Lewis acidity of the metal.^{5, 21} The $E_{1/2}$ values of the $[\text{Mn}^{\text{IV}}\text{Mn}^{\text{III}}_2/\text{Mn}^{\text{III}}_3]$ couples measured above in organic solvents were plotted against the $\text{p}K_{\text{a}}$ of the metal aqua ions, $\text{M}(\text{aqua})^{n+}$ in water,²² used here as a measure of the Lewis acidity of the metal M. A remarkable linear correlation is observed (Fig. 11) that clearly links the effect of the redox-inactive metal to the cluster reduction potential in terms of the metal's Lewis acidity. The slope provides a quantitative measure of this correlation, with each $\text{p}K_{\text{a}}$ unit shifting the potential by ca. 100 mV. This effect is likely a consequence of the interaction between the oxido moieties and redox-inactive metals vs. manganese centers. The stronger Lewis acid is expected to draw more electron density from the oxido ligands and to destabilize the higher oxidation state manganese centers.

The above findings have implications for biological and heterogeneous metal catalysts for water oxidation and other redox processes. Catalysis occurs at discrete multinuclear sites, consisting of five metal centers for the OEC in PSII and less than ten metal centers for heterogeneous manganese and cobalt oxides. The potential of the cluster is expected to vary based on structure and number of oxido ligands. For example, the reduction potential of the $[\text{Mn}^{\text{IV}}\text{Mn}^{\text{III}}_2\text{CaO}_2/\text{Mn}^{\text{III}}_3\text{CaO}_2]$ couple reported here is more positive than that of the $[\text{Mn}^{\text{IV}}_3\text{CaO}_4/\text{Mn}^{\text{IV}}_2\text{Mn}^{\text{III}}\text{CaO}_4]$ couple of the CaMn_3 cubane cluster,¹⁵ despite the higher manganese oxidation states in the latter complex, likely due to the greater number of oxido ligands. Changing the nature of the redox-inactive metal component of the cluster, without a structural change of the cluster, allows for drastic variation of the reduction potential in both directions, potentially from values that render the chemistry of interest (e.g. water oxidation) thermodynamically unfavorable to values that make it favorable. Tuning of the

reduction potentials of mixed metal-oxide cluster by Lewis acids is an appealing strategy for designing practical catalysts for water splitting.

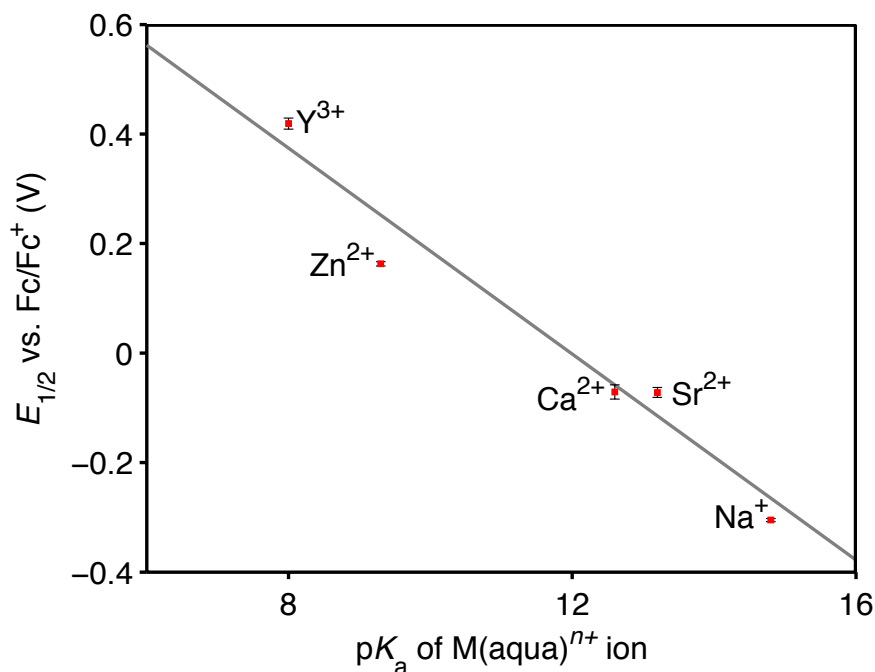


Figure 11. Dependence of $E_{1/2}$ of $Mn^{IV}Mn^{III}_2/Mn^{III}_3$ couple on pK_a of $M(aqua)^{n+}$ ion.²²

Error bars correspond to the standard deviation of the reduction potentials measured from three independent samples.

It is notable in the present series that the Ca^{2+} and Sr^{2+} variants have essentially the same potentials, which is consistent with the observation that substitution of Sr^{2+} for Ca^{2+} in PSII retains reactivity and a similar electronic structure.²³ Although a previously proposed role of Ca^{2+} (or Sr^{2+}) of the OEC in facilitating the attack of a water or hydroxide moiety on an electrophilic manganese oxo is still possible,²⁴ the reported results support a significant role in redox tuning of the cluster.

Conclusions

In summary, a series of tetrametallic dioxo complexes containing redox-inactive metal ions in the +1 to +3 oxidation states was synthesized by employing a trinucleating ligand framework. The structural characteristics of these complexes, with the oxido ligands bridging the redox-inactive metals and the manganese centers, make them particularly relevant to biological and heterogeneous metal-oxido clusters. Electrochemical studies of these compounds show that the reduction potentials are highly dependent upon the Lewis acidity of the redox-inactive metal, identifying the chemical basis for the observed differences in electrochemistry. This correlation provides evidence for the role of the Ca^{2+} ion in modulating the redox potential of the OEC and of other redox-inactive ions in tuning the redox potentials of other metal oxide electrocatalysts. The observed linear dependence between cluster potential and Lewis acidity provides a rational strategy for tuning the redox properties of heterometallic metal-oxido clusters of interest for catalysis.

Experimental Section

General Considerations

Unless indicated otherwise, reactions performed under inert atmosphere were carried out in oven-dried glassware in a glovebox under a nitrogen atmosphere. Anhydrous tetrahydrofuran (THF) was purchased from Aldrich in 18 L Pure-PacTM containers. Anhydrous dichloromethane, diethyl ether, and THF were purified by sparging with nitrogen for 15 minutes and then passing under nitrogen pressure through a column of activated A2 alumina (Zapp's). Anhydrous 1,2-dimethoxyethane (DME) was dried over sodium/benzophenone ketyl and vacuum-transferred onto molecular sieves. CD_2Cl_2 was purchased from Cambridge Isotope Laboratories, dried over calcium hydride, then

degassed by three freeze-pump-thaw cycles and vacuum-transferred prior to use. ^1H NMR spectra were recorded on a Varian 300 MHz instrument, with shifts reported relative to the residual solvent peak. ^{19}F NMR spectra were recorded on a Varian 300 MHz instrument, with shifts reported relative to the internal lock signal. Elemental analyses were performed by Midwest Microlab, LLC, Indianapolis, IN. UV–Vis spectra were taken on a Varian Cary 50 spectrophotometer at 25 °C using quartz crystal cells. Electrospray ionization mass spectrometry (ESI-MS) was performed in the positive ion mode using a LCQ ion trap mass spectrometer (Thermo) at the California Institute of Technology Mass Spectrometry Facility.

Unless indicated otherwise, all commercial chemicals were used as received. $\text{Ca}(\text{OTf})_2$, NaOTf , $\text{Y}(\text{OTf})_3$, and $\text{Zn}(\text{OTf})_2$ were purchased from Aldrich. Dimethylferrocene was purchased from Aldrich and sublimed before use. Decamethylferrocene was purchased from Strem. Iodosobenzene,²⁵ $\text{Sr}(\text{OTf})_2$,²⁶ and dimethylferrocenium triflate²⁷ were prepared according to literature procedures. $\text{LMn}_3(\text{OAc})_3$ and $[\text{LMn}_3\text{O}(\text{OAc})_3]_2\text{Ca}(\text{OTf})_2$ were prepared according to previously published procedures.^{15, 16b} Caution! Iodosobenzene is potentially explosive and should be used only in small quantities.

Synthesis of $[\text{4-Ca}(\text{DME})(\text{OTf})][\text{OTf}]_2$

Method A: In the glovebox, a round-bottom flask equipped with a stir bar was charged with $\text{LMn}_3(\text{OAc})_3$ (2.0 g, 1.67 mmol) and $\text{Ca}(\text{OTf})_2$ (0.90 g, 2.67 mmol, 1.6 equiv). DME (200 mL) was added, and the yellow suspension was stirred at room temperature for 5 min. Iodosobenzene (0.81 g, 3.68 mmol, 2.2 equiv) was added as a solid, and the mixture was stirred at room temperature for 4 h, turning from yellow to purple. The purple solid was collected via filtration, washing with DME, then extracted with dichloromethane. The red-

purple solution was concentrated *in vacuo* to yield the product as a red-purple solid (2.45 g, 84%). ^1H NMR (CD_2Cl_2 , 300 MHz): δ 77.8, 76.5, 72.3, 69.6, 60.5, 53.7, 48.4, 38.6, 37.0, 24.2, 19.9, 17.5, 15.9, 8.1, 3.3, 2.9, -19.3, -23.5, -24.9, -26.4, -29.1 ppm. ^{19}F NMR (CD_2Cl_2): δ -74.4 ppm. UV-Vis (CH_2Cl_2 , λ_{max} (ϵ)): 498 ($1410 \text{ M}^{-1} \text{ cm}^{-1}$), 846 ($640 \text{ M}^{-1} \text{ cm}^{-1}$) nm. Anal. Calcd. For $\text{C}_{68}\text{H}_{55}\text{CaF}_9\text{Mn}_3\text{N}_6\text{O}_{20}\text{S}_3$: C, 46.72; H, 3.17; N, 4.81. Found: C, 46.92; H, 3.27; N, 4.89.

Method B: In the glovebox, a scintillation vial equipped with a stir bar was charged with $[\text{LMn}_3\text{O}(\text{OAc})_3]_2\text{Ca}(\text{OTf})_2$ (0.050 g, 0.018 mmol), $\text{Ca}(\text{OTf})_2$ (0.011 g, 0.032 mmol, 1.8 equiv) and DME (5 mL). To the stirring suspension, PhIO (0.008 g, 0.036 mmol, 2 equiv) was added as a solid, and the purple mixture was stirred at room temperature, gradually becoming slightly redder after 10 min. After 30 min., the mixture was concentrated *in vacuo* to yield a red-purple solid. The ^1H NMR spectrum of a CD_2Cl_2 solution of this unpurified solid matches the ^1H NMR spectrum of the product formed in method A.

Synthesis of $[\mathbf{4}\text{-Ca}(\text{OH}_2)_3][\text{OTf}]_3$

Under ambient conditions, $[\mathbf{4}\text{-Ca}(\text{DME})(\text{OTf})][\text{OTf}]_2$ (0.046 g, 0.026 mmol) was dissolved in wet acetonitrile and the purple mixture was stirred at room temperature for 5 min. The solvent was removed *in vacuo* to yield a purple solid. This procedure was repeated, and the solid was then dried under vacuum (0.032 g, 71%). ^1H NMR (CD_2Cl_2 , 300 MHz): δ 77.3, 75.5, 72.0, 59.2, 49.4, 39.1, 36.1, 27.8, 17.4, 16.3, 8.1, -18.2, -23.4, -25.4, -27.1, -28.1 ppm. ^{19}F NMR (CD_2Cl_2): δ -76.8 ppm. Anal. Calcd. for $\text{C}_{64}\text{H}_{51}\text{CaF}_9\text{Mn}_3\text{N}_6\text{O}_{21}\text{S}_3$: C, 44.89; H, 3.00; N, 4.91. Found: C, 44.84; H, 3.05; N, 4.73.

Synthesis of [5-Ca(DME)(OTf)][OTf]

In the glovebox, a round-bottom flask equipped with a stir bar was charged with [4-Ca(DME)(OTf)]²⁺ (0.750 g, 0.429 mmol) and decamethylferrocene (0.140 g, 0.429 mmol, 1 equiv). DME (30 mL) was added, and the purple mixture was stirred at room temperature over 1 h. The gray-purple precipitate was collected on a fritted glass funnel and washed with DME, then extracted with cold THF (40 mL). The purple filtrate was concentrated to ca. 20 mL *in vacuo*, then cooled to -35 °C to precipitate out more Cp*₂Fe⁺, which was filtered off over Celite. The purple filtrate was concentrated *in vacuo* to a purple solid, then recrystallized from DME/CH₂Cl₂/hexanes to yield the product as a purple solid (0.405 g, 59%). ¹H NMR (CD₂Cl₂, 300 MHz): δ 65.1, 57.8, 50.7, 41.6, 35.3, 29.6, 15.7, 15.0, 14.2, 8.2, 3.0, -9.6, -12.6, -17.0, -17.9 ppm. ¹⁹F NMR (CD₂Cl₂): δ -74.6 ppm. UV-Vis (CH₂Cl₂, λ_{max} (ε)): 495 (710 M⁻¹ cm⁻¹), 860 (310 M⁻¹ cm⁻¹) nm. Anal. Calcd. for C₆₇H₅₅CaF₆Mn₃N₆O₁₇S₂: C, 50.32; H, 3.47; N, 5.26. Found: C, 50.04; H, 3.63; N, 5.06.

Synthesis of [4-Sr(DME)(OTf)][OTf]₂

In the glovebox, a scintillation vial equipped with a stir bar was charged with LMn₃(OAc)₃ (0.200 g, 0.167 mmol) and Sr(OTf)₂ (0.103 g, 0.267 mmol, 1.6 equiv). DME (20 mL) was added, and the mixture was stirred at room temperature for 5 min. PhIO (0.077 g, 0.351 mmol, 2.1 equiv) was added as a solid to the vial, and the mixture was stirred at room temperature for 1 h, turning purple. The purple precipitate was collected over Celite and washed with DME, then extracted with CH₂Cl₂. The purple CH₂Cl₂ filtrate was concentrated *in vacuo* to yield the product as a purple solid (0.125 g, 42%). ¹H NMR (CD₂Cl₂, 300 MHz): δ 77.4, 76.2, 72.3, 69.6, 58.9, 51.0, 47.2, 38.8, 36.6, 23.1, 19.3, 17.4, 14.4, 8.2, 3.2, -18.8, -23.1, -26.5, -27.1, -28.1 ppm. ¹⁹F NMR (CD₂Cl₂): δ -76.7 ppm.

UV-Vis (CH_2Cl_2 , λ_{max} (ϵ)): 497 ($1670 \text{ M}^{-1} \text{ cm}^{-1}$), 845 ($725 \text{ M}^{-1} \text{ cm}^{-1}$) nm. Anal. Calcd. for $\text{C}_{68}\text{H}_{55}\text{F}_9\text{Mn}_3\text{N}_6\text{O}_{20}\text{S}_3\text{Sr}$: C, 45.48; H, 3.09; N, 4.68. Anal. Calcd. for $\text{C}_{69}\text{H}_{57}\text{Cl}_2\text{F}_9\text{Mn}_3\text{N}_6\text{O}_{20}\text{S}_3\text{Sr}$ ($[\mathbf{4}\text{-Sr(DME)(OTf)}][\text{OTf}]_2 \bullet \text{CH}_2\text{Cl}_2$): C, 44.06; H, 3.05; N, 4.47. Found: C, 43.76; H, 3.50; N, 4.46.

Synthesis of $[\mathbf{5}\text{-Sr(DME)(OTf)}][\text{OTf}]$

In the glovebox, a scintillation vial equipped with a stir bar was charged with $[\mathbf{4}\text{-Sr(DME)(OTf)}][\text{OTf}]_2$ (0.200 g, 0.111 mmol) and decamethylferrocene (0.036 g, 0.111 mmol, 1 equiv). DME (10 mL) was added, and the mixture was stirred for 1 h, then cooled to -35°C for 30 min. Cp^*_2Fe^+ was filtered off over Celite, washing with cold DME. The purple DME filtrate was concentrated *in vacuo*, and the purple solid was recrystallized twice from DME/hexanes to remove the remaining Cp^*_2Fe^+ to yield the product as purple crystals (0.156 g, 85%). ^1H NMR (CD_2Cl_2 , 300 MHz): δ 62.9, 57.4, 54.4, 35.0, 33.2, 26.1, 22.3, 15.0, 13.3, 9.1, 8.2, 3.4, 3.2, -8.7 , -12.4 , -15.2 , -17.0 , -19.9 ppm. ^{19}F NMR (CD_2Cl_2): δ -76.4 ppm. UV-Vis (CH_2Cl_2 , λ_{max} (ϵ)): 500 ($750 \text{ M}^{-1} \text{ cm}^{-1}$), 850 ($330 \text{ M}^{-1} \text{ cm}^{-1}$) nm. Anal. Calcd. for $\text{C}_{67}\text{H}_{55}\text{F}_6\text{Mn}_3\text{N}_6\text{O}_{17}\text{S}_2\text{Sr}$: C, 48.87; H, 3.37; N, 5.10. Found: C, 48.60; H, 3.60; N, 5.28.

Synthesis of $[\mathbf{5}\text{-Y(DME)(OTf)}][\text{OTf}]_2$

In the glovebox, a scintillation vial equipped with a stir bar was charged with $\text{LMn}_3(\text{OAc})_3$ (0.200 g, 0.167 mmol) and $\text{Y}(\text{OTf})_3$ (0.134 g, 0.25 mmol, 1.5 equiv). DME (20 mL) was added, and the mixture was stirred at room temperature for 5 min. PhIO (0.077 g, 0.334 mmol, 2.1 equiv) was added as a solid, and the mixture was stirred at room temperature 1 h, turning purple. The purple precipitate was collected over Celite and extracted with CH_2Cl_2 . The purple CH_2Cl_2 filtrate was concentrated *in vacuo* and crystallized from

CH₂Cl₂/DME/diethyl ether to yield the product as purple crystals (0.055 g, 18%). ¹H NMR (CD₂Cl₂, 300 MHz): δ 64.7, 62.6, 59.0, 53.3, 50.9, 41.0, 38.9, 38.2, 36.6, 33.7, 19.6, 16.6, 15.6, 13.6, 13.0, 12.0, 8.0, 3.4, 3.3, -10.8, -15.6, -17.2, -19.3, -20.4, -24.7 ppm. ¹⁹F NMR (CD₂Cl₂): δ -77.0 ppm. UV-Vis (CH₂Cl₂, λ_{max} (ε)): 475 (675 M⁻¹ cm⁻¹), 806 (260 M⁻¹ cm⁻¹) nm. Anal. Calcd. for C₆₈H₅₅F₉Mn₃N₆O₂₀S₃Y: C, 45.45; H, 3.08; N, 4.68. Anal. Calcd. for C₆₉H₅₇Cl₂F₉Mn₃N₆O₂₀S₃Y ([**5**-Y(DME)(OTf)][OTf]₂•CH₂Cl₂): C, 44.03; H, 3.77; N, 4.47. Found: C, 43.94; H, 3.55; N, 4.40.

Synthesis of [4-Na]₂[OTf]₄

In the glovebox, a scintillation vial equipped with a stir bar was charged with LMn₃(OAc)₃ (0.300 g, 0.250 mmol) and NaOTf (0.086 g, 0.501 mmol, 2 equiv). DME (15 mL) was added, and the mixture was stirred for 5 min. PhIO (0.110 g, 0.501 mmol, 2 equiv) was added as a solid, and the mixture was stirred for 1 h, turning purple. The purple heterogeneous mixture was filtered through Celite to remove some purple insolubles, and diethyl ether (ca. 30 mL) was added to the filtrate to precipitate the product as a red-purple solid. This precipitate was collected over Celite, washed with more diethyl ether, then extracted with CH₂Cl₂. The purple extract was concentrated *in vacuo*, then crystallized from CH₂Cl₂/Et₂O to yield the product as a purple crystals (0.072 g, 19%). ¹H NMR (CD₂Cl₂, 300 MHz): δ 77.8, 75.6, 71.9, 54.4, 46.7, 45.0, 38.1, 22.5, 17.3, 16.4, 8.5, -16.5, -21.9, -22.5, -25.2, -26.8 ppm. ¹⁹F NMR (CD₂Cl₂): δ -78.1 ppm. UV-Vis (CH₂Cl₂, λ_{max} (ε)): 498 (1430 M⁻¹ cm⁻¹), 830 (700 M⁻¹ cm⁻¹) nm. Anal. Calcd. For C₁₂₆H₉₀F₁₂Mn₆N₁₂Na₂O₃₀S₄: C, 50.72; H, 3.04; N, 5.63. Found: C, 50.40; H, 3.17; N, 5.43.

Synthesis of [4-Zn(CH₃CN)][OTf]₃

In the glovebox, a scintillation vial equipped with a stir bar was charged with [4-Ca(DME)(OTf)]²⁺ (0.255 g, 0.146 mmol) and Zn(OTf)₂ (0.068 g, 0.172 mmol, 1 equiv) in CH₃CN (20 mL). The purple solution was stirred at room temperature for 15 min., then concentrated *in vacuo*. The solid was dissolved in CH₂Cl₂, and diethyl ether (10 mL) was added to precipitate out a purple solid, which was collected over Celite and then extracted with CH₂Cl₂. The purple filtrate was crystallized from CH₂Cl₂/diethyl ether to yield the product as a purple solid (0.083 g, 33%). ¹H NMR (CD₂Cl₂, 300 MHz): δ 80.1, 75.4, 71.1, 57.3, 52.2, 51.2, 42.1, 40.4, 32.2, 24.3, 21.0, 18.8, 18.1, 15.3, 8.3, 7.5, 6.4, -18.4, -26.1, -28.2, -31.0, -32.0, -36.0 ppm. ¹⁹F NMR (CD₂Cl₂): δ -76.4 ppm. UV-Vis (CH₂Cl₂, λ_{max} (ε)): 498 (1430 M⁻¹ cm⁻¹), 830 (700 M⁻¹ cm⁻¹) nm. Anal. Calcd. For C₆₈H₅₂Cl₄F₉Mn₃N₇O₁₈S₃Zn ([4-Zn(CH₃CN)][OTf]₂•2CH₂Cl₂): C, 43.11; H, 2.77; N, 5.18. Found: C, 42.59; H, 2.66; N, 4.48.

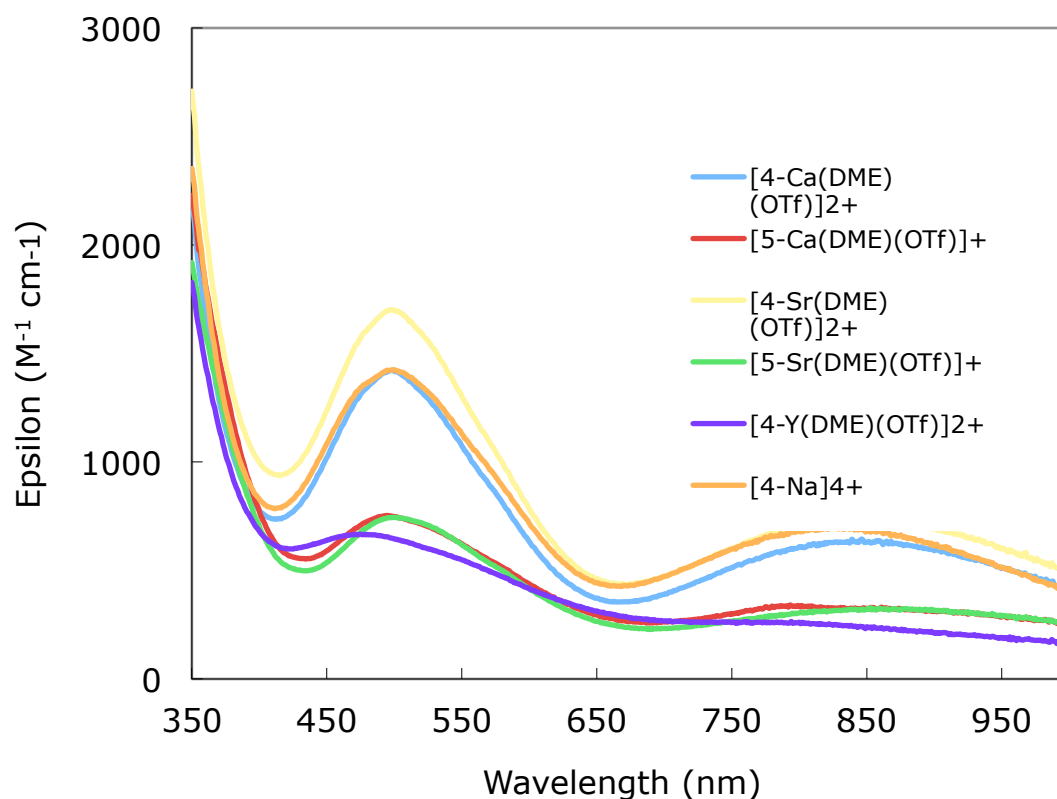


Figure 12. Electronic absorption spectra of trimanganese dioxo complexes in CH_2Cl_2 solution at room temperature.

Magnetic Susceptibility Measurements

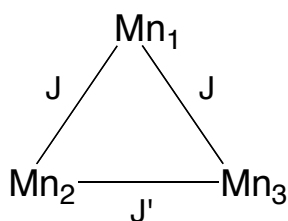
General Considerations. DC magnetic susceptibility measurements were carried out in the Molecular Materials Research Center in the Beckman Institute of the California Institute of Technology on a Quantum Design MPMS instrument running MPMS MultiVu software. Powdered samples (0.038–0.056 g) were fixed in eicosane (0.05–0.11 g) in gelatin capsules and suspended in clear plastic straws. Data were recorded at 0.5 T from 4–300 K. Diamagnetic corrections were made using the average experimental magnetic susceptibility of H_3L at 0.5 T from 100–300 K ($-593 \times 10^{-6} \text{ cm}^3/\text{mol}$) in addition to the values of Pascal's

constants for amounts of anion and solvent quantified for each sample using elemental analysis.

The $\chi_M T$ data taken at 0.5 T were fit to the magnetic susceptibility equation derived from the isotropic spin Hamiltonian for two coupling constants, J and J' [Eq. (1)].

$$\hat{H} = -2J[(\hat{S}_1 \cdot \hat{S}_2) + (\hat{S}_2 \cdot \hat{S}_3)] - 2J'(\hat{S}_3 \cdot \hat{S}_1) \quad (1)$$

The eigenvalues were determined using the Kambe method.²⁸ The data were fit from 10–300 K using Matlab²⁹ by minimizing $R = \sum |(\chi_M T)_{obs} - (\chi_M T)_{calcd}|^2 / \sum (\chi_M T)_{obs}^2$ (Table 1).



Scheme 3. Exchange coupling model employed. For compounds **4**, the spins used were $S = 3/2$, 2, and 2 for Mn1, Mn2, and Mn3 respectively. For **[5-Ca(DME)(OTf)][OTf]**, the spins used were three $S = 2$ centers.

Electrochemical Measurements

Electrochemical measurements were recorded with a Pine Instrument Company AFCBP1 bipotentiostat using the AfterMath software package.

Controlled-potential electrolysis was conducted in a sealed two-chambered H cell where the first chamber held the working and reference electrodes in 50 mL in 0.05 M LiOTf in 10:1 $\text{CH}_2\text{Cl}_2/\text{DME}$ with ca. 0.5 mM of **[4-Ca(DME)(OTf)][OTf]₂** (0.048 g, 0.027 mmol), and the second chamber held the auxiliary electrode in 25 mL of 0.05 M LiOTf in 10:1 $\text{CH}_2\text{Cl}_2/\text{DME}$. The two chambers were separated by a fine-porosity glass frit. Glassy

carbon plates (12 cm × 3 cm × 1 cm; Tokai Carbon USA) were used as the working and auxiliary electrodes. The reference electrode was a Ag/Ag⁺ NBu₄PF₆ in CH₃CN solution electrode separated from the solution by a Vycor frit. The cell was prepared and sealed in a nitrogen-filled glovebox before the beginning of the experiment. The experiment was run by holding the potential of the working electrode at -0.25 V vs. Ag/Ag⁺ for 16 h until the current was nearly at 0 A. Integration of the current showed the passage of 2.06 C (0.8 electrons per molecule of [4-Ca(DME)(OTf)][OTf]₂). The purple solution in the first chamber was then removed from the cell and concentrated *in vacuo* to yield a purple solid that was taken up in CH₂Cl₂, filtered to remove excess LiOTf, then concentrated again.

Cyclic voltammograms were recorded on ca. 1 mM solutions of the relevant complexes in the glovebox at 20 °C with an auxiliary Pt-coil electrode, a Ag/Ag⁺ reference electrode (0.01 M AgNO₃, 0.1 M *n*Bu₄NPF₆ in CH₃CN), and a 3.0 mm glassy carbon electrode disc (BASI). The electrolyte solutions were 0.1 M *n*Bu₄NPF₆ in CH₂Cl₂ ([4-Na]₂⁴⁺) or 10:1 CH₂Cl₂/DME ([4-Ca(DME)(OTf)]²⁺, [4-Sr(DME)(OTf)]²⁺, [4-Zn(CH₃CN)]³⁺, and [5-Y(DME)(OTf)]²⁺). For [4-Ca(DME)(OTf)]²⁺, [4-Sr(DME)(OTf)]²⁺, and [4-Na]₂⁴⁺, CVs were also recorded in an electrolyte solution of 0.1 M *n*Bu₄NPF₆ in CH₂Cl₂ using a hanging mercury drop electrode (BASI CGME). Using the average mass of the mercury drop (0.037 g), the surface area of the drop (assumed to be a sphere) was calculated to be 0.095 cm². All reported values are referenced to an internal ferrocene/ferrocenium couple.

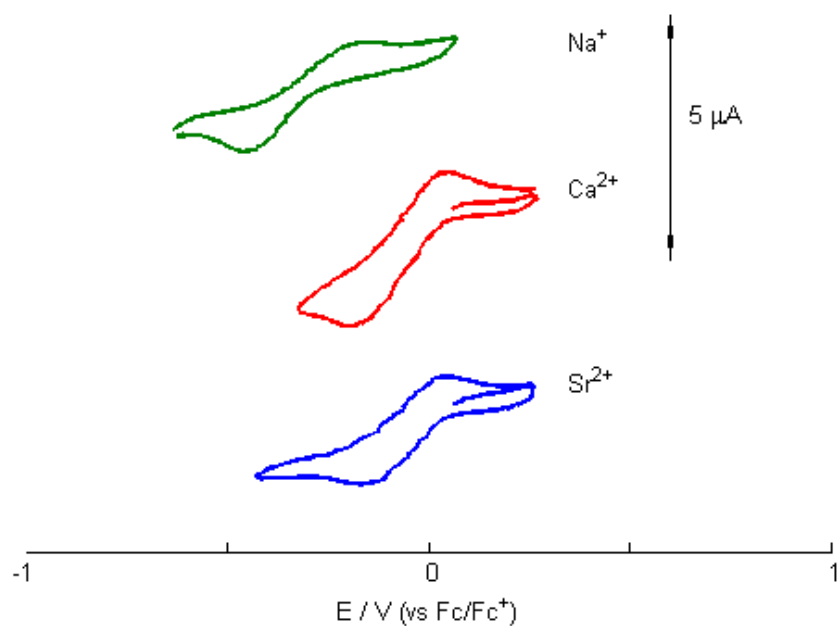


Figure 13. Cyclic voltammograms of complexes using a hanging mercury drop electrode at 20 °C at a scan rate of 100 mV/s. Each redox event corresponds to the $[\text{MMn}^{\text{IV}}\text{Mn}^{\text{III}}_2\text{O}_2]/[\text{MMn}^{\text{III}}_3\text{O}_2]$ couple referenced to an internal Fc/Fc^+ standard.

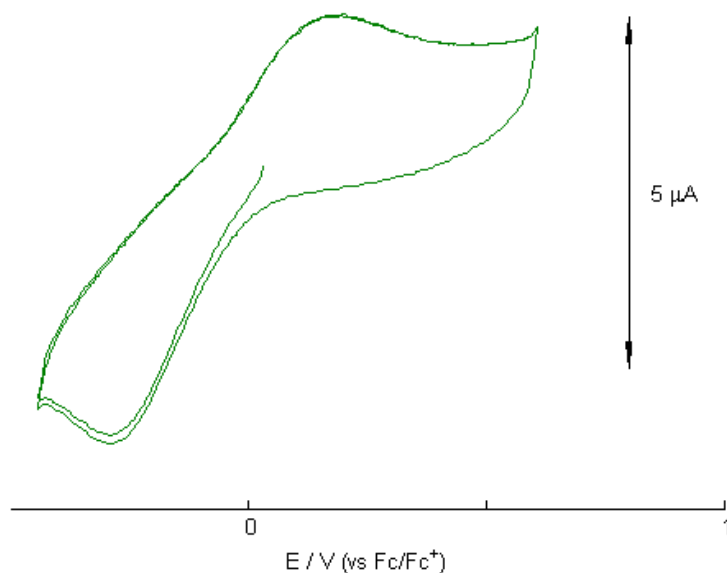


Figure 14. Cyclic voltammogram of a solution of $[\mathbf{4}\text{-Ca}(\text{H}_2\text{O})_3]^{3+}$ in 0.1 M NBu_4PF_6 in 10:1 $\text{CH}_2\text{Cl}_2/\text{DME}$ at a scan rate of 50 mV/s using a GCE. $E_{1/2} = -0.05$ V vs. Fc/Fc^+ .

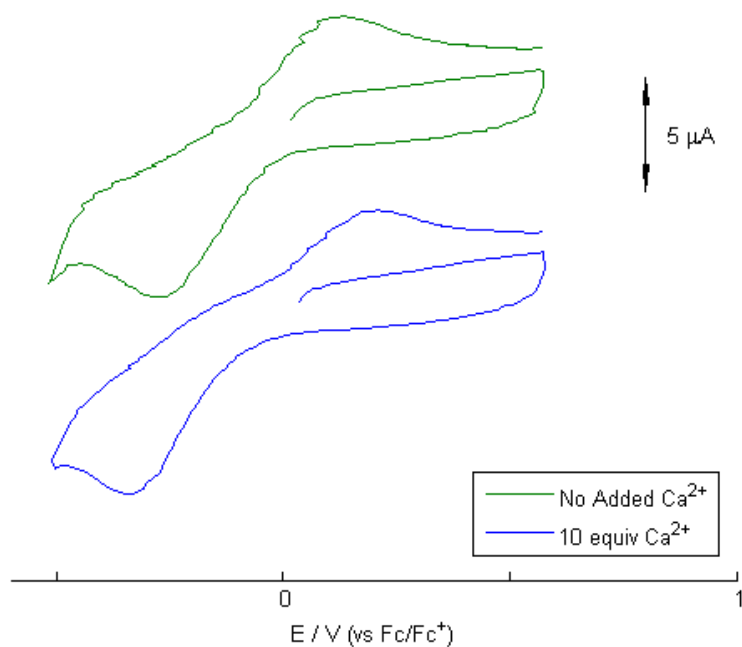
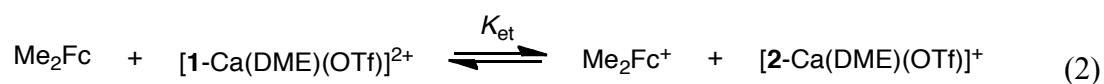


Figure 15. Cyclic voltammograms at 100 mV/s using a GCE in 0.1 M NBu₄PF₆ in 10:1 CH₂Cl₂/DME of [4-Ca(DME)(OTf)]²⁺ (green) and [4-Ca(DME)(OTf)]²⁺ with 10 equivalents of Ca(OTf)₂ (blue). $E_{1/2}$ = -0.07 V vs. Fc/Fc⁺ for both voltammograms.

Spectral Redox Titration

The titration procedures were based off of published methods.³⁰ Electron transfer from dimethylferrocene to [4-Ca(DME)(OTf)]²⁺ (6.2×10^{-4} M) and from [5-Ca(DME)(OTf)]⁺ to dimethylferrocenium triflate was measured from the spectral change in the presence of various concentrations of dimethylferrocene (4.8×10^{-4} – 1.9×10^{-3} M) at 298 K (Fig. 16) using a Cary 50 spectrophotometer with quartz cuvettes sealed with Teflon stoppers (path length = 10 mm). In a glovebox, a solution of dimethylferrocene in 10:1 CH₂Cl₂/DME was added via a microsyringe to a solution of [4-Ca(DME)(OTf)]²⁺ in 10:1 CH₂Cl₂/DME (3 mL). The concentrations of [4-Ca(DME)(OTf)]²⁺, [5-Ca(DME)(OTf)]⁺, dimethylferrocene, and dimethylferrocenium triflate were determined by spectral deconvolution using Matlab.

The equilibrium constant (K_{et}) of eq. 2 was determined by fitting the plot in Fig. 17 to then yield the E_{red} value of the reduction of $[\mathbf{4}\text{-Ca(DME)(OTf)}]^{2+}$ vs. the E_{ox} of dimethylferrocene from eq. 3.³⁰ The reduction potential vs. Fc/Fc^+ was determined by subtracting 90 mV.



$$E_{\text{red}} = E_{\text{ox}} + (RT/F) \ln K_{\text{et}} \quad (3)$$

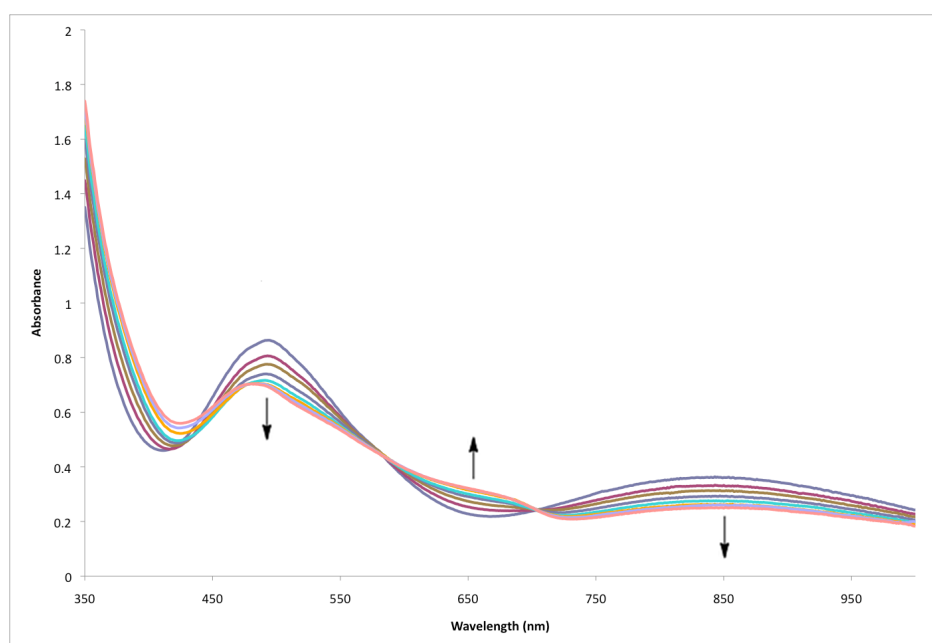


Figure 16. Spectral changes observed in electron transfer from dimethylferrocene to $[\mathbf{4}\text{-Ca(DME)(OTf)}]^{2+}$ in 10:1 $\text{CH}_2\text{Cl}_2/\text{DME}$ at 298 K.

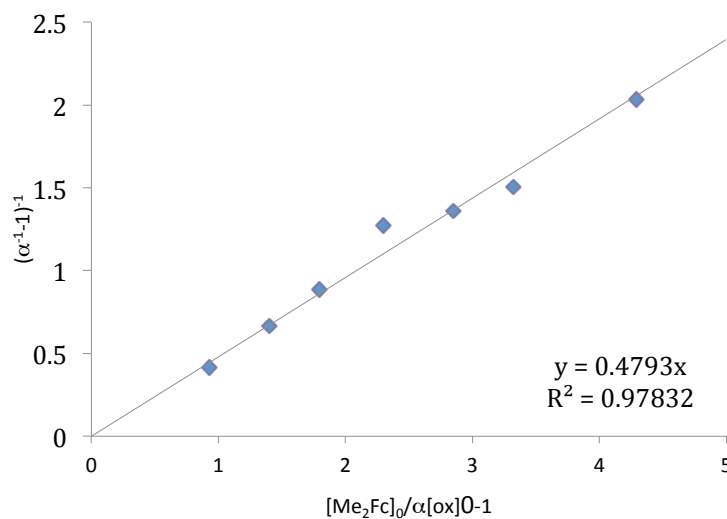


Figure 17. Plot of $(\alpha^{-1} - 1)^{-1}$ vs. $[\text{Me}_2\text{Fc}]_0/\alpha[[\mathbf{4}\text{-Ca}(\text{DME})(\text{OTf})]^{2+}]_0 - 1$ (See ref. 30 for details). The calculated $K_{\text{et}} = 0.48$, corresponding to $E_{1/2}$ of -0.11 V vs. Fc/Fc^+ .

The $E_{1/2}$ of the $[\mathbf{4}\text{-Ca}(\text{DME})(\text{OTf})]^{2+}/[\mathbf{5}\text{-Ca}(\text{DME})(\text{OTf})]^+$ couple was also determined by titrating a 10:1 $\text{CH}_2\text{Cl}_2/\text{DME}$ solution of $[\mathbf{5}\text{-Ca}(\text{DME})(\text{OTf})]^+$ (6.1×10^{-4} M) with dimethylferrocenium triflate ($8.6 \times 10^{-5} - 1.3 \times 10^{-3}$ M) (Fig. 18). By fitting the reverse reaction of eq. 2 in the same manner as above (Fig. 19), the E_{ox} of $[\mathbf{5}\text{-Ca}(\text{DME})(\text{OTf})]^+$ vs. the E_{red} of dimethylferrocenium triflate was calculated from the K_{et} .

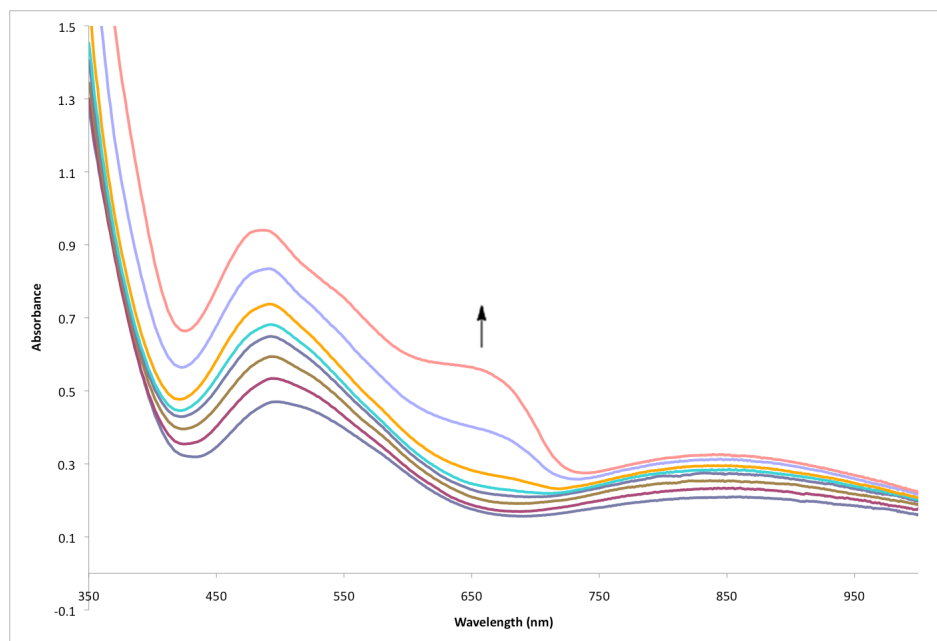


Figure 18. Spectral changes observed in electron transfer from $[\mathbf{5}\text{-Ca}(\text{DME})(\text{OTf})]^+$ to dimethylferrocenium triflate in 10:1 $\text{CH}_2\text{Cl}_2/\text{DME}$ at 298 K.

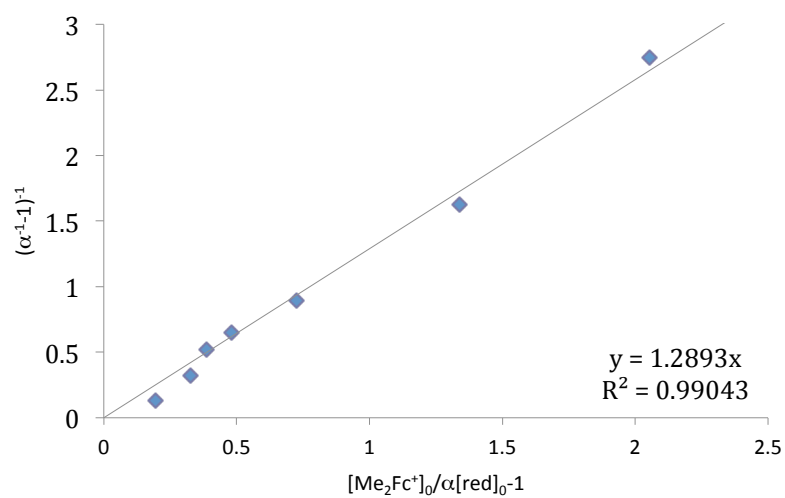


Figure 19. Plot of $(\alpha^{-1} - 1)^{-1}$ vs. $[\text{Me}_2\text{Fc}^+]_0/\alpha[[\mathbf{5}\text{-Ca}(\text{DME})(\text{OTf})]^+]_0 - 1$ (See ref. 30 for details). The calculated $K_{\text{et}} = 1.3$, corresponding to $E_{1/2}$ of -0.10 vs. Fc/Fc^+ .

¹⁸O Labeling Studies

ESI-MS Procedures

In a nitrogen glovebox, samples were dissolved in dry CH₂Cl₂ (ca. 10 μM) in 1.5 mL snap-cap vials. The line and inlet of the instrument were rinsed with dry CH₂Cl₂ before injecting the sample. Spectra were collected by averaging 70 or more scans. The fragment analyzed was that of [LCaMn₃¹⁶O₂(OAc)(OTf)₂]⁺. MS calcd. for C₆₁H₄₂CaF₆Mn₃N₆O₁₃S₂ (M⁺): 1448.99.

Synthesis of ¹⁸O-labeled [4*-Ca(DME)(OTf)][OTf]₂

In a glovebox, a scintillation vial equipped with a stir bar was charged with LMn₃(OAc)₃ (0.050 g, 0.0418 mmol), Ca(OTf)₂ (0.021 g, 0.0627 mmol, 1.5 equiv), and DME (5 mL). After stirring for 2 min., PhI¹⁸O (0.019 g, 0.0835 mmol, 2 equiv)³¹ was added as a solid, and the mixture was stirred for 2 h at room temperature, becoming a purple mixture. The purple precipitate was collected over Celite, then extracted with CH₂Cl₂ to yield the product as a red-purple solid (0.031 g, 42%). The ¹H NMR spectrum matches that of unlabeled [4-Ca(DME)(OTf)][OTf]₂. The isotopic enrichment is approximately 9:49:41 (¹⁶O₂/¹⁶O¹⁸O/¹⁸O₂) (Fig. 20, Table 4).

Crossover Experiment

In a glovebox, a scintillation vial equipped with a stir bar was charged with [4-Ca(DME)(OTf)][OTf]₂ (0.005 g, 0.003 mmol) and [4*-Ca(DME)(OTf)][OTf]₂ (0.005 g, 0.003 mmol). Dichloromethane (5 mL) was added. Aliquots were taken of the reaction mixture at 1 min. and 1 h, diluted with dichloromethane, and measured by ESI-MS. Relative isotopic amounts were calculated using Matlab²⁹ and the expected isotopic ratios of clean species.

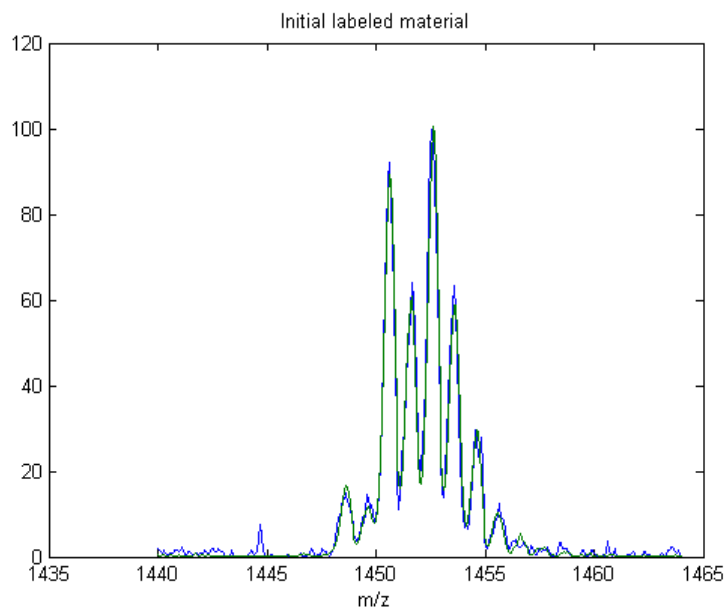


Figure 20. ESI-MS of a CH_2Cl_2 solution of $[\mathbf{4}^*\text{-Ca(DME)(OTf)}][\text{OTf}]_2$ (blue) and theoretical spectrum of mixture of isotopologs (green).

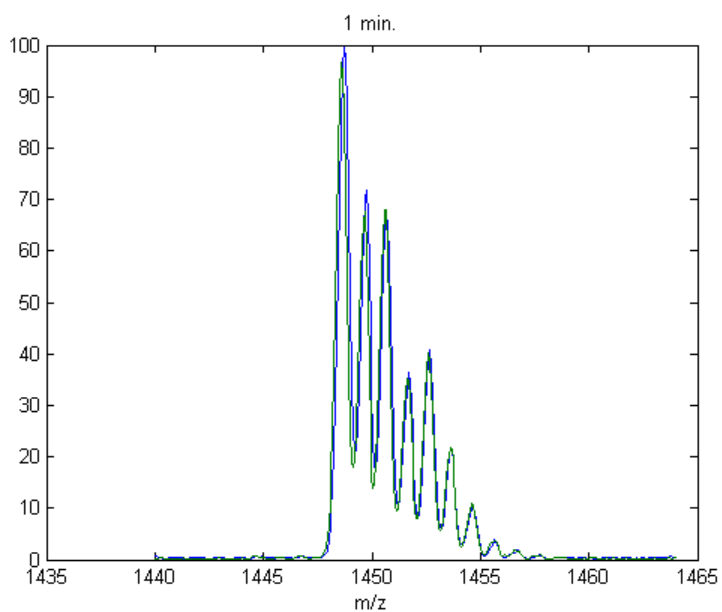


Figure 21. ESI-MS of a CH_2Cl_2 solution of a ca. 1:1 mixture of $[\mathbf{4}\text{-Ca(DME)(OTf)}]^{2+}$ and $[\mathbf{4}^*\text{-Ca(DME)(OTf)}]^{2+}$ after 1 min (blue) and theoretical spectrum from calculated isotopolog ratios (green).

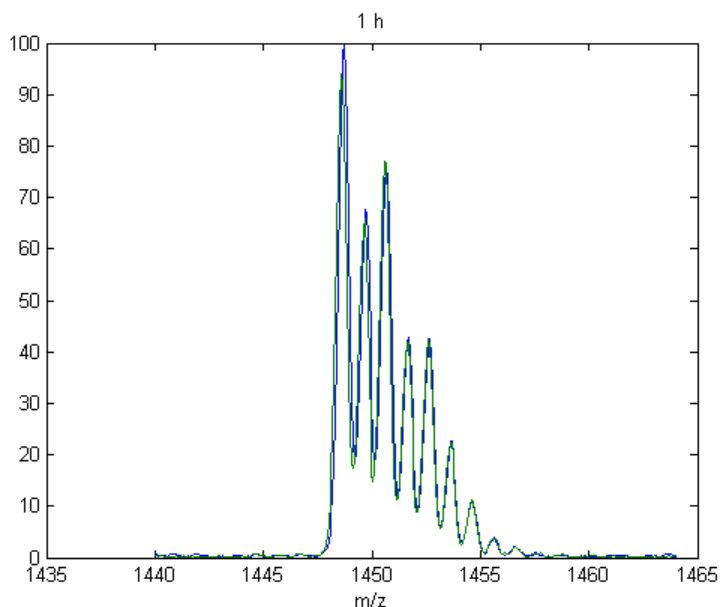


Figure 22. ESI-MS of a CH_2Cl_2 solution of a ca. 1:1 mixture of $[\mathbf{4}\text{-Ca(DME)(OTf)}]^{2+}$ and $[\mathbf{4}^*\text{-Ca(DME)(OTf)}]^{2+}$ after 1 h (blue) and theoretical spectrum from calculated isotopolog ratios (green).

Table 4. Ratios of isotopologs of $[\mathbf{4}\text{-Ca(DME)(OTf)}]^{2+}$ and calculated amount of ^{18}O -mixing.

| | Percent $^{16}\text{O}_2$ | Percent $^{16}\text{O}^{18}\text{O}$ | Percent $^{18}\text{O}_2$ | % Crossover |
|------------------------|---------------------------|--------------------------------------|---------------------------|-------------|
| Initial $\mathbf{4}^*$ | 9.3 | 49.3 | 41.4 | 0 |
| 1 min. ^a | 62.8 | 22.5 | 14.6 | 7 |
| 1 h ^a | 58.6 | 27.8 | 13.6 | 18 |

^a Ratios were calculated based upon mass spectrometry data of aliquots of a ca. 1:1 mixture of $[\mathbf{4}\text{-Ca(DME)(OTf)}]^{2+}$ and $[\mathbf{4}^*\text{-Ca(DME)(OTf)}]^{2+}$ taken at the indicated time points.

Crystallographic Information

CCDC 898246–898252 and 906249 contain the supplementary crystallographic data for this paper. These data can be obtained free of charge from The Cambridge Crystallographic Data Centre via www.ccdc.cam.ac.uk/data_request/cif.

Refinement details

In each case, crystals were mounted on a glass fiber or nylon loop using Paratone oil, then placed on the diffractometer under a nitrogen stream. Low temperature (100 K) X-ray data were obtained on a Bruker APEXII CCD based diffractometer (Mo sealed X-ray tube, $K_{\alpha} = 0.71073 \text{ \AA}$). All diffractometer manipulations, including data collection, integration and scaling were carried out using the Bruker APEXII software.³² Absorption corrections were applied using SADABS.³³ Space groups were determined on the basis of systematic absences and intensity statistics and the structures were solved by direct methods using XS³⁴ (incorporated into SHELXTL) and refined by full-matrix least squares on F^2 . All non-hydrogen atoms were refined using anisotropic displacement parameters. Hydrogen atoms were placed in idealized positions and refined using a riding model. The structure was refined (weighted least squares refinement on F^2) to convergence.

It should be noted that due to the size of these compounds, most crystals included solvent accessible voids, which tended to contain disordered solvent. In addition, due to a tendency to desolvate, the long range order of these crystals and amount of high angle data we were able to record was in some cases not ideal. These disordered solvent molecules were largely responsible for the alerts generated by the checkCIF protocol. In some cases, this disorder could be modeled satisfactorily, while in two ([**4**-Ca(H₂O)₃](OTf)₃ and [**5**-Y(DME)(OTf)](OTf)₂), the disordered solvent was removed using the SQUEEZE protocol

included in PLATON³⁵ (vide infra). In all cases, we are confident this additional electron density is attributable to solvent included in the crystal lattice and not unaccounted for counterions. Refinement details for each compound are included below.

Table 5. Crystal and refinement data.

| | [4-Ca(DME)(OTf) ₂] Ca(DME)(OTf) ₂ | [4-Ca(H ₂ O) ₃](OTf) ₃ Ca(H ₂ O) ₃ (OTf) ₃ | [5-Ca(DME)(OTf) ₂] Ca(DME)(OTf) ₂ | [4-Sr(DME)(OTf) ₂] Sr(DME)(OTf) ₂ | [5-Sr(DME)(OTf) ₂] Sr(DME)(OTf) ₂ | [4-Zn(CH ₃ CN) ₂](OTf) ₃ Zn(CH ₃ CN) ₂ (OTf) ₃ | [4-Na ₂ (OTf) ₄] Na ₂ (OTf) ₄ | [5-Y(DME)(OTf) ₂] Y(DME)(OTf) ₂ |
|--|--|--|--|---|---|--|--|--|
| empirical formula | C ₆₈ H ₅₅ CaF ₉ Mn ₃ N ₆ O ₂₀ S ₃ | C ₆₄ H ₄₅ CaF ₉ Mn ₃ N ₆ O ₂₁ S ₃ | C ₇₆ H ₆₅ CaF ₆ Mn ₃ N ₆ O ₁₉ S ₂ | C ₇₅ H ₅₇ Cl ₂ F ₉ Mn ₃ N ₆ O ₂₀ S ₃ Sr | C ₇₆ H ₆₅ F ₆ Mn ₃ N ₆ O ₁₉ S ₂ Sr | C _{67.40} H _{47.11} F ₉ Mn ₃ N _{7.70} O ₁₈ S ₃ Zn | C ₁₂₆ H ₉₀ F ₁₂ Mn ₆ N ₁₂ Na ₂ O _{31.74} S ₄ | C ₇₂ H ₆₅ F ₉ Mn ₃ N ₆ O ₂₁ S ₃ Y |
| formula wt | 1748.26 | 1706.14 | 1749.36 | 1952.79 | 1796.90 | 1750.21 | 3011.80 | 1871.21 |
| T (K) | 100 | 100 | 100 | 100 | 100 | 100 | 100 | 100 |
| a, Å | 13.5027(13) | 14.7053(8) | 11.6790(4) | 16.0744(8) | 11.7071(4) | 14.3484(8) | 13.5641(16) | 14.7253(17) |
| b, Å | 19.1805(17) | 14.7735(8) | 27.0308(9) | 26.0588(13) | 27.1019(12) | 14.3923(7) | 15.0073(17) | 25.280(3) |
| c, Å | 27.433(3) | 18.508(1) | 25.7452(9) | 20.2364(11) | 25.4494(11) | 18.5632(9) | 16.813(2) | 23.717(3) |
| α, deg | 90 | 69.988(3) | 90 | 90 | 90 | 72.643(3) | 102.848(4) | 90 |
| β, deg | 91.337(4) | 72.802(3) | 93.682(2) | 105.055(3) | 93.564(2) | 73.273(3) | 109.783(4) | 102.212(6) |
| γ, deg | 90 | 69.910(2) | 90 | 90 | 90 | 70.956(3) | 93.581(4) | 90 |
| V, Å ³ | 7102.9(11) | 3475.2(3) | 8110.8(5) | 8185.7(7) | 8059.1(6) | 3380.7(3) | 3104.2(6) | 8629.1(17) |
| Z | 4 | 2 | 4 | 4 | 4 | 2 | 1 | 4 |
| cryst syst | Monoclinic | Triclinic | Monoclinic | Monoclinic | Monoclinic | Triclinic | Triclinic | Monoclinic |
| space group | P2(1)/c | P-1 | P2(1)/c | P2(1)/n | P2(1)/c | P-1 | P-1 | P2(1)/c |
| d _{calcd} , g/cm ³ | 1.635 | 1.630 | 1.433 | 1.585 | 1.481 | 1.719 | 1.611 | 1.440 |
| θ range, deg | 1.83–27.03 | 1.20–27.50 | 1.75–32.34 | 1.65–27.50 | 1.70–25.00 | 1.54–27.50 | 1.98–24.00 | 1.63–27.50 |
| μ, mm ⁻¹ | 0.788 | 0.804 | 0.659 | 1.336 | 1.255 | 1.096 | 0.769 | 1.256 |
| abs cor | Semi-empirical from equivalents | Semi-empirical from equivalents | Semi-empirical from equivalents | Semi-empirical from equivalents | Semi-empirical from equivalents | Semi-empirical from equivalents | Semi-empirical from equivalent | Semi-empirical from equivalents |
| GOF ^c | 1.901 | 1.669 | 1.351 | 1.683 | 1.110 | 1.466 | 1.434 | 1.070 |
| R1, ^a | 0.0647, | 0.0516, | 0.0939, | 0.1018, | 0.0865, | 0.0694, | 0.0711, | 0.0515, |
| wR2 ^b | 0.0834 | 0.1732 | 0.2338 | 0.3081 | 0.1959 | 0.2015 | 0.1588 | 0.1233 |
| (I>2σ(I)) | | | | | | | | |

$$^a R1 = \sum ||F_o| - |F_c|| / \sum |F_o| \quad ^b wR2 = \{ \sum [w(F_o^2 - F_c^2)^2] / \sum [w(F_o^2)^2] \}^{1/2} \quad ^c GOF = S = \{ \sum$$

$$[w(F_o^2 - F_c^2)^2] / (n-p) \}^{1/2}$$

Special refinement details for [4-Ca(DME)(OTf)][OTf]₂

The structure contains a disordered trifluoromethanesulfonate counterion bound to the calcium center. Restraints and populations were employed to model this anion in two positions. Additionally, restraints were employed to treat the displacement parameters of some of the carbons to acceptable sizes. Crystals of this compound were weakly diffracting and had very little high angle data. The present data and solution represent the best of a number of data collections using different crystals. The CIF file and CheckCIF file output contain validation reply form items which address this issue.

Special refinement details for [5-Ca(DME)(OTf)][OTf]

The structure contains a disordered trifluoromethanesulfonate ion bound to the calcium center, and populations were employed to model the ion in two positions. Restraints were used to treat the distances, angles, and displacement parameters of the counterion. The crystal also contains some disordered solvent, which was constrained as a pentane molecule in two positions, but may also be a more disordered 1,2-dimethoxyethane molecule (both solvents were present in the crystallization mixture). We were unable to rule out one or the other due to the severe disorder. Restraints were employed to treat the displacement parameters of this disordered solvent and of the disordered triflate ion to acceptable sizes. The crystal also contains another 1,2-dimethoxyethane molecule that is not disordered and presents satisfactory thermal parameters.

Special refinement details for [4-Sr(DME)(OTf)][OTf]₂

The structure contains a disordered dichloromethane molecule, which was refined by modeling two positions and constraining the bond distances and angles. Restraints were employed to treat the displacement parameters of this disordered dichloromethane to

acceptable sizes. The crystal also contains a disordered solvent molecule that was constrained as a hexane molecule with restrained displacement parameters. Both dichloromethane and hexanes were present as crystallization solvents. The final refined R1 value is high (0.102) due to the large amount of solvent disorder, leading to loss of long range order and poor diffraction of the small crystal, but these data were the best collected from collection of multiple crystals.

Special refinement details for [5-Sr(DME)(OTf)][OTf]

The structure contains a disordered trifluoromethanesulfonate counterion bound to strontium, which was modeled in two positions using populations. Restraints were employed to treat the distances, angles, and displacement parameters of this disordered counterion to acceptable sizes. The crystal contains one DME molecule that could be modeled with acceptable thermal parameters, in addition to other disordered solvent. The solvent was constrained to be a hexane molecule (present as a crystallization solvent), and restraints were employed to treat the displacement parameters. We note the CheckCIF routine produced one Alert A item related to a solvent accessible void of 339 Å³ (4% of the total volume). We were unable to discern any solvent or electron density in this void, likely due to severe disorder. However, this void corresponds to only 103 electrons per cell, which is too few to be a third counterion; thus, this issue should not affect any conclusions drawn about the oxidation state of the complex. The CIF file and CheckCIF file output contain validation reply form items which address this issue.

Special refinement details for [4-Zn(CH₃CN)][OTf]₃

The structure contains a disordered trifluoromethanesulfonate counterion, which was modeled in two positions. Restraints were employed to treat the angles, distances, and

displacement parameters of the counterion. The acetonitrile bound to the zinc center is also disordered, and was refined in two positions using restraints to treat the displacement parameters. The crystal also contains a free molecule of acetonitrile whose population refined to 0.70.

Special refinement details for [4-Na]₂[OTf]₄

The structure contains a disordered trifluoromethanesulfonate counterion, which was modeled in two positions using populations. Restraints were used to treat the bond distances, angles, and displacement parameters of the counterion. Crystals of this compound were weakly diffracting and very little high angle data could be observed. The present data collection and solution represent the best of repeated data collections using a number of different crystals. The CIF file and CheckCIF file output contain validation reply form items which address this issue. Additionally, there was a single area of residual electron density that was modeled as a water molecule at 85% population. This water molecule (O16) is within 2.8 Å of O15B, likely indicating hydrogen bonding. Although these crystals were grown in a dry glovebox, it is possible that trace amounts of moisture entered the mixture over time.

Special refinement details for [5-Y(DME)(OTf)][OTf]₂

The structure contains a molecule of diethyl ether as solvent. The crystal also contains other disordered solvent molecules, presumably diethyl ether and/or 1,2-dimethoxyethane (both present in the crystallization) that could not be satisfactorily modeled. Due to the considerable percentage of the unit cell occupied by the solvent (1496 Å³, 17%), SQUEEZE was employed to produce a bulk solvent correction to the observed intensities.

The program accounted for 448 electrons. This is in reasonable agreement with what would be expected for two disordered molecules of 1,2-dimethoxyethane (400 electrons).

Special refinement details for $[4\text{-Ca}(\text{H}_2\text{O})_3][\text{OTf}]_3$

The structure contains three water ligands coordinated to the calcium center, for which hydrogen atoms were not modeled. Three outer-sphere trifluoromethanesulfonate atoms were located. The crystal also contains other disordered solvent molecules, presumably dichloromethane (present in the crystallization) that could not be satisfactorily modeled. SQUEEZE was employed to produce a bulk solvent correction to the observed intensities. The program accounted for 68 electrons. This is in reasonable agreement with what would be expected for two disordered molecules of dichloromethane (84 electrons).

References

1. (a) Fukuzumi, S.; Ohkubo, K. *Coord. Chem. Rev.* **2010**, *254*, 372-385; (b) Fukuzumi, S., Roles of Metal Ions in Controlling Bioinspired Electron-Transfer Systems. Metal Ion-Coupled Electron Transfer. In *Prog. Inorg. Chem.*, Karlin, K. D., Ed. John Wiley & Sons Inc: New York, 2009; Vol. 56, pp 49-153.
2. (a) Yachandra, V. K.; Yano, J. *J. Photochem. Photobiol., B* **2011**, *104*, 51-59; (b) Yocum, C. F. *Coord. Chem. Rev.* **2008**, *252*, 296-305; (c) McEvoy, J. P.; Brudvig, G. W. *Chem. Rev.* **2006**, *106*, 4455-4483.
3. Park, J.; Morimoto, Y.; Lee, Y. M.; You, Y.; Nam, W.; Fukuzumi, S. *Inorg. Chem.* **2011**, *50*, 11612-11622.
4. Fukuzumi, S.; Morimoto, Y.; Kotani, H.; Naumov, P.; Lee, Y. M.; Nam, W. *Nat. Chem.* **2010**, *2*, 756-759.
5. Morimoto, Y.; Kotani, H.; Park, J.; Lee, Y. M.; Nam, W.; Fukuzumi, S. *J. Am. Chem. Soc.* **2011**, *133*, 403-405.
6. Park, Y. J.; Ziller, J. W.; Borovik, A. S. *J. Am. Chem. Soc.* **2011**, *133*, 9258-9261.
7. Park, Y. J.; Cook, S. A.; Sickerman, N. S.; Sano, Y.; Ziller, J. W.; Borovik, A. S. *Chem. Sci.* **2013**.
8. Miller, C. G.; Gordon-Wylie, S. W.; Horwitz, C. P.; Strazisar, S. A.; Peraino, D. K.; Clark, G. R.; Weintraub, S. T.; Collins, T. J. *J. Am. Chem. Soc.* **1998**, *120*, 11540-11541.
9. (a) Risch, M.; Klingan, K.; Ringleb, F.; Chernev, P.; Zaharieva, I.; Fischer, A.; Dau, H. *ChemSuschem* **2012**, *5*, 542-549; (b) Kanan, M. W.; Yano, J.; Surendranath, Y.; Dincă, M.; Yachandra, V. K.; Nocera, D. G. *J. Am. Chem. Soc.* **2010**, *132*, 13692-13701; (c) Kanan, M. W.; Nocera, D. G. *Science* **2008**, *321*, 1072-1075.

10. (a) Wiechen, M.; Zaharieva, I.; Dau, H.; Kurz, P. *Chem. Sci.* **2012**, *3*, 2330-2339; (b) Najafpour, M. M.; Ehrenberg, T.; Wiechen, M.; Kurz, P. *Angew. Chem. Int. Ed.* **2010**, *49*, 2233-2237; (c) Najafpour, M. M.; Pashaei, B.; Nayeri, S. *Dalton Trans.* **2012**, *41*, 4799-4805.
11. (a) Umena, Y.; Kawakami, K.; Shen, J. R.; Kamiya, N. *Nature* **2011**, *473*, 55-U65; (b) Ferreira, K. N.; Iverson, T. M.; Maghlaoui, K.; Barber, J.; Iwata, S. *Science* **2004**, *303*, 1831-1838.
12. Yamada, Y.; Yano, K.; Hong, D.; Fukuzumi, S. *Phys. Chem. Chem. Phys.* **2012**, *14*, 5753-5760.
13. Symes, M. D.; Surendranath, Y.; Lutterman, D. A.; Nocera, D. G. *J. Am. Chem. Soc.* **2011**, *133*, 5174-5177.
14. (a) Yano, J.; Kern, J.; Sauer, K.; Latimer, M. J.; Pushkar, Y.; Biesiadka, J.; Loll, B.; Saenger, W.; Messinger, J.; Zouni, A.; Yachandra, V. K. *Science* **2006**, *314*, 821-825; (b) Ames, W.; Pantazis, D. A.; Krewald, V.; Cox, N.; Messinger, J.; Lubitz, W.; Neese, F. *J. Am. Chem. Soc.* **2011**, *133*, 19743-19757.
15. Kanady, J. S.; Tsui, E. Y.; Day, M. W.; Agapie, T. *Science* **2011**, *333*, 733-736.
16. (a) Tsui, E. Y.; Day, M. W.; Agapie, T. *Angew. Chem. Int. Ed.* **2011**, *50*, 1668-1672; (b) Tsui, E. Y.; Kanady, J. S.; Day, M. W.; Agapie, T. *Chem. Commun.* **2011**.
17. (a) Lacy, D. C.; Park, Y. J.; Ziller, J. W.; Yano, J.; Borovik, A. S. *J. Am. Chem. Soc.* **2012**, *134*, 17526-17535; (b) Mukherjee, S.; Stull, J. A.; Yano, J.; Stamatatos, T. C.; Pringouri, K.; Stich, T. A.; Abboud, K. A.; Britt, R. D.; Yachandra, V. K.; Christou, G. *Proc. Natl. Acad. Sci. USA* **2012**, *109*, 2257-2262; (c) Mishra, A.; Yano, J.; Pushkar, Y.; Yachandra, V. K.; Abboud, K. A.; Christou, G. *Chem. Commun.* **2007**, 1538-1540; (d) Mishra, A.; Wernsdorfer, W.; Abboud, K. A.; Christou, G. *Chem. Commun.* **2005**, 54-56; (e) Kotzabasaki, V.; Siczek, M.; Lis, T.; Milios, C. J. *Inorg. Chem. Commun.* **2011**, *14*, 213-216; (f) Hewitt, I. J.; Tang, J.-K.; Madhu, N. T.; Clerac, R.; Buth, G.; Anson, C. E.; Powell, A. K. *Chem. Commun.* **2006**, 2650-2652; (g) Nayak, S.; Nayek, H. P.; Dehnen, S.; Powell, A. K.; Reedijk, J. *Dalton Trans.* **2011**, *40*, 2699-2702.
18. Sheldrick, G. *Acta Crystallographica Section A* **2008**, *64*, 112-122.
19. Visser, H.; Anxolabéhère-Mallart, E.; Bergmann, U.; Glatzel, P.; Robblee, J. H.; Cramer, S. P.; Girerd, J.-J.; Sauer, K.; Klein, M. P.; Yachandra, V. K. *J. Am. Chem. Soc.* **2001**, *123*, 7031-7039.
20. (a) Leeladee, P.; Baglia, R. A.; Prokop, K. A.; Latifi, R.; de Visser, S. P.; Goldberg, D. P. *J. Am. Chem. Soc.* **2012**, *134*, 10397-10400; (b) Horwitz, C. P.; Ciringh, Y. *Inorg. Chim. Acta* **1994**, *225*, 191-200; (c) Horwitz, C. P.; Ciringh, Y.; Weintraub, S. T. *Inorg. Chim. Acta* **1999**, *294*, 133-139.
21. Fukuzumi, S.; Ohkubo, K. *Chem. Eur. J.* **2000**, *6*, 4532-4535.
22. Perrin, D. D., *Ionisation Constants of Inorganic Acids and Bases in Aqueous Solution*. Pergamon Press: New York, 1982.
23. Cox, N.; Rapatskiy, L.; Su, J.-H.; Pantazis, D. A.; Sugiura, M.; Kulik, L.; Dorlet, P.; Rutherford, A. W.; Neese, F.; Boussac, A.; Lubitz, W.; Messinger, J. *J. Am. Chem. Soc.* **2011**, *133*, 3635-3648.
24. Pecoraro, V. L.; Baldwin, M. J.; Caudle, M. T.; Hsieh, W. Y.; Law, N. A. *Pure Appl. Chem.* **1998**, *70*, 925-929.
25. Saltzman, H.; Sharefkin, J. G. *Org. Synth.* **1973**, *43*.

26. Forsberg, J. H.; Spaziano, V. T.; Balasubramanian, T. M.; Liu, G. K.; Kinsley, S. A.; Duckworth, C. A.; Poteruca, J. J.; Brown, P. S.; Miller, J. L. *J. Org. Chem.* **1987**, *52*, 1017-1021.
27. Adhikari, D.; Mossin, S.; Basuli, F.; Huffman, J. C.; Szilagyi, R. K.; Meyer, K.; Mindiola, D. J. *J. Am. Chem. Soc.* **2008**, *130*, 3676-3682.
28. Kambe, K. *J. Phys. Soc. Jpn.* **1950**, *5*, 48-51.
29. *Matlab*, 7.10.0.499 (R2010a); The MathWorks, Inc.: Natick, MA, 2010.
30. Lee, Y.-M.; Kotani, H.; Suenobu, T.; Nam, W.; Fukuzumi, S. *J. Am. Chem. Soc.* **2007**, *130*, 434-435.
31. Schardt, B. C.; Hill, C. L. *Inorg. Chem.* **1983**, *22*, 1563-1565.
32. *APEX2*, Bruker Analytical X-ray Systems: Madison, WI, 2006.
33. Sheldrick, G. M. *SADABS*, 2008/1; University of Göttingen, 2008.
34. Sheldrick, G. M. *Acta Crystallogr.* **2008**, *A64*, 112-122.
35. Spek, A. L. *PLATON - A Multipurpose Crystallographic Tool*, Utrecht, The Netherlands, 2006.

Chapter 4

SYNTHESIS, STRUCTURE, AND ELECTROCHEMICAL STUDIES OF HETEROMETALLIC MANGANESE TETRAOXIDO CUBANE CLUSTERS

The text for this chapter was reproduced in part from:

Kanady, J. S.; Tsui, E. Y.; Day, M. W.; Agapie T. *Science* **2011**, 333, 733-736.

Tsui, E. Y. and Agapie, T. *Proc. Natl. Acad. Sci. USA* **2013**, 110, 10084-10088.

Abstract

Understanding the effect of redox-inactive metals on the properties of biological and heterogeneous water oxidation catalysts is important both fundamentally and for improvement of future catalyst designs. In this work, heterometallic manganese-oxido cubane clusters $[\text{MMn}_3\text{O}_4]$ ($\text{M} = \text{Ca}^{2+}, \text{Sr}^{2+}, \text{Zn}^{2+}, \text{Sc}^{3+}, \text{Y}^{3+}$) structurally relevant to the oxygen-evolving complex (OEC) of photosystem II were prepared and characterized. The reduction potentials of these clusters and other related mixed metal manganese-tetraoxido complexes are correlated with the Lewis acidity of the apical redox-inactive metal in a manner similar to a related series of heterometallic manganese-dioxido clusters. The redox potentials of the $[\text{SrMn}_3\text{O}_4]$ and $[\text{CaMn}_3\text{O}_4]$ clusters are close, which is consistent with the observation that the OEC is functional only with one of these two metals. Considering our previous studies of $[\text{MMn}_3\text{O}_2]$ moieties, the present results with more structurally accurate models of the OEC ($[\text{MMn}_3\text{O}_4]$) suggest a general relationship between the reduction potentials of heterometallic oxido clusters and the Lewis acidities of incorporated cations that applies to diverse structural motifs. These findings support proposals that one function of calcium in the OEC is to modulate the reduction potential of the cluster to allow electron transfer.

Introduction

Water oxidation by plants and cyanobacteria occurs at the oxygen-evolving complex (OEC) of photosystem II, which has been structurally and spectroscopically determined to contain a CaMn_4O_x cluster (Fig. 1 left).¹ Recent single crystal X-ray diffraction structures have suggested the presence of a cuboidal CaMn_3 subsite with the remaining Mn center, the “dangler” manganese, bridged to the cluster via oxido bridges.² There have been many synthetic efforts over the past few decades toward modeling the OEC, but few compounds have successfully incorporated calcium into the manganese oxido clusters (see Chapter 1). One major challenge to preparing these clusters has been limiting oligomerization and large cluster nuclearity, as well as control of oxido content and the oxidation state of the final clusters.

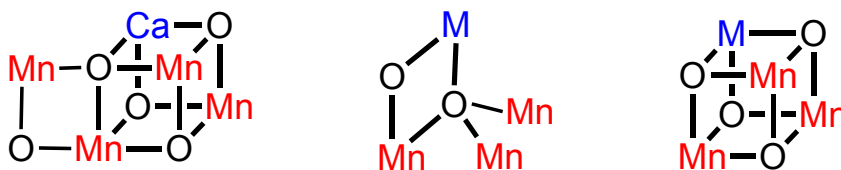


Figure 1. Proposed structure of the CaMn_4O_5 cluster in the OEC (left),² structure of the previously studied heterometallic dioxido complexes (center),³ and structure of tetraoxido complexes studied here (right).

In addition to targeting functional catalysis, biomimetic small molecule complexes are useful for probing other aspects of biological systems such as the OEC. Calcium is an obligatory cofactor for water oxidation in the OEC. The exact role of the Ca^{2+} ion in catalysis is not yet understood, but the observation that only Sr^{2+} can functionally substitute for Ca^{2+} has been attributed to the similar Lewis acidities of the two cations.⁴ The calcium center has been proposed to coordinate water or hydroxide ligands that participate in O–O bond formation.⁵ Other proposed functions include affecting proton coupled electron

transfer and the redox properties of the cluster, possibly via interactions with neighboring tyrosine residues.⁶

Many other biological and synthetic electron transfer reactions are affected by the addition of Lewis acidic metal ions.⁷ For example, synthetic Fe^{IV}–oxo complexes have shown enhanced electron transfer rates and more positive reduction potentials upon binding or addition of redox-inactive Lewis acids such as Sc³⁺ or Ca²⁺.⁸ Group 2 metal ions also enhanced the rates of dioxygen activation by monometallic Mn^{II} and Fe^{II} complexes.⁹ Alkali and alkali earth metals have also been proposed as components in heterogeneous water oxidation by cobalt and manganese oxides.¹⁰ Our group recently reported a series of heterometallic trimanganese dioxido clusters [MMn₃(μ₄-O)(μ₂-O)] (Fig. 1 middle, M = Na⁺, Ca²⁺, Sr²⁺, Zn²⁺, and Y³⁺) and demonstrated that the reduction potentials of the clusters are linearly correlated with the Lewis acidity of the redox-inactive metal (Chapter 3).³ The synthesis of these clusters also demonstrated the utility of our approach in the controlled synthesis of heterometallic manganese oxido clusters. However, these clusters are not particularly structurally accurate in mimicking the OEC, and we also desired more accurate models (higher oxidation state, more incorporated oxides).

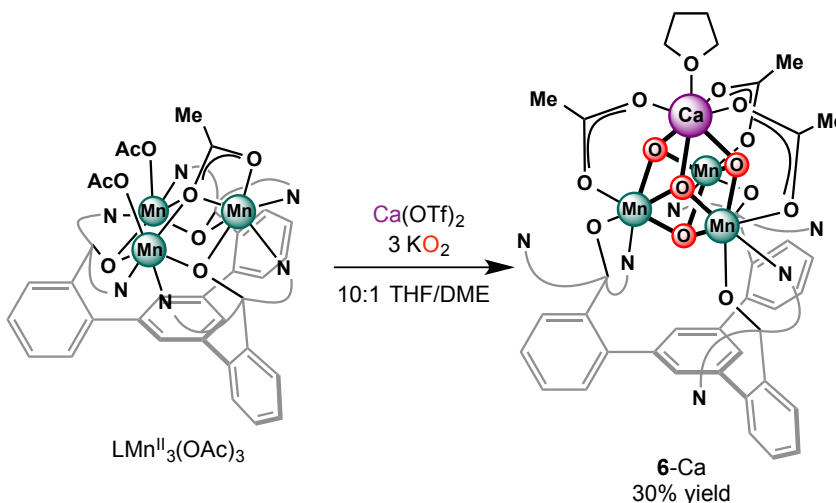
In this work, we report the synthesis of a [CaMn^{IV}₃O₄] complex that is structurally related to the CaMn₃ subsite of the OEC. We have also synthesized a structurally analogous [SrMn^{IV}₃O₄] complex important for understanding the functional substitution of Sr²⁺ for Ca²⁺ in the OEC. We also describe the synthesis of other [MMn^{IV}₃O₄] (M = Zn²⁺, Y³⁺) and [ScMn^{III}Mn^{IV}₂O₄] complexes that are structurally more similar to the cubane subsite of the OEC than the previously investigated dioxido clusters (MMn₃O₂, Fig. 1). Electrochemical studies of the isostructural series of [MMn^{IV}₃O₄] compounds (M = Ca²⁺, Sr²⁺, Zn²⁺, Y³⁺,

Sc^{3+} , Mn^{3+}) allowed the systematic investigation of the effect of redox-inactive metal ions upon the redox properties of biologically relevant manganese clusters.

Results and Discussion

4.1 Synthesis of a $[\text{CaMn}_3\text{O}_4]$ cluster

Following a similar approach as the synthesis of the dioxido clusters discussed in Chapter 3, heterometallic Ca/Mn oxido clusters were targeted using the trimanganese(II) complex $\text{LMn}^{\text{II}}_3(\text{OAc})_3$ as a convenient precursor (Scheme 1). In a synthetic route discovered by graduate student Jacob S. Kanady, a suspension of $\text{LMn}^{\text{II}}_3(\text{OAc})_3$ and $\text{Ca}(\text{OTf})_2$ (1.1 equiv) in 10:1 THF/DME was treated with KO_2 (3 equiv) as both the oxidant and source of oxygen atoms (Scheme 1). After much optimization, this route yields the product $\text{LCaMn}^{\text{IV}}_3\text{O}_4(\text{OAc})_3(\text{THF})$ (**6-Ca**) as a red solid in 30% yield.¹¹ This complex was characterized using single crystal X-ray diffraction (XRD) studies, and was found to be structurally related to the CaMn_3 subsite of the OEC (Fig. 1 right, Fig. 2).^{2, 12}



Scheme 1. Synthesis of $[\text{CaMn}^{\text{IV}}_3\text{O}_4]$ cluster **6-Ca**, first discovered by Jacob Kanady.

In the structure of **6-Ca** (Fig. 2), the three manganese centers are supported by the trinucleating ligand framework, but in a different manner from that observed for the

dioxido clusters. In **6**-Ca, the alkoxide moieties are coordinated in a terminal fashion, and three pyridyl groups remain uncoordinated. The tetraoxido [CaMn₃O₄] cubane cluster is further supported by three acetate ligands that bridge the manganese centers to the calcium center. Finally, the Ca²⁺ coordination sphere is completed by a coordinated solvent molecule, making it overall seven-coordinate. The Mn-oxo bond lengths in **6**-Ca average to 1.87 Å and do not display any axial distortions that would be consistent with a Mn^{III} d⁴ electronic configuration (Table 1). As such, the Mn centers in **6**-Ca are all assigned as the +IV oxidation state.

When the structural parameters are compared to those from the recent crystallographic study of the OEC,^{2a} there are some small differences (Tables 1 and 2). The longer Mn–O bond distances observed in the structure of the OEC could be attributed to reduction of the cluster from X-ray damage¹³ as well as distortions in the cubane motif due to the presence of the fourth “dangler” manganese center. The metal-metal bond distances observed in **6**-Ca (avg. Mn–Mn 2.834 Å, avg. Ca–Mn 3.231 Å,) are also slightly shorter than those of the OEC (Mn–Mn 2.8, 2.9, and 3.3 Å, and Mn–Ca 3.3, 3.4, and 3.5 Å), possibly due to the constraints of the three bridging acetate ligands in **6**-Ca. A recent example of an asymmetric CaMn₃O₄ cluster desymmetrized by a second calcium center prepared by Christou and co-workers shows slightly longer Ca–Mn distances that are more similar to those observed in the structure of the OEC (Table 3).¹⁴

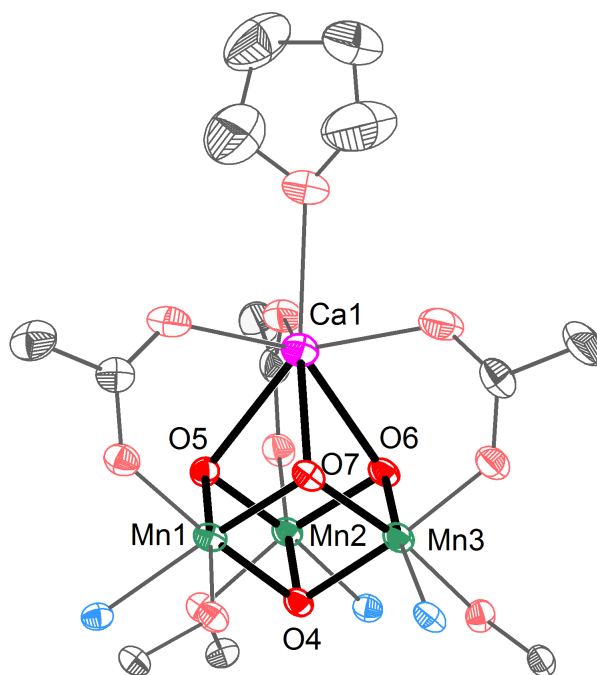
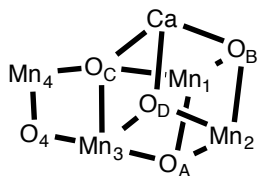


Figure 2. Truncated solid-state structure of **6-Ca** as 50% thermal ellipsoids.

Table 1. Selected structural parameters of **6-Ca** (distances in Å). Labels correspond to those of Fig. 2.

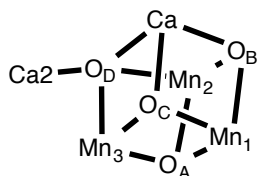
| M–Oxo | Mn1 | Mn2 | Mn3 | Ca |
|--------------|-----------|-----------|-----------|----------|
| O4 | 1.916(2) | 1.923(2) | 1.912(2) | -- |
| O5 | 1.862(2) | 1.829(2) | -- | 2.431(2) |
| O7 | 1.842(2) | -- | 1.871(2) | 2.391(2) |
| O6 | -- | 1.864(2) | 1.825(2) | 2.430(2) |
| Avg. | 1.873 | 1.872 | 1.869 | 2.417 |
| M–M | | | | |
| Mn2 | 2.8327(7) | -- | -- | -- |
| Mn3 | 2.8385(7) | 2.8301(7) | -- | -- |
| Ca | 3.2305(8) | 3.2376(9) | 3.2245(9) | -- |

Table 2. Selected structural parameters from a recent XRD study of the OEC (distances in Å).^{2a} Labels correspond to inset scheme.



| | Mn1 | Mn2 | Mn3 | Ca |
|----------------|-----|-----|-----|-----|
| M–Oxo | | | | |
| O _A | 1.8 | 2.1 | 2.1 | -- |
| O _B | 1.8 | 2.1 | -- | 2.4 |
| O _C | 2.6 | -- | 2.4 | 2.7 |
| O _D | -- | 2.1 | 1.9 | 2.5 |
| Avg. | 2.1 | 2.1 | 2.1 | 2.5 |

Table 3. Selected structural parameters of a [Ca₂Mn₃O₄] cluster prepared by Christou and co-workers (distances in Å).¹⁴ Labels correspond to inset scheme.



| | Mn1 | Mn2 | Mn3 | Ca |
|----------------|-------|-------|-------|-------|
| M–Oxo | | | | |
| O _A | 1.899 | 1.891 | 1.892 | -- |
| O _B | 1.844 | 1.862 | -- | 2.452 |
| O _C | 1.820 | -- | 1.830 | 2.470 |
| O _D | -- | 1.866 | 1.889 | 2.660 |
| Avg. | 1.854 | 1.873 | 1.870 | 2.527 |
| M–M | | | | |
| Mn2 | 2.757 | -- | -- | -- |
| Mn3 | 2.730 | 2.857 | -- | -- |
| Ca | 3.394 | 3.454 | 3.418 | -- |

4.2 Synthesis of $[MMn_3O_4]$ complexes

To study whether the correlation between Lewis acidity and redox potentials of the trimanganese dioxido complexes could be extended to the tetraoxido cubane clusters that are structurally more similar to the OEC, we targeted analogs of **6**-Ca with other metal ions substituted for calcium. The strontium compound $[LSrMn_3O_4(OAc)_3(DMF)]_2$ (**[6-Sr]₂**, Scheme 2, DMF = *N,N*-dimethylformamide) was prepared analogously to **6**-Ca from a low oxidation state trimanganese precursor supported by a triarylbenzene architecture appended with pyridine and alkoxide donors.¹⁵ Treatment of a THF suspension of $LMn^{II}_3(OAc)_3$ and $Sr(OTf)_2$ (OTf = trifluoromethanesulfonate) with KO_2 , followed by crystallization from DMF afforded the strontium cubane complex (**[6-Sr]₂**). A single crystal X-ray diffraction (XRD) study of crystals of **[6-Sr]₂** showed that **[6-Sr]₂** contains the desired $[SrMn_3O_4]$ cubane cluster in a dimeric structure, with two 9-coordinate strontium centers of different monomers bridged through acetate and coordinated DMF molecules (Fig. 3). The Mn–oxido bond distances [1.821(3)–1.913(3) Å] as well as bond valence sum (BVS) analysis of the manganese–ligand distances are consistent with all Mn^{IV} centers per $[SrMn_3O_4]$ cluster.¹⁶ Additionally, a pseudooctahedral high spin d^4 Mn^{III} center is expected to be axially elongated or compressed to accommodate the single unpaired electron in the σ -antibonding orbitals; no such axial distortion is observed. Compound **[6-Sr]₂** allows direct comparison to **6**-Ca due to their structural similarities, and is also a rare example of a molecular mixed metal Sr/Mn complex.^{3, 17}

Under the same reaction conditions, analogs of **6**-Ca and **[6-Sr]₂** containing other metal ions were not isolated, possibly due to solubility differences. However, **6**-Ca can be transmetallated using other metal sources to allow replacement of the calcium center with

other metal ions. Treatment of a DMF solution of **6**-Ca with $\text{Sc}(\text{OTf})_3$ and crystallization from acetonitrile/diethyl ether cleanly formed the scandium analog $\text{LScMn}_3\text{O}_4(\text{OAc})_3(\text{OTf})$ ($[\mathbf{6}\text{-Sc}][\text{OTf}]$, Scheme 2).^{11b} The ^1H NMR spectrum of a CD_2Cl_2 solution of $[\mathbf{6}\text{-Sc}]^+$ is similar to that of **6**-Ca, with paramagnetically shifted and broadened signals between -24 and 12 ppm. ESI-MS of an acetonitrile solution of $[\mathbf{6}\text{-Sc}]^+$ showed a single peak at 1306.1 m/z – $[\text{LScMn}_3\text{O}_4(\text{OAc})_3]^+$, which is consistent with the assignment of $[\mathbf{6}\text{-Sc}]^+$. X-ray quality single crystals of $[\mathbf{6}\text{-Sc}]^+$ were grown by slow vapor diffusion of diethyl ether into an acetonitrile solution of $[\mathbf{6}\text{-Sc}]^+$, and a XRD study of these crystals showed that the solid-state structure of $[\mathbf{6}\text{-Sc}]^+$ maintains the Mn_3MO_4 cubane core moiety of **6**-Ca, but the scandium center is further coordinated by an *O*-bound triflate anion (Fig. 4). The Mn-oxido distances of $[\mathbf{6}\text{-Sc}]^+$ ($1.8477(7)$ – $1.9116(7)$ Å) are similar to those of **6**-Ca ($1.8252(2)$ – $1.923(2)$ Å) and are consistent with the Mn^{IV}_3 oxidation state assignment.

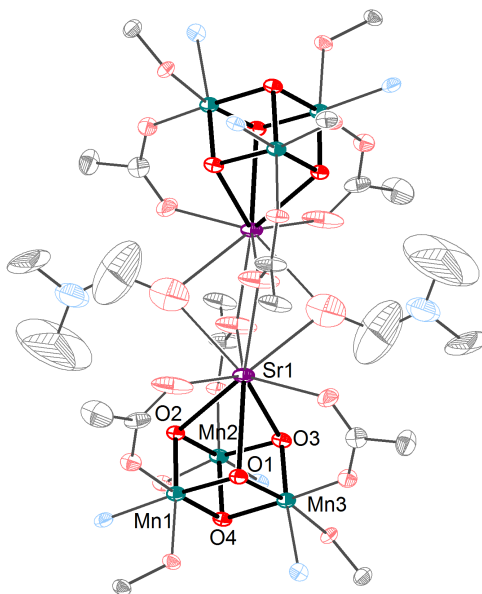
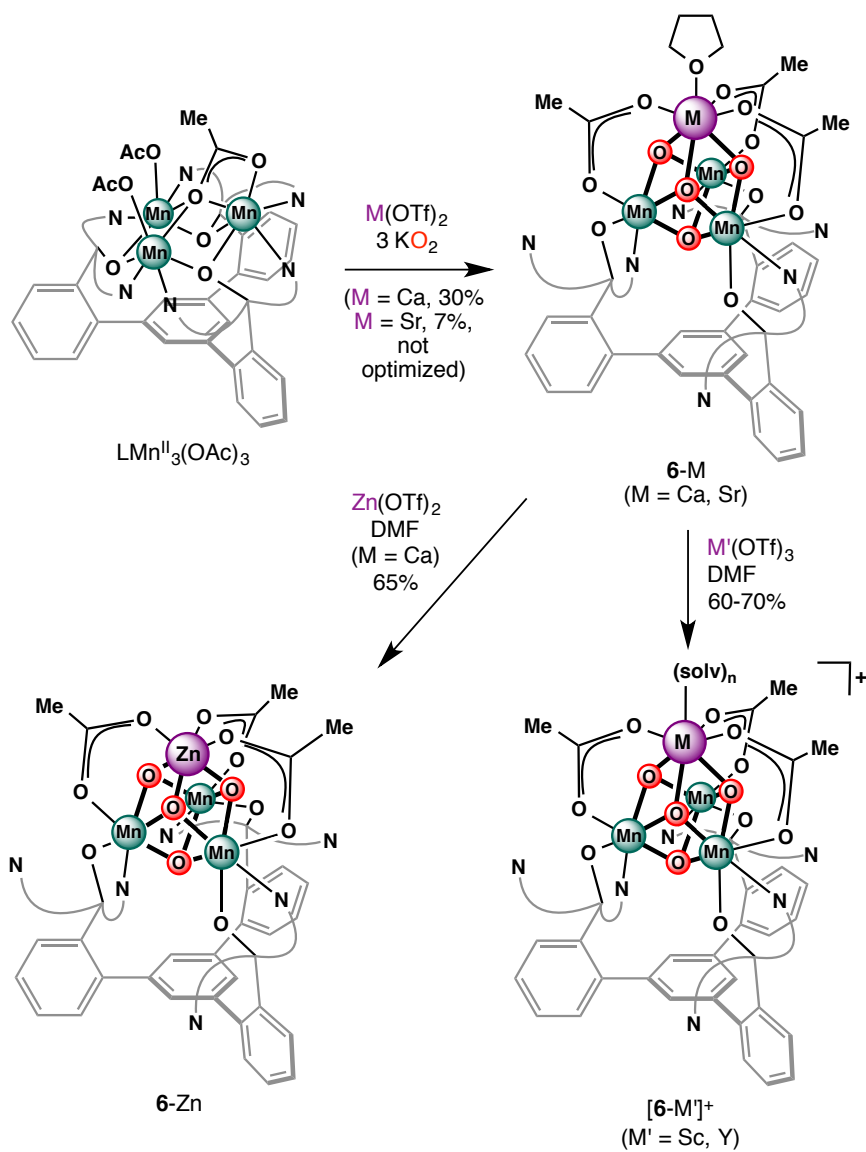


Figure 3. Truncated solid-state structure of $[\mathbf{6}\text{-Sr}]_2$ shown as 50% thermal ellipsoids. Hydrogen atoms and outer-sphere solvent molecules are omitted for clarity. Bolded bonds highlight the SrMn_3O_4 core.



Scheme 2. Synthesis of other heterometallic cubane clusters **6-M** ($\text{M} = \text{Sr}^{2+}$, Zn^{2+} , Y^{3+} , Sc^{3+}).

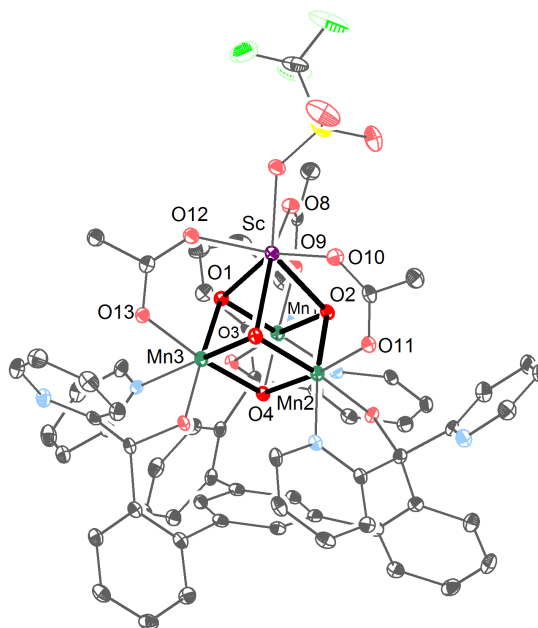


Figure 4. Solid-state structure of $[6\text{-Sc}][\text{OTf}]$. Thermal ellipsoids are drawn at 50% probability. Hydrogen atoms and solvent molecules are omitted for clarity. Bolded bonds highlight the ScMn_3O_4 core.

Similarly, when **6-Ca** was treated with $\text{Zn}(\text{OTf})_2$ in DMF (Scheme 2), electrospray ionization mass spectrometry (ESI-MS) of the reaction mixture showed a single species at 1266 m/z , corresponding to $[\text{LZnMn}_3\text{O}_4(\text{OAc})_2]^+$, with no signals corresponding to residual **6-Ca**. The clean conversion of **6-Ca** to $\text{LZnMn}_3\text{O}_4(\text{OAc})_3$ (**6-Zn**) is also demonstrated by a change in solubility; while **6-Ca** is insoluble in methylene chloride and benzene, the product after treatment with $\text{Zn}(\text{OTf})_2$ is soluble in both. A XRD study of crystals of **6-Zn** grown from benzene/diethyl ether shows that **6-Zn** contains the desired $[\text{MMn}_3\text{O}_4]$ moiety, structurally related to **6-Ca** and $[\text{6-Sr}]_2$, although the smaller zinc center is six-coordinate and does not bind solvent ligands (Fig. 5). Refinement of this structure with populations of Mn in the apical site show that the metal center is unambiguously Zn. BVS analysis $[\text{Mn}-$

oxido distances 1.822(1)–1.947(1) Å] supports the assignment of the compound as in the $[\text{Mn}^{\text{IV}}_3\text{O}_4]$ oxidation state.

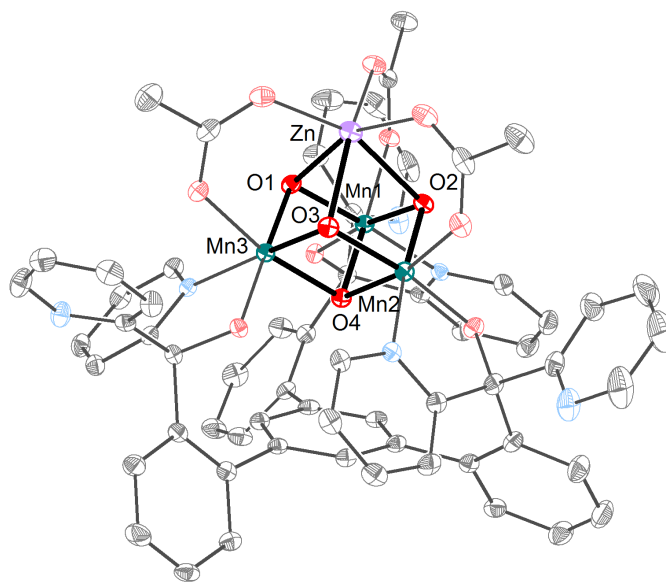


Figure 5. Solid-state structure of **6-Zn**. Thermal ellipsoids are drawn at 50% probability. Hydrogen atoms and solvent molecules are omitted for clarity. Bolded bonds highlight the ZnMn_3O_4 core.

Under the same reaction conditions using $\text{Y}(\text{OTf})_3$ instead of $\text{Zn}(\text{OTf})_2$, ESI-MS of the reaction mixture displayed a single signal at 1350 m/z , corresponding to $[\text{LYMn}_3\text{O}_4(\text{OAc})_3]^+$ (Scheme 2). A XRD study of single crystals of the product, formulated as $[\text{LYMn}_3\text{O}_4(\text{OAc})_3(\text{DMF})_2][\text{OTf}]$ (**[6-Y]**⁺) shows that the compound contains a $[\text{YMn}_3\text{O}_4]$ core (Fig. 6). The yttrium center is 8-coordinate, with two *O*-bound DMF molecules, and the triflate counterion is outer sphere. Structural parameters support the Mn^{IV}_3 oxidation state assignment [Mn–oxido distances 1.839(2)–1.912(2)]. A CD_2Cl_2 solution of **[6-Y]**⁺ displays a paramagnetically broadened ^1H NMR spectrum with signals between –21 and 16 ppm, similar to that of **[6-Sc][OTf]**.^{11b}

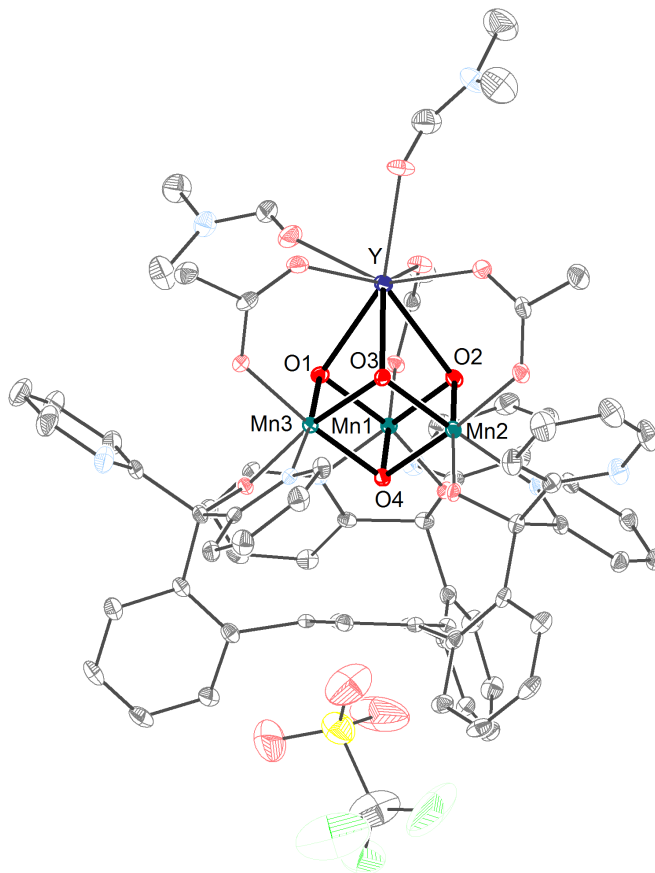


Figure 6. Solid-state structure of [6-Y][OTf]. Thermal ellipsoids are drawn at 50% probability. Hydrogen atoms and solvent molecules are omitted for clarity. Bolded bonds highlight the YMn_3O_4 core.

The structural parameters of the $[\text{MMn}^{\text{IV}}_3\text{O}_4]$ cubane clusters are compared in Table 4. Despite the variation in apical metal, the trimanganese(IV) tetraoxido core remains structurally unchanged for compounds **6**, as demonstrated by the manganese-oxido distances, which all remain very similar (average Mn–O distance of 1.87–1.88 Å). The M–oxido distances for the capping metals vary with ionic radius; the smaller ions (Sc^{3+} , Zn^{2+}) have the shortest average metal-oxido distances (2.18, 2.19 Å respectively), while the largest (Sr^{2+}) has the longest average metal-oxido distance (2.58 Å).

Table 4. Selected structural parameters of compounds **6-M**.

| | 6-Ca | [6-Sr]₂ | 6-Zn | [6-Sc][OTf] | [6-Y][OTf] |
|---------------|------------------------------------|------------------------------------|------------------------------------|---------------------------------------|------------------------------------|
| Mn1–O (Å) | 1.916(2), 1.862(2), 1.842(2) | 1.912(3), 1.821(3), 1.863(3) | 1.928(1), 1.858(1), 1.828(1) | 1.9079(7), 1.8477(7), 1.8906(7) | 1.910(2), 1.874(2), 1.840(2) |
| Mn2–O (Å) | 1.923(2), 1.829(2), 1.864(2) | 1.894(3), 1.825(3), 1.869(3) | 1.947(1), 1.822(1), 1.863(1) | 1.9085(7), 1.8546(7), 1.8985(7) | 1.910(2), 1.839(2), 1.874(2) |
| Mn3–O (Å) | 1.912(2), 1.825(2), 1.871(2) | 1.913(3), 1.842(3), 1.854(3) | 1.913(1), 1.839(1), 1.863(1) | 1.9116(7), 1.8482(7), 1.8886(7) | 1.912(2), 1.844(2), 1.877(2) |
| Avg. Mn–O (Å) | 1.87 | 1.87 | 1.87 | 1.88 | 1.88 |
| M–O (Å) | 2.391(2), 2.430(2), 2.431(2) | 2.617(3), 2.584(3), 2.552(3) | 2.129(1), 2.195(1), 2.222(1) | 2.1838(7), 2.1904(7), 2.1933(7) | 2.336(2), 2.432(2), 2.389(2) |
| Avg. M–O (Å) | 2.42 | 2.58 | 2.18 | 2.19 | 2.39 |

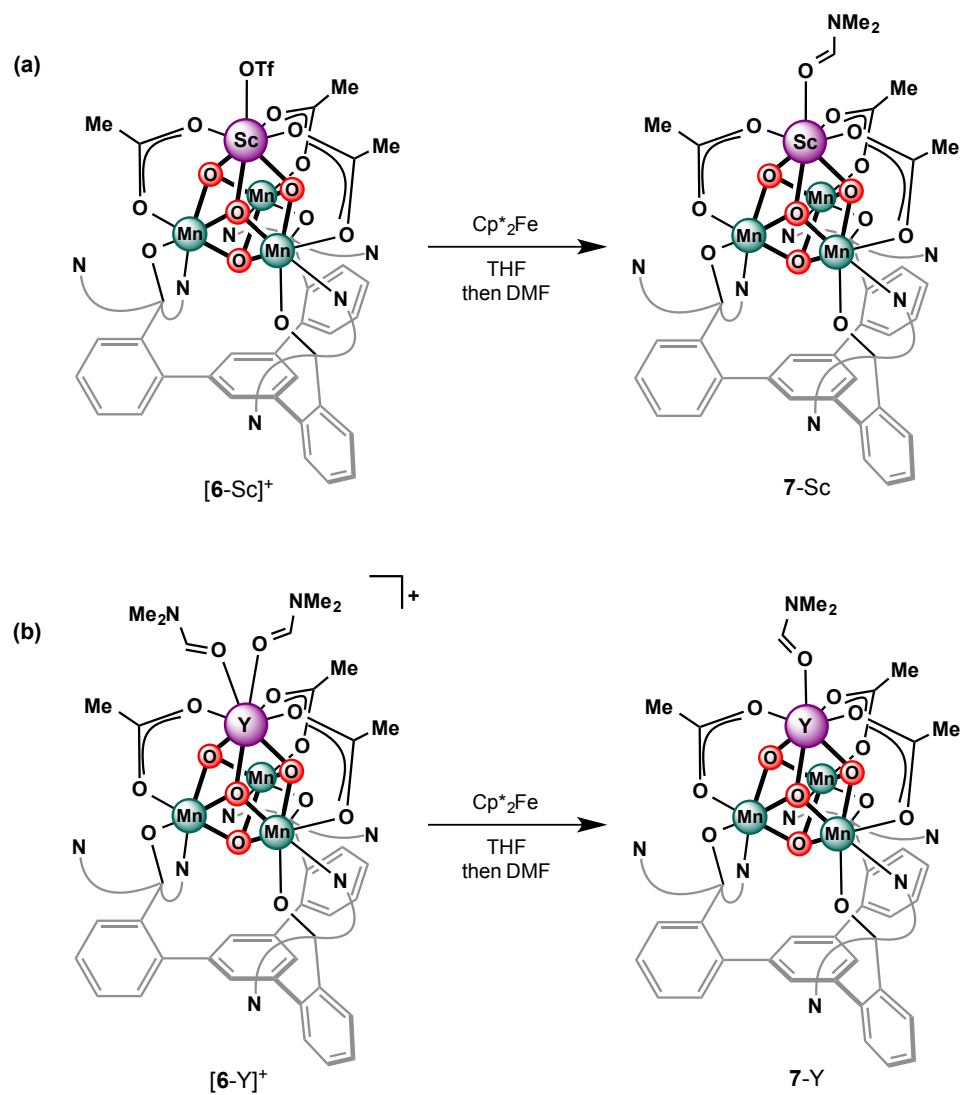
4.3 Chemical reductions of cubane complexes

The [ScMn^{IV}₃O₄] compound [6-Sc][OTf] can be reduced using one equivalent of decamethylferrocene (Cp*₂Fe) in THF ($E^0 \sim -0.48$ vs. Fc/Fc⁺ in CH₂Cl₂) to cleanly form the one-electron reduced compound LScMn^{IV}₂Mn^{III}O₄(OAc)₃(DMF) (**7-Sc**) after crystallization from DMF (Scheme 3a). The identity of the reduced product was confirmed by a XRD study (Fig. 7). BVS analysis of the Mn–ligand bond lengths indicate that the oxidation states of the Mn^{IV}₂Mn^{III} cluster are isolated. The Mn^{III} center (Mn1, Fig. 7, Table 5), shows an elongation of the O(acetate)–Mn1–O4 axis [Mn1–O(acetate) 2.134(2) Å; Mn1–O4 2.142(1) Å], while the equatorial Mn–O bond lengths are shorter [1.854(1)–1.931(1) Å]. The two Mn^{IV} centers (Mn2 and Mn3, Fig. 7, Table 5) are not axially distorted [Mn–oxido distances 1.855(1)–1.903(1) Å].

The $[\text{YMn}^{\text{IV}}_3\text{O}_4]$ compound $[\mathbf{6}\text{-Y}][\text{OTf}]$ can also be reduced in the same fashion to yield the reduced compound $\text{LYMn}^{\text{IV}}_2\text{Mn}^{\text{III}}\text{O}_4(\text{OAc})_3(\text{DMF})$ ($\mathbf{7}\text{-Y}$, Scheme 3b). A XRD study of single crystals of $\mathbf{7}\text{-Y}$ grown by vapor diffusion of diethyl ether into a DMF solution of $\mathbf{7}\text{-Y}$ shows a similar structure to $\mathbf{7}\text{-Sc}$ (Fig. 8), with the Mn^{III} center (Mn1) displaying an axial distortion [Mn1–O(acetate) 2.168(3) Å; Mn1–O4 2.206(3) Å]. The similarities of the structures of compound **7** are demonstrated when they are overlaid (Fig. 9); the bottom trimanganese tetraoxido cores match very well, while the apical metals are offset due to the larger ionic radius of Y^{3+} . Surprisingly, while the Y^{3+} center in $[\mathbf{6}\text{-Y}]^+$ is 8-coordinate with two DMF ligands bound to yttrium, the Y^{3+} center in $\mathbf{7}\text{-Y}$ is 7-coordinate, with only one DMF ligand. This change in coordination may be due to the reduced positive charge of $\mathbf{7}\text{-Y}$.

Table 5. Selected structural parameters of compounds **7-M**. Mn1 is the Mn^{III} center.

| | 7-Sc | 7-Y |
|---------------|------------------------------------|------------------------------------|
| Mn1–O (Å) | 2.142(1), 1.931(1), 1.885(1) | 2.206(3), 1.926(3), 1.896(3) |
| Mn2–O (Å) | 1.903(1), 1.888(1), 1.861(1) | 1.870(3), 1.854(3), 1.853(3) |
| Mn3–O (Å) | 1.881(1), 1.873(1), 1.855(1) | 1.886(3), 1.861(3), 1.853(3) |
| Avg. Mn–O (Å) | 1.91 | 1.91 |
| M–O (Å) | 2.200(1), 2.164(1), 2.166(1) | 2.342(3), 2.308(3), 2.297(3) |
| Avg. M–O (Å) | 2.18 | 2.32 |



Scheme 3. Synthesis of (a) reduced $[\text{ScMn}_3\text{O}_4]$ complex **2-Sc** and (b) reduced $[\text{YMn}_3\text{O}_4]$ complex **2-Y**.

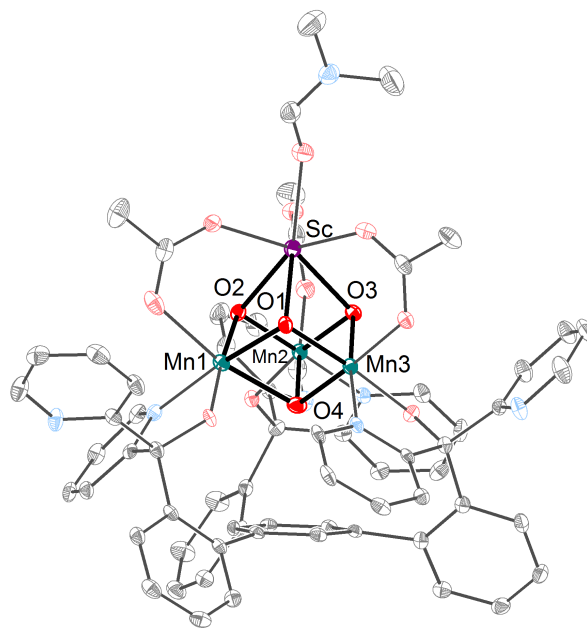


Figure 7. Solid-state structure of 7-Sc as 50% thermal ellipsoids. Bold lines emphasize the cubane core. Hydrogen atoms and outer-sphere solvent molecules not shown for clarity.

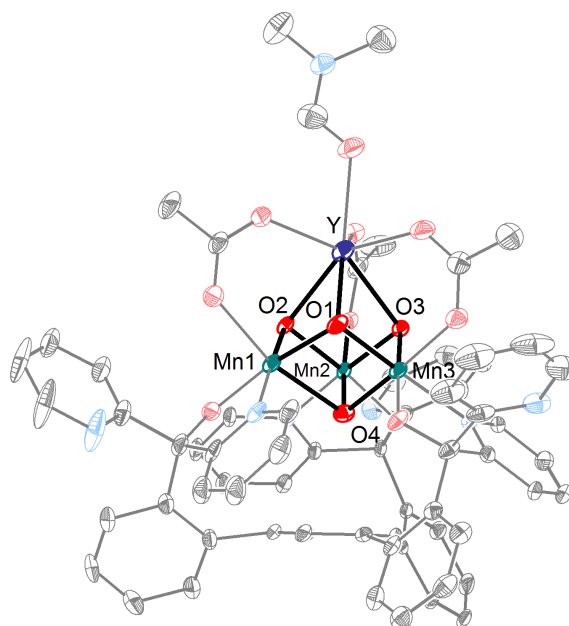


Figure 8. Solid-state structure of 7-Y as 50% thermal ellipsoids. Bold lines emphasize the cubane core. Hydrogen atoms and outer-sphere solvent molecules not shown for clarity.

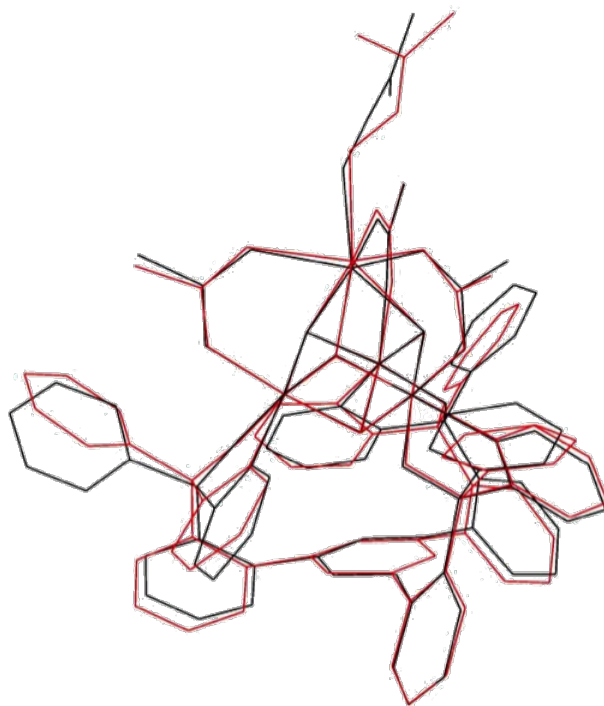


Figure 9. Structural overlay of 7-Sc (black) and 7-Y (red).

4.4 Magnetic susceptibility measurements

The magnetic properties of oxide-bridged manganese clusters have been studied extensively both experimentally and theoretically in order to further understand the OEC and other manganese systems.¹⁸ With the recent advances in the syntheses of heterometallic clusters, including two examples of clusters containing $[\text{CaMn}^{\text{IV}}_3\text{O}_4]$ units related to the structure of the OEC,^{11a, 14} understanding the experimental magnetic susceptibilities of these clusters would be useful both as benchmarks for theoretical models and to help understand spin exchange in the OEC and in water oxidation catalysts. Recent theoretical studies have predicted that these $[\text{CaMn}^{\text{IV}}_3\text{O}_4]$ cubane clusters should display ferromagnetic interactions between the manganese(IV) centers, leading to a $S = 9/2$ ground state.^{18b}

The variable temperature magnetic susceptibilities of compounds **6**-Ca, $[\mathbf{6}\text{-Sc}]^+$, and $[\mathbf{6}\text{-Y}]^+$ were measured at an applied field of 1000 Oe from 2–300 K (Fig. 10). For all three

compounds, dominant ferromagnetic coupling between the Mn ions is observed (see Table 6 for fitting parameters). At 300 K, the expected spin-only $\chi_M T$ value for three Mn^{IV} centers ($S = 3/2$, $g = 2$) is $5.625 \text{ cm}^3 \text{ mol}^{-1} \text{ K}$. The $\chi_M T$ values for all three compounds **6** measured are close to that value; for **6**-Ca, the $\chi_M T$ value at 300 K is $5.75 \text{ cm}^3 \text{ mol}^{-1} \text{ K}$, for $[\text{6-Sc}]^+$, the $\chi_M T$ value at 300 K is $5.45 \text{ cm}^3 \text{ mol}^{-1} \text{ K}$, and for $[\text{6-Y}]^+$, the $\chi_M T$ value is $5.27 \text{ cm}^3 \text{ mol}^{-1} \text{ K}$. The $\chi_M T$ values for all three compounds increase at low temperatures, although all three approach different maximum values. It is notable that the maximum $\chi_M T$ value for **6**-Ca only approaches ca. $8 \text{ cm}^3 \text{ mol}^{-1} \text{ K}$ even at low temperatures, as the predicted theoretical maximum for **6**-Ca based upon calculations has been reported to be greater than $12 \text{ cm}^3 \text{ mol}^{-1} \text{ K}$ due to the $S = 9/2$ ground state.^{18b} This discrepancy may be due to antiferromagnetic intermolecular interactions contributing to a lower overall observed spin, but further studies are needed.

The variable temperature magnetic susceptibility behaviors for **7**-Sc and $\text{cm}^3 \text{ mol}^{-1}$ and **7**-Y were also measured under the same conditions (Fig. 11). The $\chi_M T$ value at room temperature approaches $7.06 \text{ cm}^3 \text{ mol}^{-1} \text{ K}$ for **7**-Sc, which is near the expected spin-only value of $6.75 \text{ cm}^3 \text{ mol}^{-1} \text{ K}$ for a $\text{Mn}^{\text{IV}}_2\text{Mn}^{\text{III}}$ system with $g = 2$. The room temperature value for **7**-Y is higher, near $10 \text{ cm}^3 \text{ mol}^{-1} \text{ K}$, and fits to a higher g value of 2.31, which may be due to some experimental inconsistencies. For both compounds, however, dominant ferromagnetic coupling is observed.

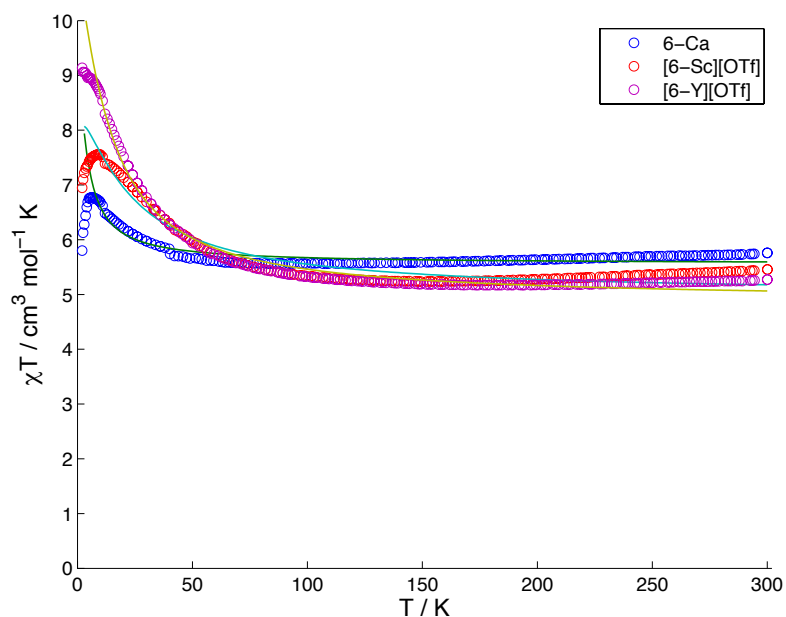


Figure 10. $\chi_M T$ vs. T data and fits (solid lines) for **6-Ca**, **[6-Sc]⁺**, and **[6-Y]⁺**. SQUID data were measured by Dr. Po-Heng Lin. See Table 6 for fitting parameters.

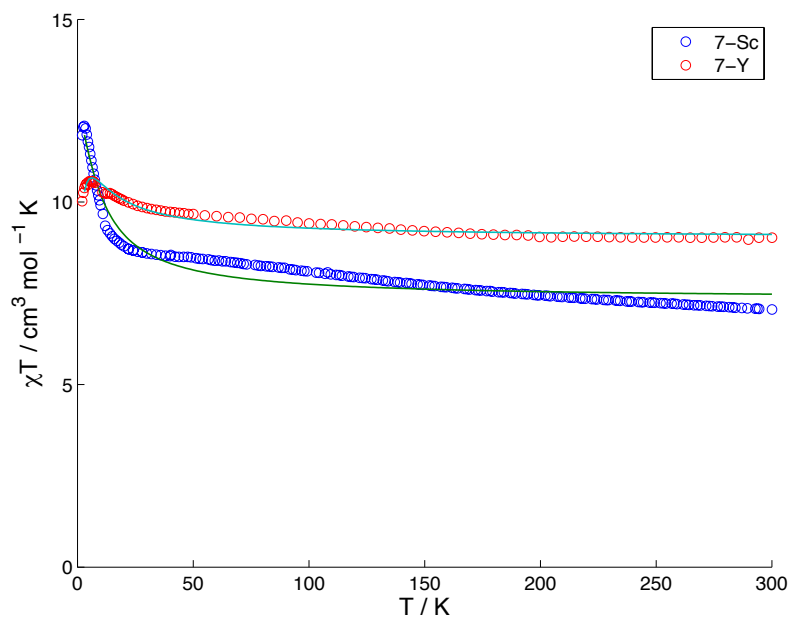


Figure 11. $\chi_M T$ vs. T data and best fit (solid line) for **7-Sc** and **7-Y**. SQUID data were measured by Dr. Po-Heng Lin. See Table 6 for fitting parameters.

Table 6. Magnetic susceptibility fitting parameters.

| Compound | J (cm ⁻¹) | J' (cm ⁻¹) | g | R ($\times 10^{-4}$) |
|------------------------------|-------------------------|--------------------------|------|------------------------|
| 6 -Ca | 0.61 | -0.34 | 1.99 | 2.3 |
| [6 -Sc] ⁺ | 3.59 | -2.00 | 1.88 | 7.1 |
| [6 -Y] ⁺ | 3.03 | -0.88 | 1.86 | 3.4 |
| 7 -Sc | 1.19 | -0.89 | 2.08 | 10 |
| 7 -Y | 0.78 | -0.98 | 2.31 | 1 |

4.5 Electrochemical studies

With these complexes in hand, in addition to the tetramanganese cluster LMn₄O₄(OAc)₃ (**8**), which was prepared and measured by Mr. Jacob S. Kanady,¹¹ the effect of changing the redox-inactive metals in the clusters was studied electrochemically. Cyclic voltammograms (CVs) of [**6**-Sc]⁺, [**6**-Y]⁺, **6**-Zn, **6**-Ca, and [**6**-Sr]₂ (0.1 M NBu₄PF₆) in *N,N*-dimethylacetamide (DMA) showed quasireversible redox couples assigned as the [MMn^{IV}₃O₄]/[MMn^{IV}₂Mn^{III}O₄] couple at potentials of -250, -430, -630, and -940 mV respectively vs. the ferrocene/ferrocenium couple (Fc/Fc⁺) (Fig. 12, Table 7).

The reduction potentials of **6**-Ca and [**6**-Sr]₂ are similar ($E_{1/2} = -940$ mV vs. Fc/Fc⁺)^{11a}, but the reduction potential of **6**-Zn is more positive by greater than 300 mV ($E_{1/2} = -630$ mV), even though Zn²⁺ is also a dicationic redox-inactive metal and all three complexes are neutral in charge. Similarly, although both [**6**-Sc]⁺ and [**6**-Y]⁺ contain tricationic redox-inactive metals, their reduction potentials differ by ca. 200 mV. This variation in redox potential is inconsistent with a purely electrostatic explanation of the differences in redox potentials¹⁹. The similarity of the redox potentials of the calcium and strontium variants in

comparison to those of the other analogs is consistent with the similar electronic structure of the Sr-substituted OEC, as well as the water oxidation activity observed (although lower than that of native photosystem II).^{4a, 20}

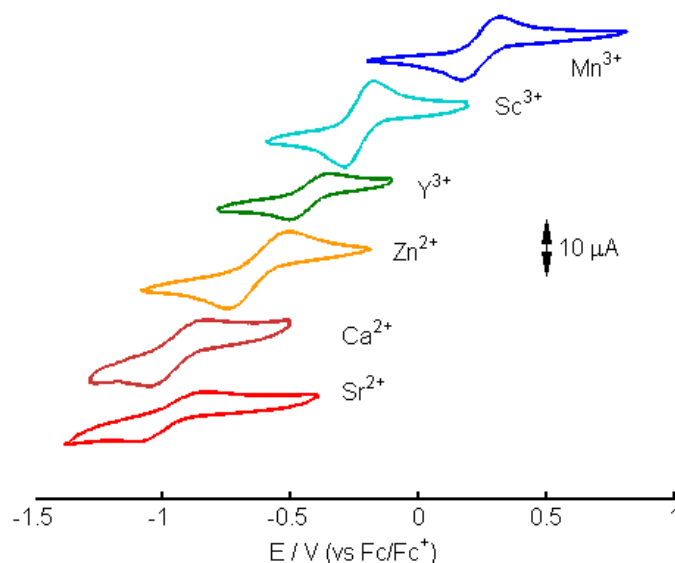


Figure 12. Cyclic voltammograms corresponding to the $[\text{MMn}^{\text{IV}}_3\text{O}_4]/[\text{MMn}^{\text{IV}}_2\text{Mn}^{\text{III}}\text{O}_4]$ redox couple ($\text{M} = \text{Mn}^{3+}, \text{Sc}^{3+}, \text{Y}^{3+}, \text{Zn}^{2+}, \text{Ca}^{2+}, \text{and Sr}^{2+}$) in 0.1 M NBu_4PF_6 in DMA. Scan rate of 100 mV/s. Potentials are referenced to Fc/Fc^+ . CV for $\text{M} = \text{Mn}^{3+}$ measured by Mr. Jacob S. Kanady.^{11a}

The $E_{1/2}$ values of the $[\text{MMn}^{\text{IV}}_3\text{O}_4]/[\text{MMn}^{\text{IV}}_2\text{Mn}^{\text{III}}\text{O}_4]$ couples measured above in DMA and those of previously prepared complexes¹¹ were plotted against the $\text{p}K_{\text{a}}$ of the metal aqua ions measured in water,²¹ used here as a measure of the Lewis acidity of cation M. As with the related series of trimanganese dioxido complexes (Chapter 3),³ a linear correlation is observed (Fig. 13). Hence, the chemical property that the reduction potentials of the clusters depend on is the Lewis acidity of the incorporated redox inactive metal. The positive shift in reduction potential with increasing Lewis acidity is likely due to the increased electron-withdrawing effect upon the μ_3 -oxido ligands, which stabilizes the more

reduced manganese oxidation state. Remarkably, both lines have similar slopes, with each pK_a unit shifting the potential by ca. 100 mV, despite the differences in cluster structure, ancillary ligands, number of oxido ligands, and manganese oxidation states. The intercepts of the two series are different by ca. 900 mV, with the $[MMn^{IV}_3O_4]$ complexes having more negative reduction potentials than the corresponding $[MMn^{IV}Mn^{III}_2O_2]$ complexes containing the same metal ions, despite the higher overall manganese oxidation state of the tetraoxido clusters. This negative shift in potential with additional oxido ligands highlights a different path for tuning the reduction potential. An increased number of oxido ligands per redox active metal shifts the potentials negatively as the cluster becomes more electron-rich and the higher Mn oxidation states are stabilized. The synthetic calcium cubane discussed here, **6**-Ca, has a very negative potential compared to the thermodynamic potential of water oxidation. However, the structurally related OEC has a lower oxide/Mn ratio, likely driving the potential positively.

Table 7. Reduction potentials of $[MMn^{IV}_3O_4]$ compounds in *N,N*-dimethylacetamide (0.1 M NBu₄PF₆).

| Compound | pK_a of M(aqua) ⁿ⁺ | Potential vs. Fc/Fc ⁺ (mV) ^a |
|---|---------------------------------|--|
| LMn ₄ O ₄ (OAc) ₃ (8) | 0.1 | 290 ^{11a} |
| [6 -Sc][OTf] | 4.7 | -250 |
| [6 -Y][OTf] | 8.0 | -430 |
| 6 -Zn | 9.3 | -630 |
| 6 -Ca | 12.6 | -940 ^{11a} |
| 6 -Sr | 13.2 | -940 |

^a Reported potentials are an average of duplicate measurements from different samples and referenced to Fc/Fc⁺.

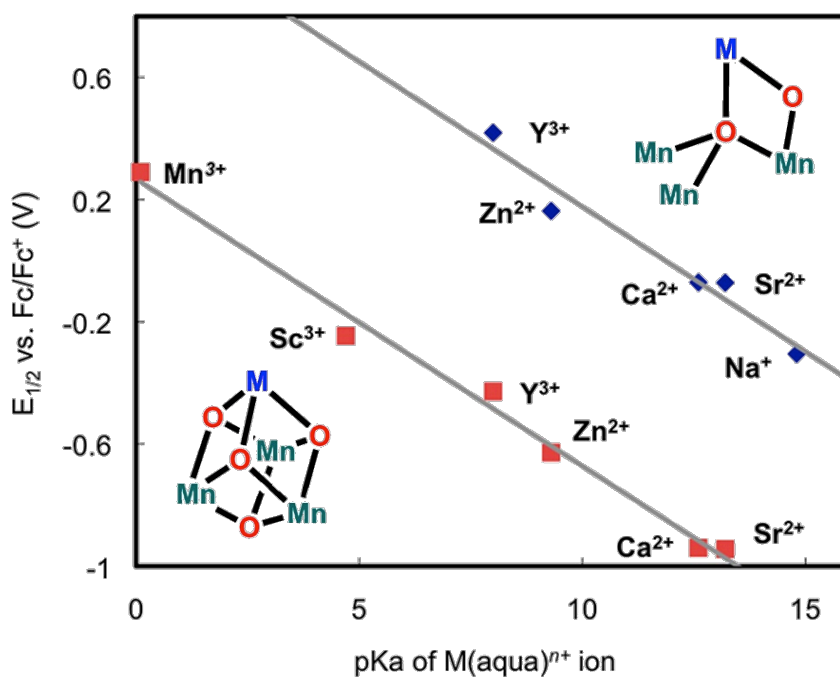


Figure 13. Reduction potentials of MMn₃O₄ complexes (red squares) and MMn₃O₂ complexes (blue diamonds, Chapter 3) vs. pK_a of the corresponding M(aqua)ⁿ⁺ ion as a measure of Lewis acidity. Potentials are referenced to ferrocene/ferrocenium.

The similar linear dependences upon Lewis acidity of the dioxido and tetraoxido complexes suggest that a more general correlation exists between the redox potentials of mixed metal oxides and the Lewis acidity of incorporated redox-inactive metals. Such a relationship may provide a quantitative method for tuning the potentials of both homogeneous and heterogeneous metal oxide electrocatalysts, either by changing the redox-inactive metal in isostructural compounds or by increasing or decreasing the oxide content. The wide range of reduction potentials found within the [MMn₃O₄] clusters demonstrates that a large change in the thermodynamics of a catalyst can be effected by simple substitution, (e.g., ca. 16 kcal/mol when substituting Sc³⁺ for Ca²⁺).

Conclusions

In summary, [MMn₃O₄] cubane clusters structurally related to the CaMn₃ subsite of the OEC substituted with divalent and trivalent redox-inactive metals were prepared. This series of compounds allowed the systematic study of the electrochemical effect of the Lewis acidic metal ions on the manganese reduction potentials. Varying the Lewis acidity of the capping metal from Mn³⁺ to Sr²⁺ shifted the redox potentials of these clusters by over 1 V. These results support proposals that in addition to its other possible functions in the OEC, Ca²⁺ plays a role in modulating the redox potential of the manganese centers via the μ -oxo ligands. Future work will include studying these effects in other metal-oxido compounds of varying structure, metal character, and oxidation state to better understand the fundamental basis for water oxidation in complex metal clusters.

Experimental Section

General Considerations. Unless indicated otherwise, reactions performed under inert atmosphere were carried out in oven-dried glassware in a glovebox under a nitrogen atmosphere. Anhydrous tetrahydrofuran (THF) was purchased from Aldrich in 18 L Pure-PacTM containers. Anhydrous acetonitrile, benzene, dichloromethane, diethyl ether, and THF were purified by sparging with nitrogen for 15 minutes and then passing under nitrogen pressure through a column of activated A2 alumina (Zapp's). CD₂Cl₂ was purchased from Cambridge Isotope Laboratories, dried over calcium hydride, then degassed by three freeze-pump-thaw cycles and vacuum transferred prior to use. ¹H NMR spectra were recorded on a Varian 300 MHz instrument, with shifts reported relative to the residual solvent peak. ¹⁹F NMR spectra were recorded on a Varian 300 MHz instrument, with shifts reported relative to the internal lock signal. Elemental analyses were performed

by Midwest Microlab, LLC, Indianapolis, IN and Robertson Microlit, Ledge wood, NJ. High resolution mass spectrometry (HRMS) was performed at the California Institute of Technology Mass Spectrometry Facility. $\text{LMn}_3(\text{OAc})_3$ was prepared according to previously published procedures.^{11, 15b}

Synthesis of $\text{LCaMn}_3\text{O}_4(\text{OAc})_3(\text{THF})$ (6-Ca).

In the glovebox, a round-bottom flask equipped with a stir bar was charged with $\text{LMn}_3(\text{OAc})_3$ (2.00 g, 1.67 mmol) and $\text{Ca}(\text{OTf})_2$ (0.62 g, 1.84 mmol, 1.1 equiv). 10:1 THF/DME (220 mL) was added, and the yellow heterogeneous mixture was stirred at room temperature for 5 min. KO_2 (0.356 g, 5.01 mmol, 3 equiv) was added to the mixture as a solid, and the mixture was stirred at room temperature for 2 d, darkening to red-brown. The mixture was filtered through Celite, then concentrated *in vacuo* to yield a red-brown solid. The solid was washed with acetonitrile (100 mL), then extracted with THF/benzene. The THF/benzene extract was concentrated *in vacuo* to yield the product as a red solid (0.48 g, 21%). ^1H NMR (C_6D_6 , 300 MHz): δ 21.7, 11.4, 10.1, 8.7, 6.0, -17.0 ppm. Anal. Calcd. For $\text{C}_{67}\text{H}_{55}\text{CaMn}_3\text{N}_6\text{O}_{14}$: C, 58.61; H, 4.04; N, 6.12. Found: C, 58.33; H, 3.90; N, 6.23.

Synthesis of $[\text{LSrMn}_3\text{O}_4(\text{OAc})_3(\text{DMF})]_2$ ([6-Sr]₂)

In a glovebox, $\text{LMn}(\text{OAc})_3$ (0.310 g, 0.259 mmol) and $\text{Sr}(\text{OTf})_2$ (0.115 g, 0.298 mmol, 1.2 equiv) were combined in a scintillation vial equipped with a stir bar. 10:1 THF/DME (20 mL) was added, and the heterogeneous yellow mixture was stirred for 5 min. KO_2 (0.055 g, 0.774 mmol, 3.0 equiv) was added in small portions over a minute, and the mixture was stirred at room temperature for 12 h, darkening to a red-brown mixture. The reaction mixture was filtered through Celite, and the filtrate was dried *in vacuo*. The red-brown solid was then washed with acetonitrile, then extracted with DMF and dried again to yield

the clean product (0.030 g, 7%). HRMS–ESI (m/z): $[M+H]^+$ calcd. for $C_{63}H_{48}N_6O_{13}Mn_3Sr$ (no solvent coordinated to Sr), 1350.0555; found, 1350.0597. Single crystals of a dimer of the complex coordinated by DMF molecules were grown by vapor diffusion of diethyl ether into a DMF solution of the product at room temperature.

Synthesis of $LZnMn_3O_4(OAc)_3$ (**6-Zn**)

In a glovebox, **6**-Ca (0.044 g, 0.032 mmol) and $Zn(OTf)_2$ (0.016 g, 0.035 mmol, 1.1 equiv) were combined in a scintillation vial equipped with a stir bar and dissolved in DMF (3 mL). The brown mixture was stirred at room temperature for 15 min., then dried *in vacuo*. Benzene (4 mL) was added to the resulting brown solid, and the mixture was filtered through Celite to remove calcium triflate salts. The filtrate was dried *in vacuo* to yield the product as a red-brown solid (0.029 g, 68%). X-ray quality single crystals were grown by vapor diffusion of diethyl ether into a benzene solution of **6-Zn** at room temperature. 1H NMR (CD_2Cl_2 , 300 MHz): δ 24.5, 11.7, 9.0, 8.0, 7.1, 4.1, 3.4, –21.8 ppm. Anal. Calcd. for $C_{63}H_{48}Mn_3N_6O_{13}Zn$: C, 57.01; H, 3.65; N, 6.33. Found: C, 56.01; H, 3.79; N, 6.11. HRMS–ESI (m/z): M^+ calcd. for $C_{63}H_{48}N_6O_{13}Mn_3Zn$, 1325.0712; found, 1325.0754.

Synthesis of $[LScMn_3O_4(OAc)_3(OTf)]$ (**[6-Sc][OTf]**)

In the glovebox, a scintillation vial equipped with a stir bar was charged with **6**-Ca (0.101 g, 0.073 mmol) and $Sc(OTf)_3$ (0.036 g, 0.073 mmol, 1.0 equiv). DMF (3 mL) was added, and the dark red-brown solution was stirred at room temperature for 5 min. Diethyl ether (35 mL) was added to precipitate a dark red-brown solid. The precipitate was collected by filtration, then recrystallized from acetonitrile/diethyl ether to afford the product as a dark brown crystals (0.069 g, 65 %). 1H NMR (CD_2Cl_2 , 300 MHz): δ 12.1, 11.8, 9.5, 8.0, 6.2, 4.4, –1.1, –23.8 ppm. ^{19}F NMR (CD_2Cl_2): δ –77.5 ppm. UV-Vis (CH_2Cl_2 , λ_{max} (ϵ [$M^{-1} cm^{-1}$]

¹)]): 243 (6.6x10⁴), 350 (shoulder, 1.2x10⁴). Anal. Calcd. for C₆₄H₄₈F₃Mn₃N₆O₁₆SSc: C, 52.80; H, 3.32; N, 5.77. Found: C, 53.07; H, 3.41; N, 5.65.

Synthesis of [LYMn₃O₄(OAc)₃(DMF)₂][OTf] ([6-Y][OTf])

In a glovebox, **6**-Ca (0.046 g, 0.0335 mmol) and Y(OTf)₃ (0.020 g, 0.0368 mmol, 1.1 equiv) were combined in a scintillation vial equipped with a stir bar and dissolved in DMF (3 mL). The brown mixture was stirred at room temperature for 15 min. Diethyl ether (40 mL) was added to precipitate the product as a red-brown solid. The precipitate was collected over Celite, washed with diethyl ether, then extracted with dichloromethane. The extract was dried *in vacuo* to yield the product as a red-brown solid (0.039 g, 71%). Single crystals for XRD were grown by vapor diffusion of diethyl ether into a DMF solution of [6-Y][OTf] at room temperature. ¹H NMR (300 MHz, CD₂Cl₂): δ 16.1, 11.9, 11.3, 9.2, 6.1, 4.6, 1.5, -21.1 ppm. ¹⁹F NMR (CD₂Cl₂): δ -78.2 ppm. Anal. Calcd. for C₇₀H₆₂F₃Mn₃N₈O₁₈SY: C, 51.08; H, 3.80; N, 6.81. Found: C, 50.79; H, 3.77; N, 6.36. HRMS-ESI (*m/z*): M⁺ calcd. for C₆₃H₄₈N₆O₁₃Mn₃Y (no solvent coordinated to Y), 1350.0479; found, 1350.0524.

Synthesis of LScMn₃O₄(OAc)₃(L') (7-Sc·L', L' = THF or DMF)

In a glovebox, a solution of decamethylferrocene (0.006 g, 0.018 mmol, 1.4 equiv) in THF (1 mL) was added to a THF solution of [6-Sc][OTf] (0.019 g, 0.013 mmol, 3 mL). The mixture was stirred 5 min., then filtered through Celite. The filtrate was dried *in vacuo*. Benzene was added, and the brown mixture was filtered through Celite to remove the remaining green decamethylferrocenium triflate. The benzene filtrate was dried *in vacuo*, then washed with diethyl ether to yield the product as a red-brown solid (0.014 g, 78%). ¹H NMR (300 MHz, C₆D₆): δ 22.4, 11.2, 10.3, 9.3, 5.6, 4.8, 3.6, -28.0 ppm. Anal. Calcd. for

$\text{C}_{66}\text{H}_{55}\text{Mn}_3\text{N}_7\text{O}_{14}\text{Sc}$ [$\text{LScMn}_3\text{O}_4(\text{OAc})_3(\text{THF})$]: C, 58.36; H, 4.09; N, 6.09. Found: C, 58.23; H, 3.36; N, 6.15. HRMS–ESI (m/z): M^+ calcd. for $\text{C}_{63}\text{H}_{48}\text{N}_6\text{O}_{13}\text{Mn}_3\text{Sc}$ (no solvent coordinated to Sc), 1306.0980; found, 1306.0996. X-ray quality single crystals of the product with coordinated DMF rather than THF were grown from DMF/diethyl ether.

Synthesis of $\text{LYMn}_3\text{O}_4(\text{OAc})_3(\text{DMF})$ (7-Y)

In a glovebox, a solution of decamethylferrocene (0.017 g, 0.0527 mmol) in THF (2 mL) was added to a solution of [6-Y][OTf] (0.079 g, 0.0527 mmol, 1 equiv) in THF (8 mL). The mixture was stirred at room temperature for 30 min., then filtered through Celite. The filtrate was dried *in vacuo*. Benzene was added, and the mixture was filtered through Celite to remove decamethylferrocenium triflate. The benzene filtrate was dried *in vacuo* to yield the product as a red-brown solid (0.063 g, 94%). X-ray quality crystals were grown by vapor diffusion of diethyl ether into a DMF solution of 7-Y. ^1H NMR (C_6D_6 , 300 MHz): δ 25.1, 13.1, 11.3, 10.2, 9.3, 7.8, 5.5, 4.5, –25.3 ppm. Anal. Calcd. For $\text{C}_{66}\text{H}_{55}\text{Mn}_3\text{N}_7\text{O}_{14}\text{Y}$: C, 55.67; H, 3.89; N, 6.89. Anal. Calcd. For $\text{C}_{69}\text{H}_{62}\text{Mn}_3\text{N}_8\text{O}_{15}\text{Y}$ (one DMF solvate): C, 55.36; H, 4.17; N, 7.49. Found: C, 53.96; H, 4.88; N, 7.26.

Synthesis of $\text{LMgMn}_3\text{O}_4(\text{OAc})_3$ (6-Mg)

In the glovebox, a scintillation vial equipped with a stir bar was charged with 6-Ca (0.016 g, 0.0115 mmol) and $\text{Mg}(\text{OTf})_2$ (0.008 g, 0.024 mmol, 2 equiv). DMF (2 mL) was added, and the mixture was stirred at room temperature for 12 h, then concentrated *in vacuo*. The residue was taken up in benzene, filtered through Celite, then concentrated under reduced pressure to yield the product as a red-brown solid. X-ray quality crystals were grown by vapor diffusion of diethyl ether into a DMF solution of 6-Zn. ^1H NMR (CD_2Cl_2 , 300 MHz): δ 22.4, 11.8, 11.1, 9.0, 7.0, 4.1, –21.2 ppm. Anal. Calcd. For $\text{C}_{63}\text{H}_{48}\text{MgMn}_3\text{N}_6\text{O}_{13}$:

C, 58.83; H, 3.76; N, 6.53. Anal. Calcd. For $C_{70}H_{65}MgMn_3N_7O_{15}$ (one DMF and one Et_2O , as in XRD structure): C, 58.65; H, 4.57; N, 6.84. Found: C, 57.74; H, 4.60; N, 6.71.

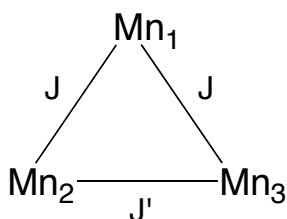
Magnetic Susceptibility Measurements

General Considerations. DC magnetic susceptibility measurements were carried out in the Molecular Instrumentation Center at UCLA on a Quantum Design MPMS instrument running MPMS MultiVu software. Powdered samples were wrapped in plastic wrap and suspended in clear plastic straws. Data were recorded at 0.1 T from 2–300 K.

The $\chi_M T$ data taken at 0.1 T were fit to the magnetic susceptibility equation derived from the isotropic spin Hamiltonian for two coupling constants, J and J' [Eq. (1)].

$$\hat{H} = -2J[(\hat{S}_1 \cdot \hat{S}_2) + (\hat{S}_2 \cdot \hat{S}_3)] - 2J'(\hat{S}_3 \cdot \hat{S}_1) \quad (1)$$

The eigenvalues were determined using the Kambe method.²² The data were fit from 10–300 K using Matlab²³ by minimizing $R = \sum |(\chi_M T)_{obs} - (\chi_M T)_{calcd}|^2 / \sum (\chi_M T)_{obs}^2$.



Scheme 4. Exchange coupling model employed. For compounds **6**, the spins used were all $S = 3/2$ for Mn1, Mn2, and Mn3. For **7-Sc**, the spins used were $S = 2$, $3/2$, and $3/2$ for Mn1, Mn2, and Mn3 respectively.

Electrochemical Measurements

Electrochemical measurements were recorded with a Pine Instrument Company AFCBP1 bipotentiostat using the AfterMath software package. Cyclic voltammograms were recorded on ca. 1 mM solutions of the relevant complexes in the glovebox at 20 °C with an

auxiliary Pt-coil electrode, a Ag/Ag⁺ reference electrode (0.01 M AgNO₃, 0.1 M ⁿBu₄NPF₆ in CH₃CN), and a 3.0 mm glassy carbon electrode disc (BASi). The electrolyte solution was 0.1 M ⁿBu₄NPF₆ in *N,N*-dimethylacetamide (DMA). Reported potentials were referenced internally to ferrocene/ferrocenium, and are an average of at least two separate CV experiments. The measured reduction potentials typically varied by less than 15 mV between experiments.

Crystallographic Information

Table 8. Crystal and refinement data for reported complexes.

| | [6-Sr] ₂ | 6-Zn | [6-Y][OTf] | [6-Sc][OTf] | [7-Y]·DMF | [7-Sc]·DMF |
|--|---|---|---|---|---|---|
| empirical formula | C ₆₉ H ₅₅ Mn ₃ N ₈ O ₁₅ Sr | C ₆₉ H ₅₄ Mn ₃ N ₆ O ₁₃ Zn | C ₇₆ H ₇₆ F ₃ Mn ₃ N ₁₀ O ₂₀ SY | C ₇₀ H ₆₁ F ₃ Mn ₃ N ₇ O ₁₇ SSc | C _{69.53} H _{63.58} Mn ₃ N _{7.47} O ₁₅ Y | C ₆₆ H ₅₅ Mn ₃ N ₇ O ₁₅ Sc |
| CCDC | 923216 | 923217 | 923218 | 901808 | -- | 923219 |
| formula wt | 1488.65 | 1405.37 | 1742.26 | 1571.10 | 1497.53 | 1395.95 |
| T (K) | 100 | 100 | 100 | 100 | 100 | 100 |
| a, Å | 14.4394(9) | 13.5517(7) | 12.9611(6) | 13.7160(7) | 15.2019(9) | 13.8808(6) |
| b, Å | 14.5514(9) | 15.2198(8) | 14.9934(7) | 15.8986(7) | 15.2276(9) | 14.6307(6) |
| c, Å | 18.0485(11) | 16.9998(8) | 19.8287(9) | 16.3736(8) | 16.696(1) | 14.8415(6) |
| α, deg | 80.763(3) | 70.865(2) | 84.492(2) | 73.250(2) | 74.449(2) | 84.969(2) |
| β, deg | 71.236(3) | 81.612(2) | 82.070(2) | 84.410(3) | 74.510(2) | 82.052(2) |
| γ, deg | 73.470(3) | 82.158(3) | 87.566(2) | 72.393(2) | 66.594(2) | 78.193(2) |
| V, Å ³ | 3432.3(4) | 3262.4(3) | 3797.2(3) | 3258.6(3) | 3360.3(3) | 2916.5(2) |
| Z | 2 | 2 | 2 | 2 | 2 | 2 |
| cryst syst | Triclinic | Triclinic | Triclinic | Triclinic | Triclinic | Triclinic |
| space group | P-1 | P-1 | P-1 | P-1 | P-1 | P-1 |
| d _{calcd} , g/cm ³ | 1.440 | 1.431 | 1.568 | 1.601 | 1.480 | 1.590 |
| θ range, deg | 1.82–29.02 | 1.99–33.15 | 1.78–30.74 | 1.77 to 43.86 | 1.48–30.77 | 1.86–32.88 |
| μ, mm ⁻¹ | 1.383 | 0.998 | 1.360 | 0.788 | 1.478 | 1.336 |
| abs cor | Semi-empirical from equivalents | Semi-empirical from equivalents | Semi-empirical from equivalents | Semi-empirical from equivalents | Semi-empirical from equivalents | Semi-empirical from equivalents |
| GOF ^c | 1.186 | 1.046 | 1.237 | 1.270 | 1.242 | 1.542 |
| R1, ^a | | | | | | |
| wR2 ^b (I > 2σ(I)) | 0.0668, 0.1559 | 0.0433, 0.1053 | 0.0536, 0.1250 | 0.0464, 0.1091 | 0.0720, 0.1835 | 0.0511, 0.0710 |

$$^a R1 = \sum ||F_o| - |F_c|| / \sum |F_o| \quad ^b wR2 = \{ \sum [w(F_o^2 - F_c^2)^2] / \sum [w(F_o^2)^2] \}^{1/2} \quad ^c GOF = S = \{ \sum$$

$$[w(F_o^2 - F_c^2)^2] / (n-p) \}^{1/2}$$

Refinement details

In each case, crystals were mounted on a glass fiber or nylon loop using Paratone oil, then placed on the diffractometer under a nitrogen stream. Low temperature (100 K) X-ray data were obtained on a Bruker APEXII CCD based diffractometer (Mo sealed X-ray tube, $K_{\alpha} = 0.71073 \text{ \AA}$). All diffractometer manipulations, including data collection, integration and scaling were carried out using the Bruker APEXII software.²⁴ Absorption corrections were applied using SADABS.²⁵ Space groups were determined on the basis of systematic absences and intensity statistics and the structures were solved by direct methods using XS²⁶ (incorporated into SHELXTL) and refined by full-matrix least squares on F^2 . All non-hydrogen atoms were refined using anisotropic displacement parameters. Hydrogen atoms were placed in idealized positions and refined using a riding model. The structure was refined (weighted least squares refinement on F^2) to convergence.

It should be noted that due to the size of these compounds, most crystals included solvent accessible voids, which tended to contain disordered solvent. In addition, due to a tendency to desolvate, the long range order of these crystals and amount of high angle data we were able to record was in some cases not ideal. These disordered solvent molecules were largely responsible for the alerts generated by the checkCIF protocol. For two compounds ($[\mathbf{6}\text{-Sr}]_2$ and $\mathbf{6}\text{-Zn}$), the disordered non-coordinated solvents were removed using the SQUEEZE protocol included in PLATON (*vide infra*).²⁷ We are confident this additional electron density is from solvent in the crystal lattice and not from unaccounted counterions.

Special refinement details for $[\text{LSrMn}_3\text{O}_4(\text{OAc})_3(\text{DMF})]_2 \cdot \text{DMF}$ (**[6-Sr]**)

The structure is a dimer of two molecules bridged by a highly disordered DMF molecule. Restraints and populations were employed to model this bridging ligand as a DMF molecule disordered in two positions. Restraints were also employed to treat the displacement parameters of the coordinated DMF molecule to acceptable sizes. The crystal lattice also contained electron density corresponding to uncoordinated solvent molecules. One DMF molecule could be located, while the remaining electron density could not be satisfactorily modeled. SQUEEZE was employed to produce a bulk solvent correction to the observed intensities. The program accounted for 91 electrons per unit cell. This is in reasonable agreement with what would be expected for two disordered molecules of DMF (40 electrons/molecule).

Special refinement details for $\text{LZnMn}_3\text{O}_4(\text{OAc})_3 \cdot \text{C}_6\text{H}_6$ (**(6-Zn)**)

The compound crystallized with two solvent molecules in the lattice. One molecule could be modeled as a single benzene molecule, while the other was disordered and likely a mixture of benzene and diethyl ether. The electron density could not be satisfactorily modeled, and SQUEEZE was employed to produce a bulk solvent correction to the observed intensities. The program accounted for 78 electrons per unit cell. This is in reasonable agreement with what would be expected for a molecule of benzene (42 electrons/molecule) or a molecule of diethyl ether (42 electrons/molecule).

Special refinement details for $[\text{LYMn}_3\text{O}_4(\text{OAc})_3(\text{DMF})_2][\text{OTf}] \cdot 2(\text{DMF})$ (**[6-Y][OTf]**)

The structure contains two DMF ligands coordinated to yttrium. One DMF ligand is slightly disordered, but the difference peaks were low, suggesting that the disordered

population is low. The structure also contains two free DMF molecules and an outer-sphere trifluoromethanesulfonate counterion, which were all satisfactorily modeled.

Special refinement details for $\text{LScMn}_3\text{O}_4(\text{OAc})_3(\text{OTf})$ ($[\mathbf{6}\text{-Sc}][\text{OTf}]$)

Crystals were grown by vapor diffusion of diethyl ether into an acetonitrile solution of $[\mathbf{6}\text{-Sc}][\text{OTf}]$ at room temperature, then mounted on a fiber using Paratone oil and then placed on the diffractometer under a nitrogen stream at 100 K. The triflate anion bound to scandium is disordered, and populations were employed to model the ion in two positions. Restraints were used to treat the distances, angles, and displacement parameters of the ion. A molecule of acetonitrile and a molecule of diethyl ether were located in the structure.

Refinement of F^2 against ALL reflections. The weighted R-factor (wR) and goodness of fit (S) are based on F^2 , conventional R-factors (R) are based on F , with F set to zero for negative F^2 . The threshold expression of $F^2 > 2\sigma(F^2)$ is used only for calculating R-factors(gt) etc. and is not relevant to the choice of reflections for refinement. R-factors based on F^2 are statistically about twice as large as those based on F , and R-factors based on ALL data will be even larger.

All esds (except the esd in the dihedral angle between two l.s. planes) are estimated using the full covariance matrix. The cell esds are taken into account individually in the estimation of esds in distances, angles and torsion angles; correlations between esds in cell parameters are only used when they are defined by crystal symmetry. An approximate (isotropic) treatment of cell esds is used for estimating esds involving l.s. planes.

Special refinement details for $\text{LScMn}_3\text{O}_4(\text{OAc})_3(\text{DMF})\cdot\text{H}_2\text{O}$ ([7-Sc]·DMF)

The structure contains a DMF ligand coordinated to scandium. Additionally, there is a water molecule in the lattice (O15). The hydrogen atoms were not located, but the distance between O15 and O1 (2.805 Å) is consistent with a hydrogen bonding interaction.

Special refinement details for $\text{LYMn}_3\text{O}_4(\text{OAc})_3(\text{DMF})$ (7-Y)

The compound crystallizes with one DMF molecule coordinated to the Y^{3+} center. A second solvent molecule was located in the lattice that was modeled as a mixture of diethyl ether and DMF. The DMF molecule was fixed using DFIX constraints, and the thermal displacement parameters were restrained using EADP commands. Refinement of the populations resulted in 53% occupancy of the diethyl ether.

References

1. Yocum, C. F. *Coord. Chem. Rev.* **2008**, *252*, 296-305.
2. (a) Umena, Y.; Kawakami, K.; Shen, J. R.; Kamiya, N. *Nature* **2011**, *473*, 55-U65; (b) Ferreira, K. N.; Iverson, T. M.; Maghlaoui, K.; Barber, J.; Iwata, S. *Science* **2004**, *303*, 1831-1838.
3. Tsui, E. Y.; Tran, R.; Yano, J.; Agapie, T. *Nat Chem* **2013**, *5*, 293-299.
4. (a) Ghanotakis, D. F.; Babcock, G. T.; Yocum, C. F. *Febs Lett* **1984**, *167*, 127-130; (b) Vrettos, J. S.; Stone, D. A.; Brudvig, G. W. *Biochemistry* **2001**, *40*, 7937-7945; (c) Lee, C.-I.; Lakshmi, K. V.; Brudvig, G. W. *Biochemistry* **2007**, *46*, 3211-3223.
5. (a) Pecoraro, V. L.; Baldwin, M. J.; Caudle, M. T.; Hsieh, W. Y.; Law, N. A. *Pure Appl. Chem.* **1998**, *70*, 925-929; (b) Vrettos, J. S.; Limburg, J.; Brudvig, G. W. *Biochim. Biophys. Acta Bioenergetics* **2001**, *1503*, 229-245; (c) Yachandra, V. K.; Yano, J. *J. Photochem. Photobiol., B* **2011**, *104*, 51-59.
6. (a) Yachandra, V. K.; Sauer, K.; Klein, M. P. *Chem. Rev.* **1996**, *96*, 2927-2950; (b) Riggs-Gelasco, P. J.; Mei, R.; Ghanotakis, D. F.; Yocum, C. F.; Penner-Hahn, J. E. *J. Am. Chem. Soc.* **1996**, *118*, 2400-2410; (c) Haumann, M.; Junge, W. *Biochim. Biophys. Acta Bioenergetics* **1999**, *1411*, 121-133; (d) Lohmiller, T.; Cox, N.; Su, J.-H.; Messinger, J.; Lubitz, W. *J. Biol. Chem.* **2012**, *287*, 24721-24733.
7. (a) Fukuzumi, S.; Ohkubo, K. *Coord. Chem. Rev.* **2010**, *254*, 372-385; (b) Fukuzumi, S., Roles of Metal Ions in Controlling Bioinspired Electron-Transfer Systems. Metal Ion-Coupled Electron Transfer. In *Prog. Inorg. Chem.*, Karlin, K. D., Ed. John Wiley & Sons Inc: New York, 2009; Vol. 56, pp 49-153.
8. (a) Fukuzumi, S.; Morimoto, Y.; Kotani, H.; Naumov, P.; Lee, Y. M.; Nam, W. *Nat. Chem.* **2010**, *2*, 756-759; (b) Morimoto, Y.; Kotani, H.; Park, J.; Lee, Y. M.; Nam, W.; Fukuzumi, S. *J. Am. Chem. Soc.* **2011**, *133*, 403-405.

9. (a) Park, Y. J.; Ziller, J. W.; Borovik, A. S. *J. Am. Chem. Soc.* **2011**, *133*, 9258-9261; (b) Park, Y. J.; Cook, S. A.; Sickerman, N. S.; Sano, Y.; Ziller, J. W.; Borovik, A. S. *Chem. Sci.* **2013**, *4*, 717-726.
10. (a) Risch, M.; Klingan, K.; Ringleb, F.; Chernev, P.; Zaharieva, I.; Fischer, A.; Dau, H. *Chemsuschem* **2012**, *5*, 542-549; (b) Wiechen, M.; Zaharieva, I.; Dau, H.; Kurz, P. *Chem. Sci.* **2012**, *3*, 2330-2339; (c) Zaharieva, I.; Najafpour, M. M.; Wiechen, M.; Haumann, M.; Kurz, P.; Dau, H. *Energy Environ. Sci.* **2011**, *4*, 2400-2408; (d) Najafpour, M. M.; Pashaei, B.; Nayeri, S. *Dalton Trans.* **2012**, *41*, 4799-4805; (e) Najafpour, M. M.; Ehrenberg, T.; Wiechen, M.; Kurz, P. *Angew. Chem. Int. Ed.* **2010**, *49*, 2233-2237.
11. (a) Kanady, J. S.; Tsui, E. Y.; Day, M. W.; Agapie, T. *Science* **2011**, *333*, 733-736; (b) Kanady, J. S.; Mendoza-Cortes, J. L.; Tsui, E. Y.; Nielsen, R. J.; Goddard, W. A.; Agapie, T. *J. Am. Chem. Soc.* **2013**, *135*, 1073-1082.
12. (a) Yano, J.; Kern, J.; Sauer, K.; Latimer, M. J.; Pushkar, Y.; Biesiadka, J.; Loll, B.; Saenger, W.; Messinger, J.; Zouni, A.; Yachandra, V. K. *Science* **2006**, *314*, 821-825; (b) Peloquin, J. M.; Campbell, K. A.; Randall, D. W.; Evanchik, M. A.; Pecoraro, V. L.; Armstrong, W. H.; Britt, R. D. *J. Am. Chem. Soc.* **2000**, *122*, 10926-10942; (c) Ames, W.; Pantazis, D. A.; Krewald, V.; Cox, N.; Messinger, J.; Lubitz, W.; Neese, F. *J. Am. Chem. Soc.* **2011**, *133*, 19743-19757.
13. Yano, J.; Kern, J.; Irrgang, K.-D.; Latimer, M. J.; Bergmann, U.; Glatzel, P.; Pushkar, Y.; Biesiadka, J.; Loll, B.; Sauer, K.; Messinger, J.; Zouni, A.; Yachandra, V. K. *Proc. Natl. Acad. Sci. USA* **2005**, *102*, 12047-12052.
14. Mukherjee, S.; Stull, J. A.; Yano, J.; Stamatatos, T. C.; Pringouri, K.; Stich, T. A.; Abboud, K. A.; Britt, R. D.; Yachandra, V. K.; Christou, G. *Proc. Natl. Acad. Sci. USA* **2012**, *109*, 2257-2262.
15. (a) Tsui, E. Y.; Day, M. W.; Agapie, T. *Angew. Chem. Int. Ed.* **2011**, *50*, 1668-1672; (b) Tsui, E. Y.; Kanady, J. S.; Day, M. W.; Agapie, T. *Chem. Commun.* **2011**, *47*, 4189-4191.
16. Thorp, H. H. *Inorg. Chem.* **1992**, *31*, 1585-1588.
17. (a) Mishra, A.; Yano, J.; Pushkar, Y.; Yachandra, V. K.; Abboud, K. A.; Christou, G. *Chem. Commun.* **2007**, 1538-1540; (b) Mishra, A.; Pushkar, Y.; Yano, J.; Yachandra, V. K.; Wernsdorfer, W.; Abboud, K. A.; Christou, G. *Inorg. Chem.* **2008**, *47*, 1940-1948.
18. (a) Pantazis, D. A.; Krewald, V.; Orio, M.; Neese, F. *Dalton Trans.* **2010**, *39*, 4959-4967; (b) Krewald, V.; Neese, F.; Pantazis, D. A. *J. Am. Chem. Soc.* **2013**, *135*, 5726-5739.
19. Horwitz, C. P.; Ciringh, Y. *Inorg. Chim. Acta* **1994**, *225*, 191-200.
20. Cox, N.; Rapatskiy, L.; Su, J.-H.; Pantazis, D. A.; Sugiura, M.; Kulik, L.; Dorlet, P.; Rutherford, A. W.; Neese, F.; Boussac, A.; Lubitz, W.; Messinger, J. *J. Am. Chem. Soc.* **2011**, *133*, 3635-3648.
21. Perrin, D. D., *Ionisation Constants of Inorganic Acids and Bases in Aqueous Solution*. Pergamon Press: New York, 1982.
22. Kambe, K. *J. Phys. Soc. Jpn.* **1950**, *5*, 48-51.
23. *Matlab*, 7.10.0.499 (R2010a); The MathWorks, Inc.: Natick, MA, 2010.
24. *APEX2*, Bruker Analytical X-ray Systems: Madison, WI, 2006.
25. Sheldrick, G. M. *SADABS*, 2008/I; University of Göttingen, 2008.

26. Sheldrick, G. *Acta Crystallographica Section A* **2008**, 64, 112-122.
27. Spek, A. L. *PLATON - A Multipurpose Crystallographic Tool*, Utrecht, The Netherlands, 2006.

*Chapter 5*REACTIVITY STUDIES OF HETEROMETALLIC MANGANESE OXIDO
CLUSTERS

Portions of the text for this chapter were reproduced in part from:

Kanady, J. S.; Mendoza-Cortes, J. L.; Tsui, E. Y.; Nielsen, R. J.; Goddard, W. A.; Agapie, T. *J. Am. Chem. Soc.* **2013**, *135*, 1073-1082.

Abstract

Redox-inactive metal ions are known to tune the reactivities of metal oxo compounds in different chemical transformations, including electron transfer, oxygen atom transfer, and hydrogen atom transfer. To expand the scope of our studies of heterometallic trimanganese dioxido and tetraoxido clusters with different incorporated apical redox-inactive metals, oxygen atom transfer reactions from the clusters to phosphine reagents were studied. For the dioxido clusters, rate enhancements in oxygen atom transfer were observed upon varying the metal from Ca^{2+} to Y^{3+} , though the final products have not been identified. Similarly, for the tetraoxido $[\text{MMn}_3\text{O}_4]$ clusters, the rate of oxygen atom transfer to trimethylphosphine decreased dramatically from $\text{M} = \text{Sc}^{3+}$ to $\text{M} = \text{Y}^{3+}$. This chapter also describes preliminary studies of hydrogen atom transfer to the clusters as well as studies of electron transfer rates. These results suggest that, as with the previously studied mononuclear metal oxo compounds, varying the constituent redox-inactive metals in multinuclear heterometallic oxido clusters can have dramatic effects on the rates and extent of their chemical reactivity.

Introduction

Lewis acidic metal ions play an essential role in many chemical transformations and biological electron transfer processes.¹ Studying these effects will advance the fundamental understanding of biological catalysts with incorporated redox-inactive metal centers like the CaMn_4O_x cluster of the oxygen-evolving complex (OEC) of photosystem II,² as well as artificial water oxidation catalysts that have been proposed to contain redox-inactive cations in their composition.³ As discussed in previous chapters, the observation that the OEC is only active for water oxidation when Ca^{2+} or Sr^{2+} are present raises questions about the function of the redox-inactive alkaline earth metal during catalysis.⁴ We and others have proposed that one role of calcium is to tune the redox potentials of the clusters for water oxidation (Chapters 3 and 4).⁵ Another proposed function of calcium is to bind water or hydroxide moieties that participate in O–O bond formation.⁶ Understanding how these ions can affect the reactivity and properties of these materials may enable the design of improved artificial water oxidation catalysts.

In synthetic small molecule and biomimetic metal oxo complexes, the addition of redox-inactive Lewis acidic metal ions has been shown to tune the reactivities of these systems in different processes. In many cases, the addition of these metal ions significantly shifts the redox potentials of the metal centers. For example, Fukuzumi, Nam, and co-workers showed that the addition of $\text{Sc}(\text{OTf})_3$ to a non-heme iron oxo (**A**, Fig. 1) promoted its two-electron reduction by ferrocene, whereas in the absence of Sc^{3+} only one-electron reduction was observed.⁷ With a different non-heme $\text{Fe}^{\text{IV}}\text{O}$ compound (**B**, Fig. 1), a shift of 0.84 V in the reduction potential was observed upon addition of $\text{Sc}(\text{OTf})_3$, and the electron transfer rates were found to be dependent upon the Lewis acidity of the added metal ions.⁸

A related manganese(IV)-oxo complex supported by the same ligand framework was also observed to undergo a shift in reduction potential upon addition of Sc^{3+} .⁹ Borovik and co-workers observed greatly enhanced rates of O_2 activation by a manganese(II) complex supported by a tripodal sulfonamide ligand (**C**, Fig. 1) in the presence of 15-crown-5 and $\text{Ca}(\text{OTf})_2$.¹⁰ When different salts such as Sr^{2+} and Ba^{2+} are used, a shift in the reduction potentials was found with both Mn and Fe complexes of this ligand.¹¹ Horwitz and co-workers have previously found that when using salen and salphen type manganese bridged oxo compounds that the addition of different salts such as KPF_6 also shifted the reduction potentials (**D**, Fig. 1), although this was attributed to an electrostatic effect.¹² Finally, as discussed in Chapters 3 and 4, varying the incorporated redox-inactive metal ions in heterometallic trimanganese dioxido (**4** and **5**)^{5c} and tetraoxido (**6**, and **7**)^{5d} changes the reduction potentials of the clusters (at manganese) with a linear dependence upon the Lewis acidities of the metals.

In addition to shifts in the reduction potentials of the metal oxo compounds, other differences in electron transfer and other processes have been observed in the presence of redox-inactive metal ions. The non-heme iron oxo complex and its related manganese(IV)-oxo compound (**B**) by Fukuzumi and co-workers show significant changes in electron transfer to the iron oxo to a more reduced iron(III) compound.⁸⁻⁹ The authors observed up to a 10^7 enhancement in electron transfer rates. Goldberg and co-workers observed valence tautomerization in a manganese corraloazinato complex upon addition of a Zn^{2+} source (**E**, Fig. 1), as well as shifts in the reduction potential of the manganese oxo and enhanced rates of hydrogen atom transfer from phenol substrates.¹³

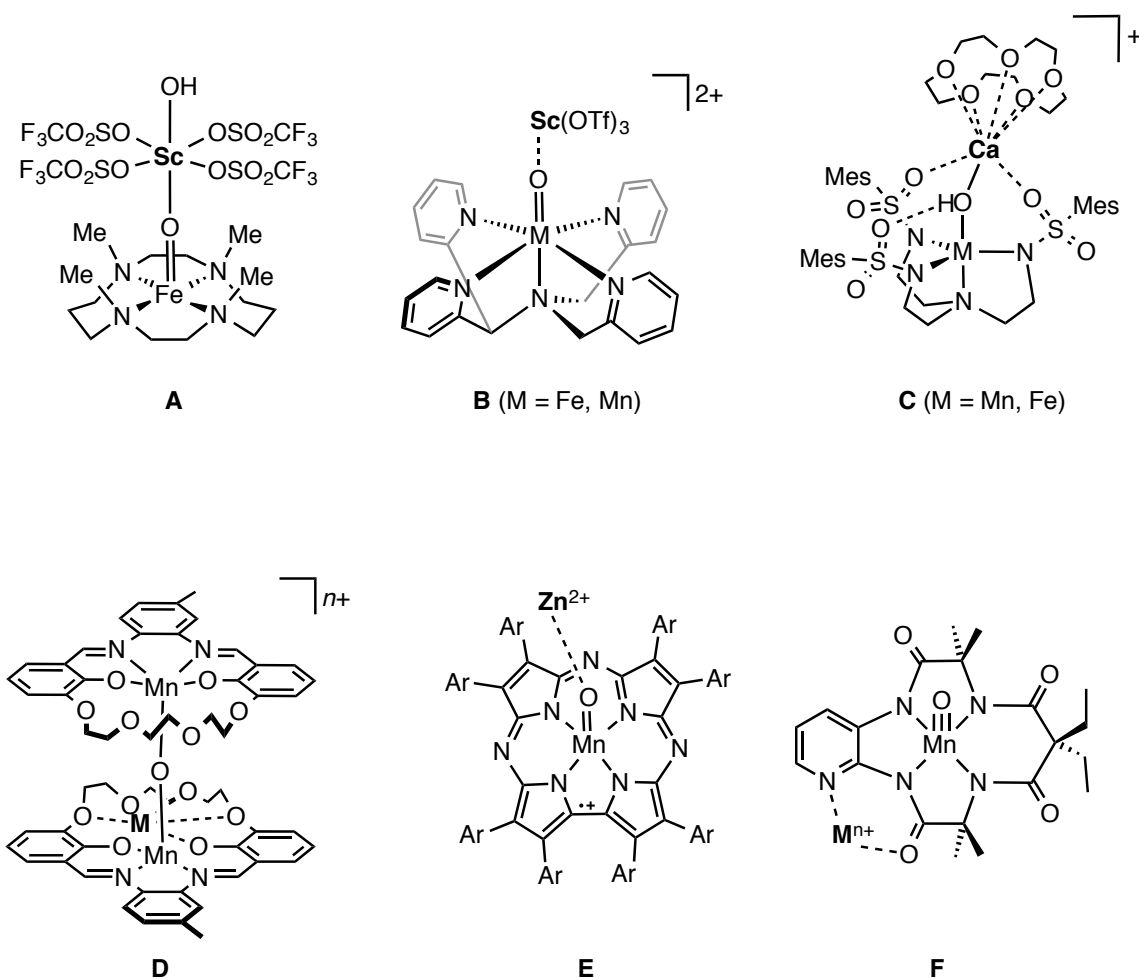


Figure 1. Selected examples of metal oxo or hydroxo compounds whose reactivity is affected by the addition of redox-inactive metals.^{5c, 5d, 7-8, 10, 12a, 13-14}

Redox-inactive metal ions have also been demonstrated to affect other transformations of metal oxo compounds, such as oxygen atom transfer and hydrogen atom transfer processes. In the manganese-oxo analogue of **B** reported by Fukuzumi and co-workers, an increase in the rates of oxidation of thioanisoles was observed upon addition of Sc^{3+} .¹⁵ The authors also described a change in the mechanism of sulfoxidation from direct oxygen atom transfer to an electron transfer pathway.⁹ Collins and co-workers have also demonstrated that a Mn^{V} -oxo system (**F**, Fig. 1) can be activated for electrophilic oxygen atom transfer from binding of a secondary ion.¹⁴ Fukuzumi and co-workers have also observed

differences in hydrogen atom transfer from organic substrates such as benzyl alcohol to metal oxo complexes upon addition of different Lewis acids.¹⁶ In the non-heme iron and manganese oxo complexes **B** explored by Fukuzumi and co-workers, the binding of multiple cations has been observed. In one example, the observation that H-atom transfer from cyclohexadiene is unexpectedly slower in the presence of Sc^{3+} has been explained as a steric crowding effect.¹⁵

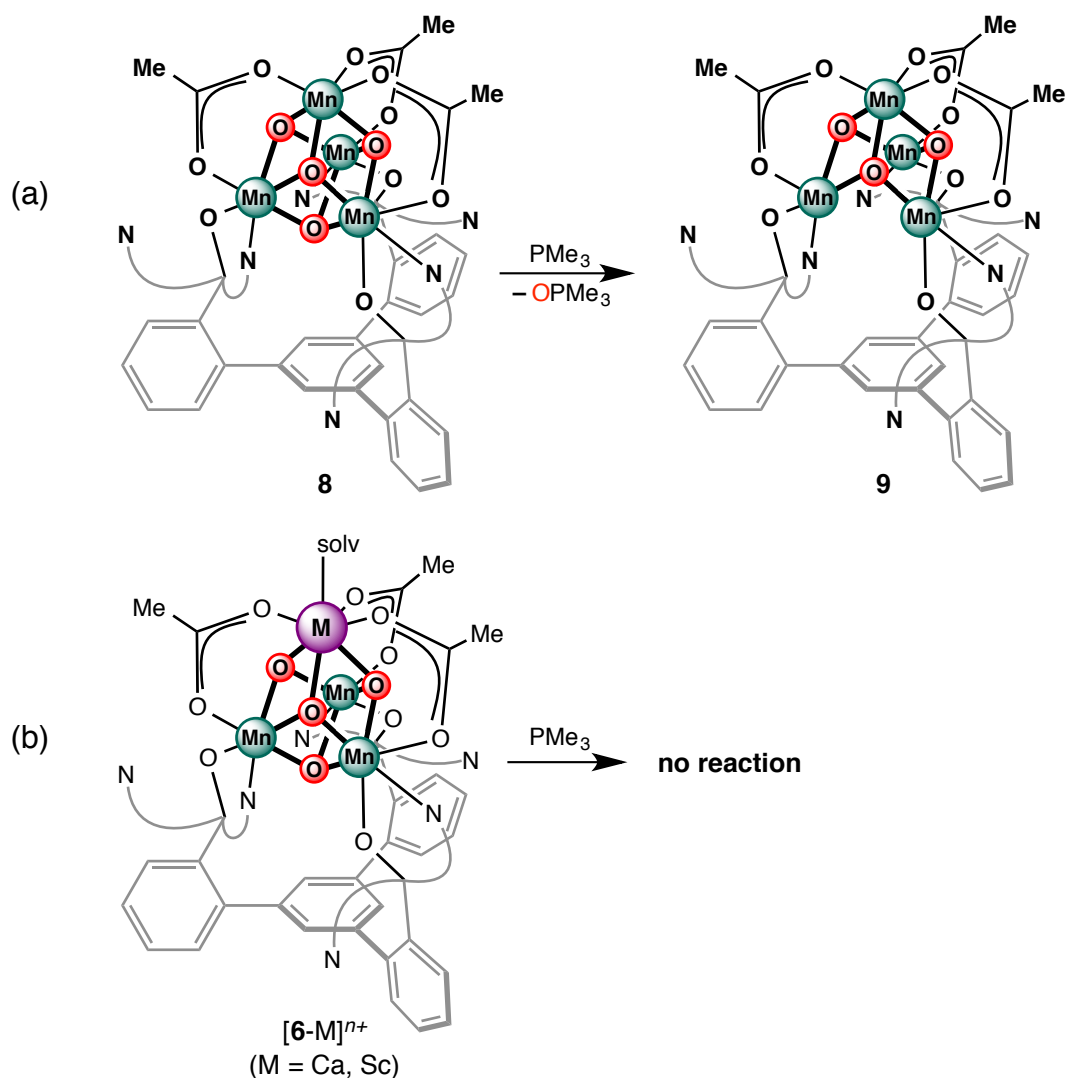
For this work, in addition to the cyclic voltammetry studies described in Chapters 3 and 4, studying the effects on different chemical processes such as electron transfer rates, oxygen atom transfer, and hydrogen atom transfer by varying the redox-inactive metals in the heterometallic trimanganese oxido complexes would provide a useful benchmark in comparison to the metal oxo examples described above because they have been structurally characterized and can be prepared with great control over the metal ion/oxido/manganese ratios. Additionally, each isostructural series of compounds all present a similar steric profile. These properties will allow us to isolate the effects of variation of the redox-inactive metals from the other metals. Herein, we describe a number of initial studies in probing the reactivities of the clusters toward oxygen atom transfer and hydrogen atom transfer.

Results and Discussion

5.1 Oxygen atom transfer of $[\text{MMn}_3\text{O}_4]$ complexes to phosphine

To test the effects of the incorporated redox-inactive metals on the oxygen atom transfer capabilities of the $[\text{MMn}_3\text{O}_4]$ clusters, we treated these compounds with known oxygen atom acceptor reagents such as phosphines. The tetramanganese tetraoxido cluster $\text{LMn}_4\text{O}_4(\text{OAc})_3$ (**8**) reacts with trimethylphosphine cleanly to form the tetramanganese

trioxide compound $\text{LMn}_4\text{O}_3(\text{OAc})_3$ (**9**) and trimethylphosphine oxide (Scheme 1a).^{5b} This reaction is a demonstration of oxygen atom transfer, as the starting material ($\text{Mn}^{\text{IV}}_2\text{Mn}^{\text{III}}_2$) has been reduced by two electrons to (Mn^{III}_4) with loss of an oxido ligand. This reaction proceeds within 15 min. at room temperature when using 2–10 equiv of PMe_3 (Fig. 2).



Scheme 1. (a) Oxygen atom transfer to trimethylphosphine from **8** to generate trimethylphosphine oxide and **9** (Jacob Kanady). (b) Treatment of **6**-Ca and **[6-Sc][OTf]** with trimethylphosphine shows no oxygen atom transfer on the same time scale.^{5b}

In contrast, when **6**-Ca or $[\mathbf{6}\text{-Sc}]^+$ are treated with excess PMe_3 , no consumption of trimethylphosphine is observed over the same time period (^{31}P NMR spectroscopy with a PPh_4^+ internal standard, Figs. 2, 3). In fact, **6**-Ca does not react with PMe_3 at all over days, though with $[\mathbf{6}\text{-Sc}][\text{OTf}]$ consumption of one equivalent of PMe_3 is observed by ^{31}P NMR spectroscopy after 18 h (trimethylphosphine oxide was not identified, possibly due to coordination to Sc^{3+}). These results suggest that compound **8** is more prone to oxygen atom transfer than **6**-Ca and $[\mathbf{6}\text{-Sc}][\text{OTf}]$ despite its more reduced state ($\text{Mn}^{\text{IV}}_2\text{Mn}^{\text{III}}_2$ vs. $\text{Mn}^{\text{IV}}_3\text{M}$). To more directly contrast the oxidizing power of these clusters as a measure of oxygen atom transfer propensity, the reduction potentials of the clusters as presented in Chapter 4 were compared (Table 1). In comparison to the $\text{Mn}^{\text{IV}}_2\text{Mn}^{\text{III}}_2/\text{Mn}^{\text{IV}}\text{Mn}^{\text{III}}_3$ reduction potential of **8** and the $\text{CaMn}^{\text{IV}}_3/\text{CaMn}^{\text{IV}}_2\text{Mn}^{\text{III}}$ reduction potential of **6**-Ca, the reduction of $[\mathbf{6}\text{-Sc}]^+$ occurs at a much more positive potential. It should be noted, however, that these are one-electron reduction potentials rather than two-electron potentials. Despite the significantly higher oxidizing power of $[\mathbf{6}\text{-Sc}]^+$, the significantly slower reaction with trimethylphosphine suggests that the difference in reactivity stems from a kinetic barrier due to the lower ligand lability of Mn^{IV} centers vs. Mn^{III} , which is in agreement with computational studies performed by Goddard and co-workers as well as carboxylate exchange studies, which demonstrated that compound **8** undergoes acetate exchange (> 1 min to statistical mixture) significantly faster than compounds **6**-Ca and **6**-Sc (ca. 50 min. to statistical mixture).^{5b}

Table 1. One-electron reduction potentials of clusters discussed here. Potentials referenced to ferrocene/ferrocenium.

| Compound | Potential (V) vs. Fc/Fc ⁺ | Oxidation state assignment |
|------------------------------|--------------------------------------|--|
| 8 | −0.70 | Mn ^{IV} ₂ Mn ^{III} ₂ / Mn ^{IV} Mn ^{III} ₃ |
| 6 -Ca | −0.94 | CaMn ^{IV} ₃ / CaMn ^{IV} ₂ Mn |
| [6 -Sc] ⁺ | −0.24 | ScMn ^{IV} ₃ / ScMn ^{IV} ₂ Mn |

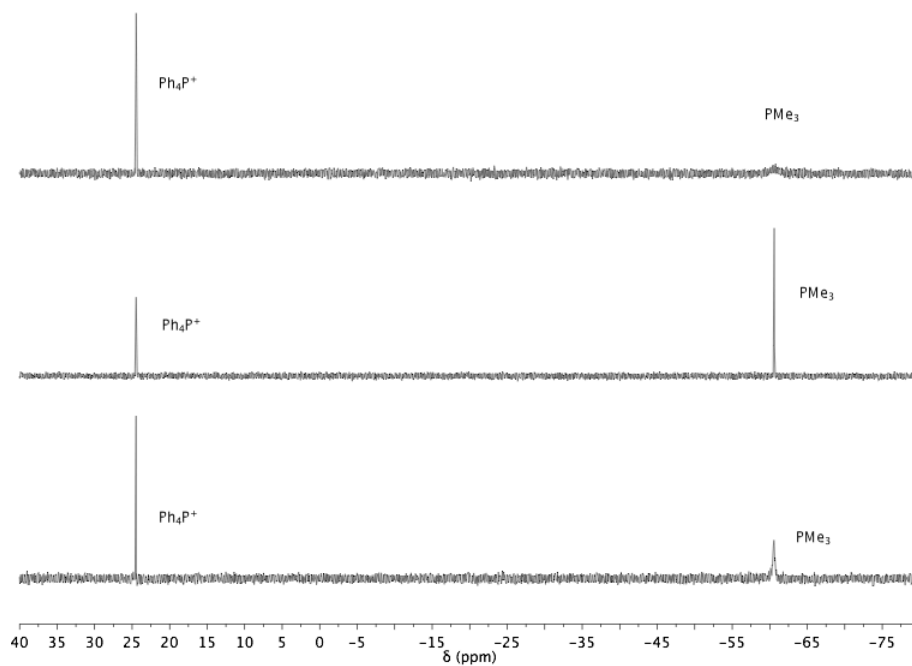


Figure 2. ³¹P NMR spectra of the reaction of **8** and PMe_3 (top), **6**-Ca and PMe_3 (middle), and **6**-Sc and PMe_3 (bottom) in DMF after 15 min. at RT. $[\text{PPh}_4][\text{BF}_4]$ (1 equiv) is present as an internal standard.

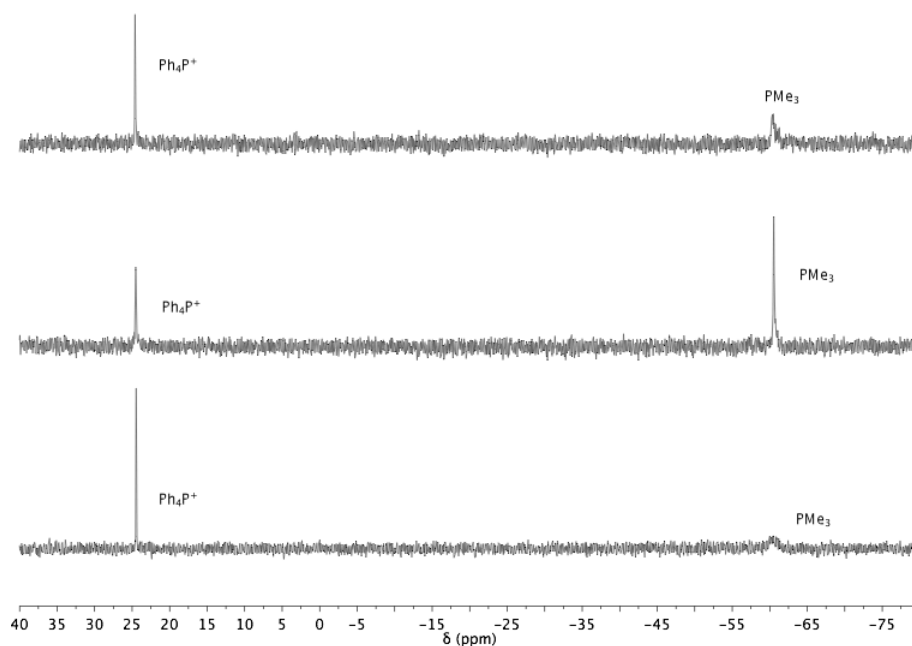


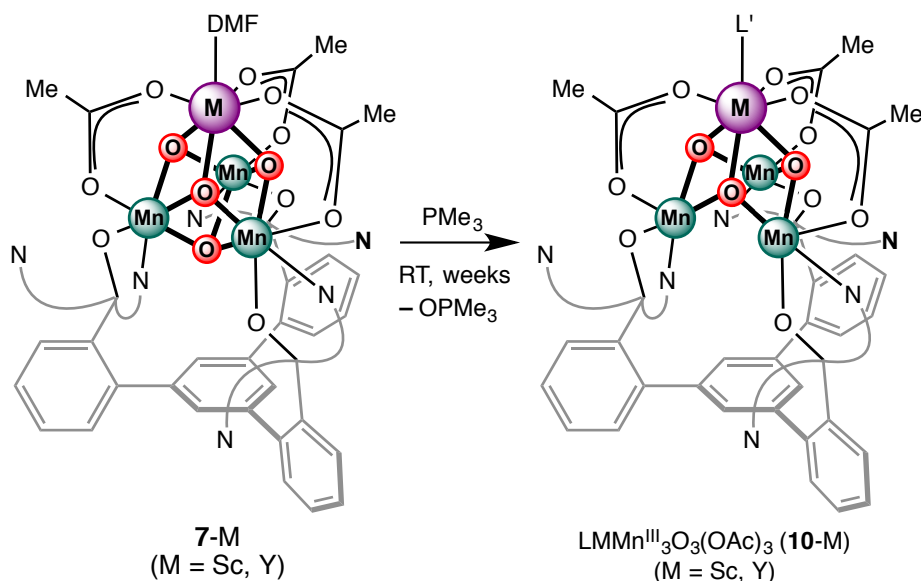
Figure 3. ^{31}P NMR spectra of the reaction of **8** and PMe_3 (top), **6-Ca** and PMe_3 (middle), and **6-Sc** and PMe_3 (bottom) in DMF after 18 hours at RT. $[\text{PPh}_4][\text{BF}_4]$ (1 equiv) is present as an internal standard.

Because this difference in reactivity is caused by a kinetic rather than thermodynamic argument, these studies do not provide a direct study of the role of the apical metal center in tuning the oxygen atom transfer processes. Compound **8** contains a more coordinatively labile Mn^{III} center in the basal trimanganese core supported by the multinucleating ligand framework, thus making acetate dissociation and phosphine approach more likely. For a more direct comparison, it would be desirable to test the reactivity of reduced heterometallic MMn_3O_4 cubanes **7** with phosphine because these also have a basal Mn^{III} center.

Carboxylate exchange studies of the reduced tetraoxido complex $\text{LScMn}^{\text{IV}}_2\text{Mn}^{\text{III}}\text{O}_4(\text{OAc})_3(\text{DMF})$ (**7-Sc**) were first conducted to confirm that the Mn^{III} center

would indeed more labile and prone to acetate dissociation. When **7-Sc** was treated with a solution of d_3 -acetate, a statistical mixture of coordinated labeled acetate ligands was observed by ESI-MS in less than one minute, consistent with compound **8**.

When a benzene solution of **7-Sc** was treated with ten equivalents of PMe_3 , consumption of **7-Sc** was slow at room temperature, proceeding over two weeks (Scheme 2), in contrast to **8**, which reacts with PMe_3 within minutes. A new species is observed by ^1H NMR spectroscopy that is assigned as the scandium analogue to the tetramanganese trioxido complex **9**, $\text{LScMn}^{\text{III}}_3\text{O}_3(\text{OAc})_3$ (**10-Sc**). When a benzene solution of **7-Y** is treated with ten equivalents of PMe_3 under the same conditions, the reaction proceeds even slower, with >40 % of **7-Y** remaining by ^1H NMR spectroscopy even after 2 weeks. These results suggest that the identity of the redox-inactive metal in the cluster can significantly affect the rates of oxygen atom transfer to phosphine. Based on these initial studies, the reaction rates follow the Lewis acidities of the apical metals, with $\text{Mn}^{3+} > \text{Sc}^{3+} > \text{Y}^{3+}$.



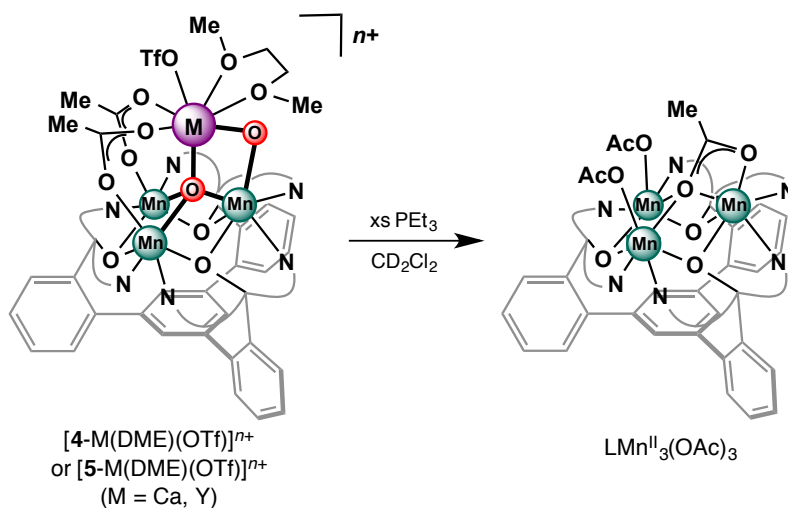
Scheme 2. Reaction of **7-Sc** and **7-Y** with PMe_3 .

5.2 Phosphine reactivity of dioxido complexes

The heterometallic trimanganese dioxido clusters (see Chapter 3) were also treated with phosphine reagents to probe their propensities for oxygen atom transfer (Scheme 3). The complexes with the greatest difference in the Lewis acidities of the incorporated redox-inactive metals that we described in Chapter 3 were $[\mathbf{5}\text{-Ca}(\text{DME})(\text{OTf})]^+$ and $[\mathbf{5}\text{-Y}(\text{DME})(\text{OTf})]^{2+}$, although there are differences in overall charge because of the tricationic yttrium center. When CD_2Cl_2 solutions of these two compounds were treated with two equivalents of PEt_3 , significant differences in reactivity were observed (Figs. 4, 5). The reaction of $[\mathbf{5}\text{-Ca}(\text{DME})(\text{OTf})]^+$ with triethylphosphine is slow; <1 equiv. of PEt_3 was consumed after 80 h at room temperature (^{31}P NMR spectroscopy, Fig. 4). In the ^1H NMR spectrum of this mixture, starting material was still observable, although a new unidentified species was also observed by ^1H NMR spectroscopy. This new species has not yet been structurally identified. In contrast, when a CD_2Cl_2 solution of $[\mathbf{5}\text{-Y}(\text{DME})(\text{OTf})]^{2+}$ was treated with two equivalents of PEt_3 under the same conditions, ca. 1.1 equiv of PEt_3 was consumed within 15 min. (^{31}P NMR spectroscopy, Fig. 5). Complete consumption of PEt_3 occurred within 2 h at room temperature. By ^1H NMR spectroscopy, the final product is the fully reduced $\text{LMn}^{\text{II}}_3(\text{OAc})_3$ trimanganese compound, presumably with loss of $\text{Y}(\text{OTf})_3$ and triethylphosphine oxide. For both of these reactions, triethylphosphine oxide was not observed by NMR spectroscopy *in situ*, but was later detected by GC/MS upon methanolysis of the product. It is proposed that triethylphosphine oxide can interact with the yttrium or calcium centers of the manganese dioxide complexes, thus paramagnetically shifting and broadening the ^{31}P NMR signal of the phosphine oxide. It should be noted that complete conversion of $[\mathbf{5}\text{-Ca}(\text{DME})(\text{OTf})]^+$ can only be effected upon addition of a large

excess (>10 equiv) of PEt_3 and is still significantly slower than the reaction with $[\mathbf{5}\text{-Y(DME)(OTf)}]^+$.

One explanation for this shift in reaction rates with PEt_3 is that the yttrium complex is more oxidizing than the calcium analogue. From Chapter 3, it was observed that the reduction potential assigned to the $[\text{Mn}^{\text{III}}_3] / [\text{Mn}^{\text{III}}_2\text{Mn}^{\text{II}}]$ couple shifts approximately 300 mV more positive upon variation from Ca^{2+} to Y^{3+} . Again, it should be noted that these are one-electron processes rather than the presumed two-electron process that oxygen atom transfer to phosphine would be. This change in oxygen atom transfer rate may also be due to a kinetic effect, since $[\mathbf{5}\text{-Y(DME)(OTf)}]^{2+}$ is dicationic in comparison to the monocationic $[\mathbf{5}\text{-Ca(DME)(OTf)}]^+$ complex. Similar effects on oxygen atom transfer rates have previously been observed by Fukuzumi and co-workers, who found that rates of thioanisole oxidation by a Mn(IV)-oxo complex increased dramatically upon addition of Sc^{3+} .¹⁵ In this example, the authors proposed that electron transfer first occurs from the thioanisole substrates to the metal complexes, followed by oxygen atom transfer. Such a mechanism could be operating in the reactions of phosphines with $\mathbf{5}\text{-M}$.



Scheme 3. Triethylphosphine reactivity of heterometallic trimanganese dioxido complexes.

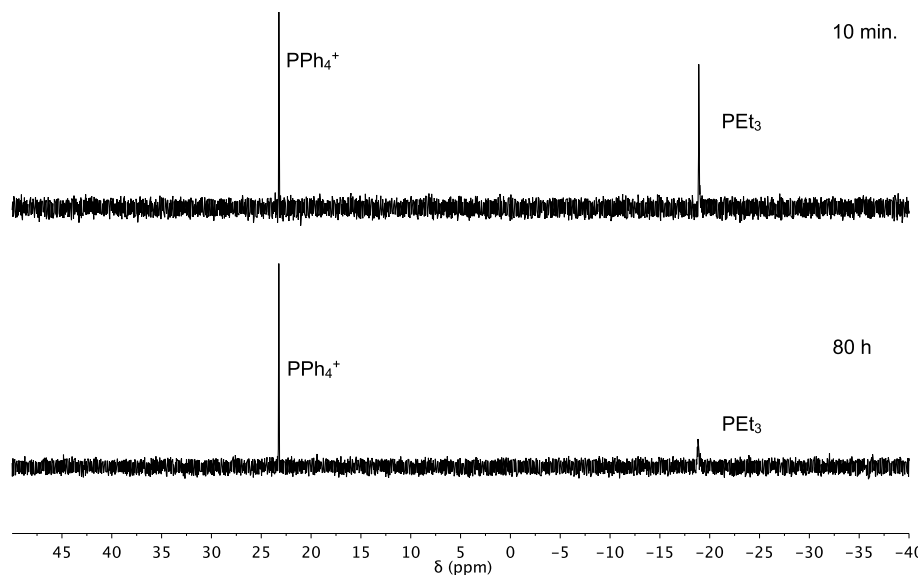


Figure 4. ^{31}P NMR spectra of CD_2Cl_2 solutions of $[\mathbf{5}\text{-Ca}(\text{DME})(\text{OTf})]^+$ after addition of 2 equiv of PEt_3 after 10 min. at room temperature (top) and after 80 h at room temperature (bottom). $[\text{PPh}_4][\text{BF}_4]$ (one equiv) is present as an internal standard. Ca. 0.4 equiv of PEt_3 consumed after 80 h.

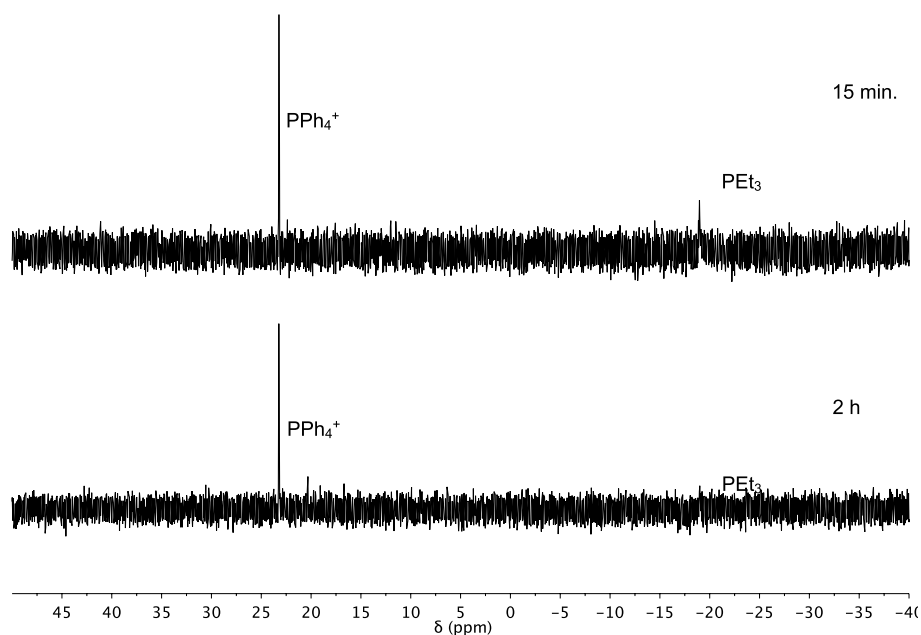
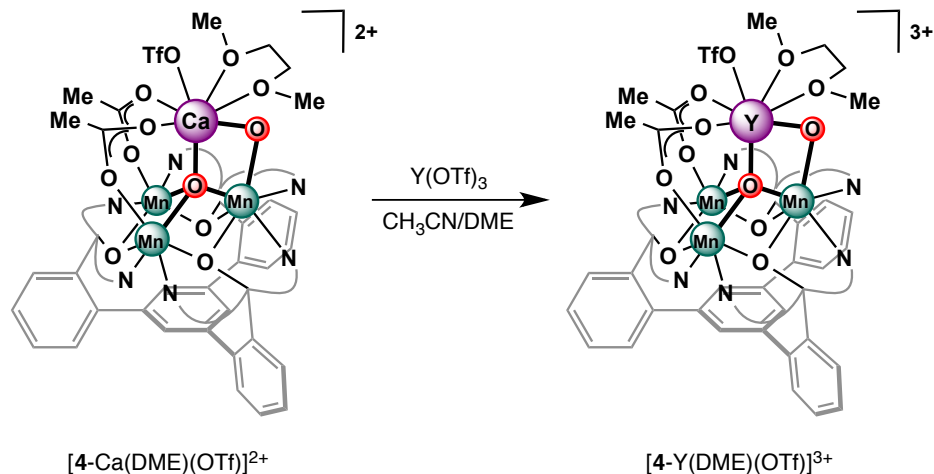


Figure 5. ^{31}P NMR spectra of CD_2Cl_2 solutions of $[\mathbf{5}\text{-Y}(\text{DME})(\text{OTf})]^{2+}$ after addition of 2 equiv of PEt_3 after 15 min. at room temperature (top) and after 2 h at room temperature (bottom). $[\text{PPh}_4][\text{BF}_4]$ (one equiv) is present as an internal standard. Ca. 1.1 equiv of PEt_3 consumed after 15 min., and no PEt_3 observed after 2 h at room temperature.

To compare the same oxygen atom transfer reactivities of the more oxidized $[\text{MMn}^{\text{IV}}\text{Mn}^{\text{III}}\text{O}_2]$ complexes **4-M**, we attempted to prepare the oxidized yttrium-containing cluster $[\mathbf{4}\text{-Y(DME)(OTf)}]^{3+}$. Oxidation of $[\mathbf{5}\text{-Y(DME)(OTf)}]^{2+}$ occurs at a rather positive potential (0.42 V vs. Fc/Fc^+). Treatment of $[\mathbf{5}\text{-Y(DME)(OTf)}]^{2+}$ with the one-electron oxidant tris(4-bromophenyl)aminium hexachloroantimonate “Magic Blue” resulted in chlorination of the complex with loss of yttrium. Transmetalation of $[\mathbf{4}\text{-Ca(DME)(OTf)}]^{2+}$ (Scheme 4) yielded a new complex by ^1H NMR spectroscopy. The ESI-MS signal of this product is in good agreement with $[\mathbf{4}\text{-Y(DME)(OTf)}]^{3+}$. Unfortunately, so far we have been unable to structurally confirm this assignment, as crystallization of this compound has eluded us. Efforts are ongoing to grow X-ray quality single crystals of this complex.



Scheme 4. Synthesis of $[\mathbf{4}\text{-Y(DME)(OTf)}]^{3+}$.

Compounds **4-M** are expected to be more electrophilic than compounds **5-M** and thus more active toward oxygen atom transfer, due to the higher oxidation. Both $[\mathbf{4}\text{-Ca(DME)(OTf)}]^{2+}$ and $[\mathbf{4}\text{-Y(DME)(OTf)}]^{3+}$ react quickly (< 1 h) with one equivalent of PEt_3 . To slow down the reaction rates, the weaker oxygen atom acceptor triphenylphosphine was used instead of triethylphosphine. Triphenylphosphine was added to CD_2Cl_2 solution of $[\mathbf{4}\text{-Ca(DME)(OTf)}]^{2+}$ and $[\mathbf{4}\text{-Y(DME)(OTf)}]^{3+}$, and the reactions

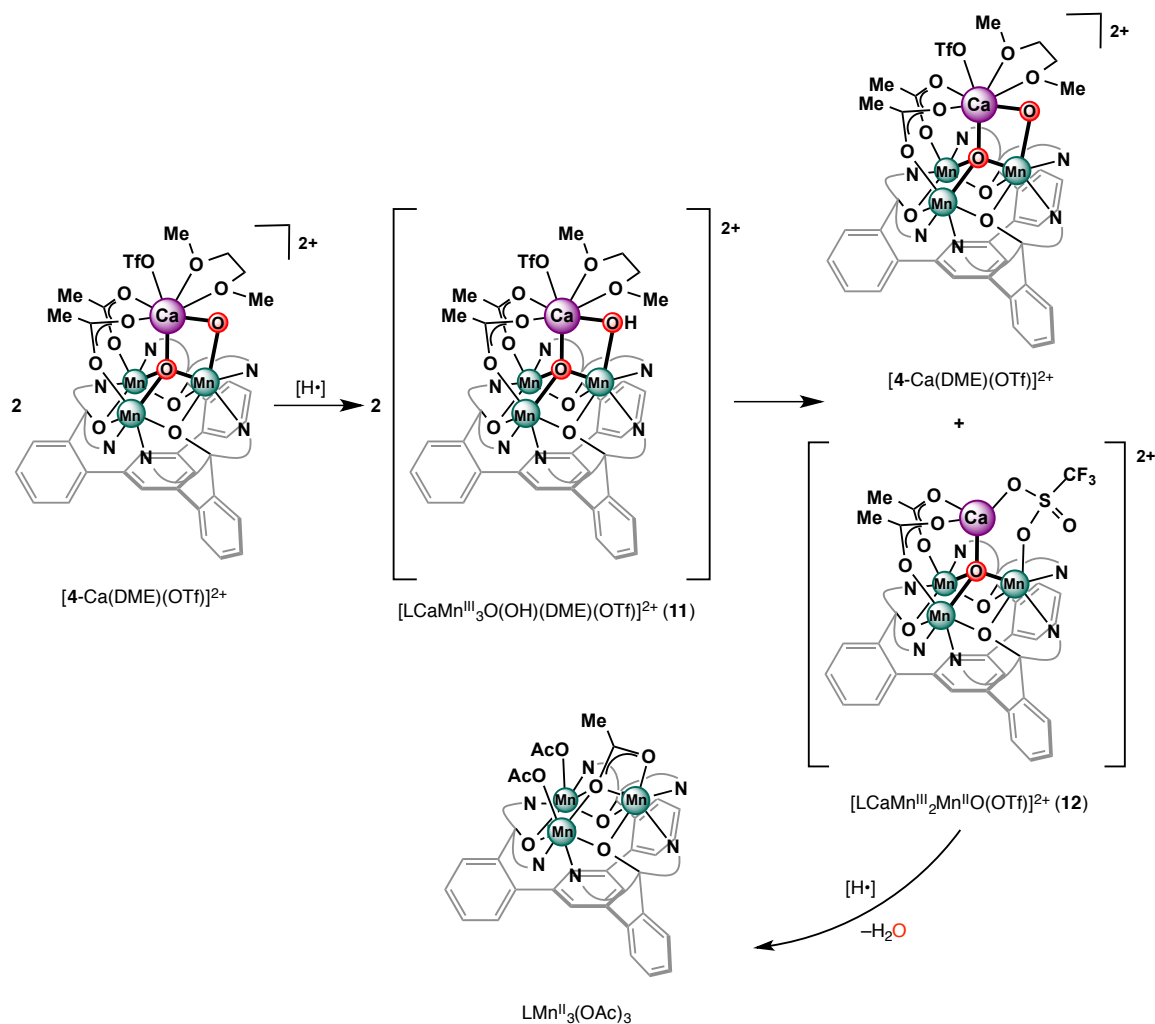
were monitored using NMR spectroscopy (see experimental section). The purple solution of $[4\text{-Y(DME)(OTf)}]^{3+}$ turns gray within 5 h, with no more starting material remaining (^1H NMR spectroscopy). In contrast, $[4\text{-Ca(DME)(OTf)}]^{2+}$ is much slower to react, turning gray only over 2 days. As with the more reduced compounds **5**, substituting Y^{3+} for Ca^{2+} results in rate enhancement of reactivity with oxygen atom acceptors. The final products of both reactions mixtures have not yet been fully characterized, although some $\text{LMn}^{\text{II}}_3(\text{OAc})_3$ is observed in the mixture by ^1H NMR spectroscopy.

Future studies will probe this enhancement in activity, although these studies are complicated by the difficulties in isolating the products after single oxygen atom transfer, since by NMR spectroscopy mixtures are often observed that include starting dioxido complexes, unidentified intermediate species, and fully reduced trimanganese(II) complexes.

5.3 Hydrogen atom transfer to dioxido clusters

The propensity of the dioxido clusters to accept hydrogen atoms was also probed. As with the phosphine reactions, treatment of $[4\text{-Ca(DME)(OTf)}]^{2+}$ with an excess of H-atom donors such as TEMPO-H or 2,4,6-tri-tert-butylphenol resulted in formation of the reduced trimanganese(II) compound $\text{LMn}^{\text{II}}_3(\text{OAc})_3$. Unfortunately, the product of a single H-atom transfer, the putative oxo/hydroxo species (**11**, Scheme 5) could not be isolated. Instead, ^1H NMR spectra of the reaction mixtures showed a mixture of $[4\text{-Ca(DME)(OTf)}]^{2+}$ and $\text{LMn}^{\text{II}}_3(\text{OAc})_3$. The observed reactivity was proposed to occur via a disproportionation reaction of **11**, first to regenerate $[4\text{-Ca(DME)(OTf)}]^{2+}$ and a monooxido cluster **12**. Although a species similar to **12** has previously been observed via protonation of $[5\text{-Ca(DME)(OTf)}]^+$ (Appendix C), **12** itself could not be isolated or identified by ^1H NMR

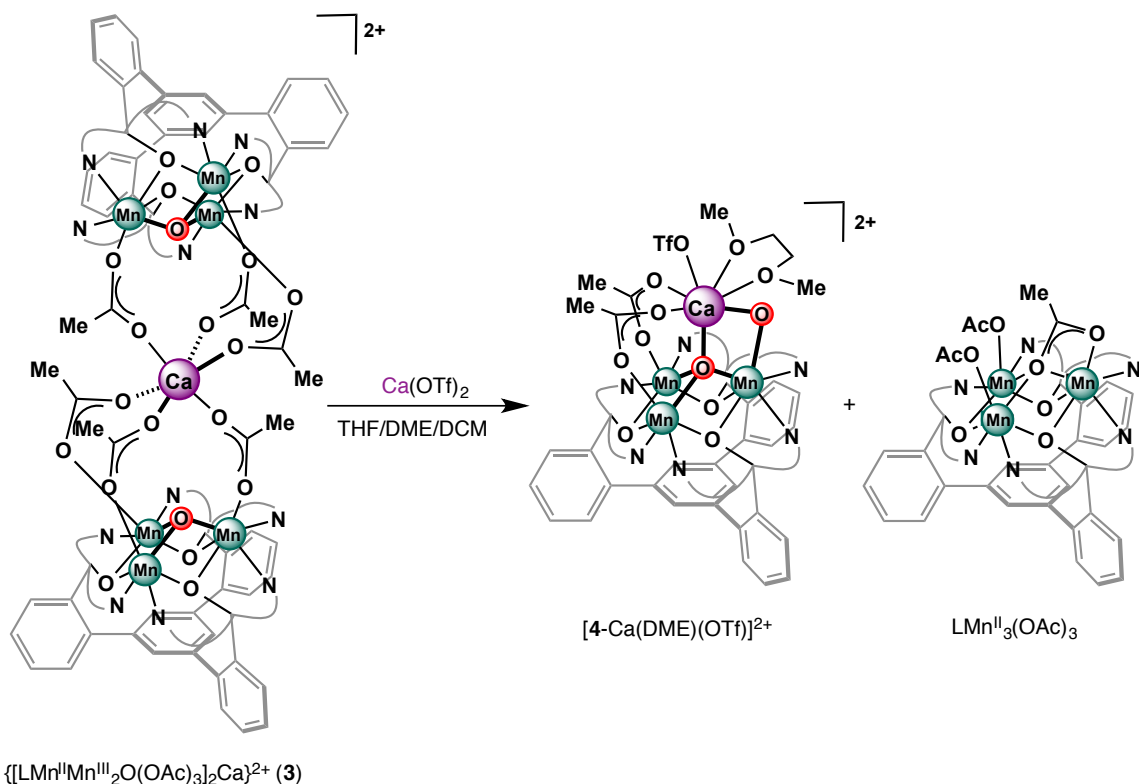
spectroscopy. It is likely that **12** reacts quickly with H-atom donors to release another equivalent of H₂O and to form the reduced species LMn^{II}₃(OAc)₃ (Scheme 5).



Scheme 5. Proposed disproportionation reaction upon H-atom transfer.

Similar disproportionation issues have complicated other reactivity studies and have hindered our ability to measure the kinetics of oxygen atom transfer and hydrogen atom transfer. We have found that the clusters can easily comproportionate and disproportionate with oxygen atom transfer or with loss of the apical redox-inactive metals. For example, to test the hypothesis that compound **12** could transfer oxygen atom equivalents, we tested the proposed monooxido compound in the same oxidation state, compound **3**, in which a single

Ca^{2+} center bridges two trimanganese units. To our surprise, no reaction was observed with PEt_3 (4 equiv) at room temperature in CD_2Cl_2 . However, upon addition of excess $\text{Ca}(\text{OTf})_2$ in THF/DME, the reaction with phosphine proceeded to form the reduced trimanganese(II) complex. In this reaction, $\text{Ca}(\text{OTf})_2$ may serve to abstract an acetate ligand from **3** in order to allow approach of the phosphine. We have also found that disproportionation can occur in the presence of $\text{Ca}(\text{OTf})_2$ and DME. Upon treatment of **3** with DME and $\text{Ca}(\text{OTf})_2$, we observed the formation of $[\mathbf{4}\text{-Ca}(\text{DME})(\text{OTf})]^{2+}$ and $\text{LMn}^{\text{II}}_3(\text{OAc})_3$ by ^1H NMR spectroscopy (Scheme 6).



Scheme 6. Disproportionation of **3** to form $[\mathbf{4}\text{-Ca}(\text{DME})(\text{OTf})]^{2+}$ and $\text{LMn}^{\text{II}}_3(\text{OAc})_3$.

5.4 Electron transfer kinetics

Finally, attempts to measure and compare the electron transfer rates of the dioxido cluster have been complicated due to the extremely fast rates. Addition of ferrocene to the

least oxidizing complex $[4\text{-Ca}(\text{DME})(\text{OTf})]^{2+}$ ($E^0 = -0.08$ V vs. Fc/Fc^+) under pseudo-first-order conditions (10 equiv. Fc) results in complete consumption of $[4\text{-Ca}(\text{DME})(\text{OTf})]^{2+}$ and formation of ferrocenium in seconds, with no further formation of ferrocenium over time. Use of less reducing ferrocene derivatives such as bromoferrocene and acetylferrocene ($E^0 = 0.17$ and 0.23 V vs. Fc/Fc^+ respectively) results in no reduction of $[4\text{-Ca}(\text{DME})(\text{OTf})]^{2+}$.

Conclusions

In summary, the reactivity of heterometallic dioxido and tetraoxido clusters was investigated in order to examine the effects of redox-inactive metal ions on properties of these complexes other than electrochemical reduction potentials (Chapter 3, 4). In particular, oxygen atom transfer to phosphine and hydrogen atom transfer to the clusters were studied. The reduced heterometallic tetraoxido cubane clusters were found to display significant deceleration in the rates of oxygen atom transfer to trimethylphosphine upon decreasing the Lewis acidity of the apical metal, with the tetramanganese cluster **8** reacting faster than **7-Sc** and **7-Y**. Although the dioxido clusters transfer oxygen atoms to phosphine, unlike the tetramanganese case simple transfer of one oxygen atom could not be observed. Instead, over-reduction to the trimanganese(II) compound $\text{LMn}^{\text{II}}_3(\text{OAc})_3$ is seen. Studying the kinetics of these reactions is complicated by facile cluster interconversion by disproportionation and comproportionation mechanisms. Further studies may help point to another role for Ca^{2+} in the OEC for O–O bond formation in water oxidation.

Experimental Section

General Considerations. Unless indicated otherwise, reactions performed under inert atmosphere were carried out in oven-dried glassware in a glovebox under a nitrogen atmosphere. Anhydrous tetrahydrofuran (THF) was purchased from Aldrich in 18 L Pure-PacTM containers. Anhydrous dichloromethane, diethyl ether, and THF were purified by sparging with nitrogen for 15 minutes and then passing under nitrogen pressure through a column of activated A2 alumina (Zapp's). Anhydrous 1,2-dimethoxyethane (DME) was dried over sodium/benzophenone ketyl and vacuum-transferred onto molecular sieves. CD₂Cl₂ was purchased from Cambridge Isotope Laboratories, dried over calcium hydride, then degassed by three freeze-pump-thaw cycles and vacuum-transferred prior to use. ¹H NMR spectra were recorded on a Varian 300 MHz instrument, with shifts reported relative to the residual solvent peak. ³¹P NMR spectra were recorded on a Varian 300 MHz instrument, with shifts reported relative either to an external 85% H₃PO₄ standard or to the internal lock signal. UV-Vis spectra were taken on a Varian Cary 50 spectrophotometer at 25 °C using quartz crystal cells. Electrospray ionization mass spectrometry (ESI-MS) was performed in the positive ion mode using a LCQ ion trap mass spectrometer (Thermo) at the California Institute of Technology Mass Spectrometry Facility.

Unless indicated otherwise, all commercial chemicals were used as received. Ca(OTf)₂ was purchased from Alfa Aesar. Y(OTf)₃ was purchased from Sigma-Aldrich. Ferrocene was purchased from Alfa Aesar and sublimed before use. Iodosobenzene¹⁷ was prepared according to literature procedures. Caution! Iodosobenzene is potentially explosive and should be used only in small quantities. LMn₃(OAc)₃, [LMn₃O(OAc)₃]₂Ca(OTf)₂ (**3**), and

$[\text{LCaMn}_3\text{O}_2(\text{OAc})_2(\text{DME})(\text{OTf})][\text{OTf}]$ ($[\text{4-Ca}(\text{DME})(\text{OTf})]^{2+}$) were prepared according to previously published procedures.^{5a, 5c, 18}

Synthesis of $[\text{4-Y}(\text{DME})(\text{OTf})]^{3+}$

In the glovebox, a scintillation vial equipped with a stir bar was charged with $[\text{4-Ca}(\text{DME})(\text{OTf})][\text{OTf}]_2$ (0.100 g, 0.0572 mmol) and $\text{Y}(\text{OTf})_3$ (0.034 g, 0.063 mmol, 1.1 equiv). DME (4 mL) and CH_3CN (10 mL) were added, and the purple mixture was stirred at room temperature for 12 h. The mixture was filtered, then concentrated *in vacuo* to yield an oily purple residue. This material was taken up in $\text{CH}_2\text{Cl}_2/\text{DME}$, filtered through Celite, then concentrated again *in vacuo*. This compound has not yet been fully characterized. See Appendix D for ^1H NMR spectrum. Reactions of $[\text{4-Y}(\text{DME})(\text{OTf})]^{3+}$ described below were carried out with this material without further purification.

Reactions of tetraoxido cubane clusters with PMe_3

In the glovebox, **8** (0.0091 g, 0.0069 mmol), **6-Ca** (0.0095 g, 0.0069 mmol), and $[\text{6-Sc}][\text{OTf}]$ (0.0079 g, 0.0054 mmol) respectively, were dissolved in 0.8 mL (0.7 mL for $[\text{6-Sc}][\text{OTf}]$) of a DMF solution of $[\text{PPh}_4][\text{BF}_4]$ (3.4 mg, 0.0079 mmol, 1.14 equiv for **8** and **6-Ca**; 2.3 mg, 0.0054 mmol, 1.0 equiv for $[\text{6-Sc}][\text{OTf}]$) and transferred to separate J. Young NMR tubes (PPh_4^+ serves as an internal standard). A solution of PMe_3 (18 μL , 0.78 M in THF, 0.014 mmol, 2.0 equiv for **8** and **6-Ca**; 20 μL , 0.78 M in THF, 0.015 mmol, 2.9 equiv for $[\text{6-Sc}][\text{OTf}]$) was added via syringe to both mixtures, and the tubes were sealed with Teflon caps. The reactions were monitored using ^{31}P NMR spectroscopy referenced to an external standard of 85% H_3PO_4 .

Within 15 min. at RT, ^{31}P NMR spectroscopy of the reaction with **8** indicates consumption of one equivalent of PMe_3 as well as a broadened PMe_3 signal. No signal

corresponding to OPMe_3 is observed. ^{31}P NMR spectroscopy of the solutions of **6**-Ca and **[6-Sc][OTf]** show no consumption of PMe_3 . No changes in the ^{31}P NMR spectra of the mixtures containing **8** and **6**-Ca are observed after 18 h at RT. Approximately one equivalent of PMe_3 has been consumed in the reaction containing **[6-Sc][OTf]**, though no OPMe_3 is detected by GC-MS, likely indicating an alternate decomposition route not involving oxygen atom transfer.

Synthesis of $\text{LScMn}_3\text{O}_3(\text{OAc})_3$ (**10**-Sc)

In the glovebox, a J. Young NMR tube was charged with a solution of **7**-Sc (0.007 g, 0.005 mmol) in C_6D_6 (0.7 mL). A solution of PMe_3 (1 M in THF, 1 equiv, 5 μL) was added via syringe, and the reaction was allowed to proceed at room temperature and monitored by ^1H NMR spectroscopy. After two weeks, the reaction was dried *in vacuo* and washed with diethyl ether. ^1H NMR (C_6D_6 , 300 MHz): δ 17.7, 11.2, 10.8, 9.5, 4.8, -19.0 ppm.

Reactions of $[\mathbf{5}\text{-M}(\text{DME})(\text{OTf})]^n+$ with PEt_3

In a glovebox, $[\mathbf{5}\text{-Ca}(\text{DME})(\text{OTf})]^+$ (0.010 g, 0.0062 mmol) and $[\mathbf{5}\text{-Y}(\text{DME})(\text{OTf})]^{2+}$ (0.011 g, 0.0062 mmol) were respectively dissolved in 0.5 mL of CD_2Cl_2 . In a separate vial, a solution of $[\text{PPh}_4][\text{BF}_4]$ (0.013 g) and PEt_3 (9.2 μL) in 1.0 mL of CD_2Cl_2 was prepared. To each of the solutions of **5**-M, 0.2 mL of this solution (2 equiv PEt_3 , 1 equiv PPh_4^+) was added, and the reaction mixtures were transferred to separate J. Young NMR tubes and sealed with Teflon caps. PPh_4^+ serves as an internal ^{31}P NMR standard. The reactions were monitored using ^1H NMR spectroscopy (Figs. 6, 7) and ^{31}P NMR spectroscopy.

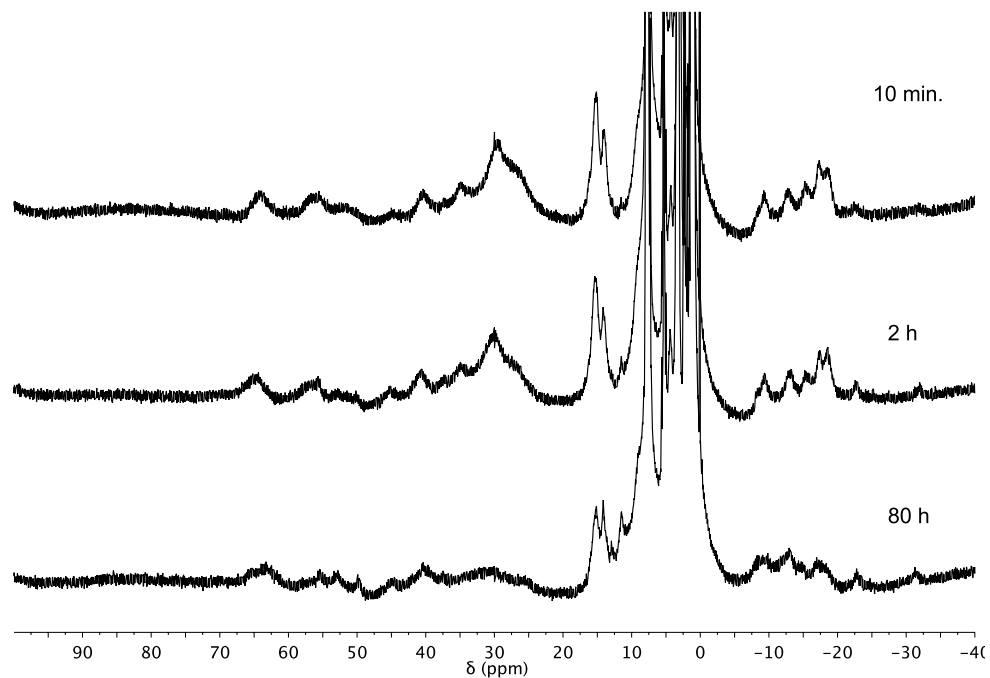


Figure 6. ^1H NMR spectra of reaction of $[\mathbf{5}\text{-Ca}(\text{DME})(\text{OTf})]^+$ with 2 equiv. of PEt_3 after 10 min. (top), 2 h (middle), and 80 h (bottom). Solvent peaks are offscale.

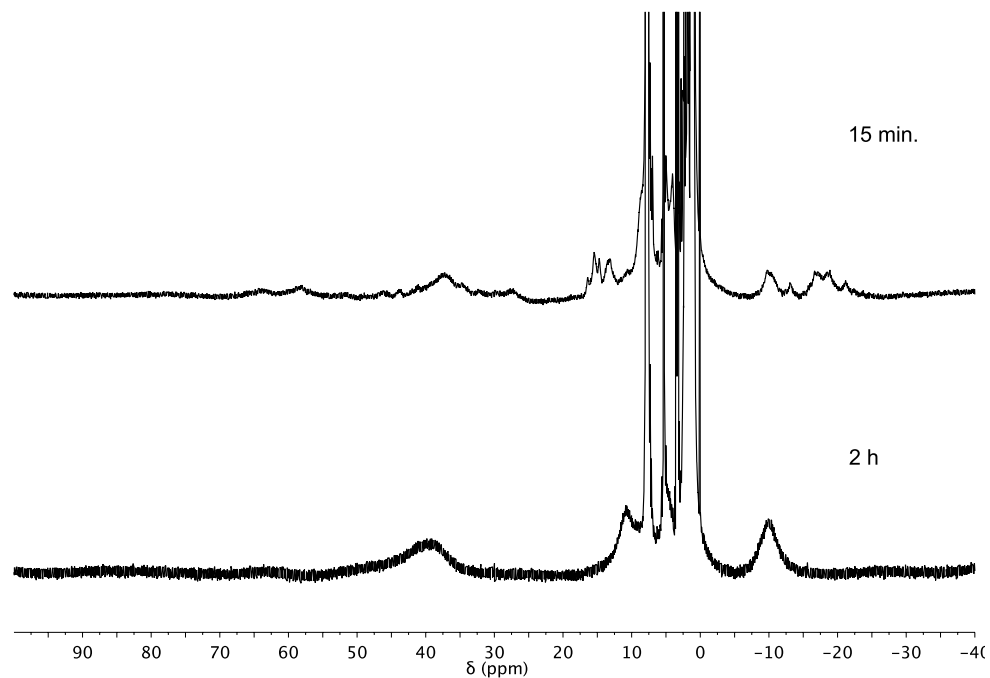


Figure 7. ^1H NMR spectra of reaction of $[\mathbf{5}\text{-Y}(\text{DME})(\text{OTf})]^{2+}$ with 2 equiv. of PEt_3 after 15 min. (top) and 2 h (bottom). Solvent peaks are offscale.

For $[\mathbf{5}\text{-Ca}(\text{DME})(\text{OTf})]^+$, no consumption of triethylphosphine is observed by ^{31}P NMR spectroscopy after 10 min. After 80 h at room temperature, only 0.4 equiv of PEt_3 was consumed (^{31}P NMR spectroscopy), and starting material is still observed by ^1H NMR spectroscopy (Fig. 6). For $[\mathbf{5}\text{-Y}(\text{DME})(\text{OTf})]^{2+}$, consumption of 1.1 equiv PEt_3 is observed by ^{31}P NMR spectroscopy within 15 min., and complete conversion to $\text{LMn}^{\text{II}}_3(\text{OAc})_3$ is observed by ^1H NMR spectroscopy after 2 h at room temperature (Fig. 7).

Reaction of $[\mathbf{4}\text{-Ca}(\text{DME})(\text{OTf})]^{2+}$ with PPh_3

In the glovebox, a vial was charged with $[\mathbf{4}\text{-Ca}(\text{DME})(\text{OTf})]^{2+}$ (0.020 g, 0.011 mmol) and PPh_3 (0.003 g, 0.011 mmol, 1 equiv). CD_2Cl_2 (0.7 mL) was added, and the mixture was transferred to a NMR tube. The reaction was monitored by ^1H NMR and ^{31}P NMR spectroscopy (Fig. 8). No change was observed within 10 min., but after 2 d at room temperature the reaction mixture became gray in color and no ^{31}P NMR signal remained. The ^1H NMR spectrum indicates the formation of a new species that has not yet been structurally identified.

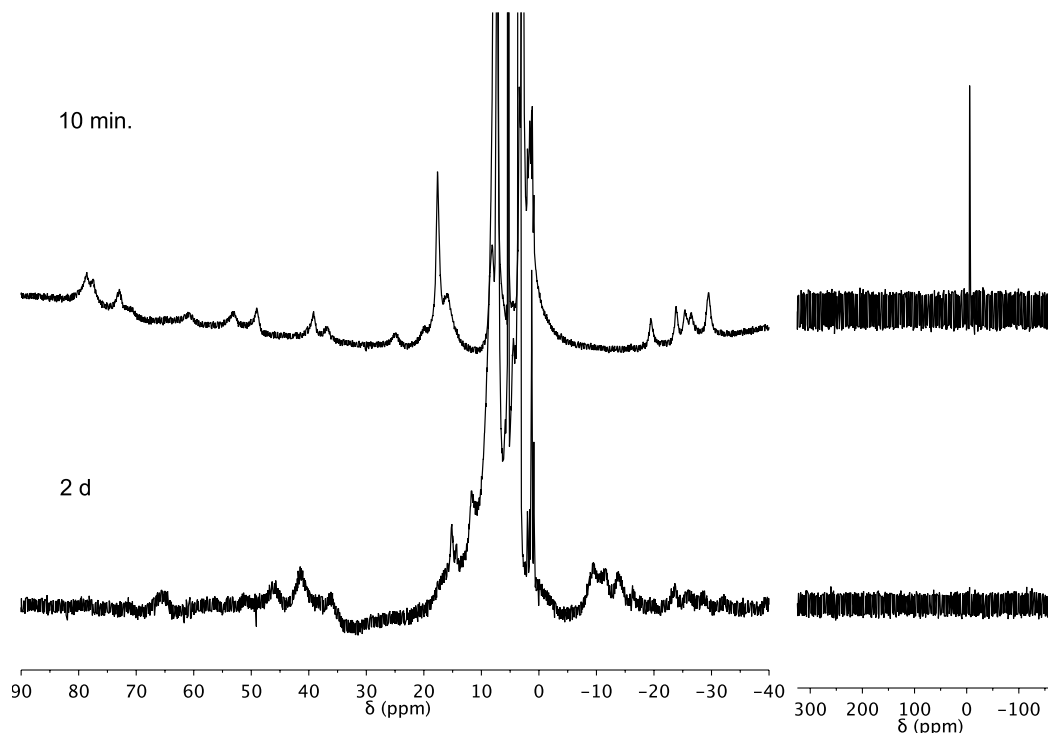


Figure 8. ^1H NMR spectra (left) and ^{31}P NMR spectra (right) of reaction of $[\mathbf{4}\text{-Ca(DME)(OTf)}]^{2+}$ and PPh_3 after 10 min. (top) and 2 d (bottom) at room temperature.

Reaction of $[\mathbf{4}\text{-Y(DME)(OTf)}]^{3+}$ with PPh_3

In the glovebox, a scintillation vial was charged with $[\mathbf{4}\text{-Y(DME)(OTf)}]^{3+}$ (0.010 g, 0.0051 mmol) and PPh_3 (0.004 g, 0.015 mmol, 3 equiv). CD_2Cl_2 (0.7 mL) was added, and the reaction was monitored by ^1H and ^{31}P NMR spectroscopy. No starting material remains by ^1H NMR spectroscopy after 5 h at room temperature, and the reaction mixture turned from purple to gray in color. Triphenylphosphine oxide was not detected by ^{31}P NMR spectroscopy of the reaction mixture.

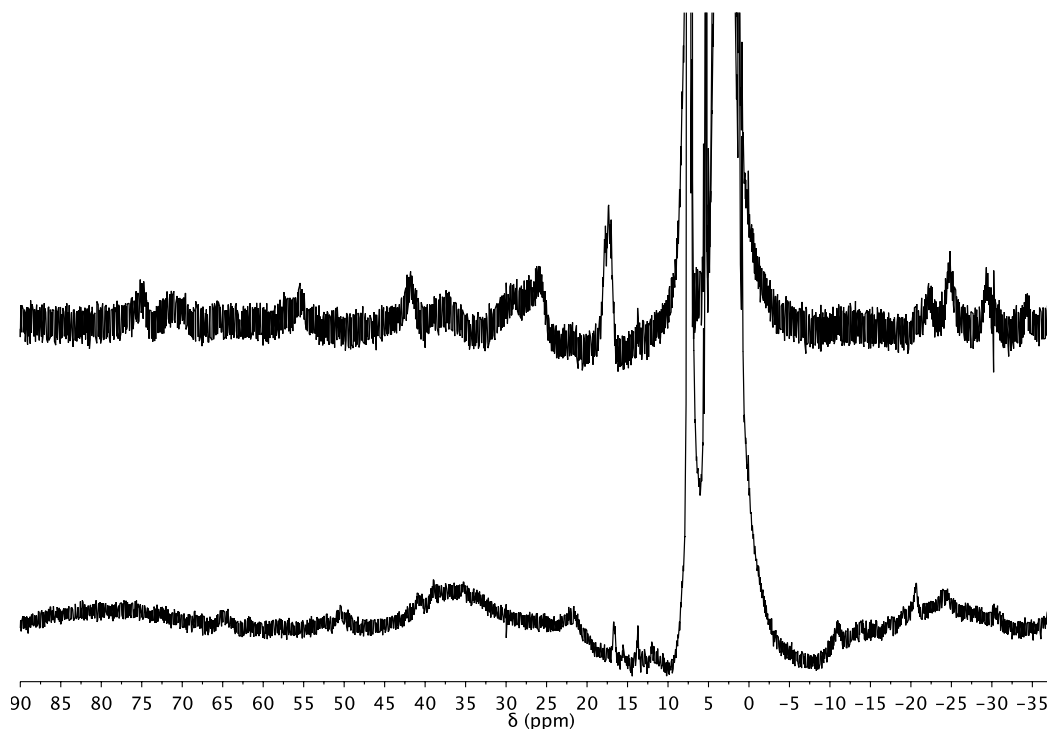


Figure 9. ^1H NMR spectra of the reaction of $[\text{4-Y(DME)}(\text{OTf})]^{3+}$ and PPh_3 (3 equiv) after 10 min. (top) and 5 h (bottom) at room temperature.

References

1. (a) Fukuzumi, S., Roles of Metal Ions in Controlling Bioinspired Electron-Transfer Systems. Metal Ion-Coupled Electron Transfer. In *Prog. Inorg. Chem.*, Karlin, K. D., Ed. John Wiley & Sons Inc: New York, 2009; Vol. 56, pp 49-153; (b) Fukuzumi, S.; Ohkubo, K. *Coord. Chem. Rev.* **2010**, 254, 372-385.
2. (a) McEvoy, J. P.; Brudvig, G. W. *Chem. Rev.* **2006**, 106, 4455-4483; (b) Brudvig, G. W. *Philos. Trans. R. Soc. London, Ser. B* **2008**, 363, 1211-1218.
3. (a) Symes, M. D.; Surendranath, Y.; Lutterman, D. A.; Nocera, D. G. *J. Am. Chem. Soc.* **2011**, 133, 5174-5177; (b) Risch, M.; Klingan, K.; Ringleb, F.; Chernev, P.; Zaharieva, I.; Fischer, A.; Dau, H. *Chemsuschem* **2012**, 5, 542-549; (c) Zaharieva, I.; Najafpour, M. M.; Wiechen, M.; Haumann, M.; Kurz, P.; Dau, H. *Energy Environ. Sci.* **2011**, 4, 2400-2408; (d) Wiechen, M.; Zaharieva, I.; Dau, H.; Kurz, P. *Chem. Sci.* **2012**; (e) Zaharieva, I.; Chernev, P.; Risch, M.; Klingan, K.; Kohlhoff, M.; Fischer, A.; Dau, H. *Energy Environ. Sci.* **2012**, 5, 7081-7089.
4. (a) Ghanotakis, D. F.; Babcock, G. T.; Yocum, C. F. *Febs Lett* **1984**, 167, 127-130; (b) Boussac, A.; Zimmermann, J. L.; Rutherford, A. W. *Biochemistry* **1989**, 28, 8984-8989; (c) Yocum, C. F. *Coord. Chem. Rev.* **2008**, 252, 296-305; (d) Yocum, C. F. *Biochim. Biophys. Acta Bioenergetics* **1991**, 1059, 1-15.
5. (a) Kanady, J. S.; Tsui, E. Y.; Day, M. W.; Agapie, T. *Science* **2011**, 333, 733-736; (b) Kanady, J. S.; Mendoza-Cortes, J. L.; Tsui, E. Y.; Nielsen, R. J.; Goddard, W.

- A.; Agapie, T. *J. Am. Chem. Soc.* **2013**, *135*, 1073-1082; (c) Tsui, E. Y.; Tran, R.; Yano, J.; Agapie, T. *Nat Chem* **2013**, *5*, 293-299; (d) Tsui, E. Y.; Agapie, T. *Proc. Natl. Acad. Sci. USA* **2013**, *110*, 10084-10088.
6. (a) Pecoraro, V. L.; Baldwin, M. J.; Caudle, M. T.; Hsieh, W. Y.; Law, N. A. *Pure Appl. Chem.* **1998**, *70*, 925-929; (b) Vrettos, J. S.; Limburg, J.; Brudvig, G. W. *Biochim. Biophys. Acta Bioenergetics* **2001**, *1503*, 229-245; (c) Vrettos, J. S.; Stone, D. A.; Brudvig, G. W. *Biochemistry* **2001**, *40*, 7937-7945.
 7. Fukuzumi, S.; Morimoto, Y.; Kotani, H.; Naumov, P.; Lee, Y. M.; Nam, W. *Nat. Chem.* **2010**, *2*, 756-759.
 8. Morimoto, Y.; Kotani, H.; Park, J.; Lee, Y. M.; Nam, W.; Fukuzumi, S. *J. Am. Chem. Soc.* **2011**, *133*, 403-405.
 9. Yoon, H.; Lee, Y.-M.; Wu, X.; Cho, K.-B.; Sarangi, R.; Nam, W.; Fukuzumi, S. *J. Am. Chem. Soc.* **2013**, *135*, 9186-9194.
 10. Park, Y. J.; Ziller, J. W.; Borovik, A. S. *J. Am. Chem. Soc.* **2011**, *133*, 9258-9261.
 11. Park, Y. J.; Cook, S. A.; Sickerman, N. S.; Sano, Y.; Ziller, J. W.; Borovik, A. S. *Chem. Sci.* **2013**, *4*, 717-726.
 12. (a) Horwitz, C. P.; Ciringh, Y. *Inorg. Chim. Acta* **1994**, *225*, 191-200; (b) Horwitz, C. P.; Ciringh, Y.; Weintraub, S. T. *Inorg. Chim. Acta* **1999**, *294*, 133-139.
 13. Leeladee, P.; Baglia, R. A.; Prokop, K. A.; Latifi, R.; de Visser, S. P.; Goldberg, D. P. *J. Am. Chem. Soc.* **2012**, *134*, 10397-10400.
 14. Miller, C. G.; Gordon-Wylie, S. W.; Horwitz, C. P.; Strazisar, S. A.; Peraino, D. K.; Clark, G. R.; Weintraub, S. T.; Collins, T. J. *J. Am. Chem. Soc.* **1998**, *120*, 11540-11541.
 15. Chen, J.; Lee, Y.-M.; Davis, K. M.; Wu, X.; Seo, M. S.; Cho, K.-B.; Yoon, H.; Park, Y. J.; Fukuzumi, S.; Pushkar, Y. N.; Nam, W. *J. Am. Chem. Soc.* **2013**, *135*, 6388-6391.
 16. (a) Park, J.; Morimoto, Y.; Lee, Y. M.; You, Y.; Nam, W.; Fukuzumi, S. *Inorg. Chem.* **2011**, *50*, 11612-11622; (b) Park, J.; Morimoto, Y.; Lee, Y.-M.; Nam, W.; Fukuzumi, S. *J. Am. Chem. Soc.* **2011**, *133*, 5236-5239; (c) Morimoto, Y.; Park, J.; Suenobu, T.; Lee, Y.-M.; Nam, W.; Fukuzumi, S. *Inorg. Chem.* **2012**, *51*, 10025-10036.
 17. Saltzman, H.; Sharefkin, J. G. *Organic Syntheses* **1973**, *43*.
 18. Tsui, E. Y.; Kanady, J. S.; Day, M. W.; Agapie, T. *Chem. Commun.* **2011**.

*Appendix A***BIMETALLIC COMPLEXES OF A DINUCLEATING BIS(N-HETEROCYCLIC
CARBENE) FRAMEWORK**

Abstract

The synthesis of dinuclear or bimetallic complexes supported by new ligand architectures may allow the development of new catalytic reactions involving the transfer of multiple electrons for the activation of small molecules. In this work, a series of dinucleating bis(N-heterocyclic carbene) ligands that are structurally related to a *p*-terphenyl diphosphine ligand previously used in the Agapie group was designed and synthesized in moderate yield in three steps from commercially available materials. Dinuclear complexes of copper(I), cobalt(II), and nickel(I) were prepared using this ligand framework and structurally characterized. The dinickel(I) dichloride complex can be reduced to form a dinickel(0) compound that reacts with carbon dioxide. Cleavage of the C–O bond of CO₂ to yield bridging carbonyl ligands is observed. The nickel complexes can also form higher nuclearity complexes with different ligand activation modes.

Introduction

In recent years, multimetallic complexes have become attractive synthetic targets due to their potential uses in chemical transformations involving the transfer of multiple electrons through cooperative substrate binding and functionalization. As such, there have been many efforts to design and synthesize new binucleating ligand frameworks.¹ Our group has used a *para*-terphenyl diphosphine ligand to support a variety of dinuclear Ni (Fig. 1, left, **A.1**), Pd, Fe, and Co complexes.² Labile metal-arene interactions between the metal centers and the central aryl moiety serve to stabilize these bimetallic compounds.

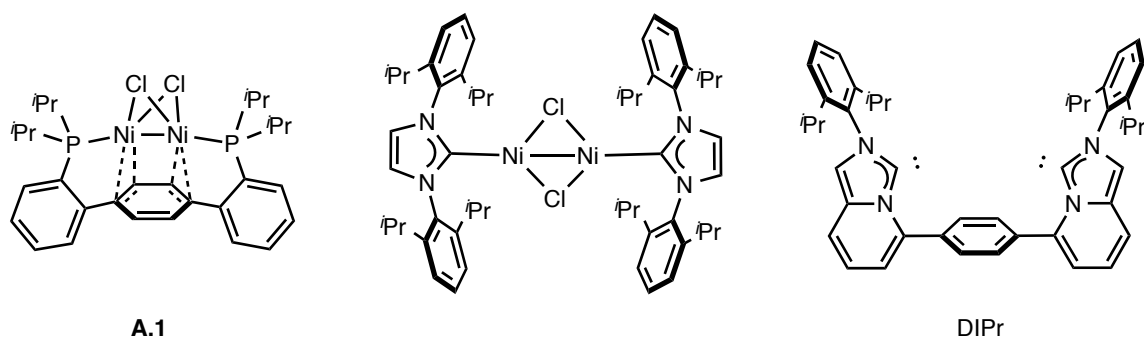


Figure 1. Dinickel(I) dichloride complexes supported by diphosphine **P2** (**A.1**, left)^{2a} and by N-heterocyclic carbene ligand 1,3-bis(2,6-diisopropylphenyl)imidazol-2-ylidene (IPr, center).³ This work: dinucleating bis(N-heterocyclic carbene) framework DIPr (right).

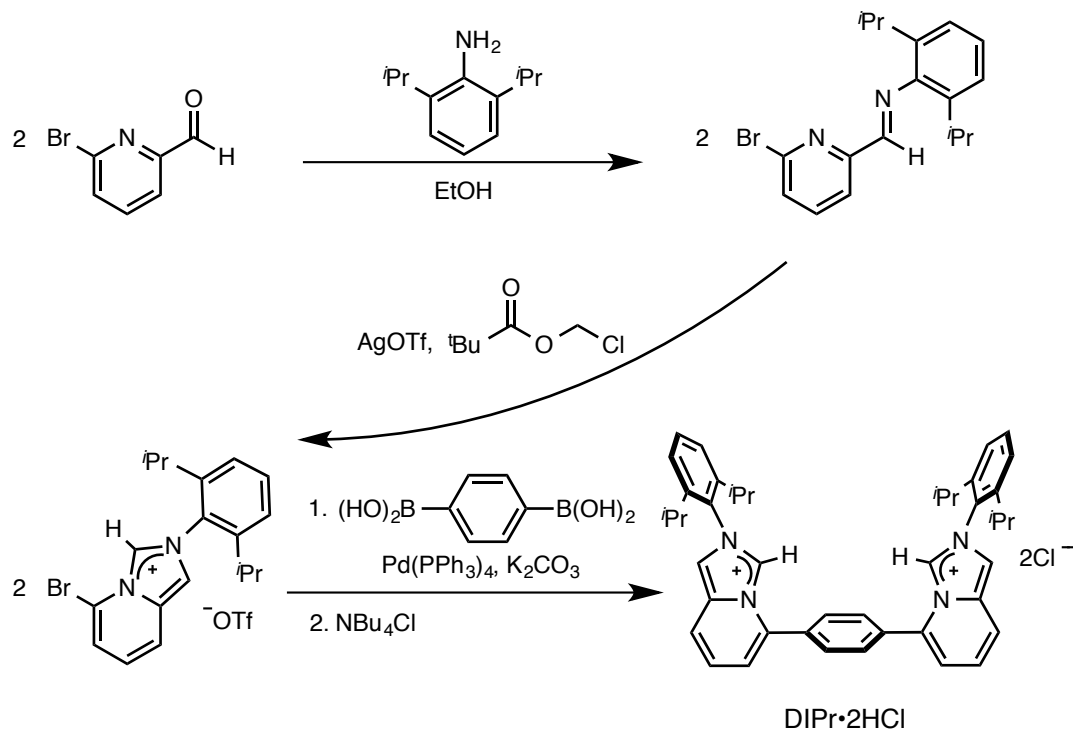
Over the past two decades, N-heterocyclic carbene (NHC) ligands have gained prominence in organometallic chemistry and catalysis since they were first popularized by Arduengo and co-workers.⁴ There have been many examples of polydentate NHC ligand frameworks; although these have primarily been chelating ligands that support a single metal center,⁵ some have been designed with potentially bridging moieties in mind for the support of multimetallic complexes.⁶

A new dinucleating NHC framework (Fig. 1, right) containing an aryl linker was designed to incorporate both the hemilabile arene moiety of **P2** and the different donor properties of the NHC donors compared to phosphines. This ligand framework may also accommodate structural variations in supported multimetallic complexes compared to complexes of **P2** due to the presence of shorter M–C bond distances compared to M–P bond distances as well as a smaller bite angle. In this work, we describe the synthesis of this ligand framework and of bimetallic copper(I), cobalt(II), and nickel complexes of this ligand, as well as initial reactivity studies.

Results and Discussion

A.1 Ligand synthesis

The bis(carbene) precursor, abbreviated DIPr•2HCl, was prepared in three steps from commercially available starting materials based upon a previously published route.⁷ Condensation of 2-bromo-6-pyridinecarboxaldehyde with 2,6-diisopropylaniline yielded the corresponding imine (Scheme 1). Cyclization by treatment with silver triflate and chloromethyl pivalate formed the bromo-substituted imidazo[1,5-a]pyridinium salt. Suzuki coupling of this imidazo[1,5-a]pyridinium triflate with 1,4-benzenediboronic acid, followed by anion substitution using tetrabutylammonium chloride, yielded the ligand precursor DIPr•2HCl. This synthetic route can be extended to other ligand variants with different aryl substituents on the carbene heterocyclic rings (Fig. 2).



Scheme 1. Synthesis of DIPr•2HCl.

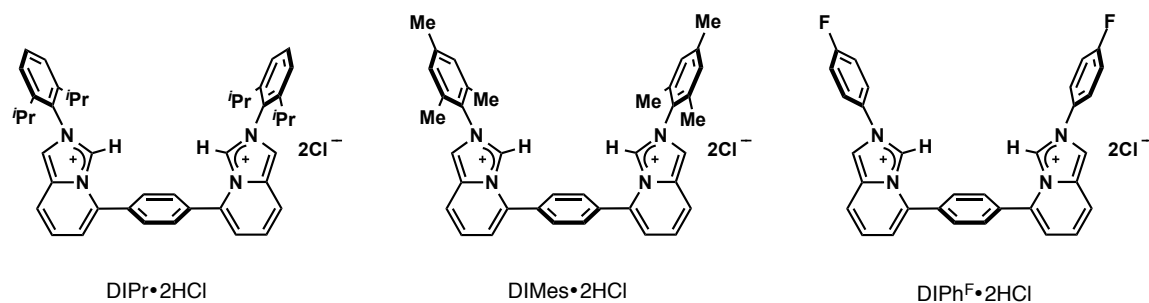


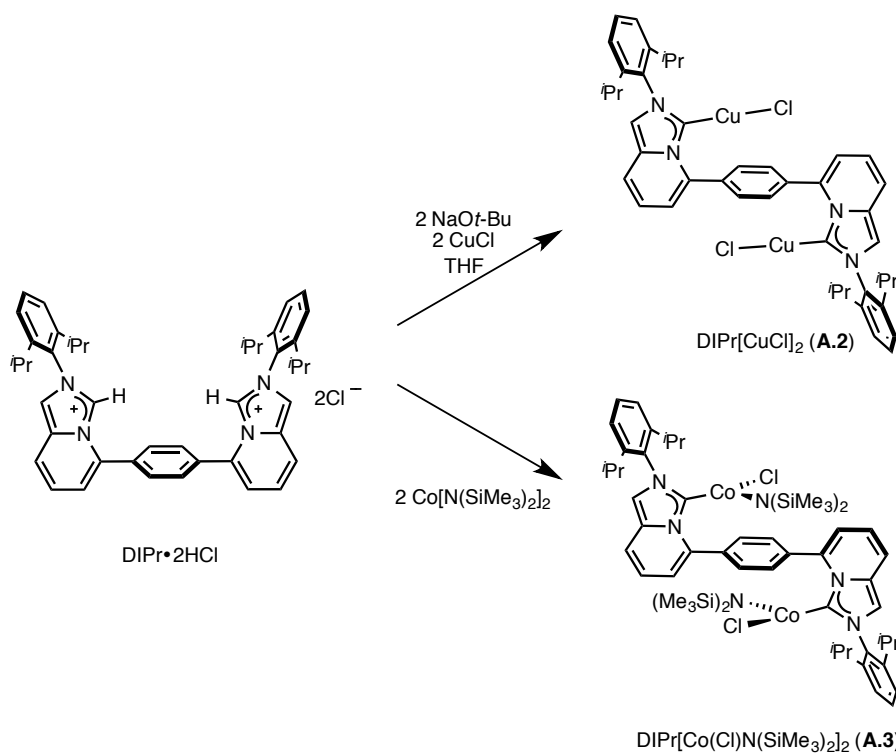
Figure 2. Different ligand variants prepared.

A.2 Metallation of biscarbene ligand framework

With the ligand precursor in hand, bimetallic complexes of the bis(carbene) framework were targeted. Attempts to deprotonate DIPr•2HCl using bases such as sodium *tert*-butoxide, sodium hydride, or sodium bis(trimethylsilyl)amide to yield the free bis(carbene) resulted in intractable mixtures of insoluble products, possibly due to decomposition of the free carbene. Fortunately, one-pot metallation reactions of DIPr•2HCl proved to be more

successful. Treatment of $\text{DIPr}\cdot 2\text{HCl}$ with two equivalents of sodium *tert*-butoxide and two equivalents of copper(I) chloride in THF formed the corresponding dicopper(I) dichloride compound $\text{DIPr}[\text{CuCl}]_2$ (**A.2**, Scheme 2). X-ray quality crystals were grown from vapor diffusion of diethyl ether into a dichloromethane solution of **A.2**. A X-ray diffraction (XRD) study of these crystals (Fig. 3 left) showed that the two copper(I) centers are oriented on opposite faces of the central arene, and are coordinated in a linear geometry (C–Cu–Cl angle of $175.3(2)^\circ$). Compound **A.2** is structurally related to the monomeric compound IPrCuCl ,⁸ whose solid-state structure displayed a Cu–Cl distance of $2.106(2)$ Å and a C–Cu distance of $1.881(7)$ Å.⁹ In comparison, compound **A.2** has a Cu–C distance of $1.886(2)$ and a Cu–Cl distance of $2.210(5)$ Å. No interactions with the central arene are observed in the XRD structure (shortest Cu–C(arene) distance 3.06 Å); this is also borne out in the ^1H NMR spectrum, in which the signal corresponding to the central arene protons is located at 7.79 ppm.

Rather than use an exogenous base, $\text{DIPr}\cdot 2\text{HCl}$ can also be metallated via aminolysis of metal amide compounds. The addition of two equivalents of $\text{Co}[\text{N}(\text{SiMe}_3)_2]_2$ to $\text{DIPr}\cdot 2\text{HCl}$ in benzene forms, after two days at room temperature, yellow crystals of the dicobalt(II) compound $\text{DIPr}[\text{Co}(\text{Cl})\text{N}(\text{SiMe}_3)_2]_2$ (**A.3**, Fig. 3 right). As with **A.2**, the two metal centers are oriented on opposite faces of the central arene and no metal-arene interactions are observed (shortest Co–C(arene) distance 2.95 Å). The coordination sphere of each cobalt(II) center is further completed by a single chloride and bis(trimethylsilyl)amide ligand. A related compound with one NHC donor has previously been isolated and characterized.¹⁰ Compound **A.3** is paramagnetic, and the ^1H NMR spectrum of a C_6D_6 solution of **A.3** contains signals that are broadened and shifted.



Scheme 2. Synthesis of dicopper(I) compound **A.2** and dicobalt(II) compound **A.3**.

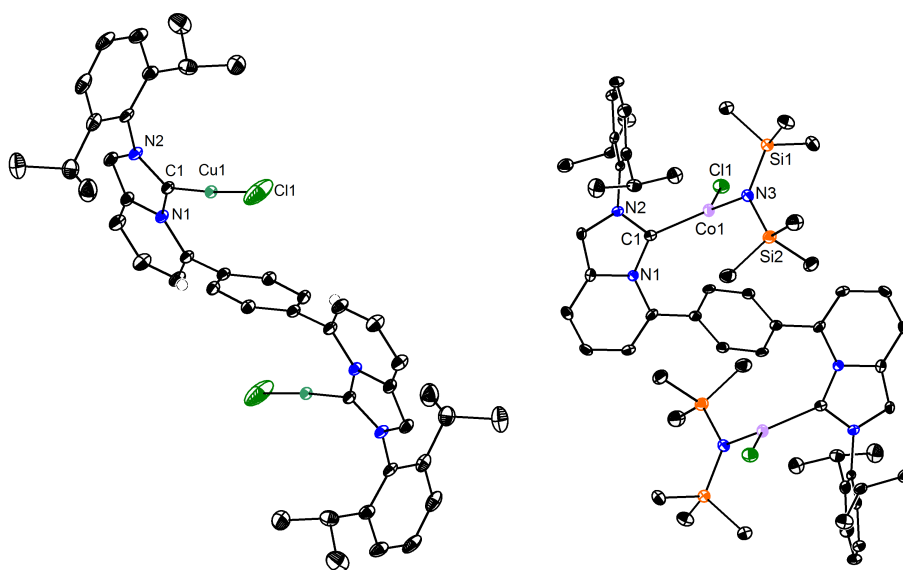
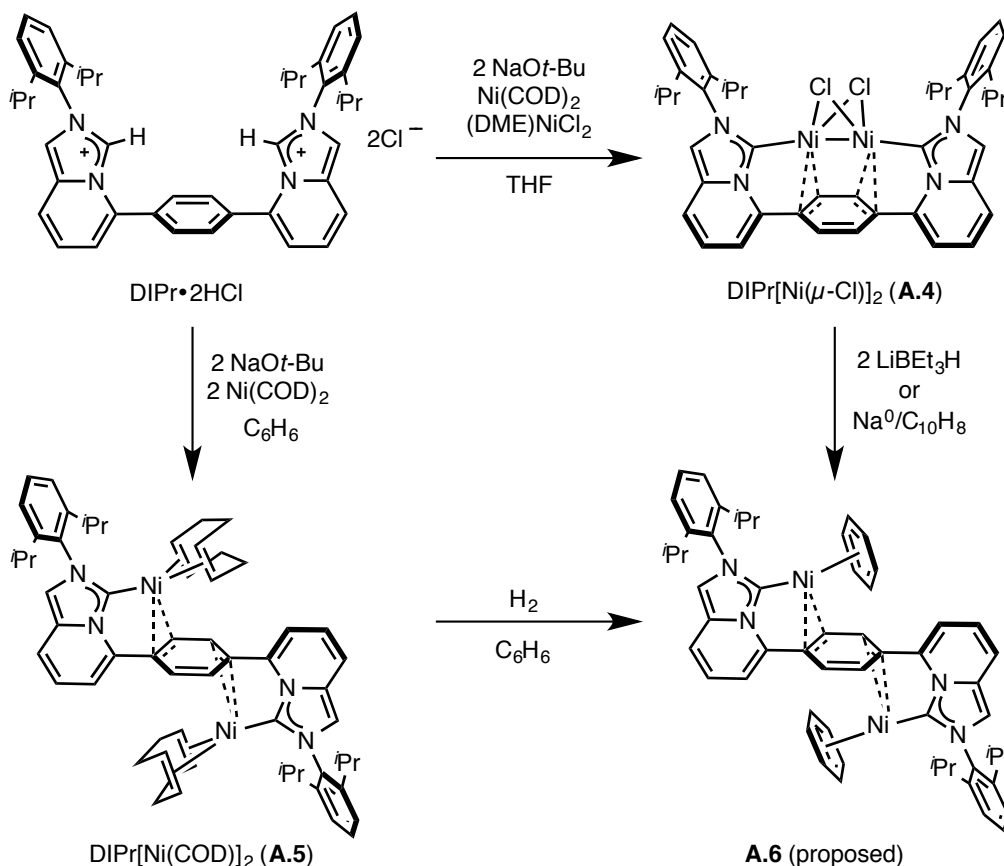


Figure 3. Solid-state structures of **A.2** (left) and **A.3** (right) as 50% thermal ellipsoids. Hydrogen atoms and solvent molecules not shown for clarity. Structure of **A.2** contains a mixture of bromide and chloride ligands.

A.3 Synthesis of dinickel complexes

Although compounds **A.2** and **A.3** are bimetallic complexes, they display no metal-metal interactions. However, both NHC ligands and diphosphine **P2** have been shown to support dinickel(I) dichloride complexes containing a $\text{Ni}^{\text{I}}\text{--Ni}^{\text{I}}$ bond. These complexes were prepared by the comproportionation of $\text{NiCl}_2(\text{dme})$ ($\text{dme} = 1,2\text{-dimethoxyethane}$) and $\text{Ni}(\text{COD})_2$ ($\text{COD} = 1,5\text{-cyclooctadiene}$) (Fig. 1, left and center).^{2a, 3} When a THF suspension of $\text{DIPr}\cdot 2\text{HCl}$ was treated with sodium *tert*-butoxide (2 equiv), $\text{Ni}(\text{COD})_2$ (1 equiv), and $\text{NiCl}_2(\text{dme})$ (1 equiv), the desired comproportionation product $\text{DIPr}[\text{Ni}(\mu\text{-Cl})]_2$ (**A.4**) was isolated as a dark brown solid (Scheme 3). As with both the NHC-supported and diphosphine-supported complexes, the ^1H NMR spectrum of **A.4** is diamagnetic, revealing a $\text{Ni}^{\text{I}}\text{--Ni}^{\text{I}}$ interaction. The signal corresponding to the central arene protons is a significantly downshifted singlet at 14.24 ppm. In comparison, the central arene ^1H NMR signal of the corresponding diphosphine-supported dinickel(I) dichloride complex **A.1** is shifted upfield from that of free ligand,^{2a} indicating differences in the nickel-arene interactions. That the signal is a singlet at room temperature, as well as the observation of only one methine signal for the isopropyl moieties, suggests that the dinickel(I) unit exchanges positions over the central arene quickly at room temperature.



Scheme 3. Synthesis of dinickel complexes.

Single crystals of **A.4** were grown by vapor diffusion of pentane into a diethyl ether solution of the complex. A XRD study shows that the two nickel(I) centers are located on the same face of the arene ring and have a short nickel-nickel distance of 2.589(3) Å (Fig. 4), with the two chlorides bridging the nickel centers. There is a strong interaction between the nickel centers and the central arene moiety, with short C–Ni distances (2.05–2.17 Å). Additionally, the C–C bond distances of the central arene show significant bond localization (Fig. 4 inset). The solid-state structure of compound **A.1** shows similar nickel-arene interaction (Ni–C distance 2.05–2.10 Å), but similar central arene bond localization distances. Due to the longer Ni–P distances (2.17–2.18 Å) compared to the Ni–C(carbene) distances (1.91 Å), the terphenyl backbone of the diphosphine ligand is more distorted to

accommodate the dinickel moiety, with the outer aryl rings of the diphosphine bent 15–17° out of the plane vs. 9–10° for **A.4**. Compound **A.4** displays a torsion angle of 62.72–68.75°, while the pendant aryl groups of **A.1** are oriented closer to perpendicular to the central arene, with torsion angles of 74.4 and 78.8°. As a result, the nickel(I) centers of **A.4** are located more over the C–H bonds rather than over the diene of the central arene, potentially causing the differences in the ^1H NMR spectra.

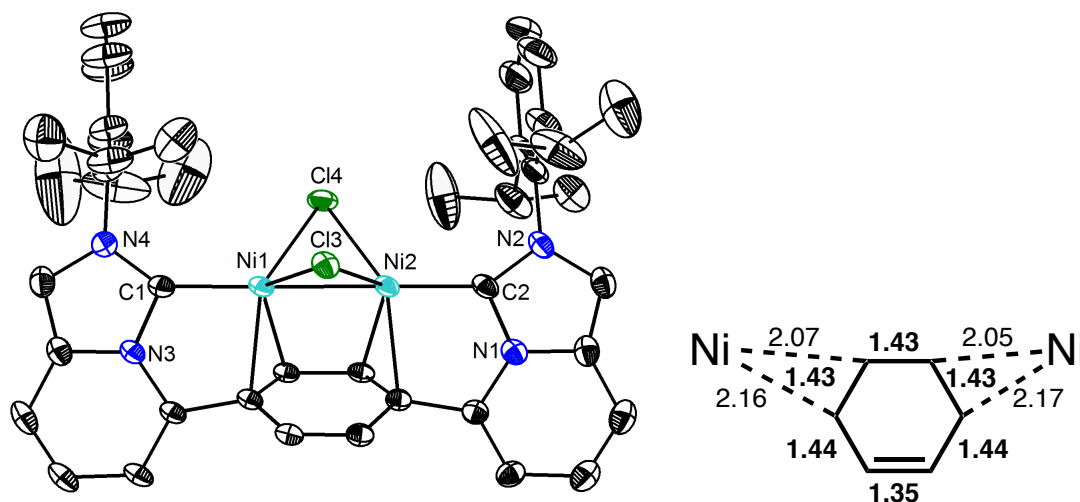


Figure 4. Solid-state structure of $\text{DIPr}[\text{Ni}(\mu\text{-Cl})]_2$ (**A.4**) as 50% thermal ellipsoids. Hydrogen atoms and solvent molecules not shown for clarity. Inset: selected bond distances (Å). Ni–Ni distance: 2.3936(3) Å.

More reduced dinickel(0) compounds were also targeted, as a previous example of a carbene-supported dinickel(0) compound was demonstrated to be capable of a new binding mode of CO_2 as well as CO_2 deoxygenation, presumably by the formation of an equivalent of a nickel carbonate species.¹¹ It was hoped that by supporting a dinickel(0) complex with a binucleating ligand framework that loss of mononuclear nickel side products could be avoided. A benzene suspension of $\text{DIPr}\cdot 2\text{HCl}$ was treated with sodium *tert*-butoxide (2 equiv) and $\text{Ni}(\text{COD})_2$ (2 equiv) to form a dark brown compound **A.5** (Scheme 3). The ^1H

NMR spectrum of a C_6D_6 solution of **A.5** contains two broad signals at 4.2 and 1.9 ppm corresponding to the protons of the coordinated 1,5-cyclooctadiene ligands. Additionally, some interactions between the nickel(0) centers and the central arene was observed, as the signal corresponding to the central arene protons is shifted upfield to 6.25 ppm. A XRD study of single crystals of **A.5** grown from THF/hexanes at $-35\text{ }^{\circ}\text{C}$ (Fig. 5) confirmed the structure to be a dinickel(0) complex in which each nickel(0) center is located on the opposite face of the central arene, each displaying an η^2 -interaction with the vicinal diene of the central arene moiety (Ni–C distances 2.13–2.15 Å).

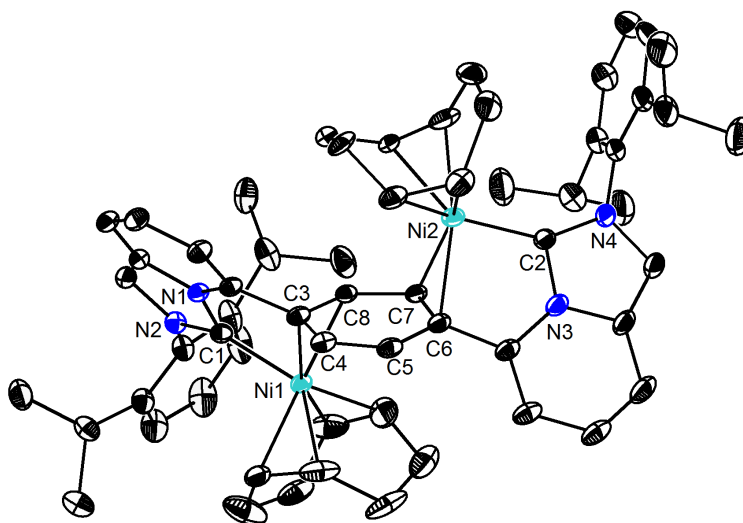


Figure 5. Solid-state structure of $\text{DIPr}[\text{Ni}(\text{COD})_2]$ (**A.5**) as 50% thermal ellipsoids. Hydrogen atoms and outer sphere solvent molecules not shown for clarity.

In benzene solution, compound **A.5** was observed to be in equilibrium with a second ligand-containing complex (**A.6**), along with free COD. Addition of excess COD resulted in clean conversion to **A.5**. Compound **A.6** is proposed to be the benzene adduct of the dinickel(0) complex. Addition of excess dihydrogen to a benzene solution of **A.5** facilitates hydrogenation of the COD ligands and formation of clean **A.6**. Compound **A.6**

can also be independently prepared by reduction of the dinickel(I) compound **A.4** with two equivalents of LiBEt_3H or two equivalents of sodium naphthalenide in THF, followed by benzene. Unfortunately, compound **A.6** is unstable at room temperature in solution and in the solid-state, decomposing within several hours. As such, it has been challenging to grow X-ray quality single crystals of **A.6**, and structural confirmation of its assignment via XRD has not been achieved yet. The ^1H NMR spectrum of a C_6D_6 solution of **A.6** displays two singlets that integrate to 2 protons corresponding to the central arene at 5.56 and 3.53 ppm, both shifted far upfield relative to **A.5**, consistent with greater backbonding into the central arene ligand due to weaker backbonding into the coordinated benzene ligands compared to COD. The observation of two central arene signals, as well as two isopropyl methine signals, indicates that the fluxional motion of the nickel centers is slower than that of **A.4** and **A.5**, again consistent with stronger metal-arene interactions. In comparison, reduction of **A.1** or metallation of **P2** with nickel(0) sources has typically yielded only a mononickel(0) complex rather than dinickel complexes, except in cases in which the compounds are stabilized via bridging carbonyl ligands.^{2d, 12} These differences may be attributed to the differences in the donor-metal bond distances and ligand bite angles of **P2** and DIPr.

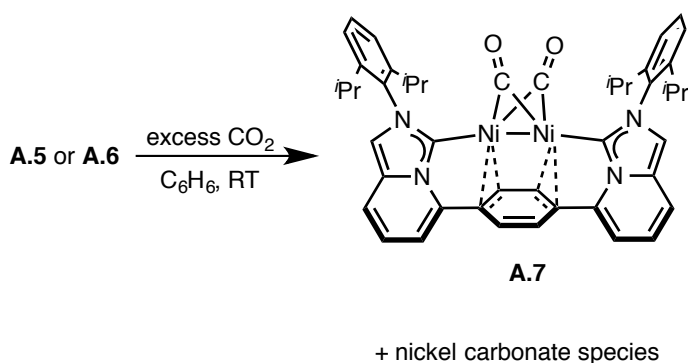
A.4 CO₂ reactivity studies

Nickel complexes have long been examined for carbon dioxide reduction activity due to the proposed role of the nickel center in carbon monoxide dehydrogenase.¹³ The first known example of a nickel carbon dioxide complex, $(\text{Cy}_3\text{P})_2\text{Ni}(\text{CO}_2)$ was prepared by Aresta and co-workers in 1975.¹⁴ In this example, the CO_2 complex was found to yield small amounts of carbonyl and carbonate products upon heating via the metal-mediated

disproportionation of CO₂. Other examples of tri- and diphosphine supported nickel(0) complexes have been demonstrated to cleave CO₂ via the formation of nickel carbonyl and carbonate complexes, or via the oxidation of the phosphine ligands to form phosphine oxides.¹⁵ A recent report by Caulton and co-workers described the cleavage of the C–O bond of CO₂ by a PNP pincer-supported nickel(I) complex to transpose an oxygen center from CO₂ with the amide nitrogen of the ligand framework.¹⁶ Multinickel complexes have also been studied for the reduction of carbon dioxide. Sadighi and co-workers reported a dinickel(0) compound that reacts with CO₂ to form a carbonyl-bridged dinickel complex with proposed concomitant loss of an unobserved nickel carbonate species.¹¹ A recent example of dinickel(I) complexes supported by β -diketiminato ligands also demonstrated the formation of carbonyl, carbonate, and oxalate nickel complexes.¹⁷ Finally, dinickel and trinickel complexes have also been reported as effective electrocatalysts in the reduction of CO₂ to CO.¹⁸

When benzene solutions of **A.5** or **A.6** were treated with an excess of CO₂, complete consumption of starting material was observed by ¹H NMR spectroscopy within minutes to form one major species. Over 7 hours at room temperature, this species slowly converts to a mixture of products, with one major species (**A.7**) observed by ¹H NMR spectroscopy whose spectrum displays one signal for the isopropyl methine protons and a broad singlet at 6.2 ppm corresponding to the central arene ring, indicating nickel-arene interactions, albeit weaker than those observed in **A.6**. An IR spectrum of **A.7** shows a strong stretch at 1825 cm⁻¹, which is consistent with the presence of a bridging CO moiety, and compound **A.7** was assigned as a dinickel complex containing two bridging carbonyl ligands (Scheme 4).¹⁹ When ¹³CO₂ was added to **A.5**, a signal at 171 ppm was initially observed in the ¹³C

NMR spectrum (see supporting information), possibly indicating a carbon dioxide complex of nickel, while the final product mixture showed two sharp signals at 161 ppm, consistent with nickel carbonate complexes.²⁰ The ^{13}C signal corresponding to the bridging carbonyl ligands of **A.7** could not be observed by ^{13}C NMR spectroscopy even at elevated temperatures, possibly due to fluxional exchange processes of the dinickel unit about the central arene ring. Compound **A.7** was also independently synthesized by the addition of two equivalents of paraformaldehyde to a benzene solution of **A.5**.



Scheme 4. Reaction of dinickel(0) complexes **A.5** and **A.6** with CO_2 .

A XRD study of crystals grown from vapor diffusion of pentane into a diethyl ether solution of **A.7** reveals the structure to be a dinickel(0) complex in which the two nickel centers are located on the same face of the central arene and are bridged by two $\mu_2\text{-CO}$ ligands (Figure 6). The nickel centers also interact with the vicinal diene of the central arene in a similar manner as **A.4**, with bond localization of the central arene C–C bonds (Figure 6, inset). However, the dinickel moiety is located further from the *ipso*-carbons of the central arene than that of **A.4**, with torsion angles of 50.38–51.28 ° between the pendant and central aryl groups. The structure of compound **A.7** also displays an unusually short Ni–Ni distance (2.248(1) Å). In comparison, the Ni–Ni distance of compound **A.4** is 2.2936(3) Å and the median Ni–Ni distance of carbonyl-bridged species from a CSD

search of dinickel complexes is 2.387 Å. This shorter vector compared to other carbonyl-bridged nickel species may be due to the constraints of the dinucleating ligand framework.

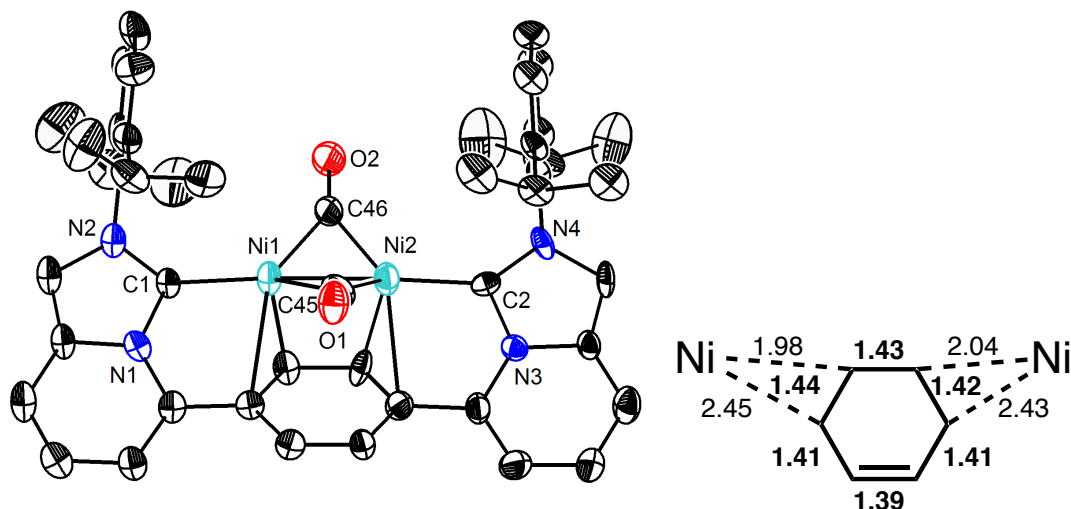


Figure 6. Solid-state structure of **A.7** as 50% thermal ellipsoids. Hydrogen atoms and solvent molecules not shown for clarity. Ni–Ni: 2.248(1) Å.

When the hexanes wash of the $\text{DIPr}[\text{Ni}(\text{COD})]_2$ synthesis was stored at $-35\text{ }^\circ\text{C}$ for over a year, single crystals of a new compound **A.8** were isolated. A XRD study of these crystals revealed the structure to be a trinuclear cluster coordinated by two allylic $\eta^3\text{-C}_8\text{H}_{13}$ ligands presumably derived from insertion and rearrangement of 1,5-cyclooctadiene into nickel hydride moieties (Fig. 7).²¹ Notably, two of the C–H bonds of the central arene have been activated, and the resulting benzyne-like moiety bridges the three nickel centers. Such trinuclear complexes containing μ_3 -bridging benzyne ligands have previously been isolated with osmium,²² ruthenium,²³ and nickel.²⁴ To the author's knowledge, however, this is the first example of direct arene C–H activation by nickel to form such a trinuclear cluster; the previous examples have involved the addition of haloarene compounds.²⁴ Compound **A.8** is proposed to be formed by oxidative addition of the central aryl C–H bond to a nickel(0)

center; the resulting nickel hydride then inserts 1,5-cyclooctadiene, which rearranges via β -hydride elimination and reinsertion processes to form the resulting allylic C_8H_{13} ligands.

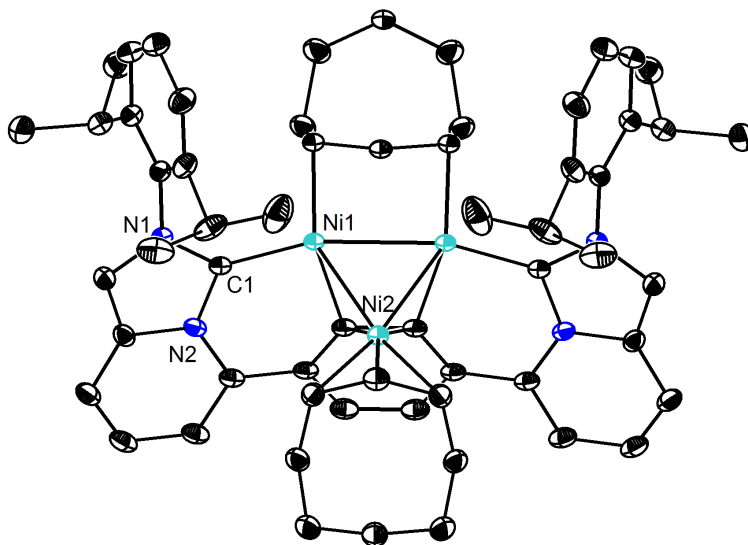


Figure 7. Solid-state structure of **A.8** as 50% thermal ellipsoids. Hydrogen atoms and solvent molecules not shown for clarity.

Conclusions

In summary, a novel bis(N-heterocyclic carbene) framework containing a hemi-labile central arene donor was designed and synthesized as a carbene analogue to the previously described para-terphenyl diphosphine ligand **P2**. This ligand framework contains two fused ring N-heterocyclic carbene donors with a hemilabile central arene unit as a potential donor/ π -acceptor. Multiple ligand variants with different aryl substituents on the N-heterocyclic carbene donors could be prepared. Dicopper(I), dicobalt(II), and dinickel complexes of varying oxidation state were prepared and characterized. Dinickel(0) complexes of this ligand framework were found to react with CO_2 to form a carbonyl-bridged dinickel(0) product.

Experimental Section

General Considerations. Unless stated otherwise, all synthetic manipulations were carried out using standard Schlenk techniques under a nitrogen atmosphere, or in a M. Braun glovebox under a nitrogen atmosphere. Reactions were carried out in oven-dried glassware cooled under vacuum. Anhydrous THF was purchased from Aldrich in 18 L Pure-PacTM containers. Anhydrous benzene, hexanes, pentane, diethyl ether, and THF were purified by sparging with nitrogen for 15 minutes and then passing under nitrogen pressure through a column of activated A2 alumina (Zapp's). All non-dried solvents used were reagent grade or better. Deuterated solvents were purchased from Cambridge Isotope Laboratories, Inc. C₆D₆ was dried over sodium/benzophenone ketyl, degassed by three freeze-pump-thaw cycles and vacuum-transferred prior to use. Deuterated dichloromethane (CD₂Cl₂) was dried over calcium hydride, degassed by three freeze-pump-thaw cycles, and vacuum-transferred prior to use. ¹H NMR and ¹³C NMR spectra were recorded on Varian 300, 400, or 500 MHz instruments, with shifts reported relative to the residual solvent peaks (7.16 and 128.06 ppm respectively for C₆D₆, 5.32 and 53.84 ppm respectively for CD₂Cl₂, and 7.27 and 77.16 pm respectively for CDCl₃). ¹⁹F NMR spectra were referenced relative to the lock signal of the solvent. Elemental analyses were performed by Robertson Microlit, Ledgewood, NJ. High resolution mass spectrometry (HRMS) was performed at the California Institute of Technology Mass Spectrometry Facility.

Unless indicated otherwise, all reagents were used as received. Silver triflate were purchased from Alfa Aesar. Chloromethyl pivalate was purchased from Alfa Aesar and distilled from calcium hydride. Copper(I) chloride, nickel bis(cyclooctadiene), sodium *tert*-butoxide, and nickel(II) chloride dimethoxyethane adduct were purchased from Strem.

$\text{Co}[\text{N}(\text{SiMe}_3)_2]_2$,²⁵ 1,4-benzenediboronic acid²⁶ and 2-(2,6-diisopropylphenyl)imine-6-bromopyridine²⁷ were prepared according to literature procedures.

Preparation of 5-bromo-2-(2',6'-diisopropylphenyl)imidazo[1,5a]pyridinium triflate.

In the glovebox, silver trifluoromethanesulfonate (5.21 g, 20.27 mmol) was suspended in methylene chloride (15 mL) in a scintillation vial equipped with a stir bar. Chloromethyl pivalate (2.92 mL, 20.27 mmol) was added via syringe, and the mixture was stirred at room temperature in the dark for 45 min., changing to a dark red mixture. The mixture was filtered through Celite to remove silver chloride and washed with methylene chloride, then added to a solution of 2-(2,6-diisopropylphenyl)imine-6-bromopyridine (5.0 g, 14.48 mmol) in methylene chloride (5 mL). The dark red-brown solution was transferred to a reaction bomb equipped that was then sealed with a Teflon stopper. The reaction was stirred at 45 °C in the dark for 16 h, then cooled to room temperature. Ethanol (10 mL) was added to quench the reaction and the mixture was concentrated *in vacuo* to yield a viscous brown oil that crystallizes upon standing. The solid was washed with diethyl ether and then recrystallized from diethyl ether/methylene chloride to yield the product as a white solid (5.27 g, 72%). ¹H NMR (CDCl_3 , 300 MHz): δ 9.24 (d, J = 1.8 Hz, 1 H, NC(H)N), 8.48 (d, J = 1.8 Hz, 1 H), 8.33 (d, J = 9.0 Hz, 1 H, *o*-Br), 7.63 (t, J = 8.0 Hz, 1 H, *m*-Br), 7.57 (d, J = 7.2 Hz, 1 H), 7.40–7.33 (m, 3 H), 2.14 (sept, J = 6.6 Hz, 2 H, $\text{CH}(\text{CH}_3)_2$), 1.22 (d, J = 6.6 Hz, 6 H, CH_3), 1.21 (d, J = 6.6 Hz, 6 H, CH_3) ppm. ¹³C NMR (126 MHz, CDCl_3) δ 145.2, 132.7, 132.6, 130.4, 126.6, 125.7, 125.0, 124.0, 119.7, 119.5, 112.0, 28.9, 24.6, 24.4 ppm. HRMS (FAB+, m/z) for $\text{C}_{18}\text{H}_{22}\text{BrN}_2$: 357.0966. Found: 357.0951.

Preparation of DIPr•2HCl.

A reaction bomb equipped with a stir bar was charged with 5-bromo-*N*-(2,6-diisopropylphenyl)imidazo[1,5-*a*]pyridinium triflate (12.915 g, 25.45 mmol), 1,4-benzenediboronic acid (2.11 g, 12.73 mmol), potassium carbonate (10.55 g, 76.36 mmol), toluene (200 mL), ethanol (40 mL), and water (40 mL). The mixture was degassed via three freeze-pump-thaw cycles, then Pd(PPh₃)₄ (0.735 g, 0.636 mmol) was added under N₂. The flask was sealed with a Teflon stopper, then heated to 100 °C for 22 h. The mixture was cooled to room temperature, then the organic were extracted with ethyl acetate and dichloromethane, dried over magnesium sulfate, filtered, then concentrated under reduced pressure. The resulting brown solid was recrystallized from diethyl ether/dichloromethane to yield an off-white solid. The solid was dissolved in dichloromethane (50 mL), then tetrabutylammonium chloride (2.75 g) was added. The mixture was stirred for 2 h, then concentrated under reduced pressure. The residue was taken up in diethyl ether/THF, and the solid was collected, washed with THF, then recrystallized from diethyl ether/chloroform to yield the product as a white solid (2.43 g, 27%). ¹H NMR (CDCl₃, 300 MHz): δ 12.19 (s, 2 H, NC(H)N), 7.99 (d, *J* = 9.3 Hz, 2 H, Ar-H), 7.87 (s, 4 H, central arene), 7.85 (d, *J* = 1.5 Hz, 2 H, Ar-H), 7.56 (t, *J* = 7.8 Hz, 2 H, Ar-H), 7.49 (dd, *J* = 9.3, 6.9 Hz, 2 H, Ar-H), 7.30 (d, *J* = 7.8 Hz, 4 H, Ar-H), 7.25 (d, *J* = 6.9 Hz, 2 H, Ar-H), 2.06 (sept, *J* = 6.9 Hz, 4 H, CH(CH₃)₂), 1.15 (d, *J* = 6.9 Hz, 12 H, CH₃), 1.11 (d, *J* = 6.9 Hz, 12 H, CH₃). ¹³C NMR (CD₂Cl₂, 75.463 MHz): δ 141.7, 135.8, 134.4, 133.6, 131.80, 131.75, 131.0, 129.8, 129.1, 126.0, 118.8, 118.7, 115.7, 21.3, 17.8 ppm. HRMS (FAB+) for C₄₄H₄₈N₄Cl: 667.3567. Found: 667.3560.

Preparation of 5-bromo-2-(2',4',6'-trimethylphenyl)imidazo[1,5a]pyridinium triflate.

The title compound was prepared in the same way as the diisopropylphenyl-substituted variant. ^1H NMR (CDCl_3 , 300 MHz): δ 9.40 (s, 1 H, NC(H)N), 8.30 (s, 1 H), 8.17 (d, $J = 9.3$ Hz, 1 H), 7.51 (d, $J = 7.5$ Hz, 1 H), 7.29 (dd, $J = 7.5, 9.3$ Hz, 1 H), 7.07 (s, 2 H, $\text{C}_6\text{Me}_3\text{H}_2$), 2.38 (s, 3 H, $p\text{-Me}$), 2.05 (s, 6 H, $o\text{-Me}$) ppm.

Preparation of DIMes•2HCl.

The title compound was prepared in the same manner as DIPr•2HCl. ^1H NMR (CD_2Cl_2 , 300 MHz): δ 11.61 (s, 2 H, NC(H)N), 8.08 (d, $J = 7.8$ Hz, 2 H), 8.06 (s, 2 H), 7.90 (s, 4 H), 7.45 (dd, $J = 9.3, 6.9$ Hz, 2 H), 7.21 (d, $J = 6.9$ Hz, 2 H), 7.04 (s, 4 H), 2.35 (s, 6 H, CH_3), 2.04 (s, 12 H, CH_3) ppm. ^{13}C NMR (CD_2Cl_2): δ 211.36, 141.72, 135.81, 134.45, 133.56, 131.78, 131.73, 130.94, 129.82, 129.05, 126.01, 118.78, 118.72, 115.68, 21.30, 17.82 ppm.

Preparation of 5-bromo-2-(4'-fluorophenyl)imidazo[1,5a]pyridinium triflate.

The title compound was prepared in the same way as the diisopropylphenyl-substituted variant. ^1H NMR (CDCl_3 , 300 MHz): δ 9.79 (s, 1 H), 8.53 (s, 1 H), 7.90 (m, 6 H), 7.41 (d, 7.5 Hz, 1 H), 7.28 (m, 2 H), 7.19 (m, 1 H) ppm. ^{19}F NMR (CDCl_3): δ -78.4 (3 F, OTf), -107.4 (1 F, ArF) ppm.

Preparation of DIPr[CuCl] $_2$ (A.2).

In the glovebox, a scintillation vial equipped with a stir bar was charged with DIPr•2HCl (0.040 g, 0.057 mmol), sodium *tert*-butoxide (0.011 g, 0.11 mmol, 2 equiv), and copper(I) chloride (0.011 g, 0.11 mmol, 2 equiv). THF (5 mL) was added, and the yellow mixture was stirred at room temperature for 2 h. The mixture was filtered through Celite to remove an insoluble yellow precipitate, and the yellow filtrate was concentrated *in vacuo*. The mixture was washed with benzene, then extracted with THF and concentrated again under

reduced pressure to yield a yellow solid. This solid was washed with acetonitrile to yield the product as a yellow solid (0.011 g, 23%). ^1H NMR (CD_2Cl_2 , 400 MHz): δ 7.79 (s, 4 H, central arene), 7.52 (d, $J = 7.6$ Hz, 2 H, Ar-H), 7.48 (d, $J = 9.6$ Hz, 2 H, Ar-H), 7.38 (s, 2 H, benzylic H), 7.30 (d, $J = 8.0$ Hz, 4 H, Ar-H), 7.13–7.09 (m, 4 H, Ar-H), 2.26 (sept, $J = 6.8$ Hz, 4 H, $\text{CH}(\text{CH}_3)_2$), 1.20 (d, $J = 6.8$ Hz, 12 H, CH_3), 1.14 (d, $J = 6.8$ Hz, 12 H, CH_3) ppm. ^{13}C NMR (CD_2Cl_2 , 101 MHz): δ 145.8, 139.4, 136.3, 136.2, 132.1, 130.1, 130.7, 124.4, 124.3, 117.3, 116.6, 114.3, 28.7, 24.7, 24.4 ppm. Anal. Calcd. For $\text{C}_{44}\text{H}_{46}\text{Cl}_2\text{Cu}_2\text{N}_4$: C, 63.76; H, 5.59; N, 6.76 %. Found: C, 63.51; H, 5.31; N, 6.51 %.

Preparation of $\text{DIPr}[\text{Co}(\text{Cl})\text{N}(\text{SiMe}_3)_2]_2$ (A.3).

In the glovebox, a scintillation vial equipped with a stir bar was charged with $\text{DIPr}\cdot 2\text{HCl}$ (0.046 g, 0.065 mmol) and $\text{Co}[\text{N}(\text{SiMe}_3)_2]_2$ (0.050 g, 0.13 mmol, 2 equiv). Benzene (6 mL) was added, and the green mixture was stirred for 12 h, then filtered through Celite and concentrated under reduced pressure. The yellow-brown residue was washed with pentane, then extracted with diethyl ether and concentrated in vacuo. A benzene solution was allowed to stand at room temperature, slowly forming the product as yellow crystals (0.008 g, 11%). This procedure has not been optimized. ^1H NMR (C_6D_6 , 300 MHz): δ 89.0, 64.6, 36.1, 10.1 (bs), 3.3, -2.3, -7.2, -15.2, -51.1, -54.8 (bs), -70.0 (bs) ppm.

Preparation of $\text{DIPr}[\text{Ni}(\mu\text{-Cl})]_2$ (A.4).

In the glovebox, a round-bottom flask equipped with a stir bar was charged with $\text{DIPr}\cdot 2\text{HCl}$ (1.18 g, 1.68 mmol), sodium *tert*-butoxide (0.327 g, 3.4 mmol), nickel bis(cyclooctadiene) (0.459 g, 1.67 mmol), and nickel dichloride dimethoxyethane adduct (0.367 g, 1.67 mmol). THF (100 mL) was added, and the brown mixture was stirred at room temperature for 12 h. The dark brown mixture was filtered through Celite, washing

with THF (50 mL), and the filtrate was concentrated *in vacuo*. The brown residue was taken up in benzene (60 mL), filtered through Celite, then concentrated *in vacuo*. The resulting brown solid was washed with pentane (30 mL), and dried under vacuum to yield the product as a brown solid (0.300 g, 22%). This yield has not yet been optimized. ^1H NMR (C_6D_6 , 500 MHz): δ 14.34 (s, 4 H, central arene), 8.49 (s, 2 H, benzylic H), 7.59 (d, J = 7.0 Hz, 4 H, Ar-H), 7.53 (t, J = 7.0 Hz, 2 H, Ar-H), 7.19 (d, J = 9.5 Hz, 2 H, Ar-H), 6.94 (d, J = 6.5 Hz, 2 H, Ar-H), 5.86 (dd, J = 6.5, 9.5 Hz, 2 H, Ar-H), 2.86 (sept, J = 6.5 Hz, 4 H, $\text{CH}(\text{CH}_3)_2$), 1.64 (d, J = 6.5 Hz, 12 H, CH_3), 1.12 (d, J = 6.5 Hz, 12 H, CH_3) ppm. ^{13}C NMR (C_6D_6 , 126 MHz): δ 157.4, 150.7, 150.0, 149.4, 148.7, 147.9, 147.4, 147.2, 131.1, 125.0, 122.3, 117.4, 109.3, 33.18, 27.8, 25.6 ppm.

Preparation of $\text{DIPr}[\text{Ni}(\text{COD})]_2$ (A.5).

In the glovebox, an oven-dried round-bottom flask equipped with a stir bar was charged with $\text{DIPr}\cdot 2\text{HCl}$ (0.200 g, 0.284 mmol), sodium *tert*-butoxide (0.055 g, 0.572 mmol, 2 equiv), and $\text{Ni}(\text{COD})_2$ (0.150 g, 0.546 mmol, 1.9 equiv). Benzene (40 mL) was added, and the mixture was stirred for 90 min. at room temperature, turning from yellow to green to dark brown. The mixture was then filtered through Celite, then concentrated *in vacuo* to yield a dark brown solid. This residue was washed with hexanes (50 mL) and diethyl ether (10 mL), then dried under vacuum to yield the product as a dark brown solid (0.150 g, 55%). Due to the equilibrium between **A.5** and **A.6** in benzene solution, NMR spectra were collected after the addition of 2 equivalents of excess 1,5-cyclooctadiene. ^1H NMR (C_6D_6 , 400 MHz): δ 7.26 (t, J = 7.6 Hz, 2 H, Ar-H), 7.13 (d, J = 7.6 Hz, 4 H, Ar-H), 6.79 (s, 2 H, Ar-H), 6.65 (d, J = 8.8 Hz, 2 H, Ar-H), 6.45 (d, J = 6.4, 10.4 Hz, 2 H, Ar-H), 6.34 (d, J = 6.8 Hz, 2 H, Ar-H), 6.25 (bs, 4 H, central arene), 4.2 (bs, 8 H, $\text{Ni}(\text{COD})$ vinyl H), 2.82

(sept, $J = 6.8$ Hz, 4 H, $\text{CH}(\text{CH}_3)_2$), 1.9 (bs, 12 H, Ni(COD) methylene H), 1.28 (d, $J = 6.8$ Hz, 12 H, CH_3), 0.96 (d, $J = 6.8$ Hz, 12 H, CH_3) ppm. ^{13}C NMR (C_6D_6 , 100.5 MHz): δ 194.33, 148.09, 146.27, 138.10, 130.78, 129.74, 128.83, 125.14, 123.75, 112.49, 111.88, 106.14, 81.04, 30.70, 28.72, 26.54, 22.36 ppm.

Preparation of $\text{DIPr}[\text{Ni}(\text{C}_6\text{H}_6)]_2$ (A.6).

Procedure A: In the glovebox, a scintillation vial equipped with a stir bar was charged with a solution of $\text{DIPr}\cdot 2\text{HCl}$ (0.272 g, 0.333 mmol) in THF (10 mL). A 1 M THF solution of LiBEt_3H (0.67 mL, 0.666 mmol) was added via syringe. The mixture was stirred at room temperature for 10 min. and the mixture was concentrated *in vacuo*. The brown residue was taken up in benzene, filtered through Celite, then concentrated *in vacuo*. The resulting solid was washed with hexanes and diethyl ether to yield the product as a brown solid (0.074 g, 25%). ^1H NMR (C_6D_6 , 500 MHz): δ 7.15 (2 H, overlapped with solvent residual peak, identified by gCOSY), 7.07 (d, $J = 7.5$ Hz, 2 H, Ar-H), 6.99 (d, $J = 7.5$ Hz, 2 H, Ar-H), 6.89 (d, $J = 6.5$ Hz, 2 H, Ar-H), 6.85 (d, $J = 9.0$ Hz, 2 H, Ar-H), 6.80 (s, 2 H, Ar-H), 6.56 (t, $J = 8.0$ Hz, 2 H, Ar-H), 5.56 (s, 2 H, central arene H), 3.53 (s, 2 H, central arene H), 2.63 (sept, $J = 7.0$ Hz, 2 H, $\text{CH}(\text{CH}_3)_2$), 2.17 (sept, $J = 7.0$ Hz, 2 H, $\text{CH}(\text{CH}_3)_2$), 1.15 (d, $J = 7.0$ Hz, 6 H, CH_3), 1.01 (d, $J = 7.0$ Hz, 6 H, CH_3), 0.93 (d, $J = 7.0$ Hz, 6 H, CH_3), 0.91 (d, $J = 7.0$ Hz, 6 H, CH_3) ppm. ^{13}C NMR (C_6D_6 , 500 MHz): δ 129.4, 147.6, 147.1, 145.4, 137.3, 130.7, 129.7, 125.3, 123.8, 123.5, 112.8, 112.4, 106.8, 105.7, 97.3, 42.4, 28.6, 28.5, 26.7, 24.7, 24.2, 22.6 ppm.

Procedure B: In the glovebox, a Schlenk flask equipped with a stir bar was charged with a benzene solution of A.5. The solution was degassed with three freeze-pump-thaw cycles, then placed under an atmosphere of dihydrogen. The reaction mixture was stirred for 30

min. at room temperature, then dried *in vacuo*. The resulting brown solid was washed with pentane to yield the product as a brown solid (0.023 g, 82%).

Preparation of DIPr[Ni(μ_2 -CO)]₂ (A.7).

Procedure A: In the glovebox, a J. Young NMR tube was charged with a solution of **A.6** (0.017 g, 0.019 mmol) in C₆D₆ (0.7 mL). The solution was degassed via three freeze-pump-thaw cycles, then placed under an atmosphere of CO₂. The reaction was allowed to proceed at room temperature, and monitored by ¹H NMR spectroscopy. Compound **A.7** was identified as the major species in the mixture by ¹H NMR spectroscopy after 20 h.

Procedure B: In the glovebox, a scintillation vial equipped with a stir bar was charged with **A.5** (0.021 g, 0.022 mmol) and paraformaldehyde (0.015 g, 0.044 mmol, 2 equiv). THF (5 mL) was added, and the brown mixture was stirred at room temperature for 1 h, turning dark purple. The mixture was concentrated *in vacuo*, then crystallized from diethyl ether/pentane to yield the product as a brown-purple solid (0.008 g, 47%). ¹H NMR (C₆D₆, 500 MHz): δ 7.10 (t, J = 7.0 Hz, 2 H, Ar-H), 7.03 (d, J = 7.0 Hz, 4 H, Ar-H), 6.81 (s, 2 H, Ar-H), 6.74 (dd, J = 2.0, 7.8 Hz, 2 H, Ar-H), 6.38 (m, 4 H, Ar-H), 6.24 (bs, 4 H, central arene), 2.64 (sept, J = 7.0 Hz, 4 H, CH(CH₃)₂), 1.27 (d, J = 7.0 Hz, 12 H, CH₃), 0.99 (d, J = 7.0 Hz, 12 H, CH₃) ppm. ¹³C NMR (C₆D₆, 126 MHz): δ 184.9, 145.5, 142.9, 137.4, 129.8, 127.2, 124.1, 123.8, 115.0, 114.3, 112.5, 109.9, 98.3 (bs, located at 50 °C). 28.6, 24.8, 23.8 ppm. The ¹³C signal corresponding to the carbonyl ligands could not be located, presumably due to fluxional exchange processes. FT-IR (ATR film, C₆D₆): 1825 cm⁻¹ (CO).

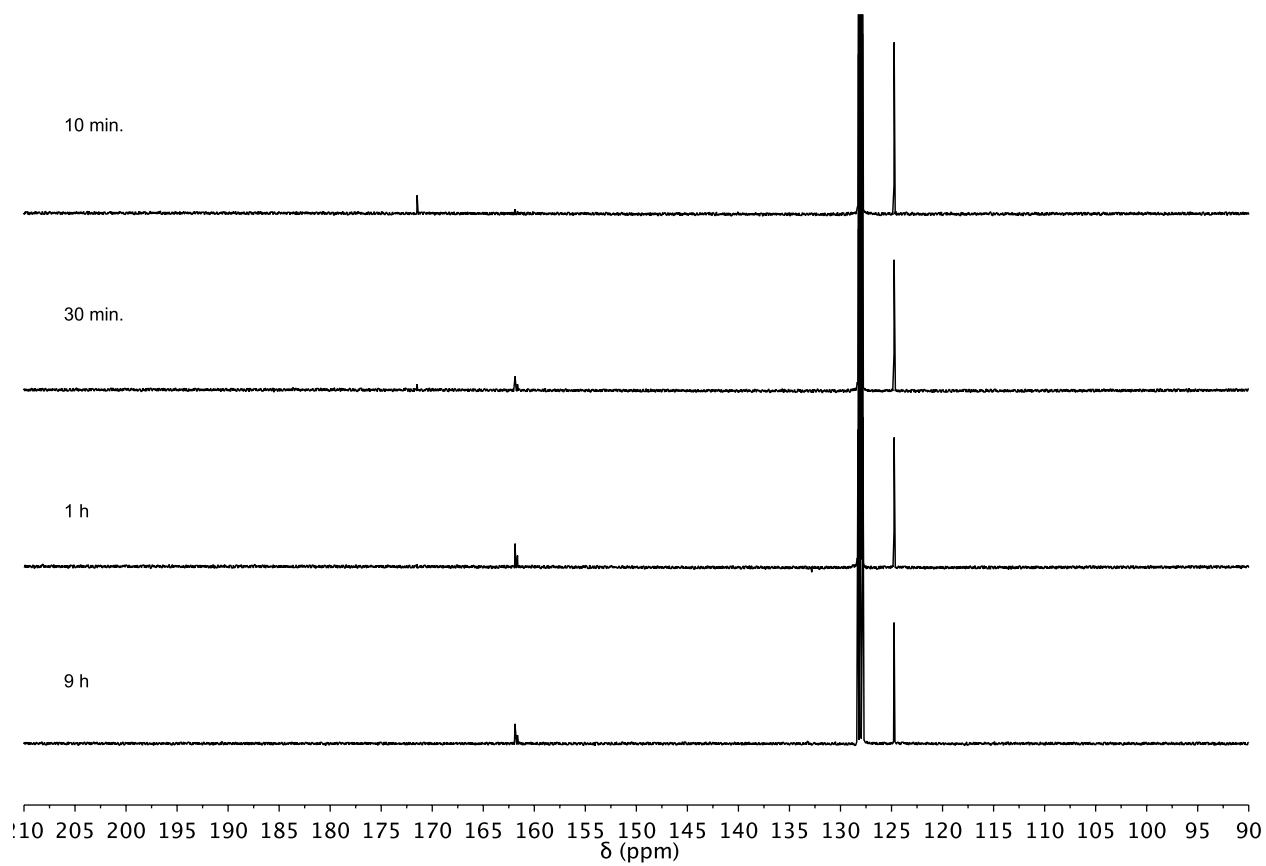


Figure 8. ^{13}C NMR spectra over time of addition of excess $^{13}\text{CO}_2$ to **A.5** in C_6D_6 .

Crystallographic Information

CCDC 999595-999599 contain the supplementary crystallographic data for this chapter.

Table 1. Crystal and refinement data for reported complexes.

| | A.2 | A.3 | A.4 | A.5 | A.7 | A.8 |
|--|--|---|--|--|--|--|
| empirical formula | C ₄₆ H ₅₀ Br _{1.37} C | C ₁₀₄ H ₁₃₀ Cl ₂ C | C ₄₉ H ₅₆ Cl ₂ N ₄ | C ₆₃ H ₇₃ N ₄ Ni ₂ | C ₅₀ H ₅₆ N ₄ Ni ₂ | C ₆₆ H ₇₀ N ₄ Ni ₃ |
| formula | I _{4.64} Cu ₂ N ₄ | O ₂ N ₆ Si ₄ | Ni ₂ | | O ₃ | |
| wt | 1059.59 | 1765.26 | 889.30 | 1003.67 | 878.41 | 1096.39 |
| T (K) | 100 | 100 | 100 | 100 | 100 | 100 |
| a, Å | 10.4614(4) | 11.973(2) | 16.723(1) | 16.237(2) | 13.792(2) | 20.560(1) |
| b, Å | 20.3391(8) | 13.496(2) | 15.480(1) | 16.4657(8) | 17.418(2) | 17.9058(9) |
| c, Å | 10.9427(4) | 16.495(3) | 19.180(1) | 20.628(1) | 17.948(2) | 14.9536(7) |
| α, deg | 90 | 71.164(2) | 90 | 90 | 90 | 90 |
| β, deg | 95.206(2) | 82.751(5) | 114.167(1) | 112.705(2) | 160.03(4) | 90 |
| γ, deg | 90 | 83.297(4) | 90 | 90 | 90 | 90 |
| V, Å ³ | 2318.7(2) | 2494.2(7) | 4530.1(6) | 5087.5(4) | 4143.8(8) | 5505.2(5) |
| Z | 2 | 1 | 4 | 4 | 4 | 4 |
| cryst syst | Monoclinic | Triclinic | Monoclinic | Monoclinic | Monoclinic | Orthorhombic |
| space group | P2 ₁ /n | P-1 | P2 ₁ /n | P2 ₁ /c | P2 ₁ /c | Pnma |
| d _{calcd} , g/cm ³ | 1.518 | 1.175 | 1.304 | 1.310 | 1.408 | 1.322 |
| θ range, deg | 2.00-39.54 | 1.60-35.27 | 1.76-39.17 | 1.84-37.81 | 1.54 to 29.46 | 1.68-36.56 |
| μ, mm ⁻¹ | 2.401 | 0.482 | 0.987 | 0.785 | 0.958 | 1.060 |
| abs cor | Semi-empirical from equivalents | None | Semi-empirical from equivalents | Semi-empirical from equivalents | Semi-empirical from equivalents | None |
| GOF ^c | 1.676 | 0.993 | 1.406 | 1.397 | 2.042 | 0.982 |
| R1, ^a wR2 ^b (I > 2σ(I)) | 0.0451, 0.1273 | 0.0461, 0.0682 | 0.0559, 0.1555 | 0.0644, 0.1890 | 0.0946, 0.1598 | 0.0408, 0.1166 |

$$^a R1 = \sum ||F_o| - |F_c|| / \sum |F_o| \quad ^b wR2 = \{ \sum [w(F_o^2 - F_c^2)^2] / \sum [w(F_o^2)^2] \}^{1/2} \quad ^c GOF = S = \{ \sum [w(F_o^2 - F_c^2)^2] / (n-p) \}^{1/2}$$

Refinement Details

In each case, crystals were mounted on a glass fiber or nylon loop using Paratone oil, then placed on the diffractometer under a nitrogen stream. Low temperature (100 K) X-

ray data were obtained on a Bruker APEXII CCD based diffractometer (Mo sealed X-ray tube, $K_{\alpha} = 0.71073 \text{ \AA}$). All diffractometer manipulations, including data collection, integration and scaling were carried out using the Bruker APEXII software.²⁸ Absorption corrections were applied using SADABS.²⁹ Space groups were determined on the basis of systematic absences and intensity statistics and the structures were solved by direct methods using XS³⁰ (incorporated into SHELXTL) and refined by full-matrix least squares on F^2 . All non-hydrogen atoms were refined using anisotropic displacement parameters. Hydrogen atoms were placed in idealized positions and refined using a riding model. The structure was refined (weighted least squares refinement on F^2) to convergence.

Special refinement details for $\text{DIPr}[\text{CuX}]_2$ (A.2)

Because the compound was synthesized from the bromide salt of the ligand precursor and with copper(I) chloride, the structure contains a mixture of halides and the two copper centers, which were related by symmetry, were each modelled in two different positions. Upon refinement of the populations, the $[\text{CuBr}]:[\text{CuCl}]$ ratio was found to be about 70%. The Cu–X distances ($2.210(5) \text{ \AA}$ for $\text{X} = \text{Cl}$, $2.225(1) \text{ \AA}$ for $\text{X} = \text{Br}$) are reasonable based upon a CCDC structure search of NHC copper complexes. An additional molecule of CH_2Cl_2 was found in the structure and appropriately modelled.

Special refinement details for $\text{DIPr}[\text{Co}(\text{Cl})\text{N}(\text{SiMe}_3)_2]_2$ (A.3)

Four solvent benzene molecules were found in the asymmetric unit and appropriately modelled.

Special refinement details for $\text{DIPr}[\text{NiCl}]_2$ (A.4)

One solvent pentane molecule was located in the lattice and appropriately modelled.

Special refinement details for $\text{DIPr}[\text{Ni}(\text{COD})_2]_2$ (A.5)

One solvent molecule was located in the asymmetric unit and modelled using DFIX and DANG restraints as a benzene molecule. The cyclooctadiene ligand coordinated to Ni2 was found to be disordered and modelled in two positions. Refinement of the populations showed a 54% occupancy in one position.

Special refinement details for $\text{DIPr}[\text{Ni}(\text{CO})]_2$ (A.7)

One solvent molecule was located in the asymmetric unit and was modelled as a diethyl ether molecule.

Special refinement details for A.8.

There is a solvent molecule of *n*-hexane located in the lattice that is disordered in two positions about a center of symmetry. The molecule was modelled using DFIX and DANG constraints as a hexane molecule using the PART -1 operator. Additionally, SIMU and DELU restraints were used to appropriately restrain the thermal displacement parameters of C39 in the disordered hexane molecule.

References

1. Gavrilova, A. L.; Bosnich, B. *Chem. Rev.* **2004**, *104*, 349-384.
2. (a) Velian, A.; Lin, S.; Miller, A. J. M.; Day, M. W.; Agapie, T. *J. Am. Chem. Soc.* **2010**, *132*, 6296-6297; (b) Lin, S.; Day, M. W.; Agapie, T. *J. Am. Chem. Soc.* **2011**, *133*, 3828-3831; (c) Lin, S.; Herbert, D. E.; Velian, A.; Day, M. W.; Agapie, T. *J. Am. Chem. Soc.* **2013**, *135*, 15830-15840; (d) Horak, K. T.; Velian, A.; Day, M. W.; Agapie, T. *Chem. Commun.* **2014**, *50*, 4427-4429.
3. Dible, B. R.; Sigman, M. S.; Arif, A. M. *Inorg. Chem.* **2005**, *44*, 3774-3776.
4. (a) Arduengo, A. J.; Harlow, R. L.; Kline, M. *J. Am. Chem. Soc.* **1991**, *113*, 361-363; (b) Herrmann, W. A.; Köcher, C. *Angew. Chem. Int. Ed.* **1997**, *36*, 2162-2187; (c) Díez-González, S.; Marion, N.; Nolan, S. P. *Chem. Rev.* **2009**, *109*, 3612-3676; (d) Fortman, G. C.; Nolan, S. P. *Chem. Soc. Rev.* **2011**, *40*, 5151-5169.
5. (a) Mata, J. A.; Poyatos, M.; Peris, E. *Coord. Chem. Rev.* **2007**, *251*, 841-859; (b) Pugh, D.; Danopoulos, A. A. *Coord. Chem. Rev.* **2007**, *251*, 610-641; (c) Poyatos, M.; Mata, J. A.; Peris, E. *Chem. Rev.* **2009**, *109*, 3677-3707.
6. (a) Scheele, U. J.; John, M.; Dechert, S.; Meyer, F. *Eur. J. Inorg. Chem.* **2008**, *2008*, 373-377; (b) Lee, K.-M.; Chen, J. C. C.; Lin, I. J. B. *J. Organomet. Chem.*

- 2001**, 617–618, 364–375; (c) Scheele, U. J.; Dechert, S.; Meyer, F. *Inorg. Chim. Acta* **2006**, 359, 4891–4900; (d) Scheele, U. J.; Dechert, S.; Meyer, F. *Tetrahedron Lett.* **2007**, 48, 8366–8370; (e) Li, Y.; Yang, L.; Chen, Q.; Cao, C.; Guan, P.; Pang, G.; Shi, Y. *Z. Anorg. Allg. Chem.* **2013**, 639, 575–581; (f) Liu, B.; Chen, C.; Zhang, Y.; Liu, X.; Chen, W. *Organometallics* **2013**, 32, 5451–5460; (g) Reindl, S. A.; Poethig, A.; Drees, M.; Bechlars, B.; Herdtweck, E.; Herrmann, W. A.; Kuehn, F. E. *Organometallics* **2013**, 32, 4082–4091; (h) Yang, L.; Zhao, J.; Li, Y.; Ge, K.; Zhuang, Y.; Cao, C.; Shi, Y. *Inorg. Chem. Commun.* **2012**, 22, 33–36; (i) Zhao, J.; Yang, L.; Ge, K.; Chen, Q.; Zhuang, Y.; Cao, C.; Shi, Y. *Inorg. Chem. Commun.* **2012**, 20, 326–329; (j) Zhou, Y.; Xi, Z.; Chen, W.; Wang, D. *Organometallics* **2008**, 27, 5911–5920.
7. Burstein, C.; Lehmann, C. W.; Glorius, F. *Tetrahedron* **2005**, 61, 6207–6217.
 8. Jurkauskas, V.; Sadighi, J. P.; Buchwald, S. L. *Org. Lett.* **2003**, 5, 2417–2420.
 9. Mankad, N. P.; Gray, T. G.; Laitar, D. S.; Sadighi, J. P. *Organometallics* **2004**, 23, 1191–1193.
 10. (a) Danopoulos, A. A.; Braunstein, P.; Stylianides, N.; Wesolek, M. *Organometallics* **2011**, 30, 6514–6517; (b) Danopoulos, A. A.; Braunstein, P. *Dalton Transactions* **2013**, 42, 7276–7280.
 11. Lee, C. H.; Laitar, D. S.; Mueller, P.; Sadighi, J. P. *J. Am. Chem. Soc.* **2007**, 129, 13802–13803.
 12. Suseno, S.; Horak, K. T.; Day, M. W.; Agapie, T. *Organometallics* **2013**, 32, 6883–6886.
 13. Jeoung, J.-H.; Dobbek, H. *Science* **2007**, 318, 1461–1464.
 14. Aresta, M.; Nobile, C. F.; Albano, V. G.; Forni, E.; Manassero, M. *J. Chem. Soc., Chem. Commun.* **1975**, 636–637.
 15. (a) Bianchini, C.; Mealli, C.; Meli, A.; Sabat, M. *Inorg. Chem.* **1984**, 23, 2731–2732; (b) Anderson, J. S.; Iluc, V. M.; Hillhouse, G. L. *Inorg. Chem.* **2010**, 49, 10203–10207.
 16. Fullmer, B. C.; Fan, H.; Pink, M.; Caulton, K. G. *Inorg. Chem.* **2008**, 47, 1865–1867.
 17. Horn, B.; Limberg, C.; Herwig, C.; Braun, B. *Chem. Commun.* **2013**, 49, 10923–10925.
 18. (a) DeLaet, D. L.; Del Rosario, R.; Fanwick, P. E.; Kubiak, C. P. *J. Am. Chem. Soc.* **1987**, 109, 754–758; (b) Ratliff, K. S.; Lentz, R. E.; Kubiak, C. P. *Organometallics* **1992**, 11, 1986–1988; (c) Simón-Manso, E.; Kubiak, C. P. *Organometallics* **2004**, 24, 96–102.
 19. Jutzi, P.; Redeker, T.; Neumann, B.; Stammeler, H.-G. *J. Organomet. Chem.* **1995**, 498, 127–137.
 20. Horn, B.; Limberg, C.; Herwig, C.; Feist, M.; Mebs, S. *Chem. Commun.* **2012**, 48, 8243–8245.
 21. Hatnean, J. A.; Beck, R.; Borrelli, J. D.; Johnson, S. A. *Organometallics* **2010**, 29, 6077–6091.
 22. (a) Deeming, A. J.; Underhill, M. *J. Chem. Soc., Dalton Trans.* **1974**, 1415–1419; (b) Goudsmit, R. J.; Johnson, B. F. G.; Lewis, J.; Raithby, P. R.; Rosales, M. J. *J. Chem. Soc., Dalton Trans.* **1983**, 2257–2261; (c) Bradford, C. W.; Nyholm, R. S.; Gainsford, G. J.; Guss, J. M.; Ireland, P. R.; Mason, R. *J. Chem. Soc., Chem.*

- Commun.* **1972**, 87-89; (d) Gainsford, G. J.; Guss, J. M.; Ireland, P. R.; Mason, R.; Bradford, C. W.; Nyholm, R. S. *J. Organomet. Chem.* **1972**, 40, C70-C72; (e) Deeming, A. J.; Kimber, R. E.; Underhill, M. *J. Chem. Soc., Dalton Trans.* **1973**, 2589-2595; (f) Deeming, A. J.; Rothwell, I. P.; Hursthouse, M. B.; Backer-Dirks, J. D. *J. Chem. Soc., Dalton Trans.* **1981**, 1879-1885.
23. Bruce, M. I.; Guss, J. M.; Mason, R.; Skelton, B. W.; White, A. H. *J. Organomet. Chem.* **1983**, 251, 261-271.
24. (a) Bennett, M. A.; Griffiths, K. D.; Okano, T.; Parthasarathi, V.; Robertson, G. B. *J. Am. Chem. Soc.* **1990**, 112, 7047-7048; (b) Keen, A. L.; Doster, M.; Johnson, S. A. *J. Am. Chem. Soc.* **2007**, 129, 810-819.
25. Andersen, R. A.; Faegri, K.; Green, J. C.; Haaland, A.; Lappert, M. F.; Leung, W. P.; Rypdal, K. *Inorg. Chem.* **1988**, 27, 1782-1786.
26. Lemonnier, J.-F. o.; Guénée, L.; Bernardinelli, G. r.; Vigier, J.-F. o.; Bocquet, B.; Piguet, C. *Inorg. Chem.* **2010**, 49, 1252-1265.
27. Irrgang, T.; Keller, S.; Maisel, H.; Kretschmer, W.; Kempe, R. *Eur. J. Inorg. Chem.* **2007**, 2007, 4221-4228.
28. *APEX2*, Bruker Analytical X-ray Systems: Madison, WI, 2006.
29. Sheldrick, G. M. *SADABS*, 2008/l; University of Göttingen, 2008.
30. Sheldrick, G. *Acta Crystallogr. A* **2008**, 64, 112-122.

*Appendix B*SYNTHESIS AND PRELIMINARY METALLATION REACTIONS OF AN
ASYMMETRIC MULTINUCLEATING LIGAND FRAMEWORK

Abstract

To prepare a more accurate structural mimic of the oxygen-evolving complex of photosystem II, it is necessary to desymmetrize the heterometallic trimanganese tetraoxido cubane complexes discussed in Chapter 4 and to incorporate a fourth manganese center to the cluster. One possible strategy to effect this transformation is to desymmetrize the multinucleating ligand at the base of the cluster that coordinates to the three manganese centers. In this chapter, asymmetric variants of the H_3L ligand used in previous chapters of this dissertation were designed and prepared. Preliminary metallation reactions of these ligand variants are also discussed.

Introduction

As described in previous chapters, the oxygen-evolving complex (OEC) of photosystem II is known to be a CaMn_4O_x cluster in which a CaMn_3 subsite is bridged to a fourth manganese center via oxide ligands (see Chapter 1).¹ Although our group has synthesized heterometallic trimanganese tetraoxido complexes that structurally resemble the cubane-like CaMn_3 subsite (Chapter 4),² these complexes are all pseudo- C_3 -symmetric, unlike the actual OEC. Christou and co-workers have recently isolated a $\text{Ca}_2\text{Mn}_3\text{O}_4$ cluster in which a second calcium center is located near a CaMn_3O_4 cubane.³ The authors stated that the distortion in the cubane cluster caused by the second Ca^{2+} center makes the compound more structurally relevant to the OEC. These distortions may lead to spectroscopic changes that would more accurately parallel the biological system.

Altering one face of the threefold-symmetric cubane cluster may allow selective addition of one manganese center that would then become a model of the full structure of the OEC (Fig. 1). As such, there have been many different efforts within our group to explore ways to access asymmetric variants of the $[\text{MMn}_3\text{O}_4]$ clusters that we have previously prepared and characterized.

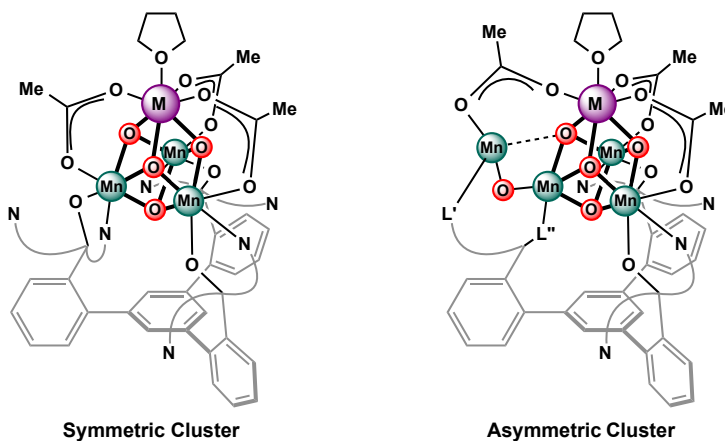


Figure 1. Desymmetrization of $[\text{MMn}_3\text{O}_4]$ cubane clusters.

In this chapter, we explore one strategy for desymmetrization of the cubane clusters. Namely, we target changes in one “arm” of the H₃L ligand framework used to support the [MMn₃O₄] clusters discussed in Chapter 4. Two different ligand precursors with different donor moieties rather than the dipyridylalkoxy group of the multinucleating ligand framework were prepared, and preliminary metallation reactions are discussed. Although this is a promising strategy, additional studies will be necessary to know whether it is viable in comparison to other strategies currently explored in the group.

Results and Discussion

B.1 Ligand design and synthesis

We envisioned that desymmetrization of the cubane architecture could be achieved by modifying the multinucleating ligand framework that supports the basal trimanganese core. After the assembly of the cubane core, the only donors to manganese from the multinucleating ligand are a terminal alkoxide group and a pyridyl donor, it may be possible to functionalize the pendant arm to add additional donors (Fig. 2). The functionalized aryl “arm” could then still support one manganese center in the cubane core while the additional donors could bridge to a fourth manganese center. A carboxylate moiety would be particularly desirable in this position, as in the biological OEC structure there is a carboxylate ligand bridging from the CaMn₃ subsite to the dangler manganese center.^{1a}

The targeted asymmetric ligand framework was prepared in four steps from tribromide **B.1** that was previously described in Chapter 2 (Scheme 1). Compound **B.1** was selectively monolithiated via lithium-halogen exchange using *n*-butyllithium, then quenched with *N,N*-dimethylformamide (DMF) to form the monoaldehyde dibromide product (**B.2**). The

aldehyde moiety was functionalized with an acetal protecting group upon condensation with ethylene glycol (**B.3**). The remaining two bromide moieties of acetal **B.3** were lithiated via lithium-halogen exchange using *tert*-butyllithium and quenched with dipyridylketone to yield the tetrapyridyl aldehyde product (**B.4**). Compound **B.4** was used as a versatile starting material for later ligand precursors, since the aldehyde moiety is easily functionalized to accommodate other donors.

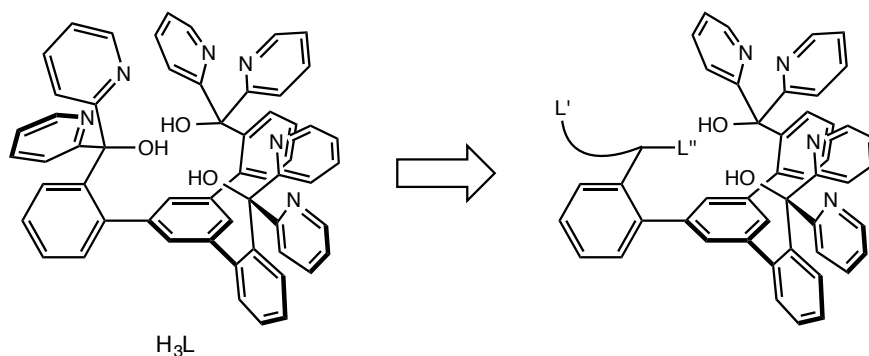
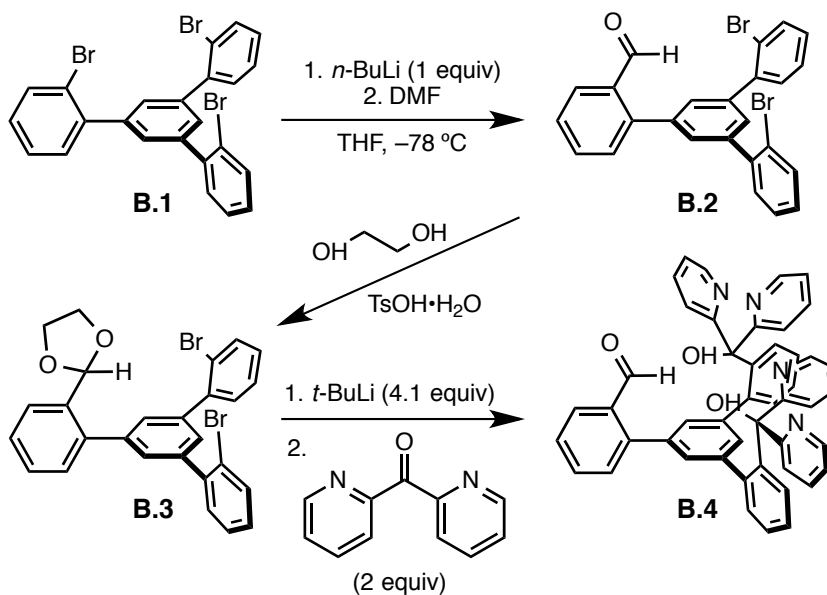


Figure 2. Desymmetrization of ligand framework and general targeted ligand geometry.

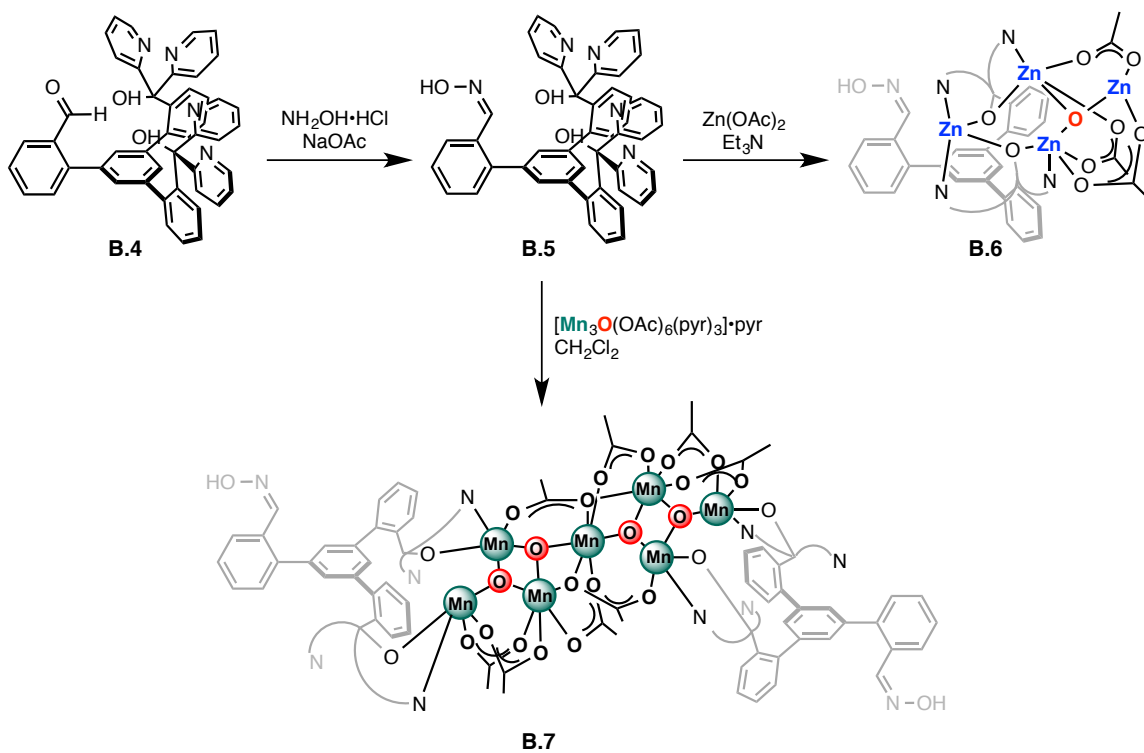


Scheme 1. Synthesis of asymmetric **B.4**.

B.2 Metallation of monooxime ligand

The first ligand precursor targeted was an oxime donor, since there are several examples of heterometallic manganese complexes supported by oxime ligands.⁴ Monooxime **B.5** was prepared by facile condensation with hydroxylamine hydrochloride and **B.4** in the presence of sodium acetate as a base (Scheme 2). Upon treatment with $\text{Zn}(\text{OAc})_2$ in the presence of triethylamine to deprotonate the oxime and hydroxyl moieties, a tetrazinc(II) complex was formed (Figure 3, **B.6**). Unfortunately, in this instance the oxime group was not deprotonated and did not coordinate to a metal center. Instead, the two dipyridylalkoxy arms coordinate three Zn^{2+} centers. The fourth Zn^{2+} center is bridged to two of the other zinc centers via a μ_3 -oxido (or hydroxo) bridge and bridging acetate ligands. There are many related structures found in the Cambridge Structural Database.

Compound **B.5** was also treated with a trimanganese μ_3 -oxido cluster⁵ in the hope that the preformed trinuclearity would be maintained in the final product. Unfortunately, X-ray quality single crystals of the product of this reaction revealed the structure to be a higher nuclearity heptamanganese compound instead (Figure 4, **B.7**). Again, the oxime moieties were found to be not coordinated to the metal centers and presumably are still protonated. Future work will include first deprotonating the metal centers prior to treatment with transition metal sources, in the hope that the oximate moiety may be more coordinating.



Scheme 2. Synthesis and reactions of oxime ligand **B.5**.

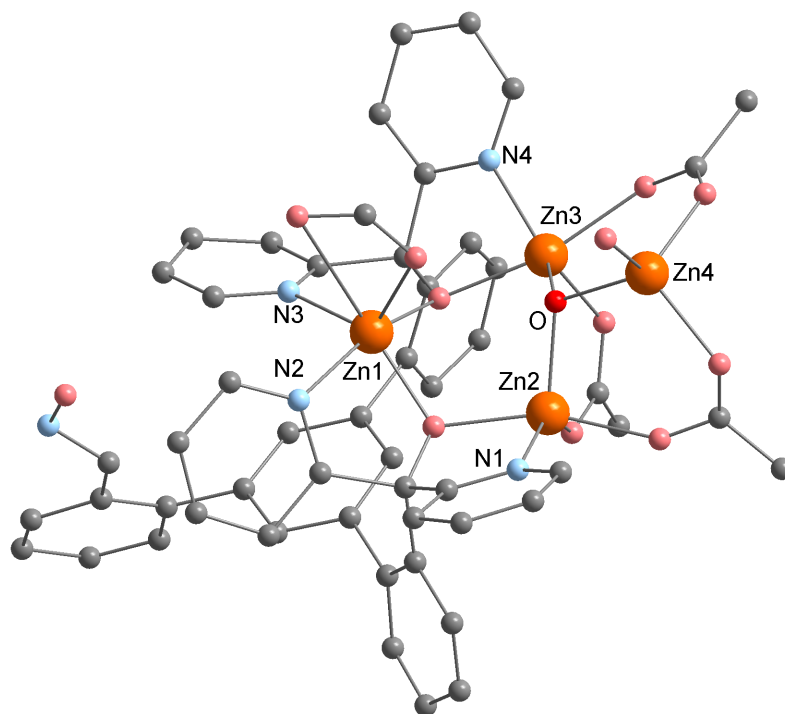


Figure 3. Preliminary solid-state structure of **B.6**.

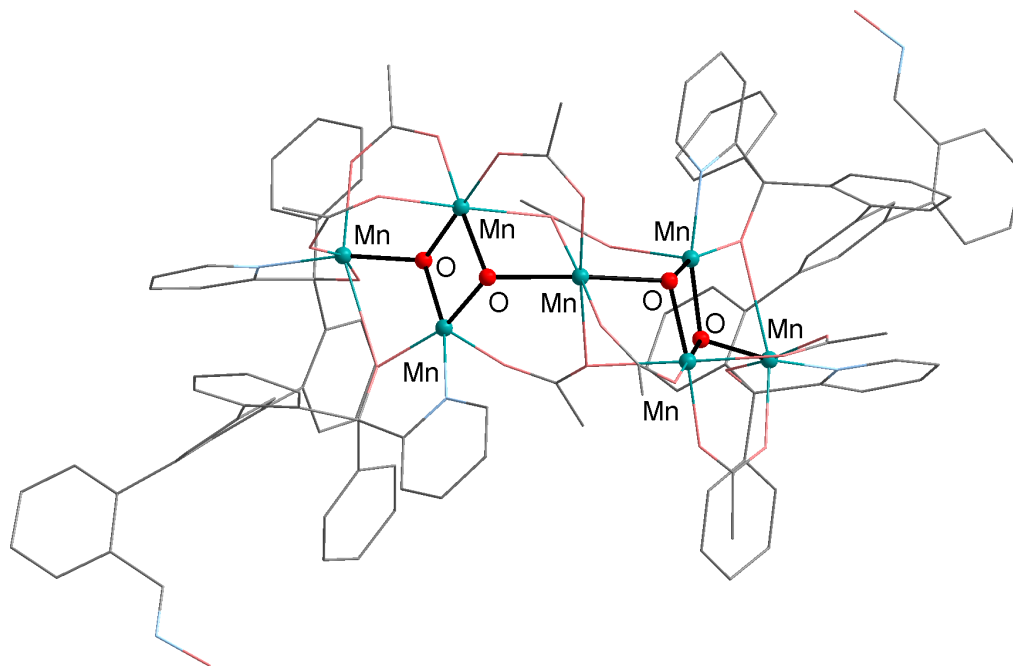
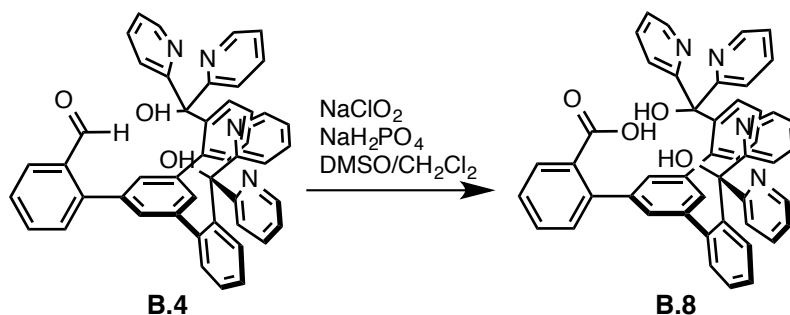


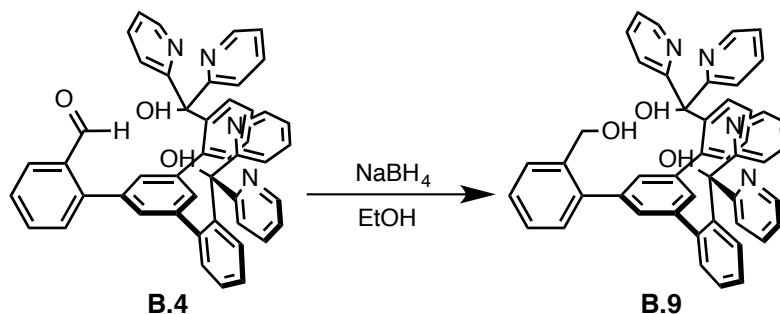
Figure 4. Preliminary solid-state structure of **B.7**.

B.3 Synthesis of other ligand variants

A monocarboxylate variant of the asymmetric ligand was also targeted for a closer structural mimic to the OEC, which is supported by carboxylate bridges. A Pinnick-type oxidation of **B.4** cleanly yields the carboxylic acid (**B.8**), as assigned by ^1H NMR spectroscopy and ESI-MS (Scheme 3). Currently metallation reactions of **B.8** are ongoing, but no products have been structurally identified by XRD studies yet. A reduced ligand variant (**B.9**) was prepared via reduction of the aldehyde moiety of **B.4** (Scheme 4). Similarly, no metal complexes of **B.9** have yet to be structurally identified.



Scheme 3. Oxidation of **B.4** to form monocarboxylate ligand precursor **B.8**.



Scheme 4. Reduction of **B.4** to form hydroxymethyl ligand variant **B.9**.

Conclusions

In summary, progress has been made toward the strategy of desymmetrizing the basal multinucleating ligand frameworks. Unfortunately, similar heterometallic trimanganese oxido clusters have yet to be identified structurally. Efforts are ongoing for this. However, the monoaldehyde compound **B.4** is a versatile precursor that can be easily functionalized and derivatized to form other asymmetric ligand frameworks that may be useful for supporting multimetallic clusters. There are also other ligand variants that can be tried that are more similar to H_3L , such as a variant with a pyridazine moiety rather than a pyridyl group (Fig. 5, **B.10**). It should be possible to prepare this ligand variant via nucleophilic substitution of the aldehyde moiety of **B.4**. Because **B.10** is more similar to the original H_3L , it may be more straightforward to prepare and isolate similar manganese oxido clusters.

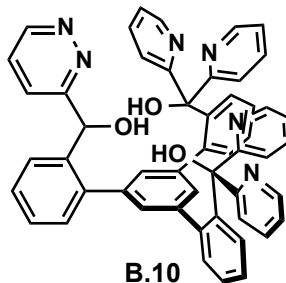


Figure 5. An asymmetric ligand framework that can be prepared from **B.4**.

Experimental Section

General Considerations. Unless stated otherwise, all synthetic manipulations were carried out using standard Schlenk techniques under a nitrogen atmosphere, or in a M. Braun glovebox under an atmosphere of nitrogen. Reactions were carried out in oven-dried glassware cooled under vacuum. Anhydrous THF was purchased from Aldrich in 18 L Pure-PacTM containers. Anhydrous dichloromethane, acetonitrile, diethyl ether, and THF were purified by sparging with nitrogen for 15 minutes and then passing under nitrogen pressure through a column of activated A2 alumina (Zapp's). All non-dried solvents used were reagent grade or better. All NMR solvents were purchased from Cambridge Isotope Laboratories, Inc. NMR solvents were dried as follows: CD₂Cl₂ and CD₃CN over calcium hydride. All NMR solvents were degassed by three freeze-pump-thaw cycles and vacuum-transferred prior to use. ¹H NMR and ¹³C NMR spectra were recorded on a Varian 300 MHz instrument, with shifts reported relative to the residual solvent peak.

The tribromide compound **B.1** was prepared according to literature procedures.⁶ The acetate-bridged trimanganese monooxo complex [Mn₃O(OAc)₆(pyr)₃]•pyr was prepared according to literature procedures.⁵ Di(2-pyridyl)ketone was purchased from Anvia.

Synthesis of B.2.

A 500-mL Schlenk flask equipped with a stir bar was charged with **B.1** (10.0 g, 18.41 mmol) under nitrogen flow. Anhydrous THF (300 mL) was added via cannula transfer, and the flask was cooled to $-78\text{ }^{\circ}\text{C}$. A solution of *n*-butyllithium in hexane (2.5 M, 7.73 mL, 19.33 mmol, 1.05 equiv) was added over 10 min. via syringe, and the yellow solution was stirred at $-78\text{ }^{\circ}\text{C}$ for 30 min. Anhydrous DMF (2.9 mL, 36.83 mmol, 2 equiv) was added via syringe, and the mixture was stirred at $-78\text{ }^{\circ}\text{C}$ for 30 min., then at $0\text{ }^{\circ}\text{C}$ for 30 min. The reaction mixture was quenched with methanol and a saturated sodium bicarbonate solution. The volatiles were removed under vacuum and then extracted three times with ethyl acetate. The organics were dried over MgSO_4 , filtered, and dried *in vacuo*. The yellow residue was purified by column chromatography using 1:1 hexanes/ CH_2Cl_2 , then dried under vacuum to yield the product as a white foamy solid (4.42 g, 49%). ^1H NMR (CDCl_3 , 300 MHz): δ 10.23 (s, 1H, CHO), 8.08 (dd, $J = 7.8, 1.5\text{ Hz}$, 1H), 7.71 (dd, $J = 8.2, 1.5\text{ Hz}$, 2H, *o*-CHO), 7.68 (td, $J = 7.5, 1.5\text{ Hz}$, 1H), 7.59 (d, $J = 8.5\text{ Hz}$, 1H), 7.55 (t, $J = 1.5\text{ Hz}$, 1H), 7.53 (t, $J = 7.5\text{ Hz}$, 1H), 7.50 (d, $J = 1.5\text{ Hz}$, 2H), 7.46 (dd, $J = 7.8, 1.5\text{ Hz}$, 2H), 7.40 (td, $J = 7.5, 1.5\text{ Hz}$, 2H), 7.25 (td, $J = 7.8, 2.0\text{ Hz}$, 2H) ppm. ^{13}C NMR (CDCl_3): 192.6 (CHO), 145.5, 141.6, 141.2, 137.3, 134.0, 133.8, 133.4, 131.5, 131.1, 130.4, 130.3, 129.3, 128.2, 127.8, 127.7, 122.8 ppm. HRMS (FAB+): calcd. For $\text{C}_{25}\text{H}_{17}\text{OBr}^{18}\text{Br}$: 492.9626; found: 42.9645 [M+H].

Acetal protection of B.2 (B.3).

Under ambient conditions, a 500-mL round-bottom flask equipped with a stir bar was charged with **B.2** (4.05 g, 8.23 mmol), ethylene glycol (0.5 mL, 9.05 mmol, 1.1 equiv), and *p*-toluenesulfonic acid monohydrate (0.313 g, 1.65 mmol, 0.2 equiv). A Dean-Stark

apparatus was connected to the flask, and the mixture was refluxed for 15 h. The mixture was quenched with saturated sodium bicarbonate solution, then extracted with ethyl acetate, dried over MgSO_4 , filtered, and dried under vacuum to yield product as an off-white solid (4.2 g, 95%). The resulting material was carried on without further purification.

Synthesis of aldehyde (B.4).

In the glovebox, a solution of **B.3** (0.200 g, 0.371 mmol) in THF (10 mL) was added to an oven-dried 25-mL pear Schlenk flask equipped with a stir bar. The flask was capped with a septum and then put under a nitrogen atmosphere on the Schlenk line. The flask was cooled to $-78\text{ }^{\circ}\text{C}$ in a dry ice/acetone bath, then a solution of *t*-BuLi (1.7 M in pentane, 0.89 mL, 1.52 mmol, 4.1 equiv) was added via syringe. The solution darkened from pale yellow to orange-brown. The reaction mixture was stirred at $-78\text{ }^{\circ}\text{C}$ for 20 min. and a solution of di(2-pyridyl)ketone (0.137 g, 0.742 mmol, 2 equiv) in dry THF (3 mL) was added via syringe. The reaction mixture turned green and was stirred at $-78\text{ }^{\circ}\text{C}$ for 1 h, then warmed to $0\text{ }^{\circ}\text{C}$. 3 M HCl (1 mL) was added to quench the reaction, and the mixture was stirred overnight at room temperature, turning orange. Saturated NaHCO_3 solution was added to neutralize the acid and the mixture was extracted three times with CH_2Cl_2 . The combined organics were washed with brine, dried over MgSO_4 , filtered, then concentrated *in vacuo* to form a gooey yellow residue. This residue was purified on a plug column of silica gel by washing with CH_2Cl_2 to remove impurities, then eluting the purified product using 3:1 $\text{CH}_2\text{Cl}_2/\text{Et}_3\text{N}$ (0.168 g, 64%). ^1H NMR (CDCl_3 , 300 MHz): δ 9.82 (s, 1 H, CHO), 8.33 (d, $J = 5.1\text{ Hz}$, 4 H), 8.01 (d, $J = 7.8\text{ Hz}$, 1 H), 7.66 (d, $J = 8.1\text{ Hz}$, 4 H), 7.61 (d, $J = 7.5\text{ Hz}$, 1 H), 7.46 (t, $J = 7.5\text{ Hz}$, 6 H), 7.36 (t, $J = 7.5\text{ Hz}$, 2 H), 7.21 (t, $J = 7.5\text{ Hz}$, 2 H), 7.13 (d, $J = 7.5\text{ Hz}$, 2 H), 7.07 (s, 1 H), 6.97 (bm, 6 H), 6.81 (s, 2 H), 6.75 (d, $J = 8.1\text{ Hz}$, 2 H) ppm.

Synthesis of monooxime **B.5**.

Under ambient conditions, a solution of **B.4** (0.100 g, 0.141 mmol) in methanol (10 mL) was added to a round-bottom flask equipped with a stir bar. $\text{NH}_2\text{OH}\cdot\text{HCl}$ (0.011 g, 0.156 mmol, 1.1 equiv) and sodium acetate (0.014 g, 0.170 mmol, 1.2 equiv) were added, and the homogeneous yellow solution was stirred at room temperature for 2 h. The volatiles were removed *in vacuo*, and the resulting yellow solid was washed with water.

Synthesis of tetrazinc compound **B.6**.

Under ambient conditions, **B.5** (0.037 g, 0.052 mmol) and $\text{Zn}(\text{OAc})_2$ (0.028 g, 0.16 mmol, 3 equiv) were combined in CH_3CN (2 mL) in a scintillation vial equipped with a stir bar. A solution of NaOH (0.006 g, 0.16 mmol, 3 equiv) in water (2 mL) was added, and the reaction mixture becomes homogeneous and colorless. The reaction mixture was stirred at room temperature. Single crystals were grown via vapor diffusion of diethyl ether into a dichloromethane solution of the mixture.

Synthesis of heptamanganese complex **B.7**

Under ambient conditions, **B.5** (0.015 g, 0.021 mmol) and $[\text{Mn}_3\text{O}(\text{OAc})_6(\text{pyr})_3]\cdot\text{pyr}$ (0.018 g, 0.021 mmol, 1 equiv) were combined in a vial, and CH_3CN (0.7 mL) and CH_2Cl_2 (3 mL) were added. The brown solution was stirred for 5 min. at room temperature, then the volatiles were removed *in vacuo*. The brown residue was fractionated into benzene, acetonitrile, and dichloromethane. X-ray quality crystals were grown from the acetonitrile fraction via vapor diffusion of diethyl ether into a dichloromethane solution of the compound.

Synthesis of monocarboxylate B.8.

Under ambient conditions, **B.4** (0.200 g, 0.28 mmol) was dissolved in 6:1 DMSO/CH₂Cl₂ (14 mL) in a round-bottom flask equipped with a stir bar. A solution of NaH₂PO₄•2H₂O (0.055 g, 0.4 mmol, 1.4 equiv) in H₂O (2 mL) was added to the mixture. While stirring, a solution of NaClO₂ (0.067 g, 0.074 mmol, 2.6 equiv) in H₂O (2 mL) was added dropwise over 2 h via an addition funnel. The mixture slowly turned yellow, and was stirred at room temperature overnight. The reaction mixture was quenched with 1 M HCl (40 mL), turning colorless. After stirring for several hours, the mixture was washed with dichloromethane. The aqueous layer was then neutralized with saturated NaHCO₃ solution, then extracted three times with CH₂Cl₂. The combined organics were washed with brine, dried over Na₂SO₄, filtered, and concentrated *in vacuo*. ¹H NMR (CDCl₃, 300 MHz): δ 8.32 (d, *J* = 4.8 Hz, 4 H), 7.65 (m, 5 H), 7.47 (t, *J* = 7.2 Hz, 4 H), 7.27 (m, 2 H), 7.14 (t, *J* = 7.8 Hz, 2 H), 7.02 (d, *J* = 7.5 Hz, 2 H), 6.96 (m, 5 H), 6.86 (s, 2 H), 6.73 (d, *J* = 7.8 Hz, 2 H), 6.63 (s, 1 H) ppm.

Synthesis of B.9.

Under ambient conditions, **B.4** (0.300 g, 0.424 mmol) and NaBH₄ (0.024 g, 0.637 mmol) were combined in a round-bottom flask equipped with a stir bar, and ethanol (10 mL) and CH₂Cl₂ (10 mL) were added. The reaction mixture was stirred at room temperature for 20 min., then concentrated *in vacuo*. The residue was taken up in CH₂Cl₂ and filtered to remove excess NaBH₄, then concentrated *in vacuo*. ¹H NMR (CDCl₃, 300 MHz): δ 8.37 (d, *J* = 4.8 Hz, 4 H), 7.67 (d, *J* = 7.8 Hz, 4 H), 7.49 (t, *J* = 6.9 Hz, 4 H), 7.32 (m, 5 H), 7.19 (t, *J* = 7.5 Hz, 2 H), 7.03 (m, 9 H), 6.85 (s, 2 H), 6.74 (m, 3 H), 4.62 (d, *J* = 6.3 Hz, 2 H), 2.95 (t, *J* = 6.3 Hz, 1 H) ppm.

References

1. (a) Umena, Y.; Kawakami, K.; Shen, J. R.; Kamiya, N. *Nature* **2011**, *473*, 55-U65; (b) Ferreira, K. N.; Iverson, T. M.; Maghlaoui, K.; Barber, J.; Iwata, S. *Science* **2004**, *303*, 1831-1838.
2. (a) Kanady, J. S.; Tsui, E. Y.; Day, M. W.; Agapie, T. *Science* **2011**, *333*, 733-736; (b) Kanady, J. S.; Mendoza-Cortes, J. L.; Tsui, E. Y.; Nielsen, R. J.; Goddard, W. A.; Agapie, T. *J. Am. Chem. Soc.* **2013**, *135*, 1073-1082; (c) Tsui, E. Y.; Agapie, T. *Proc. Natl. Acad. Sci. USA* **2013**, *110*, 10084-10088.
3. Mukherjee, S.; Stull, J. A.; Yano, J.; Stamatatos, T. C.; Pringouri, K.; Stich, T. A.; Abboud, K. A.; Britt, R. D.; Yachandra, V. K.; Christou, G. *Proc. Natl. Acad. Sci. USA* **2012**, *109*, 2257-2262.
4. (a) Koumoussi, E. S.; Mukherjee, S.; Beavers, C. M.; Teat, S. J.; Christou, G.; Stamatatos, T. C. *Chem. Commun.* **2011**, *47*, 11128-11130; (b) Ross, S.; Weyhermüller, T.; Bill, E.; Bothe, E.; Flörke, U.; Wieghardt, K.; Chaudhuri, P. *Eur. J. Inorg. Chem.* **2004**, *2004*, 984-997.
5. Vincent, J. B.; Chang, H. R.; Folting, K.; Huffman, J. C.; Christou, G.; Hendrickson, D. N. *J. Am. Chem. Soc.* **1987**, *109*, 5703-5711.
6. Feng, X. L.; Wu, J. S.; Enkelmann, V.; Mullen, K. *Org. Lett.* **2006**, *8*, 1145-1148.

Appendix C

SIDE PRODUCTS AND OTHER STRUCTURES

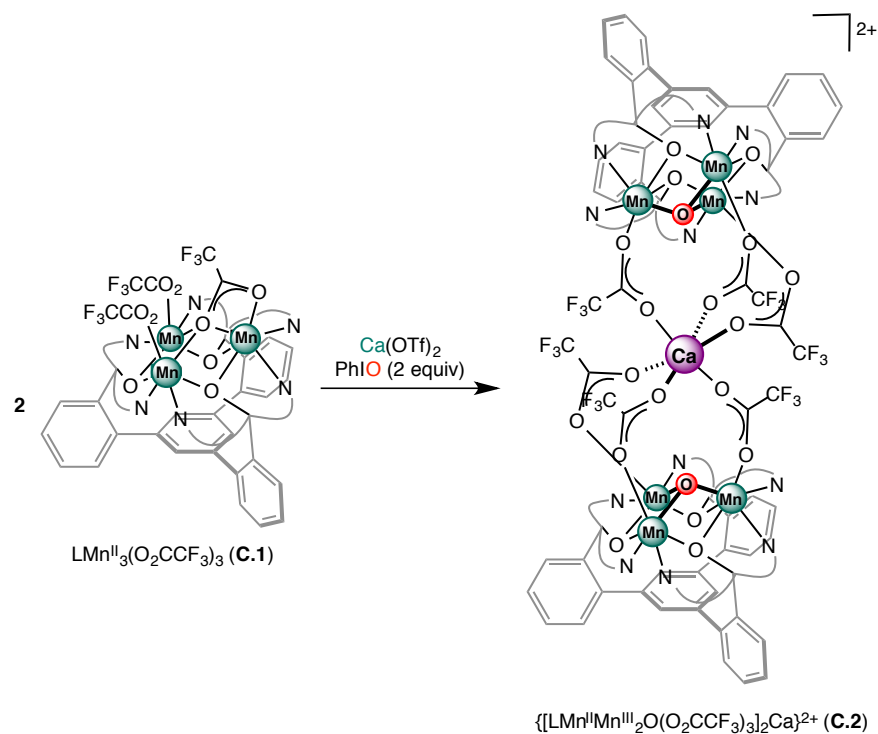
Introduction

The strategy of using a multinucleating ligand framework to control the structure and nuclearity of multimetallic clusters that we described in Chapter 1 has allowed us to access a variety of different trinuclear and tetranuclear species with unprecedented control over structure and composition (Chapters 2–4). However, during the course of developing the methodology for preparing these different complexes, unexpected complexes are sometimes formed. This chapter describes some of these compounds. Many of these complexes are not fully characterized other than via single crystal X-ray diffraction studies or with ^1H NMR spectroscopy or electrospray ionization mass spectrometry. In the interest of organization, the compounds will primarily be organized by nuclearity and oxido content.

Results and Discussion

C.1 Trinuclear complexes

The clusters discussed in the preceding chapters all contain bridging acetate ligands. Carboxylate groups are well known to stabilize multinuclear manganese clusters.¹ We briefly explored using weaker carboxylate supporting ligands in the hope that they would be more easily substituted. As such, we were able to prepare the trimanganese(II) complex $\text{LMn}^{\text{II}}_3(\text{O}_2\text{CCF}_3)_3$ (**C.1**) in analogy to the trimanganese(II) tris(acetate) complex that was the common precursor to most of the complexes discussed in Chapters 3 and 4 (Scheme 1, Fig. 1). Heterometallic clusters can also be formed with this cluster, as treatment of **C.1** with $\text{Ca}(\text{OTf})_2$ and iodosobenzene forms a calcium-bridged hexamanganese complex (**C.2**) analogous to complex **3** (Scheme 1, Fig. 2). Compound **C.2** was also structurally characterized and is very similar to **3**.



Scheme 1. Formation of trifluoroacetate-bridged hexamanganese cluster (**C.2**) from $\text{LMn}_3(\text{O}_2\text{CCF}_3)_3$ (**C.1**).

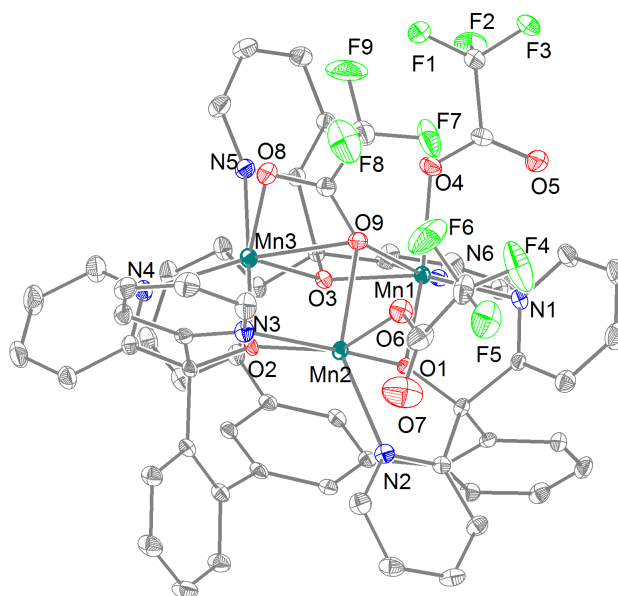


Figure 1. Solid-state structure of $\text{LMn}^{\text{II}}_3(\text{O}_2\text{CCF}_3)_3$ (**C.1**) as 50% thermal ellipsoids. Hydrogen atoms and solvent molecules not shown for clarity.

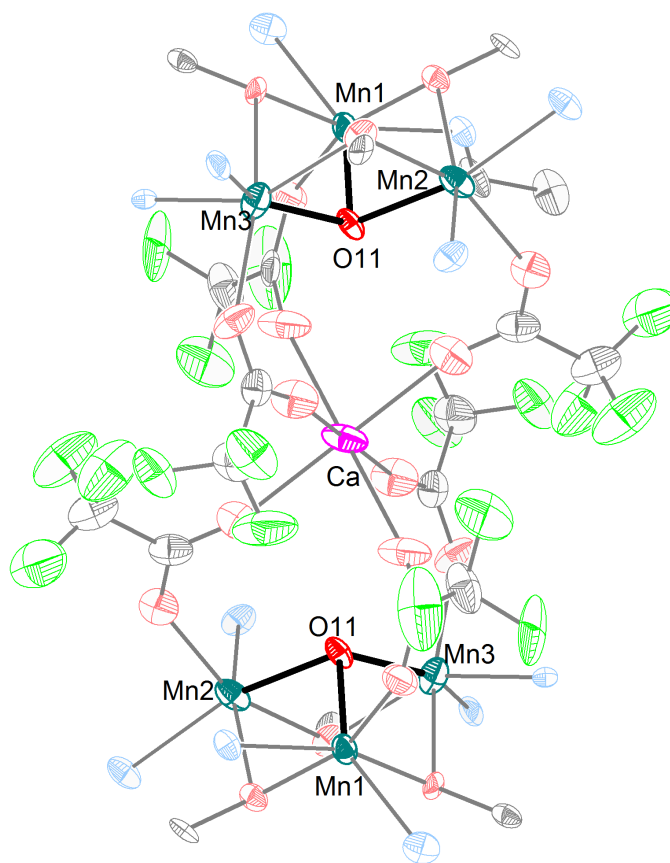
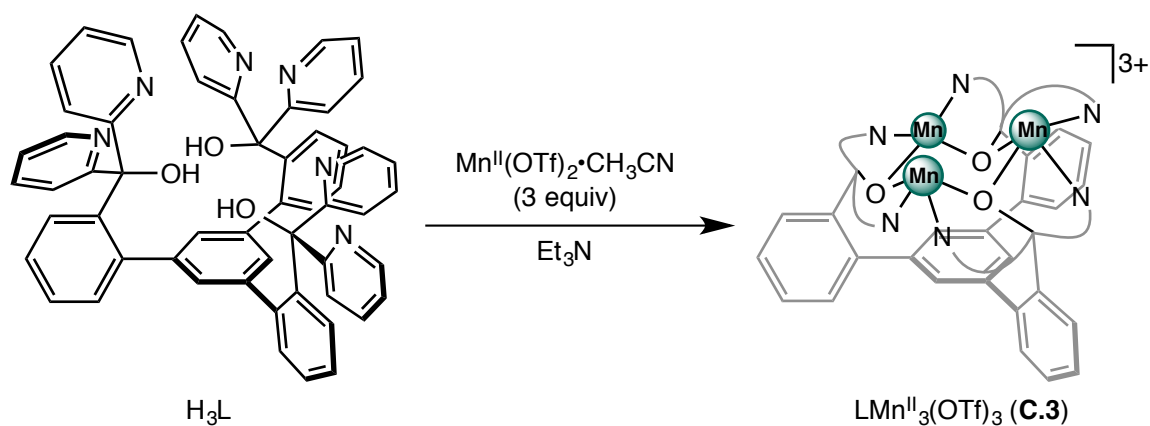


Figure 2. Solid-state structure of **C.2** as 50% thermal ellipsoids. Hydrogen atoms, outer sphere anions, and solvent molecules not shown for clarity.

We also attempted to prepare a trimanganese(II) compound without carboxylate groups. Targeting $\text{LMn}^{\text{II}}_3(\text{OTf})_3$, treatment of H_3L with three equivalents of $\text{Mn}^{\text{II}}(\text{OTf})_2 \cdot \text{CH}_3\text{CN}$ and base formed a yellow compound (Scheme 2, **C.3**) whose ^1H NMR spectrum was paramagnetically shifted and broadened, as might be expected for a trimanganese(II) compound. Single crystals were grown from vapor diffusion of diethyl ether into an acetonitrile solution of **C.3**. A XRD study of these crystals reveals the desired trimanganese(II) structure (Fig. 3), though there seems to be an oxygen atom, possibly a hydroxide ligand, that crystallized bridging the three manganese centers (oxidation is

unlikely because the compound remained colorless. It was not possible to fully identify the number of outer sphere anions due to some disorder.



Scheme 2. Synthesis of $\text{LMn}_3(\text{OTf})_3$ (**C.3**).

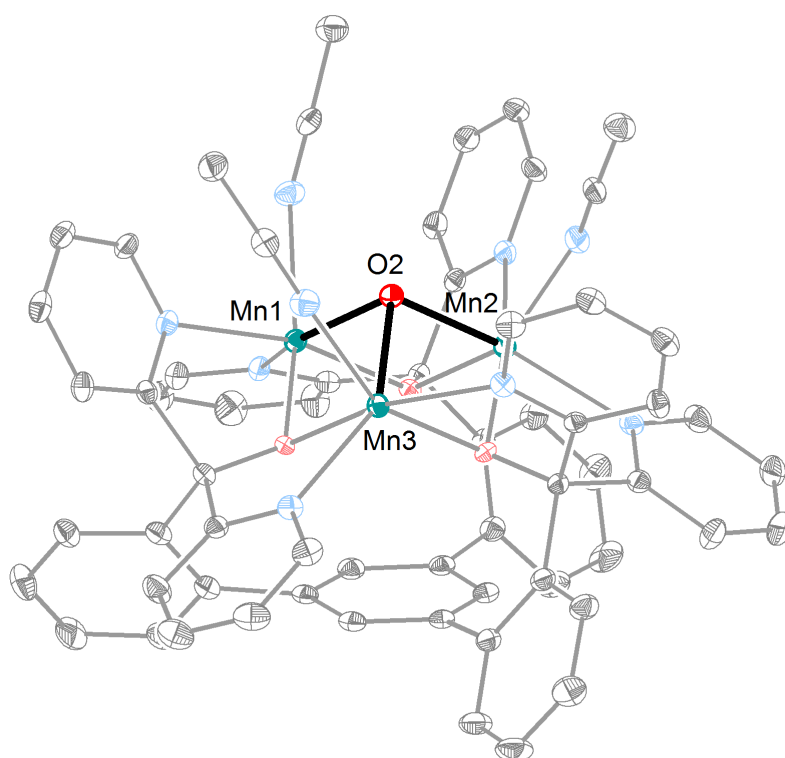
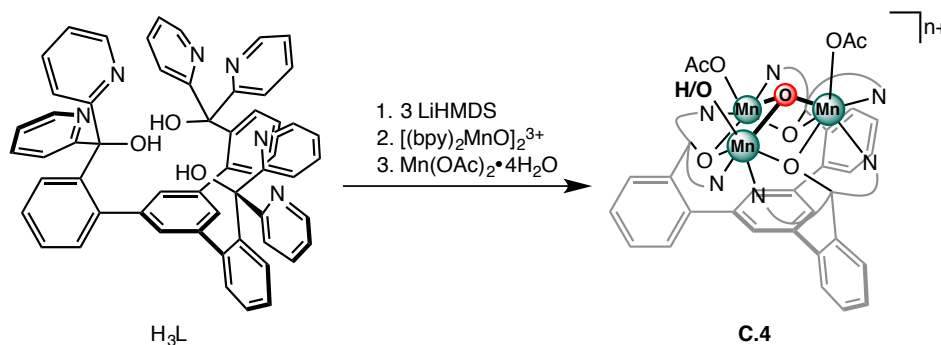


Figure 3. Solid-state structure of **C.3** as 50% thermal ellipsoids. Outer sphere triflate anions and hydrogen atoms not shown for clarity.

In addition to treating H_3L with divalent transition metal salts in the presence of base, we also investigated an alternate metallation strategy wherein we use higher oxidation manganese sources. Specifically, deprotonation of H_3L with lithium bis(trimethylsilyl)amide (3 equivalents) followed by treatment with a mixed-valent Mn^{III}/Mn^{IV} bis(μ -oxo) dimer $[(bpy)_2MnO]_2(ClO_4)_3 \cdot H_2O$ and addition of $Mn^{II}(OAc)_2 \cdot 4H_2O$ formed a brown species with a sharp 1H NMR spectrum (Scheme 3, **C.4**). X-ray quality single crystals were grown by slow evaporation of a CH_2Cl_2 solution of **C.4** (Fig. 4). Compound **C.4** is a trimanganese cluster with a μ_3 -oxido or hydroxo moiety with terminal acetate ligands on two of the manganese centers and a terminal hydroxide on the third. Unfortunately, due to disorder in the structure the number of outer sphere perchlorate anions could not be quantified, so assignment of the oxidation state of this complex is currently uncertain.



Scheme 3. Synthesis of **C.4**.

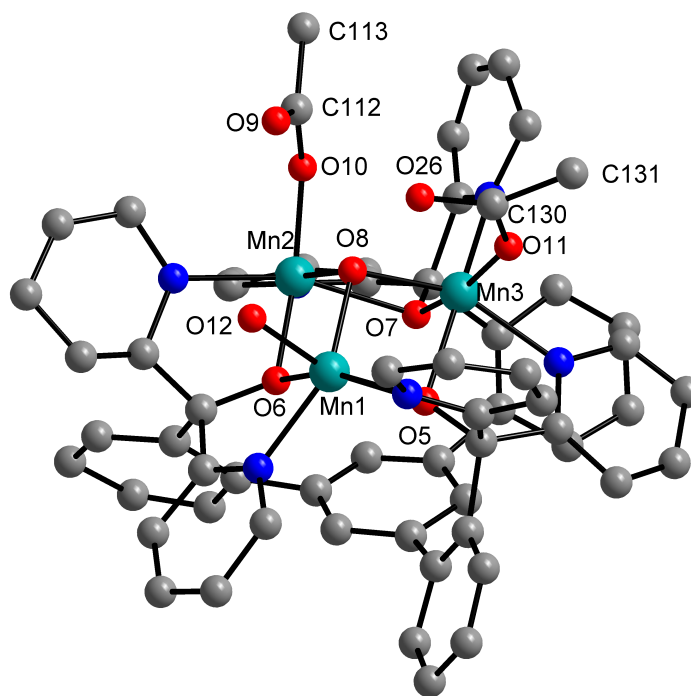
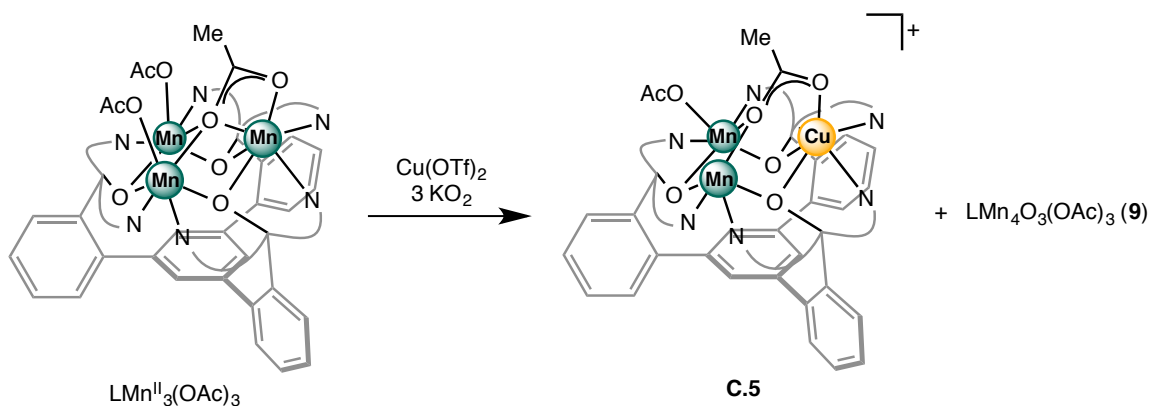


Figure 4. Preliminary solid-state structure of **C.4**.

Finally, a serendipitous route to forming mixed-metal trinuclear clusters was found when we attempted to prepare a Cu^{2+} -capped tetraoxido cubane cluster. Treatment of $\text{LMn}^{\text{II}}_3(\text{OAc})_3$ with $\text{Cu}(\text{OTf})_2$ and KO_2 in THF, in analogy to the procedure for forming the $[\text{CaMn}_3\text{O}_4]$ cubane cluster **6-Ca**, instead forms $\text{LMn}_4\text{O}_3(\text{OAc})_3$ (**9**) and a green mixed-metal $[\text{LMn}_2\text{Cu}(\text{OAc})_2]^+$ cluster (**C.5**) with outer sphere triflate ions (Scheme 4). A XRD study of single crystals of **C.5** shows a trinuclear core with two coordinate acetate ligands and an outer sphere triflate anion. As such, the compound is tentatively assigned to be in the $\text{Mn}^{\text{II}}_2\text{Cu}^{\text{II}}$ oxidation state (Fig. 5).



Scheme 4. Synthesis of **C.5**.

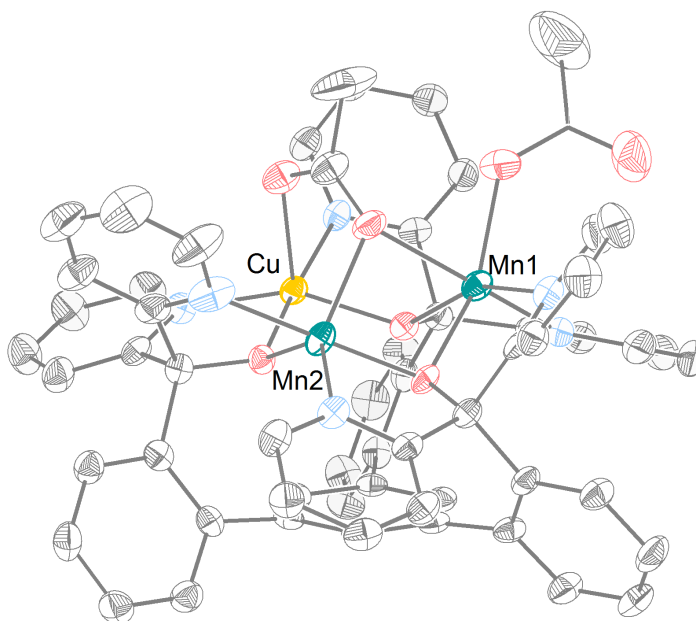


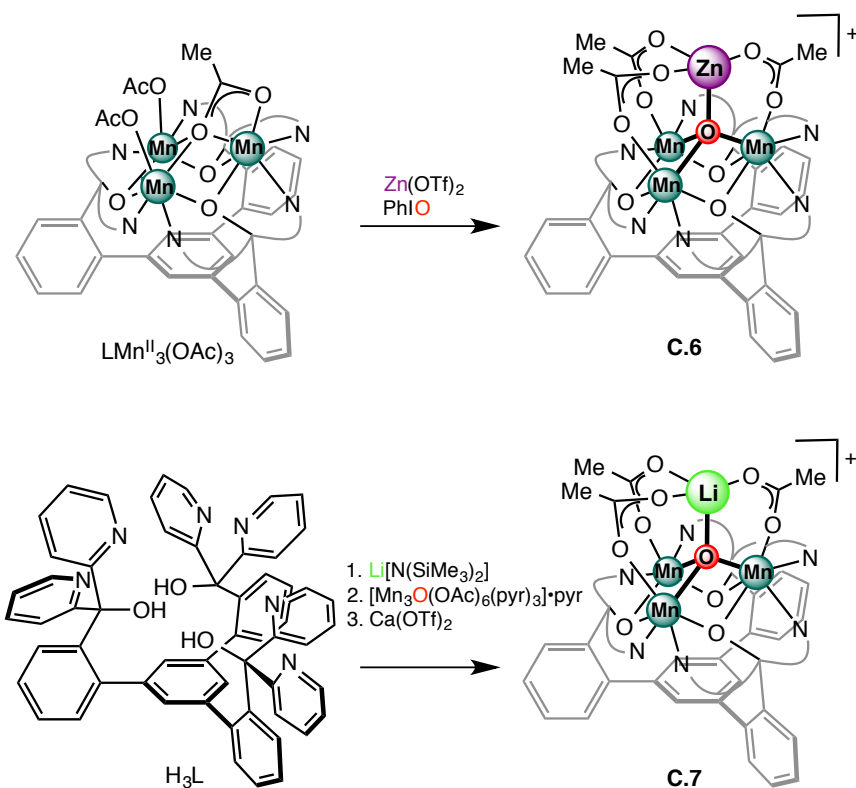
Figure 5. Preliminary solid-state structure of **C.5**.

The above structures show that it is possible to achieve a trimetallic complex via a few different metallation strategies. The compounds also demonstrate that the alkoxide-bridged trinuclear core motif is very robust.

C.2 Tetrametallic monooxo complexes

We also targeted other heterometallic complexes that are related to compound **3**, in which a μ_3 -oxido ligand bridges the three manganese centers, with the redox-inactive metal

ion bridged to the complex via acetate ligands. Treatment of a mixture of $\text{LMn}^{\text{II}}_3(\text{OAc})_3$ and $\text{Zn}(\text{OTf})_2$ with iodosobenzene forms a zinc monooxido compound **C.6** (Scheme 5). A XRD study of single crystals of **C.6** reveals that the Zn^{2+} ion is, as expected, bridged to the trimanganese core via acetate ligands, but also via a μ_4 -oxo ligand (Fig. 6). The smaller ionic radius of Zn^{2+} in comparison to Ca^{2+} may allow it to coordinate the oxo ligand. In the crystal structure, only one triflate anion could be located, suggesting that the oxidation state may be $\text{Mn}^{\text{III}}\text{Mn}^{\text{II}}_2$, which is different from the oxidation state observed for the Ca^{2+} analogue (**3**).



Scheme 5. Synthesis of heterometallic monooxido complexes **C.6** and **C.7**.

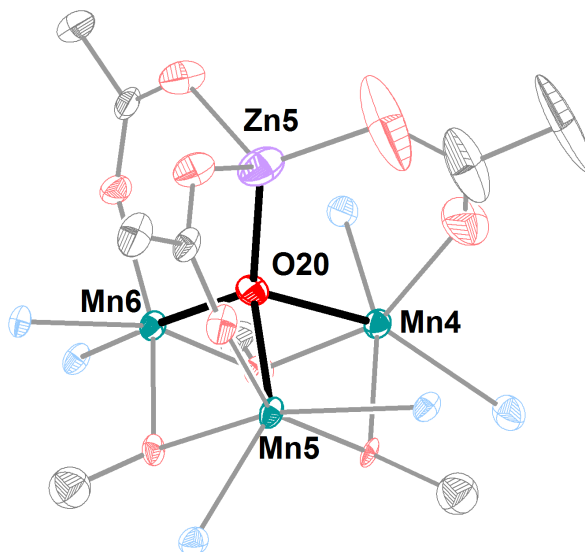


Figure 6. Truncated preliminary solid-state structure of **C.6** as 50% thermal ellipsoids. Outer sphere anions and hydrogen atoms not shown for clarity.

A related lithium monooxo compound **C.7** was prepared when H_3L was deprotonated with lithium bis(trimethylsilyl)amide, then treated with $[\text{Mn}_3\text{O}(\text{OAc})_6(\text{pyr})_3]\cdot\text{pyr}$ and $\text{Ca}(\text{OTf})_2$. Although we initially expected that this route would yield the Ca^{2+} -bridged compound **3**, we instead found that the product displayed a different ^1H NMR spectrum. A XRD study of single crystals of **C.7** revealed that the compound is a lithium monooxo compound with a similar structure to **C.6** (Fig. 7). Again, the redox-inactive capping metal is bridged to the trimanganese core via a μ_4 -oxo ligand, and the coordination sphere of the lithium ion is completed via acetate ligands that bridge to the basal manganese centers. One triflate ion could be located in the lattice (presumably originating from $\text{Ca}(\text{OTf})_2$), thus allowing the oxidation state of the cluster to be assigned as $\text{Mn}^{\text{III}}_2\text{Mn}^{\text{II}}$.

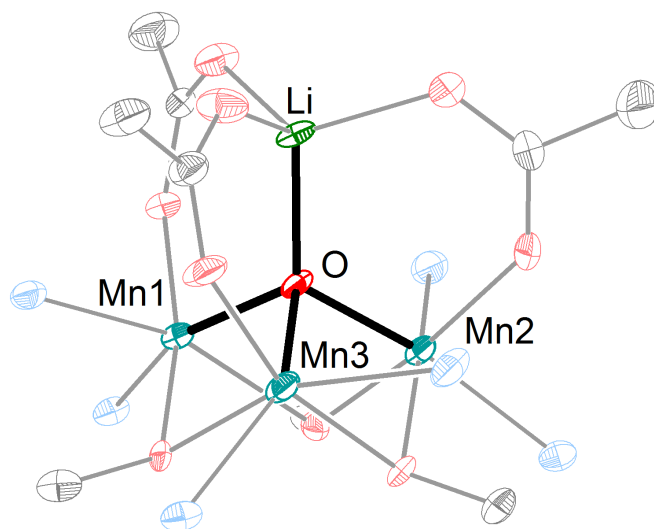
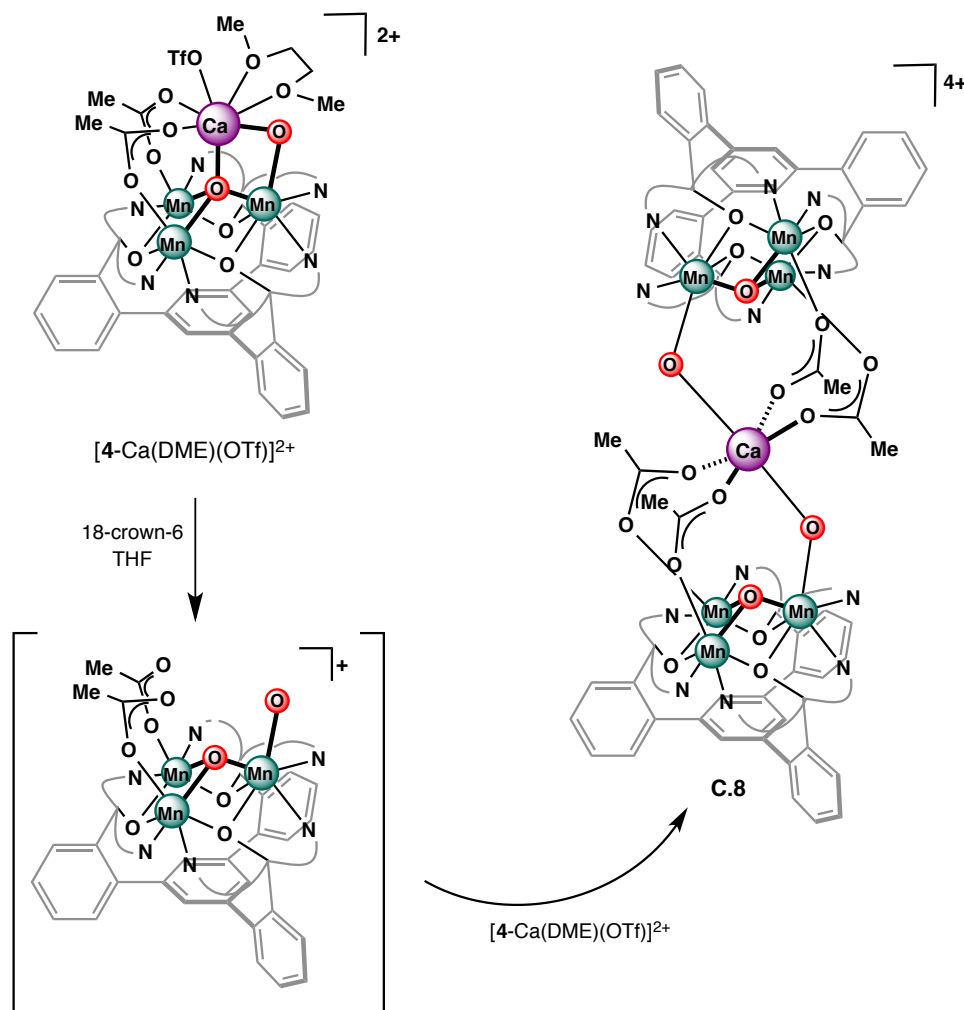


Figure 7. Truncated preliminary solid-state structure of **C.7** as 50% thermal ellipsoids. Outer sphere anions, hydrogen atoms, and solvent molecules not shown for clarity.

C.3 Complexes derived from dioxido clusters

The dioxido clusters are fairly reactive in comparison to the monooxido or tetraoxido clusters and are more prone to transformations such as comproportionation and disproportionation (Chapter 5). We came upon a variety of new structural motifs in the course of investigating the reactivity of complexes **4** and **5**. For example, we originally targeted a trimanganese dioxido complex without an incorporated fourth redox-inactive metal in order to provide a control for the electrochemical studies described in Chapter 3. One approach for the synthesis of such a complex would be to remove the Ca^{2+} center from a complex such as $[\mathbf{4}\text{-Ca}(\text{DME})(\text{OTf})]^{2+}$. When a THF solution of $[\mathbf{4}\text{-Ca}(\text{DME})(\text{OTf})]^{2+}$ is treated with 18-crown-6, a new species **C.8** is formed by ^1H NMR spectroscopy (Scheme 6). The ^1H NMR spectrum of **C.8** is asymmetric and similar to $[\mathbf{4}\text{-Ca}(\text{DME})(\text{OTf})]^{2+}$, suggesting that the reaction was successful. However, when single crystals were grown of **C.8**, a XRD study revealed that the complex is instead a hexamanganese complex bridged

by a single Ca^{2+} center in which each trimanganese unit has a μ_3 -oxo that is not associated with the Ca^{2+} center, and one oxido ligand that bridges a single manganese center to the calcium (Fig. 8). It is likely that after the Ca^{2+} is removed, the resulting “naked” dioxido complex can react with another equivalent of $[\text{4-Ca}(\text{DME})(\text{OTf})]^{2+}$, thus forming the sandwich compound **C.8** that is stable to 18-crown-6 (Scheme 6).



Scheme 6. Formation of hexamanganese tetraoxido cluster **C.8**.

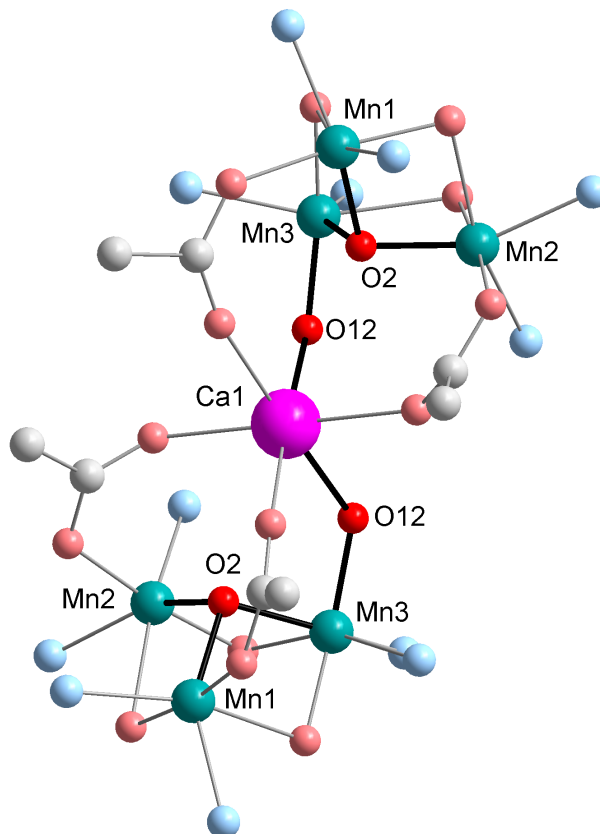


Figure 8. Truncated preliminary solid-state structure of **C.8**.

Oxidizing the dioxido clusters also yielded compounds with new structural motifs. When $[4\text{-Ca}(\text{DME})(\text{OTf})]^{2+}$ is treated with Na_2O_2 , a mixture of products is formed. Crystals have been isolated from the reaction mixtures that correspond both to the cubane cluster **6**-Ca as well as a new hexamanganese cluster (**C.9**) with a single Ca^{2+} center bridging two trimanganese units that each are bound to three oxygenic ligands: one μ_4 -oxido coordinates three manganese centers and the Ca^{2+} center, one μ_2 -oxido ligand bridges the Ca^{2+} and a single manganese center, and a third, terminal ligand is bound to another manganese center (Fig. 9). The Mn–O distances of this ligand range from 1.84–1.87 Å in the preliminary structure, which is slightly longer than previously isolated terminal Mn^{III} -oxo compounds, albeit of different symmetry (1.77 and 1.80 Å),² but within the range of

Mn-hydroxide compounds. However, as the Mn centers of **C.9** are pseudo-octahedral, some axial elongation would not be unexpected for a Mn^{III} center due to population of the antibonding orbitals. As such, distinguishing between a terminal oxido or hydroxide ligand cannot yet be accomplished.

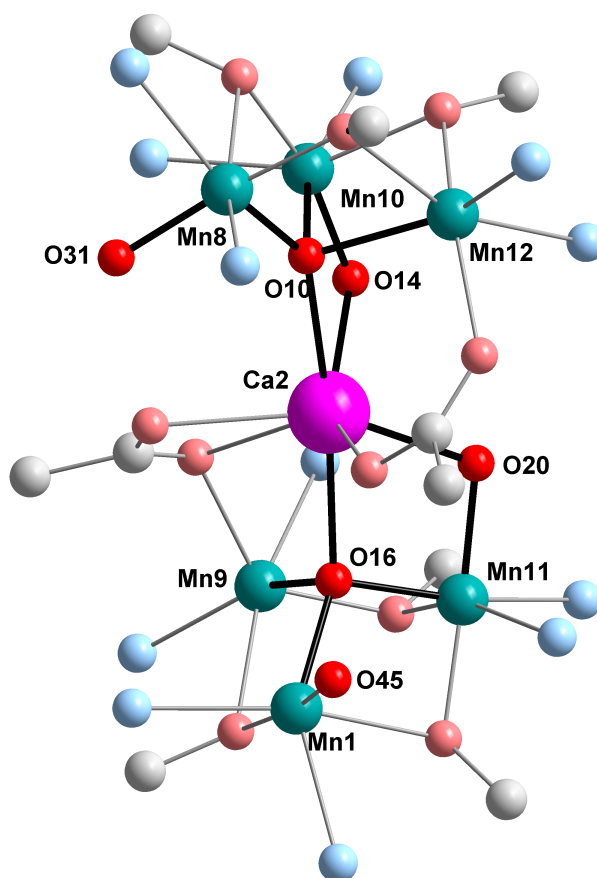


Figure 9. Truncated preliminary solid-state structure of **C.9**

Finally, where oxo ligands can be added via oxidation or removed via reduction (see Chapter 5), they can also be removed via protonation. When an acetonitrile solution of $[\mathbf{5}\text{-Ca}(\text{DME})(\text{OTf})]^+$ is treated with two equivalents of *p*-cyanoanilinium triflate, a new species (**C.10**) is formed by ^1H NMR spectroscopy. A XRD study of single crystals of **C.10** shows that the μ_2 -oxo has been protonated off and been replaced by a bridging triflate

ligand. There is a μ_3 -oxido ligand still bridging the basal manganese centers (previously μ_4). The structure itself is dimeric, with the Ca^{2+} center bridged to another Ca^{2+} via acetate ligands (Fig. 10).

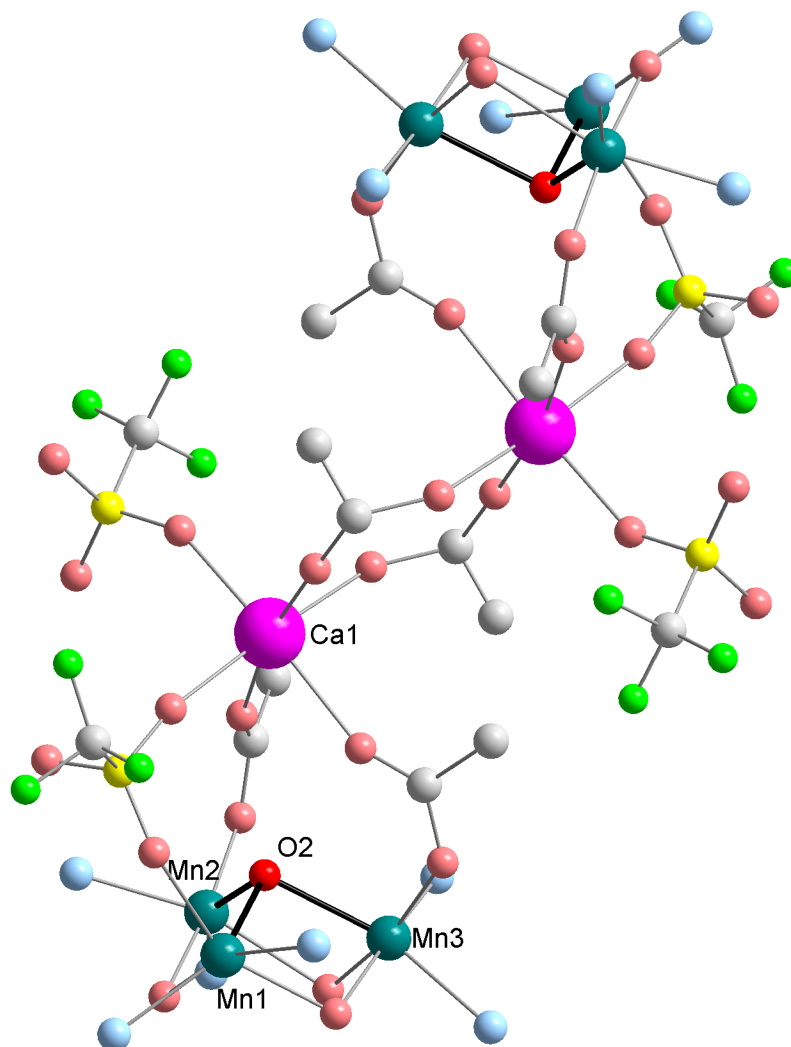
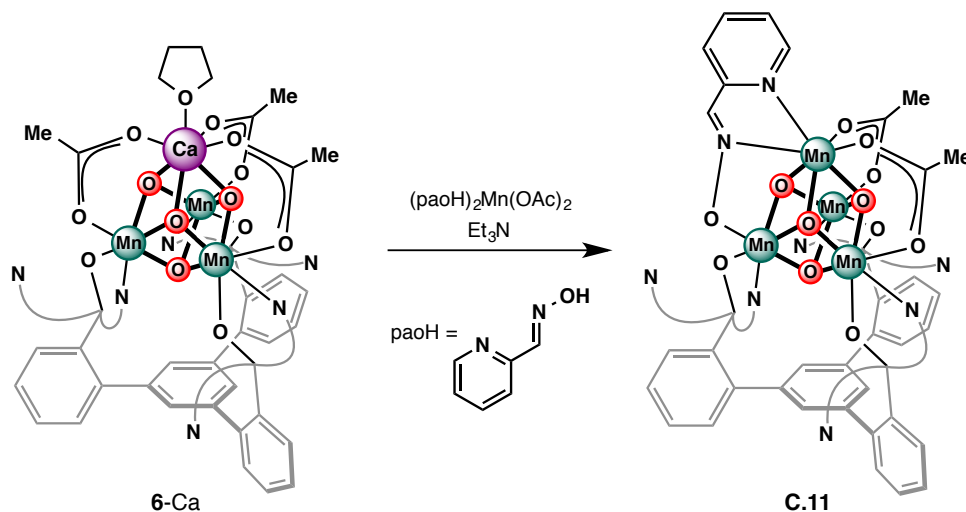


Figure 10. Truncated preliminary solid-state structure of **C.10**.

As demonstrated above, the heterometallic trimanganese dioxido complexes can be easily converted into new mono-, di-, tri-, and tetraoxido species. However, one common problem that is encountered is the propensity of the complexes to form higher nuclearity sandwich or dimer-type complexes, rather than simple tetrametallic units.

C.4 Products derived from tetraoxido cubane clusters

Given that the tetraoxido $[\text{MMn}_3\text{O}_4]$ cubane clusters are the complexes that are the most structurally relevant to the OEC, we have also spent significant efforts in making new derivatives, with varying degrees of success. One problem has been the propensity of complex **6**-Ca to transmetallate rather than undergo ligand exchange at Ca^{2+} . For example, when **6**-Ca was treated with a pyridinealdoxime-supported Mn^{II} source in an effort to attach a fourth manganese center that would bridge to the Ca/Mn cluster via bridged oximate ligands, a tetramanganese cubane cluster **C.11** was isolated instead (Scheme 7). In this example, manganese has substituted for the calcium center, and one of the bridging acetate ligands of **6**-Ca has been substituted for an oximate ligand (Fig. 11). Interestingly, in comparison to $\text{LMn}_4\text{O}_4(\text{OAc})_3$ (**8**), which has two Mn^{IV} centers and two Mn^{III} centers, **C.11** appears to be valence localized, with the apical manganese center displaying bond lengths consistent with Mn^{II} , while the basal manganese centers remain Mn^{IV} .



Scheme 7. Synthesis of **C.11**.

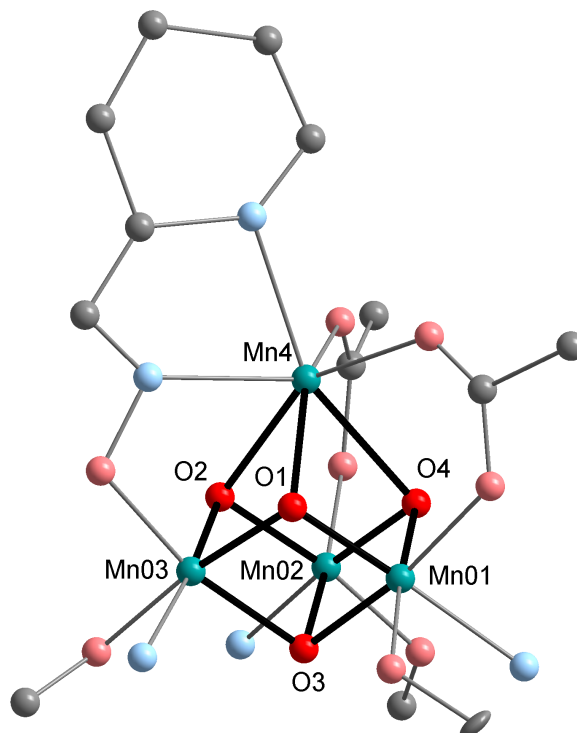
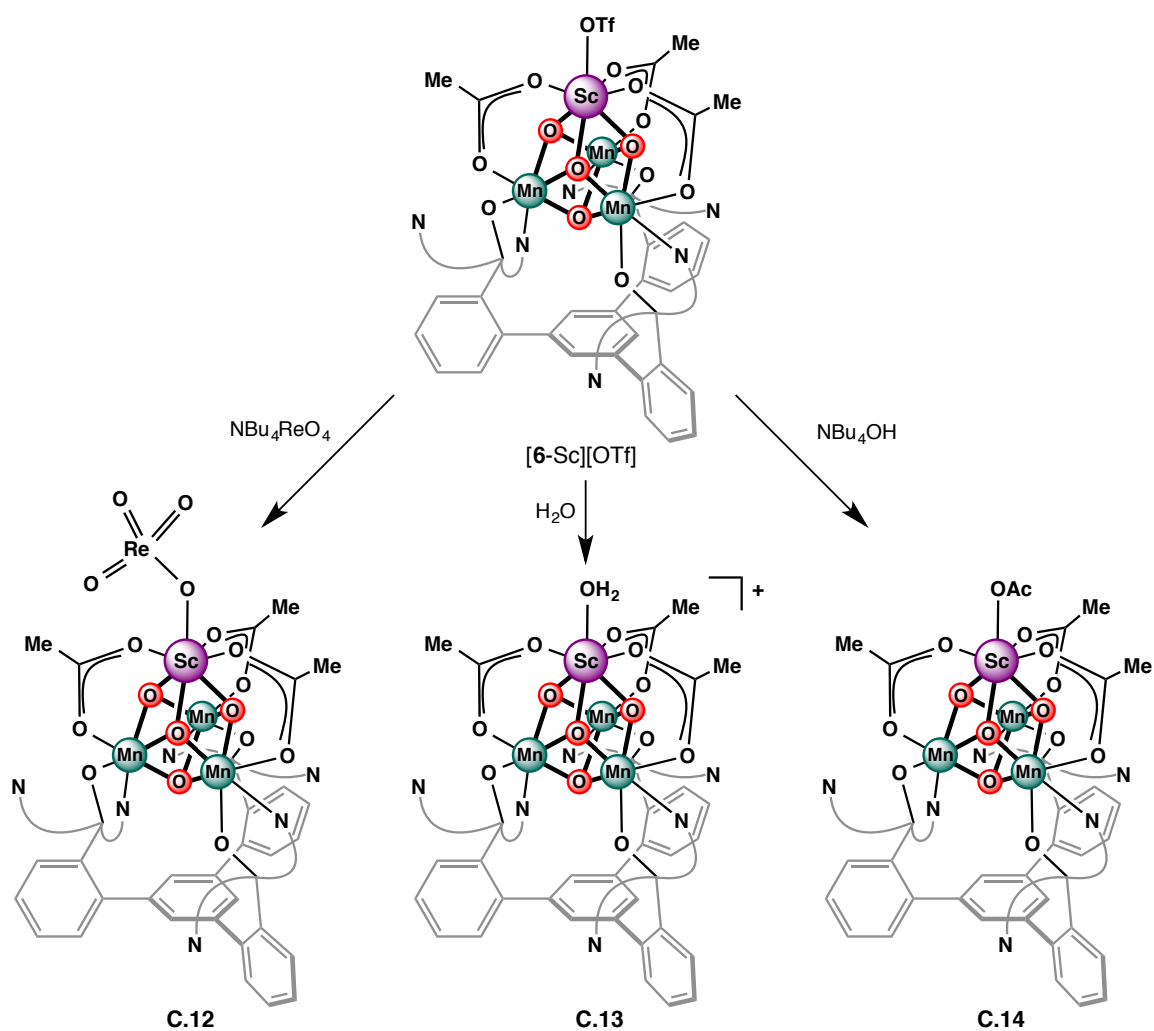


Figure 11. Truncated preliminary solid-state structure of **C.11**.

Compound $[\mathbf{6}\text{-Sc}][\text{OTf}]$ is more stable to transmetallation because Sc^{3+} is more Lewis acidic than Ca^{2+} . As such, we have isolated several different compounds with different ligands coordinated to the Sc^{3+} center. Compound $[\mathbf{6}\text{-Sc}][\text{OTf}]$ can be treated with $\text{NBu}_4[\text{ReO}_4]$ to undergo anion exchange (Scheme 8), and the resulting $[\text{ScMn}_3\text{O}_4]$ cluster can be crystallographically characterized with a coordinated perrhenate ligand (Fig. 12, **C.12**). Alternatively, Sc^{3+} can also be coordinated by a neutral donor, as when $[\mathbf{6}\text{-Sc}][\text{OTf}]$ is treated with H_2O , and the aquo complex with an outer sphere triflate anion is isolated (Fig. 13, **C.13**). When $[\mathbf{6}\text{-Sc}][\text{OTf}]$ is treated with hydroxide, an acetate-capped complex was crystallographically characterized, presumably through some sort of cluster degradation with loss of a side product (Fig. 14, **C.14**).



Scheme 8. Ligand substitutions of [6-Sc][OTf].

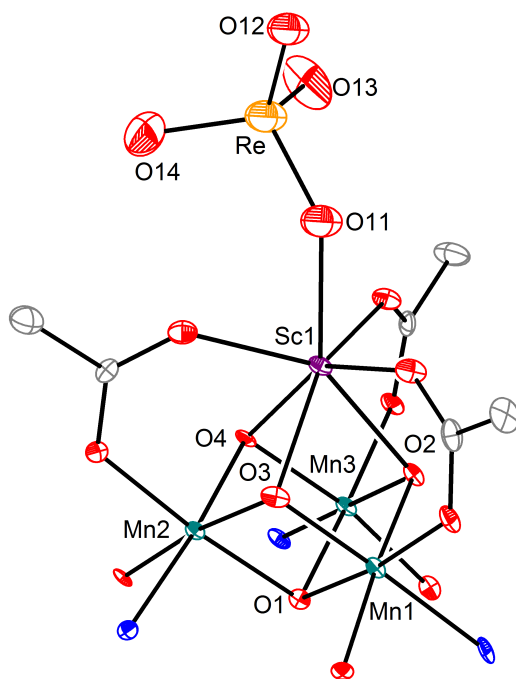


Figure 12. Truncated solid-state structure of LScMn₃O₄(OAc)₄(ReO₄) (**C.12**).

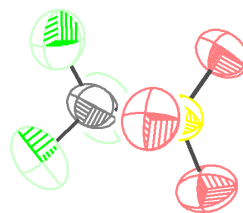
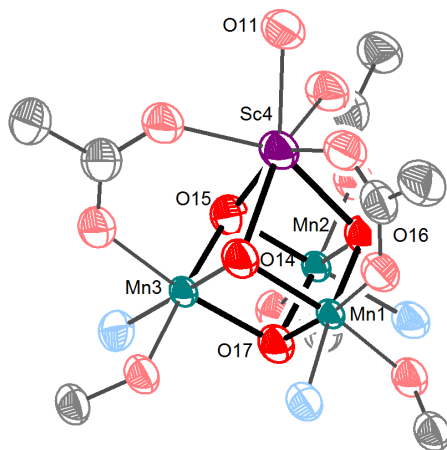


Figure 13. Truncated solid-state structure of [LScMn₃O₄(OAc)₃(OH₂)][OTf] (**C.13**).

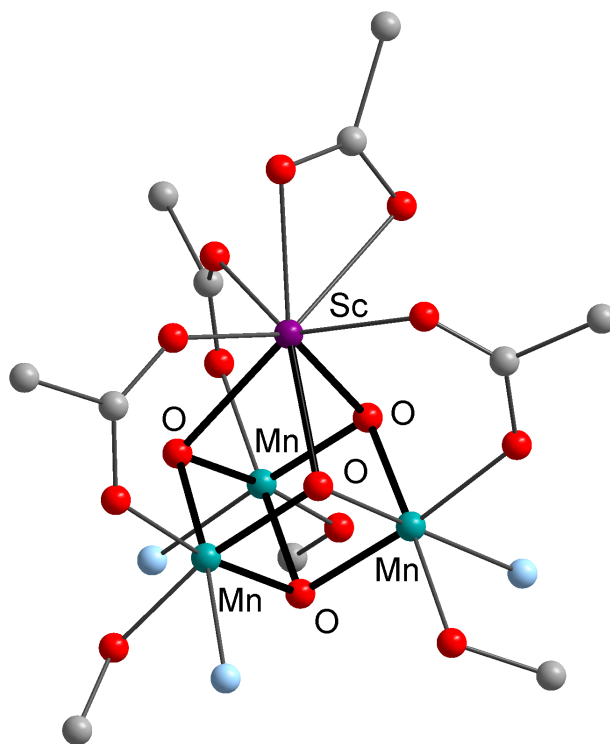


Figure 14. Truncated solid-state structure of $\text{LScMn}_3\text{O}_4(\text{OAc})_4$ (**C.14**).

One of the most unexpected XRD structures during the course of these studies was formed when attempting to prepare a $[\text{Mn}_3\text{O}_4]$ cubane cluster with an incorporated Ba^{2+} ion. When a mixture of $\text{LMn}^{\text{II}}_3(\text{OAc})_3$ and $\text{Ba}(\text{OTf})_2$ was treated with excess KO_2 in THF, then crystallized from DMF/diethyl ether, single crystals of an octamanganese complex with six oxido moieties per tetramanganese unit were isolated (**C.15**). This compound has one of the highest oxo/manganese ratios out of all the complexes characterized thus far. Although the $[\text{Mn}_4\text{O}_4]$ cubane cluster is maintained, two of the acetate ligands have been substituted for oxygenic ligands, with only one bridging acetate ligand remaining. There is one terminal ligand currently assigned as a hydroxide ($\text{Mn}-\text{O}$ distance ca. 1.96 Å) per tetramanganese unit, and μ_2 -oxo ligand ($\text{Mn}-\text{O}$ distances 1.78, 1.82 Å) that bridges to the

other dimeric subunit (Fig. 15). This structure demonstrates that three carboxylate ligands are not strictly necessary to maintain the structural stability of the cubane core.

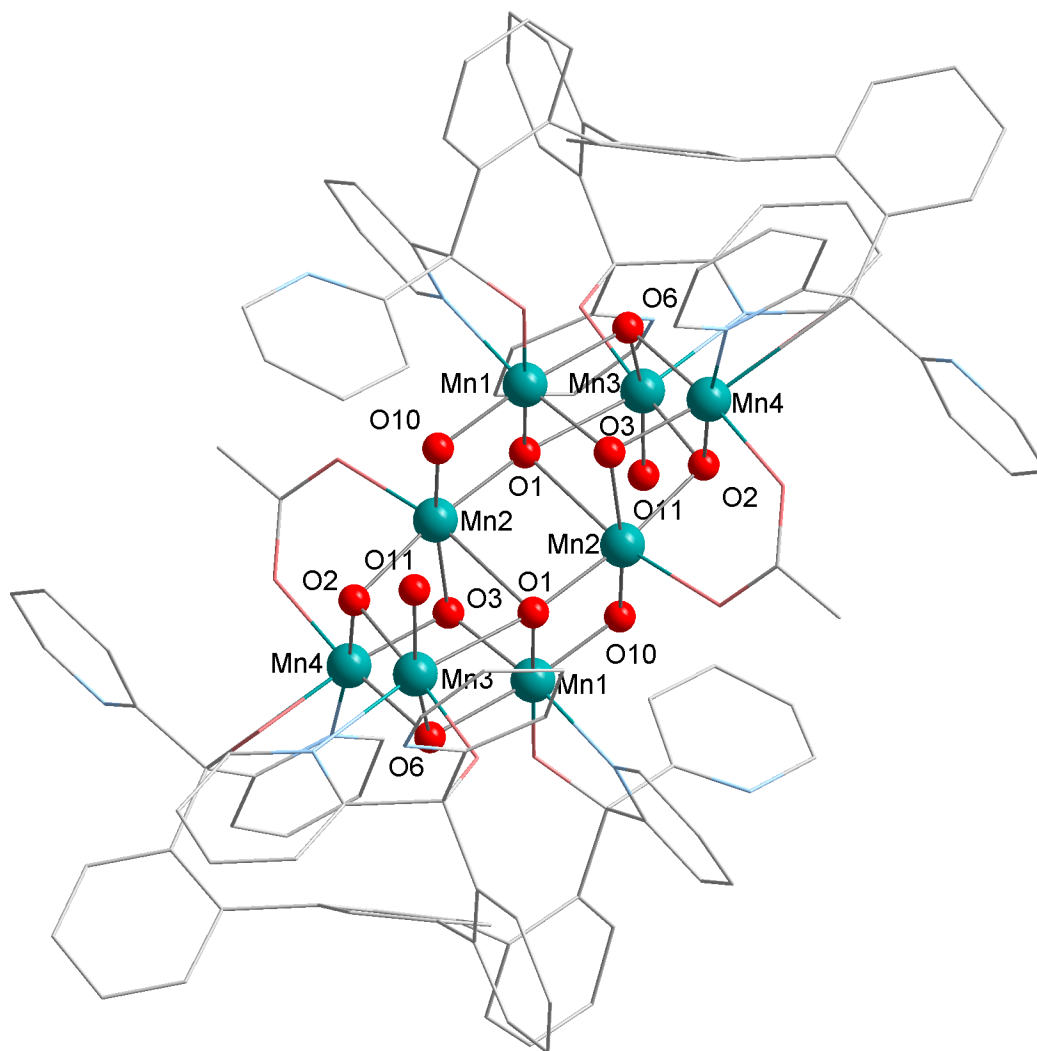


Figure 15. Preliminary solid state structure of octamanganese complex **C.15**.

Conclusions

In summary, we have demonstrated that there are several other multimetallic oxido cluster architectures that these complexes can access. The trinuclear basal core remains fairly stable and robust, but upon oxidation and incorporation of other metals, clusters of greater nuclearity can form that can lead to unpredictable results.

Experimental Section

General Considerations. Unless stated otherwise, all synthetic manipulations were carried out using standard Schlenk techniques under a nitrogen atmosphere, or in a M. Braun glovebox under an atmosphere of nitrogen. Reactions were carried out in oven-dried glassware cooled under vacuum. Anhydrous THF was purchased from Aldrich in 18 L Pure-PacTM containers. Anhydrous dichloromethane, acetonitrile, diethyl ether, and THF were purified by sparging with nitrogen for 15 minutes and then passing under nitrogen pressure through a column of activated A2 alumina (Zapp's). All non-dried solvents used were reagent grade or better. All NMR solvents were purchased from Cambridge Isotope Laboratories, Inc. NMR solvents were dried as follows: CD₂Cl₂ and CD₃CN over calcium hydride. All NMR solvents were degassed by three freeze-pump-thaw cycles and vacuum-transferred prior to use. ¹H NMR and ¹³C NMR spectra were recorded on a Varian 300 MHz instrument, with shifts reported relative to the residual solvent peak.

The acetate-bridged trimanganese monooxo complex [Mn₃O(OAc)₆(pyr)₃]•pyr was prepared according to literature procedures.³ The ligand framework H₃L, the trimanganese(II) precursor LMn^{II}₃(OAc)₃, and compounds **4**, **5**, and **6** were prepared according to literature procedures.⁴ Lithium bis(trimethylsilyl)amide was purchased from Sigma-Aldrich and used as received. Cu(OTf)₂ was purchased from Strem and used as received. Ca(OTf)₂ was purchased from Alfa Aesar and used as received. [(bpy)₂MnO₂Mn(bpy)₂][ClO₄]₃•H₂O was prepared according to literature procedures.⁵

Synthesis of LMn₃(O₂CCF₃)₃ (C.1). In the glovebox, a scintillation vial equipped with a stir bar was charged with a solution of H₃L (0.102 g, 0.119 mmol) in THF (5 mL). Triethylamine (0.07 mL, 0.475 mmol) was added, and a solution of Mn(O₂CCF₃)₂ (0.100 g,

0.356 mmol) was added. The yellow solution was stirred at room temperature for 2 h. Lithium bis(trimethylsilyl)amide (0.060 g, 2 equiv) was added as a solid, and the yellow solution became turbid within 20 min. After 5 h, the mixture was filtered through Celite and washed with THF. The white solid was extracted from the Celite with dichloromethane, then concentrated *in vacuo* to yield the product as a white solid (0.048 g, 30%). Yield is not yet optimized.

Synthesis of $[\text{LMn}_3\text{O}(\text{O}_2\text{CCF}_3)_3]_2\text{Ca}\cdot 2\text{OTf}$ (C.2). In the glovebox, a scintillation vial equipped with a stir bar was charged with $\text{LMn}_3(\text{O}_2\text{CCF}_3)_3$ (0.030 g, 0.022 mmol) and THF (5 mL). While stirring, $\text{Ca}(\text{OTf})_2$ (0.004 g, 0.011 mmol) was added as a solid and the mixture was stirred at room temperature for 3 min. Iodosobenzene (0.005 g, 0.022 mmol) was added as a solid, and the mixture was stirred at room temperature for 30 min., turning a dark purple-brown color and becoming more homogeneous. The mixture was filtered through Celite and concentrated under reduced pressure to yield a brown solid. The precipitate collected over the Celite was extracted using dichloromethane and also concentrated under reduced pressure to yield a brown solid. This fraction was recrystallized from dichloromethane at room temperature to yield X-ray quality crystals.

Synthesis of $\text{LMn}_3(\text{OTf})_3\cdot 3\text{CH}_3\text{CN}$ (C.3). In the glovebox, a scintillation vial equipped with a stir bar was charged with H_3L (0.200 g, 0.233 mmol) and THF (8 mL). $\text{Mn}(\text{OTf})_2\cdot\text{CH}_3\text{CN}$ (0.275 g, 0.698 mmol) was added in THF (2 mL) and the mixture was stirred at room temperature for 2 min. LiHMDS (0.120 g, 0.717 mmol) was added as a solid and the yellow mixture was stirred at room temperature for 2 h. The yellow mixture was filtered through Celite and the collected pale yellow solid was washed with THF, then extracted with acetonitrile and concentrated *in vacuo* to yield a pale yellow solid (0.150 g).

X-ray quality crystals were grown by vapor diffusion of diethyl ether into an acetonitrile solution of the product at room temperature.

Synthesis of C.4. In the glovebox, H_3L (0.500 g, 0.582 mmol) was weighed into an oven-dried Schlenk tube equipped with a stir bar. THF (10 mL) was added, then a solution of lithium bis(trimethylsilyl)amide (0.292 g, 1.75 mmol, 3 equiv) was added in THF. Dry CH_3CN (20 mL) was added to the orange mixture, which turned greenish-yellow. The mixture was stirred at room temperature for 15 min., then on the Schlenk line under positive N_2 flow, $[(\text{bpy})_2\text{Mn}^{\text{III}}\text{O}_2\text{Mn}^{\text{IV}}(\text{bpy})_2][\text{ClO}_4]_3 \cdot \text{H}_2\text{O}$ (0.96 g, 0.873 mmol, 1.5 equiv) was added as a solid. The mixture turned a red-brown color. The reaction mixture was stirred under N_2 at room temperature for 16 h, at which point the dark brown mixture was concentrated *in vacuo*. Under ambient conditions, the brown residue was washed with THF and CH_2Cl_2 . The remaining solid was extracted with CH_3CN . To 50 mg of this material, $\text{Mn}(\text{OAc})_2 \cdot 2\text{H}_2\text{O}$ (0.0093 g, 0.0346 mmol) was added in CH_3CN , and the brown mixture was heated to 80 °C. X-ray quality crystals were grown by slow evaporation from CH_2Cl_2 . ^1H NMR (CD_2Cl_2 , 300 MHz): δ 77.4, 70.1, 43.0, 25.2, 17.8, 14.7, -21.7, -27.2 ppm.

Synthesis of $\text{LCuMn}_2(\text{OAc})_2(\text{OTf})$ (C.5). In the glovebox, a scintillation vial equipped with a stir bar was charged with $\text{LMn}_3(\text{OAc})_3$ (0.050 g, 0.039 mmol) and $\text{Cu}(\text{OTf})_2$ (0.015 g, 0.041 mmol). THF (5 mL) was added. The reaction mixture was stirred at room temperature for 5 min. and began to turn slightly green. KO_2 (0.011 g, 0.143 mmol) was added as a solid, and the mixture was stirred at room temperature for 16 h, turning dark brown. The mixture was filtered through Celite. The green filtrand was extracted with CH_2Cl_2 and crystallized to yield **C.5** (15 mg). ^1H NMR (CDCl_3 , 300 MHz): δ 41.5, 36.7,

34.4, 26.9, 25.6, 13.5, 10.8, 8.9, -8.9, -17.5 ppm. The brown THF filtrate was assigned as $\text{LMn}_4\text{O}_3(\text{OAc})_3$ (**9**) by ^1H NMR spectroscopy.

Synthesis of $\text{LMn}_3\text{ZnO}(\text{OAc})_3(\text{OTf})$ (C.6). In the glovebox, a scintillation vial equipped with a stir bar was charged with $\text{LMn}_3(\text{OAc})_3$ (0.100 g, 0.084 mmol) and THF (8 mL). While stirring, $\text{Zn}(\text{OTf})_2$ (0.030 g, 0.084) was added with the aid of THF (2 mL) and the yellow mixture was stirred at room temperature for 5 min. Iodosobenzene (0.018 g, 0.084 mmol) was added as a solid, and the mixture was stirred at room temperature for 30 min., turning more homogeneous and a darker purple-brown color. Potassium superoxide (0.006 g, 0.084 mmol) was added as a solid, and the mixture was stirred at room temperature for 14 h. The mixture was filtered through Celite and washed with THF. The collected purple solid was extracted with dichloromethane, then concentrated *in vacuo* to yield the product as a purple solid (0.070 g, 53%). ^1H NMR (CD_2Cl_2 , 300 MHz): δ 48.91, 43.18, 34.46, 29.95, 11.29, 8.76, -7.69, -10.92 ppm.

Synthesis of $\text{LMn}_3\text{LiO}(\text{OAc})_3(\text{OTf})$ (C.7). In the glovebox, a solution of lithium bis(trimethylsilyl)amide (0.058 g, 0.349 mmol, 3 equiv) in THF (2 mL) was added to a solution of H_3L (0.100 g, 0.116 mmol, 1 equiv) in THF (3 mL). The mixture darkened to yellow. After 5 min., this mixture was added to a suspension of $[\text{Mn}_3\text{O}(\text{OAc})_6(\text{pyr})_3]\cdot\text{pyr}$ (0.099 g, 0.116 mmol, 1 equiv) and $\text{Ca}(\text{OTf})_2$ (0.030 g, 0.0887 mmol, 0.7 equiv) in THF (2 mL). The mixture was stirred at room temperature overnight, becoming purple but staying heterogeneous. The precipitate was collected over Celite, then washed with THF and extracted with CH_2Cl_2 . The dichloromethane extract was concentrated *in vacuo* to yield 80 mg of a purple solid. X-ray quality crystals were grown by vapor diffusion at room

temperature of diethyl ether into an acetonitrile solution of **C.7**. ^1H NMR (CD_2Cl_2 , 300 MHz): δ 67.3, 62.4, 32.5, 24.7, 15.2, 8.6, -11.1 , -17.6 ppm.

Synthesis of C.8. In the glovebox, a scintillation vial equipped with a stir bar was charged with $[\text{4-Ca}(\text{DME})(\text{OTf})]^{2+}$ (0.015 g, 0.0086 mmol) and 18-crown-6 (0.002 g, 0.009 mmol, 1 equiv). THF was added (1 mL), and the mixture was stirred for 1 h, resulting in the formation of some purple precipitate. The precipitate was collected over Celite, then extracted with CH_2Cl_2 , dried *in vacuo*, taken up in DME, and concentrated again. X-ray quality crystals were grown by vapor diffusion of diethyl ether into an acetonitrile solution of **C.8** at room temperature.

Synthesis of C.10. In the glovebox, a scintillation vial was charged with $[\text{5-Ca}(\text{DME})(\text{OTf})]^+$ (0.015 g, 0.009 mmol) and *p*-cyanoanilinium triflate (0.005 g, 0.019 mmol, 2 equiv). Acetonitrile (2 mL) was added. X-ray quality crystals were grown by vapor diffusion of diethyl ether into an acetonitrile solution of the product. ^1H NMR (CD_3CN , 300 MHz): δ 84.7, 75.6, 73.3, 56.7, 50.0, 44.9, 37.0, 35.0, 21.1, 16.6, 15.5, -14.1 , -19.2 , -24.2 , -27.1 ppm.

Synthesis of C.11. In the glovebox, made a solution of **6-Ca** (0.020 g, 0.015 mmol) in benzene (5 mL) with one drop of THF. Under ambient conditions, added a solution of $(\text{paoH})_2\text{Mn}(\text{OAc})_2$ (0.004 g, 0.015 mmol, 1 equiv) in CH_2Cl_2 (2 mL), then added triethylamine (0.004 mL, 0.029 mmol, 2 equiv) via syringe. Stirred the brown mixture at room temperature for 5 min., then concentrated under reduced pressure. X-ray quality crystals were grown by vapor diffusion of diethyl ether into a dichloromethane solution of **C.11** at room temperature. ^1H NMR (CD_2Cl_2 , 300 MHz): δ 20.0, 10.9, 8.8, 8.4, -12.7 , -17.0 ppm.

References

1. Christou, G. *Acc. Chem. Res.* **1989**, *22*, 328-335.
2. (a) Shirin, Z.; Hammes, B. S.; Young, V. G.; Borovik, A. S. *J. Am. Chem. Soc.* **2000**, *122*, 1836-1837; (b) Gupta, R.; MacBeth, C. E.; Young, V. G.; Borovik, A. S. *J. Am. Chem. Soc.* **2002**, *124*, 1136-1137.
3. Vincent, J. B.; Chang, H. R.; Folting, K.; Huffman, J. C.; Christou, G.; Hendrickson, D. N. *J. Am. Chem. Soc.* **1987**, *109*, 5703-5711.
4. (a) Tsui, E. Y.; Day, M. W.; Agapie, T. *Angew. Chem. Int. Ed.* **2011**, *50*, 1668-1672; (b) Tsui, E. Y.; Kanady, J. S.; Day, M. W.; Agapie, T. *Chem. Commun.* **2011**; (c) Kanady, J. S.; Tsui, E. Y.; Day, M. W.; Agapie, T. *Science* **2011**, *333*, 733-736; (d) Tsui, E. Y.; Tran, R.; Yano, J.; Agapie, T. *Nat Chem* **2013**, *5*, 293-299.
5. Cooper, S. R.; Calvin, M. *J. Am. Chem. Soc.* **1977**, *99*, 6623-6630.

Appendix D

NMR SPECTRA

NMR Spectra

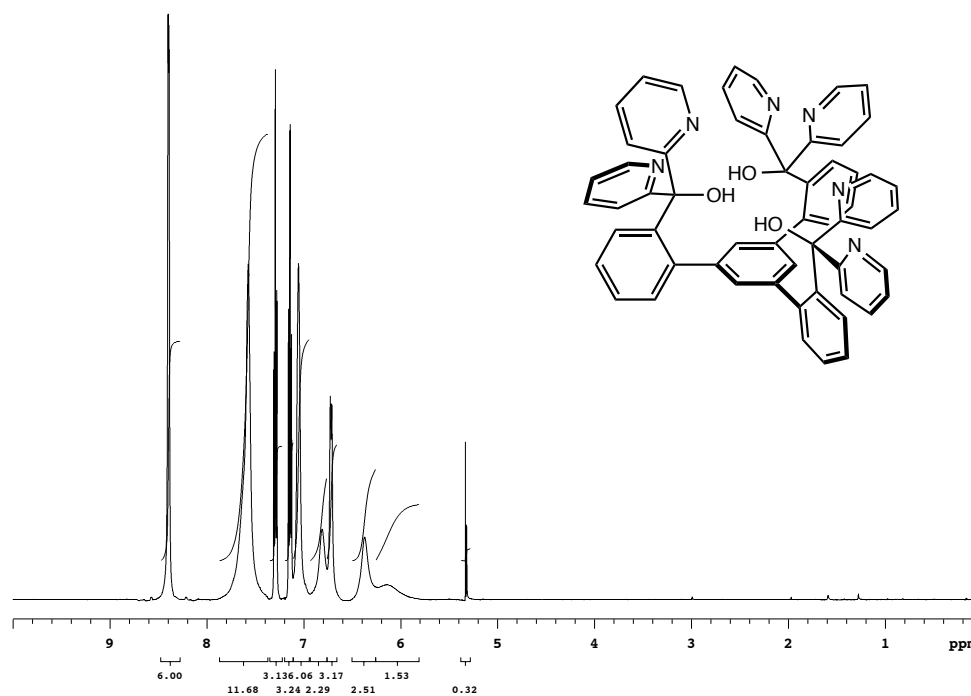


Figure 1. ^1H NMR spectrum of H_3L in CD_2Cl_2 at 25°C .

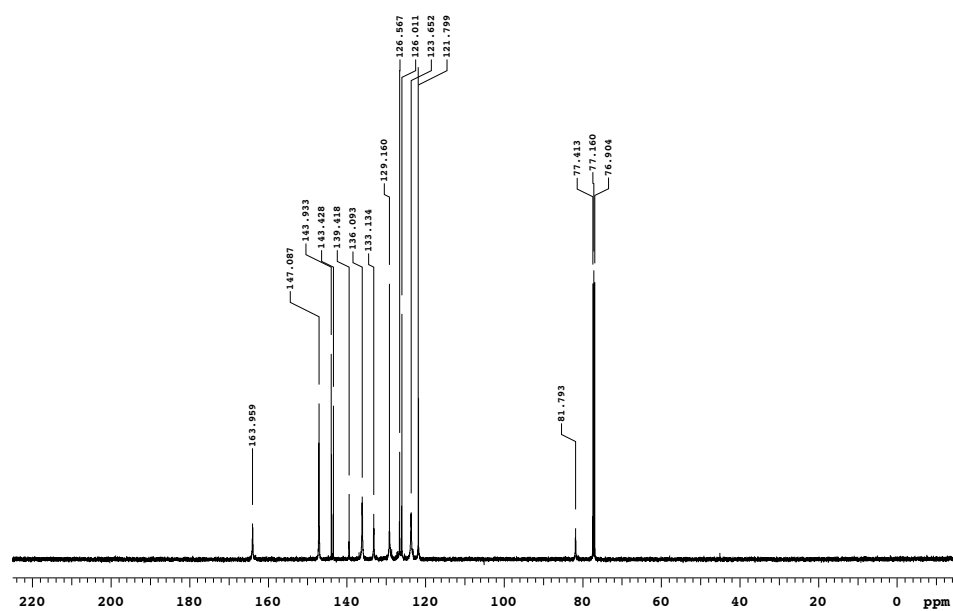


Figure 2. ^{13}C NMR spectrum of H_3L in CDCl_3 at 25°C .

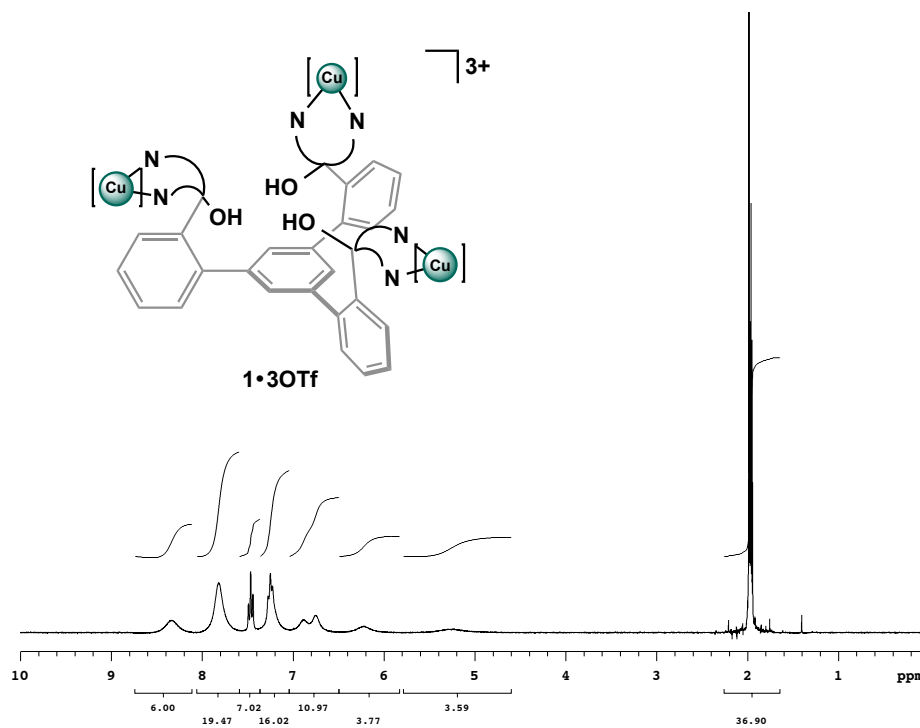


Figure 3. ^1H NMR spectrum of **1•3OTf** in CD_3CN at 25 °C. CH_3CN peak is offscale.

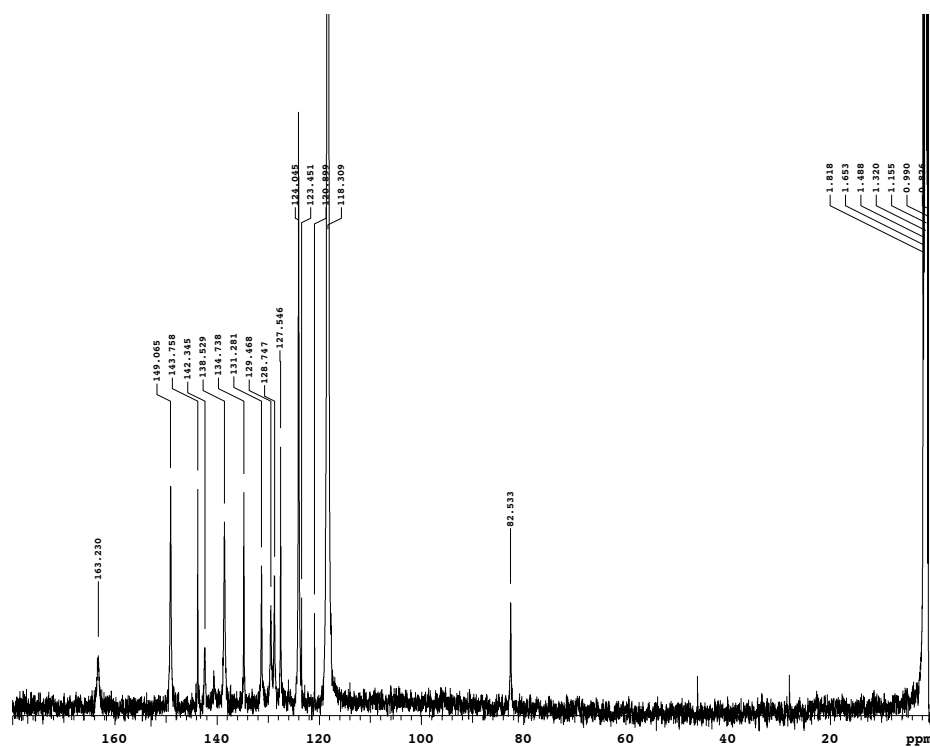


Figure 4. ^{13}C NMR spectrum of **1•3OTf** in CD_3CN at 25 °C. CD_3CN residual peaks are offscale.

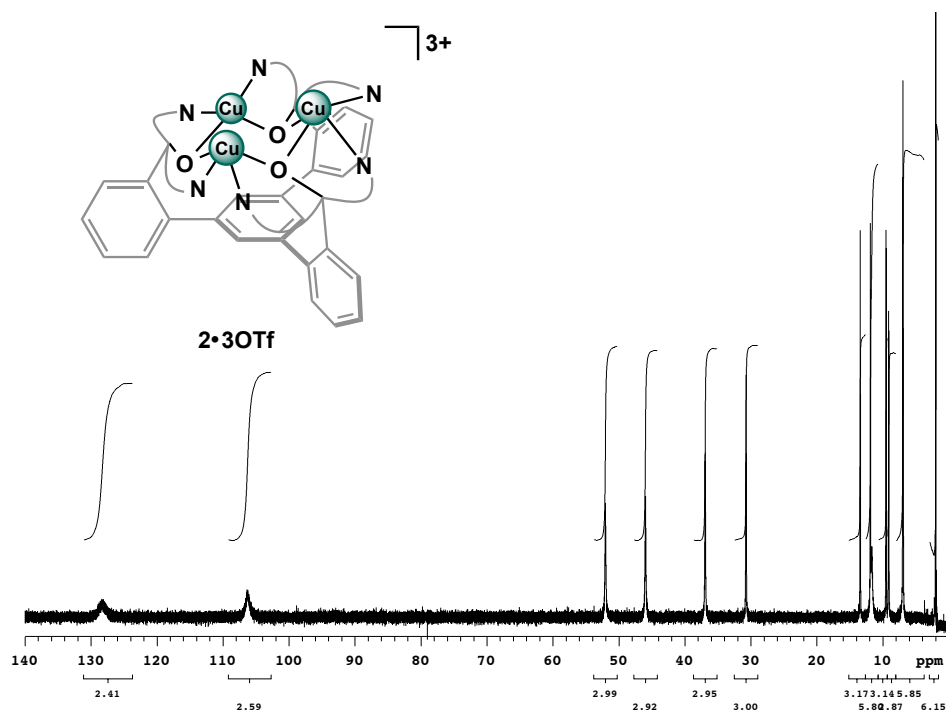


Figure 5. ^1H NMR spectrum of **2•3OTf** in CD_3CN at 25 °C. CD_3CN solvent residual peak is offscale.

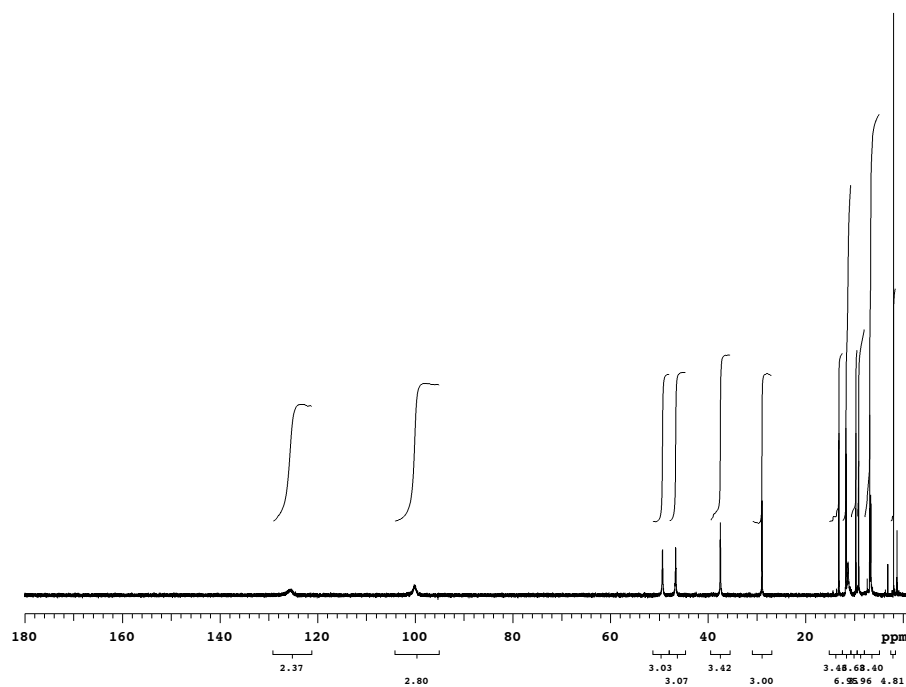


Figure 6. ^1H NMR spectrum of **2•3BF₄** in CD_3CN at 25 °C.

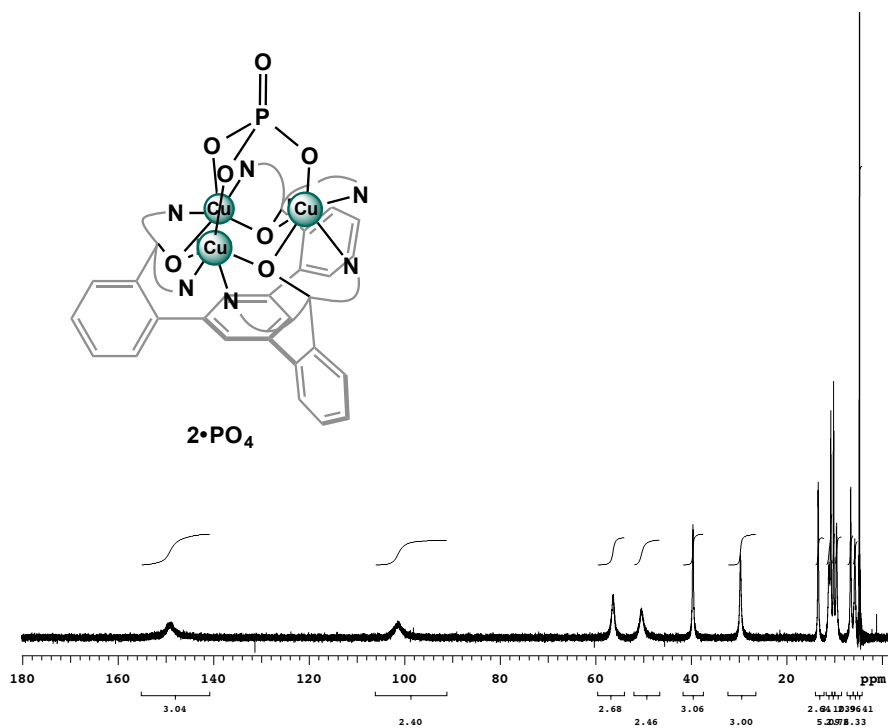


Figure 7. ^1H NMR spectrum of $2\cdot\text{PO}_4$ in D_2O at $25\text{ }^\circ\text{C}$. D_2O solvent residual peak is offscale.

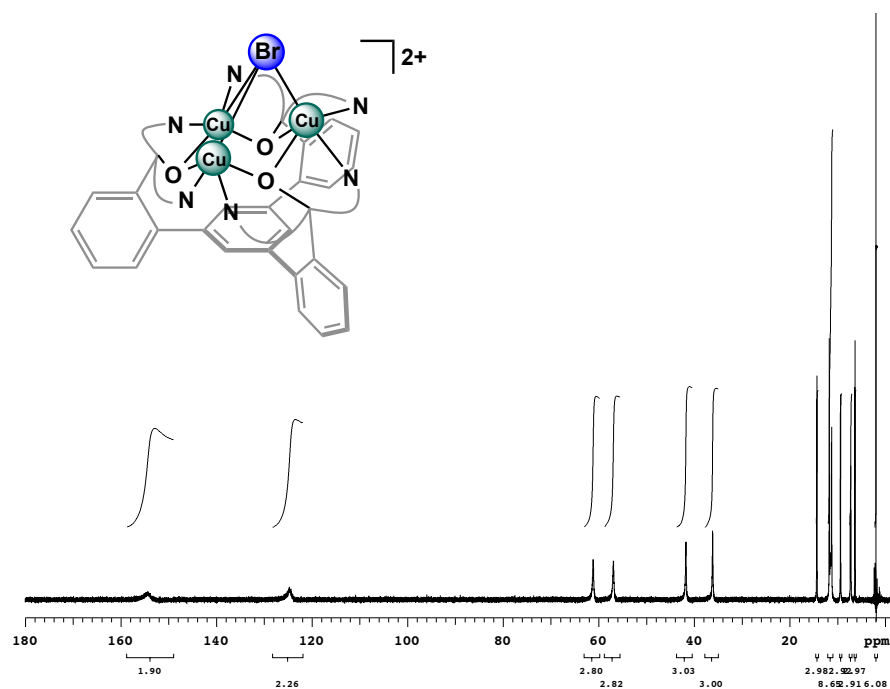


Figure 8. ^1H NMR spectrum of $2\cdot\text{Br}\cdot 2\text{OTf}$ in CD_3CN at $25\text{ }^\circ\text{C}$. CD_3CN residual peak is offscale.

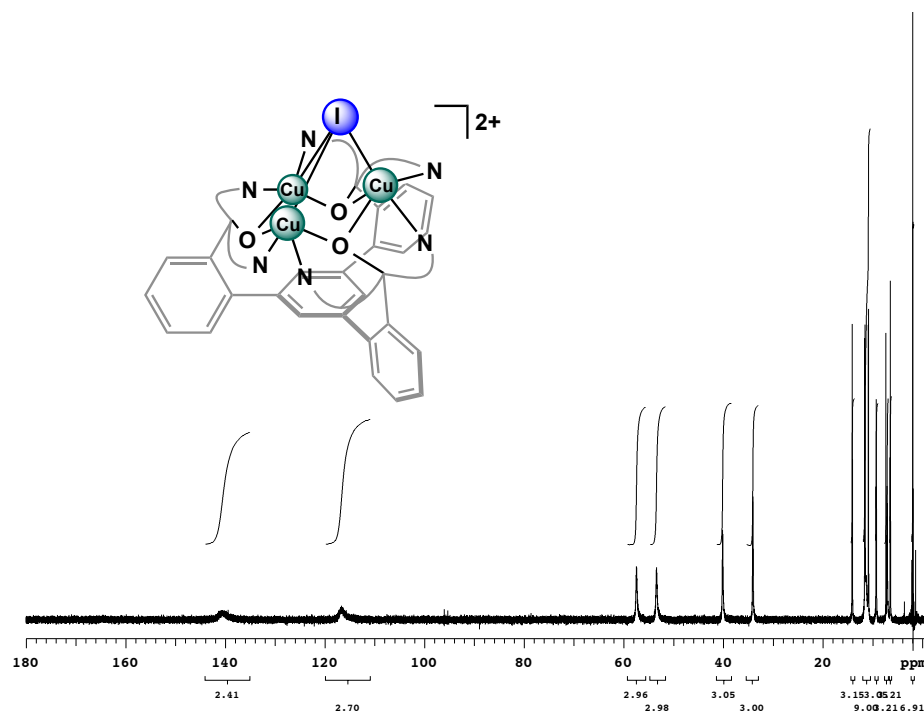


Figure 9. ^1H NMR spectrum of $2 \cdot \text{I} \cdot 2\text{OTf}$ in CD_3CN at 25°C . CD_3CN residual peak is offscale.

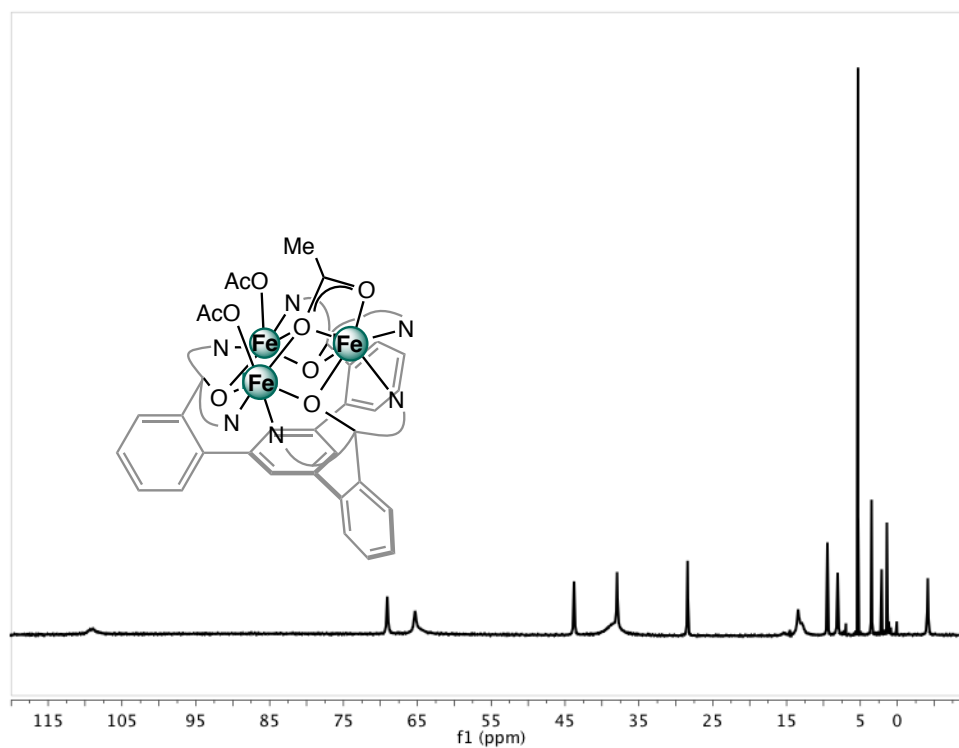


Figure 10. ^1H NMR spectrum of $\text{LFe}_3(\text{OAc})_3$ in CD_2Cl_2 at 25°C .

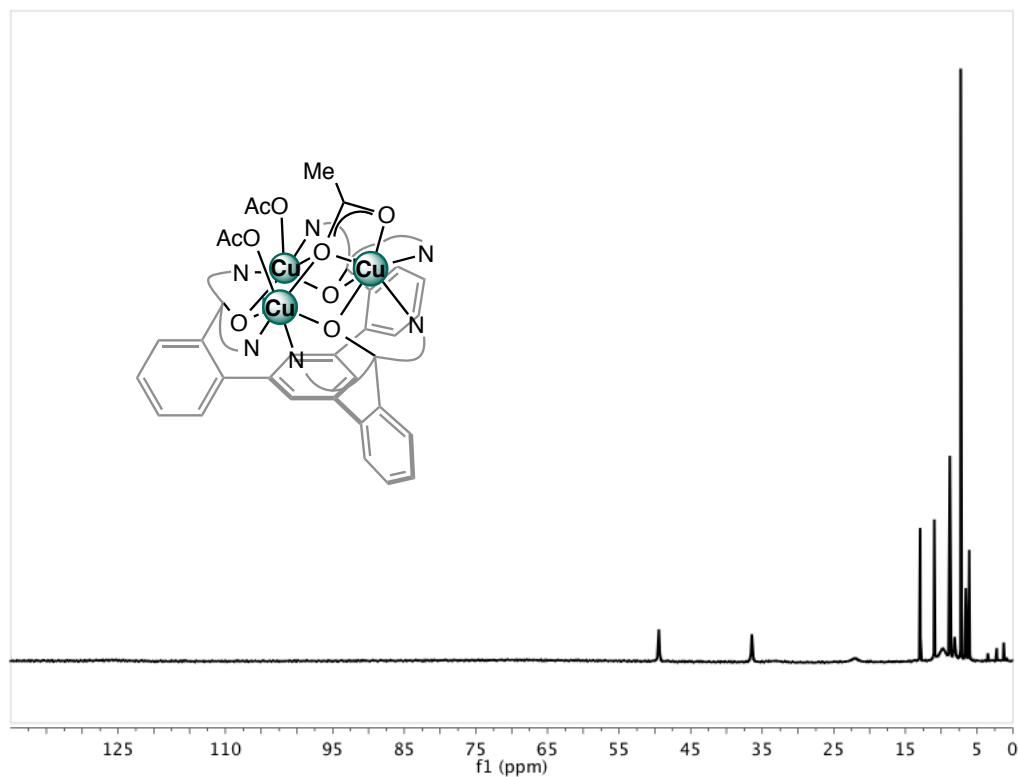


Figure 11. ^1H NMR spectrum of $\text{LCu}_3(\text{OAc})_3$ in CDCl_3 at 25°C .

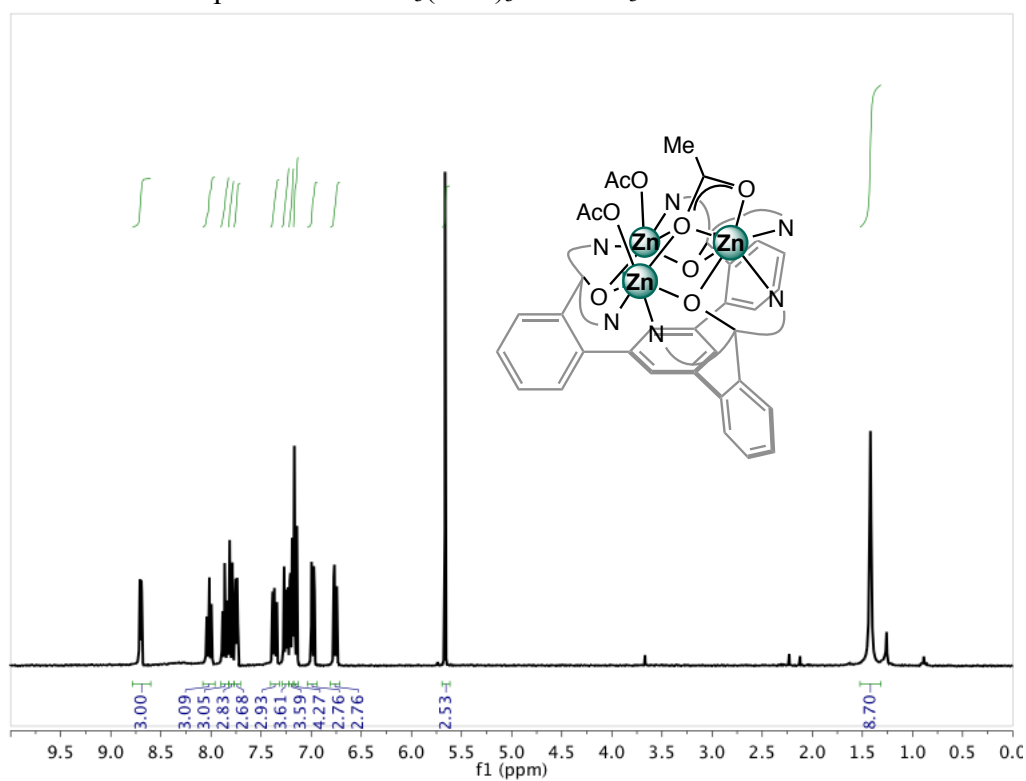


Figure 12. ^1H NMR spectrum of $\text{LZn}_3(\text{OAc})_3$ in CDCl_3 at 25°C .

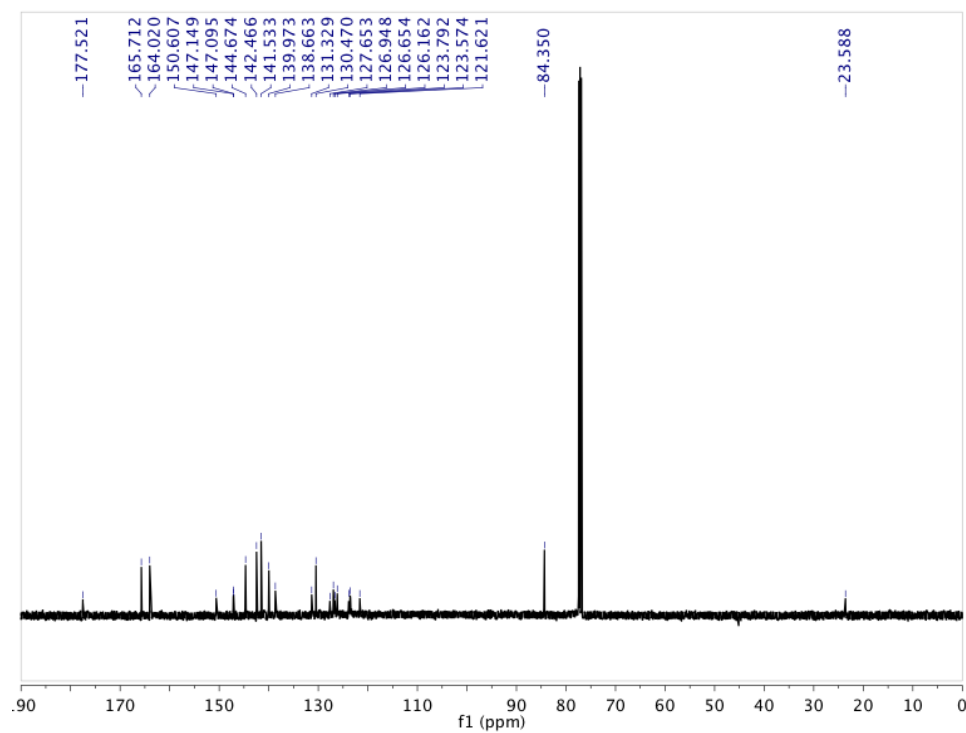


Figure 13. ^{13}C NMR spectrum of $\text{LZn}_3(\text{OAc})_3$ in CDCl_3 at 25 °C.

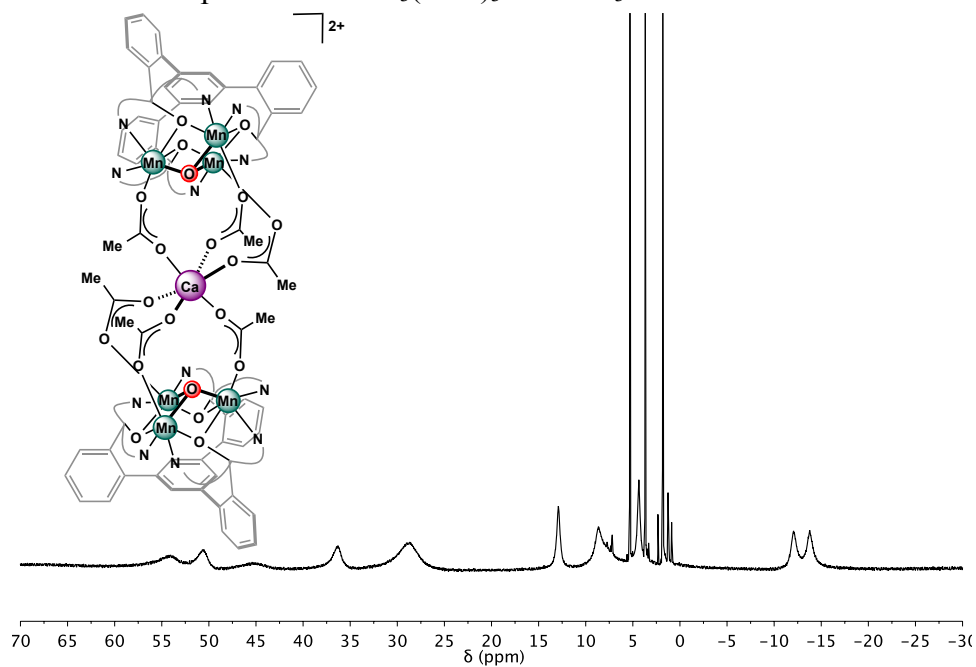


Figure 14. ^1H NMR spectrum of **3** in CD_2Cl_2 at 25 °C. Solvent peaks are offscale.

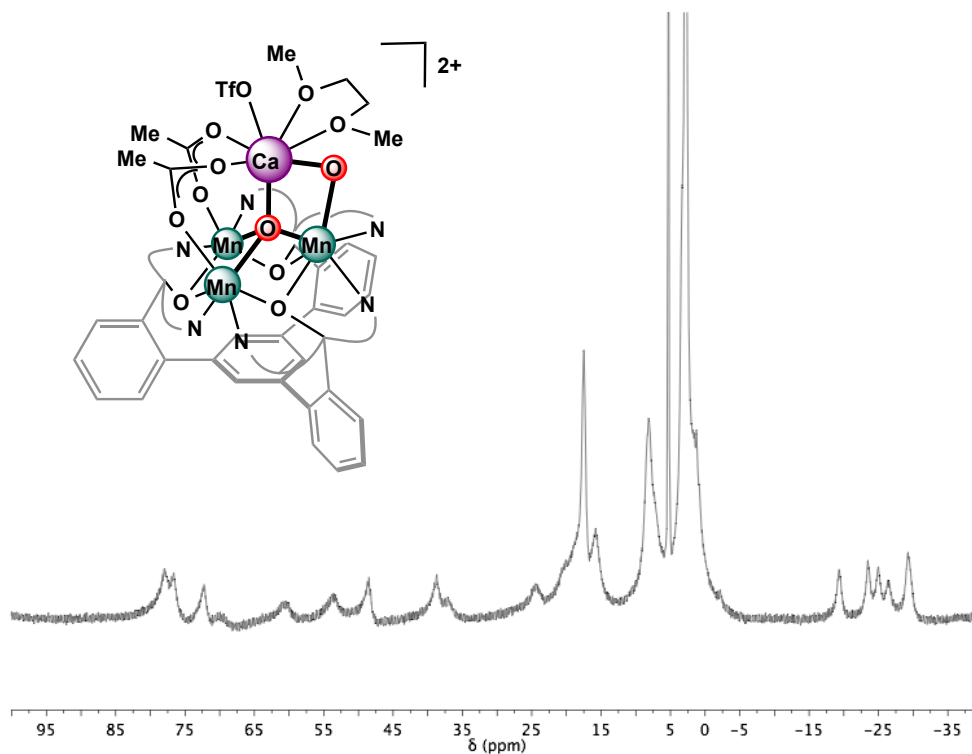


Figure 15. ^1H NMR spectrum of $[4\text{-Ca}(\text{DME})(\text{OTf})]^{2+}$ in CD_2Cl_2 at $25\text{ }^\circ\text{C}$.

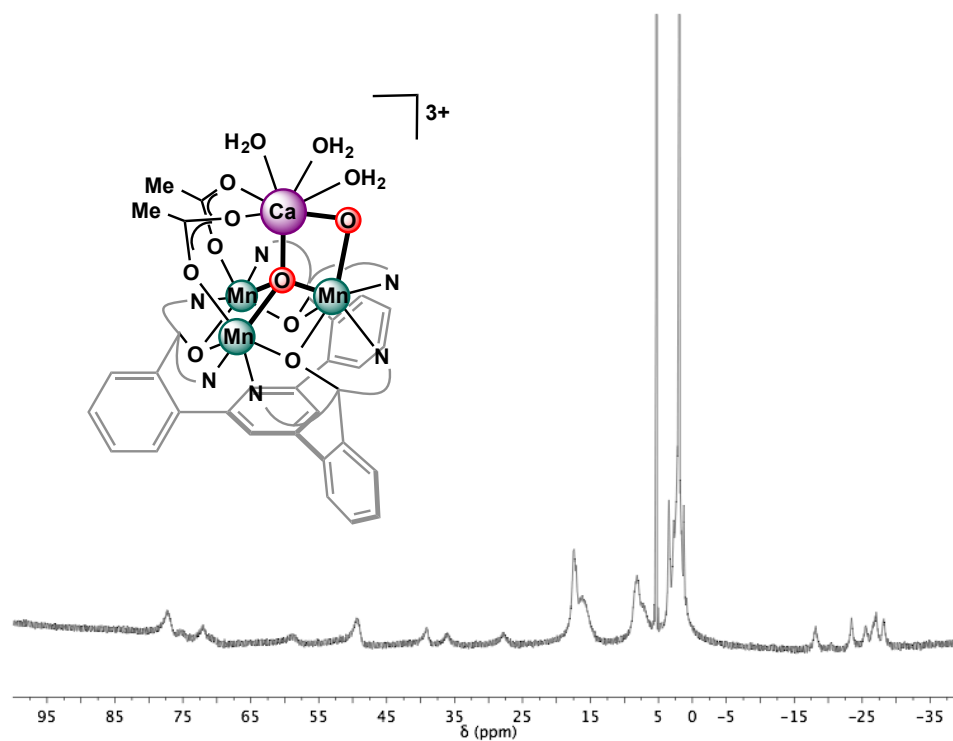


Figure 16. ^1H NMR spectrum of $[4\text{-Ca}(\text{OH}_2)_3]^{3+}$ in CD_2Cl_2 at $25\text{ }^\circ\text{C}$.

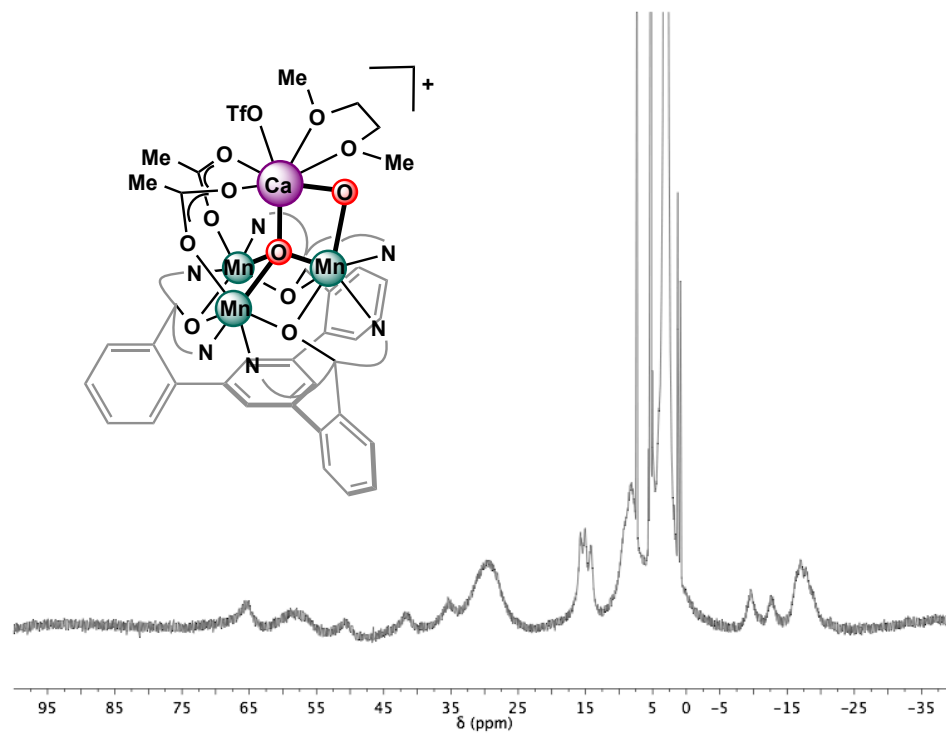


Figure 17. ^1H NMR spectrum of $[\mathbf{5}\text{-Ca}(\text{DME})(\text{OTf})]^+$ in CD_2Cl_2 at 25°C .

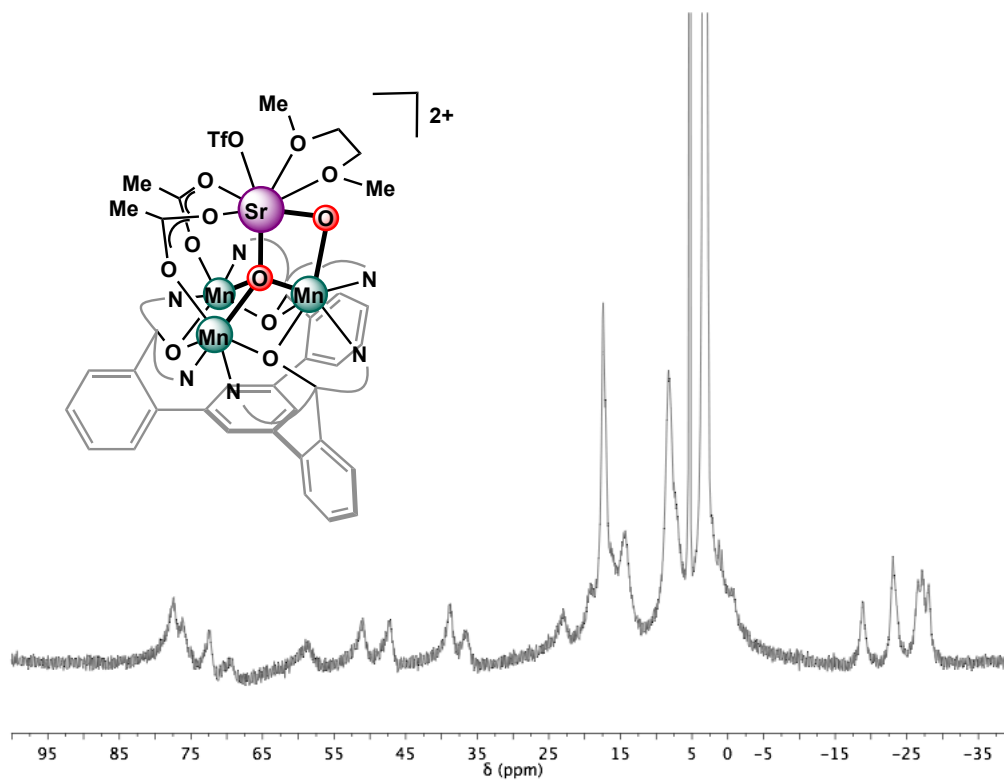


Figure 18. ^1H NMR spectrum of $[\mathbf{4}\text{-Sr}(\text{DME})(\text{OTf})]^{2+}$ in CD_2Cl_2 at 25°C .

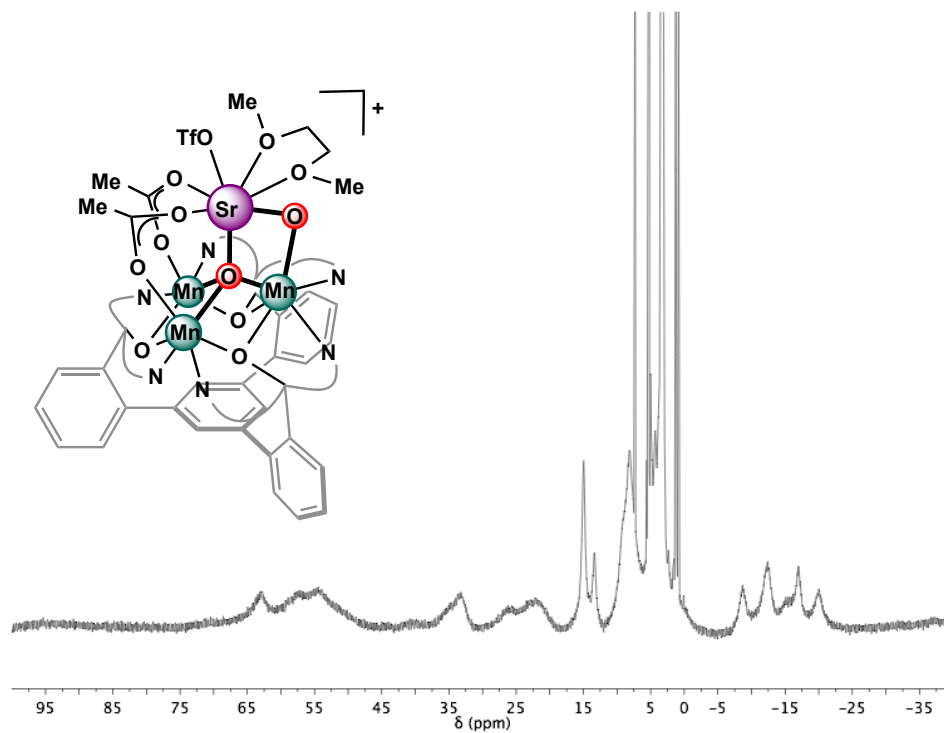


Figure 19. ^1H NMR spectrum of $[\mathbf{5}\text{-Sr}(\text{DME})(\text{OTf})]^+$ in CD_2Cl_2 at $25\text{ }^\circ\text{C}$.

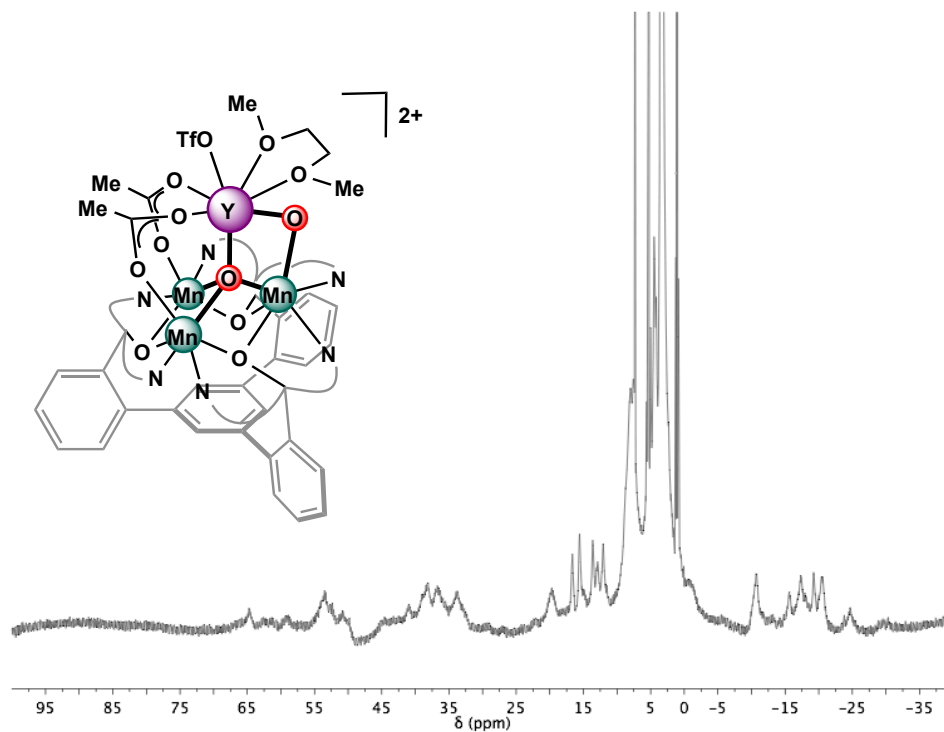


Figure 20. ^1H NMR spectrum of $[\mathbf{5}\text{-Y}(\text{DME})(\text{OTf})]^{2+}$ in CD_2Cl_2 at $25\text{ }^\circ\text{C}$.

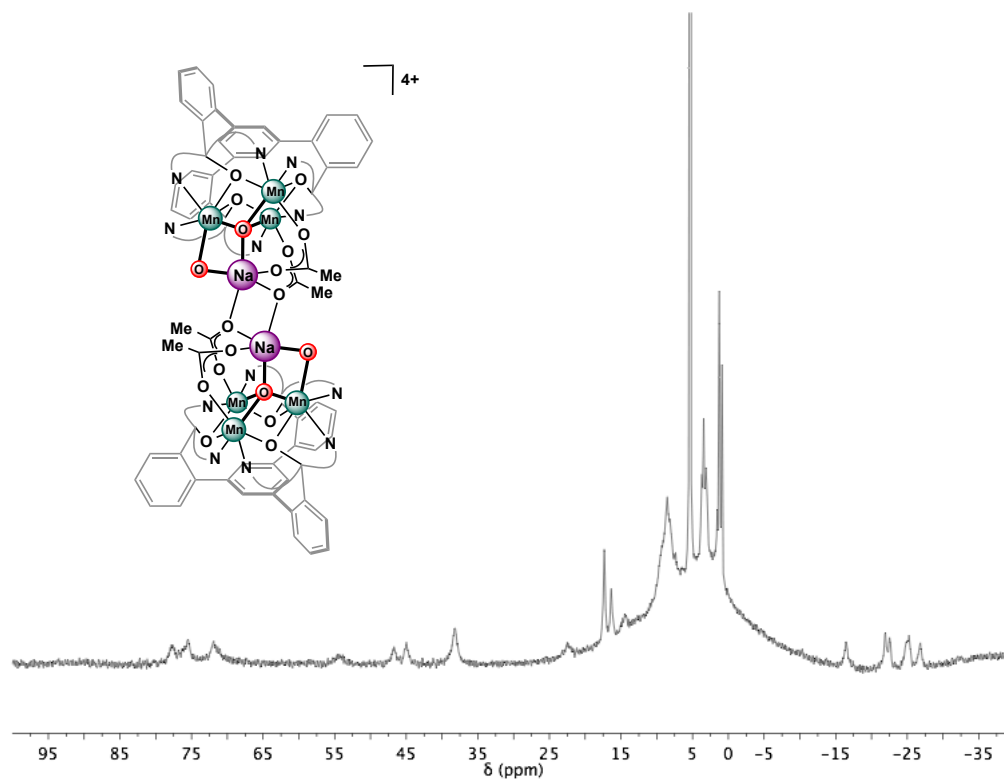


Figure 21. ^1H NMR spectrum of $[\mathbf{4}\text{-Na}]_2^{4+}$ in CD_2Cl_2 at 25°C .

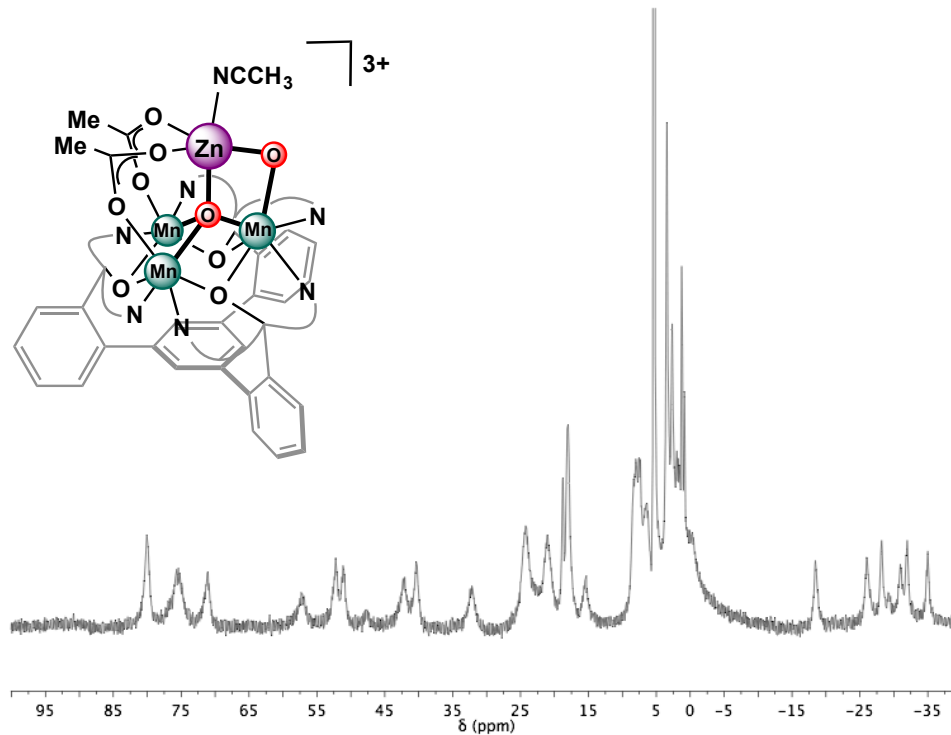


Figure 22. ^1H NMR spectrum of $[\mathbf{4}\text{-Zn}(\text{CH}_3\text{CN})]^{3+}$ in CD_2Cl_2 at 25°C .

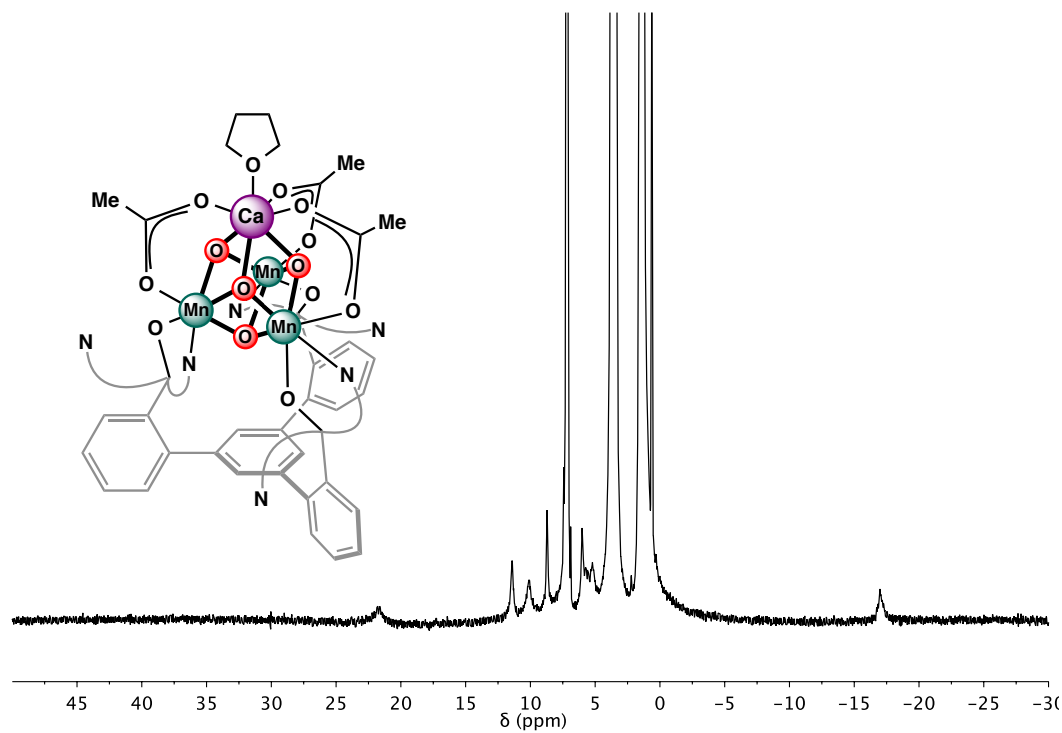


Figure 23. ^1H NMR spectrum of **6-Ca** in C_6D_6 at 25 °C.

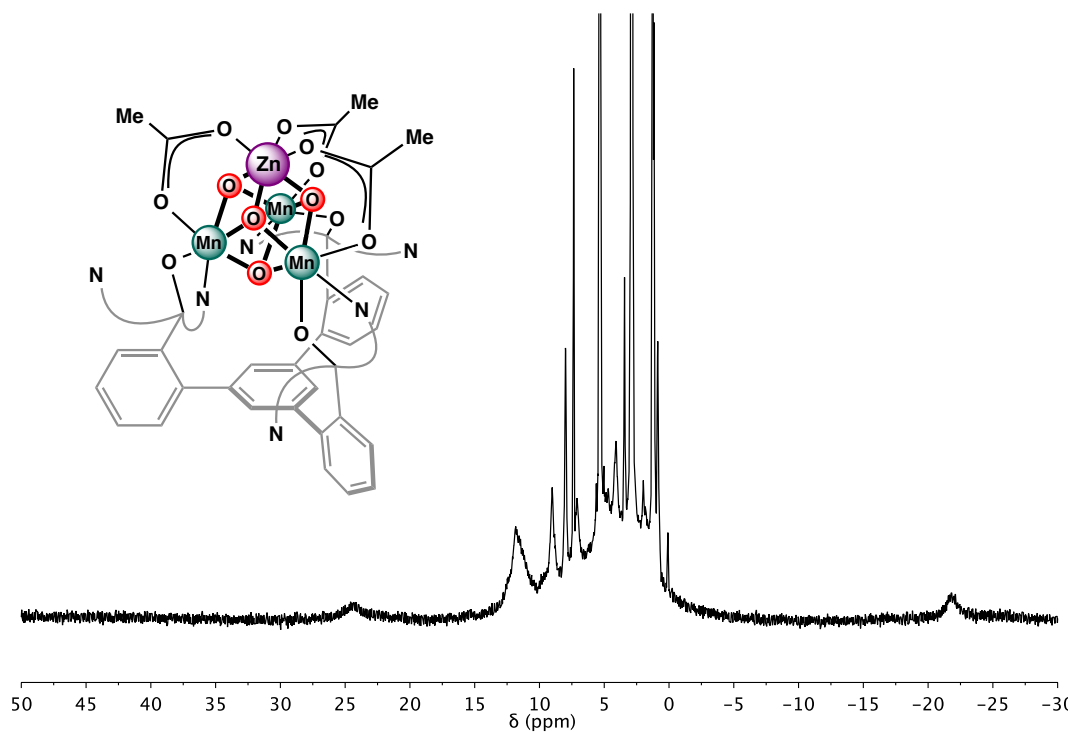


Figure 24. ^1H NMR spectrum of **6-Zn** in CD_2Cl_2 at 25 °C.

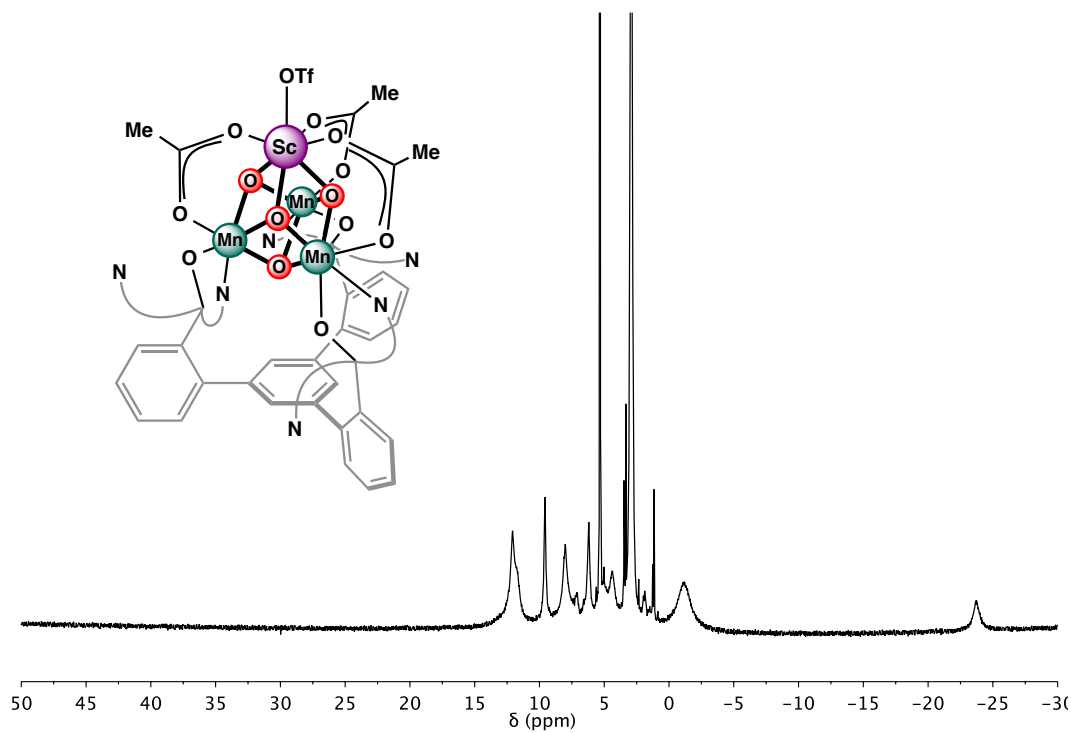


Figure 25. ^1H NMR spectrum of [6-Sc][OTf] in CD_2Cl_2 at 25 $^\circ\text{C}$.

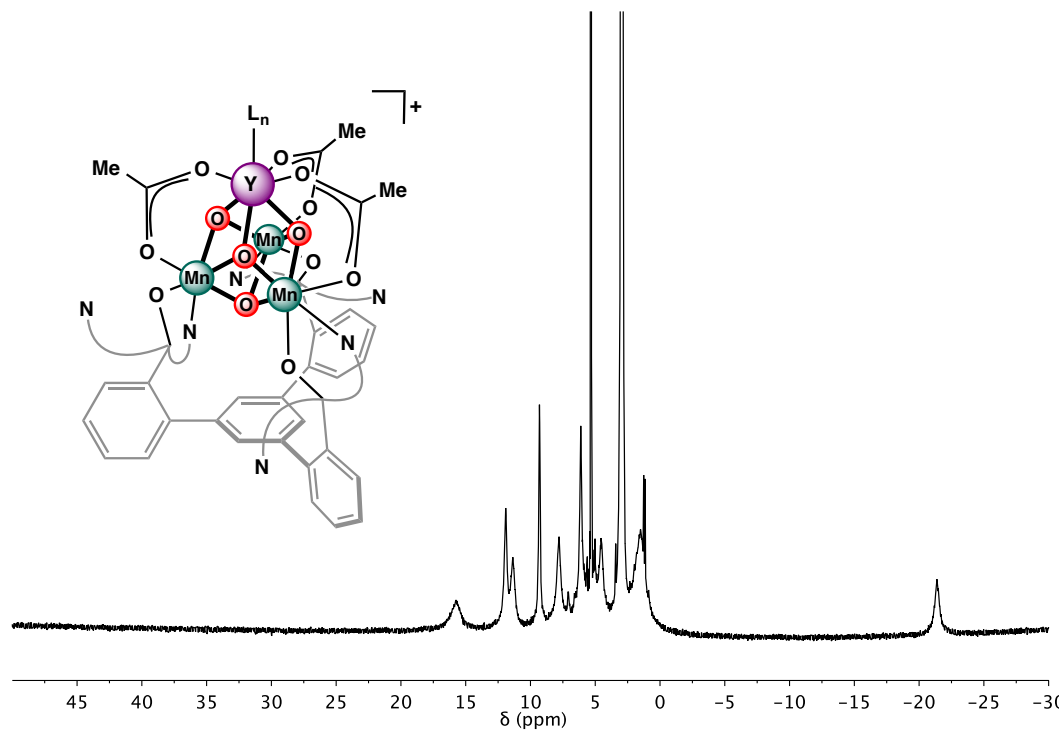


Figure 26. ^1H NMR spectrum of [6-Y][OTf] in CD_2Cl_2 at 25 $^\circ\text{C}$.

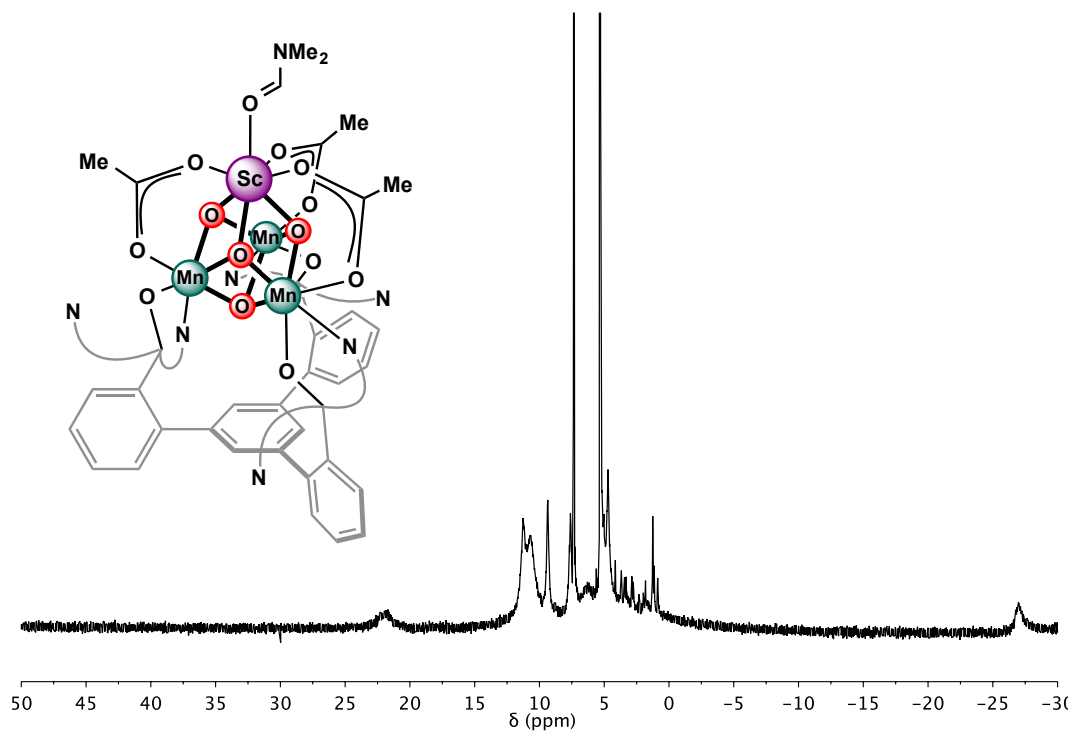


Figure 27. ^1H NMR spectrum of **7-Sc** in CD_2Cl_2 at 25 °C.

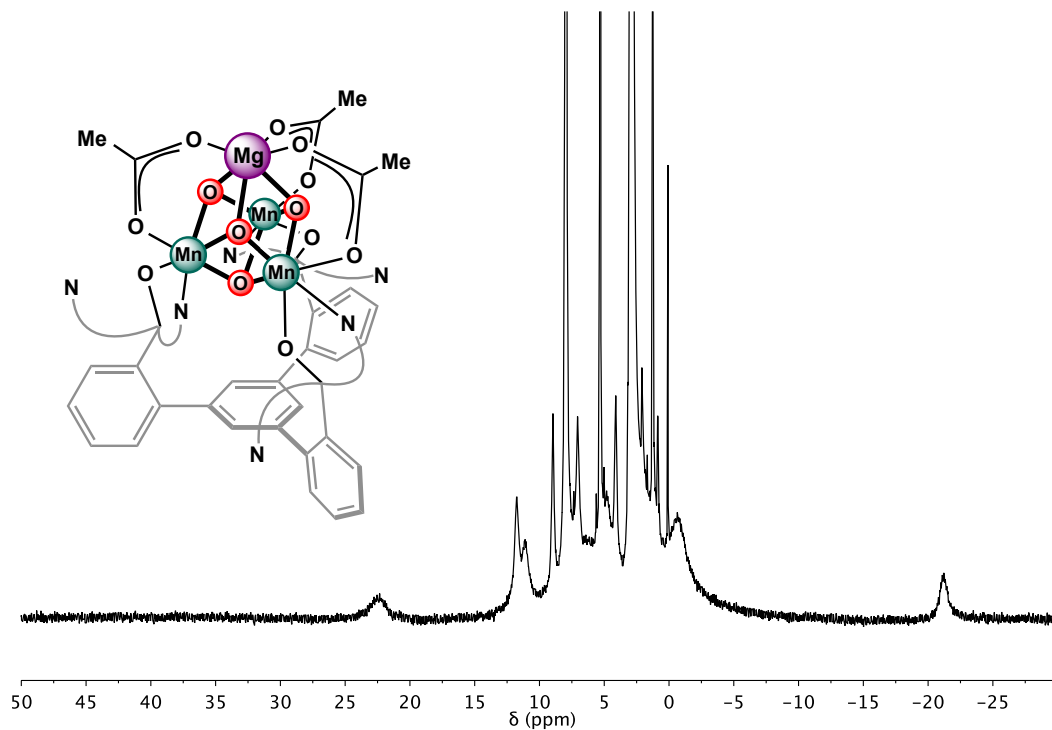


Figure 28. ^1H NMR spectrum of **6-Mg** in CD_2Cl_2 at 25 °C.

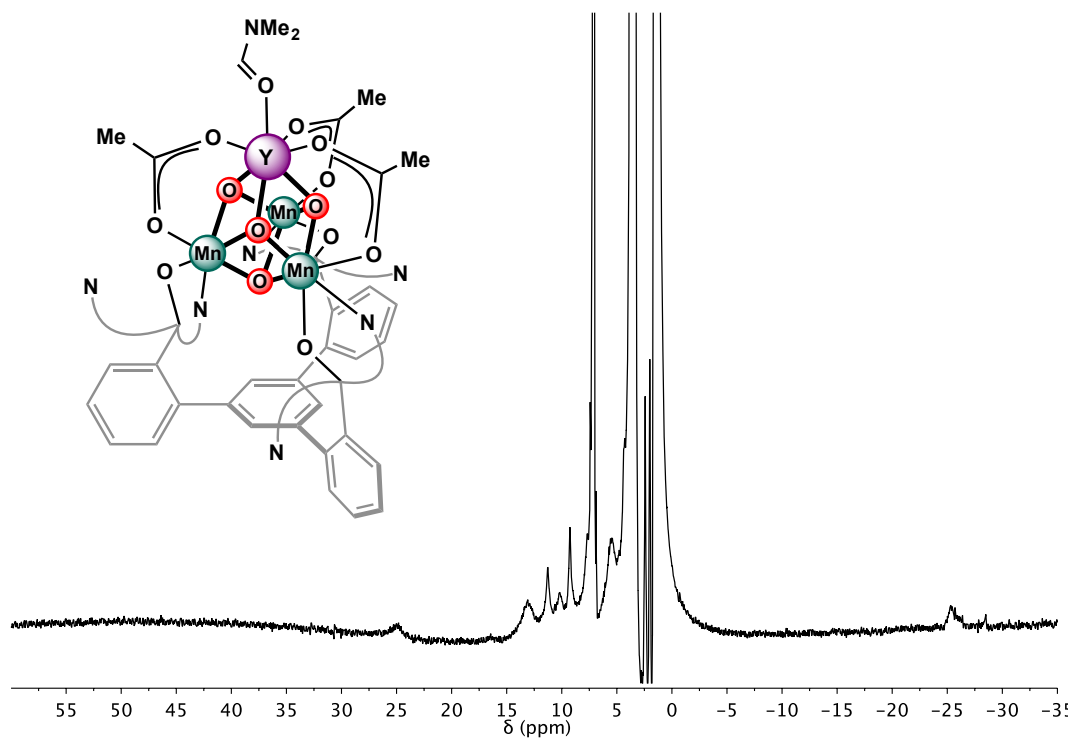


Figure 29. ^1H NMR spectrum of **7-Y** in C_6D_6 at $25\text{ }^\circ\text{C}$.

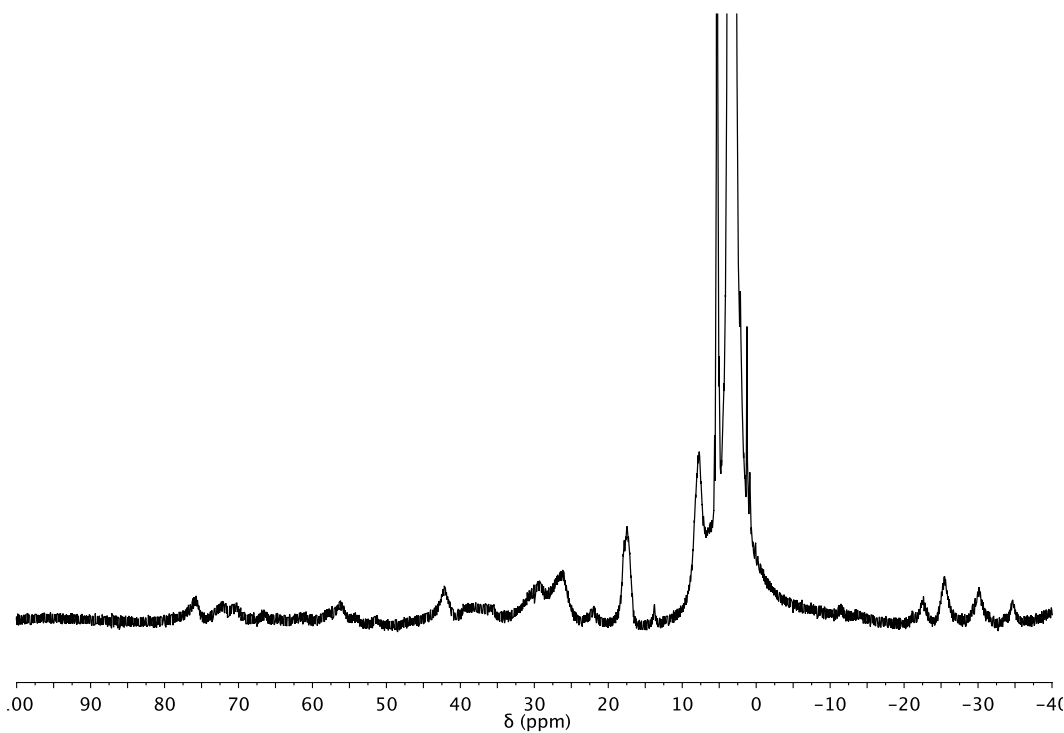


Figure 30. ^1H NMR spectrum of $[\mathbf{4}\text{-Y}(\text{DME})(\text{OTf})]^{3+}$ in CD_2Cl_2 (one drop DME added for solubility) at $25\text{ }^\circ\text{C}$.

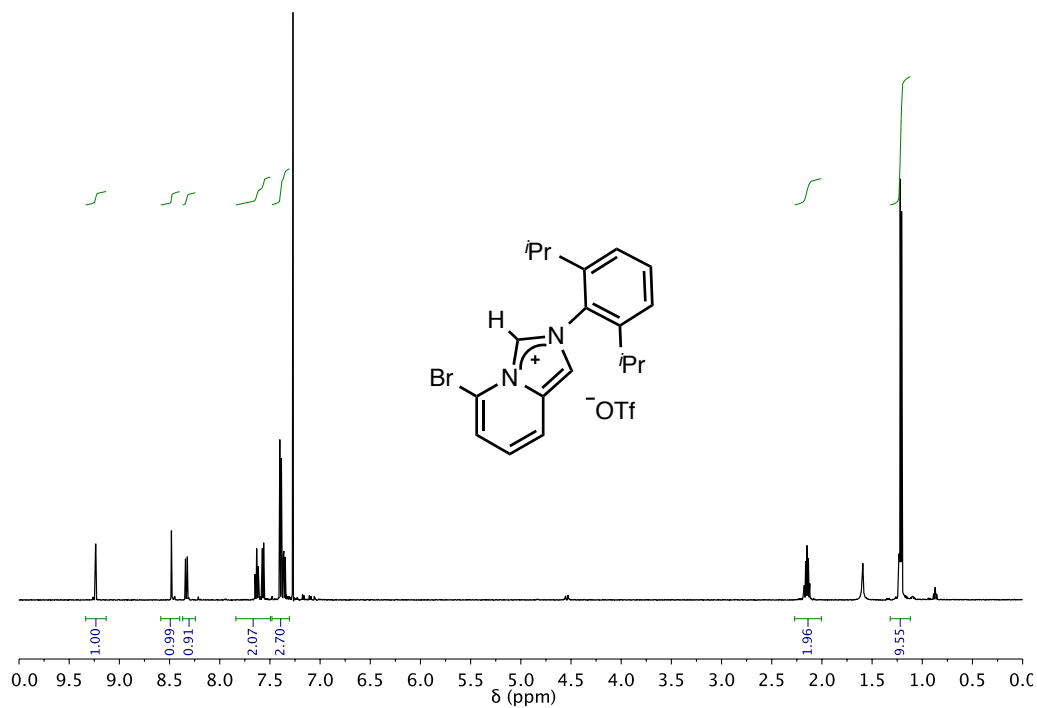


Figure 31. ¹H NMR spectrum of 5-bromo-2-(2',6'-diisopropylphenyl)imidazo[1,5a]pyridinium triflate in CDCl₃ 25 °C.

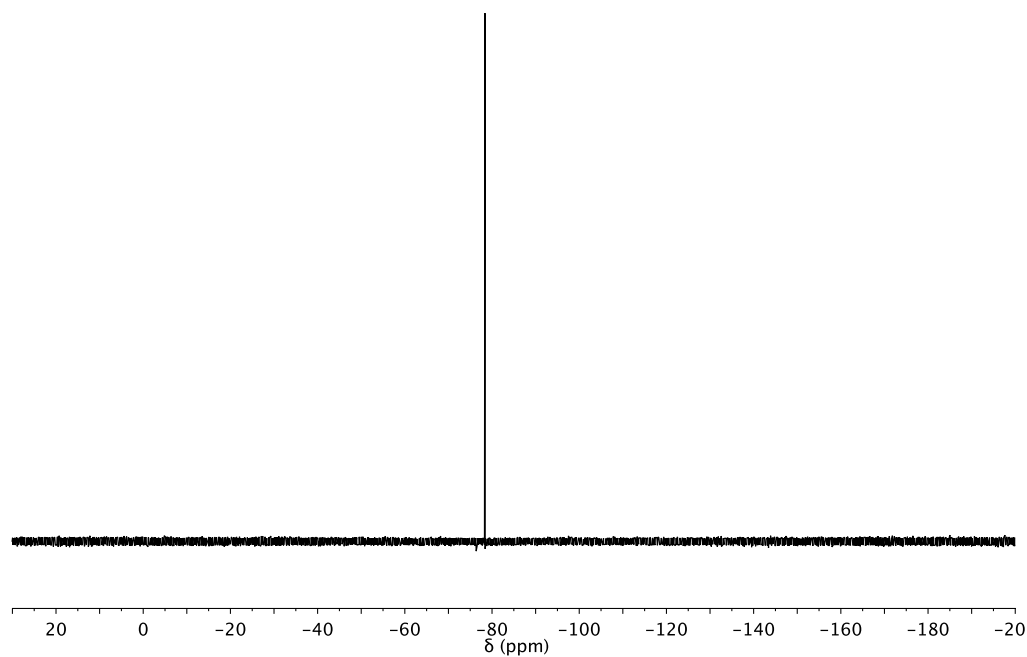


Figure 32. ¹⁹F NMR spectrum of 5-bromo-2-(2',6'-diisopropylphenyl)imidazo[1,5a]pyridinium triflate in CDCl₃ 25 °C.

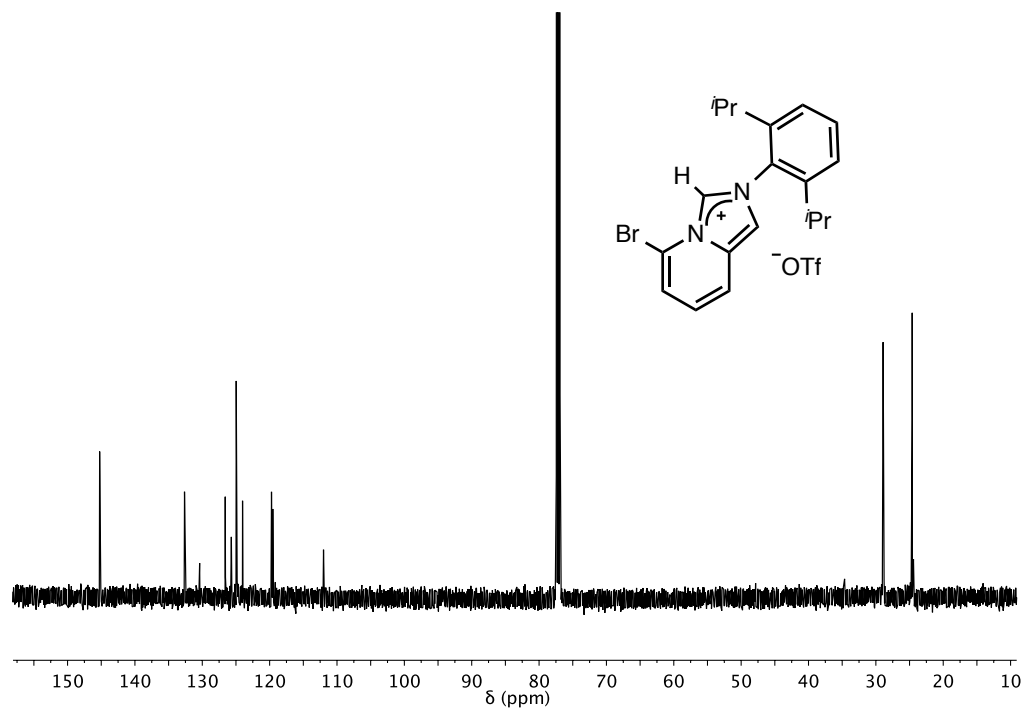


Figure 33. ^{31}C NMR spectrum of 5-bromo-2-(2',6'-diisopropylphenyl)imidazo[1,5a]pyridinium triflate in CDCl_3 25 °C

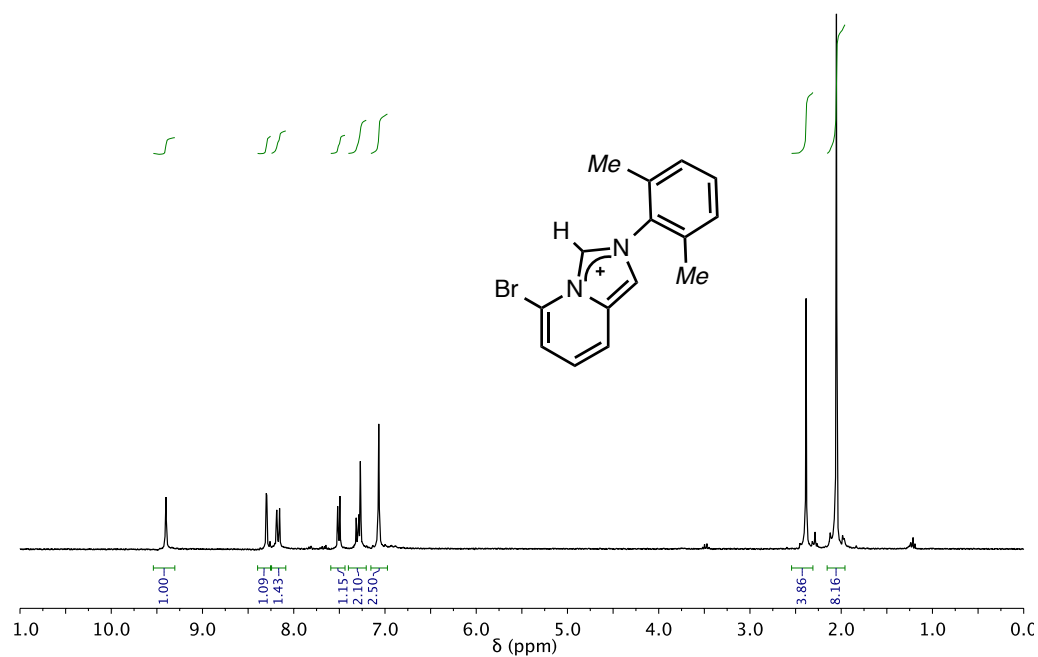


Figure 34. ^1H NMR spectrum of 5-bromo-2-(mesityl)imidazo[1,5a]pyridinium triflate in CDCl_3 at 25 °C.

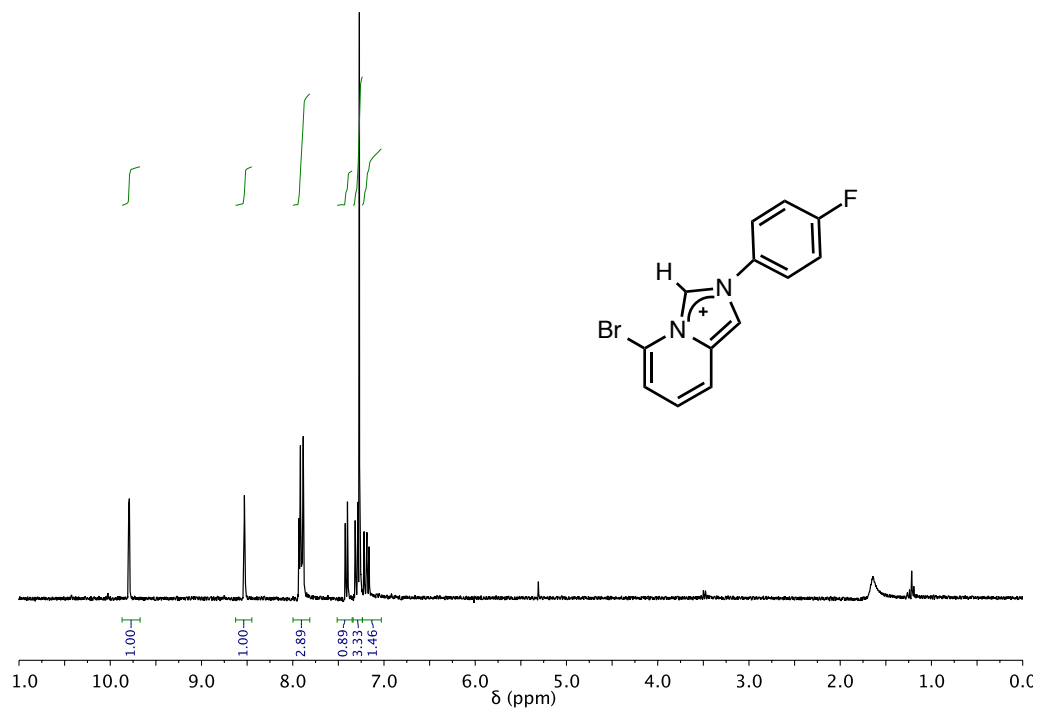


Figure 35. ¹H NMR spectrum of 5-bromo-2-(4'-fluorophenyl)imidazo[1,5a]pyridinium triflate in CDCl₃ at 25 °C.

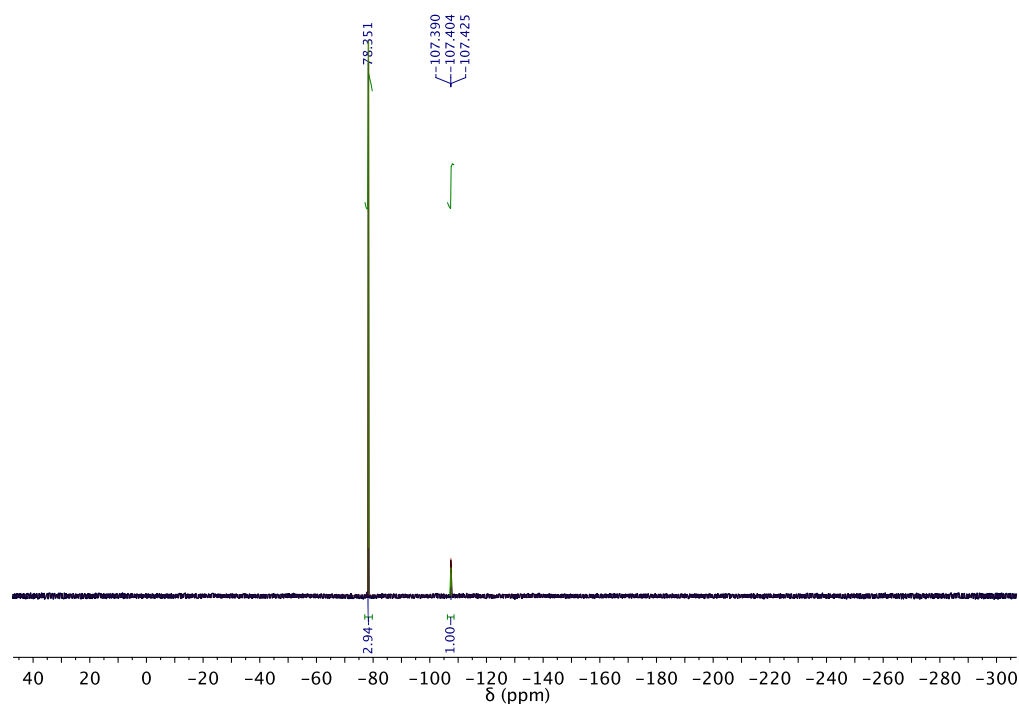


Figure 36. ¹⁹F NMR spectrum of 5-bromo-2-(4'-fluorophenyl)imidazo[1,5a]pyridinium triflate in CDCl₃ at 25 °C.

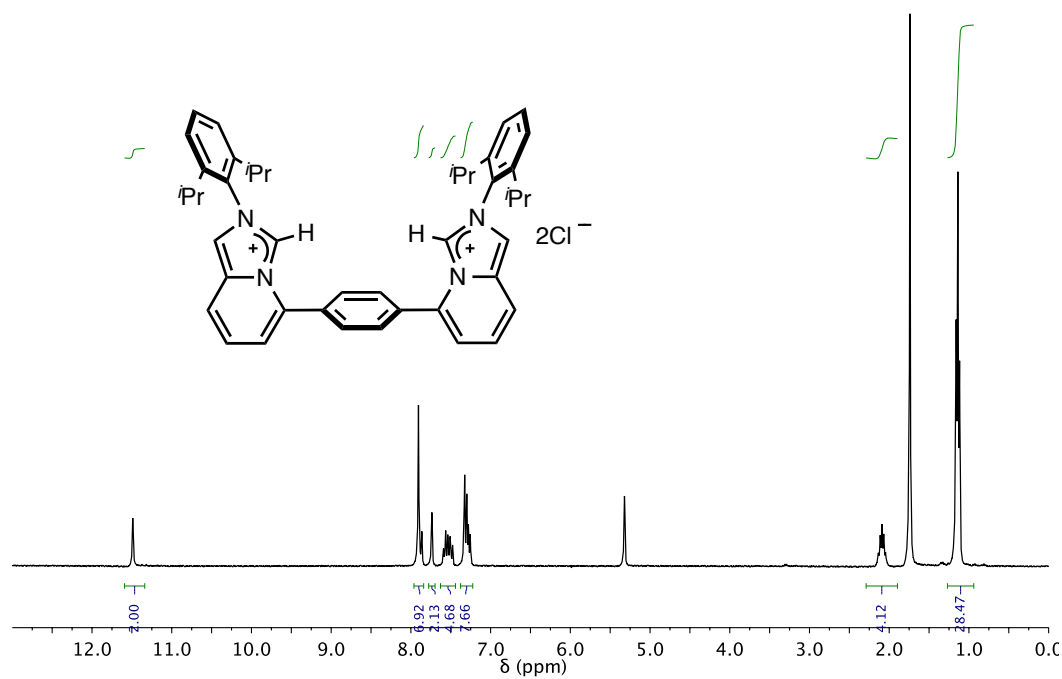


Figure 37. ^1H NMR spectrum of DIPr•2HCl in CD_2Cl_2 at 25 °C.

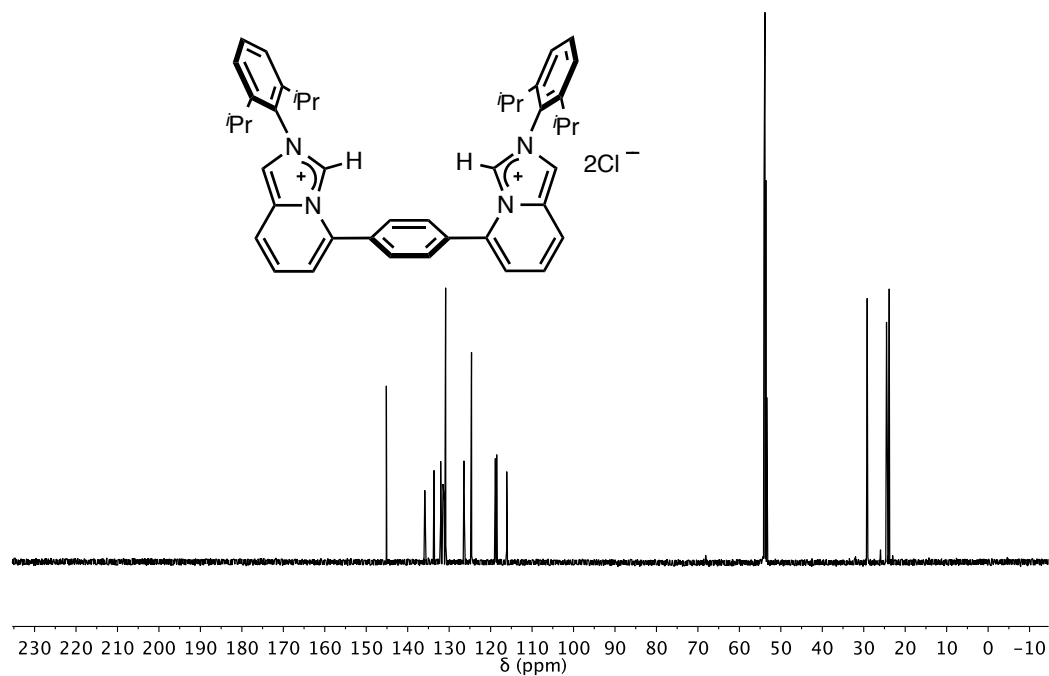


Figure 38. ^{13}C NMR spectrum of DIPr•2HCl in CD_2Cl_2 at 25 °C.

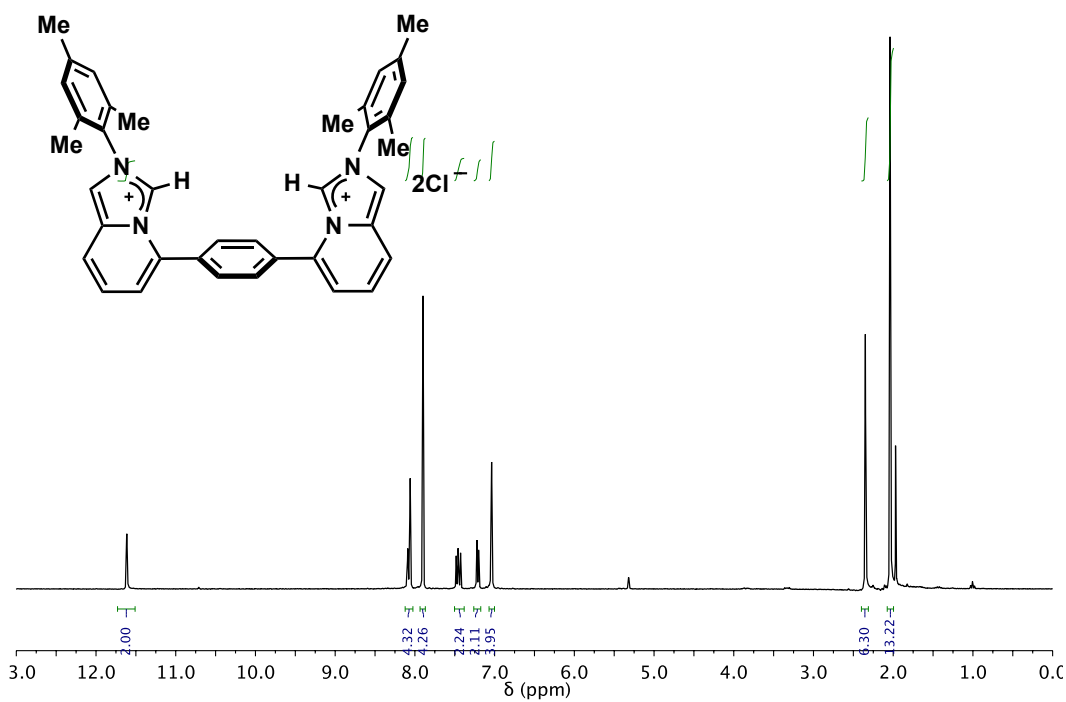


Figure 39. ¹H NMR spectrum of DIMes•2HCl in CD₂Cl₂ at 25 °C.

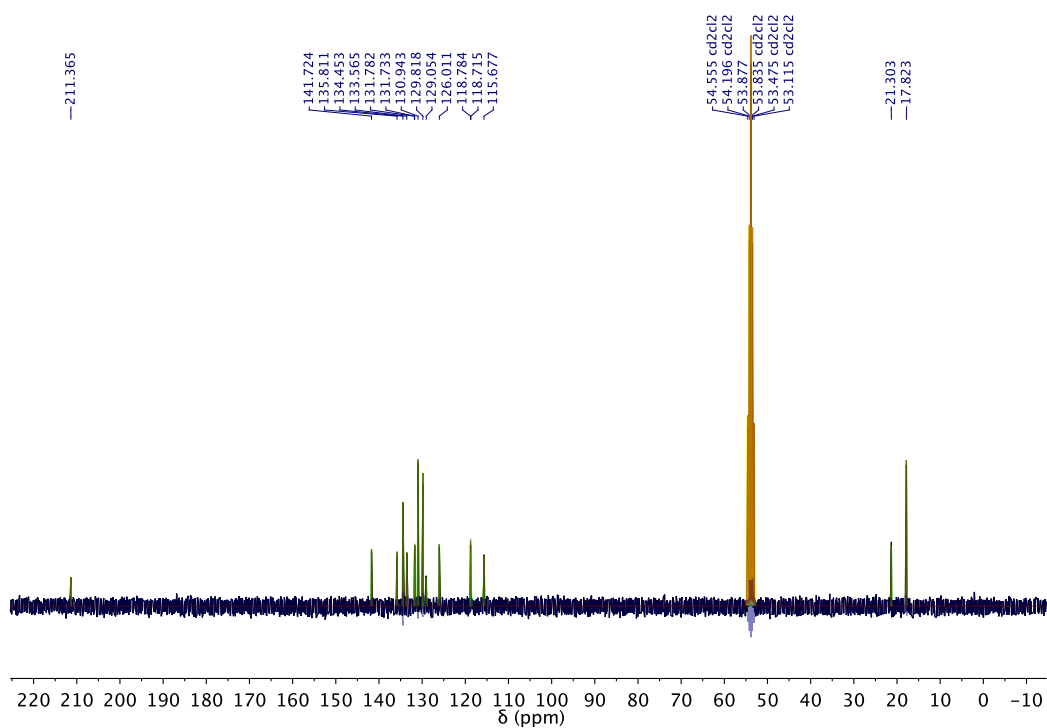


Figure 40. ¹³C NMR spectrum of DIMes•2HCl in CD₂Cl₂ at 25 °C.

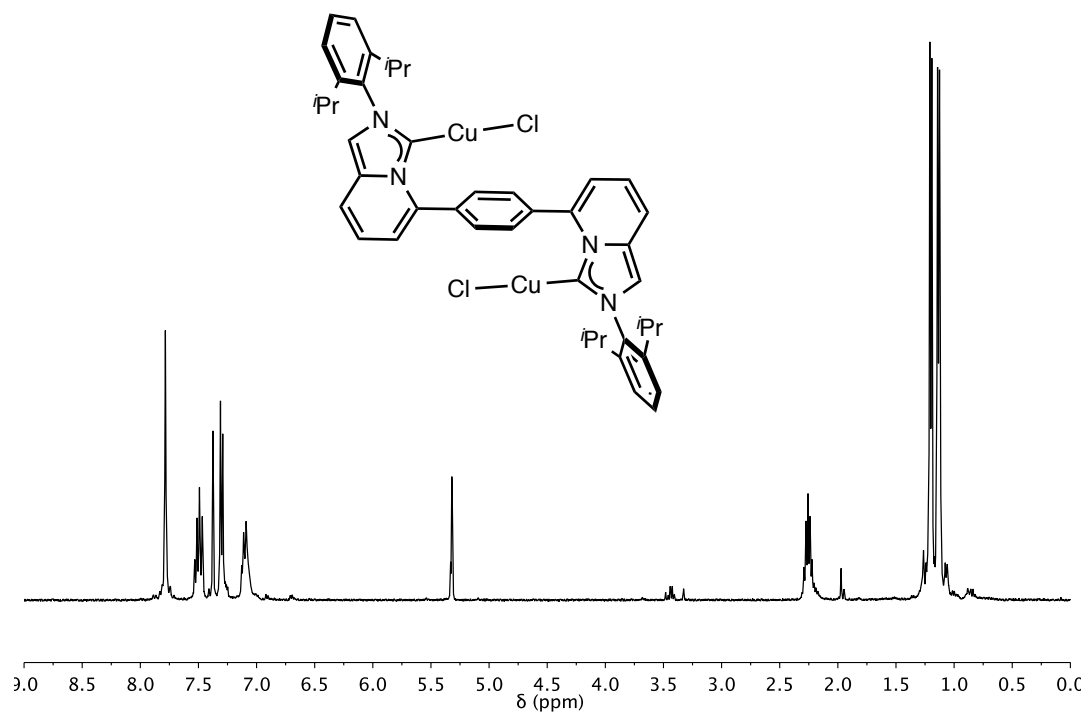


Figure 41. ^1H NMR spectrum of $\text{DIPr}[\text{CuCl}]_2$ (A.2) in CD_2Cl_2 at 25 °C.

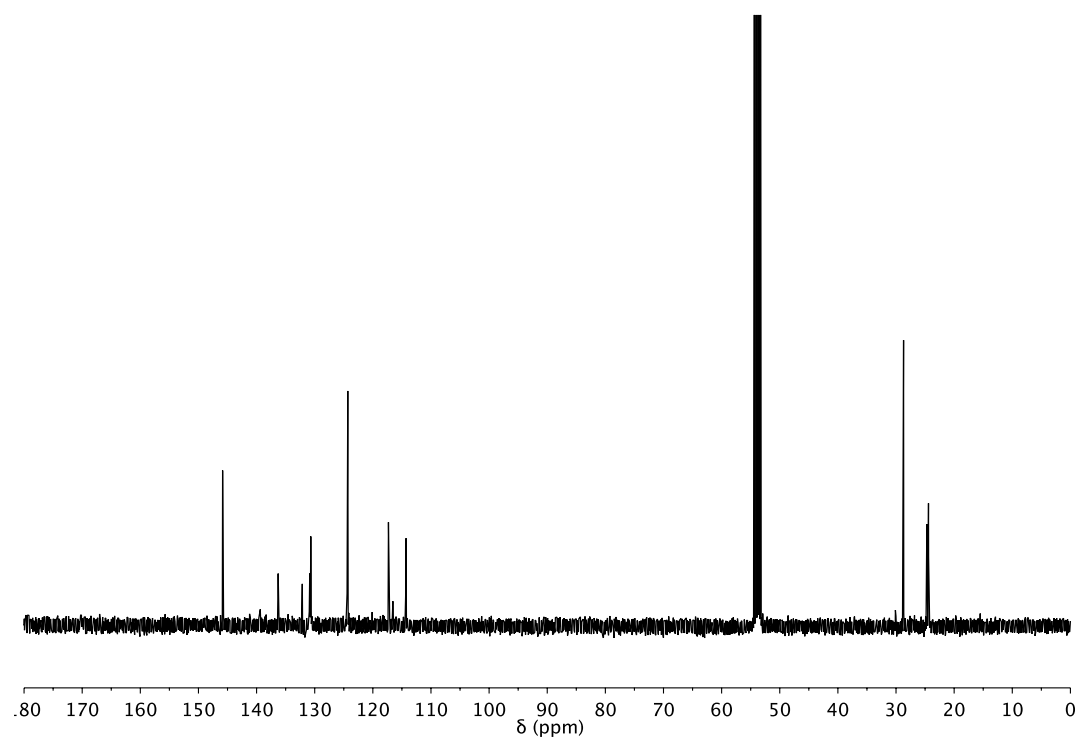


Figure 42. ^{13}C NMR spectrum of $\text{DIPr}[\text{CuCl}]_2$ (A.2) in CD_2Cl_2 at 25 °C.

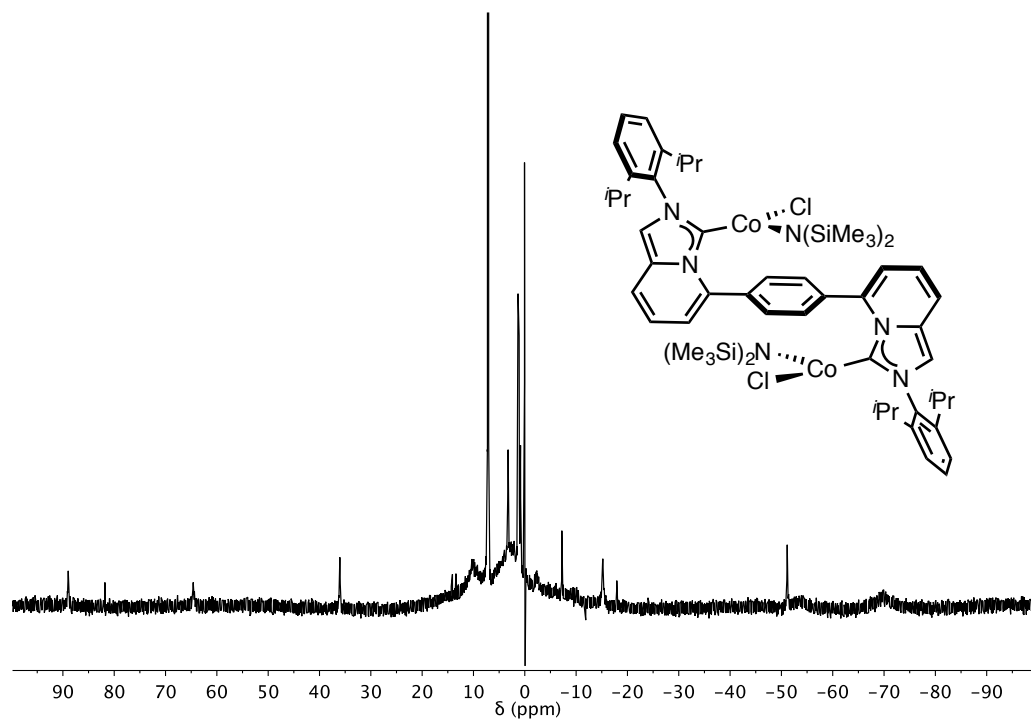


Figure 43. ^1H NMR spectrum of $\text{DIPr}[\text{Co}(\text{Cl})\text{N}(\text{SiMe}_3)_2]_2$ (**A.3**) in C_6D_6 at 25°C .

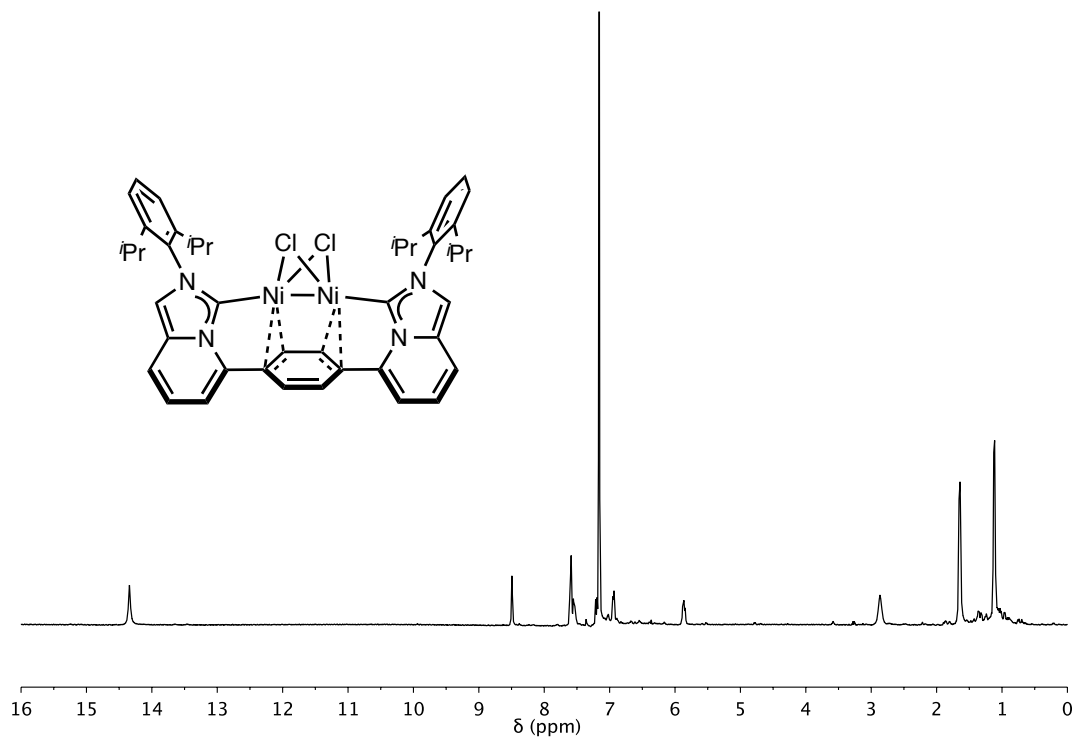


Figure 44. ^1H NMR spectrum of $\text{DIPr}[\text{Ni}(\mu\text{-Cl})_2]_2$ (**A.4**) in C_6D_6 at 25°C .

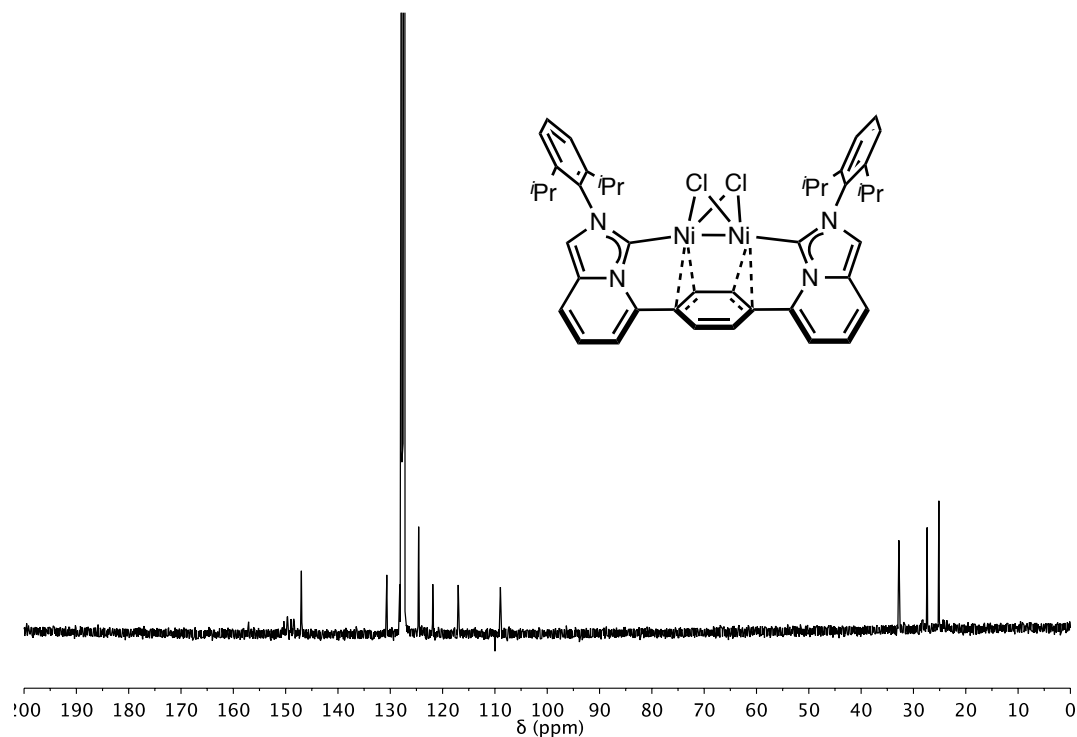


Figure 45. ^{13}C NMR spectrum of $\text{DIPr}[\text{Ni}(\mu\text{-Cl})_2]$ (A.4) in C_6D_6 at 25°C .

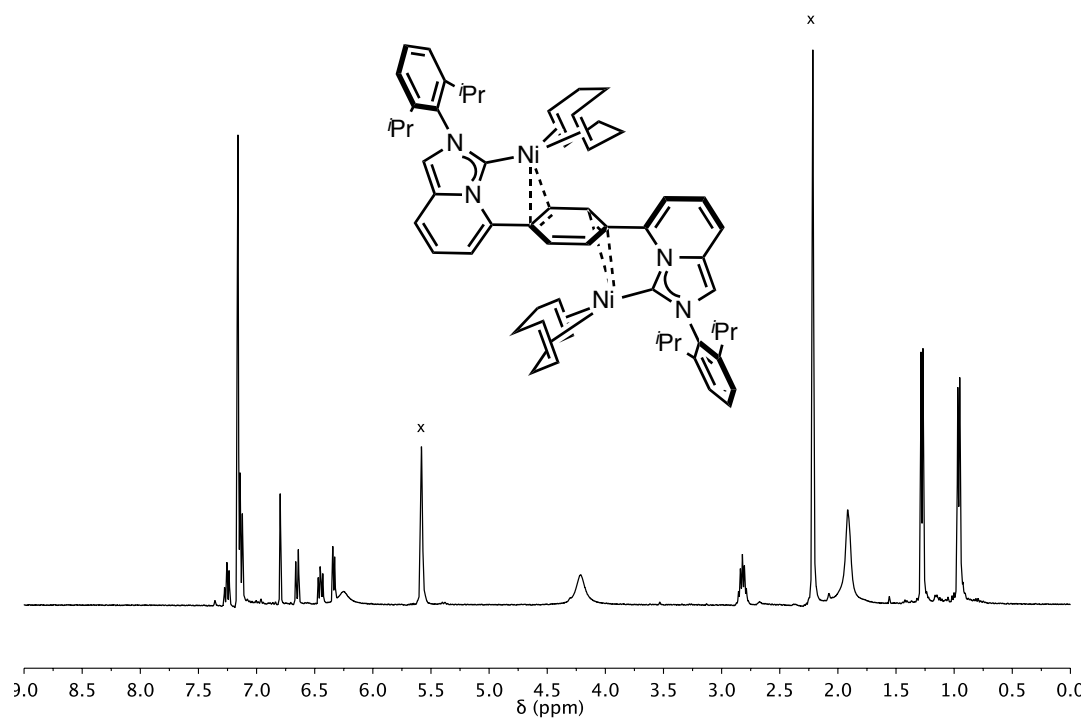


Figure 46. ^1H NMR spectrum of $\text{DIPr}[\text{Ni}(\text{COD})_2]$ (A.5) and COD in C_6D_6 at 25°C . Added 1,5-cyclooctadiene is present (x).

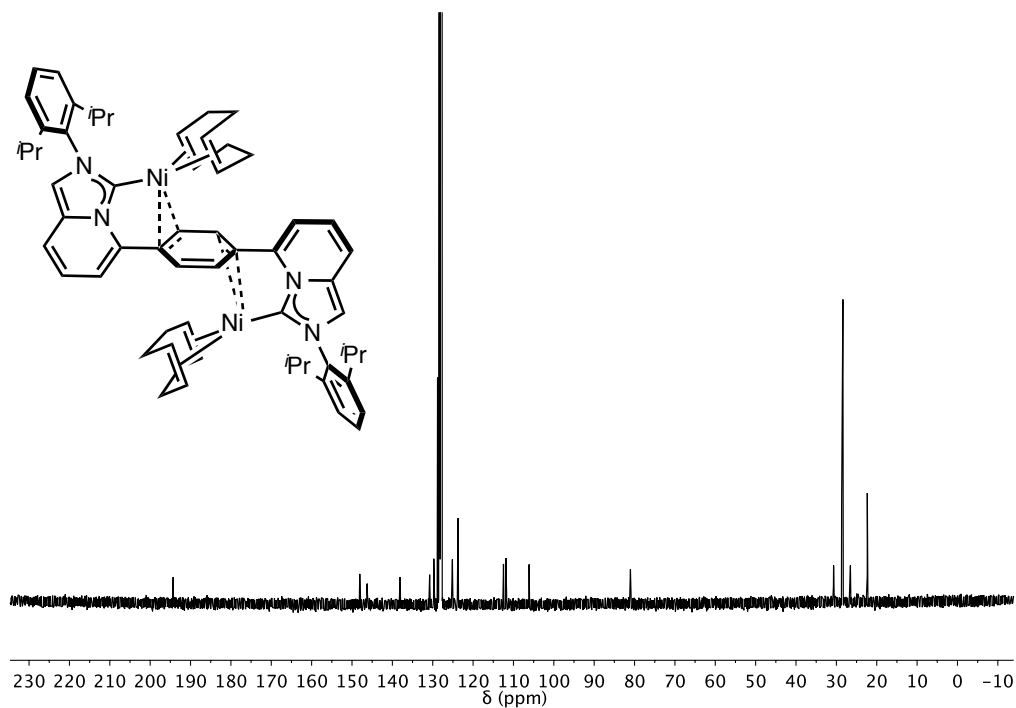


Figure 47. ^{13}C NMR spectrum of $\text{DIPr}[\text{Ni}(\text{COD})]_2$ (**A.5**) and COD in C_6D_6 at 25 °C. Added 1,5-cyclooctadiene is present.

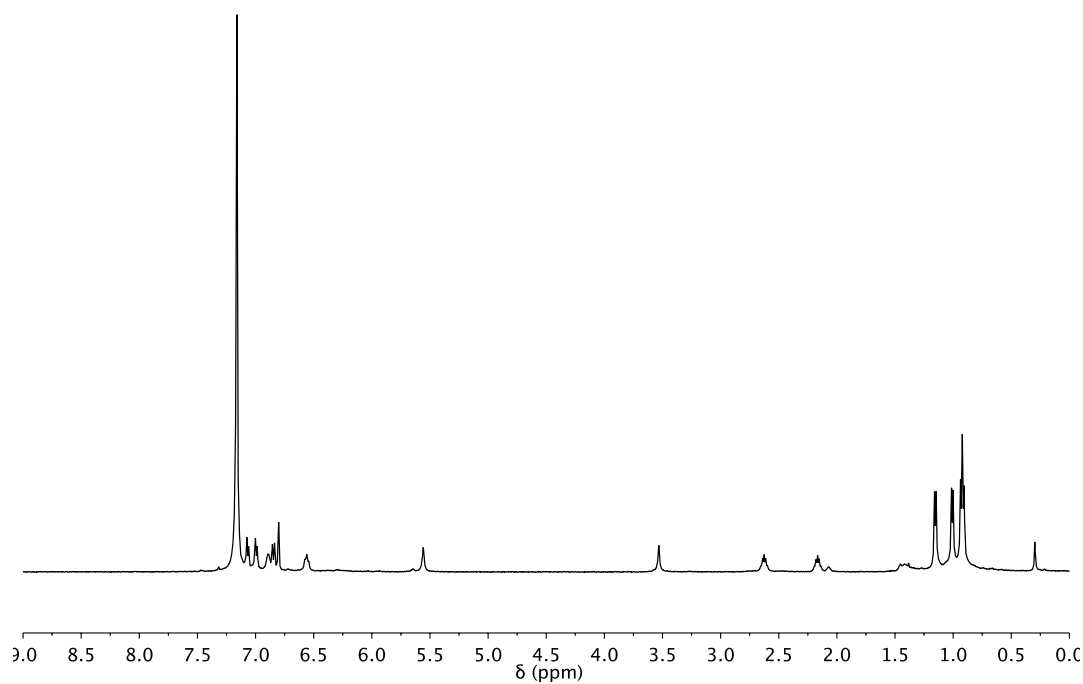


Figure 48. ^1H NMR spectrum of $\text{DIPr}[\text{Ni}(\text{C}_6\text{H}_6)]_2$ (**A.6**) in C_6D_6 at 25 °C.

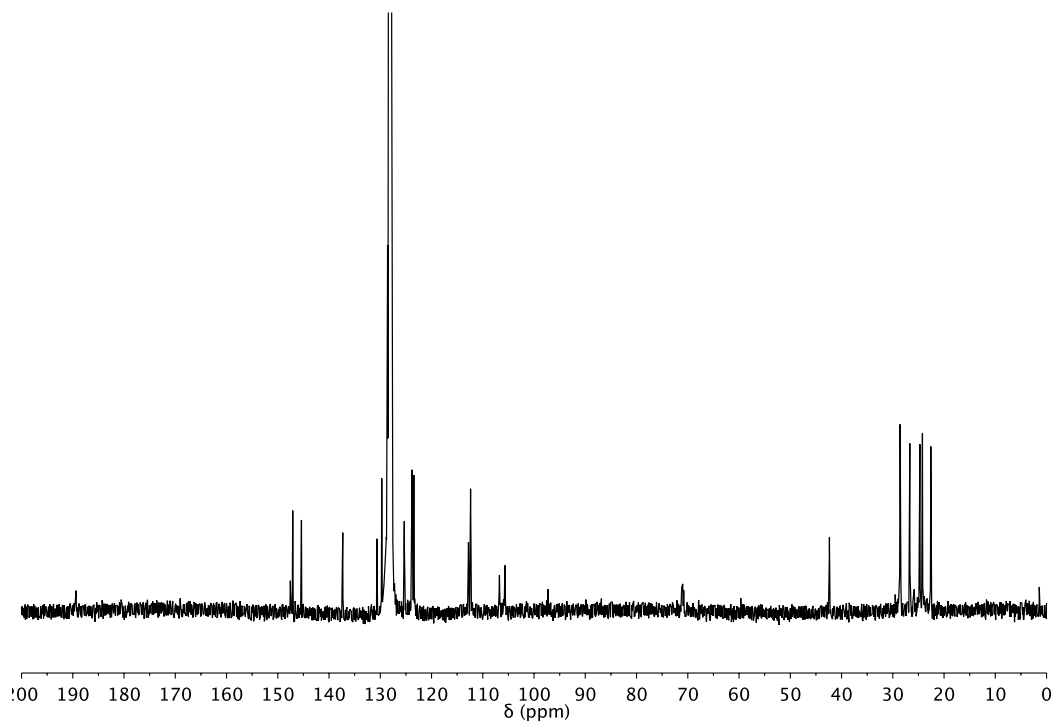


Figure 49. ^{13}C NMR spectrum of $\text{DIPr}[\text{Ni}(\text{C}_6\text{H}_6)]_2$ (**A.6**) in C_6D_6 at 25 °C.

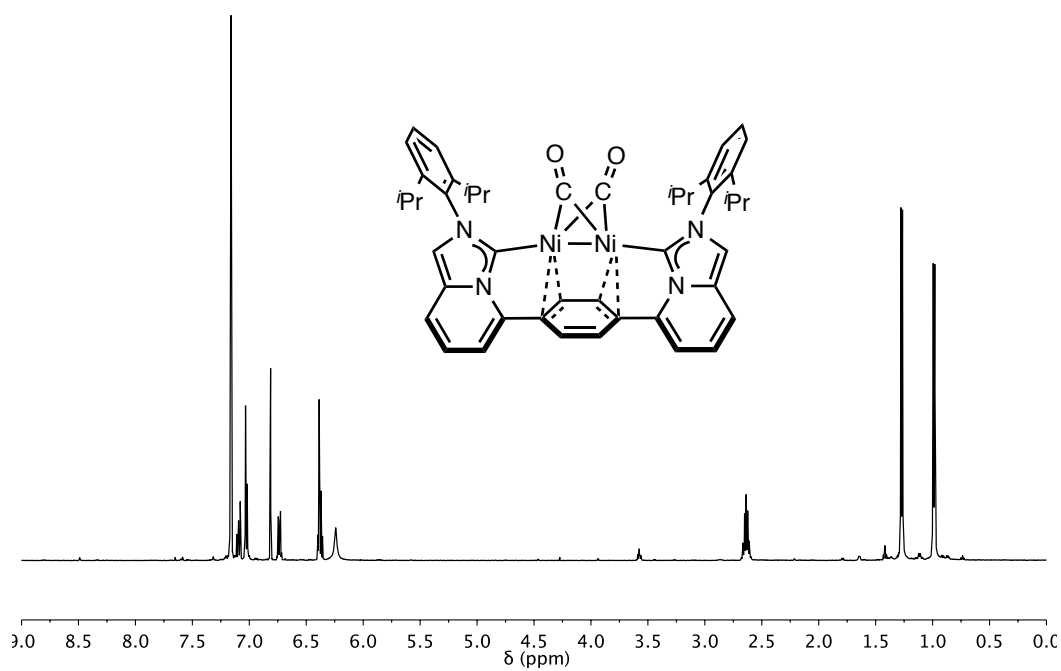


Figure 50. ^1H NMR spectrum of $\text{DIPr}[\text{Ni}(\mu\text{-CO})]_2$ (**A.7**) in C_6D_6 at 25 °C.

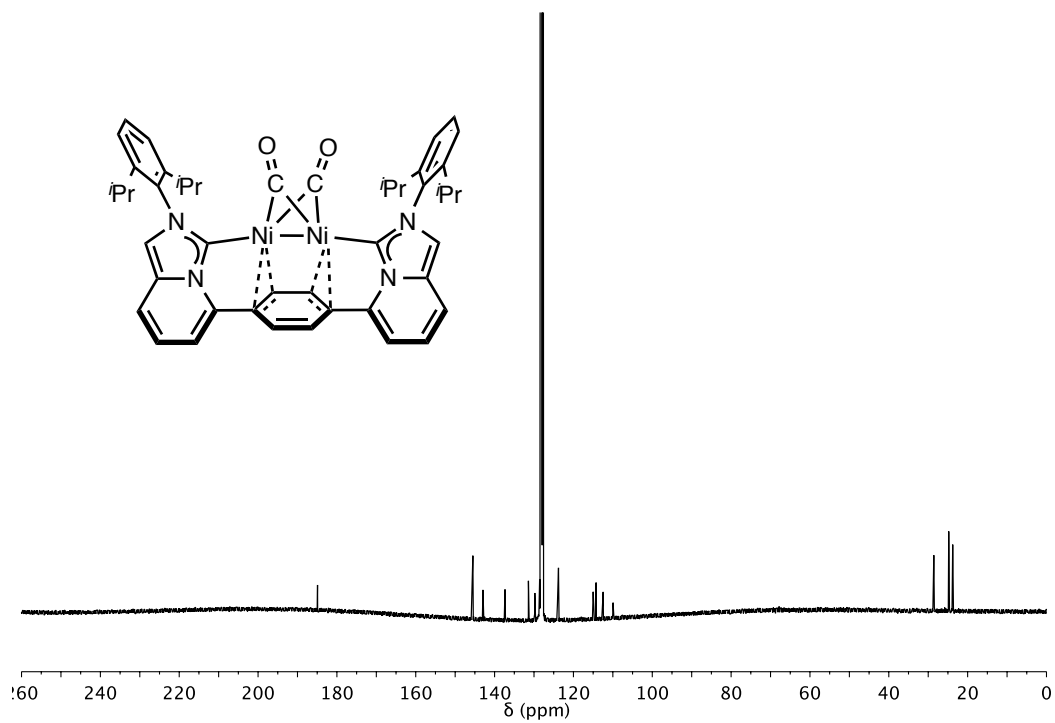


Figure 51. ^{13}C NMR spectrum of $\text{DIPr}[\text{Ni}(\mu\text{-CO})]_2$ (A.7) in C_6D_6 at 25 °C.

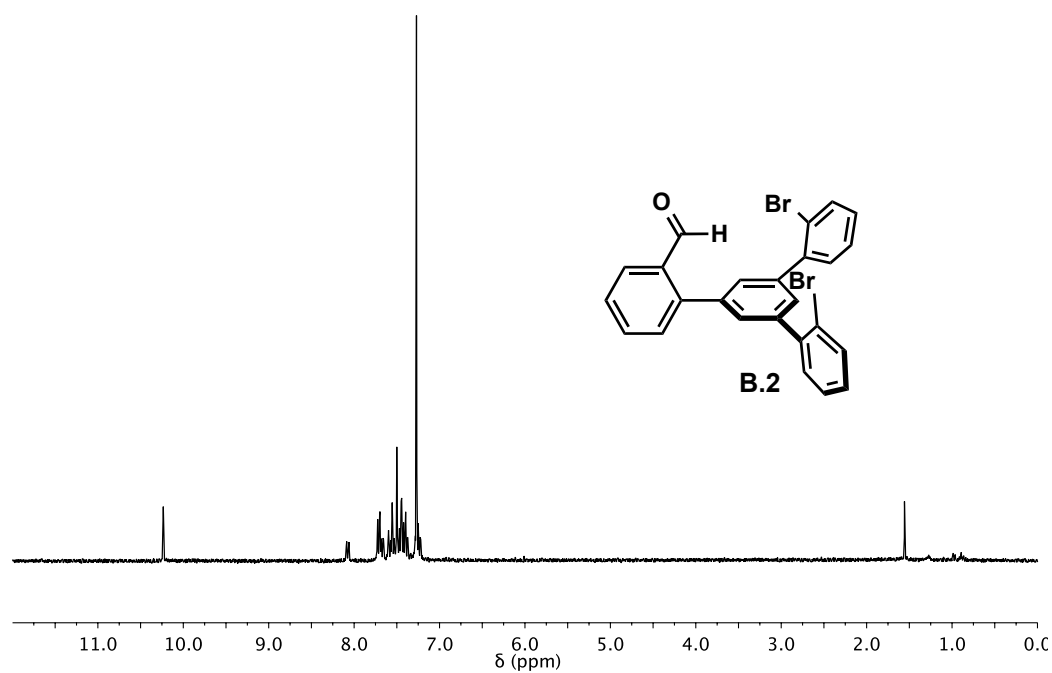


Figure 52. ^1H NMR spectrum of B.2 in CDCl_3 at 25 °C.

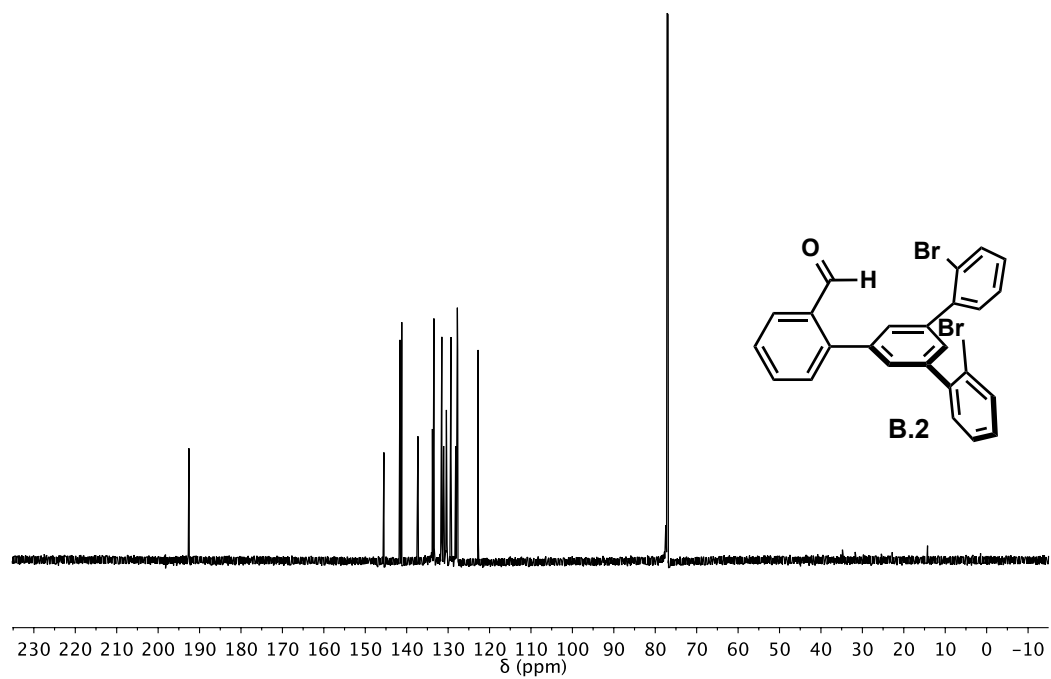


Figure 53. ^{13}C NMR spectrum of **B.2** in CDCl_3 at 25 °C.

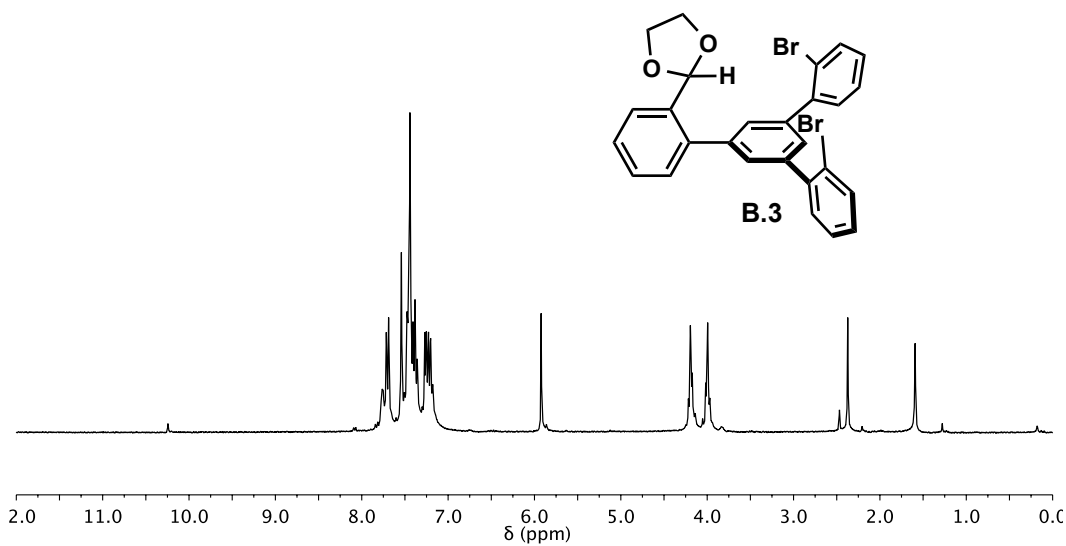


Figure 54. ^1H NMR spectrum of **B.3** in CDCl_3 at 25 °C (approximately 95% pure).

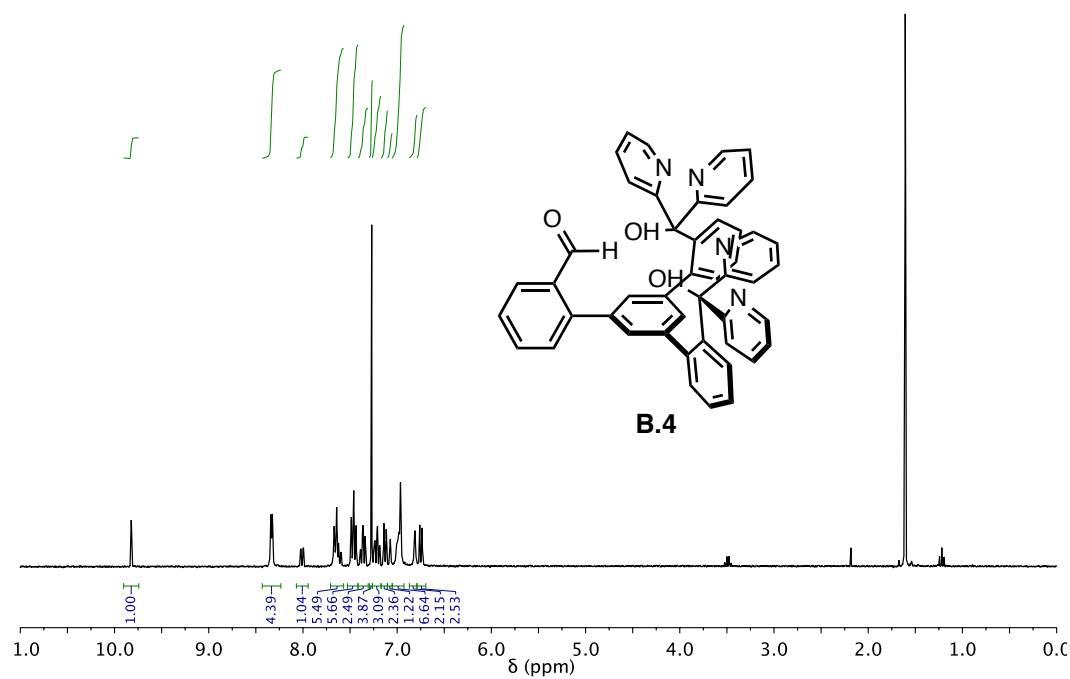


Figure 55. ^1H NMR spectrum of **B.4** in CDCl_3 at room temperature.

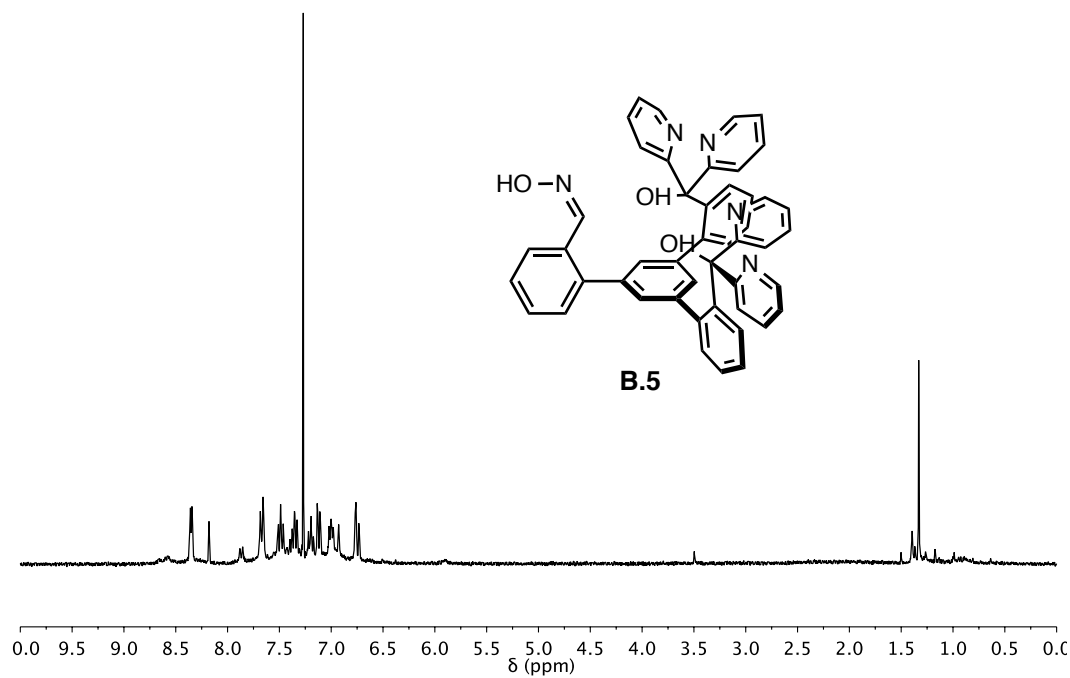


Figure 56. ^1H NMR spectrum of **B.5** in CDCl_3 at room temperature.

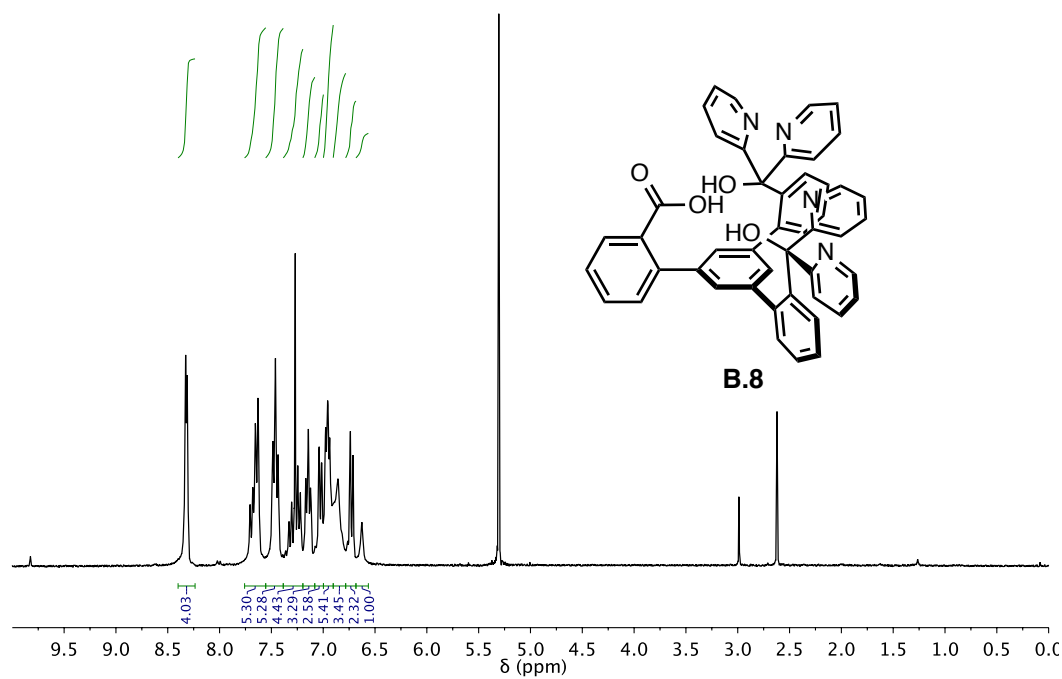


Figure 57. ^1H NMR spectrum of **B.8** in CDCl₃ at room temperature.

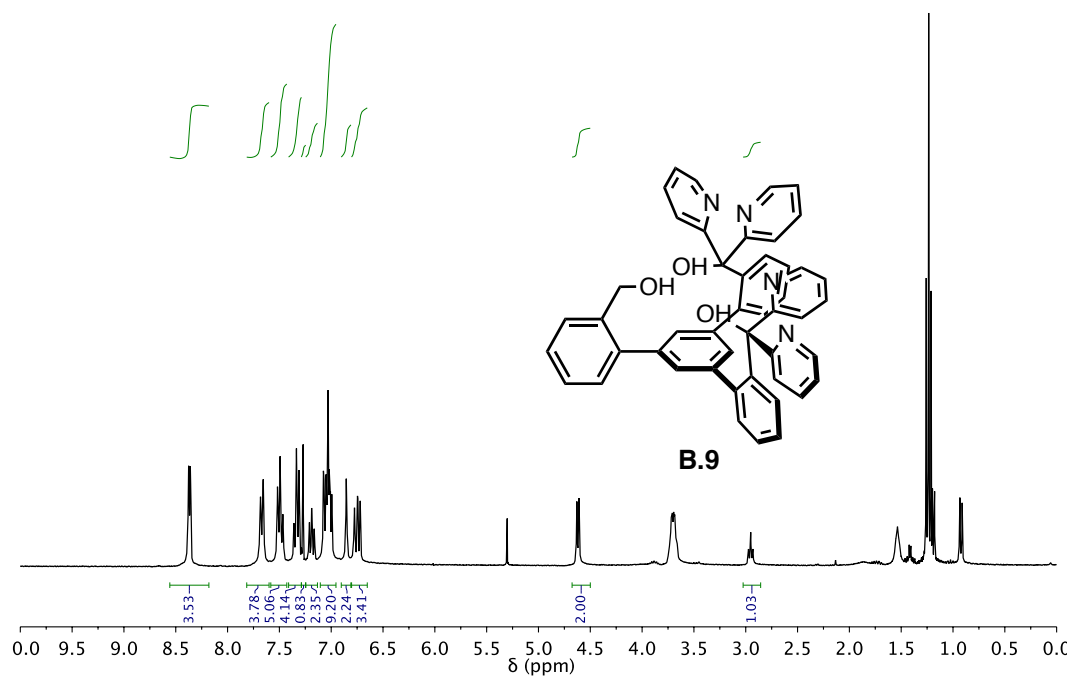


Figure 58. ^1H NMR spectrum of **B.9** in CDCl₃ at room temperature.

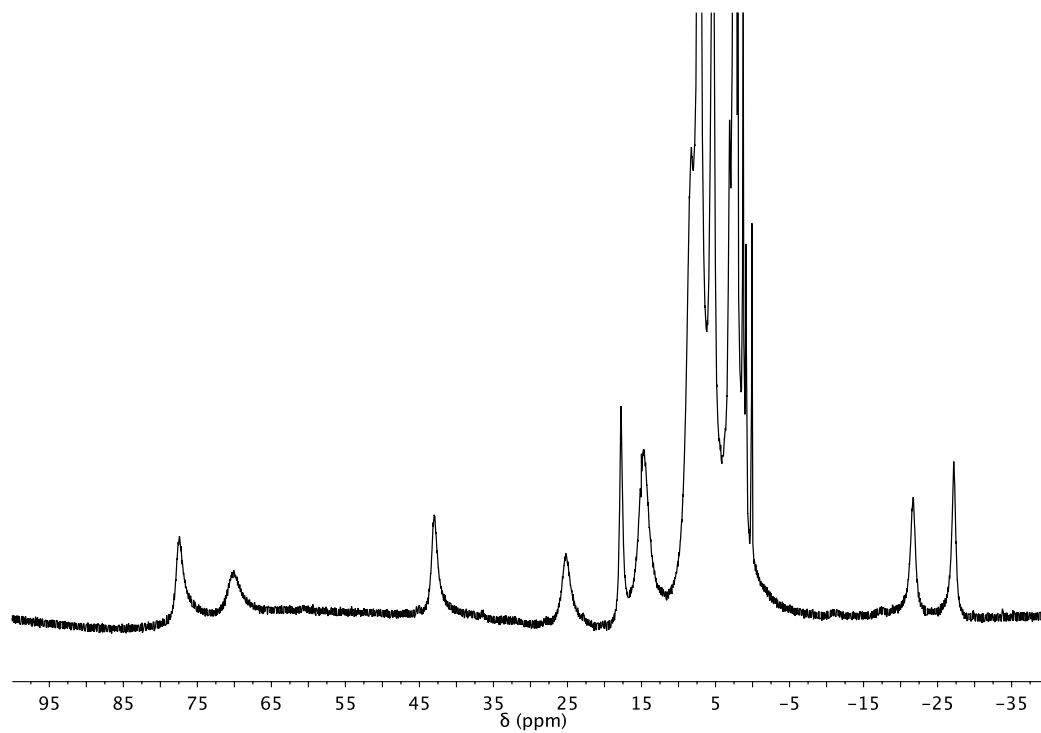


Figure 59. ^1H NMR spectrum of **C.4** in CD_2Cl_2 at room temperature.

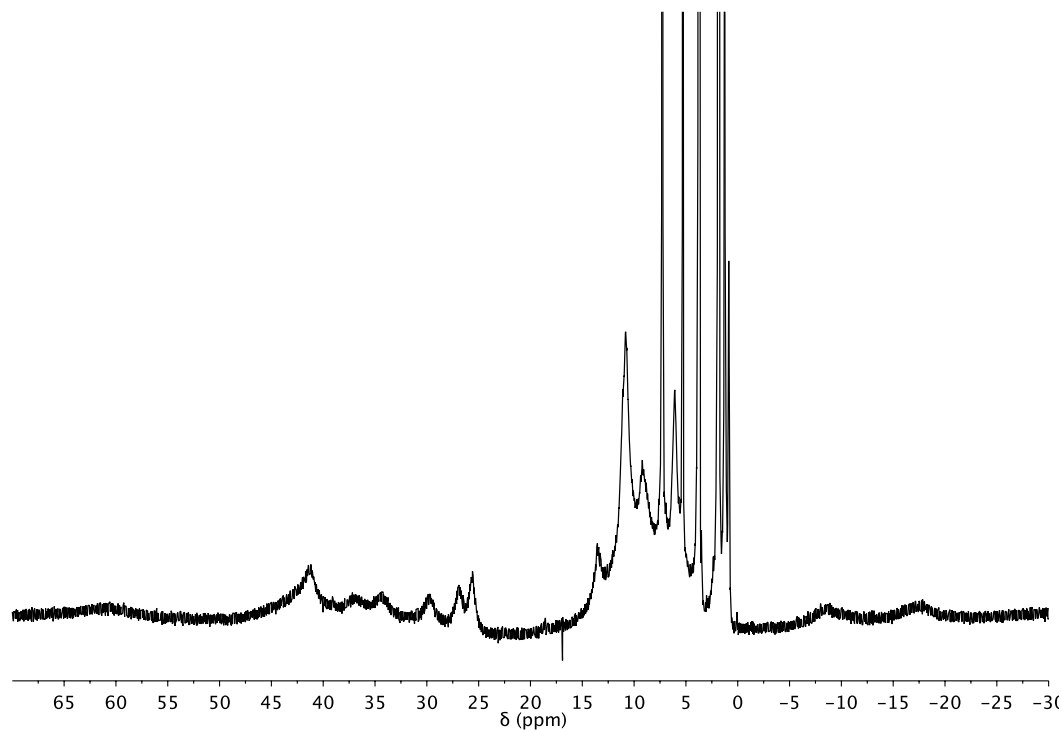


Figure 60. ^1H NMR spectrum of $\text{LCuMn}_2(\text{OAc})_2(\text{OTf})$ (**C.5**) in CDCl_3 at room temperature.

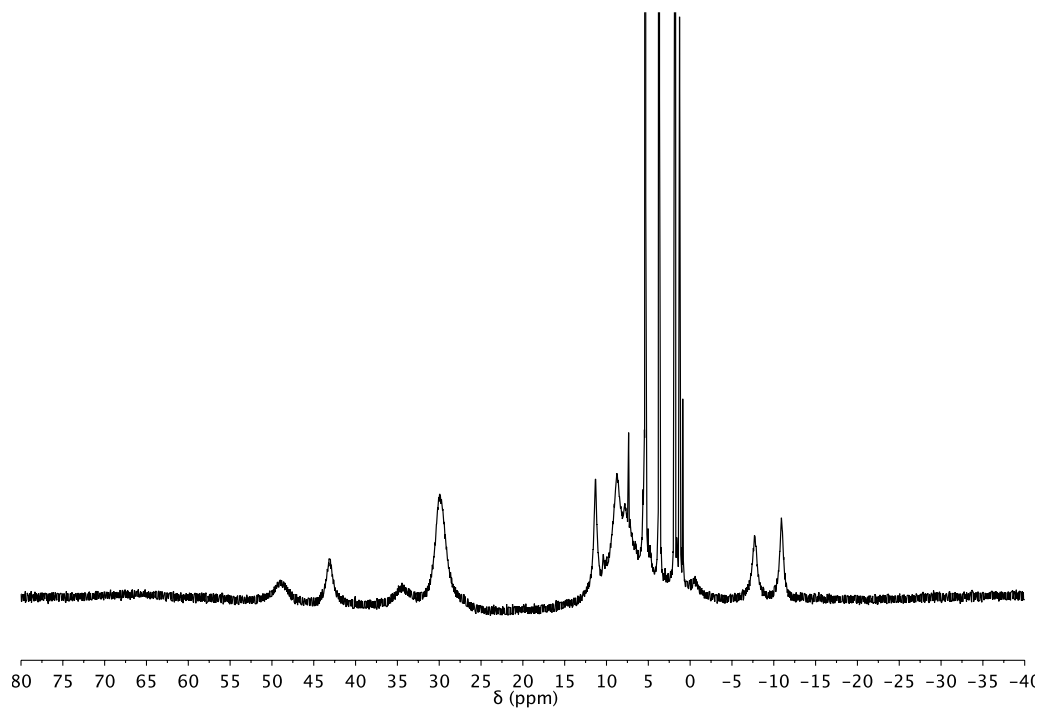


Figure 61. ^1H NMR spectrum of $[\text{LZnMn}_3\text{O}(\text{OAc})_3][\text{OTf}]_n$ (**C.6**) in CD_2Cl_2 at room temperature.

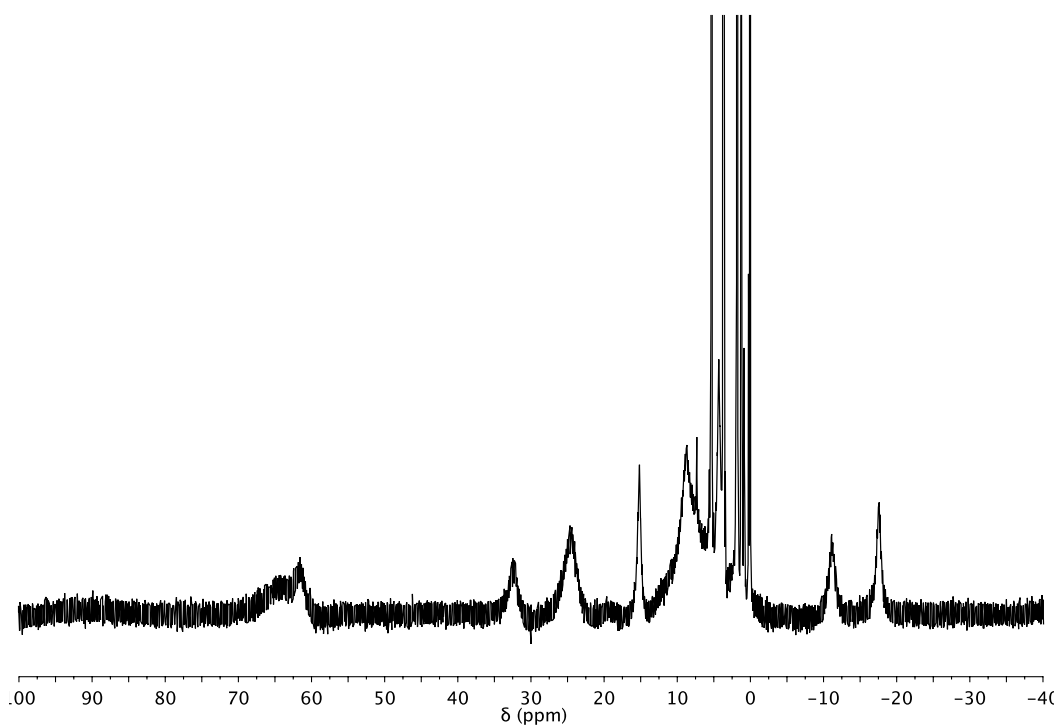


Figure 62. ^1H NMR spectrum of $[\text{LMn}_3\text{LiO}(\text{OAc})_3][\text{OTf}]$ (**C.7**) in CD_2Cl_2 at room temperature.

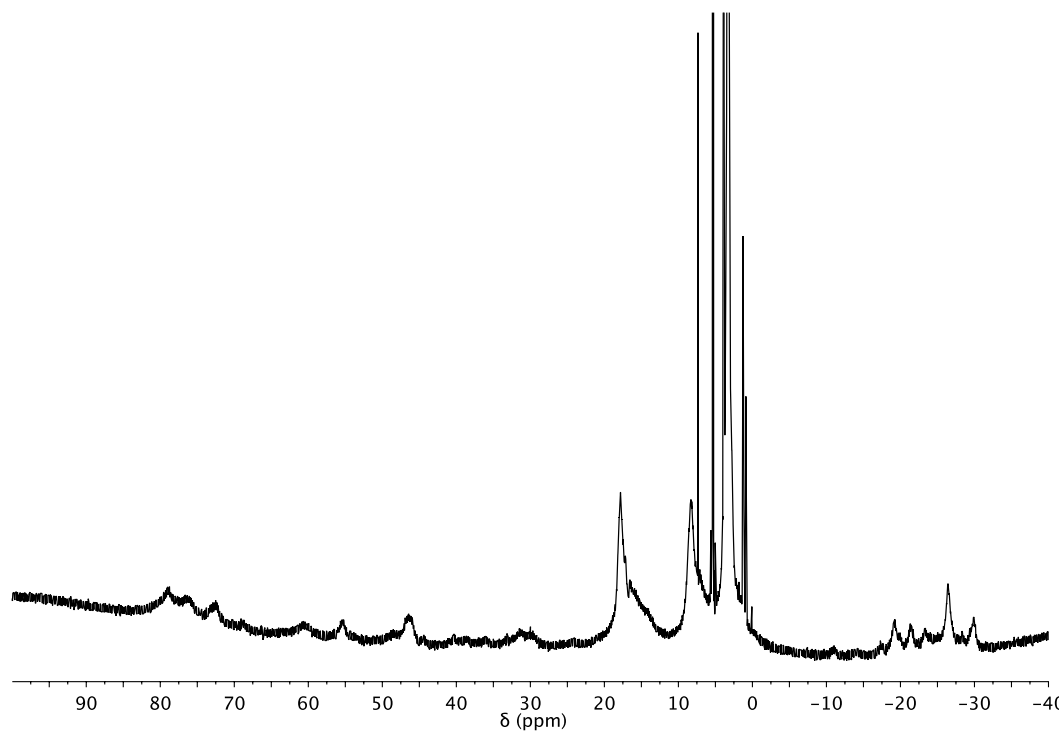


Figure 63. ^1H NMR spectrum of impure **C.8** in CD_2Cl_2 at room temperature.

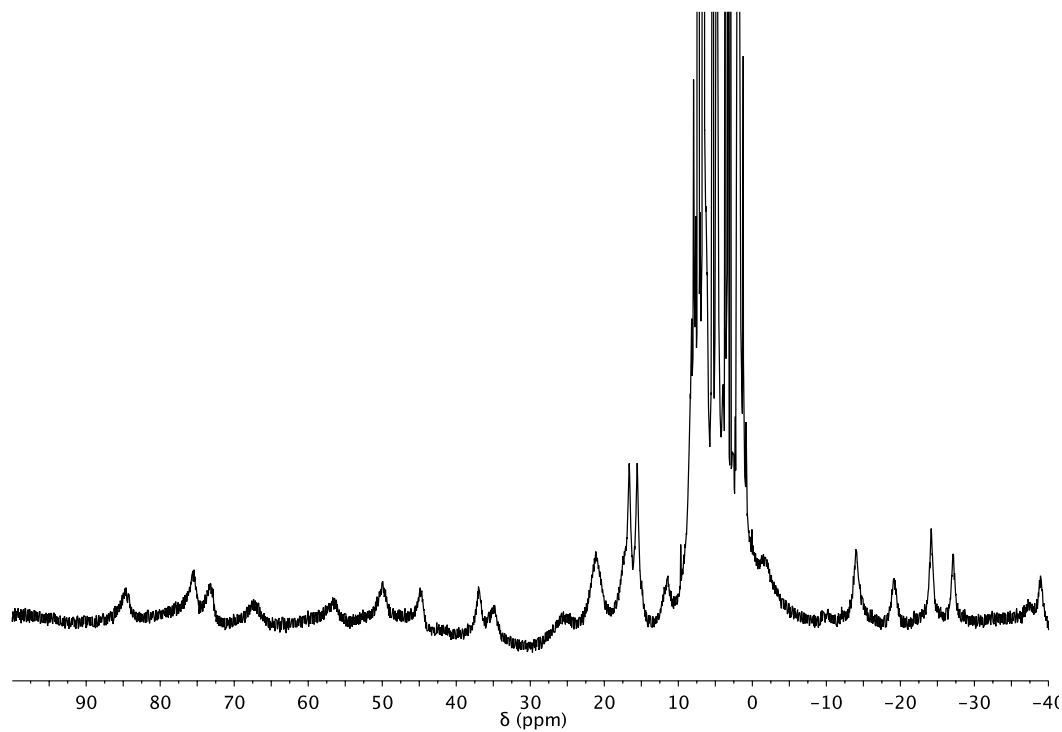


Figure 64. ^1H NMR spectrum of **C.10** in CD_3CN at room temperature.

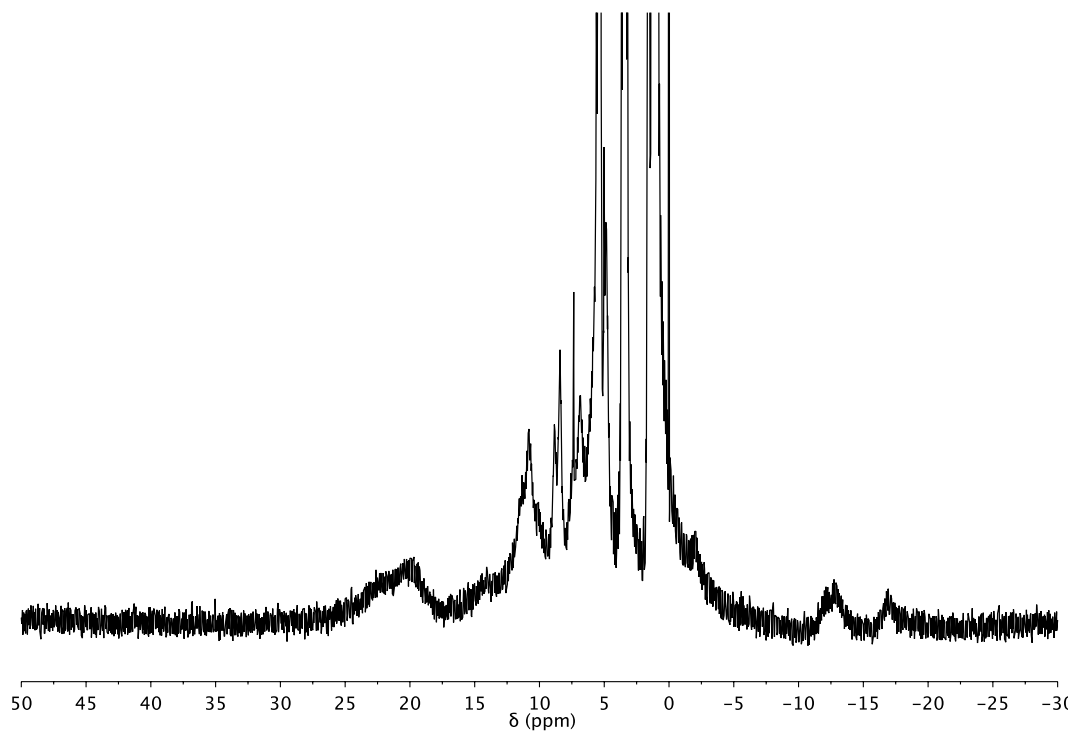


Figure 65. ^1H NMR spectrum of **C.11** in CD_2Cl_2 at room temperature.

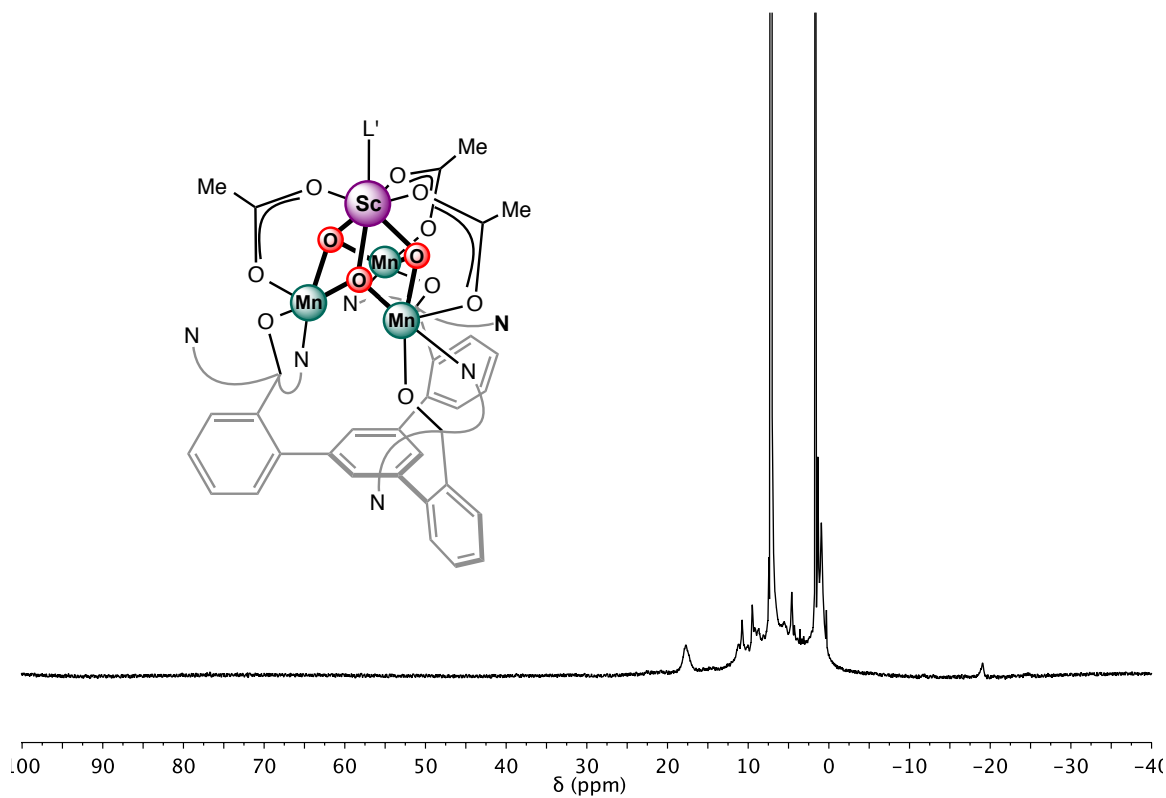


Figure 66. ^1H NMR spectrum of **10-Sc** in C_6D_6 at room temperature.